

**Springer Theses**  
Recognizing Outstanding Ph.D. Research

Holger Kluck

# Production Yield of Muon-Induced Neutrons in Lead

Measured at the Modane  
Underground Laboratory



Springer

# **Springer Theses**

Recognizing Outstanding Ph.D. Research

## **Aims and Scope**

The series “Springer Theses” brings together a selection of the very best Ph.D. theses from around the world and across the physical sciences. Nominated and endorsed by two recognized specialists, each published volume has been selected for its scientific excellence and the high impact of its contents for the pertinent field of research. For greater accessibility to non-specialists, the published versions include an extended introduction, as well as a foreword by the student’s supervisor explaining the special relevance of the work for the field. As a whole, the series will provide a valuable resource both for newcomers to the research fields described, and for other scientists seeking detailed background information on special questions. Finally, it provides an accredited documentation of the valuable contributions made by today’s younger generation of scientists.

## **Theses are accepted into the series by invited nomination only and must fulfill all of the following criteria**

- They must be written in good English.
- The topic should fall within the confines of Chemistry, Physics, Earth Sciences, Engineering and related interdisciplinary fields such as Materials, Nanoscience, Chemical Engineering, Complex Systems and Biophysics.
- The work reported in the thesis must represent a significant scientific advance.
- If the thesis includes previously published material, permission to reproduce this must be gained from the respective copyright holder.
- They must have been examined and passed during the 12 months prior to nomination.
- Each thesis should include a foreword by the supervisor outlining the significance of its content.
- The theses should have a clearly defined structure including an introduction accessible to scientists not expert in that particular field.

More information about this series at <http://www.springer.com/series/8790>

Holger Kluck

# Production Yield of Muon-Induced Neutrons in Lead

Measured at the Modane Underground  
Laboratory

Doctoral Thesis accepted by  
Karlsruhe Institute of Technology,  
Karlsruhe, Germany



Springer

<i>Author</i>	<i>Supervisor</i>
Dr. Holger Kluck Institute of Atomic and Subatomic Physics Vienna University of Technology Vienna Austria	Prof. Johannes Blümer Institute for Nuclear Physics Karlsruhe Institute of Technology Karlsruhe Germany

ISSN 2190-5053

Springer Theses

ISBN 978-3-319-18526-2

DOI 10.1007/978-3-319-18527-9

ISSN 2190-5061 (electronic)

ISBN 978-3-319-18527-9 (eBook)

Library of Congress Control Number: 2015942785

Springer Cham Heidelberg New York Dordrecht London

© Springer International Publishing Switzerland 2015

This work is subject to copyright. All rights are reserved by the Publisher, whether the whole or part of the material is concerned, specifically the rights of translation, reprinting, reuse of illustrations, recitation, broadcasting, reproduction on microfilms or in any other physical way, and transmission or information storage and retrieval, electronic adaptation, computer software, or by similar or dissimilar methodology now known or hereafter developed.

The use of general descriptive names, registered names, trademarks, service marks, etc. in this publication does not imply, even in the absence of a specific statement, that such names are exempt from the relevant protective laws and regulations and therefore free for general use.

The publisher, the authors and the editors are safe to assume that the advice and information in this book are believed to be true and accurate at the date of publication. Neither the publisher nor the authors or the editors give a warranty, express or implied, with respect to the material contained herein or for any errors or omissions that may have been made.

Printed on acid-free paper

Springer International Publishing AG Switzerland is part of Springer Science+Business Media  
([www.springer.com](http://www.springer.com))

*Seht ihr den Mond dort stehen?  
Er ist nur halb zu sehen,  
Und ist doch rund und schön!  
So sind wohl manche Sachen,  
Die wir getrost belachen,  
Weil unsre Augen sie nicht sehn.*

—Matthias Claudius

# Supervisor's Foreword

The Swiss physicist and astronomer Fritz Zwicky noted in 1933 that the Coma cluster of galaxies had a spread of individual velocities that was “too large”: the mass of the cluster itself—deduced from the visible objects—was too small to keep the galaxies bound together. Turning the argument around using the virial theorem he found that the Coma Cluster must contain a large amount of matter not accounted for by the light of the stars. He called it “Dark Matter”.

Since then astronomers, cosmologists and physicists have found more evidence for the existence of Dark Matter. Galaxies rotate faster than Newtonian gravitation would suggest. Precision measurements of the cosmic microwave background radiation can only be explained by a certain mixture of ordinary matter, Dark Matter and an even more mysterious substance called “Dark Energy”. Dark Matter is electrically neutral and interacts very weakly with ordinary matter. A nice example is the so called “bullet” cluster (1E 0657–558, Fig. 2.4 of this book). Here, galaxy clusters have penetrated each other. A superposition of optical, radio and x-ray images shows that gas clouds are interacting violently and are left behind their clusters while most of the mass is at the center of the galaxy clusters, measured by the gravitational lensing effect.

What is Dark Matter? We don't know, but serious speculations say that new kinds of particles should exist, so-called supersymmetric particles that relate to the known zoo of subatomic particles. A generic name is WIMP for Weakly Interacting Massive Particle. If that model is correct, then also our own galaxy should be filled with a cloud of WIMPs and the Sun and the Earth are moving through. WIMPs would gather almost everywhere, preferentially bound in gravitational fields. They would move rather slowly due to their large mass, ranging from a few to thousands of proton masses.

How can we find WIMPs? There are essentially three ways. First, WIMPs may scatter off ordinary atomic nuclei, but very rarely so. If the recoiling nucleus is part of a very sensitive detector material, a tiny energy release might be detected. Second, WIMPs could annihilate with each other somewhere in the Universe, leading to a characteristic radiation, which in turn can be observed by astronomers.

Finally, WIMPs might be produced at accelerators like the Large Hadron Collider LHC at CERN, Geneva. They would leave the detectors without a trace, but the energy-momentum balance of the other, well-measured particles would indicate their creation and escape. My student Holger Kluck was part of a team—the EDELWEISS collaboration—that pursues the first kind of WIMP search.

The difficulties in the three kinds of WIMP searches are different. For the third method, LHC detectors must work very well to account for so-called missing mass. For the so-called indirect searches astronomers must be sure that no ordinary radiation source is mistaken for WIMP annihilation. For the direct search with sensitive detectors, the expected scattering in any target material is very rare indeed. Radioactivity and other particles may mimic a WIMP signal, e.g. from cosmic rays that impinge all the time on Earth. Therefore, the EDELWEISS detector is well shielded in the Modane Underground Laboratory in the French Alps, located in the middle of the Frejus tunnel between France and Italy. A particularly nasty kind of background signal arises from neutrons, which may be produced by cosmic rays in the surrounding material close to the detector. They may wander around unseen by veto detectors, hit a detector nucleus and release a tiny amount of energy just as a WIMP would. Holger's task was to perform a detailed study of this background.

In this thesis Holger Kluck presents a unique summary of the research on WIMPs emphasizing on the origin and the suppression of this neutron background which could compromise the WIMP search. He describes the physical processes in great detail and offers a comprehensive account of all measurements to date. That wouldn't have been possible without a dedicated interpretation of data and—importantly—of very detailed simulations. Holger's own measurements using a neutron detector developed at the Karlsruhe Institute of Technology (KIT), his model and his extensions of the GEANT4 software package are finally consistent with each other and in accordance with newer results from other groups.

Holger's thesis in this form has become a handbook of cosmic-induced neutrons that is relevant for understanding and suppressing neutron reactions. The community of WIMP searchers is grateful for his effort, and so am I that Springer has agreed to make this research easily accessible.

Karlsruhe Institute of Technology  
January 2015

Prof. Johannes Blümer

# Abstract

Muon-induced neutrons are an important background source for rare event searches such as Dark Matter searches looking for nuclear recoils induced by the elastic scattering of galactic WIMPs off nuclei. Due to a shielding of 4800 mwe against muons at the *Laboratoire Souterrain de Modane* (LSM), the rate of muon-induced neutrons in EDELWEISS is too low, to be studied in situ with satisfying statistical accuracy. One thus relies on Monte Carlo (MC) modelling of the relevant processes, using e.g. the package Geant4. However, the reliability of MC simulations is debatable, as the published differences between simulation and measurement is often larger than a factor two.

The lack of reliable data on the neutron production yield in lead at LSM and the dubious accuracy of the MC simulations motivated this work and lead to the following results:

A high statistics reference data set of muon-induced neutrons at LSM was collected by running a dedicated neutron counter consisting of a lead target below a neutron multiplicity meter based on 1000 l liquid scintillator loaded with gadolinium. Within a live-time of 964.5 d from 2009 to 2012, a sample of 5583 tagged muons were measured in coincidence with 313 candidates for muon-induced neutrons distributed over 181 neutron cascades.

Using the modelling package Geant4, we propagated about  $5.5 \cdot 10^7$  muons ( $\mu^+/\mu^- \approx 1.37$ ) through a detailed three-dimensional geometry and tracked all electromagnetic and hadronic shower products. Albeit more than 95.5 % of all neutrons which terminated in the liquid scintillator were produced within a distance of 1.19 m around the neutron counter, only 78.2 % of them originated from the lead target. This highlights the importance of a detailed geometry implemented in simulation packages.

Taking into account a calibrated detector response model on an event-by-event basis, the measured and simulated *absolute* integral rates of neutron candidates agree within the statistical, systematic, and theoretical uncertainties. The experimental value of  $(3.2_{-0.3}^{+0.5}) \cdot 10^{-1}$  neutrons per day is reproduced by MC to within

15 %. Also the measured *absolute* multiplicity spectrum is well reproduced by our model.

The neutron production yield in lead at LSM is, for the first time, derived to be  $\langle y \rangle = (2.7^{+1.0}_{-0.7}) \cdot 10^{-3} \text{ cm}^2 \text{ g}^{-1}$  for muon energies  $\overline{\langle E_\mu \rangle} = 267 \text{ GeV}$ .

This work demonstrates that Geant4 can reliably model the production and detection of muon-induced neutrons once all relevant production processes and a detailed description of the detector response and geometry are implemented in the model. Thus, one of the most prominent background sources for Dark Matter search can be accurately modelled and eventually suppressed.

# Acknowledgments

I want to thank all people who have supported my work in several ways during the past years.

First of all I want to thank my supervisor Prof. Dr. J. Blümer who gave me the opportunity to pursue my study at the Institute for Nuclear Physics of KIT. I also thank Prof. Dr. G. Quast for acting as second examiner.

I am obliged to Dr. K. Eitel for his initial proposal to study the muon-induced neutron production at the LSM and for his everyday support of my work. Whenever I had a question, he had time for a helping discussion.

I am grateful to Dr. V.Y. Kozlov for his patience, to discuss with me many of my initial ideas and helping to find the possible flaws in them. I also greatly enjoyed our common work during the installation and running of the neutron counter.

The work of St. Jokisch and N. Bechthold in the institute's workshops were essential for the development and the assembly of the neutron counter and thus for the success of this work. During the development, they rapidly and skilfully reacted on even the most sudden request for modification on the electronics and mechanics of the detector.

I thank my colleagues in the EDELWEISS collaboration for the possibility to run the neutron counter as part of the EDELWEISS experiment. I especially want to thank Dr. V.A. Kudryavtsev for many helpful discussions and hints on the simulation of underground muon flux and muon-induced neutron production.

For a friendly and intellectually stimulating atmosphere, I thank all my colleagues at the institute. For helping me with cross reading my thesis I am particularly in debt to Dr. K. Eitel, Dr. V.Y. Kozlov, and the late Dr. J. Engler. Of course, I am solely responsible for any remaining incorrectness.

Last, but not least, I thank my family for their boundless support during the past years, when I had to spend more time with my thesis than with them.

# Contents

<b>1</b>	<b>Introduction</b>	<b>1</b>
	References	5
<b>2</b>	<b>Searching Dark Matter: The Quest for the Missing Mass</b>	<b>9</b>
2.1	Motivation for WIMP-Like Dark Matter	9
2.1.1	Dark Matter as Solution for the Missing Mass Problem	10
2.1.2	Supersymmetric WIMPs as Dark Matter Candidates	17
2.1.3	Constraints on the WIMP Parameter Space Including Latest LHC Results	22
2.1.4	Limits on the WIMP Self-annihilation Cross Section by Astroparticle Data	25
2.1.5	WIMP Signature in Direct Searches for Dark Matter	29
2.2	Overview of Direct Searches for Galactic WIMPs	32
2.2.1	Scintillators	33
2.2.2	Ionisation Detectors	35
2.2.3	Cryogenic Crystal Detectors	36
2.2.4	Two-Phase Noble Liquids	38
2.2.5	Single-Phase Noble Liquids	41
2.2.6	Superheated Liquids	42
2.2.7	Directional Experiments	43
2.2.8	Tension Between Signal Claims and Exclusion Limits	43
2.3	Dark Matter Search at LSM with EDELWEISS	47
2.3.1	The Experimental Set-up at LSM	47
2.3.2	Event Categories and Event Selection	51
2.3.3	Results of EDELWEISS-II and Outlook on EDELWEISS-III	55
	References	59

<b>3 Review of Muon-Induced Neutron Production at Underground Sites</b> . . . . .	77
3.1 Muon Flux at Sea Level . . . . .	77
3.1.1 Cosmic Rays as Muon Source . . . . .	78
3.1.2 Influence of the Earth's Atmosphere on Muon Production. . . . .	79
3.1.3 Gaisser's Parametrization of the Muon Flux at Sea Level. . . . .	81
3.2 Muon Energy Loss in Rock. . . . .	82
3.2.1 General Parametrization of Energy Loss . . . . .	83
3.2.2 Electronic Contribution to the Energy Loss . . . . .	85
3.2.3 Energy Loss via Bremsstrahlung . . . . .	87
3.2.4 Energy Loss via Direct Pair Production . . . . .	88
3.2.5 The Landau-Pomeranchuk-Migdal Effect and the Ter-Mikaelian Effect. . . . .	88
3.2.6 Energy Loss via Muon Spallation . . . . .	89
3.2.7 References for Total Muon Energy Loss. . . . .	89
3.2.8 Total Energy Loss in LSM Rock . . . . .	90
3.3 Muon Flux at LSM . . . . .	92
3.3.1 Muon Survival Probabilities . . . . .	92
3.3.2 Rock Overburden Above LSM . . . . .	93
3.3.3 Local Muon Flux at LSM . . . . .	95
3.4 Production Mechanisms for Muon-Induced Neutrons . . . . .	98
3.4.1 Capture of Negative Muons on Nuclei . . . . .	100
3.4.2 Quasielastic Scattering on Nuclei . . . . .	101
3.4.3 Muon Spallation . . . . .	102
3.4.4 Neutron Production in Electromagnetic Showers . . . . .	103
3.4.5 Neutron Production in Hadronic Showers . . . . .	104
3.4.6 Photonuclear Cross Section . . . . .	105
3.5 Measurements of Muon-Induced Neutrons. . . . .	106
3.5.1 Overview of Existing Measurements. . . . .	107
3.5.2 Angular and Lateral Correlation of Neutrons with Muons. . . . .	111
3.5.3 Energy and Multiplicity Spectrum . . . . .	113
3.5.4 Dependence of the Neutron Production Yield on Energy and Target. . . . .	116
3.5.5 Currently Running and Future Experiments . . . . .	126
3.6 Implementation of Muon Interactions in Geant4. . . . .	128
3.6.1 Electromagnetic Interactions . . . . .	128
3.6.2 Muon Spallation . . . . .	130

3.6.3	Photo-Nuclear and Electron-/Positron-Nuclear Interactions . . . . .	131
3.6.4	Hadronic Interactions . . . . .	132
3.7	Conclusion . . . . .	135
	References . . . . .	137
<b>4</b>	<b>Long Term Measurement of Muon-Induced Neutrons at LSM . . . . .</b>	<b>151</b>
4.1	Functionality of a Neutron Multiplicity Meter . . . . .	151
4.1.1	Neutron Detection via Capture on Gadolinium. . . . .	152
4.1.2	Possible Sources for Background . . . . .	160
4.1.3	Assessing the Neutron Detection Efficiency. . . . .	162
4.2	Experimental Set-Up of the Neutron Counter. . . . .	164
4.2.1	Neutron Multiplicity Meter (NMM) . . . . .	164
4.2.2	Muon Telescope . . . . .	170
4.2.3	Light Pulser . . . . .	171
4.2.4	Data Acquisition Electronics . . . . .	172
4.2.5	Adjustment of High Tension and Discriminator Threshold . . . . .	180
4.2.6	Data Acquisition Software and Dead Time . . . . .	184
4.3	Signatures for Muon-Induced Neutrons . . . . .	186
4.4	Detector Live-Time and Stability . . . . .	188
4.4.1	Live-Time and Chronological Performance of the Experiment . . . . .	188
4.4.2	Precipitation of the Gadolinium Out of the Liquid Scintillator. . . . .	190
4.4.3	Deterioration of the Transparency of the Liquid Scintillator . . . . .	193
4.4.4	Long Term Shifts in the DAQ Electronics. . . . .	196
4.5	Measured Muon-Induced Neutrons . . . . .	197
4.5.1	Particle Identification . . . . .	197
4.5.2	Rate of Muon-Induced Neutron Candidates . . . . .	201
	References . . . . .	202
<b>5</b>	<b>Simulation of Muon-Induced Neutrons at LSM with Geant4 . . . . .</b>	<b>207</b>
5.1	Implementation of the Detector Set-Up and Its Environment . . . . .	207
5.2	Physics List for Modelling Interactions . . . . .	213
5.3	Muon Generation in Geant4 . . . . .	216
5.3.1	Muon Generator. . . . .	217
5.3.2	Simulating the Local Muon Spectrum at LSM . . . . .	227
5.3.3	Absolute Normalization of the Simulated Muon Flux . . . . .	231

5.4	MC Model of the Detector Response . . . . .	235
5.4.1	Simulation of Energy Deposits . . . . .	236
5.4.2	Scintillation Light Production, Propagation, and Absorption . . . . .	242
5.4.3	Event Building . . . . .	251
5.4.4	Calibration of the Model . . . . .	254
5.5	MC Modelling of Muon-Induced Neutron Production and Detection . . . . .	264
5.5.1	Muon-Induced Neutron Production . . . . .	264
5.5.2	Definition of the Neutron Yield . . . . .	270
5.5.3	Neutron Production Rate and Detection Efficiency . . . . .	279
5.5.4	Estimation of Systematic Uncertainties in the Simulation . . . . .	283
5.5.5	Background Estimation . . . . .	293
5.5.6	Prospect to Deduce Neutron Multiplicity and Energy Spectra . . . . .	298
	References . . . . .	300
<b>6</b>	<b>Assessment of Geant4 to Simulate the Neutron Yield in Lead at LSM . . . . .</b>	<b>305</b>
6.1	MC Prediction of Muon-Induced Neutron Candidates . . . . .	305
6.1.1	Counting Rate . . . . .	305
6.1.2	Differential Counting Spectra . . . . .	308
6.2	Cosmic Induced Neutron Production Yield at LSM . . . . .	312
6.2.1	Calculation of the Neutron Yield . . . . .	312
6.2.2	Neutron Yield in Comparison with Existing Measurements . . . . .	314
6.2.3	Neutron Yield in Comparison with Geant4 Simulations . . . . .	316
6.2.4	Neutron Production at Shower Equilibrium . . . . .	317
	References . . . . .	319
<b>7</b>	<b>Conclusion and Outlook . . . . .</b>	<b>321</b>
	References . . . . .	331
<b>Appendix</b>	<b>335</b>	
<b>Curriculum Vitae</b>	<b>381</b>	

# Acronyms

List of recurring acronyms, i.e. used in more than one subsection

ADC	Analog-to-digital converter
ADS	Astrophysics Data System of the NASA, online data base for astronomy and physics papers ( <a href="http://adsabs.harvard.edu">http://adsabs.harvard.edu</a> )
ASD	Artemovsk Scintillation Detector, an underground detector
BERT	Bertini cascade, a physics model in Geant4
BiC	Binary cascade, a physics model in Geant4
CAMAC	Computer Automated Measurement And Control, a bus standard for DAQ (ANSI/IEEE 583-1982)
cdf	Cumulative distribution function
CDMS	Cryogenic Dark Matter Search, an experiment searching for dark matter
CHIPS	Chiral invariant phase space, a physics model in Geant4
CJPL	China Jin-Ping underground Laboratory, a Chinese underground laboratory
CL	Confidence level
CMSSM	Constrained Minimal Supersymmetric Standard Model, a supersymmetric extension of the standard model
CODATA	Committee on Data for Science and Technology, author of recommended values of fundamental physical constants
CSDA	Continuous-slowing-down approximation, for muon energy loss
CUBE	Cosmic-ray Underground Background Experiment, an underground detector
DAQ	Data acquisition systems
DIR	Depth-intensity-relation of muon flux at underground sites
DOI	Digital object identifier ( <a href="http://www.doi.org">http://www.doi.org</a> )
ECL	Emitter-coupled logic, a transistor logic family, which defines also signal levels

EDELWEISS	Experience pour <b>DE</b> tecter <b>Les</b> Wimps <b>En</b> <b>SI</b> te <b>Souterrain</b> , an experiment searching for dark matter
ENDF	<b>E</b> valuated <b>N</b> uclear <b>D</b> ata <b>F</b> ile, data base of recommended nuclear data of the NDS ( <a href="http://www-nds.iaea.org/exfor/endf.htm">http://www-nds.iaea.org/exfor/endf.htm</a> )
EURECA	<b>E</b> uropean <b>U</b> nderground <b>R</b> are <b>E</b> vent <b>C</b> alorimeter <b>A</b> rray, a projected experiment searching for dark matter
FADC	<b>F</b> lash <b>A</b> DC, a direct conversion ADC
FID	<b>F</b> ull <b>I</b> nter <b>Digit, a detector design of EDELWEISS, improvement of the ID detectors</b>
FPGA	<b>F</b> ield- <b>P</b> rogrammable <b>G</b> ate <b>A</b> rray, a type of integrated circuit
FTF	<b>F</b> ri <b>T</b> o <b>F</b> string, a physics model in Geant4
FTFP	<b>F</b> TF model in Geant4, using the <b>p</b> recompound model for deexcitation
FWHM	<b>F</b> ull <b>W</b> idth <b>at</b> <b>h</b> alf <b>m</b> aximum
GDR	<b>G</b> iant <b>d</b> ipole <b>r</b> esonance, a collective excitation of atomic nuclei
GEANT	<b>G</b> EOmetry <b>A</b> ND <b>T</b> racking, a series of MC simulation programs, the latest iteration is Geant4 ( <a href="http://geant4.cern.ch">http://geant4.cern.ch</a> )
GPS	<b>G</b> eneral <b>p</b> article <b>s</b> ource in Geant4
HP	<b>H</b> igh <b>precision physics model in Geant4</b>
IAEA	<b>I</b> nternational <b>A</b> tomic <b>E</b> nergy <b>A</b> gency ( <a href="http://www.iaea.org">http://www.iaea.org</a> )
ICRU	<b>I</b> nternational <b>C</b> ommission on <b>R</b> adiation <b>U</b> nits and <b>M</b> easurements ( <a href="http://www.icru.org">http://www.icru.org</a> )
ID	<b>I</b> nterDigit, a detector design of EDELWEISS
IKP	<b>I</b> nstitut <b>f</b> ür <b>K</b> ern <b>p</b> hysik (German), Institute for Nuclear Physics of the KIT ( <a href="http://www.ikp.kit.edu">http://www.ikp.kit.edu</a> )
IPE	<b>I</b> nstitut <b>f</b> ür <b>P</b> rozessdatenverarbeitung <b>u</b> nd <b>E</b> lektronik (German), Institute for Data Processing and Electronics of the KIT ( <a href="http://www.ipe.kit.edu">http://www.ipe.kit.edu</a> )
IRQ	<b>I</b> nterrupt <b>r</b> equest
JENDL	<b>J</b> apanese <b>E</b> valuated <b>N</b> uclear <b>D</b> ata <b>L</b> ibrary, data base of recommended nuclear data ( <a href="http://wwwndc.jaea.go.jp/jendl/jendl.html">http://wwwndc.jaea.go.jp/jendl/jendl.html</a> )
KamLAND	<b>K</b> amioka <b>L</b> iquid <b>S</b> cintillator <b>A</b> nti- <b>N</b> eutrino <b>D</b> etector, an underground detector
keV <sub>ee</sub>	kilo <b>e</b> lectron <b>V</b> olt <b>e</b> lectron <b>e</b> quivalent, energy scale normalized to electronic interactions
KIT	<b>K</b> arlsruhe <b>I</b> nstitute of <b>T</b> echnology ( <a href="http://www.kit.edu">http://www.kit.edu</a> )
LAr	<b>L</b> iquid <b>A</b> rgon
LED	<b>L</b> ight- <b>e</b> mitting <b>diode</b>
LEP	<b>L</b> ow <b>e</b> nergy <b>p</b> arameterised physics model in Geant4
LHC	<b>L</b> arge <b>H</b> adron <b>C</b> ollider, a particle accelerator
LNe	<b>L</b> iquid <b>N</b> eon
LNGS	<b>L</b> aboratori <b>N</b> azionali <b>d</b> el <b>G</b> ran <b>S</b> asso (Italian), an Italian underground laboratory ( <a href="http://www.lngs.infn.it">http://www.lngs.infn.it</a> )

LSC	Laboratorio Subterráneo de Canfranc (Spain), a Spain underground laboratory ( <a href="http://www.lsc-canfranc.es">http://www.lsc-canfranc.es</a> )
LSD	Large Scintillator Detector, an underground detector
LSM	Laboratoire Souterrain de Modane (French), a French underground laboratory ( <a href="http://www-lsm.in2p3.fr">http://www-lsm.in2p3.fr</a> )
LSP	Lightest Supersymmetric Particle
LUX	Large Underground Xenon, an experiment searching for dark matter
LVD	Large Volume Detector, an underground detector
LXe	Liquid Xenon
MC	Monte Carlo simulation
MCNPX	Monte Carlo N-Particle eXtended, a MC radiation transport code ( <a href="http://mcnpx.lanl.gov">http://mcnpx.lanl.gov</a> )
MOND	Modified Newtonian Dynamics
MSSM	Minimal Supersymmetric Standard Model, a supersymmetric extension of the standard model of particle physics
mwe	Meter water equivalent, i.e. $10^2$ g cm $^{-2}$
NASA	National Aeronautics and Space Administration of the United States ( <a href="http://www.nasa.gov">http://www.nasa.gov</a> )
ndf	Number of degrees of freedom
NDS	Nuclear Data Services of the IAEA ( <a href="http://www-nds.iaea.org">http://www-nds.iaea.org</a> )
NIM	Nuclear Instrumentation Module, standard that defines also signal level
NIST	National Institute of Standards and Technology of the United States Department of Commerce ( <a href="http://www.nist.gov">http://www.nist.gov</a> )
NMM	Neutron multiplicity meter, a type of neutron detector
NTD	Neutron Transmutation Doped, a type of thermal sensor
PC	Precompound, a physics model in Geant4, otherwise personal computer
pdf	Probability density function
PMMA	Poly(methyl methacrylate), i.e. acrylic glass like PLEXIGLASS
PMT	Photomultiplier tube
PMTG <sup>M</sup>	Group of muon PMTs
PMTG <sup>N</sup>	Group of neutron PMTs
PMT <sup>M</sup>	Muon PMT
PMT <sup>N</sup>	Neutron PMT
QDC	Charge-to-digital converter, a charge integrating ADC
QGS	Quark-gluon string, a physics model in Geant4
QGSC	QGS model in Geant4, using the CHIPS model for deexcitation
QGSP	QGS model in Geant4, using the precompound model for deexcitation
SSH	Secure Shell, a network protocol
SUSY	Super Symmetry, a hypothetical symmetry in particle physics
TDC	Time-to-digital converter

VMbus	<b>VERSA</b> module Eurocard <b>bus</b> , a computer bus standard (ANSI/IEEE 1014-1987)
WIMP	<b>Weakly Interacting Massive Particle</b> , a category of particle candidates for dark matter

# Symbols

List of recurring symbols, i.e. used in more than one subsection. Values for physical constants are given according to CODATA.

$x_0$	In context of atmospheric muons, the index ‘0’ indicates quantities taken at sea level
$a$	Electronic contribution to the muon energy loss
$A$	Depending on the context either the atomic weight or the molar mass (i.e. atomic weight times $1 \text{ g mol}^{-1}$ ) of a substance
$\alpha$	Empirical index to fit $Y _A(\langle E_\mu \rangle)$
$\alpha^{-1}$	Absorption length
$\alpha_{440}^{-1}$	Absorption length at 440 nm
$b$	Radiative contribution to the muon energy loss
$\beta$	Empirical index to fit $Y _{E_\mu}(A)$
$\beta$	Velocity relative to the speed of light, i.e. $\beta = v/c$
$c$	Speed of light in vacuum, i.e. $c = 299,792,458 \text{ ms}^{-1}$
$x_{\text{can},y}$	The index ‘can’ indicates quantities $x$ related to candidates of an entity $y$
$\chi$	Particular a neutralino, in general any WIMP
$\delta x$	Uncertainty of $x$
$\Delta E$	Energy loss
$\Delta t$	Period between entrance of a neutron in the NMM and its capture, experimentally measured with the NMM as interval between the primary hit and any secondary hit
$\Delta t_{\text{ADC}}$	Width of an ADC gate
$\Delta t_{\text{bin}}$	Width of a time bin $T_k$ in the detector response model
$\Delta t_{\text{DAQ}}$	Width of the DAQ window
$E_{\text{dep}}$	Deposit energy
$E_\mu$	Kinetic energy of a muon
$E_n$	Kinetic energy of a neutron
$E_R$	Resonance energy

$E_{\text{rec}}$	Recoil energy
$E_s$	Depending on the context either the energy of a particle shower or the initial energy of a simulated muon
$E_{\text{th}}$	Thermal energy, i.e. $E_{\text{th}} = 25.3$ MeV at 20.4 °C
$E_{\text{vis}}$	Visible energy deposit
$\epsilon$	Critical energy of the muon energy loss
$\epsilon_{\text{cap}}$	Neutron capture efficiency, fraction of neutrons captured in the NMM with $E_{\text{dep}} \geq 3$ MeV
$\epsilon_{\text{MT}}$	Agreement between reference measurement and detector response model for the muon telescope
$\epsilon_n$	Neutron detection efficiency
$\epsilon_{\text{NMM}}$	Agreement between reference measurement and detector response model for the NMM
$\eta_{n,\text{cas}}$	Ratio of neutrons to neutron cascades
$\eta_{n,\mu}$	Ratio of neutrons to muons
$x_{\text{exp}}$	The index ‘exp’ indicates experimental obtained values $x$
$F_{\text{LED}}$	Signal to flag an LED sequence
$G_x$	Within the detector response model, the effective gain of detector $x$
$x_n$	Within the detector response model, the index $n$ count the ADC channel
$x_g$	Within the detector response model, the index $g$ count the ADC gate
$\Gamma$	Decay width
$\gamma$	Integral spectral index
$\gamma$	Lorentz factor, i.e. $\gamma = 1/\sqrt{1 - \beta^2}$
$\gamma_\mu$	Spectral index for muons
$h$	Altitude above sea level
$H_0$	Present Hubble’s constant, i.e. $H_0 = 67.4 \text{ km s}^{-1} \text{ Mpc}^{-1}$
$h_0$	In context of the MC simulation, it is the distance between the muon starting position and the centre of the LSM model; otherwise the <i>reduced</i> Hubble’s constant $h_0 = H_0/100 \text{ km s}^{-1} \text{ Mpc}^{-1}$ at the present epoch
$\hbar$	Reduced Planck constant, i.e. $\hbar = 6.58211928(15) \cdot 10^{-16} \text{ eV s}$
$x_i$	Within the detector response model, the index $i$ count the PMT group
$x_j$	Within the detector response model, the index $j$ count the PMT within a given PMT group
$x_k$	Within the detector response model, the index $k$ count the time bin
$k_{\text{B}}$	Boltzmann constant, i.e. $k_{\text{B}} = 8.6173324(78) \cdot 10^{-5} \text{ eV K}^{-1}$
$k_B$	Quenching parameter
$l$	Particle track length
$\Lambda$	Effective attenuation length
$\lambda_{\text{dec}}$	Decay length
$\lambda_{\text{int}}$	Interaction length
$\lambda_s$	Mean path length between scatterings
$\lambda$	Reduced deBroglie wavelength, i.e. $\lambda = \lambda/(2\pi) = \hbar/(mv)$

$m$	Mass
$m_\chi$	In general the mass of a WIMP of any type, in particular the mass of a neutralino
$m_e$	Electron mass, i.e. $m_e c^2 = 510.998928(11)$ KeV
$m_\mu$	Muon mass, i.e. $m_\mu c^2 = 105.6583715(35)$ MeV
$M_n$	Neutron multiplicity
$m_{\text{Pl}}$	Planck mass, i.e. $m_{\text{Pl}} c^2 = 1.220932(73) \cdot 10^{19}$ GeV
$x_{\text{M50}}$	Quantity $x$ related to the muon module 50
$x_{\text{M50}}$	Quantity $x$ related to the muon module 51
$x_{\text{MC}}$	The index ‘MC’ indicates values $x$ obtained by MC simulations
$\mu$	Linear attenuation coefficient
$x_N$	Quantity $x$ related to the NMM
$n_x$	Number of entities $x$ within a given data set
$N$	Nucleon
$N_A$	Avogadro constant, i.e. $N_A = 6.02214129(27) \cdot 10^{23}$ mol $^{-1}$
$n_{\text{Gd}}$	Content of gadolinium in the liquid scintillator, nominal value is $n_{\text{Gd}} = 0.2\%$ w/w
$n_n$	Number of neutrons
$N_{\text{ph}}$	Number of emitted scintillation photons
$n_s$	Average number of scatterings needed to moderate a neutron
$n_x$	Amount of $x$
$\nu$	Fractional energy loss
$\Omega$	Solid angle
$\hat{\omega}$	Direction vector
$P$	Probability
$\hat{p}$	Set of best fitting parameter of the detector response model in standard configuration
$P_N(x; \mu, \sigma)$	Normal distribution of $x$ with mean $\mu$ and variance $\sigma^2$
$\Phi$	Fluence
$\phi$	Azimuth angle
$\dot{\Phi}$	Flux, i.e. $\dot{\Phi} = d\Phi/dt$
$q$	Quenching factor
$q^2$	Squared four-momentum transfer
$R_x$	Within the detector response model, the effective energy resolution of detector x
$x_r$	In context of the muon generator, the index ‘r’ indicated quantities taken when the simulated muon is started in the rock overburden
$\langle r_E^2 \rangle$	Average squared distance needed for a neutron to pass the energy $E$
$r_e$	Classical electron radius, i.e. $r_e = 2.8179403267(27) \cdot 10^{-15}$ m

$R_x$	Counting rate of entity x
$\rho$	Material density
$S$	Scintillation light yield
$S_i^x$	Signal on channel $i$ of detector $x$
$S_n$	Neutron binding energy
$\Sigma$	Macroscopic interaction cross section
$\sigma$	Interaction cross section
$\Sigma_a$	Macroscopic absorption cross section
$\langle \sigma_a v \rangle$	Thermal average of the WIMP self-annihilation cross section times the relative velocity
$\sigma_{n\gamma}$	Cross section for radiative neutron capture
$\Sigma_s$	Macroscopic scattering cross section
$\sigma_s$	Scattering cross section
$\delta x^{\text{stat}}$	The index ‘stat’ indicates statistical uncertainties
$\delta x^{\text{sys}}$	The index ‘sys’ indicates systematic uncertainties
$T$	Temperature
$T_x$	Within the detector response model, the effective threshold of detector x
$t$	Depending on the context either the depth of a underground site or time
$T_{\text{exp}}$	Experimental live-time
$T_k$	The $k$ -th time bin
$T_M$	Trigger signal of the muon veto
$T_{\text{MC}}$	Live-time of the MC simulation
$T_N$	Trigger signal of the NMM
$\tau$	Life time of a particle
$\tau_{\text{cap}}$	Mean time between the subsequent capture of thermalized neutrons
$\delta x^{\text{theo}}$	The index ‘theo’ indicates theoretical uncertainties
$\Theta(x)$	Heaviside step function
$\theta$	Zenith angle
$v$	Velocity
$w_c$	Weight to normalize the simulated data set $ic$ with respect to its charge fraction $c$
$w'_i$	Weight to normalize the simulated data set $ic$ with respect to its energy range $i$
${}^A_Z X$	Nucleus with mass number $A$ and atomic number $Z$
$X$	Column density of a material, e.g. the slant depth of Earth’s atmosphere
$\hat{x}$	A hat indicates values obtained in the standard configuration of the MC simulations, i.e. the standard parameter set for the muon generator, the GdNeutronHPCapture model for the neutron capture on gadolinium, the best fitting parameter set $\hat{p}$ for the detector response model, and $n_{Gd} = 0.2$ % w/w loading with gadolinium
$\hat{\vec{x}}$	A unit vector in $\mathbb{R}^3$

$\vec{x}$	A vector in $\mathbb{R}^3$
$\xi$	Average logarithmic energy decrement
$Y$	Neutron yield
$Y_{\text{equi}}$	Neutron yield at shower equilibrium
$Y_{\text{ext}}$	External neutron yield
$Z$	Atomic number

# Chapter 1

## Introduction

Many of the most exciting experiments in astroparticle physics like the search for proton decay [41], the observation of neutrino oscillations [39] or the direct search for dark matter [22] require an event by event identification of a potentially very rare signal. The capability to efficiently reject background is therefore a central requirement. A background component common to all of these experiments are neutrons induced by the muonic component of cosmic rays [28], hence called muon-induced neutrons [27]. The main objective of this work is the measurement of the muon-induced neutron production in the *Laboratoire Souterrain de Modane* (LSM) and to assess the capability of the Monte Carlo (MC) package Geant4 [3, 8] to correctly model this kind of neutron production. A reliable MC code is a basic ingredient to correctly model the muon-induced background. Only then, improved strategies for background suppression can be developed. Therefore, a better understanding of muon-induced neutrons will contribute to more sensitive studies of several exciting research topics. Among those, one of the biggest mystery in contemporary physics: The quest for understanding the nature of dark matter.

Various astrophysical and cosmological observations e.g. of the dynamic behaviour of gravitational bound systems like galaxy clusters and galaxies [48], the cosmic microwave background [43], or gravitational lensing [34, 47] indicated during the last 80 years the existence of *dark matter* [52], also in the halo of our Galaxy [46]. Despite the various indications of its existence, up to now no particle constituent of dark matter is known, albeit some properties could be deduced from the observations. As an example, studies of the large scale structure formation in the universe show that the dark matter particle has to be *massive*, i.e. non-relativistic at the time of de-coupling [22, 33]. The observed abundance of dark matter as observed today would be naturally matched if the particle is further *weakly interacting*. Particles fulfilling these requirements are therefore called *weakly interacting massive particles* (WIMPs) [22, 33]. A natural candidate for a WIMP is the lightest supersymmetric particle, e.g. the neutralino  $\chi$  in the minimal supersymmetric standard model [33, 40, 45]. Many experiments world-wide are searching for WIMPs [7, 18, 26], see especially [22] for an instructive introduction.

The EDELWEISS (*Expérience pour DEtecter Les Wimps En SIté Souterrain*) experiment [14] searches for the nuclear recoils induced by elastic scattering of galactic WIMPs off germanium nuclei in cryogenic bolometers [24]. In combination with the similar CDMS II (Ge) experiment [4], EDELWEISS is the most sensitive experiment using germanium targets [5], third only to the XENON [11] and LUX [6] experiments using liquid xenon as target. The combined EDELWEISS-II and CDMS II (Ge) analysis sets an upper limit in the spin-independent WIMP-nucleon cross section of  $\sigma_{\chi,N}^{\text{SI}} < 3.3 \times 10^{-8} \text{ pb}$ <sup>1</sup> at 90 % CL for a WIMP mass of  $m_\chi c^2 = 90 \text{ GeV}$ <sup>2</sup> and excludes significant parts of the supersymmetric parameter space [5]. Albeit the exclusion is confirmed by the majority of dark matter searches, it is in tension with observed signal excesses over known background in the experiments CDMS II (Si) [2], CoGeNT [1], CRESST [9], and an annual modulation observed by DAMA [21]. These indications motivated further experiments like the current EDELWEISS-III or the future EURECA, aiming for improved sensitivities of  $\sigma_{\chi,N}^{\text{SI}} < 10^{-9} \text{ pb}$  [16] and  $\sigma_{\chi,N}^{\text{SI}} < 2 \times 10^{-11} \text{ pb}$  [10], respectively. The current situation highlights also the importance of a well understood background model, where muon-induced neutrons are an important component.

EDELWEISS can reject electromagnetic background from  $\alpha$ -,  $\beta$ -, and  $\gamma$ -decay via the simultaneous measurement of ionisation and heat signals [14]. However, the background of nuclear recoils caused by neutrons is not rejectable by this technique alone. For the recent EDELWEISS-II experiment, the three main neutron sources in decreasing order of its relative contributions were [14]: uranium/thorium decay in the materials of the experimental set-up, neutron production induced by atmospheric muons, and  $(\alpha, n)$ -reaction in the concrete and rock of the laboratory's walls. As muon-induced neutron production scales with the atomic weight of the target [38], one important source is the lead of the gamma shield of EDELWEISS [44]. For the current EDELWEISS-III experiment, it is expected that the *relative* contribution of muon-induced neutrons rise further due to increased radiopurity of the materials [15, 44], thus establishing muon-induced neutrons as central background source.

Muon-induced neutrons can be *rejected* by tagging the parent muon with a muon veto system, and they can be *suppressed* by going deep underground to reduce the flux of atmospheric muons [27]. For this reason, EDELWEISS is located at the LSM with a shielding power equivalent to 4800 m of water [14]. As only muons with an energy in the TeV range or above can penetrate such massive shielding, the energy spectrum of the remaining muons get harder. After passing the rock above LSM, the mean energy of muons reaches  $\sim 260 \text{ GeV}$ . In this energy regime, several physical processes contribute to the neutron production [27, 38], e.g. muon-induced spallation of nuclei in deep-inelastic scatterings and inelastic scattering of neutrons which produce secondary neutrons. Albeit the latter process is more probable, the

---

<sup>1</sup>*Barn* (symbol b) is a unit of cross section area used in particle physics. One barn is equivalent to  $100 \text{ fm}^2 = 10^{-28} \text{ m}^2$ .

<sup>2</sup>*Electronvolt* (symbol eV) is a unit of energy used in particle physics. One electronvolt is the energy needed to move one elementary charge  $e$  against a potential difference of one volt, i.e.  $1 \text{ eV} \approx 1.602 \times 10^{-19} \text{ J}$ .

muon-induced neutrons can reach higher energies, up to several GeVs. Due to these high energies, a detailed knowledge about the flux and energy spectrum is needed to develop strategies to reduce this background of muon-induced neutrons.

As a consequence of the reduced muon flux and the subsequent suppression of the muon-induced neutron production, an on-site study of muon-induced neutrons is difficult due to the limited statistics. Even more important, the complex physics of deep-inelastic scattering of muons and the production mechanism of secondary neutrons are not well understood. Therefore, one strongly relies on MC simulations to understand this background, to design active and passive shielding, and to evaluate its efficiency to suppress and eventually reject muon-induced background.

Unfortunately, the modelling of muon-induced neutron production is no mature field and the accuracy of the MC codes is debatable. This is especially true for heavy target materials with high neutron yield like lead which is commonly used as shield against radioactivity from  $\gamma$ -decay. As several targets and energy dependent neutron production processes contribute to the muon-induced neutron yield [27], the specific implementation differs between MC packages like FLUKA [17, 25] and Geant4, and also between different versions of the same package. In addition, several user modifications are described in literature, e.g. [35, 37]. Typically, a factor of up to two is stated in literature as possible deviation between different MC codes [36, 37], reducing the reliability of results obtained from MC simulations. To improve the reliability and accuracy, a verification of the simulation against experimental results was necessary. This is the subject of this work.

An in situ measurement of the muon-induced neutron production with direct dark matter searches is difficult, due to the typically low event rate. Therefore, long-term measurement campaigns with dedicated neutron detectors are necessary to collect the needed reference data sets of muon-induced neutrons. However, for heavy target materials only few such measurements were undertaken at different average muon energies [19, 20, 23, 29–32, 42], up to this work none at the LSM. It is also not straightforward to compare the derived results: a simple scaling of the measured neutron production yield with the average muon energy is not consistent, e.g. [50]. It is proposed in literature that not all measurements are properly corrected for site and detector specifics, e.g. the contribution of muon-induced showers to the neutron yield [51]. A reproduction of the published measurements with MC simulation is also difficult and deviated by more than a factor of two for complex composite materials [35]. As possible reason, a breakdown of the physics model is proposed [12, 37, 49], but also a poor documentation of especially the older experiments and their limited accuracy in implementing the geometry in MC is discussed in literature [13, 36, 37]. During the time of this work, the possibility to reduce this discrepancy by detailed documented measurements was shown in [13, 37, 42].

The great uncertainties in measurements and simulations of muon-induced neutron production motivated this thesis. As a reliable MC code is important for experiments searching for rare events, like EDELWEISS, this work aims to assess the suitability of Geant4 to model the muon-induced neutron production by comparing simulation to measurement. The first objective of this thesis is the collection of a well-documented reference data set of muon-induced neutrons. To ensure the utility

of this work for EDELWEISS, despite possible site-dependence, the measurement was performed at the LSM, the site of the EDELWEISS experiment. The second objective is to simulate the neutron production and detection with Geant4, taken into account the detector response based on a fully implemented geometry including detector response functions. Based on the carefully analysed data and the detailed modelling, the reliability of Geant4 can be assessed and the neutron production at the LSM can be derived.

To achieve the first objective, a dedicated neutron detector was installed at the LSM and operated in coincidence with a muon detector. The neutron detector was based on 10001 of gadolinium loaded liquid scintillator, which provides an efficient way to detect neutrons. After thermalizing in the large volume of liquid scintillator, the neutrons get captured on the gadolinium nuclei with a cross section of up to  $\approx 200$  kb for  $^{157}\text{Gd}$ . The gadolinium nuclei deexcite via the emission of several gamma rays with a sum energy of  $\approx 8$  MeV, providing a clear signal above the energy regime common for natural  $\gamma$ -radioactivity, i.e.  $\approx 2$  MeV. The neutron detector was placed above a layer of lead, a target with a high production yield for muon-induced neutrons. When a remaining atmospheric muon passes through the target, it is registered by the muon detector. Hence, the coincidence between neutron and muon detector selects a very clear sample of muon-induced neutrons which is used as reference data set.

The challenge of the second objective is to simulate exactly the same quantity which was measured as reference data, i.e. not only the rate of neutrons produced by the passing muon, but the rate of detected neutron signals in coincidence with muon signals. Therefore, it is necessary to simulate the production, propagation, and detection of neutrons together with the propagation and detection of muons. To consider also the possible contribution of neutrons induced by the muon before or after it passes the lead target, e.g. in the rock floor below or in the nearby EDELWEISS experiment, it is also necessary to implement the entire detector surrounding. To derive the efficiency to detect neutrons, a dedicated detector response model was developed. The free model parameters were determined via a log likelihood fit to data obtained in calibration measurements. The reliability of Geant4 to simulate the production, transport, and detection of muon-induced neutrons can be assessed by comparing the measured rate of neutron events in coincidence with a passing muon with the expected rate of such events based on the simulation.

The following text is structured along the above given outline:

Chapter 2 motivates WIMPs as solution for one of the most exciting physics problems, the quest for the particle constituent of dark matter. The status of experiments searching for the very rare interaction of WIMPs with earth based detectors is reviewed. Describing the example of the EDELWEISS experiment, the need for a very low background, including muon-induced neutrons, is shown. Thus, this chapter puts the investigation of muon-induced neutrons into a broader context.

Chapter 3 reviews the literature relevant for muon-induced neutron production on deep underground sites like LSM, both concerning measurements and simulation. This chapter starts with an overview of muon production in the atmosphere, the propagation through the rock overburden above the LSM, and the resulting muon flux in the LSM. Afterwards the individual neutron production processes are reported.

Finally, the existing measurements and simulations of muon-induced neutrons are discussed.

Chapter 4 describes the experimental set-up of the dedicated neutron detectors, its detection principle and results. The theory of neutron detection and the properties of the actual detector are used to define the signature of muon-induced neutrons. Based on this signature, the measured data set is analysed and rates of muon-induced neutrons are derived.

Chapter 5 comprises the results of the Geant4 simulation of the production and detection of muon-induced neutrons. It reports the implemented detector geometry and physics processes, and it documents the used algorithm to generate muons. Afterwards, the response model for both the neutron and muon detector is developed and the free model parameters are determined. Folding the simulated muons and neutrons with the response model, the expected rate of detector signals is obtained.

Finally, based on the comparison of measurement and simulation, Chap. 6 gives the physics results of this study, i.e. the assessment of Geant4's reliability and quantification of the muon-induced neutron production at LSM. Also the agreement between this result and results from literature is discussed.

We close with a summary discussing some implications for future experiments in Chap. 7.

## References

1. Aalseth CE et al [CoGeNT Collaboration] (2011) Results from a search for lightmass dark matter with a  $p$ -type point contact germanium detector. *Phys Rev Lett* 106(13):131301. doi:[10.1103/PhysRevLett.106.131301](https://doi.org/10.1103/PhysRevLett.106.131301). arXiv:[1002.4703](https://arxiv.org/abs/1002.4703) [astro-ph]
2. Agnese R et al [CDMS Collaboration] (2013) Dark matter search results using the silicon detectors of CDMS II. arXiv:[1304.4279](https://arxiv.org/abs/1304.4279) [hep-ex]
3. Agostinelli S et al [GEANT4 Collaboration] (2003) GEANT4—a simulation toolkit. *Nucl Instrum Methods Phys Res Sect A* 506(3):250–303. doi:[10.1016/S0168-9002\(03\)01368-8](https://doi.org/10.1016/S0168-9002(03)01368-8)
4. Ahmed Z et al [CDMS II Collaboration] (2010) Dark matter search results from the CDMS II experiment. *Science* 327(5973):1619–1621. doi:[10.1126/science.1186112](https://doi.org/10.1126/science.1186112)
5. Ahmed Z et al [CDMS and EDELWEISS Collaborations] (2011) Combined limits on WIMPs from the CDMS and EDELWEISS experiments. *Phys Rev D* 84(1):011102. doi:[10.1103/PhysRevD.84.011102](https://doi.org/10.1103/PhysRevD.84.011102). arXiv:[1105.3377](https://arxiv.org/abs/1105.3377) [astro-ph.CO]
6. Akerib DS et al [LUX Collaboration] (2013) First results from the LUX dark matter experiment at the Sanford Underground Research Facility. arXiv:[1310.8214](https://arxiv.org/abs/1310.8214) [astro-ph.CO]
7. Akimov D (2011) Techniques and results for the direct detection of dark matter (review). In: VCI 2010 - proceedings of the 12th international Vienna conference on instrumentation, special issue. *Nucl Instrum Methods Phys Res Sect A* 628(1):50–58. doi:[10.1016/j.nima.2010.06.283](https://doi.org/10.1016/j.nima.2010.06.283)
8. Allison J et al (2006) Geant4 developments and applications. *IEEE Trans Nucl Sci* 53(1):270–278. doi:[10.1109/TNS.2006.869826](https://doi.org/10.1109/TNS.2006.869826)
9. Angloher G et al (2012) Results from 730 kg days of the CRESST-II dark matter search. *Eur Phys J C* 72:1971. doi:[10.1140/epjc/s10052-012-1971-8](https://doi.org/10.1140/epjc/s10052-012-1971-8). arXiv:[1109.0702](https://arxiv.org/abs/1109.0702)
10. Angloher G et al (2014) EURECA conceptual design report. *Phys Dark Universe* 3:41–74. doi:[10.1016/j.dark.2014.03.004](https://doi.org/10.1016/j.dark.2014.03.004)
11. Aprile E et al [XENON100 Collaboration] (2012) Dark matter results from 225 live days of XENON100 data. *Phys Rev Lett* 109(18):181301. doi:[10.1103/PhysRevLett.109.181301](https://doi.org/10.1103/PhysRevLett.109.181301). arXiv:[1207.5988](https://arxiv.org/abs/1207.5988) [astro-ph.CO]

12. Araújo H et al (2005) Muon-induced neutron production and detection with GEANT4 and FLUKA. *Nucl Instrum Methods Phys Res Sect A* 545(1–2):398–411. doi:[10.1016/j.nima.2005.02.004](https://doi.org/10.1016/j.nima.2005.02.004). arXiv:[hep-ex/0411026](https://arxiv.org/abs/hep-ex/0411026)
13. Araújo H et al (2008) Measurements of neutrons produced by high-energy muons at the Boulby Underground Laboratory. *Astropart Phys* 29(6):471–481. doi:[10.1016/j.astropartphys.2008.05.004](https://doi.org/10.1016/j.astropartphys.2008.05.004)
14. Armengaud E et al [EDELWEISS Collaboration] (2011) Final results of the EDELWEISS-II WIMP search using a 4-kg array of cryogenic germanium detectors with interleaved electrodes. *Phys Lett B* 702(5):329–335. doi:[10.1016/j.physletb.2011.07.034](https://doi.org/10.1016/j.physletb.2011.07.034). arXiv:[1103.4070](https://arxiv.org/abs/1103.4070) [astro-ph.CO]
15. Armengaud E et al [EDELWEISS Collaboration] (2013) Background studies for the EDELWEISS dark matter experiment. *Astropart Phys* 47(1–9):1. doi:[10.1016/j.astropartphys.2013.05.004](https://doi.org/10.1016/j.astropartphys.2013.05.004). arXiv:[1305.3628](https://arxiv.org/abs/1305.3628) [physics.insdet]
16. Arnaud Q [For the EDELWEISS Collaboration] (2014) The EDELWEISS experiment status. In: Augé E, Dumarchez J, Trần Thanh Vân J (eds) ARISF proceedings of the 49th RENCON-TRES DE MORIOND. Cosmology, La Thuile, Aosta Valley, Italy, 22–29 March 2014, pp 175–178. [http://moriond.in2p3.fr/Proceedings/2014/Moriond\\_Cosmo\\_2014.pdf](http://moriond.in2p3.fr/Proceedings/2014/Moriond_Cosmo_2014.pdf)
17. Battistoni G et al (2007) The FLUKA code: description and benchmarking. In: Albrow M, Raja R (eds) Hadronic shower simulation workshop, Batavia, 6–8 September 2006. AIP conference proceedings, vol 896. AIP Publishing, Melville, pp 31–49. doi:[10.1063/1.2720455](https://doi.org/10.1063/1.2720455)
18. Baudis L (2012) Direct dark matter detection: the next decade. Next decade in dark matter and dark energy, special issue. *Phys Dark Universe* 1(1–2):94–108. doi:[10.1016/j.dark.2012.10.006](https://doi.org/10.1016/j.dark.2012.10.006). arXiv:[1211.7222](https://arxiv.org/abs/1211.7222)
19. Bergamasco L (1970) Experimental results on the pion and neutron production by muons at 60 and 110 m w.e. *Nuovo Cim B* 66(1):120–128. doi:[10.1007/BF02710194](https://doi.org/10.1007/BF02710194)
20. Bergamasco L, Costa S, Picchi P (1973) Experimental results on neutron production by muons at 4300 m w.e. *Nuovo Cim A* 13:403–412. doi:[10.1007/BF02827344](https://doi.org/10.1007/BF02827344)
21. Bernabei R (2012) Dark matter particles in the galactic halo: DAMA/LIBRA results and perspectives. *Ann Phys* 524(9–10):497–506. doi:[10.1002/andp.201200094](https://doi.org/10.1002/andp.201200094)
22. Bertone G (ed) (2010) Particle dark matter. Observations models and searches. Cambridge University Press, Cambridge
23. Crouch MF, Sard RD (1952) The distribution of multiplicities of neutrons produced by cosmic-ray  $\mu$ -mesons captured in lead. *Phys Rev (2nd ser)* 85(1):120–129. doi:[10.1103/PhysRev.85.120](https://doi.org/10.1103/PhysRev.85.120)
24. Enss C (ed) (2005) Cryogenic particle detection, vol 99. Topics in applied physics. Springer, Berlin. doi:[10.1007/b12169](https://doi.org/10.1007/b12169)
25. Ferrari A et al (2005) FLUKA: a multi-particle transport code. <http://cdsweb.cern.ch/record/898301/files/CERN-2005-010.pdf>
26. Figueiroa-Feliciano E (2011) Direct detection searches for WIMP dark matter. *Prog Part Nucl Phys* 66(3):661–673. doi:[10.1016/j.ppnp.2011.01.003](https://doi.org/10.1016/j.ppnp.2011.01.003)
27. Formaggio JA, Martoff CJ (2004) Backgrounds to sensitive experiments underground. *Annu Rev Nucl Part Sci* 54:361–412. doi:[10.1146/annurev.nucl.54.070103.181248](https://doi.org/10.1146/annurev.nucl.54.070103.181248)
28. Gaisser TK (1991) Cosmic rays and particle physics. 1. publ., repr. ed. Cambridge University Press, Cambridge
29. Gorshkov GV, Zyabkin VA (1968) Production of neutrons in Pb, Cd, Fe, and Al under the influence of cosmic-ray muons at a depth of 150 in water equivalent (trans: Adashko JG). *Sov J Nucl Phys* 7(4):470–474. Orig. pub. as *Yad Fiz* 7:770–777 [in Russian]
30. Gorshkov GV, Zyabkin VA (1971) Neutron production in Pb at a depth of 150 m w.e. under the influence of cosmic-radiation mesons traveling at large zenith angles (trans: Adashko JG). *Sov J Nucl Phys* 12(2):187–190. Orig. pub. as *Yad Fiz* 12:340–346 [in Russian]
31. Gorshkov GV, Zyabkin VA, Yakovlev RM (1974) Production of neutrons in Pb, Cd, Fe, and Al by high energy muons (trans: Adashko JG). *Sov J Nucl Phys* 18(1): 57–61. Orig. pub. as *Yad Fiz* (1973) 18:109–117 [in Russian]

32. Gorshkov GV, Zyabkin VA, Yakovlev RM (1971) Production of neutrons in Pb, Cd, Fe, and Al and fission of Pb nuclei by cosmic rays in the depth range 0–1000 m water equiv (trans: Robinson CS). Sov J Nucl Phys 13(4):450–452. Orig. pub. as *Yad Fiz* 13:791–796 [in Russian]
33. Griest K, Kamionkowski M (2000) Supersymmetric dark matter. *Phys Rep* 333–334:167–182. doi:[10.1016/S0370-1573\(00\)00021-1](https://doi.org/10.1016/S0370-1573(00)00021-1)
34. Hoekstra H, Jain B (2008) Weak gravitational lensing and its cosmological applications. *Annu Rev Nucl Part Sci* 58(1):99–123. doi:[10.1146/annurev.nucl.58.110707.171151](https://doi.org/10.1146/annurev.nucl.58.110707.171151)
35. Horn OM (2007) Simulations of the muon-induced neutron background of the EDELWEISS-II experiment for Dark Matter search. Scientific report FZKA 7391. Forschungszentrum Karlsruhe. <http://bibliothek.fzk.de/zb/berichte/FZKA7391.pdf>. Orig. pub. as PhD dissertation, Universität Karlsruhe (TH) <http://digibib.ubka.uni-karlsruhe.de/volltexte/1000007402>
36. Kudryavtsev V, Pandola L, Tomasello V (2008) Neutron- and muon-induced background in underground physics experiments. *Eur Phys J A* 36(2):171–180. doi:[10.1140/epja/i2007-10539-6](https://doi.org/10.1140/epja/i2007-10539-6)
37. Lindote A et al (2009) Simulation of neutrons produced by high-energy muons underground. *Astropart Phys* 31:366–375. doi:[10.1016/j.astropartphys.03.008](https://doi.org/10.1016/j.astropartphys.03.008). arXiv:[0810.1682](https://arxiv.org/abs/0810.1682) [hep-ex]
38. Mal'gin A, Ryazhskaya O (2008) Neutrons from muons underground. *Phys At Nucl* 71(10):1769–1781. doi:[10.1134/S1063778808100116](https://doi.org/10.1134/S1063778808100116)
39. Mariani C (2012) Review of reactor neutrino oscillation experiments. *Mod Phys Lett A* 27(8):1230010. doi:[10.1142/S0217732112300108](https://doi.org/10.1142/S0217732112300108). arXiv:[1201.6665](https://arxiv.org/abs/1201.6665) [hep-ex]
40. Martin SP (2008) A supersymmetry primer. arXiv:[hep-ph/9709356](https://arxiv.org/abs/hep-ph/9709356)
41. Perkins DH (1984) Proton decay experiments. *Annu Rev Nucl Part Sci* 34(1):1–50. doi:[10.1146/annurev.ns.34.120184.000245](https://doi.org/10.1146/annurev.ns.34.120184.000245)
42. Reichhart L et al (2013) Measurement and simulation of the muon-induced neutron yield in lead. *Astropart Phys* 47:67–76. doi:[10.1016/j.astropartphys.2013.06.002](https://doi.org/10.1016/j.astropartphys.2013.06.002). arXiv:[1302.4275](https://arxiv.org/abs/1302.4275) [physics.ins-det]
43. Samtleben D, Staggs S, Weinstein B (2007) The cosmic microwave background for pedestrians: A review for particle and nuclear physicists. *Annu Rev Nucl Part Sci* 57(1):245–283. doi:[10.1146/annurev.nucl.54.070103.181232](https://doi.org/10.1146/annurev.nucl.54.070103.181232)
44. Schmidt B et al [EDELWEISS Collaboration] (2013) Muon-induced background in the EDELWEISS dark matter search. *Astropart Phys* 44:28–39. doi:[10.1016/j.astropartphys.2013.01.014](https://doi.org/10.1016/j.astropartphys.2013.01.014). arXiv:[1302.7112](https://arxiv.org/abs/1302.7112) [astro-ph.CO]
45. Signer A (2009) ABC of SUSY. *J Phys G Nucl Part Phys* 36(7):073002. doi:[10.1088/0954-3899/36/7/073002](https://doi.org/10.1088/0954-3899/36/7/073002). arXiv:[0905.4630](https://arxiv.org/abs/0905.4630) [hep-ph]
46. Sofue Y (2012) A grand rotation curve and dark matter halo in the Milky Way galaxy. *Publ Astron Soc Japan* 64(4):75. arXiv:[1110.4431](https://arxiv.org/abs/1110.4431) [astro-ph.GA]. <http://www.ioa.s.u-tokyo.ac.jp/~sofue/htdocs/2012DarkHalo/>
47. Treu T (2010) Strong lensing by galaxies. *Annu Rev Astron Astrophys* 48(1):87–125. doi:[10.1146/annurev-astro-081309-130924](https://doi.org/10.1146/annurev-astro-081309-130924)
48. Trimble V (1987) Existence and nature of dark matter in the universe. *Annu Rev Astron Astrophys* 25:425–472. doi:[10.1146/annurev.aa.25.090187.002233](https://doi.org/10.1146/annurev.aa.25.090187.002233)
49. Wang Y-F et al (2001) Predicting neutron production from cosmic-ray muons. *Phys Rev D* 64:013012. doi:[10.1103/PhysRevD.64.013012](https://doi.org/10.1103/PhysRevD.64.013012). arXiv:[hepex/0101049](https://arxiv.org/abs/hepex/0101049)
50. Wulandari H et al (2004) Neutron background studies for the CRESST dark matter experiment. arXiv:[hep-ex/0401032v1](https://arxiv.org/abs/hep-ex/0401032v1)
51. Zbiri K (2010) Remark on the studies of the muon-induced neutron background in the liquid scintillator detectors. *Nucl Instrum Methods Phys Res Sect A* 615(2):220–222. doi:[10.1016/j.nima.2010.01.035](https://doi.org/10.1016/j.nima.2010.01.035)
52. Zwicky F (1933) Die Rotverschiebung von extragalaktischen Nebeln [in German]. *Helv Phys Acta* 6(2):110–127. doi:[10.5169/seals-110267](https://doi.org/10.5169/seals-110267)

# Chapter 2

## Searching Dark Matter: The Quest for the Missing Mass

An increasing number of observations indicates the existence of *dark matter*, which led to one of the greatest discoveries of modern physics: the well known normal matter is only a minor contribution to the total matter and energy content of the Universe. The major matter content of the Universe is of an unknown type. This results in a central question: what is the particle nature for dark matter? The fact that it cannot be one of the constituents of known matter is one of the strongest hints to a new kind of physics beyond the standard model of particle physics. Several experiments look for hints of this new physics, e.g. *direct searches* for dark matter like EDELWEISS.

One prominent candidate for dark matter is a *weakly interacting massive particle* (WIMP). If WIMPs are the constituents of dark matter, direct searches have to be sensitive to a very rare signal, i.e. around one interaction per tonne detector mass and per year observation time. Therefore, a detailed understanding of the background is needed to decrease the background rate below the expected interaction rate.

A central background for direct searches are muon-induced neutrons. To motivate the significance of muon-induced neutrons as background for the direct dark matter search with EDELWEISS, a summary of dark matter induced signals, and hence the properties of dark matter itself, is needed.

We will first review evidences for and properties of WIMP-like dark matter in Sect. 2.1. In Sect. 2.2, we give an overview of the current state of direct dark matter searches. Finally, in Sect. 2.3 experimental aspects of direct searches for WIMPs are discussed in more detail on the example of EDELWEISS. As an important background for direct searches, muon-induced neutrons will be the topic of Chap. 3.

### 2.1 Motivation for WIMP-Like Dark Matter

In this section we will motivate WIMP-like dark matter as solution of the *missing mass problem*. The defining property of *dark matter* is its non-luminosity as opposite to the luminous matter visible in astronomical observations, originally referred only to

the visible light [259], nowadays extended to other wavelength ranges like infrared, X-rays, gamma-rays, and even particles like  $\nu_e$  from the Sun or neutrinos from supernovae, often described as a *multi messenger approach* in astroparticle physics. Under the assumption that Newtonian physics is valid for the description of non-relativistic dynamics, the dynamical behaviour of gravitationally bound systems can not be explained by their visible mass alone, raising the *problem of missing mass*.

Astronomical indications for dark matter as solution for the missing mass problem will be given in Sect. 2.1.1. Thereafter, we introduce a supersymmetric WIMP as one possible particle candidate for dark matter (Sect. 2.1.2).

To detect dark matter and to specify its properties, three experimental approaches are viable: *accelerator based* experiments including the search for the missing transverse momentum associated with the production of dark matter (Sect. 2.1.3), *indirect detection* experiments searching for the products of dark matter self-annihilation (Sect. 2.1.4), and *direct detection* experiments searching for the scattering of galactic dark matter off terrestrial targets (Sect. 2.1.5).

We will review the first two approaches briefly and will focus on direct detection with the example of EDELWEISS in the next two Sects. 2.2 and 2.3.

### 2.1.1 Dark Matter as Solution for the Missing Mass Problem

We will first motivate dark matter as solution to the problem of missing mass via a historic review of classic indications relying on the dynamical behaviour of gravitationally bound systems, like galaxy clusters and galaxies,<sup>1,2</sup> Afterwards, we will discuss the standing of the dark matter paradigm against the alternative solution of modified gravity on the example of weak gravitational lensing. Possible particle candidates for dark matter will be discussed in Sect. 2.1.2.

In the original meaning as non-visible mass, F. Zwicky used the term in 1933 to describe the discrepancy between the mass of luminous matter and the total, dynamic mass he observed in the Coma cluster, a gravitationally bound group of galaxies [325, pp. 124f.], [326].

F. Zwicky's original intention was to determine the velocity of Coma for a further validation of Hubble's law, the proportionality between distance and velocity of an astronomical object. In his work F. Zwicky noted an unusual great spread of the single galaxies within the cluster. By applying the virial theorem<sup>3</sup>

---

<sup>1</sup>We find it convenient to the focus on gravitationally bound systems like our Galaxy in contrast to cosmological arguments because the experiments reported in Sect. 2.2 search for dark matter in the galactic halo.

<sup>2</sup>Besides these selected cases, further indications for dark matter in the sense of missing mass related to the dynamics in gravitationally bound astronomical systems, e.g. binary galaxies, are listed in [312].

<sup>3</sup>In his original work, F. Zwicky denotes Newtons gravitational constant, nowadays usually abbreviated as  $G$ , with  $\Gamma$ .

$$M = \frac{5R\bar{v}^2}{3G} \quad (2.1)$$

on the mean velocity of the clusters galaxies  $\sqrt{\bar{v}^2} = 1000 \text{ km s}^{-1}$  he found a dynamical mass  $M$  within the cluster radius  $R$  of 400-times the mass of luminous matter of the cluster. The latter one he approximated as the number of cluster galaxies times the averaged galaxy mass. The discrepancy between dynamical mass and luminous mass he attributed to a non-luminous, hence *dark*, mass that contributes to the dynamics of the cluster.

The discrepancy observed by F. Zwicky was confirmed over the last 80 years and is still valid. After his introduction of the virial theorem in astronomy [86], other galaxy clusters and groups were weighted with the same technique. So find R. Carlberg et al. [140] by averaging over 16 clusters with roughly 1000 galaxies a mass-to-luminosity ratio of  $M/L = (295(53)) h M_{\odot} L_{\odot}^{-1}$  where  $h$  is the Hubble constant and  $M_{\odot}$  ( $L_{\odot}$ ) the mass (luminosity) of the sun. For galaxy groups, like the local group containing the Milky Way, a smaller ratio of  $M/L \approx 12 M_{\odot} L_{\odot}^{-1}$  is found [209, 230]. The difference in  $M/L$  can be explained by assuming that big galaxy clusters are dominated by the dark matter distributed throughout their gravitational well, whereas small-size galaxy groups are dominated by dark matter concentrated around the single galaxies [209].

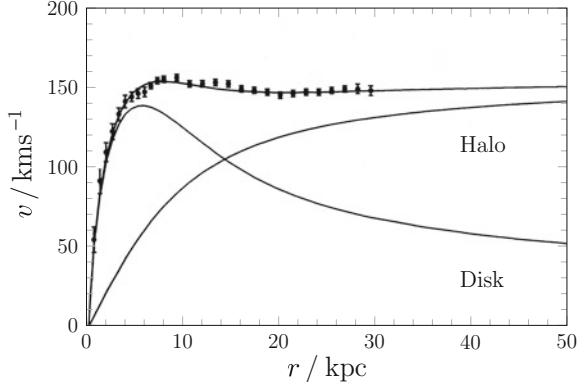
The concept of dark matter concentrated around single galaxies was first applied in 1970 by K.C. Freeman for the galaxies M33 and NGC300. Again, a discrepancy between luminous matter and dynamical mass could be derived. In the *rotation curves*  $v - r$ , see e.g. Fig. 2.1 for a more recent example, he recognized a deviation of the orbits of stars around the galaxy centre from the Keplerian predictions (the *disk*-curve in Fig. 2.1): beyond a characteristic radius that depends on the actual mass-density profile of the galaxy, a drop of rotation velocity  $v$  inversely proportional to the radius  $r$  of the orbit is expected:  $v^2 \propto 1/r$ . He found no such drop in the rotation curve  $v - r$  over the whole visible galaxy (visible light and radio emissions) and concluded the existence of additional ‘undetected matter’, extending further than the luminous matter [184, p. 828], [185].

In 1974, the dark matter within the galaxy clusters was connected to the dark matter in individual galaxies. The existence of ‘coronas’ [167] or ‘spheres’ [260] of dark matter around galaxies were postulated after it was found that the stars orbits could be explained by a spherical distribution of additional dark matter. These *dark halos* as they are called today are therefore also contributing to the mass of the host galaxy cluster. For example, Fig. 2.1 shows a fit of a spherical dark halo on the rotation curve of NGC 3198.<sup>4</sup>

Finally V.C. Rubin, N. Thonnard, and W.K. Ford Jr. showed in 1980 by the then largest systematic observation of galactic rotations that the anomalous rotation curves were no exception. Contrary, they found out of 21 spiral galaxies no single one that followed the expected Keplerian behaviour [274]. Five years later, V.C. Rubin et al.

<sup>4</sup>Albeit J. Einasto, A. Kaasik, and E. Saar provide an earlier fit of a dark halo to a rotation curve in [167], we chose the example of [48] for the sake of clarity as it shows the individual components.

**Fig. 2.1** Observed rotation curve of NGC 3198 (data points), i.e. circular velocity  $v$  of stars as function of their distance to the galaxy centre  $r$ , fitted by a combination of an exponential disk containing the visible mass and a dark, spherical halo. Figure adapted from [48, Fig. 4]



could describe the rotation curves for all spiral galaxies of a given type and luminosity  $L$  with one general formula, after the radius  $r$  is scaled to the optical radius  $r_{\text{opt}}$ , at which the luminosity drops under a certain threshold. Additionally, the similarity between these general curves was noted [275]. And in the 1990s, it was shown by M. Persic and P. Salucci that the rotation curve  $v(r/r_{\text{opt}})$  of all spiral galaxies can be described by the same formula after they were normalized to the total luminosity  $L_*$ , assuming a visible disk and a dark halo [262, 263]. This universal rotation curve was then reproduced in 1996 by numerical simulation of the galaxy formation, assuming a *Navarro-Frenk-White* (NFW)-distribution of the dark matter density  $\rho(r)$  [250, 251], which can be parametrized as [121]

$$\rho = \frac{\rho_0}{\left(\frac{r}{R}\right)^\gamma \left[1 + \left(\frac{r}{R}\right)^\alpha\right]^{(\beta-\gamma)/\alpha}} \quad (2.2a)$$

$$\alpha = 1.0, \quad \beta = 3.0, \quad \gamma = 1.0, \quad R = 20 \text{ kpc} \quad (2.2b)$$

with the dark matter density of the halo  $\rho_0$  and a characteristic scale  $R$ . However, the behaviour of the rotational curve near the galactic centre is debatable, see the reviews in [121, 206], and several models for the halo exist, see references in [97, 169, 207]. Also the existence of substructure of dark matter clumps is discussed [107]. Nevertheless, the given NFW-model fits well the outer parts of the galaxies, as Fig. 2.2 shows for the example of our Galaxy. The existence of dark matter in our Galaxy indicates also the possibility to detect dark matter with earth based experiments, which will be discussed in Sect. 2.1.5.

The cluster and rotation curves are clear indications of missing matter, but no final proofs. The observed discrepancy may be explained not only by dark matter, i.e. correcting our experimental knowledge about the source distribution of gravity, but also by modifying gravity, i.e. correcting our theoretical model of gravity.

To explain the missing mass problem without an introduction of an additional kind of matter, M. Milgrom proposed in 1983 a modification of Newton's second law [242]. As M. Milgrom pointed out, all experimental validation of Newton's

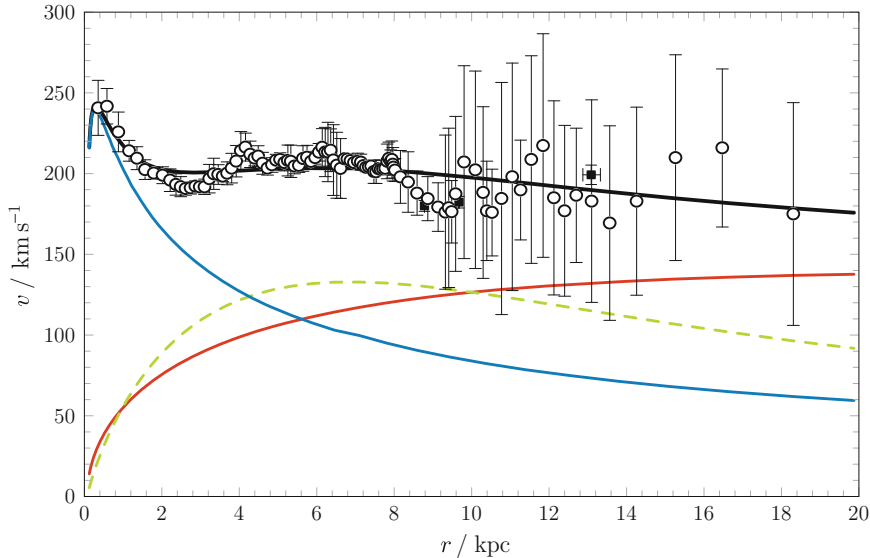


**Fig. 2.2** Rotation curve of the Milky Way, i.e. circular velocity  $v$  as function of the distance  $r$  to the galactic center, for the innermost 20 kpc. Fitted to the data points are the sum (black line) of three components: A visible bulge (blue line) and disk (dashed green line), together with a dark halo based on a NFW-parametrisation (red line). Figure adapted from [293, Figs. 2 and 5], references for the data compilation therein

second law were made within the range of our solar system and for accelerations higher than the typically intra-galactic accelerations. Therefore it may be possible that on intra-galactic scales the inertial force and the gravitational mass of a body is not anymore related by Newton's second law, but by a more generalized function  $\mu(x)$  [242, p. 366]:

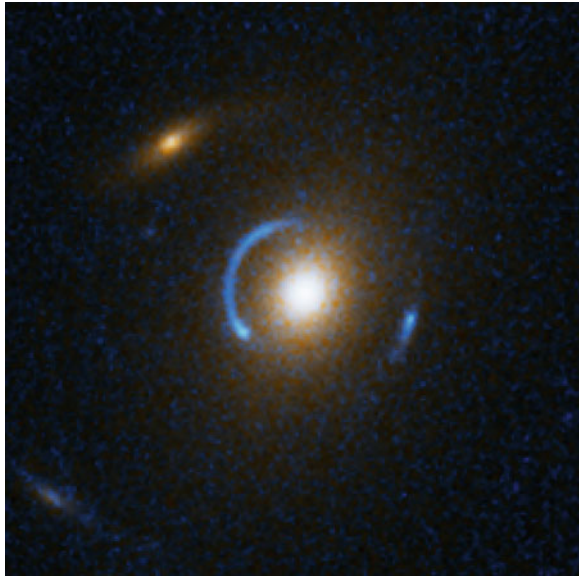
$$\vec{F} = \vec{a} \cdot \mu(a/a_0) \cdot m_g \quad (2.3)$$

known as *Modified Newtonian Dynamics* (MOND). By demanding that for accelerations higher than a threshold  $a_0$  Newton's second law is valid  $\mu(x \gg 1) \approx 1$ , and that for accelerations below the threshold a modification  $\mu(x \ll 1) \approx x$  occurs, the function  $\mu(x)$  is constrained.

M. Milgrom noted a good reproduction of the rotation curves for  $a_0 \approx 2.10^{-8} \text{ cm s}^{-2}$  without the need of non-visible mass [243]. As all the systems under considerations are bound by gravity the modified dynamics (Eq. 2.3) can be expressed by a modified gravitational field [242]: But as M. Milgrom stated himself: The modification “can at most be considered an effective working formula. [...] We are thus still in need of a theory for the modified dynamics even in the nonrelativistic regime” [242, p. 366].

A non-relativistic theory of gravity leading to Eq. 2.3 was first given by Bekenstein and Milgrom [92], and named AQUAL (derived from *AQuadratic Lagrangian* [95]):

**Fig. 2.3** Einstein ring SDSS J120540.43+491029.3: Multiple, arc-like images of a background galaxy (blue) caused by strong gravitational lensing from a foreground galaxy (center, yellow) [187]. Picture reprinted from [294]. Credit NASA, ESA, A. Bolton (Harvard-Smithsonian CfA) and the SLACS Team



the Lagrangian leading to the Poisson equation for the gravitational potential  $\Phi$  is no longer quadratic in  $\nabla\Phi$ , but depends on  $f((\nabla\Phi)^2/a_0^2)$  instead. For  $f(x^2) = \mu(x)$ , the dynamics described by Eq. 2.3 follow. AQUAL fits the rotation curves of several hundred galaxies as successfully as MOND [95, 278], but it is challenged by results from *gravitational lensing*: the gravitational potential of a mass in the foreground causes a distortion of background light sources, ranging from a slight shearing of the background image (*weak gravitational lensing* [201]) to the split into multiple images (*strong gravitational lensing* [311]). Strong lensing is in tension with MOND/AQUAL, as it reveals a missing mass problem also in regions of galaxies where  $a > a_0$ , i.e. where MOND/AQUAL behaves by definition Newtonian, leading again to the need of dark matter [176]. However, the possibility remains that gravitational lensing in a relativistic formulation of AQUAL could behave differently [176]. A relativistic theory of MOND/AQUAL is TeVeS (derived from *Tensor-Vector-Scalar* [93]), in the sense that the non-relativistic limit is AQUAL. The success of TeVeS to explain strong lensing is controversial. It is claimed [95, 154], that TeVeS can explain strong lensing systems like SDSS J120540.43+491029.3 [154], see Fig. 2.3, with an additional amount of neutrinos with  $m_\nu \approx 2\text{eV}$  [150]. However, even with such massive neutrinos, more recent investigations claim that TeVeS will fail to explain strong lensing without additional, non-neutrino dark matter [178]. Contrary, dark matter can explain the observed strong lensing, like Fig. 2.3 [177], without modifying gravity.

The challenge for theories like TeVeS is even greater for *weak gravitational lensing*: An example for a system showing weak gravitational lensing is the galaxy cluster 1E 0657–558, named *Bullet Cluster*, which consists of two sub-cluster, one less massive than the other [156], see Fig. 2.4. Both are moving away from each other, after

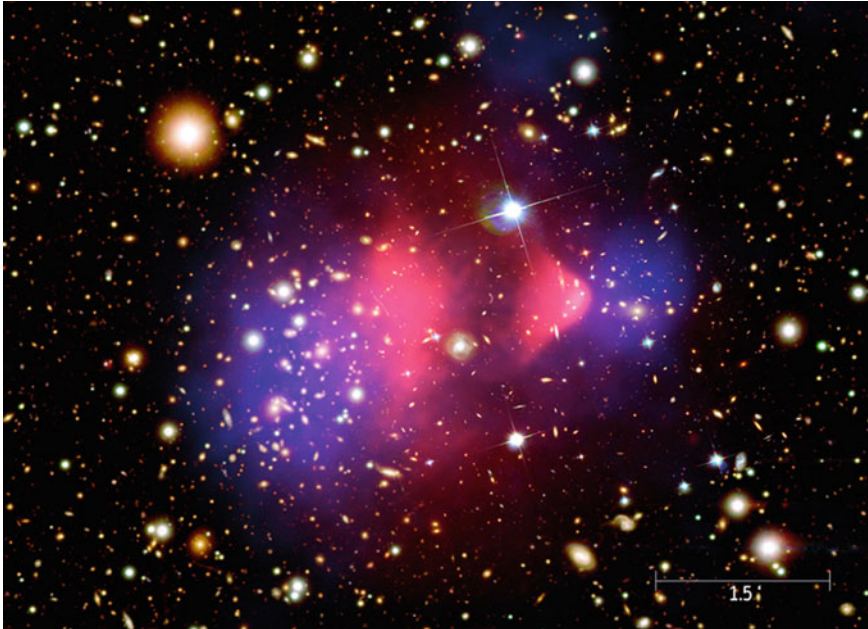


**Fig. 2.4** Galaxy cluster merger 1E 0657–558 ('bullet cluster') observed via X-rays (red) and the corresponding shear map (blue) obtained via weak gravitational lensing [156]. Via self-interaction, the hot intracluster medium was slowed down and is nowadays located in the centre of the cluster. In the dark matter paradigm, the shear field shows that most of the gravitating mass is different from the intracluster medium and located at the position of the sub-clusters. In modified gravity paradigm, the difference between the peaks in sheer field are caused by the intracluster medium via position dependent gravitational coupling. For details see text. Picture reprinted from [198]. Credit X-ray: NASA/CXC/CfA/M.Markevitch et al.; Optical: NASA/STScI; Magellan/U.Arizona/D.Clowe et al.; Lensing Map: NASA/STScI; ESO WFI; Magellan/U.Arizona/D.Clowe et al.

the cluster cores passed through each other in a collision roughly 100 million years ago [156]. While the single galaxies of the sub-clusters were not affected by the collision, acting as collision-less particles, the hot intracluster medium, containing most of the visible mass [248], acts fluid-like and was heated. The location and extension of the intracluster medium therefore can be tracked by the X-ray emission. The total gravitational mass of the cluster can be traced by weak gravitation lensing which causes a distortion of the shape of a background object. As the original shape of a single background object is unknown, the average shape over a sample of background objects away from the cluster can serve as reference and can then be compared with the average shape of background objects behind the cluster. The resulting shear map is related with the mass density map via the theory of gravitation under consideration, for an overview over weak lensing see [201]. The X-ray observations reveal that the intracluster medium is located roughly in the middle between the visible centres of the sub-clusters. In contrast, the mass-density map revealed from the weak lensing

observations shows two centres coincident with the centres of the visible sub-cluster. The superposition of both observations results in the famous Fig. 2.4, resembling a blue bullet (mass density of the smaller cluster) punching through a red wall (X-ray emission of intracluster medium), hence the popular name of the cluster.<sup>5</sup>

Whereas the astronomical observation could be reproduced with other clusters (see [130] and references therein), the interpretation of the observations depends on the used paradigm. Supporters of both paradigms agree that nearly the total of the luminous mass is traced via X-ray emission. But the interpretation of the shear map is different:

For a MOND based theory like TeVeS, the centre of baryonic matter should coincide with the measured centres of shear [94, 170, 304], which is not the case. This is accepted by supporters of MOND, like J. D. Bekenstein:

[TeVeS] does not account for the observed distortion [of weak lensing] without the help of invisible matter [=dark matter] in addition to a reasonable dose of massive neutrinos. [...] dramatized by a handful of colliding clusters, [...] MOND has never dealt perfectly with the dynamics of clusters. So TeVeS, which was designed with MOND in mind, could not [be] expected to do well in this business, and modification of it may be in order. [...] clusters may well contain large amounts of as yet invisible [baryonic] matter [95, p. 559c]

However, more generalized theories of gravity can accommodate to this difference by introducing a position dependent gravitational coupling [245].

Within the dark matter paradigm, the centres of the shear map are coincident with the centres of collisional-less dark matter. As the dark matter halos of the sub-cluster do not interact with each other during the collision, like the visible cluster content, they are already separated again, and coincident with the centre of the visible sub-clusters [156]. If the dark matter paradigm is correct, such cluster merger would allow to measure the self-interaction rate of dark matter [267]. In general, weak lensing is a suitable tool to map the large scale distribution of dark matter [164, 270], e.g. in galaxy clusters like Cl0024+17 [205], see Fig. 2.5.

In summary, over the last 80 years, astronomical observations from galaxies clusters and single galaxies showed strong evidence for a gap between the visible mass and the dynamic mass of the system, leading to the problem of missing mass. Proposed solutions are additional *dark matter* or a modified theory of gravity like *MOND*. Strong and weak gravitational lensing reject the simpler MOND-like theories. The remaining, more complex theories are forced to incorporate an additional amount of dark matter in form of massive neutrinos and baryonic matter, contrary to their original intention. Albeit this does not disprove theories of modified gravity as possible explanation for the missing mass problem, it certainly reduces their attractivity. The identification of a new kind of particles leading to the density distributions needed to substitute the dark halos would be a strong support for the dark matter paradigm and disfavour an explanation of the missing mass problem by modified gravity. Needed properties for such a particle candidate and its galactic distribution are the topic of Sect. 2.1.2.

---

<sup>5</sup>Some of the X-ray features, like the red bow shock behind the blue bullet in Fig. 2.4, are also visible by radio observations of the cluster [232, 286].

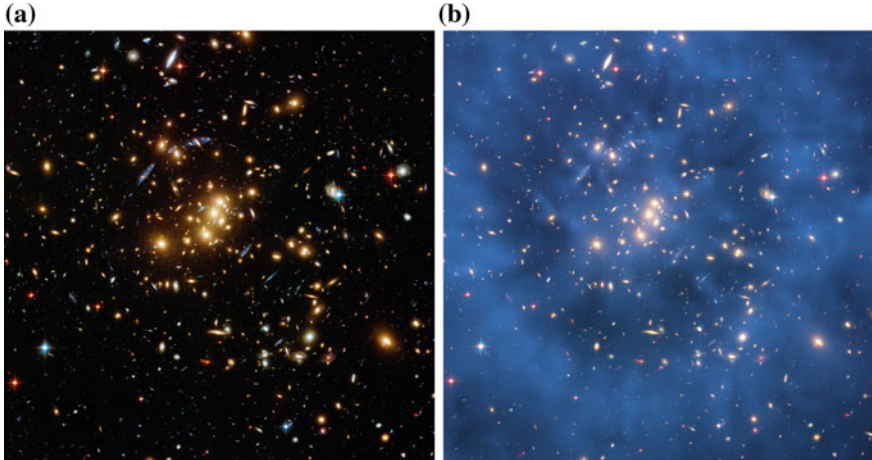


**Fig. 2.5** **a** The rich galaxy cluster Cl0024+17 features both weak and strong gravitational lensing, the latter is visible as *arc* like structure around the centre of the image. *Credit* NASA, ESA, M.J. Jee and H. Ford (Johns Hopkins University). **b** Based on weak and strong gravitational lensing, the projected distribution of dark matter is obtained as *ring* like structure (*blue*) around the cluster center. The ring structure may be the result of a high-speed collision of two clusters along the line-of-sight [205]. *Credit* NASA, ESA, M.J. Jee and H. Ford (Johns Hopkins University). Pictures reprinted from [295]

### 2.1.2 Supersymmetric WIMPs as Dark Matter Candidates

The astronomical observations discussed in the previous section, ranging from velocity dispersion in galaxy clusters over galactic rotation curves to weak lensing maps of rich galaxy clusters, are strong evidences for dark matter. However, these observations do not reveal the constituents of dark matter. In this section, we will shortly review the properties for such constituents, deduced from astrophysical and cosmological observations. Subsequently, we list well motivated particle candidates for dark matter, focusing on the classic example of supersymmetric particles like the neutralino. In the next section we will review the impact of the Higgs discovery and the latest LHC results on the parameter space for supersymmetric *weakly interacting massive particles* (WIMPs) as candidates for cold, non-baryonic dark matter.

The observations reported in Sect. 2.1.1 show that dark matter is non-luminous and has a small self-interaction, as shown by merging clusters (Fig. 2.4). The merging clusters also show that at this length scale dark matter is mostly *non-baryonic*: the main mass is distinct from the intercluster medium [248], which contains most of the baryonic mass of a galaxy cluster [193] especially if it is traced until the outskirts of the cluster [290]. This is further supported by observations on galactic scale. A possible source for non-luminous, baryonic matter on galactic scale could be *massive compact halo objects* (MACHOs), e.g. in form of stellar remnants [141]. However, searches for microlensing events caused by the transit of such an MACHO in front

of a star could limit the MACHO contribution to the mass of the galactic halo to less than 8 % [307].

Large scale structures and their distribution can solve the question whether if the dark matter was non-relativistic (*cold*) or relativistic (*hot*) at the time of recombination. The free-streaming of *hot dark matter*, like neutrinos, suppresses the growth of structures below a certain scale [124]. The comparison between observed and simulated matter power spectra ruled out a major contribution of hot dark matter [58, 305]. This is further supported by the success of N-body simulations based on *cold dark matter* (CDM) to reproduce the observed hierarchical clustering [252] from individual galaxies [196, 214] over galaxy clusters [216] to super clusters [298] in the local universe. An often quoted disadvantage of CDM structure formation is the over-prediction of smaller dark halos (see [215] and references therein). If they are identified as hosts of dwarf galaxies, then the simulated numbers are often in disagreement with the observed number of dwarf galaxies. However, recent simulations reduce the predicted numbers of dwarf galaxies by tidal disruption caused by bigger galaxies nearby [166, 291] and by feed-back of star formation, supernovae wind, and ultraviolet radiation of the luminous matter [188, 194]. Also newer observations increased significantly the number of ultra-faint dwarf galaxies [99, 308] and dark matter dominated satellites [314]. Combining both effects, an agreement between simulations and observations seems possible. Recent weak lensing observation confirms also the predicted filaments of CDM between individual galaxies [164].

From studies of the *cosmic microwave background* (CMB), the energy density  $\Omega$  in units of the critical density (see Eq. A.7) of the total non-relativistic matter ( $\Omega_m$ ), of the baryonic matter ( $\Omega_b$ ), and of active neutrinos ( $\Omega_\nu$ ) can be deduced on cosmological scale. As neutrinos affect the matter power spectrum,  $\Omega_\nu$  can be deduced from its effect on the CMB via weak gravitational lensing since the time of recombination [226]. The peak-height ratio of the acoustic oscillations in the CMB power spectrum (Fig. 2.6) are sensitive to  $\Omega_m$ ,  $\Omega_b$  at the time of recombination [203, 277]. Consequently, the cold dark matter density can be calculated:  $\Omega_{cdm} = \Omega_m - \Omega_b$ . Observation of the CMB with the PLANCK satellite [28] gives the latest values for the energy densities<sup>6</sup>:

$$\Omega_m = 0.313 \quad (2.4a)$$

$$\Omega_{cdm} = 0.263 \quad (2.4b)$$

$$\Omega_b = 0.0486 \quad (2.4c)$$

$$\Omega_\nu < 0.0156 \quad (2.4d)$$

---

<sup>6</sup>The energy densities for matter, cold dark matter, and baryons are calculated from the PLANCK best fit values  $\Omega_m h^2 = 0.1423$  [28, Eq. 15],  $\Omega_{cdm} h^2 = 0.1196$  [28, Eq. 18], and  $\Omega_b h^2 = 0.02207$  [28, Eq. 17] with a Hubble constant of  $H_0 = h \cdot 100 \text{ km s}^{-1} \text{Mpc}^{-1} = 67.4 \text{ km s}^{-1} \text{Mpc}^{-1}$  [28, Eq. 13]. The energy density of active neutrinos is based on  $\Omega_\nu h^2 = \sum_i m_i / 93.14 \text{ eV}$  [226, 296] with  $\sum_i m_i < 0.66 \text{ eV}$  [28, Eq. 69]. All densities are given to three decimal places.

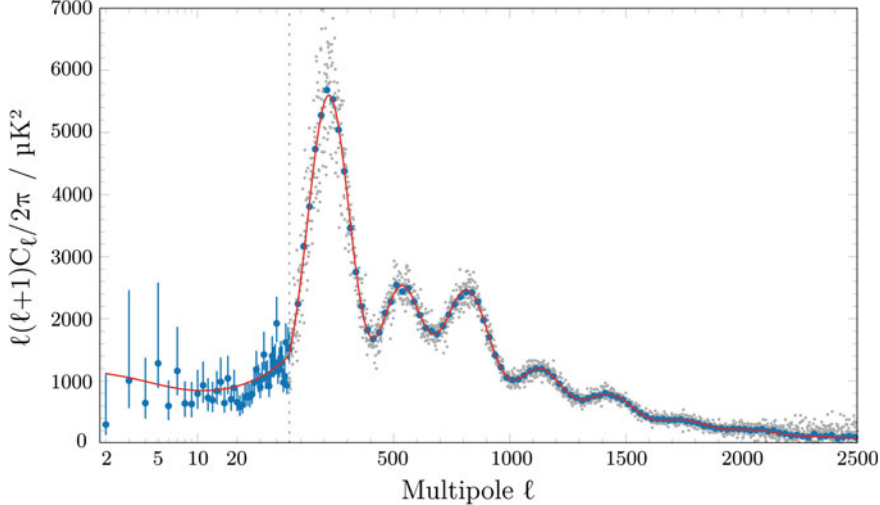


**Fig. 2.6** Foreground-subtracted temperature power spectrum on a logarithmic-linear hybrid scale as observed by Planck. Power spectrum shown as multipole-by-multipole (grey points) and averaged over width of 31 (blue). The red line shows the temperature spectrum for the best-fit based  $\Lambda$ CDM cosmology. The dashed line indicates the change from logarithmic scale to linear scale. Figure and description adapted from [28, Fig. 1]

The relative small contribution of baryonic matter is in agreement with results from the big bang nucleosynthesis [301]. These numbers clearly show that most of the matter content of the Universe is provided by non-baryonic, cold dark matter.

According to the production process, candidates for nonbaryonic CDM are divided into two groups, either being produced in nonthermal processes or produced in thermal equilibrium in the early universe, hence called *thermal relict*. Even particles from both categories may contribute to the observed  $\Omega_{\text{cdm}}$  in context of multicomponent scenarios [120, 173].

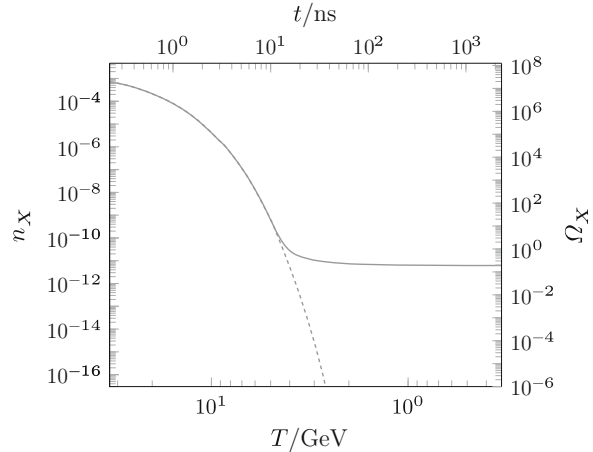
An example for nonthermally produced candidates is the *axion*. It is the pseudo-Nambu-Goldstein boson of the Peccei-Quinn symmetry postulated to solve the strong CP problem [212, 261]. If the Peccei-Quinn symmetry exists, it would be broken by the Peccei-Quinn phase transition when the Universe cools below the axion decay constant  $f_a$ , resulting in the nonthermal production of axions with mass  $m_a$ . As the axion is not yet observed, the observed  $\Omega_{\text{cdm}}$  can be produced by a wide range of the axion parameter space [173]:

$$10^{12} \text{ GeV} \theta^{-2} \gtrsim f_a \gtrsim 10^9 \text{ GeV} \quad (2.5)$$

$$6 \mu \text{eV} \theta^2 \lesssim m_a c^2 \lesssim 6 \text{ meV},$$

where  $\theta \lesssim 1$  depends on the phase transition.

**Fig. 2.7** Comoving number density  $n_X$  and resulting relic density  $\Omega_X$  as function of the temperature  $T$  and age  $t$  of the Universe for a WIMP with 100 GeV. The *solid line* is the number density of a particle that freezes out, the *dashed line* for a particle that remains in thermal equilibrium. Figure adapted from [173, Fig. 2]



A thermal relic particle  $X$  produced in the early universe, was initially in thermal equilibrium. When the temperature  $T$  drops below the particle mass  $m_X$ , its comoving number density  $n_X$  becomes Boltzmann suppressed:  $n_X \sim (m_X T / 2\pi)^{3/2} \exp(-m_X / T)$  [173, 206]. As the Universe expands with the inverse Hubble's constant  $1/H$ , the particles eventually become chemically decoupled [269], and they *freeze out* as their number density approaches a constant *relic density* [153, 323]. The actual evolution of the number density  $n_X$  is described by the Boltzmann equation [173, 206],

$$\frac{dn_X}{dt} = -3Hn_X - \langle \sigma_a v \rangle (n_X^2 - n_{X,\text{eq}}^2) \quad (2.6)$$

where  $\langle \sigma_a v \rangle$  is the thermal average of the annihilation cross section times the relative velocity and  $n_{X,\text{eq}}$  is the number density in thermal equilibrium. A numerical solution is shown in Fig. 2.7. The number density  $n_f = H/\langle \sigma_a v \rangle$  at decoupling can be approximated as [173]

$$n_f \simeq \frac{T_f^2}{m_{\text{Pl}} \langle \sigma_a v \rangle}, \quad (2.7)$$

with the Planck mass  $m_{\text{Pl}}$  and the freeze-out temperature  $T_f$ . This leads to a present day relic density of [173]:

$$\Omega_X \sim \frac{m_X T_0^3}{\rho_c m_{\text{Pl}} T_f} \langle \sigma_a v \rangle^{-1}. \quad (2.8)$$

For a weakly interacting particle, the cross section can be approximated in leading order by [173]

$$\sigma_a v \approx \frac{g^4}{16\pi^2 m_X^2} \begin{cases} 1, & \text{S-wave annihilation} \\ v^2, & \text{P-wave annihilation} \end{cases} \quad (2.9)$$

with the weak interaction gauge coupling  $g \simeq 0.65$ . As a consequence, the *WIMP miracle* [173, 206] occurs: Each *weakly interacting massive particle* (WIMP) with  $m_X \sim 1 \text{ TeV}$  can produce the observed amount ( $\Omega_X \sim \Omega_{\text{cdm}}$ ) of cold ( $T_f \approx m_X/20$  [186, 206]) dark matter. To reproduce the observed dark matter abundance (Eq. 2.4b), an annihilation cross section of [264]

$$\langle \sigma_a v \rangle \approx 3 \times 10^{-26} \text{ cm}^3 \text{ s}^{-1} \quad (2.10)$$

is necessary.

Several theories like universal extra dimensions or *supersymmetry* (SUSY) can motivate particle candidates that qualify as WIMPs [173]. In the following we will focus on the classical example of supersymmetric WIMPs.

SUSY is a symmetry between bosons and fermions: it transforms each boson (fermion) of the standard model of particle physics, called *particle*, in a yet undiscovered fermion (boson), called *sparticle*, and vice versa [240]. Supersymmetry is motivated by the *gauge hierarchy problem* of the standard model: the loop-corrections  $\Delta m_b$  of the Higgs mass  $m_h^2 = m_{h0}^2 + \Delta m_h^2$  are only limited by an ultraviolet momentum cut-off  $\Lambda$ . The cut-off is assumed to be on the order of the Planck mass  $m_{\text{Pl}}$  where the standard model is expected to break down [173, 240]:

$$\Delta m_h^2 \sim \frac{\lambda^2}{16\pi^2} \int^\Lambda \frac{d^4 p}{p^2} \sim \frac{\lambda^2}{16\pi^2} \Lambda^2, \quad (2.11)$$

with a dimensionless coupling  $\lambda \sim \mathcal{O}(1)$ .

However, the recent discovery of the Higgs boson [2, 147] fixed its mass to  $126 \text{ GeV} \ll m_{\text{Pl}}$ , i.e. the single contributions to the loop correction must cancel out within 1 part in  $10^{36}$  [173]. As the contribution of fermions to Eq. 2.11 differs from the contribution of bosons by a sign change, an exact SUSY would lead to the needed cancellation as it provides a fermionic (bosonic) sparticle for every bosonic (fermionic) particle. As up to now no sparticles were detected, they must be heavier than the standard model particle, and hence SUSY must be broken with a mass splitting between particles  $m_{\text{SM}}$  and corresponding sparticle  $m_{\text{SUSY}}$ . This results in a loop correction to the Higgs mass of [173, 240]:

$$\Delta m_h^2 \sim \frac{\lambda^2}{16\pi^2} \int^\Lambda \frac{d^4 p}{p^2} \Big|_{\text{SM}} - \frac{\lambda^2}{16\pi^2} \int^\Lambda \frac{d^4 p}{p^2} \Big|_{\text{SUSY}} \quad (2.12)$$

$$\sim \frac{\lambda^2}{16\pi^2} \left( m_{\text{SUSY}}^2 - m_{\text{SM}}^2 \right) \ln \frac{\Lambda}{m_{\text{SUSY}}}, \quad (2.13)$$

and therefore stabilizes the gauge hierarchy problem for  $m_{\text{SM}} \sim m_{\text{SUSY}} \ll m_{\text{Pl}}$ . From the experimental constraints on the Higgs mass, one can deduce the mass splitting, and therefore the mass of the *lightest supersymmetric particle* (LSP), to be of  $\mathcal{O}(1 \text{ TeV})$ . This is the same mass scale needed for a WIMP to produce the observed relic density  $\Omega_{\text{cdm}}$ . Quantitative constraints on the WIMP mass from global fits of SUSY to recent observations will be discussed in Sect. 2.1.3.

As further advantage, the LSP is stable in SUSY theories with preserved *R-parity*. The R-parity  $P_R$  of a given particle or sparticle is a discrete symmetry [240]

$$P_R = (-1)^{3(B-L)+2s} \quad (2.14)$$

$$= \begin{cases} +1, & \text{particle} \\ -1, & \text{sparticle} \end{cases} \quad (2.15)$$

associated with baryon-number  $B$ , lepton-number  $L$ , and spin  $s$ . It is motivated to prevent any baryon- and lepton-number violation, as under conserved R-parity only pairs of sparticle can be produced or annihilate. Consequently, a stable LSP results.

The *minimal supersymmetric standard model* (MSSM) contains all sparticle partners to the known particles, the latter are extended by an extra Higgs doublet [206], and it conserve R-parity [240]. Depending on the parameter space, the MSSM-LSP  $\chi$  is usually the lightest of four *neutralinos*  $\tilde{\chi}_1^0, \dots, \tilde{\chi}_4^0$ , i.e. it is a linear combination of *gauginos* ( $\tilde{B}, \tilde{W}^3$ ) and *higgsinos* ( $\tilde{H}_1^0, \tilde{H}_2^0$ ) [206, 240]:

$$\chi = n_{10}^* \tilde{B} + n_{20}^* \tilde{W}^3 + n_{30}^* \tilde{H}_1^0 + n_{40}^* \tilde{H}_2^0. \quad (2.16)$$

Here,  $\tilde{B}, \tilde{W}^3$  are the supersymmetric partners of the  $U(1)$  gauge field  $B$  and the third component of the  $SU(2)$  gauge field  $W^3$  that mix to the photon and  $Z^0$  boson, and  $\tilde{H}_1^0, \tilde{H}_2^0$  are neutral Higgs bosons [206].

Therefore, the neutralino provided by the MSSM is the classic example of a supersymmetric WIMP as particle candidate for non-baryonic, cold dark matter.

### 2.1.3 Constraints on the WIMP Parameter Space Including Latest LHC Results

As discussed in the previous section, a supersymmetric WIMP is a well motivated particle candidate for dark matter. Furthermore, the observed thermal relic abundance constrains the supersymmetric parameter space. Therefore the question arises whether this constraint is consistent with various accelerator based measurements which affect also the parameter space, like searches for sparticle production. A prominent example of a recent result that affects the parameter space is the discovery of the Higgs boson at the *Large Hadron Collider* (LHC).

This section starts with a short review of the relevant supersymmetric parameters in the most common models. Afterwards, we will list the most recent global fits [85, 137, 182, 302] to results from direct dark matter searches, thermal relic abundance, and results from the LHC. Finally, we note the implications for future direct searches for dark matter.

The general soft supersymmetry-breaking Lagrangian of the MSSM that is consistent with gauge invariance and R-parity conservation has 105 free parameter [240, Ref. 77]. Consequently, usually simplified phenomenological SUSY models are used

to interpret experimental results, like the *Constrained Minimal Supersymmetric Standard Model* (CMSSM) which serves as canonical model for supersymmetric studies [174]. In the CMSSM, the supersymmetry breaking is mediated by gravity, hence it is also called *minimal supergravity* (MSUGRA) [240, Refs. 152, 153]. The number of free parameter is reduced to 5 ( $m_0$ ,  $M_{1/2}$ ,  $A_0$ ,  $\tan \beta$ , sign  $\mu$ ) at the GUT scale  $\approx 2 \times 10^{16}$  GeV, under the three assumptions of [208]: a universal gaugino mass  $M_{1/2}$ , a universal scalar mass  $m_0$ , and a common trilinear scalar coupling  $A_0$ .

Some regions of the parameter space are named according to the possible interactions that could contribute to the LSP self-annihilation [240]: a resonance annihilation with the neutral Higgs scalar  $A^0$  of the MSSM is possible in the *A-funnel*, a coannihilation with the lightest stau or stop is possible in the *sfermion coannihilation region*,  $t$ -channel squark or slepton exchange and coannihilation can occur in the *focus point*.

Global fits of the CMSSM parameter space consider as inputs [85, 137, 182, 302]: the thermal WIMP relic abundance from CMB observations (see Sect. 2.1.2), limits from direct dark matter searches which will be discussed in Sects. 2.2 and 2.3, and constraints from accelerator results. Usually all of the following three categories of accelerator based observations are used to fit the CMSSM parameter space<sup>7</sup>:

As already mentioned in the previous section, the mass of the lightest Higgs boson is sensitive to the supersymmetric particle spectrum via radiative corrections [206]. Additional, SUSY may open new, invisible channels for the Higgs decay [139]. Recently, the ATLAS [2] and CMS [147] experiments discovered at the LHC a new particle at  $\approx 126$  GeV, consistent with evidence from the D0 and CDF experiments [11], and in agreement with the Higgs boson of the standard model. It is therefore an important test to reproduce this Higgs mass within the CMSSM.

It is expected that a hadron collider like the LHC will produce mainly colored supersymmetric particles [174] e.g. stops. As astronomical observation favours a weakly interacting LSP, the strong interaction particles have to decay. Their cascade decay to the LSP would cause a high jet ( $j$ ) multiplicity as signature [174, 221]. The signature for the LSP would be missing transverse energy ( $\cancel{E}_T$ ) in the final state accompanied by standard model particles [174]. Both ATLAS and CMS searched for these signatures in several final states, e.g.  $(\cancel{E}_T + j)$  [3, 83, 146, 211],  $(\cancel{E}_T + l)$  [1],  $(\cancel{E}_T + \gamma)$  [149],  $(\cancel{E}_T + l^+l^-)$  [148], but found no signal so far.

Also precision measurements of electroweak interactions, e.g. the anomalous magnetic moment of the muon  $a_\mu = (g_\mu - 2)/2$  [102], and b-physics is used to constrain the CMSSM parameters. An example for the latter category is the exclusive dimuon decay of  $B_s^0, B^0$  mesons which are helicity suppressed in the standard model, but its branching ratios are enhanced in SUSY models [82]. Therefore, the CMSSM parameter space is sensitive to the limits on  $BR(B^0 \rightarrow \mu^+\mu^-)$  [4, 82] and the observation of  $B_s^0 \rightarrow \mu^+\mu^-$  at the LHC [4].

---

<sup>7</sup>The examples we give in the text may differ from the specific data set used in [137, 182, 302] as we try to select the common and recent references. For the actually used data sets we refer to the references in [137, 182, 302].

For the following review, we will focus on the global fits from O. Buchmueller et al. [137], C. Strege et al. [302], and A. Fowlie et al. [182], as they contain predictions for the elastic WIMP-nucleon scattering cross section (Sect. 2.1.5), an important parameter for the direct dark matter searches listed in Sect. 2.2. Here, O. Buchmueller et al. and C. Strege et al. used the most recent results.

The actual best-fit values of these studies are less robust and depend on the used technique (frequentist or Bayesian with logarithmic or flat prior), however the contours seem more robust [182, 302], see Fig. 2.8: to some extent all fit contours enclose the stau coannihilation region ( $m_0 c^2 \lesssim 0.5$  TeV) and the A-funnel region ( $m_{1/2} c^2 \simeq 1.2$  TeV). O. Buchmueller et al. [137] found in the frequentist approach a best fit value in the stau coannihilation region, but the contour also encloses the A-funnel, this is confirmed by C. Strege et al. [302] in the Bayesian approach. A. Fowlie et al. [182] has the best-fit point in the A-funnel, but the contour also enclose the coannihilation region. However, the A-funnel is excluded in the frequentist approach of C. Strege et al. According to C. Strege et al. and O. Buchmueller et al. (as cited in [302]), the deviation between the frequentist approaches in [137, 302] can be explained by differences in the used code. C. Strege et al. accuse A. Fowlie et al. to have used unreliable code settings, resulting in the different best-fit points in [182, 302].

Therefore, we will not discuss actual predictions for sparticle masses or spin-independent WIMP nucleon scattering cross section, but reproduce some of the discussed contours in the  $m_0 - m_{1/2}$ - and  $\sigma_{\chi, N}^{\text{SI}} - m_\chi$ -plane in Fig. 2.8. The results of O. Buchmueller et al. for  $\sigma_{\chi, N}^{\text{SI}}(m_\chi)$  are shown in Fig. 2.11. However, by comparing the results some general tendencies can be stated:

The rather high mass of the discovered Higgs has a significant impact, as pre-Higgs constraints favoured a lower best-fit value of  $m_h c^2 \approx 116$  GeV [302]. The measured value can be fitted either by including radiative corrections or allowing maximal mixing scenarios. The first is most sensitive to the stop mass and favours large  $m_0$  in the A-funnel, the second favours small  $m_{1/2}$  in the stau coannihilation region [137, 182, 302], but the best-fit for the Higgs mass of all three studies is below the experimental value [137, 182, 302].

However, the A-funnel is disfavoured in the frequentist approach by the measured anomalous magnetic moment  $a_\mu$ . Its strong deviation from the standard model prediction favours new physics, e.g. in form of a significant SUSY contribution. Therefore, small masses in the coannihilation region are favoured by  $a_\mu$  [137, 302].

This is in tension with the results for  $BR(B^0 \rightarrow \mu^+ \mu^-)$ ,  $BR(B_s^0 \rightarrow \mu^+ \mu^-)$  which are consistent with the standard model prediction and disfavour new physics at low masses [137, 182]. Also the null-result of SUSY particle production at the LHC is in tension with  $a_\mu$  [137, 302]. A. Fowlie et al. and C. Strege et al. argued that remaining uncertainties in the modelling of  $a_\mu$  may justify to remove it from the constraints. By doing so, they found a greatly improved goodness of fit [182, 302].

Higher  $m_0$  values are limited by the XENON100 direct dark matter search [68], which disfavor the complete focus-point region (large  $m_0$  and small  $m_{1/2}$ ) [137, 302]. The more sensitive result of the LUX experiment [42] may further strengthen this exclusion, but it is not yet included in global fits.

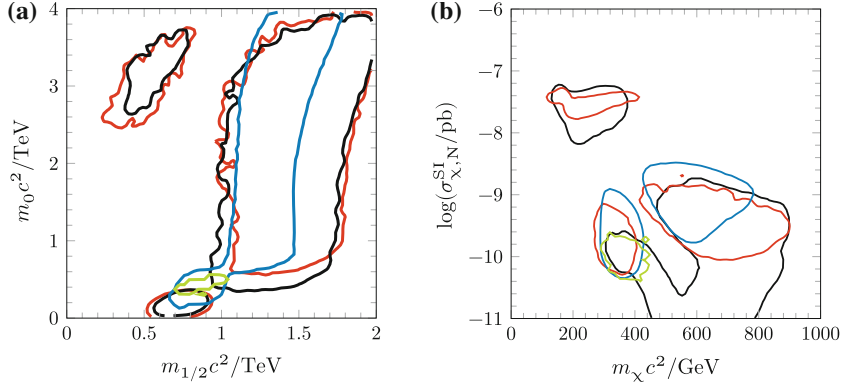


**Fig. 2.8** Overview of current global fits of the CMSSM, 95 % CL regions in **a** the  $m_0 - m_{1/2}$ -plane and **b**  $\sigma_{\chi,N}^{\text{SI}} - m_\chi$ -plane: [302] Bayesian with logarithmic prior including  $a_\mu$  (blue), [302] Profile likelihood including  $a_\mu$  (green), [182] Bayesian with logarithmic prior including  $a_\mu$  (red), [182] Bayesian with logarithmic prior excluding  $a_\mu$  (black)

All three studies discussed have different best-fit values and different 95 % CL contours. However, all three contours overlap in one region of the  $\sigma_{\chi,N}^{\text{SI}} - m_\chi$ -plane, see Figs. 2.8b and 2.11. Therefore, a WIMP with  $m_\chi c^2 \approx 400 \text{ GeV}$  at  $\sigma_{\chi,N}^{\text{SI}} \approx 10^{-10} \text{ pb}$  seems in agreement with all three studies [137, 182, 302] at 95 % CL.

The question whether the CMSSM is still a reliable model to fit the data is open: O. Buchmueller et al. state a  $p$ -value of 0.085 and emphasize the tension between  $a_\mu$  and null-results for SUSY production at LHC. Consequently, they call to look for alternatives beyond CMSSM [137]. C. Strege et al. state a  $p$ -value of 0.21 and argue that the CMSSM is not ruled out by any statistical significance [302]. However, they admit that the parameter space is shrinking [302]. The underestimation of the Higgs mass in all three studies increase the pressure on CMSSM. The MSSM may be an alternative, but it seems to need fine tuning to get a suitable Higgs mass. Such fine tuning could be avoided in the *next to minimal supersymmetric standard model* (NMSSM) [138].

### 2.1.4 Limits on the WIMP Self-annihilation Cross Section by Astroparticle Data

As shown in the Sect. 2.1.2, the WIMP miracle can lead to the observed relic abundance of non-baryonic, cold dark matter if WIMPs are self-annihilating. To match the thermal relic density (Eq. 2.4b) an annihilation cross section of  $\langle \sigma_a v \rangle \approx 3 \times 10^{-26} \text{ cm}^3 \text{s}^{-1}$  (Eq. 2.10) would be needed. This prediction can be tested by searching for particles produced in present day WIMP annihilation. Signatures for annihilation products are predicted for various astroparticle data, including cosmic rays, gamma rays, and neutrinos. In this section we will follow the reviews [206, 264] and will

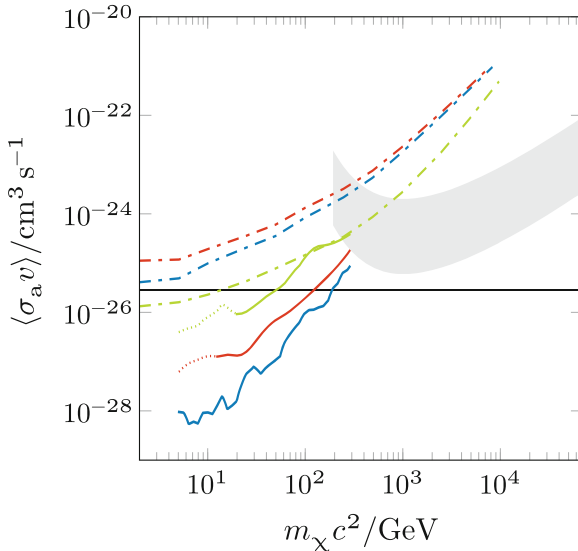


**Fig. 2.9** Compilation of exclusion limits at 95 % CL on  $\langle \sigma_a v \rangle$  as function of  $m_\chi$ . The results from AMS [108, Fig. 3] (solid lines) and from FermiLAT [26, Fig. 5] (dashed-dot lines) are shown for the final states  $e^-e^+$  (blue),  $\mu^-\mu^+$  (red)  $\tau^-\tau^+$  (green). The gray area indicates the uncertainty due to the dark halo model in the H.E.S.S. exclusion limit [34, Fig. 1]. The dotted parts of the AMS results are potentially affected by solar modulation [108]. The black solid line indicates  $\langle \sigma_a v \rangle = 3 \times 10^{-26} \text{ cm}^3 \text{s}^{-1}$ , the value necessary to match the WIMP relic abundance, often called *natural scale*

briefly list the most recent results, the associated techniques, and report the obtained limits on  $\sigma_a$  in Fig. 2.9.

Searching for a dark matter signal via the potential annihilation products is commonly known as *indirect search*. The *direct search* for scattering of galactic dark matter off terrestrial targets will be discussed in Sect. 2.1.5.

The type of annihilation products depends on the dark matter candidate and its interaction with standard model particles. Therefore, only given dark matter models are testable. Within the MSSM, the annihilation products depend on the LSP, its mass, and the MSSM mass spectrum. In principle, the dark matter particle may annihilate to any standard model particle as final state:  $Z$ ,  $W^\pm$ ,  $g$ ,  $l$ ,  $q$ ,  $\nu$  [264]. Even an annihilation to monochromatic  $\gamma$ -rays is possible, but suppressed to loop level, as the parent particle is by definition *dark matter* [206]. The source spectrum for standard model particles is the convolution of the annihilation final states and the branching ratios. To be more independent from the involved dark matter physics, most searches express the limits for specific final states like  $\gamma$ ,  $\mu^+\mu^-$ , or  $bb$ .

Assuming the final state particle to be unstable, it will decay or hadronize until reaching a stable particle like  $\gamma$ ,  $e^-$ ,  $\nu_e$ ,  $\nu_\mu$ ,  $\nu_\tau$ ,  $p$ ,  $d$ , and their respective anti-particles. Each of these particles can undergo secondary processes like inverse-Compton scattering in case of  $\gamma$ . These messengers can be divided in three categories: cosmic rays

$(e^-/e^+, p/\bar{p}, d/\bar{d})$ ,  $\gamma$ -rays, and neutrinos ( $\nu_e, \nu_\mu, \nu_\tau \nu_\tau$ ). For each category we will shortly report the results from the most recent experiments.

Besides being directly the final states,  $e^\pm$  can be produced via  $\mu^\pm$ - and  $\tau^\pm$ -decay and via  $\pi^\pm$ -decay subsequent to  $W^\pm$ - and  $Z$ -decay or hadronization. Charged hadrons ( $p/\bar{p}, d/\bar{d}$ ) can be produced via  $W^\pm$ -, and  $Z$ -decay or hadronization.

Charged cosmic rays scatter on magnetic fields in the interstellar medium and the galactic halo, therefore their incident direction get mostly randomized. Furthermore, energy loss via inverse-Compton scattering limits the sources of  $e^\pm$  with  $\lesssim 100$  GeV to a few kiloparsec around the Earth. Therefore, the propagation through and interaction with the interstellar medium has to be considered, adding additional model dependence to potential signals.

As little directional information is available for charged cosmic rays, one relies on the spectral shape to distinguish it from background. In most scenarios it is a hard continuum spectrum on top of the background, with a bump or edge near the WIMP mass [264].

The *Advanced Thin Ionization Calorimeter* (ATIC) [145] and the *Balloon-borne Electron Telescope with Scintillating fibers on the Polar Patrol Balloon* (PPB-BETS) [310] found a bump in the combined  $e^- + e^+$  spectrum at  $\approx 300$ – $800$  GeV [264]. This bump was not confirmed with the more precise data of the satellite experiment *Fermi Large Area Telescope* (FermiLAT), but it found a smaller excess at  $\approx 200$  GeV [13]. However, these excesses can be explained with additional, non-exotic sources like pulsars [266].

As the WIMP annihilation produces the same amounts of matter and anti-matter, anti-matter is a potentially better signal due to its lower astrophysical background [264]. A positron background arises from the collision of cosmic ray protons with the interstellar medium [108]. The space-based *Payload for Antimatter Matter Exploration and Light-nuclei Astrophysics* (PAMELA) [29, 30] observed a positron excess in the  $e^+/e^-$ -fraction at  $\gtrsim 100$  GeV over the background. Contrary, the  $\bar{p}/p$ -fraction is in agreement with the prediction. The observation may be explained as a dark matter signal, but it would require an exotic scenario where the dark matter annihilates predominantly into leptons, e.g. [155]. Contrary, also additional, yet unknown nearby pulsars are proposed to explain the excess, e.g. [163].

The positron excess is confirmed by the *Alpha Magnetic Spectrometer* (AMS) on the International Space Station [108]. However, a fit of the observed spectral shape found no indication of the expected sharp, edge-like feature from dark matter annihilation. Consequently, AMS data can be used to set limits on  $\langle \sigma_a v \rangle$ , depending on the final states of the decay [108], see Fig. 2.9.

A  $\gamma$ -ray signal may be produced directly as final state of the annihilation, but also via  $\pi^0$ -decay subsequent to  $W^\pm$ -,  $Z$ -, and hadronic  $\tau^\pm$ -decay; or hadronization [264]. As  $\gamma$ -rays are unaffected by magnetic fields, they indicate the direction of their source.

Contrary to the case of charged cosmic rays,  $\gamma$ -ray signals can be distinguish from background by their directional information. As the annihilation rate is proportional to the density squared, an increased signal from dark matter self-annihilation is expected from regions with high dark matter densities, like the centre of the galaxy, the

centers of galaxy clusters, or dark matter dominated dwarf galaxies [264]. Therefore, the predicted  $\gamma$ -flux due to annihilation is strongly affected by uncertainties in the dark matter distribution from N-body simulations. A background of diffuse  $\gamma$ -emission arises from propagation and interaction of cosmic rays: inelastic collision of nuclei with the interstellar gas can produce  $\pi^0$ , and its subsequent decay leads to  $\gamma$ -rays;  $e^\pm$  can produce  $\gamma$ -rays via bremsstrahlung and inverse-Compton scattering with the interstellar radiation field. Searches for  $\gamma$ -signals therefore also strongly depend on a correct modelling of the propagation and interaction of cosmic rays.

The FermiLAT experiment searched for monochromatic  $\gamma$ -lines from the galactic centre [15] and studied also the diffuse galactic [14] and extragalactic [16, 18]  $\gamma$ -emission. C. Weniger [316] found in 43 months of FermiLAT data an indication of a  $\gamma$ -line at  $\approx 130$  GeV and stated a significance of  $3.2\sigma$ , considering the look-elsewhere effect. However, reanalysis with data of 4.4 years and including the systematic effect of different data selection chains reduces the global significance to less than  $1.0\sigma$  [197]. In case of diffuse galactic emission, the proposed excess in the data of the older EGRET experiment [125] was not confirmed by FermiLAT. Based on the absence of a galactic monochromatic  $\gamma$ -line, an upper limit on the  $\gamma$ -flux from annihilation could be set. Depending on the used dark matter halo model it corresponds to  $\langle \sigma_a v \rangle \lesssim 10^{-27} \text{ cm}^3 \text{s}^{-1}$  [15].

Dwarf galaxies, especially *dwarf spheroidals* (dSph), have a high mass-to-light ratio and thus a presumably high abundance of dark matter [291]. They have probably a low  $\gamma$ -background and only a few pulsars [264]. Three imaging atmospheric Cherenkov telescopes searched for dark matter signal in dwarf galaxies: MAGIC observed the Draco [49] and Segue 1 [51]; VERITAS observed also Segue 1 [53] and the galaxies Draco, Ursa Minor, Boötes 1, and Willman 1 [24]; and H.E.S.S. observed Sagittarius [32, 34] and Canis Major [33] Sculptor and Carina dSph [21]. No dark matter signal was found and exclusion limits on  $\langle \sigma_a v \rangle$  were set. A simultaneous fit to 15 Milky Way dwarf spheroidal satellite galaxies out of 25 observed by FermiLAT set the most competitive limit on  $\langle \sigma_a v \rangle$  [17, 26], see Fig. 2.9, as FermiLAT has a lower threshold than the imaging atmospheric Cherenkov telescopes [264].

A search in galaxy clusters by MAGIC [50] and FermiLAT [22, 25] found also no dark matter signal. FermiLAT set an exclusion limit which can go down to  $\langle \sigma_a v \rangle < 10^{-24} \text{ cm}^3 \text{s}^{-1}$ , depending on the used halo model [25]. Searches in galaxy clusters are difficult due to the strong  $\gamma$ -background from e.g. active galactic nuclei [264].

Neutrinos may be produced via  $\mu^\pm$ -,  $\tau^\pm$ -decay, in addition to direct production as final states. Due to their low interaction probability, neutrinos, like  $\gamma$ -rays, provide the direction of their source. The direction is used to search for neutrinos capture inside the Sun or Earth. Due to scattering during passing through celestial bodies, WIMPs may lose enough energy to get gravitationally bound to them. Consequently, a neutrino signal from dark matter annihilation in the Sun or Earth is not only sensitive to the annihilation cross section  $\sigma_a$ , but also on the scattering cross section  $\sigma_{\chi, N}$  (Eq. 2.20a). Depending on the theory, the energy of the neutrino signal can reach up to 1/3 of the WIMP mass [206]. Thus, WIMPs annihilating inside the sun would produce a high energy neutrino signal which is clearly distinct from solar neutrinos.

The IceCube neutrino telescope at the South Pole search for Cherenkov light caused by neutrino-induced interactions in the ice. Including its denser subarray DeepCore, the IceCube experiment searched for neutrinos from the sun caused by WIMP annihilation in the range  $20 \text{ GeV} < m_\chi c^2 < 500 \text{ GeV}$ . The measurement was consistent with atmospheric muon and neutrino background, and IceCube set limits on the spin-dependent and spin-independent cross section for elastic WIMP-proton scattering [12]. Its results are therefore comparable to the direct searches, see Fig. 2.11, which we will discuss in Sect. 2.2.

In Fig. 2.9 we compiled the exclusion limits from FermiLAT [26], AMS [108], and from the H.E.S.S. observation of the Sagittarius dwarf [34]. As far as we know, the latter is the leading exclusion limit for imaging atmospheric Cherenkov telescopes. AMS and FermiLAT already reached the  $\langle \sigma_a v \rangle$  value needed to match the WIMP relic density (Eqs. 2.4b and 2.10), assuming  $e^- e^+$  in the final state. Thus, they indicate WIMPs with  $m_\chi c^2 \gtrsim 10\text{--}100 \text{ GeV}$ .

### 2.1.5 WIMP Signature in Direct Searches for Dark Matter

Astronomical and cosmological observations strongly indicate the existence of dark matter (see Sect. 2.1.1), and *indirect searches* try to further constrain its properties (Sect. 2.1.4). Possible particle candidates for dark matter are motivated by extensions of the standard model of particle physics (Sect. 2.1.2) and their existence is tested at accelerators (Sect. 2.1.3). However, even if a particle candidate exists and its properties match the astronomical observations, this is no unambiguous proof that the constituent of cosmic dark matter is identical to the candidate. *Direct searches* try to establish this identity by searching for scatterings between galactic dark matter and terrestrial targets. In this controlled conditions, a more detailed comparison with possible candidates is possible.

In this section we review the connection between the microscopic physics of supersymmetric WIMP candidates, the galactic WIMP distribution, and the signatures in direct searches. This will prepare the discussion of the results of current direct searches in Sects. 2.2 and 2.3.

Assuming the lightest neutralino as WIMP candidate, in direct searches one usually restricts WIMP interaction with ordinary matter to WIMP-quark coupling.<sup>8</sup> Consequently, scattering of WIMPs off target nuclei leads finally to recoiling nuclei in the detector [206]. The energy of the recoiling nucleus  $E_r$  with mass  $m_{\text{nucl}}$  can be given as function of the scattering angle in the centre of mass frame  $\theta$  [120]:

$$E_r = \frac{\mu^2 v^2 (1 - \cos \theta)}{m_{\text{nucl}}}, \quad \mu = \frac{m_\chi m_{\text{nucl}}}{m_\chi + m_{\text{nucl}}}. \quad (2.17)$$

---

<sup>8</sup>However, we note that also WIMP coupling to leptons is studied, e.g. [115] and references therein.

In general the WIMP-nucleus cross section has contributions from spin-dependent (SD) and spin-independent (SI) interactions and can be expressed as [120]:

$$\frac{d\sigma_{\chi,\text{nucl}}}{dE_r} = \frac{m_{\text{nucl}}}{2\mu^2 v^2} \left( \sigma_0^{\text{SI}} F_{\text{SI}}^2(E_r) + \sigma_0^{\text{SD}} F_{\text{SD}}^2(E_r) \right), \quad (2.18)$$

with the spin-independent ( $\sigma_0^{\text{SI}}$ ) and spin-dependent ( $\sigma_0^{\text{SD}}$ ) cross sections at zero momentum transfer and  $v$  denoting the WIMP velocity relative to the nucleus. The dependence on the momentum transfer and the loss of coherence for heavy WIMPs or nuclei are considered by the form factors<sup>9</sup>  $F_{\text{SI}}, F_{\text{SD}}$ .

The spin-dependent contribution arises from the coupling of the WIMP to the axial-current of the quark, which leads to [120, 206]:

$$\sigma_0^{\text{SD}} \propto (a_p \langle S_p \rangle + a_n \langle S_n \rangle) (J + 1), \quad (2.19)$$

where  $\langle S_p \rangle$  ( $\langle S_n \rangle$ ) are the expectation values of the spin content of the proton (neutron) group of the nucleus and  $J$  is the nucleus spin. The  $a_n, a_p$  depend on the theoretical WIMP-quark coupling and the quark spin distribution in the nucleon, which has to be experimentally determined from polarized deep inelastic scattering.

The spin-independent contribution arises via scalar–scalar and vector–vector coupling leading to [120, 206]:

$$\sigma_0^{\text{SI}} \propto (f^p Z + f^n (A - Z))^2 \quad (2.20a)$$

$$\approx A^2. \quad (2.20b)$$

Similar to the  $a_n, a_p$ , the terms  $f^p, f^n$  depend on the theoretical WIMP-quark coupling and the experimental quark densities in the nucleon. In most cases  $f^p \approx f^n$ , i.e. the WIMP couples in a similar way to neutrons and protons, and the cross section scales with the atomic weight  $A^2$  of the target.

Both, the nucleon number and the form factor, have to be considered by selecting a target for direct searches. In example, on one side xenon has a higher spin-independent cross section than germanium due to its higher atomic mass, but on the other side it has a larger form factor suppression of events with high momentum transfer [186].

Finally, the properties of the galactic WIMP distribution affects the differential event rate  $dR/dE_r$  of recoiling target nuclei [97, 120, 227]:

$$\frac{dR}{dE_r} = \frac{\rho_0}{m_{\text{nucl}} m_\chi} \int_{v_{\text{min}}}^{v_{\text{esc}}} v f(\vec{v}, \vec{v}_E) \frac{d\sigma_{\chi,\text{nucl}}}{dE_r}(v, E_r) d\vec{v} \quad (2.21a)$$

$$v_{\text{min}} = \sqrt{\frac{m_{\text{nucl}} E_r}{2\mu^2}}, \quad (2.21b)$$

---

<sup>9</sup>For the spin-independent case, the form factor of R.H. Helm [199] is usually used in direct searches.

resulting in a quasi-exponentially falling spectrum. Here,  $f(\vec{v}, \vec{v}_E)$  is the distribution of the WIMP velocity  $\vec{v}$  in the reference frame of the detector and  $\vec{v}_E$  is the velocity of the detector relative to the galactic frame. The local WIMP density is  $\rho_0$ . The distribution  $f(\vec{v}, \vec{v}_E)$  is limited by the escape velocity for gravitationally bound WIMPs,  $v_{\text{esc}}$ , and by the minimal velocity  $v_{\text{min}}$  that is needed to induce a recoil with  $E_r$  above an experimental threshold.

Because the actual galactic WIMP distribution is still unknown and numerical simulation results are not commonly accepted, see Sect. 2.1.1, a canonical distribution is assumed in context of direct dark matter searches. This is the *isothermal* halo (Eq. 2.2a with  $\alpha = 2.0$ ,  $\beta = 2.0$ ,  $\gamma = 1.0$ ,  $R = 3.5$  kpc) [121]. The isothermal halo leads to a Maxwellian velocity distribution [120]:

$$f(\vec{v}, \vec{v}_E) = \frac{1}{\sqrt{2\pi}\sigma} \exp\left(-\frac{|\vec{v} + \vec{v}_E|^2}{2\sigma^2}\right), \quad \sigma = \sqrt{\frac{3}{2}}v_0 \quad (2.22)$$

with the local circular speed  $v_0$ . Most of the direct detection experiments listed in Sect. 2.2 apply the following standard values [120]<sup>10</sup>:

$$v_{\text{esc}} = 544 \text{ km s}^{-1}, \quad v_0 = 220 \text{ km s}^{-1}, \quad \rho_0 c^2 = 0.3 \text{ GeV cm}^{-3}. \quad (2.23)$$

Reasonable variations of the halo model may affect the detection rate by about ten percent [207].

Earth's absolute velocity projected on the galactic plane [97] can be parametrized as

$$v_E = v_{\text{sun}} + v_{\text{rot}} \cos \gamma \cos \left( \frac{2\pi}{T}(t - t_0) \right) \quad (2.24)$$

where  $v_{\text{sun}}$  is the proper motion of the sun and  $v_{\text{rot}}$  is the rotation velocity around the sun with a period of  $T = 1$  year, a phase of  $t_0 \sim 2$ nd June, and an inclination of  $\gamma$  relative to the galactic plane.

Therefore, nuclear recoils induced by galactic WIMPs features an annual modulated event rate following a cosine [120, 227]. However, the cosine may be distorted in the presence of halo substructures such as streams [281]. Additionally, the incident WIMP flux in the lab frame is peaked in the direction of Earth's motion due to the motion of the detector relative to the galactic restframe. This produces a directional dependence of a potential WIMP signal. As both, the annual modulation and the directional dependence, do not depend on the assumption of the WIMP physics,

---

<sup>10</sup>J.D. Lewin and P.F. Smith [227] originally proposed slightly different values:  $v_{\text{esc}} = 600 \text{ km s}^{-1}$ ,  $v_0 = 230 \text{ km s}^{-1}$ . Within the stated uncertainties, they agree with the more recent values from [120].

potential signals with these characteristics are regarded as *model independent*. An overview of experiments using these characteristics as detection signature are given in Sects. 2.2.1 and 2.2.7.

Without such characteristic features, one has to search for an excess in the measured event rate over the known background of the experiment. For  $\sigma^{\text{SI}} \approx 10^{-10} \text{ pb}$  as expected in some theoretical models, see Fig. 2.8b, only one event within an exposure of 3 t.yr is expected [76]. This event has to be identified against the background, especially neutrons which also induce nuclear recoils. Possible sources for neutron background in direct dark matter searches are [181]: neutrons from uranium/thorium decay or  $(\alpha, n)$ -reactions near the detector, and neutrons induced by atmospheric muons. The latter ones can reach kinetic energies up to several hundred GeV, which makes a passive shielding of the detector difficult. Instead, one has to use active muon vetos to reject events associated with tagged muons and to go deep underground to reduce the muon flux.

Another difficulty, maybe even a final background for direct searches is the coherent scattering of neutrinos on the target nucleus which starts at  $\sigma^{\text{SI}} \approx 10^{-13} \text{ pb}$  [123]. However, this is no limitation for running experiments, as this magnitude of cross section is only reachable for the most ambitious future experiments, see Sect. 2.2 and especially Sect. 2.2.4.

In any case, direct dark matter experiments search for a very rare signal and need therefore a good knowledge of the expected background where muon-induced neutrons are a central component.

## 2.2 Overview of Direct Searches for Galactic WIMPs

In the previous section, we motivated the existence of dark matter and introduced the WIMP as possible particle candidate. This section will give an overview of current results of direct searches for WIMPs.<sup>11</sup> We will focus on running experiments and their obtained exclusion limits or claimed signals for elastic, spin-independent WIMP-nucleon scattering. Detailed reviews of finished, running, and planned direct dark matter searches can be found in e.g. [45, 88, 120, 151, 179, 284, 297]. An overview of already finished experiments from mid-1980s till mid-2000, e.g. IGEX, UKDMC, and HDMS, is given in [186, Tables 1 and 2].

Most theories predict a very weak signal, e.g. in CMSSM a cross section of roughly  $\sigma^{\text{SI}} \approx 10^{-10} \text{ pb}$  is expected for elastic WIMP-nucleon scattering (Sect. 2.1.3). Therefore, the experiments aim to measure signals as rare as one WIMP-induced nuclear recoil event within an exposure of 3 t.yr, see Sect. 2.1.5. To reach this sensitivity, a low background is important. Typical background sources are  $\beta$ - and  $\gamma$ -decays which result in electron recoils. Neutrons, either from  $(\alpha, n)$  reactions or induced by cosmic muons, cause nuclear recoils [186]. Especially neutrons are an important background,

---

<sup>11</sup>We note that planned experiments searching for neutrinoless double beta decay, like MAJORANA [10] and CUORE [265], will be also sensitive to dark matter [190, 315].

as they can mimic WIMP induced nuclear recoils (Sect. 2.1.5). Active and passive techniques are used to suppress these kinds of background. On the active side, most of the experiments feature some kind of rejection for electron recoils, like pulse shape analysis (e.g. GoGeNT [9] and COUPP [91]) or a dedicated detector design using the simultaneous measurement of two signal channels (e.g. EDELWEISS [76] and XENON [68]). Also a muon veto to tag muon-induced background produced inside the veto is not unusual, e.g. [7, 63, 283]. On the passive side, most experiments have neutron and gamma shields, and usually they are located at deep underground sites to reduce the cosmogenic background. An overview of the underground laboratories where most of the experiments are located is given in [122], their shielding power being expressed in *meter water equivalent* (mwe). The physics of this shielding and the creation of muon-induced neutrons will be discussed in detail in Chap. 3.

We will first shortly introduce the experiments and their latest results, classified by the used technique: scintillators (Sect. 2.2.1), ionisation detectors (Sect. 2.2.2), cryogenic detectors like EDELWEISS (Sect. 2.2.3), two-phase and single-phase noble liquids (Sects. 2.2.4 and 2.2.5), superheated liquids (Sect. 2.2.6), and directional experiments (Sect. 2.2.7). If not stated otherwise, the results are given for a standard isothermal halo [227], (Eq. 2.23).

Most of the experiments set upper limits on the cross section for elastic WIMP-nucleon scattering, but some claimed also indication for a WIMP signal. Due to the  $A^2$ -enhancement, the limits on spin-independent scattering are lower than the limits on spin-dependent scattering, see Sect. 2.1.5. In the following we will focus on limits on the spin-independent cross section for WIMP-nucleon scattering  $\sigma_{\chi,N}^{\text{SI}}(m_\chi)$  (Eq. 2.20a). An overview of the possible signals is shown in Fig. 2.10. The upper limits on  $\sigma_{\chi,N}^{\text{SI}}(m_\chi)$  at 90 % CL, hereafter called *exclusion limits*, of the discussed experiment are shown on Fig. 2.11. The tension between the possible signals and the exclusion limits will be discussed in Sect. 2.2.8. Section 2.3 will then discuss the experimental aspects and possible background contributions based on the example of the EDELWEISS experiment.

## 2.2.1 Scintillators

Scintillators are in principle capable to discriminate events with high stopping power  $dE/dX$  like nuclear recoils via pulse shape analysis. However, the low light yield prevents an event-by-event discrimination at low energy [297].

The DAMA [109, 116] experiment claims a discovery of galactic dark matter interacting with their target based on an annual modulation of the count rate statistic. As stated above, this is extracted without specifying the kind of interaction on an event-by-event base. Experiments like KIMS [213, 225], ANAIS [56], and DM-ICE [152] are aimed to test this claim and possible systematic effects with similar targets but different experimental set-ups. KIMS already finished its data taking, whereas ANAIS and DM-ICE are in their prototype stages.

The *DAMA* project searched, with two experimental set-ups, for WIMP signatures in NaI(Tl) crystals at the *Laboratori Nazionali del Gran Sasso* (LNGS, Italy) at a depth of 3600 mwe [109, 117]. Until July 2002, the *DAMA/NaI* set-up collected in 7 years [111] 107,731 kg.d exposure with nine crystals of 9.7 kg mass [112]. Afterwards the set-up was upgraded to *DAMA/LIBRA* with 25 crystals of the same individual mass [114], which collected additional 317,697 kg.d until September 2009 [116]. Already in the *DAMA/NaI* data, the *DAMA* collaboration found a sinusoidal modulation of the residual hit rate at low energy with a period of 1 year and a phase equivalent to a peak in June 2nd [110], as expected for the interaction of galactic WIMPs with an Earth based detector, see also Sect. 2.1.5. As expected for the low interaction cross section of a WIMP, the modulation is only observed in single hits, i.e. when only one crystal fires [110]. This modulation persisted in the combined exposure of *DAMA/NaI* and *DAMA/LIBRA* (1.17 t.yr) at a significance of  $8.9\sigma$  CL, spanning 13 annual cycles [109]. According to the *DAMA* collaboration, possible modulated backgrounds, like muon-induced neutrons, can not explain the observed topology of the events and amplitude of the modulation [109, 116, 117]. Therefore, the *DAMA* collaboration claims evidence for a dark matter induced signal [109, 116]. Since January 2011 *DAMA/LIBRA* is running in *phase 2*, using new PMTs with higher quantum efficiency. The aim of phase 2, among others, is an increased sensitivity at low energies and the investigation of the distribution of dark matter in the galactic halo [118, 119].

The *DAMA* collaboration stresses that their observation is *model independent* as far as the modulation would occur regardless of the specific dark matter particle candidate [109, 116]. To compare the *DAMA* signal with the results of other experiments in the  $\sigma_{\chi, N}^{\text{SI}} - m_\chi$ -plane (Sect. 2.2.8), we use in this work the interpretation [98] as suggested by [109, 127].<sup>12</sup> In the *light neutralino model* [127], the observed modulation would correspond to a particle mass of  $7 \text{ GeV} < m_\chi c^2 < 50 \text{ GeV}$  [98], see also Fig. 2.10. Including constraints from the LHC reduces the mass range to  $18 \text{ GeV} < m_\chi c^2 < 38 \text{ GeV}$  [127].

The *Korea Invisible Mass Search* (KIMS) experiment searched for elastic scattering of WIMPs with CsI(Tl) crystals at the *Yangyang Underground Laboratory* (Republic of Korea, 2000 mwe) [224, 225]. Twelve crystals, each of 8.7 kg mass, were installed in the last stage [213]. Identifying nuclear recoils via pulse shape analysis, no excess was found in the total exposure of 24524.3 kg.d and an exclusion limit at 90 % CL is set [213].

The *Annual Modulation with NaI(Tl) Scintillators* experiment (ANAIS) at the *Canfranc Underground Laboratory* (LSC) (Spain, 2450 mwe) aims to confirm or refute the annual modulation observed by *DAMA* [109, 116] with the same target and technique [56]. It plans to operate in total 250 kg of ultrapure NaI(Tl) crystals. Currently it investigates the intrinsic background with a sample of two NaI(Tl) crystals of 12.5 kg each [56].

---

<sup>12</sup>However, the analysis used non-standard parameter for their isothermal galactic halo ( $\rho_0 c^2 = 0.45 \text{ GeV cm}^{-3}$ ,  $v_0 = 270 \text{ km s}^{-1}$ ,  $v_{\text{esc}} = 650 \text{ km s}^{-1}$  [98]), therefore it is questionable if the analysis is really comparable to the results of other experiments.

The *DM-ICE* collaboration [165] proposed to test the DAMA signal [109, 116] with 250kg of NaI(Tl) crystals installed at a depth of 2450m below the IceCube neutrino detector at the south pole [152]. As seasonal effects are opposite on the northern and southern hemisphere, a dark matter induced annual modulation in DM-ICE that agrees with DAMA's signal will occur 6 months out of phase from seasonal modulated background [152]. Currently, data are taken with a prototype of two crystals of 17kg total mass deployed at 2450m depth [152].

### 2.2.2 Ionisation Detectors

Experiments like CoGeNT and TEXONO search for an ionisation signal caused by WIMP-induced recoils in diodes. By using high purity germanium (HPGe) or silicon crystals as target, these experiments have a low intrinsic background, but they lack the capability for a discrimination between nuclear recoils, as expected for WIMP interactions, and electron recoils, as expected for  $\gamma$ -background via Compton scattering [297]. However, the situation may be improved in future detectors: recently experiments searching for neutrinoless double beta decays, like GERDA [23] and MAJORANA [10], developed segmented diodes, enabling the active rejection of Compton background due to their multiple, spatially separated interactions [297].

The dual use of this detector techniques for dark matter searches and neutrino physics is illustrated by CoGeNT [8, 9] and TEXONO [229, 233]. Both experiments started searching for low energy neutrino interactions, but published recently results for their dark matter searches.

The *Coherent Germanium Neutrino Technology* (CoGeNT) [9] collaboration uses a p-type point contact (PPC) germanium detector (HPGe) [5], a detector design with low threshold and noise but large mass and high energy resolution, suitable for searches of coherent neutrino scattering, but also WIMP scattering [87]. First measurements were taken at the *Chicago's Tunnel And Reservoir Plan* (US, 330mwe) [5, 6], later measurements with a 440g detector at the *Soudan Underground Laboratory* (US, 2100mwe) for 145kg.d live days [7–9]. Here, the experiment reports an irreducible excess of bulk-like events above the analysis threshold of 400eV<sub>ee</sub>. Based on fits to the exponential spectrum, neither the hypothesis of pure background nor the hypothesis of an additional WIMP signal was favored [7]. However, later investigations found  $\approx 2.8\sigma$  significance for an annual modulation of the event rate as one would expect for a WIMP signal, with a best fitting mass of  $m_\chi c^2 = 7\text{ GeV}$  [8], see also Fig. 2.10. Known backgrounds like muon-induced neutrons or  $\alpha$ -recoils from radon contamination can not explain the measured excess [7–9]. Also a comparison with the measured annual modulation of the radon level in the laboratory and the muon flux found no correlation with the observed signal by CoGeNT [27]. The CoGeNT collaboration plans to further investigate the observation with the *C-4* upgrade. Its aims are: an increase of the target mass to four PPCs of up to 1.3kg mass each, a lowering of the threshold, an improved muon veto, and an increased shielding against  $\gamma$ - and neutron background [126].

The *TEXONO* experiment is located at the *Kuo-Sheng Power Plant* in Taiwan at 30 mwe. Its main objective is low energy neutrino physics, such as neutrino-nucleus coherent scattering [287]. However, the experiment searches also for elastic scattering of WIMPs [229, 233]. The latest results are obtained with a PPC of 840 g fiducial mass and an analysis threshold of 500 eV<sub>ee</sub> [229]. Due to the low threshold, the obtained exclusion limit at 90 % from a fiducial exposure of 39.5 kg.d [229] is especially sensitive at low  $m_\chi$ -values, see Fig. 2.11.

The dark matter search was later separated from the neutrino investigation and is continued by the CDEX-TEXONO collaboration as *China Dark Matter Experiment* (CDEX) at the *China Jin-Ping Underground Laboratory* (CJPL) (PR China, 6720 mwe [320]), taken advantage from the increased shielding against cosmic background [322]. First data are obtained with a PPC-Ge of 994 g total mass [324]. However, as the rejection of Compton and surface background is not yet applied, the obtained exclusion limit [324] is slightly worse than the latest TEXONO result [229].

### 2.2.3 Cryogenic Crystal Detectors

Contrary to experiments which measured only scintillation light or ionisation, experiments like EDELWEISS, CDMS, or CRESST measure two signal channels in parallel: heat and ionisation in EDELWEISS and CDMS, and heat and scintillation in CRESST.

The heat channel enables true colorimetric measurements at mK temperature as the heat capacity follows Debye's law, being proportional to  $T^3$ , therefore the energy deposit from a single nuclear recoil can yield a measurable temperature increase [189].

The second channel, ionisation or scintillation light, is *quenched* and allows a discrimination of events with high energy loss  $dE/dX$ . For example, compared to electron recoils (low  $dE/dX$ ), nuclear recoils (high  $dE/dX$ ) of the same energy produce the same heat signal, but a reduced ionisation signal [189, 297]. Consequently, this technique allows an event-by-event discrimination of nuclear recoils, as expect from elastic WIMP scattering, over electron recoils as expected from  $\gamma$ -background. This will be discussed in detail on the example of EDELWEISS in Sect. 2.3.

The advantage of active background rejection led to intensive developments since its first proposal and is reported in detail elsewhere, see e.g. [189, 297] and references therein. Currently the experiments CDMS [37–39], EDELWEISS [38, 76, 77], and CRESST [63] published results. ROSEBUD [158] was more focused on R&D of new target materials, but was defunct in 2012 [168]. EDELWEISS and CRESST plan to merge to EURECA in the future [64, 218, 219].

The *EDELWEISS* experiment is located at the *Laboratoire Souterrain de Modane* (LSM) (France, 4850 mwe [106]). It will be discussed in detail in Sect. 2.3. As result of its second stage (EDELWEISS-II), EDELWEISS can set an upper limit of  $4.4 \times 10^{-8}$  pb on  $\sigma_{\chi, N}^{\text{SI}}$  at 90 % CL for  $m_\chi c^2 = 85$  GeV [76]. To further improve the

exclusion limits, the exposure of EDELWEISS-II [76] was combined [38] with the exposure of CDMS II (Ge) [37], also a direct search experiment using cryogenic germanium bolometers. The combined exclusion limit is with  $\sigma_{\chi,N}^{\text{SI}} < 3.3 \times 10^{-8} \text{ pb}$  at 90 % CL minimal at  $m_\chi c^2 = 90 \text{ GeV}$  [38]. The obtained exclusion limits are the most sensitive limits for any germanium based experiment and third only to the xenon based experiments XENON100 [68] and LUX [42]. With a special data selection [77], the exclusion limit is extended to lower WIMP masses:  $\sigma_{\chi,N}^{\text{SI}} < 10^{-5} \text{ pb}$  at 90 % CL for  $m_\chi c^2 = 10 \text{ GeV}$  [77].

For the *Cryogenic Dark Matter Search*, the most recent results are published for the second stage (CDMS-II), which was located at the Soudan Underground Laboratory [37]. It used *Z-sensitive Ionization and Phonon* detectors (ZIP) to search for WIMP-induced nuclear recoils in germanium (19 detectors with 250 g each) and silicon (11 detectors with 100 g each) [37, 39]. With the germanium detectors, an exposure of 121.3 kg.d was taken between October 2006 and July 2007 [36] and an exposure of 612 kg.d between July 2007 and September 2008 [37]. In the last period, the CDMS collaboration found two events in their WIMP search region [37]. By an estimated background of 0.8 evts from surface electron recoils and 0.1 evts from neutrons, the result is no evidence for a WIMP signal. Combining both data sets, CDMS-II set an exclusion limit with a minimum of  $\sigma_{\chi,N}^{\text{SI}} < 3.8 \times 10^{-8} \text{ pb}$  at  $m_\chi c^2 = 70 \text{ GeV}$  [37]. To increase the sensitivity on  $\sigma_{\chi,N}^{\text{SI}}$ , the CDMS and EDELWEISS collaborations had combined their data as mentioned above. Selecting only data from germanium detectors with especially low threshold, a reanalysis [39] of the data set [36, 37] together with older data taken with germanium and silicon detectors at the shallow *Stanford Underground Facility* (SUF) (US, 17 mwe) [41] results in an improved exclusion limit below  $m_\chi c^2 = 9 \text{ GeV}$ . Also, no evidence for a modulation in the low mass CDMS-II data [39] was found [40]. Within the 140.2 kg.d exposure taken with 8 silicon detector between July 2007 and September 2008, in total 3 event were identified in the WIMP search region [31]. Albeit a profile likelihood test favoured the hypothesis that the events were caused by a signal of a WIMP with  $m_\chi c^2 = 8.6 \text{ GeV}$ , see also Fig. 2.10, the CDMS collaboration stated that this result does not rise to the level of a discovery [31]. CDMS-II was upgraded to *SuperCDMS* [268] with detectors of higher mass and a more efficient rejection of surface events using interleaved electrodes, similar to EDELWEISS, and additional phonon sensors. Currently, SuperCDMS is running with 15 of these new *iZIP* detectors at Soudan Underground Laboratory, aiming for a sensitivity of  $\sigma_{\chi,N}^{\text{SI}} < 5 \times 10^{-9} \text{ pb}$  [268]. The next stage is to move SuperCDMS to *SNOLAB* (Canada, 6000 mwe) due to the increased shielding against cosmogenic background and to further increase the individual detector mass [268].

The *Cryogenic Rare Event Search with Superconducting Thermometers* (CRESST) experiment is located at the LNGS [63]. Initially, it measured the thermal signals of sapphire crystals ( $\text{Al}_2\text{O}_3$ ) (CRESST-I) [61]. In its current second stage (CRESST-II) a dual readout of phonon and scintillation signals from  $\text{CaWO}_4$  is used [63]. Within 730 kg.d of exposure between July 2009 and March 2011, 67 events in the WIMP search region were found [63]. With a significance of  $4\sigma$ , a maximum

likelihood analysis shows that the estimated background from leaking electromagnetic events,  $\alpha$ -particle and recoiling nuclei from  $\alpha$ -decay, and neutron scattering is not sufficient to explain the observed events. Also a dedicated Geant4 simulation confirmed that ambient and muon-induced neutrons are only a minor contribution to the observed events [285]. In case scattering WIMPs are the missing contribution and considering the different nuclei in the target, a maximum likelihood analysis found two maxima in the  $\sigma_{\chi,N}^{\text{SI}}-m_\chi$ -parameter space, corresponding to potential WIMP signals at 11.6 and 25.3 GeV, respectively [63]. Figure 2.10, shows the contours at 95.45 % CL for these excesses. This is in mild tension with earlier results from CRESST-II [62], both in the analysis provided by the CRESST collaboration [63] and in the analysis by A. Brown et al. [135], as they partially exclude the potential WIMP signals from [63]. To investigate this situation further, the experiment was recently upgraded to reduce the still high background contribution: depending on the chosen likelihood maximum, a background of 37.6 events or 42.8 events remains, mainly recoiling nuclei and  $\alpha$ -particles from  $\alpha$ -decay [63].

The *Rare Objects SEArch with Bolometers UndergrounD* (ROSEBUD) [142, 158] at the LSC investigated the prospects of different target materials (BGO,  $\text{Al}_2\text{O}_3$ , LiF) for WIMP searches and in situ neutron monitoring based on the dual measurement of phonon and scintillation signals.

Finally, EDELWEISS, CRESST and new groups merged to the *European Underground Rare Event Calorimeter Array* (EURECA) [64, 218, 219], planned to be installed in the extension of the LSM [220]. In the final stage, it aims for a sensitivity of  $<2 \times 10^{-11}$  pb with a target mass of  $\approx 1000$  kg [64, 218]. A multi-target (e.g. Ge,  $\text{Al}_2\text{O}_3$ ) approach is planned to control systematic effects and to investigate the  $A^2$  dependence (Eq. 2.20a) in case of a detected WIMP candidate [218]. To reduce the neutron background with respect to current experiments like EDELWEISS, CRESST, it is planned [218] to shield the cryostat by  $\approx 3$  m of water, with the cryostat immersed in a water Cherenkov detector [309], also used as muon veto. The amount of muon-induced neutrons will be further reduced by a reducing high- $Z$  material near the detectors [283]. The mechanism of muon-induced neutron production will be discussed in Chap. 3.

## 2.2.4 Two-Phase Noble Liquids

Similar to cryogenic crystal detectors, existing and planned experiments based on two-phase noble liquids, like ZEPLIN, XENON, WArP, LUX, ArDM, DarkSide, XAX, MAX, LZ, or DARWIN, use the dual measurement of two signals to identify nuclear recoils as dark matter signature: the first signal is scintillation light, the second the ionisation signal which is quenched relative to the scintillation signal [45, 151].

As experimental design a time projection chamber is used, filled with noble gas in a liquid phase as target and a gaseous phase. An interaction in the liquid phase will cause scintillation light and free charge carriers via ionisation. The latter are

drifted into a gaseous phase above the noble liquid via electric fields and are mostly measured indirectly via electroluminescence [45, 151]. Only the ArDM experiment proposed to use large electron multiplier for a direct detection of the ionisation signal [273]. As target mostly liquid xenon (LXe,  $A = 131.3$  [65]) is used, i.e. in XENON and LUX, as its high atomic weight makes it a suitable target for spin-independent interaction which scales like  $A^2$  and a good kinetic match to likely WIMP masses [297]. However, also liquid argon (LAr,  $A = 40.0$  [65]) is used, currently only in DarkSide, as it has three advantages: first to test the  $A^2$ -scaling (Eq. 2.20a) of a possible dark matter signal with a lighter target, second it has better discrimination power for nuclear recoils, and third it is cheaper than LXe [297].

To suppress the background further, most of the experiments use *self-shielding* [151]. As noble liquids can be purified to high levels, the target is usually separated in an inner *fiducial* volume and an outer region. Whereas the inner fiducial volume is used to search for dark matter signals, the outer region acts as shield against ambient backgrounds, but produces little background by itself due to its high radiopurity. With respect to radiopurity, LAr has, with the long-lived radioactive isotope  $^{39}\text{Ar}$ , an intrinsic background which requires the sourcing from special, depleted underground reservoirs [151, 179, 297].

The experiments ZEPLIN [47, 223], XENON [60, 68], WArP [101], and LUX [42] have recently published results of their search for dark matter, whereas ArDM [84, 273], and DarkSide [52, 318] are still under construction or in commissioning. Proposals for future experiments are Panda-X [231], XAX [73], MAX [72], Darwin [89], and LZ [238].

The ZEPLIN programme spans the experiments ZEPLIN I, ZEPLIN II, and ZEPLIN III, using targets of liquid xenon (LXe) at Boulby Underground Science Facility (UK, 2800 mwe) [54]. ZEPLIN I used pulse shape analysis to identify scintillation caused by nuclear recoils in  $\approx 5$  kg LXe [54]. Starting with ZEPLIN II (31 kg LXe), the simultaneous readout of scintillation and ionisation signals was used to identify nuclear recoils [55]. ZEPLIN III, a two-phase xenon time-projection chamber containing 12 kg LXe, collected data in two science runs: first in 2008 and later between June 2010 and May 2011 [47, 223]. During the second run, ZEPLIN III was equipped with a gadolinium based anti-coincidence veto system to reject neutron background [46]. In the combined fiducial exposure of 1344 kg.d 13 events were found in the WIMP search region in agreement with the expected background from electron recoils [47]. The resulting exclusion limit is  $\sigma_{\chi, \text{N}}^{\text{SI}} < 3.9 \times 10^{-8} \text{ pb}$  at  $m_\chi c^2 = 52 \text{ GeV}$  [47].

The multi-stage experiment XENON is a dual phase liquid xenon time projection chamber at the LNGS [59]. The target mass is continuously increased over the individual stages: XENON10 had a target of 25 kg [66] (5.4 kg fiducial mass [59]), the current stage XENON100 has a target of 62 kg [67] (34 kg fiducial mass [68]), and for XENON1T a target of  $\approx 2500$  kg (1000 kg fiducial mass) is planned [67, 100]. Within an exposure of 7636.4 kg.d, collected by XENON100 during 2011 and 2012, two events were found in the WIMP search region [68]. The expected background, mainly leakage of  $\beta$ - and  $\gamma$ -radioactivity in the WIMP search region,

is estimated to 1.0(2) event [68]. The minor contribution from ambient and muon-induced neutrons is deduced to  $0.17^{+0.12}_{-0.07}$  [69]. Therefore the observed events are no indication for a dark matter signal. Consequently a 90 % CL exclusion limit of  $\sigma_{\chi,N}^{\text{SI}} < 2.0 \times 10^{-9}$  pb at  $m_\chi c^2 = 55$  GeV [68] is set. Based on data collected during 12.5 live days in 2006 with XENON10, also an limit of  $\sigma_{\chi,N}^{\text{SI}} < 7.0 \times 10^{-6}$  pb for light WIMPs with  $m_\chi c^2 = 7$  GeV could be set [60]. With a background reduced by a factor 100 with respect to XENON100, it is planned to start data taking with XENON1T in 2015 [100]. The next stage is *XENONnT*, an upgrade to  $\approx 6$  t target mass [136].

The *Large Underground Xenon* (LUX) experimentally uses a two-phase detector with 370 kg LXe (250 kg active monitored volume) aiming for  $\sigma_{\chi,N}^{\text{SI}} < 2 \times 10^{-10}$  pb [42, 44]. After a test run of the fully assembled detector at surface [43], the detector was installed in 2012 at the Davis laboratory (4300 mwe) of the *Sanford Underground Research Facility* (US)[317]. Over 85.3 live-days between April 2013 and August 2013, it collected first physics data with a fiducial volume of 118 kg [42]. The observed 160 events are consistent with the predicted background of electron recoils. Therefore, it could set a 90 % CL exclusion limit on  $\sigma_{\chi,N}^{\text{SI}} < 7.6 \times 10^{-10}$  pb for  $m_\chi c^2 = 33$  GeV, cutting also into the range of low mass WIMPs due to a lower threshold than XENON100 [42]. It is planned to continue the search until 2015 with an improved set-up and aiming for 300 live-days of data.

The *Wimp ARgon Programme* (WArP) at the LNGS [175] is a two-phase drift chamber searching for WIMP recoils in 2.6 kg (1.83 kg fiducial mass) liquid argon (LAr) [101]. In an exposure of 96.5 kg.d no events were found in the WIMP search region and an exclusion limit at 90 % CL was published 2008 [101]. The next stage of the programme is the WArP 100L detector, containing 100 l of LAr [303]. The project is continued as the *DarkSide* experiment [168].

The multi-stage *DarkSide* programme at LNGS uses a two-phase time projection chamber with depleted argon, to reduce background from  $^{39}\text{Ar}$  [318]. The prototype detector DarkSide-10 with 10 kg LAr is currently running at LNGS [52, 318]. The first stage to collect physics data will be DarkSide-50 with 50 kg LAr [318], featuring a neutron veto based on boron-loaded liquid scintillator [319]. Currently, DarkSide-50 is under construction at LNGS [276]. The next stage would be DarkSide G2 with a multi-tonne target [72, 276].

The *Argon Dark Matter* experiment (ArDM) is a two-phase detector with a tonne-scale LAr target [84, 273]. Instead of relying on electroluminescence to measure the ionisation signal, it extracts the ionisation signal via large electron multipliers in the gaseous phase [273]. After detector assembling and testing at surface [239], the detector was deployed at the LSC and is currently commissioned [84].

*Panda-X* is a multi-stage experiment, planned to be installed at the CJPL [231]. The first stage of the LXe dual-phase detector will contain 25 kg LXe, going up to 1.5 t LXe in the final stage [231].

The  $^{129/131}\text{Xenon}$ -Argon- $^{136}\text{Xenon}$  (XAX) experiment is a proposal to use three different targets of 10 t mass each [73]: LXe enriched with  $^{129}\text{Xe}$ ,  $^{131}\text{Xe}$  to search for spin-dependent interaction of WIMPs, LXe enriched with  $^{136}\text{Xe}$  for spin-independent

interaction, and LAr to compare possible interactions in LXe to a target with lower atomic weight. A similar multi-target experiment is *MAX*, proposed by a consortium of the XENON and DarkSide collaborations [72].

*Dark matter wimp search with noble liquids* (DARWIN) is a design study for a dual-phase detector with a multi-tonne target of LAr or LXe, aiming for a sensitivity of  $\sigma_{\chi, N}^{\text{SI}} < 10^{-12} \text{ pb}$  [89].

The *LUX-ZEPLIN* programme (LZ) aims for a sensitivity of  $\sigma_{\chi, N}^{\text{SI}} < 5 \times 10^{-13} \text{ pb}$  with a two stage experiment at *Sanford Underground Research Facility* [238]: the dual-phase detector will contain 1.5–3 t LXe in the first stage (LZS) and 20 t LXe in the second stage (LZD).

### 2.2.5 Single-Phase Noble Liquids

Contrary to experiments using two-phase noble liquids, single-phase experiments like XMASS and CLEAN/DEAP use only the scintillation light as signal. Therefore, a gaseous phase is missing and the target consists only of a liquefied noble gas.

A passive background reduction is still possible by using the self-shielding of the target [297]. For an active background rejection and discrimination of nuclear recoils, a pulse shape analysis of the scintillation signal is possible [297].

XMASS [19, 20] is the only experiment using this technique that recently published results on dark matter search. The first detectors of the CLEAN/DEAP project dedicated to search for dark matter, i.e. MiniCLEAN and DEAP-3600 are currently under construction [129, 192, 200].

The XMASS detector is located at the Kamioka underground laboratory (Japan, 2700 mwe), using a target of 835 kg LXe [19]. Commissioning runs ended in 2012 [19]. With an exposure of 5591.4 kg.d taken in February 2012 and a low threshold of 0.3 keV<sub>ee</sub>, the experiment set an exclusion limit, dedicated for low-mass WIMPs [20]. However, the systematic uncertainty of the scintillation efficiency for nuclear recoils relative to electron recoils has a large impact in the limit, see [20, Fig. 8].

The *Dark matter Experiment using Argon Pulse shape discrimination/Cryogenic Low Energy Astrophysics with Noble liquids* (DEAP/CLEAN) programme proposed and built several experiments based on single-phase detectors using LAr and noble neon (LNe) targets [192] including four prototypes: DEAP-0 and picoCLEAN were R&D prototypes, microCLEAN measured the nuclear quenching factor and DEAP-1 studied discrimination based on pulse shape analysis. The first detectors expected to deliver physics data are currently under construction at SNOLAB: MiniCLEAN and DEAP-3600 [192]. MiniCLEAN will have a LAr target of 500 kg mass (150 kg fiducial mass) [200]. DEAP-3600 will be a detector with 3.6 t LAr, its commissioning is expected for the end of 2013 [129].

### 2.2.6 Superheated Liquids

Experiments using superheated liquids (PICASSO [70], COUPP [91], SIMPLE [172]) detect the bubble-nucleation after interactions occur. Via tuning of temperature and pressure, the detectors become insensitive to ionising particles with low stopping power  $dE/dX$ , such as electron recoils. Only events with high stopping power, like nuclear recoils, cause nucleation [88]. All experiments have an increased sensitivity to spin-dependent interaction via  $^{19}\text{F}$  in their targets. However, they also published limits on the spin-independent interaction cross section.

The *Project In Canada to Search for Supersymmetric Objects* (PICASSO) [70, 128] at SNOLAB uses  $\text{C}_4\text{F}_{10}$  as target. With a subset of 10 detectors, a combined exposure of  $114.3\text{ kg.d}$  was collected [70]. A low background allowed to lower the threshold as low as  $1.7\text{ keV}$ , resulting in an increased sensitivity for WIMPs with mass below  $10\text{ GeV}$  with a minimum at  $\sigma_{\chi,\text{N}}^{\text{SI}} < 6.1 \times 10^{-5}\text{ pb}$  for  $m_\chi c^2 = 20\text{ GeV}$  at 90 % CL [70].

The *Superheated Instrument for Massive ParticLe Experiments* (SIMPLE) at the *Low Noise Underground Laboratory* (France, 1500 mwe) use  $\text{C}_2\text{ClF}$  as target [171, 172]. The experiment's second stage (SIMPLE-II) collected data in two runs: in the first run [171] an exposure of  $14.1\text{ kg.d}$  was obtained with  $208\text{ g}$  active mass and in the second run [172] an exposure of  $13.67\text{ kg.d}$  with  $215\text{ g}$  active mass. The combined exposure contained eleven events in the WIMP search region, in agreement with the estimated neutron background [172]. Therefore an exclusion limit of  $\sigma_{\chi,\text{N}}^{\text{SI}} < 7.6 \times 10^{-6}\text{ pb}$  for  $m_\chi c^2 = 35\text{ GeV}$  was obtained [172]. It is planned to increase the active mass by a factor of 25 and add additional neutron shielding for SIMPLE-III [191].

The *Chicagoland Observatory for Underground Particle Physics* (COUPP) uses  $\text{CF}_3\text{I}$  as target [90, 91]. Between September 2010 and August 2011 a total exposure of  $553.0\text{ kg.d}$  was collected with a  $4.0\text{ kg}$ -target at SNOLAB. Within the exposure 20 events in the WIMP search region were observed, with an estimated background of 5.3 events. However, the observed events show a clustering in time which is unlikely for true nuclear recoils induced by WIMPs. Therefore, no discovery is claimed, but an exclusion limit is set [91]. The upper exclusion limit at 90 % is presented as a band to consider systematic uncertainties in the nucleation efficiency due to  $^{19}\text{F}$  and  $^{12}\text{C}$  recoils [91]. The next stages contain a  $60\text{ kg}$  target (COUPP-60 kg) currently installed at SNOLAB and a tonne scale detector (COUPP-500 kg) currently in R&D phase [313].

The *PICASSO-COUPP* (PiCo) experiment is a merger of both groups, aiming for a target volume of  $250\text{ l}$  at SNOLAB [71, 159].

### 2.2.7 *Directional Experiments*

This section focuses on spin-independent interaction and thus excludes the experiments searching for a directional signal as they investigate spin-dependent interactions with targets containing  $^{19}\text{F}$  and did not publish limits on spin-independent interactions.

Four directional experiments try to establish a correlation between the galactic motion and the track of recoiling nuclei in gaseous time projection chambers [88, 179, 297]: *Directional Recoil Identification From Tracks* (DRIFT) at Boulby Underground Science Facility [160, 247], the *Dark Matter Time Projection Chamber* (DMTPC) at the *Waste Isolation Pilot Plant* (US, 1600 mwe) [35, 246], the *NEw generation WIMP search with an Advanced Gaseous tracking device Experiment* (NEWAGE) at Kamioka underground laboratory [244, 249], and the *MIMAC* experiment at LSM [195, 271]. All these experiments are using at least partially  $\text{CF}_4$  as target, therefore they are sensitive to spin-dependent interactions. DRIFT [160], DMTPC [35], and NEWAGE [244] already published limits on the spin-dependent scattering cross section.

### 2.2.8 *Tension Between Signal Claims and Exclusion Limits*

As shown in Sects. 2.2.1–2.2.7, 13 experiments published currently results of their search for dark matter.<sup>13</sup> In three cases<sup>14</sup> an excess above the known background was found, but no discovery was claimed so far. Only DAMA/LIBRA claimed discovery of dark matter via an annually modulated signal. In twelve cases<sup>15</sup> no excess over the known background was found and consequently exclusion limits were set. A compilation of the published signals and limits are shown<sup>16</sup> in Figs. 2.10 and 2.11, together with a theoretical prediction [137], see Sect. 2.1.4. In Fig. 2.11 we show also the limits obtained from the indirect search by IceCube [12], see Sect. 2.1.4.

<sup>13</sup>In the following, an asterisk will indicate a dedicated analysis for low WIMP mass.

<sup>14</sup>CDMS II (Si) [31], CoGeNT [7, 8], CRESST-II [63].

<sup>15</sup>CDEX [324], CDMS II (Ge) [37], CDMS II (Ge) + EDELWEISS II [38], CDMS II (Ge)\* [39], CDMS (SUF)\* [41], COUPP [91], EDELWEISS-II [76], EDELWEISS-II\* [77], KIMS [213], LUX [42], SIMPLE [172], TEXONO [229], WArP [101], XENON 10\* [60], XENON 100 [68], XMASS\* [20], ZEPLIN III [47].

<sup>16</sup>The data for CDMS II (Ge) [37], CDMS II (Ge)\* [39], CDMS SUF\* [41], CDMS II (Ge) + EDELWEISS II [38], CRESST-II [63], CoGeNT [7, 8], COUPP [91], DAMA/LIBRA [282], EDELWEISS-II [76], KIMS [213], LUX [42], SIMPLE [172], WArP [101], XENON 100 [68], XENON 10\* [60], ZEPLIN-III [47], and the prediction for the coherent neutrino background [123] were obtained from the *DMTools* (<http://dmtools.brown.edu>). The data for CDMS II (Si) [31], CDEX [324], DAMA/LIBRA [98, Fig. 1,rightpanel], EDELWEISS-II\* [77], IceCube [12], TEXONO [229], XMASS [20], and the theoretical model [137] were copied directly from the original publication. For PICASSO [70], no data in the logarithmical scale needed for Fig. 2.11 was found.

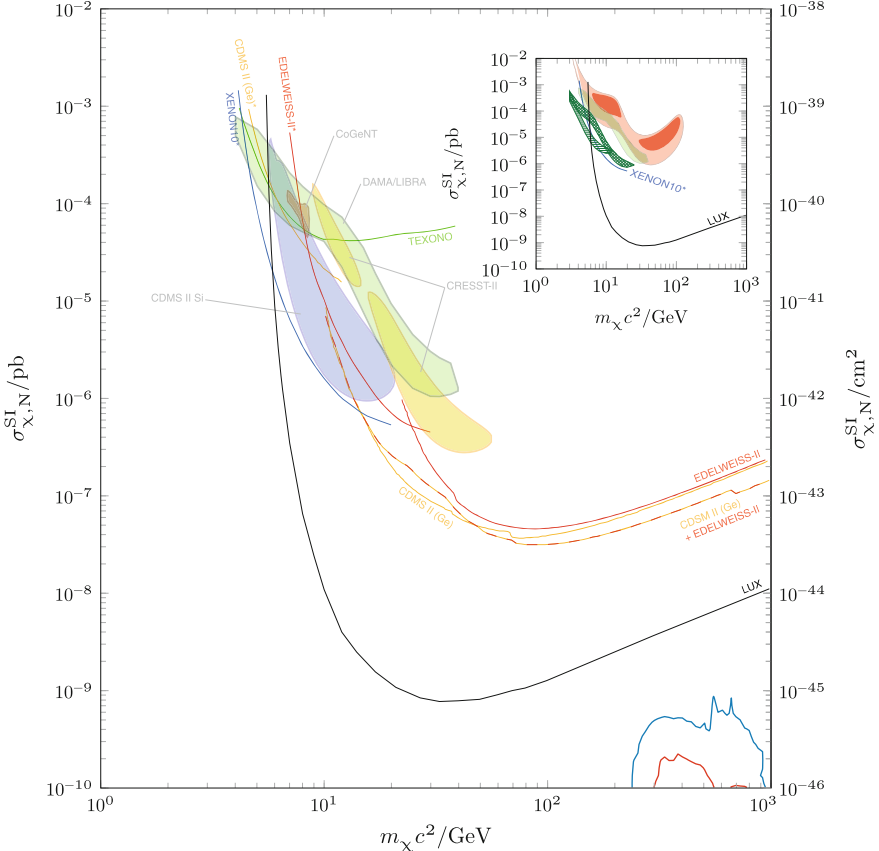


**Fig. 2.10** Possible WIMP signals in the  $\sigma_{\chi,N}^{\text{SI}} - m_\chi$ -plane: contours of the CoGeNT signal at 90% CL [7, 8], the excess measured by CDMS II with silicon detectors at 90% CL [31], the CRESST-II excess at 95.45% CL [63] and of the DAMA/LIBRA signal under the assumption of light neutralino dark matter [98] (We note that this contour indicates *not* the usual CL. It “represent the domain where the likelihood-function values differ more than  $7.5\sigma$  from the null hypothesis (absence of modulation)” [98, Fig. 1,right panel]. Nevertheless, we show it, as it is the analysis favoured by the DAMA/LIBRA collaboration [109, 127]. Also shown are the conventional analysis [282]). Also shown are the leading exclusion limits of LUX [42], XENON10\* [60], TEXONO [229], CDMS II (Ge) [37, 39], EDELWEISS-II [76, 77], and CDMS II (Ge) + EDELWEISS-II [38]. The *inset* shows the effect of channeling (green horizontally-hatched region) and the effect of energy dependent Na and I quenching factors (green cross-hatched region) on the DAMA signal (green filled region) according to [98, Fig. 1, right panel]. The alternative analysis [282] is shown at  $3\sigma$  CL (dark red) and  $5\sigma$  CL (light red) for no channeling. Shown in the *right lower corner* are 68% CL (red) and 95% CL (blue) expectation for a global CMSSM fit [137]

In this section we will discuss the tension between these exclusion limits and the observed excesses/signals and give a short review on the possible solutions discussed in literature. Also a comparison between experimental findings and theoretical predictions (Sect. 2.1.2) will be given. For the exclusion limits, we will focus on LUX

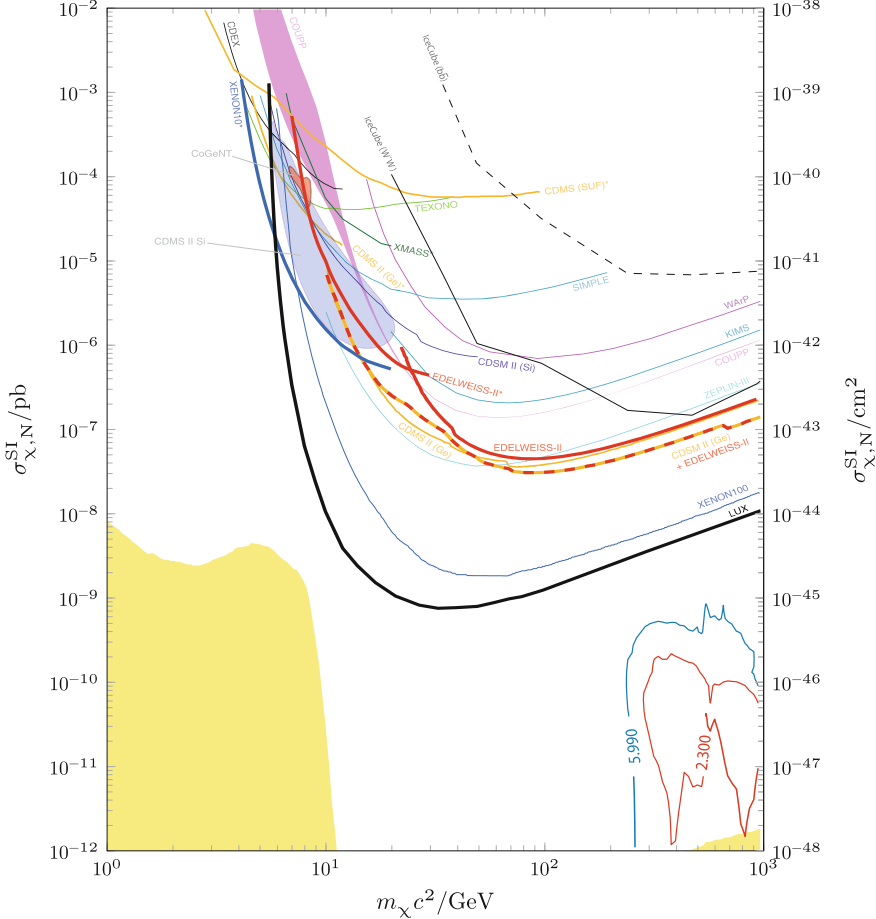


**Fig. 2.11** Experimental upper limits at 90 % CL on the spin-independent cross section for elastic scattering of WIMPs off various targets,  $\sigma_{\chi, N}^{\text{SI}}$ , normalized per nucleon, as function of the WIMP mass  $m_\chi$  (CDEX [324], CDMS II (Ge) [37], CDMS II (Si) [31], CDSM II + EDELWEISS II [38], COUPP [91], EDELWEISS-II [76], KIMS [213], IceCube for  $W^+ W^-$ ,  $b \bar{b}$  final states [12], LUX [42], SIMPLE [172], TEXONO [229], WArP [101], XENON100 [68], ZEPLIN-III [47]). Dedicated analyses for low WIMP masses are indicated by an asterisk (CDMS II (Ge) [39], CDMS (SUF) [41], EDELWEISS-II [77], XENON10 [60], XMASS [20]). Also shown are the CoGeNT signal [7, 8] and the excess measured by CDMS II with silicon detectors [31], both at 90 % CL. The yellow area indicate the background from coherent neutrino scattering [123]. Shown in the right lower corner are 68 % CL (red) and 95 % CL (blue) expectations for a global CMSSM fit [137]

[42] and the combined results of CDMS II (Ge) + EDELWEISS-II [38] as they are the leading limits for xenon and germanium targets, respectively.

If the excesses observed by CoGeNT [7, 8], CRESST [63] and CDMS II (Si) [31] and the annual modulation observed by DAMA/LIBRA [98, 114, 116] are interpreted as signals of an elastic scattered neutralino, the masses of the proposed

candidates lie between  $m_\chi \approx 7$  GeV for CoGeNT and  $m_\chi \approx 25$  GeV for CRESST. The leading exclusion limits of LUX ( $\sigma_{\chi,N}^{\text{SI}} < 7.6 \times 10^{-10}$  pb) and CDMS II (Ge) + EDELWEISS-II ( $\sigma_{\chi,N}^{\text{SI}} < 3.3 \times 10^{-8}$  pb) are less restricting for this *low mass WIMP* signal, see Fig. 2.10, as the respective experiments have their highest sensitivities between  $m_\chi \approx 33$  GeV for LUX and  $m_\chi \approx 90$  GeV for CDMS II (Ge) + EDELWEISS II, as the MSSM predicts *heavy WIMPs*, cf. Figs. 2.8b and 2.10.

However, reanalysis of the XENON10\* [60], CDMS II (Ge)\* [39], and EDELWEISS-II\* [77] results, aimed for lower mass at the cost of a reduced total sensitivity, strongly limit the allowed parameter space for these light WIMPs. As Fig. 2.10 shows, the combined XENON10\* and LUX limits exclude the preferred regions for the CRESST, CoGeNT, and CDSM II (Si) signal completely, and strongly limit the DAMA/LIBRA region. This strong reduction of the signal region is also confirmed by other experiments: Also CDSM II (Ge) + EDELWEISS-II, in sensitivity third only to LUX and XENON100, exclude the CRESST excess and strongly limit the parameter space for the CoGeNT, CDSM II (Si), and DAMA/LIBRA signal. This is confirmed, albeit with lower sensitivity, by experiments with a lower target mass like SIMPLE [172] or with a low threshold like TEXONO [229]. It has to be noted that possible signal is also at much lower mass and higher cross section than the predictions from the canonical CMSSM, e.g. [137], cf. Fig. 2.10.

To solve this tension between the observed excesses in some experiments and no signal in other experiments, several hypotheses are discussed in literature. They can be roughly divided into three categories: systematic effects on the experiments, alternative dark matter distribution in the galaxy like triaxial models [97] or tidal streams [210], and non-standard interactions between dark matter particles and the target such as a coupling to electrons instead to quarks [115] or iso-spin dependent interactions which suppress scattering off heavy targets like xenon [183]. However, it seems unlikely that fine tuning of the astrophysical and particle physics properties alone will yield a mutual solution for all observations [217].

Therefore, a correct understanding of possible systematic effects on the experiments is important. Exemplary, the tension between the results of DAMA/LIBRA and LUX may be removed by shifting the DAMA/LIBRA signal via channeling or energy dependent quenching factors [98, 113], see Fig. 2.10. It shows also the alternative interpretations [282] of a subset of the DAMA/LIBRA data [114]. For the tension between DAMA/LIBRA and the older XENON100 results, the tension may be reduced by relaxing the XENON limit by possible uncertainties in the relative scintillation efficiency of LXe at low energies [157, 306]. But also trivial explanations like an unknown background is possible, e.g. the CRESST excess may be caused by secondary cascades of nuclear recoils caused by  $^{210}\text{Po}$  decay [222]. To identify such possible systematic uncertainties, it is important to maintain also in the future at least two detectors with different targets and detector designs [297]. EURECA would be an example for such a *complementary* approach within one experiment, i.e. heat and ionisation signals from germanium diodes, and heat and light from scintillators.

Future experiments with target masses up to a Multi-tonne scale will also be necessary to probe further the theoretical predictions. Increasing the target mass up to multi-tonne scale will potentially allow to observe statistically significant rates

at  $\sigma_{\chi,N}^{\text{SI}} < 10^{-11} \text{ pb}$  as theoretically predicted for the LSP [297], see Fig. 2.8b. At scattering cross sections below  $10^{-12} \text{ pb}$ , the background from coherent scattering of atmospheric neutrinos will limit the prospects of direct dark matter searches. For low WIMP masses ( $m_\chi c^2 < 10 \text{ GeV}$ ), coherent scattering of solar neutrinos will limit the WIMP search already at  $\sigma_{\chi,N}^{\text{SI}} < 10^{-8} \text{ pb}$  [123], see Fig. 2.11.

## 2.3 Dark Matter Search at LSM with EDELWEISS

In Sect. 2.2, we gave an overview of the current state of direct searches for WIMPs. Here, we will discuss the experimental aspects of EDELWEISS in more detail.

EDELWEISS uses cryogenic germanium bolometers to search for nuclear recoils induced by galactic WIMPs scattering off the nuclei. It is situated in the *Laboratoire Souterrain de Modane* (LSM) [76, 258]. The very first phase of the experiment started in the mid-1990s [96], developed into the EDELWEISS-I [143, 144, 280] and EDELWEISS-II [76, 77] stages. It is now in the installation phase of EDELWEISS-III [74, 258]. Continuous improvements of the detectors [258] resulted in a high power to reject background and now qualify to aim for a sensitivity of  $\sigma_{\chi,N}^{\text{SI}} \lesssim 10^{-9} \text{ pb}$  with EDELWEISS-III [80]. A sophisticated detector design and the simultaneous measurement of ionisation and phonon signals allows an event-by-event separation of the searched nuclear recoils from electronic recoils caused by  $\gamma$ - and  $\beta$ -radioactivity in the bulk and on the surface of the detector [133, 134].

In this section we will focus mainly on EDELWEISS-II, starting with a description of its experimental set-up in Sect. 2.3.1. Then, the rejection of electronic recoils is discussed in Sect. 2.3.2. Finally, the obtained physical results, exclusion limit and background, of EDELWEISS-II are given together with an outlook to EDELWEISS-III (Sect. 2.3.3). One kind of background, muon-induced neutrons, will then be discussed in detail in Chap. 3.

### 2.3.1 The Experimental Set-up at LSM

To reduce cosmogenic background, EDELWEISS is located at the Laboratoire Souterrain de Modane (LSM) besides a road tunnel below the Pointe du Fréjus in the Alps at the French-Italian border. Figure 2.12 shows the location of EDELWEISS in the main hall of the LSM, until 2011 [289] the NEMO 3 experiment [81] was installed next to EDELWEISS. To attenuate the remaining background, the cryostat with the germanium crystals is surrounded by passive  $\gamma$ - and neutron shields and an active muon veto [76]. To allow maintenance access to the cryostat, the upper part (called *Niveau 1*) of the shields and veto is divided and movable in an open and closed configuration. Contrary, the lower part (*Niveau 0*) is fixed. The exact position

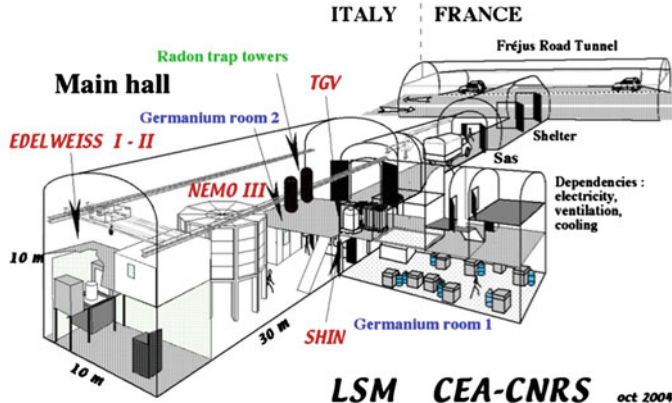


**Fig. 2.12** Location of EDELWEISS in the main hall of the LSM. Until 2011 the NEMO 3 experiment was installed nearby. Figure provided by the LSM

of the movable parts are regularly monitored via laser distance measurements [283]. For an illustration of the complete set-up, see Fig. 5.1b.

To investigate sources of neutron background, additional auxiliary detectors were temporarily installed, a  ${}^3\text{He}$  counter for the investigation of thermal neutrons [272], and a dedicated neutrons counter for muon-induced neutrons which is a main part of this work, see Chap. 4.

The muon flux at the LSM is attenuated by a rock overburden of 4800 mwe and measured via the EDELWEISS muon veto to  $5.2 \text{ m}^{-2} \text{ D}^{-1}$  [283]. A more detailed discussion with regard to the simulation of the muon flux will be given in Sect. 5.3. The flux of ambient neutrons is  $1.06 \times 10^{-6} \text{ cm}^{-2} \text{ s}^{-1} (E_n > 1 \text{ MeV})$  [180], an overview of neutron measurements at LSM will be given in Sect. 4.1.2. The radon level at LSM is  $\approx 20 \text{ Bq m}^{-3}$ , due to the ventilation system renewing the entire lab volume 1.5 times per hour [78]. The whole EDELWEISS set-up is surrounded by a clean room and permanently flushed with deradonized air [74], reducing the radon level to  $\approx 20 \text{ mBq m}^{-3}$  [78].

The active muon veto is the outermost layer of EDELWEISS. It consists of 46 individual plastic scintillator modules (called *muon modules* hereafter) and is capable of muon track reconstruction. They are mounted in a stainless steel frame attached to the neutron shield [283]. The modules have a cross section of  $65 \text{ cm} \times 5 \text{ cm}$  and lengths of 200 cm, 315 cm, 375 cm, 400 cm, for technical details of the muon modules see also Sect. 4.2.2. In total, the muon veto covers a surface of  $100 \text{ m}^2$  [283]. Due to prominent gaps in Niveau 0 for the cryogenic supply lines and the pillars on which the experiment is mounted, the geometrical efficiency to tag throughgoing muons is 98% [283].

A throughgoing muon deposits an energy between 11.8 MeV (horizontal modules) and 24 MeV (vertical modules) [202]. Aimed for an as high as possible efficiency to tag also grazing muons, the average trigger threshold is set to  $\approx 5 \text{ MeV}$  [283]. Consequently, the trigger rate of  $\approx 1 \text{ s}^{-1}$  is dominated by ambient background, whereas

muon candidates, selected by requiring a coincidence between non-adjacent modules, contributes only  $\approx 3.5 \times 10^{-4} \text{ s}^{-1}$  [283]. Including detector response and averaging over all muon modules, the detection efficiency for muons is 95 % [283]. MC simulation considering the geometrical coverage and the muon module efficiency results in a total muon veto efficiency for a closed Niveau 1 of 93.6(15) % in agreement with an experimental estimation of  $\geq 93.5$  % at 90 % CL [283].

On the inside of the muon veto follows the shield against ambient neutrons, made of polyethylene ensuring a minimal thickness of 50 cm towards the cryostat [76, 78]. The innermost shield is the  $\gamma$ -shield, consisting of an outer layer of 18 cm modern lead and an inner layer of 2 cm roman lead [228] with a reduced  $\gamma$ -activity from  $^{210}\text{Pb}$  [78, 283].

The central part of the set-up is the cryostat, able to cool down up to 40 kg of target mass to a stabilized temperature of 18 mK [74, 75]. EDELWEISS uses a cryostat with reversed geometry, i.e. the dilution unit is below the detectors, see [78, Fig. 1]. The detectors are placed within the thermal shields at 0.01, 1, 4.2, 40, 100 K, and are shielded by 14 cm roman lead against the cold electronics, the dilution unit, and the cryogenic parts [78].

All materials in the detectors' vicinity within the 10 mK thermal shield are tested for radiopurity by dedicated HPGe detectors [74, 78], e.g. the individual casings of the detectors are of 99.99 % pure electrolytic copper [78]. Also the Teflon holders of the detectors [254] are selected for lowest possible radioactivity [255, 256]. In the EDELWEISS-III stage, also the more distant parts of the cryostat, e.g. the thermal shields at higher temperature and the vacuum chamber at 300 K are specially selected for radiopurity [78].

Within the cryostat, the detectors are arranged in an array of towers, each tower with two to three detectors, to increase the granularity of the target mass [75, 76]. The cryogenic bolometers consist of a cylindrical absorber made of a HPGe monocrystal ( $< 10^{10} \text{ cm}^{-3}$  impurities [75]) equipped with sputtered aluminium electrodes and a glued Ge-NTD (Neutron Transmutation Doped) sensor [76, 256], see Fig. 2.13a. The dual readout of ionisation and phonon signal allows the rejection of electronic recoils with a power of  $3(1) \times 10^{-5}$  [74], see Sect. 2.3.2 for details. An overview of the historic detector development from EDELWEISS-I to EDELWEISS-III is given in [258]. The bolometer type used in EDELWEISS-II was *InterDigit* (ID) [258], explained later in more detail. In total, ten bolometers with a diameter of 70 mm and a height of 20 mm were installed in EDELWEISS-II [75, 76, 256]. Five detectors had bevelled edges at an angle of  $45^\circ$  and an average mass of 370 g<sup>17</sup> and five cylindrical detectors of 410 g [76].

The NTD measured the temperature of the crystal via the change of its resistance,  $\approx 1 \text{ M } \Omega$  at 17 mK [241]. With an optimized heat exchange with the absorber [256], the reached sensitivity is  $60 \text{ nV keV}^{-1}$  [258]. The FWHM baseline resolution of this heat channel ranged from 0.6–2.0 keV<sub>ee</sub> with an average of 1.2 keV<sub>ee</sub> [76, 258].

---

<sup>17</sup>However, [75] gives 360 g.

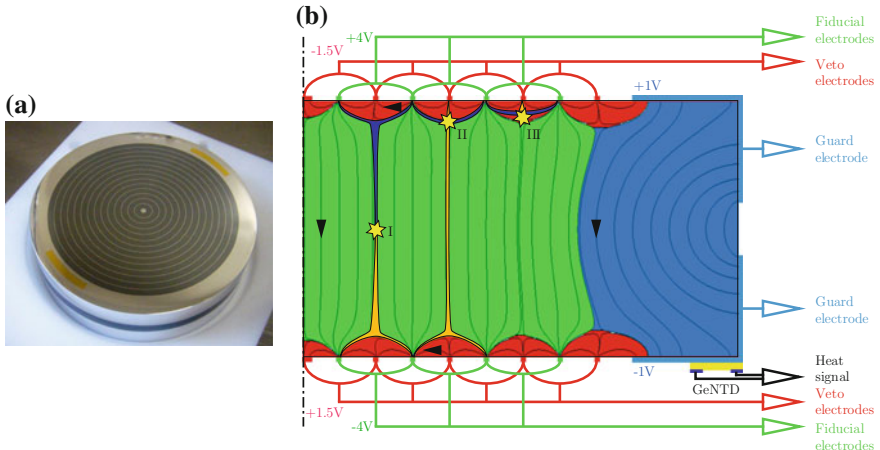


**Fig. 2.13** **a** Picture of a 410g InterDigit detector. Clearly seen are the interleaved electrodes on top and the guard electrodes on side. The NTD is glued on the bottom and therefore not visible. **b** Scheme of the heat and the six ionisation channels of the InterDigit detector and the related volumes in the detector cross section: guard volume (*light blue*), veto volume (*red*), and fiducial volume (*green*). Illustrated are the trajectories of positive (*orange*) and negative (*dark blue*) charge carriers for three event types: I) bulk ionisation, II) ionisation in low field area, III) near surface ionisation. Figures provided by the EDELWEISS collaboration and adapted by the author according to [75], [133, Fig. 1a]

The name of the InterDigit bolometer type comes from the used electrode design. Each germanium crystal has two types of aluminium electrodes sputtered on its passivated surface [134, 288]. There are two plane electrodes at the edge, called *guard electrodes*, and on the top and bottom two sets of annular concentric electrodes. In total, each crystal has six sets of electrodes [76], which enables the rejection of near surface events [133, 134, 161, 162] with a power of  $6 \times 10^{-5}$  [76], see Sect. 2.3.2 for details.

The concentric electrodes are a variation of the coplanar grid design [57, 131, 237], instead of disk shape electrodes it uses four sets of interleaved strips [133, 134]. The stripes are  $200\text{ }\mu\text{m}$  wide and  $250\text{ nm}$  thick, the distance between each concentric electrode is  $2\text{ mm}$  [133, 134]. Each electrode is connected via ultra-sonic bonding to its next but one neighbour, resulting in the earlier mentioned two sets of electrodes, called *fiducial* and *veto* electrode [133, 134].

The fiducial electrodes are biased with the highest potentials of  $\pm 4\text{ V}$  creating an axial electric field in the detector bulk [75]. The bias of  $\mp 1.5\text{ V}$  on the veto links adjacent electrodes via an electric field approximately parallel to the surface [75]. Plain guard electrodes cover the detector edges with a bias voltage of  $\pm 1\text{ V}$  [75]. See Fig. 2.13b for a map of the resulting field lines in the detector and Sect. 2.3.2 for the application in event selection. For the fiducial electrode, the chosen bias voltages and the electrode design results in a FWHM baseline resolution ranging from  $0.7\text{--}1.1\text{ keV}_{\text{ee}}$  with an average of  $0.9\text{ keV}_{\text{ee}}$  [76, 258].

The DAQ of the bolometers is independent from the DAQ of the muon veto, but synchronized via a common clock. The heat and ionisation signals of the bolometers are continuously sampled at  $100\text{ kS s}^{-1}$  [75, 283]. In case the heat channel of one bolometer crosses the threshold, pulse traces of all bolometers within the given tower are stored [76]. The trigger threshold on the heat channels was continuously adjusted online to a trigger rate of a fraction of Hz [76]. To reject muon-induced background in the bolometer data, an offline search tags coincidences between any bolometer and the muon veto with a time resolution of  $\approx 10\text{ }\mu\text{s}$ , defined by the sampling rate of the bolometer [283]. In case of a coincidence, any bolometer within  $\pm 1\text{ ms}$  around the muon tag is rejected [283].

### 2.3.2 Event Categories and Event Selection

With the experimental set-up described in Sect. 2.3.1, EDELWEISS-II is able to discriminate between nuclear recoils as expected from scattering WIMPs and electronic recoils. This is a main advantage, as it provides an active rejection of background from  $\gamma$ - and  $\beta$ -radioactivity. In this section we report the basic functionality of this rejection technique, which enables EDELWEISS-II to obtain its physical results discussed in Sect. 2.3.3.

The events occurring in the cryogenic bolometers of EDELWEISS can be categorized according to their interaction type and the penetration depth [103]: Nuclear recoils are expected to be induced by elastic scattering of WIMPs, and are also induced by neutrons and recoiling nuclei from  $\alpha$ -decays, like the  $^{210}\text{Po}(\alpha, \gamma)^{206}\text{Pb}$  reaction of the radon daughter nucleus  $^{210}\text{Po}$  [103]. Whereas WIMP and neutron scattering occurs throughout the crystal, recoiling nuclei are restricted to the surface due to the short penetration depth. Similar, electronic recoils are induced by Compton scattering of ambient  $\gamma$ -rays throughout the crystals, whereas  $\beta$ -particles interact electronically near the surface.

Aiming for a sensitivity of  $\sigma_{\chi, \text{N}}^{\text{SI}} < 5 \times 10^{-8}\text{ pb}$  for  $20\text{ GeV} \leq m_\chi c^2 \leq 100\text{ GeV}$ , the challenge is to detect a nuclear recoil rate of  $< 5 \times 10^{-3}\text{ evts kg.d}^{-1}$  in germanium at  $15\text{ keV} \leq E_{\text{rec}} \leq 65\text{ keV}$  [134]. However, already the average  $\gamma$ -rate within the EDELWEISS shield is  $\approx 10\text{ evts kg.d}^{-1}$ , hence an active rejection of electronic recoils better than  $10^{-4}$  is needed [134].

As electron recoils have a three times higher ionisation yield<sup>18</sup>  $Q_i$  as nuclear recoils, the dual measurement of ionisation and phonon signals with the cryogenic bolometers allows an active, event-by-event rejection of electronic recoils [74, 133]. However, this technique is limited by surface events where poor charge collection mimics nuclear recoils in the bulk of the detector [133]. Therefore, a clean inner fiducial volume has to be defined [74]. In the following, we will first introduce the rejection of electronic recoils in the bulk and then the rejection of surface events.

---

<sup>18</sup>Sometimes also called *quenching factor*, see e.g. [280].

The responses  $E_h$  of the phonon channel and  $E_i$  of the ionisation channel to a nuclear recoil with energy  $E_{\text{rec}}$  is normalized to the response to an electronic recoil of the same energy. As a result,  $E_h$  and  $E_i$  are given in *electronvolt electron equivalent* (eV<sub>ee</sub>) and can be parametrized as [105]:

$$E_{i,\gamma} = E_{\text{rec}} \quad (2.25a)$$

$$E_{i,n} = Q_i E_{\text{rec}} \quad (2.25b)$$

$$E_{h,\gamma} = E_{\text{rec}} \quad (2.25c)$$

$$E_{h,n} = \frac{Q_h + Q_i v}{1 + v} E_{\text{rec}} \quad v = \frac{e|V|}{\epsilon} \quad (2.25d)$$

Here,  $\epsilon = 3.0 \text{ eV}$  is the energy needed to create an electron-hole pair in cryogenic germanium [105] and  $e$  is the elementary charge. Equation 2.25d also corrects the signal for the Luke-Neganov-effect [236, 257] i.e. the Joule heating of the detector via the drifting charges along the bias potential  $V$  of the electrode [75]. Also the effect of energy leakage out of the bolometer, e.g. via photon emission, is considered and experimentally described via the heat quenching factor  $Q_h = 0.91$  [105].

For nuclear recoils, the ionisation yield  $Q_i = Q_i(E_{\text{rec}})$  depends on the electronic and nuclear stopping power  $dE/dX$  of germanium ions in germanium [105] and is described by the Lindhard theory [234, 235]. However, instead of a theoretical description EDELWEISS [75, 241, 279] uses an experimental fit [300]:

$$Q_i = 0.16 \cdot E_{\text{rec}}^{0.18} \quad (2.26)$$

It also includes systematic effects like the heat quenching, therefore no separate  $Q_h$  values are needed [300]. Consequently, the recoil energy is [241, 280]:

$$E_{\text{rec}} = \left(1 + \frac{e|V|}{\epsilon}\right) E_h - \frac{e|V|}{\epsilon} E_i \quad (2.27a)$$

$$= \frac{E_h}{1 + Q_i \frac{e|V|}{\epsilon}} \left(1 + \frac{e|V|}{\epsilon}\right) \quad (2.27b)$$

Figure 2.14 shows the distribution of events from a neutron calibration in the  $Q_i - E_{\text{rec}}$ -plane. Two clear populations from bulk events are visible: caused by the normalization of the detector response (Eq. 2.25a), the electronic recoils form a population around  $Q_i = 1$  and the nuclear recoils form a population around the central line according to Eq. 2.26 [279]. Between both populations are situated electronic recoils near the surface, below the bulk nuclear recoils occur nuclear recoils near the surface [105]. The distributions of the ionisation yield  $Q$  in the electronic and nuclear recoil bands are to a good approximation Gaussian and can be calculated from the experimental baseline resolution [76, 241]. These populations are parametrized by the *gamma band* and the *nuclear recoil band*: Assuming a Gaussian fluctuation of the  $Q_i$ , the gamma band reached 99.99% ( $7.72\sigma$ ) below unity [76]. The nuclear

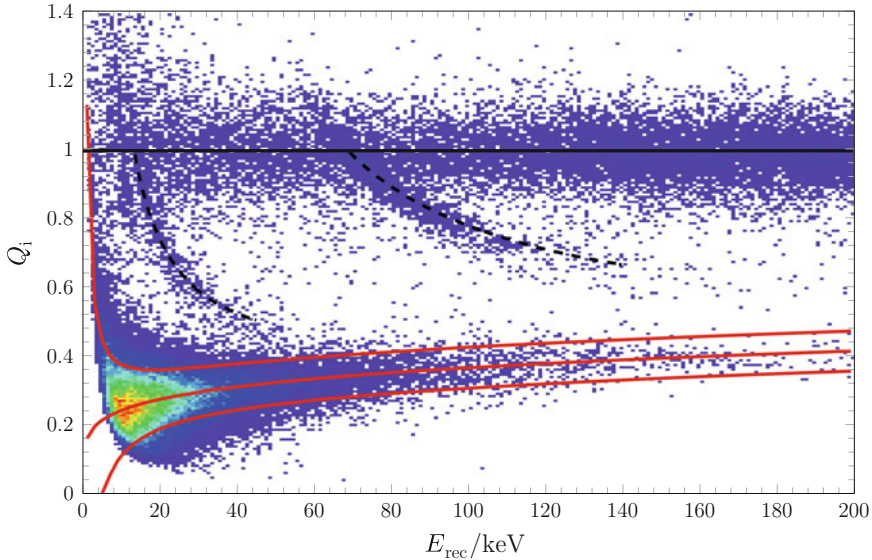


**Fig. 2.14** Ionisation yield  $Q_i$  as function of the recoil energy  $E_{\text{rec}}$  of fiducial events recorded during neutron calibration. The two main populations are pure electron ( $Q_i = 1$ , black solid line) and nuclear recoils ( $Q_i \approx 0.3$ ). The red lines indicate the  $Q_i(E_{\text{rec}})$ -parametrization for nuclear recoils according to Eq. 2.26 together with the 90 % CL band. Deexcitation of short lived states of  $^{73}\text{Ge}$  results in inelastic nuclear recoils with associated electromagnetic energies of 13.26 keV and 68.75 keV (dashed black lines). Figure adapted from [76]

recoil band is the 90 % ( $1.64\sigma$ ) acceptance region around Eq. 2.26, considering the online-adjusted trigger threshold on the heat channel and the baseline FWHM resolution of the heat and ionisation channel [76]. The intersection of gamma band and nuclear recoil band at 10–20 keV [76], depending on the detector, defines the lower threshold the gamma rejection. Therefore, EDELWEISS used a threshold of 20 keV for the standard WIMP analysis [76].

Necessary for a great rejection power is a precise estimation of the ionisation yield via an effective charge collection. However, a long standing issue of cryogenic germanium detectors is the reduced charge collection efficiency near the surface [75]. Surface events are caused mainly by interaction of  $\beta^-$ -particles and X-rays in the first 20–100  $\mu\text{m}$  below the electrodes where the collection of free-charge carriers is reduced due to efficient charge trapping and recombination in the electrode [253]. The reduced charge collection results in a leaking of electronic recoil events from the gamma band down in the nuclear recoil band. For instance, EDELWEISS-I was limited by the leaking of electron recoils, caused by  $\beta$ -decay of residual  $^{210}\text{Pb}$  on all surfaces [258].

In EDELWEISS-II, the detector sensitivity to surface events is reduced via passive and active techniques. First, the surface is passivated by an amorphous layer of silicon or germanium, which creates a potential barrier in the band structure and prevents the charge carriers to access the electrode [256]. To increase the rejection power, three types of active techniques are possible [253]: via pulse shape discrimination or via measurements of athermal phonons<sup>19</sup> or via an interleaved electrode design, the latter being used by EDELWEISS [75, 134].

To reject near surface events, the charge carrier trajectories in the electric field caused by the fiducial, veto, and guard electrodes are used [132]. Figure 2.13b shows the field and event topologies which are discussed in the following. Free charge carriers caused by ionisation in the bulk of the detector will follow the strong axial field between the fiducial electrodes on the top and bottom side, consequently they induce a signal on both fiducial electrodes. Charge carriers caused near the surface will be collected by the veto electrodes of the given surface and will only induce a signal there. Similarly, any interaction near the side of the cylindrical detectors give a signal on the guard electrodes. Even events in a low field volume provide signals on fiducial and veto electrodes [133, 134] due to the extension of the carrier clouds by Coulomb interaction [132].

The fiducial volume of the detector is the bulk of the detector with the volumes of reduced charge collection near the surface. Events in the fiducial volume are redundantly defined by the missing of any signal above the noise level on the veto and guard electrodes, and by requiring that the signals on the fiducial electrodes on the opposite sides have the same timing and amplitude [75, 76]. The mass of the fiducial volume was experimentally determined to  $160(5)\text{ g}$ , averaged over all ten detectors [76]. A cut to the fiducial volume allows an experimentally determined surface rejection of  $6 \times 10^{-5}$  [76]. Its influence on the  $\gamma$ -rejection is illustrated by Fig. 2.15: out of  $1.82 \times 10^5$  measured electronic interactions within  $20\text{ keV} < E_{\text{rec}} < 200\text{ keV}$  only six events occur in the the nuclear recoil band after fiducial cut. This is a  $\gamma$ -rejection power of  $3(1) \times 10^{-5}$  for  $20\text{ keV} < E_{\text{rec}} < 200\text{ keV}$  [76].

Therefore, background caused by  $\gamma$ - and  $\beta$ -decays can be actively rejected due to their different event signature. In contrast, neutrons mimic the WIMP event signature: both particles induce nuclear recoils throughout the complete detector volume, the only difference is the higher scattering cross section for neutrons. The neutron background can be suppressed by rejecting coincidences between multiple bolometers. In a similar way, muon-induced neutrons can be suppressed by rejecting coincidences between any bolometer and the muon veto [283].

---

<sup>19</sup>As done by the CDMS experiment [37, 39], see also Sect. 2.2.3.

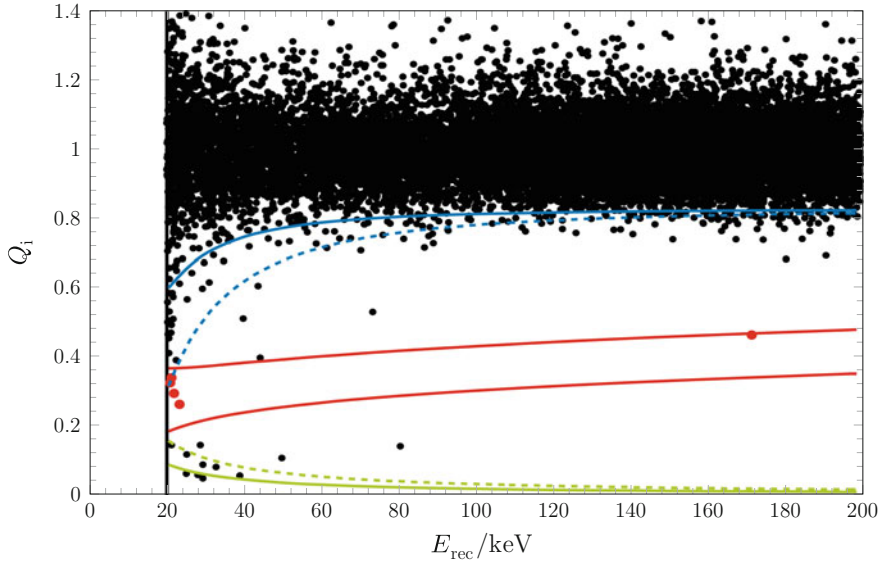


**Fig. 2.15** Ionisation yield  $Q_i$  as function of the recoil energy  $E_{\text{rec}}$  of fiducial events recorded by EDELWEISS-II within an exposure of 427 kg.d. Highlighted in red are five WIMP candidates in the WIMP search region, i.e. in the 90 % acceptance band for nuclear recoils (red) and with energies between 20 and 200 keV. The solid blue line shows the averaged one-sided 99.99 % rejection limit for electron recoils and the solid green line the average ionisation threshold. Dashed lines indicate the worst case of the respective quality. Figure adapted from [76]

### 2.3.3 Results of EDELWEISS-II and Outlook on EDELWEISS-III

Having reported the experimental set-up of EDELWEISS-II in Sect. 2.3.1 and its technique of active background rejection in Sect. 2.3.2, we give the obtained physical results of EDELWEISS-II. Here, we are focusing on the spin-independent cross-section for elastic scattering of WIMPs off nucleons<sup>20</sup> [76] and estimated remaining background [78, 283]. A comparison of the EDELWEISS result with other current direct searches was given in Sect. 2.2.8 and for the set exclusion limits see Fig. 2.11.

EDELWEISS-II takes physics data from July 2008 till November 2008 and from April 2009 till May 2010 with a duty cycle of 85 % and all 10 ID detectors [76]. In total 417 live-days of WIMP data was collect [76]. This live-time is reduced by quality cuts to exclude noisy periods, pile-ups, and coincidences between the bolometers or between any bolometer and the muon veto. The total fiducial exposure after all cuts is 427 kg.d, within the 90 % nuclear recoil band the exposure is 384 kg.d [76].

<sup>20</sup>However, the data of EDELWEISS-I and EDELWEISS-II was also analysed for different interaction models: for inelastic scattering [76], for spin-dependent coupling to  $^{73}\text{Ge}$  (natural abundance of 4.8 % in the bolometers) [104], and for the sensitivity of EDELWEISS on axions [79].

For the recorded fiducial exposure, one expects a background of  $\leq 5.0$  evts within  $20 \text{ keV} < E_{\text{rec}} < 200 \text{ keV}$ , mainly caused by  $\gamma$ -decays and neutron scattering:

- From a surface rejection with a power of  $6 \times 10^{-5}$  at 90 % CL, a background of  $\leq 0.3$  evts from  $\beta$ -decays is expected [76, 78].
- The contribution of muon-induced WIMP-like events was estimated with MC simulation, considering also muon-induced neutrons. It showed that  $>90\%$  of the muon-induced neutrons are produced in the lead of the  $\gamma$ -shield inside the muon veto, therefore they can be tagged by the muon veto. After rejecting muon-veto and multiple bolometer coincidences, one expects an irreducible background of  $\leq 0.7$  evts at 90 % CL, dominated by a small period without running muon veto [283].
- Based on calibration measurements,  $\leq 0.9$  evts at 90 % CL are expected from non-Gaussian fluctuations of electronic recoils out of the gamma band [76]. MC simulations indicate three source which may contribute most to the  $\gamma$ -background: daughter nuclei from the U/Th decay chain and  $^{60}\text{Co}$  in the copper of the thermal shields and the 10 mK parts may contribute 39–52 %, a contamination of  $^{210}\text{Pb}$  near the detectors or their casings may contribute 17–18 %, and the decay of  $^{226}\text{Ra}$  and  $^{228}\text{Ra}$  at the 300 K stage of the set-up may contribute 27–37 % [78].
- The ambient neutron background was deduced via MC simulations [78], taken into account the various shieldings and their holes due to pillars and cryogenic lines. The simulated neutron transport through the shields was checked with a strong AmBe source ( $2 \times 10^5 \text{ s}^{-1}$ ) [78]. It showed that ambient neutrons passing through the shield make only a minor contribute of  $< 0.11$  evts, whereas neutron sources within the shields are predominant, mostly from cables and connectors (1.5 evts). In total the estimated contribution form ambient neutrons is  $\leq 3.1$  evts at 90 % CL [78].
- Surface recoils from  $\alpha$ -decay are negligible according to calibration measurements with  $\alpha$ -source [76].

In total  $1.8 \times 10^4$  evts within  $20 \text{ keV} < E_{\text{rec}} < 200 \text{ keV}$  are recorded [76] in four categories in agreement with [103], see Fig. 2.15: Most events are bulk electromagnetic recoils in the gamma band. Between gamma band and nuclear recoil band ( $Q < 0.65$ ) four events are found. However, from calibration only  $< 1.5$  evts electronic surface events at 90 % CL are expected. Below the nuclear recoil band 11 events were found, probably induced by nuclear surface recoils of  $^{210}\text{Pb}$ . Within the nuclear recoil band there were 5 events [76].

The number of nuclear recoils is consistent with the most recent background estimation [78]. However, even with the original background estimate of 3.0 evts [76], EDELWEISS-II does not indicate evidence for WIMPs [76]. Consequently, EDELWEISS-II sets an exclusion limit on the spin-independent WIMP-nucleon cross section  $\sigma_{\chi, \text{N}}^{\text{SI}}$ .

The exclusion limit was calculated with the optimal interval method [321] from the measured event rate without background subtraction. The galactic WIMP distribution is modeled as Maxwellian with  $v_{\text{rms}} = 270 \text{ km s}^{-1}$ , a WIMP density of  $\rho_0 c^2 = 0.3 \text{ GeV cm}^{-3}$ , an average earth velocity of  $\bar{v}_{\text{earth}} = 235 \text{ km s}^{-1}$ , and a

galactic escape velocity of  $v_{\text{esc}} = 544 \text{ km s}^{-1}$  [292], see also Eq. 2.23. As result, EDELWEISS-II can exclude a minimal cross section of  $\sigma_{\chi, \text{N}}^{\text{SI}} < 4.4 \times 10^{-8} \text{ pb}$  at 90 % CL for  $m_{\chi} c^2 = 85 \text{ GeV}$  [76]. This is more than one order of magnitude improvement compared to EDELWEISS-I [279]. At  $\approx 10^{-8} \text{ pb}$  the experiment probes already predictions from the MSSM (Sect. 2.1.5) [76]. For a comparison between theoretical predictions and experimental exclusion limits see Fig. 2.11.

To further improve the detection sensitivity, the data set of EDELWEISS-II [76] was combined [38] with the one of CDMS II (Ge) [37], also a direct search experiment using cryogenic germanium bolometer. For more information about CDMS II (Ge), see Sect. 2.2.3. The individual sets of events can simply be merged by considering the respective exposure-weighted efficiencies and applying the optimal interval method [321] on the combined event set [38]. The combined exclusion limit is with  $\sigma_{\chi, \text{N}}^{\text{SI}} < 3.3 \times 10^{-8} \text{ pb}$  at 90 % CL minimal at  $m_{\chi} c^2 = 90 \text{ GeV}$  [38]. The gain of the combined data set relative to the previous most sensitive data set (CDMS II) reaches 1.57 at the highest mass [38]. The obtained exclusion limits are the most sensitive limits for any germanium based experiment and third only to the xenon based experiments XENON100 [68] and LUX [42].

With a special data selection [77], the sensitivity is extended to lower WIMP masses: the base line resolution is improved from 1.2 to 0.8 keV<sub>ee</sub> for the heat channel and from 0.9 to 0.7 keV<sub>ee</sub> for the fiducial ionisation channel. Consequently, the exposure decreased from 384 [76] to 113 kg.d [77]. This results in an exclusion of  $\sigma_{\chi, \text{N}}^{\text{SI}} < 10^{-5} \text{ pb}$  at 90 % CL for  $m_{\chi} c^2 = 10 \text{ GeV}$  [77]. It excludes the WIMP interpretation of the CREST-II excess [63] and sets restrictions on the excesses of CoGeNT [8], CDMS II (Si) [31], and DAMA/LIBRA [98], see also Fig. 2.10.

EDELWEISS-III aims to improve the sensitivity by roughly one order of magnitude in two steps: in a first step the goal is  $\sigma_{\chi, \text{N}}^{\text{SI}} < 5 \times 10^{-9} \text{ pb}$  within 3000 kg.d [74] and in a second step with increased target mass  $\sigma_{\chi, \text{N}}^{\text{SI}} < 10^{-9} \text{ pb}$  within 12,000 kg.d [80]. To reach this improvement, two strategies are applied: Increasing the fiducial target mass and to reduce the background by active and passive techniques.

An increased fiducial mass is provided by the new *FullInterDigit* (FID) design. Figure 2.16 shows a picture of a FID detector together with a scheme of the electric field lines in the detector. The mass of the germanium crystal is roughly doubled to 800 g. The detector is equipped with two NTDs [74]. By replacing the guard electrodes of the ID design with interleaved electrodes also on the detector side of the FID, the relative fiducial volume is increased to  $\approx 75\%$  [258] compared to  $\approx 40\%$  [76] for the ID design. It is planned to install 40 FIDs with a total fiducial mass of 24 kg [74]. Large statistics gamma calibration showed also an improved rejection power for FID detector compared to ID detectors [258].

For the passive background reduction, the main sources for background in EDELWEISS-II are considered: neutrons originated within the shields and  $\gamma$ -radioactivity in the not-radiopure-copper of the thermal shield of the cryostat [78]. By replacing the thermal shields and the copper parts at 10 mK with new ones made from ultra pure copper, the  $\gamma$ -activity is expected to be reduced by at least a factor two [78]. MC simulation predicts a reduction of the neutron background

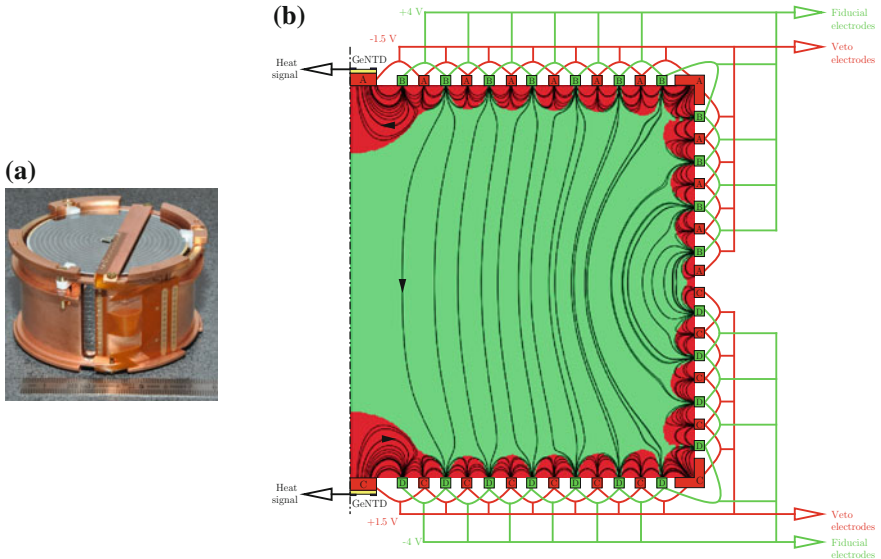


**Fig. 2.16** **a** Picture of an 800g FullInterDigit detector. Seen are the interleaved electrodes on *top* and also on *side*. Two NTDs are glued on the *top* and the *bottom* of the detector. **b** Scheme of the two heat and the four ionisation channels of the FullInterDigit detector and the related volumes in the detector cross section: veto volume (red) and fiducial volume (green). Also indicated are the two NTD sensors. Figures provided by the EDELWEISS collaboration and modified by the author

from  $\leq 8.1 \times 10^{-3}$  evts  $\text{kg} \cdot \text{d}^{-1}$  in EDELWEISS-II to  $\leq 1.9 \times 10^{-4}$  evts  $\text{kg} \cdot \text{d}^{-1}$  in EDELWEISS-III by new infrastructure (cabling, cold electronics, cryogenics, and acquisition) and an additional inner polyethylene shield inside the cryostat [74, 78]. The upgraded infrastructure aims also at a reduction of the microphonic noise [258]. Beyond EDELWEISS-III is the R&D work on *NbSi superconductive resistive meanders* as new heat sensors with the potential of decreased threshold and increased energy resolution [258].

A fully running muon veto and the increased granularity caused by the increased number of detectors will reduce the muon-induced WIMP-like background to  $(0.6^{+0.7}_{-0.6})$  events at 90 % CL for 3000 kg.d exposure [283]. This is the same order of magnitude as the contribution of ambient neutrons:  $\leq 1.9 \times 10^{-4}$  evts  $\text{kg} \cdot \text{d}^{-1}$ .  $3000 \text{ kg} \cdot \text{d} = 0.57$  evts [78]. Therefore, with an improved suppression of ambient backgrounds, the relative contribution of muon-induced background increases. This highlights the importance of a reliable understanding of muon interactions in the experiment, especially of muon-induced neutrons as they can mimic the WIMP signature.

In conclusion, EDELWEISS is together with CDMS, the leading experiment searching for elastic scattering of WIMPs in germanium. A further improvement by one order of magnitude in the sensitivity is planned for EDELWEISS-III. Due

to the improved reduction of ambient background, the relative importance of muon-induced background and its understanding will increase.

## References

1. Aad G et al [ATLAS Collaboration] (2012) Search for supersymmetry in final states with jets, missing transverse momentum and one isolated lepton in  $\sqrt{s}=7$  TeV pp collisions using  $1\text{ fb}^{-1}$  of ATLAS data. *Phys Rev D* 85(1):012006. doi:[10.1103/PhysRevD.85.012006](https://doi.org/10.1103/PhysRevD.85.012006). arXiv:[1109.6606](https://arxiv.org/abs/1109.6606) [hep-ex]
2. Aad G et al [ATLAS Collaboration] (2012) Observation of a new particle in the search for the standard model Higgs boson with the ATLAS detector at the LHC. *Phys Lett B* 716(1):1–29. doi:[10.1016/j.physletb.2012.08.020](https://doi.org/10.1016/j.physletb.2012.08.020). arXiv:[1207.7214](https://arxiv.org/abs/1207.7214) [hep-ex]
3. Aad G et al [ATLAS Collaboration] (2013) Search for squarks and gluinos with the ATLAS detector in final states with jets and missing transverse momentum using  $4.7\text{ fb}^{-1}$  of  $\sqrt{s} = 7$  TeV proton-proton collision data. *Phys Rev D* 87(1):012008. doi:[10.1103/PhysRevD.87.012008](https://doi.org/10.1103/PhysRevD.87.012008). arXiv:[1208.0949](https://arxiv.org/abs/1208.0949) [hep-ex]
4. Aaij R et al [LHCb Collaboration] (2013) First evidence for the decay  $b_s^0 \rightarrow \mu^+ \mu^-$ . *Phys Rev Lett* 110(2):021801. doi:[10.1103/PhysRevLett.110.021801](https://doi.org/10.1103/PhysRevLett.110.021801). arXiv:[1211.2674](https://arxiv.org/abs/1211.2674) [hep-ex]
5. Aalseth CE et al [CoGeNT Collaboration] (2008) Experimental constraints on a dark matter origin for the DAMA annual modulation effect. *Phys Rev Lett* 101(25):251301. doi:[10.1103/PhysRevLett.101.251301](https://doi.org/10.1103/PhysRevLett.101.251301). arXiv:[0807.0879v3](https://arxiv.org/abs/0807.0879v3) [astro-ph]
6. Aalseth CE et al (2009) Erratum: Experimental constraints on a dark matter origin for the DAMA annual modulation effect [Phys Rev Lett 101:251301 (2008)]. *Phys Rev Lett* 102(10):109903. doi:[10.1103/PhysRevLett.102.109903](https://doi.org/10.1103/PhysRevLett.102.109903)
7. Aalseth CE et al [CoGeNT Collaboration] (2011) Results from a search for lightmass dark matter with a *p*-type point contact germanium detector. *Phys Rev Lett* 106(13):131301. doi:[10.1103/PhysRevLett.106.131301](https://doi.org/10.1103/PhysRevLett.106.131301). arXiv:[1002.4703](https://arxiv.org/abs/1002.4703) [astro-ph]
8. Aalseth CE et al [CoGeNT Collaboration] (2011) Search for an annual modulation in a *p*-type point contact germanium dark matter detector. *Phys Rev Lett* 107(14):141301. doi:[10.1103/PhysRevLett.107.141301](https://doi.org/10.1103/PhysRevLett.107.141301). arXiv:[1106.0650](https://arxiv.org/abs/1106.0650) [astro-ph.CO]
9. Aalseth CE et al [CoGeNT Collaboration] (2013) CoGeNT: a search for low-mass dark matter using *p*-type point contact germanium detectors. *Phys Rev D* 88(1):012002. doi:[10.1103/PhysRevD.88.012002](https://doi.org/10.1103/PhysRevD.88.012002). arXiv:[1208.5737](https://arxiv.org/abs/1208.5737) [astroph.CO]
10. Aalseth C et al [Majorana Collaboration] (2004) The majorana neutrinoless doublebeta decay experiment. *Phys At Nucl* 67(11):2002–2010. doi:[10.1134/1.1825519](https://doi.org/10.1134/1.1825519)
11. Aaltonen T et al [CDF and D0 Collaborations] (2012) Evidence for a particle produced in association with weak bosons and decaying to a bottom-antibottom quark pair in higgs boson searches at the tevatron. *Phys Rev Lett* 109(7):071804. doi:[10.1103/PhysRevLett.109.071804](https://doi.org/10.1103/PhysRevLett.109.071804). arXiv:[1207.6436](https://arxiv.org/abs/1207.6436) [hep-ex]
12. Aartsen MG et al [IceCube Collaboration] (2012) Search for dark matter annihilations in the Sun with the 79-string IceCube detector. *Phys Rev Lett* 110(13):131302. doi:[10.1103/PhysRevLett.110.131302](https://doi.org/10.1103/PhysRevLett.110.131302). arXiv:[1212.4097](https://arxiv.org/abs/1212.4097) [astroph.HE]
13. Abdo AA et al [Fermi LAT Collaboration] (2009) Measurement of the cosmic ray  $e^+$  plus  $e^-$  spectrum from 20 GeV to 1 TeV with the Fermi Large Area Telescope. *Phys Rev Lett* 102(18):181101. doi:[10.1103/PhysRevLett.102.181101](https://doi.org/10.1103/PhysRevLett.102.181101). arXiv:[0905.0025](https://arxiv.org/abs/0905.0025) [astro-ph.HE]
14. Abdo AA et al [Fermi LAT Collaboration] (2009) Fermi large area telescope measurements of the diffuse gamma-ray emission at Intermediate Galactic Latitudes. *Phys Rev Lett* 103(25):251101. doi:[10.1103/PhysRevLett.103.251101](https://doi.org/10.1103/PhysRevLett.103.251101). As cited in Ref. [264]
15. Abdo AA et al [Fermi LAT Collaboration] (2010) Fermi large area telescope search for photon lines from 30 to 200 GeV and dark matter implications. *Phys Rev Lett* 104(9):091302. doi:[10.1103/PhysRevLett.104.091302](https://doi.org/10.1103/PhysRevLett.104.091302). As cited in Ref. [264]

16. Abdo AA et al [Fermi LAT Collaboration] (2010) Spectrum of the isotropic diffuse gamma-ray emission derived from first-year Fermi Large Area Telescope data. *Phys Rev Lett* 104(10):101101. doi:[10.1103/PhysRevLett.104.101101](https://doi.org/10.1103/PhysRevLett.104.101101). As cited in Ref. [264]
17. Abdo AA et al (2010) Observations of milky way dwarf spheroidal galaxies with the Fermi-Large Area Telescope detector and constraints on dark matter models. *Astrophys J* 712(1):147–158. doi:[10.1088/0004-637X/712/1/147](https://doi.org/10.1088/0004-637X/712/1/147)
18. Abdo AA et al (2010) Constraints on cosmological dark matter annihilation from the Fermi-LAT isotropic diffuse gamma-ray measurement. *J Cosmol Astropart Phys* 2010(4):014. doi:[10.1088/1475-7516/2010/04/014](https://doi.org/10.1088/1475-7516/2010/04/014)
19. Abe K et al (2013) XMASS detector. *Nucl Instrum Methods Phys Res Sect A* 716:78–85. doi:[10.1016/j.nima.2013.03.059](https://doi.org/10.1016/j.nima.2013.03.059)
20. Abe K et al (2013) Light WIMP search in XMASS. *Phys Lett B* 719(1–3):78–82. doi:[10.1016/j.physletb.2013.01.001](https://doi.org/10.1016/j.physletb.2013.01.001)
21. Abramowski A et al (2011) H.E.S.S. constraints on dark matter annihilations towards the sculptor and carina dwarf galaxies. *Astropart Phys* 34(8):608–616. doi:[10.1016/j.astropartphys.2010.12.006](https://doi.org/10.1016/j.astropartphys.2010.12.006)
22. Abramowski A et al (2012) Search for dark matter annihilation signals from the formax galaxy cluster with H.E.S.S. *Astrophys J* 750(2):123. doi:[10.1088/0004-637X/750/2/123](https://doi.org/10.1088/0004-637X/750/2/123). arXiv:[1202.5494](https://arxiv.org/abs/1202.5494) [astro-ph.HE]
23. Abt I et al (2007) Background reduction in neutrinoless double beta decay experiments using segmented detectors-A Monte Carlo study for the GERDA setup. *Nucl Instrum Methods Phys Res Sect A* 570(3):479–486. doi:[10.1016/j.nima.2006.10.188](https://doi.org/10.1016/j.nima.2006.10.188)
24. Acciari VA et al (2010) VERITAS search for VHE gamma-ray emission from dwarf spheroidal galaxies. *Astrophys J* 720(2):1174–1180. doi:[10.1088/0004-637X/720/2/1174](https://doi.org/10.1088/0004-637X/720/2/1174)
25. Ackermann M et al (2010) Constraints on dark matter annihilation in clusters of galaxies with the Fermi large area telescope. *J Cosmol Astropart Phys* 2010(5):025. doi:[10.1088/1475-7516/2010/05/025](https://doi.org/10.1088/1475-7516/2010/05/025)
26. Ackermann M et al [Fermi-LAT Collaboration] (2013) Dark matter constraints from observations of 25 Milky Way satellite galaxies with the Fermi Large Area Telescope. *Phys Rev D* 89(4):042001. doi:[10.1103/PhysRevD.89.042001](https://doi.org/10.1103/PhysRevD.89.042001). arXiv:[1310.0828](https://arxiv.org/abs/1310.0828) [astro-ph.HE]
27. Adamson P et al [MINOS Collaboration] (2013) Comparisons of annual modulations in MINOS with the event rate modulation in CoGeNT. *Phys Rev D* 87(3):032005. doi:[10.1103/PhysRevD.87.032005](https://doi.org/10.1103/PhysRevD.87.032005). arXiv:[1212.1776](https://arxiv.org/abs/1212.1776) [hep-ex]
28. Ade PAR et al [Planck Collaboration] (2013) Planck 2013 results: XVI. Cosmological parameters. *Astron Astrophys* 571:A16. doi:[10.1051/0004-6361/201321591](https://doi.org/10.1051/0004-6361/201321591). arXiv:[1303.5076](https://arxiv.org/abs/1303.5076) [astro-ph.CO]
29. Adriani O et al [PAMELA Collaboration] (2009) An anomalous positron abundance in cosmic rays with energies 1.5–100 GeV. *Nature* 458:607–609. doi:[10.1038/nature07942](https://doi.org/10.1038/nature07942). arXiv:[0810.4995](https://arxiv.org/abs/0810.4995) [astro-ph]
30. Adriani O et al (2013) Cosmic-ray positron energy spectrum measured by PAMELA. *Phys Rev Lett* 111(8):081102. doi:[10.1103/PhysRevLett.111.081102](https://doi.org/10.1103/PhysRevLett.111.081102). arXiv:[1308.0133](https://arxiv.org/abs/1308.0133) [astro-ph.HE]
31. Agnese R et al [CDMS Collaboration] (2013) Dark matter search results using the silicon detectors of CDMS II. arXiv:[1304.4279](https://arxiv.org/abs/1304.4279) [hep-ex]
32. Aharonian F et al (2008) Observations of the Sagittarius dwarf galaxy by the HESS experiment and search for a dark matter signal. *Astropart Phys* 29(1):55–62. doi:[10.1016/j.astropartphys.2007.11.007](https://doi.org/10.1016/j.astropartphys.2007.11.007)
33. Aharonian F et al (2009) A search for a dark matter annihilation signal toward the canis major overdensity with H.E.S.S. *Astrophys J* 691(1):175–181. doi:[10.1088/0004-637X/691/1/175](https://doi.org/10.1088/0004-637X/691/1/175)
34. Aharonian F et al (2010) Erratum to Observations of the Sagittarius dwarf galaxy by the HESS experiment and search for a dark matter signal [Astropart. Phys. 29(1) (2008) 55–62]. *Astropart Phys* 33(4):274–275. doi:[10.1016/j.astropartphys.2010.01.007](https://doi.org/10.1016/j.astropartphys.2010.01.007)
35. Ahlen S et al [DMTPC Collaboration] (2011) First dark matter search results from a surface run of the 10-L DMTPC directional dark matter detector. *Phys Lett B* 695(1–4):124–129. doi:[10.1016/j.physletb.2010.11.041](https://doi.org/10.1016/j.physletb.2010.11.041). arXiv:[1006.2928](https://arxiv.org/abs/1006.2928)

36. Ahmed Z et al [CDMS Collaboration] (2009) Search for weakly interacting massive particles with the first five-tower data from the cryogenic dark matter search at the soudan underground laboratory. *Phys Rev Lett* 102(1):011301. doi:[10.1103/PhysRevLett.102.011301](https://doi.org/10.1103/PhysRevLett.102.011301)
37. Ahmed Z et al [CDMS II Collaboration] (2010) Dark matter search results from the CDMS II experiment. *Science* 327(5973):1619–1621. doi:[10.1126/science.1186112](https://doi.org/10.1126/science.1186112)
38. Ahmed Z et al [CDMS and EDELWEISS collaborations] (2011) Combined limits on WIMPs from the CDMS and EDELWEISS experiments. *Phys Rev D* 84(1):011102. doi:[10.1103/PhysRevD.84.011102](https://doi.org/10.1103/PhysRevD.84.011102). arXiv:[1105.3377](https://arxiv.org/abs/1105.3377) [astro-ph.CO]
39. Ahmed Z et al [CDMS Collaboration] (2011) Results from a low-energy analysis of the CDMS II germanium data. *Phys Rev Lett* 106(13):131302. doi:[10.1103/PhysRevLett.106.131302](https://doi.org/10.1103/PhysRevLett.106.131302). arXiv:[1011.2482](https://arxiv.org/abs/1011.2482) [astro-ph.CO]
40. Ahmed Z et al [CDMS Collaboration] (2012) Search for annual modulation in lowenergy CDMS-II data. arXiv:[1203.1309](https://arxiv.org/abs/1203.1309) [astro-ph.CO]
41. Akerib DS et al [CDMS Collaboration] (2010) Low-threshold analysis of CDMS shallow-site data. *Phys Rev D* 82(12):122004. doi:[10.1103/PhysRevD.82.122004](https://doi.org/10.1103/PhysRevD.82.122004). arXiv:[1010.4290](https://arxiv.org/abs/1010.4290) [astro-ph.CO]
42. Akerib DS et al [LUX Collaboration] (2013) First results from the LUX dark matter experiment at the Sanford Underground Research Facility. arXiv:[1310.8214](https://arxiv.org/abs/1310.8214) [astro-ph.CO]
43. Akerib D et al (2013) Technical results from the surface run of the LUX dark matter experiment. *Astropart Phys* 45:34–43. doi:[10.1016/j.astropartphys.2013.02.001](https://doi.org/10.1016/j.astropartphys.2013.02.001). arXiv:[1210.4569](https://arxiv.org/abs/1210.4569) [astro-ph.IM]
44. Akerib D et al (2013) The large underground xenon (LUX) experiment. *Nucl Instrum Methods Phys Res, Sect A* 704:111–126. doi:[10.1016/j.nima.2012.11.135](https://doi.org/10.1016/j.nima.2012.11.135). arXiv:[1211.3788](https://arxiv.org/abs/1211.3788) [physics.ins-det]
45. Akimov D (2011) Techniques and results for the direct detection of dark matter (review). In: VCI 2010—proceedings of the 12th international Vienna conference on instrumentation, special issue. *Nucl Instrum Methods Phys Res Sect A* 628(1):50–58. doi:[10.1016/j.nima.2010.06.283](https://doi.org/10.1016/j.nima.2010.06.283)
46. Akimov D et al (2010) The ZEPLIN-III anti-coincidence veto detector. *Astropart Phys* 34(3):151–163. doi:[10.1016/j.astropartphys.2010.06.010](https://doi.org/10.1016/j.astropartphys.2010.06.010)
47. Akimov D et al (2012) WIMP-nucleon cross-section results from the second science run of ZEPLIN-III. *Phys Lett B* 709(1–2):14–20. doi:[10.1016/j.physletb.2012.01.064](https://doi.org/10.1016/j.physletb.2012.01.064). arXiv:[1110.4769](https://arxiv.org/abs/1110.4769) [astro-ph.CO]
48. van Albada TS et al (1985) Distribution of dark matter in the spiral galaxy NGC 3198. *Astrophys J* 295:305–313. doi:[10.1086/163375](https://doi.org/10.1086/163375). ADS: 1985ApJ...295..305V
49. Albert J et al (2008) Upper limit for  $\gamma$ -ray emission above 140 GeV from the Dwarf Spheroidal Galaxy Draco. *Astrophys J* 679(1):428–431. doi:[10.1086/529135](https://doi.org/10.1086/529135)
50. Aleksic J et al [MAGIC Collaboration] (2010) MAGIC gamma-ray telescope observation of the perseus cluster of galaxies: Implications for cosmic rays, dark matter, and NGC 1275. *Astrophys J* 710(1):634–647. doi:[10.1088/0004-637X/710/1/634](https://doi.org/10.1088/0004-637X/710/1/634)
51. Aleksic J et al [MAGIC Collaboration] (2011) Searches for dark matter annihilation signatures in the Segue 1 satellite galaxy with the MAGIC-I telescope. *J Cosmol Astropart Phys* 2011(6):035. doi:[10.1088/1475-7516/2011/06/035](https://doi.org/10.1088/1475-7516/2011/06/035)
52. Alexander T et al (2013) Light yield in DarkSide-10: a prototype two-phase argon TPC for dark matter searches. *Astropart Phys* 49:44–51. doi:[10.1016/j.astropartphys.2013.08.004](https://doi.org/10.1016/j.astropartphys.2013.08.004)
53. Aliu E et al [VERITAS Collaboration] (2012) VERITAS deep observations of the dwarf spheroidal galaxy Segue 1. *Phys Rev D* 85(6):062001. doi:[10.1103/PhysRevD.85.062001](https://doi.org/10.1103/PhysRevD.85.062001)
54. Alner G et al (2005) First limits on nuclear recoil events from the ZEPLIN I galactic dark matter detector. *Astropart Phys* 23(5):444–462. doi:[10.1016/j.astropartphys.2005.02.004](https://doi.org/10.1016/j.astropartphys.2005.02.004)
55. Alner G et al [ZEPLIN] (2007) First limits on WIMP nuclear recoil signals in ZEPLINII: a two-phase xenon detector for dark matter detection. *Astropart Phys* 28(3):287–302. doi:[10.1016/j.astropartphys.2007.06.002](https://doi.org/10.1016/j.astropartphys.2007.06.002)
56. Amarè J et al (2013) Preliminary results of ANAIS-25. arXiv:[1308.3478](https://arxiv.org/abs/1308.3478)

57. Amman M, Luke P (2000) Three-dimensional position sensing and field shaping in orthogonal-strip germanium gamma-ray detectors. *Nucl Instrum Methods Phys Res Sect A* 452(1–2):155–166. doi:[10.1016/S0168-9002\(00\)00351-X](https://doi.org/10.1016/S0168-9002(00)00351-X). As cited in Ref. [133]
58. Anderson L et al (2012) The clustering of galaxies in the SDSS-III baryon oscillation spectroscopic survey: baryon acoustic oscillations in the data release 9 spectroscopic galaxy sample. *Mon Not R Astron Soc* 427(4):3435–3467. doi:[10.1111/j.1365-2966.2012.22066.x](https://doi.org/10.1111/j.1365-2966.2012.22066.x). arXiv:[1203.6594](https://arxiv.org/abs/1203.6594) [astro-ph.CO]
59. Angle J et al [XENON10 Collaboration] (2008) Limits on spin-dependent wimp-nucleon cross sections from the XENON10 experiment. *Phys Rev Lett* 101(9):091301. doi:[10.1103/PhysRevLett.101.091301](https://doi.org/10.1103/PhysRevLett.101.091301)
60. Angle J et al [XENON10 Collaboration] (2011) Search for light dark matter in XENON10 data. *Phys Rev Lett* 107(5):051301. doi:[10.1103/PhysRevLett.107.051301](https://doi.org/10.1103/PhysRevLett.107.051301)
61. Angloher G et al (2002) Limits on WIMP dark matter using sapphire cryogenic detectors. *Astropart Phys* 18(1):43–55. doi:[10.1016/S0927-6505\(02\)00111-1](https://doi.org/10.1016/S0927-6505(02)00111-1)
62. Angloher G et al (2009) Commissioning run of the CRESST-II dark matter search. *Astropart Phys* 31(4):270–276. doi:[10.1016/j.astropartphys.2009.02.007](https://doi.org/10.1016/j.astropartphys.2009.02.007). arXiv:[0809.1829v2](https://arxiv.org/abs/0809.1829v2) [astro-ph]
63. Angloher G et al (2012) Results from 730 kg days of the CRESST-II dark matter search. *Eur Phys J C* 72:1971. doi:[10.1140/epjc/s10052-012-1971-8](https://doi.org/10.1140/epjc/s10052-012-1971-8). arXiv:[1109.0702](https://arxiv.org/abs/1109.0702)
64. Angloher G et al (2014) EURECA conceptual design report. *Phys Dark Universe* 3:41–74. doi:[10.1016/j.dark.2014.03.004](https://doi.org/10.1016/j.dark.2014.03.004)
65. Aprile E, Baudis L (2010) Liquid noble gases. In: Bertone G (ed) Particle dark matter: observations, models and searches. Cambridge University Press, Cambridge (Chap 21)
66. Aprile E et al (2010) Design and performance of the XENON10 dark matter experiment. arXiv:[1001.2834](https://arxiv.org/abs/1001.2834) [astro-ph.IM]
67. Aprile E et al [XENON100 Collaboration] (2012) The XENON100 dark matter experiment. *Astropart Phys* 35(9):573–590. doi:[10.1016/j.astropartphys.2012.01.003](https://doi.org/10.1016/j.astropartphys.2012.01.003). arXiv:[1107.2155](https://arxiv.org/abs/1107.2155) [astro-ph.IM]
68. Aprile E et al [XENON100 Collaboration] (2012) Dark matter results from 225 live days of XENON100 data. *Phys Rev Lett* 109(18):181301. doi:[10.1103/PhysRevLett.109.181301](https://doi.org/10.1103/PhysRevLett.109.181301). arXiv:[1207.5988](https://arxiv.org/abs/1207.5988) [astro-ph.CO]
69. Aprile E et al (2013) The neutron background of the XENON100 dark matter experiment. *J Phys G Nucl Part Phys* 40(11):115201. doi:[10.1088/0954-3899/40/11/115201](https://doi.org/10.1088/0954-3899/40/11/115201). arXiv:[1306.2303](https://arxiv.org/abs/1306.2303) [astro-ph.IM]
70. Archambault S et al (2012) Constraints on low-mass WIMP interactions on 19F from PICASSO. *Phys Lett B* 711(2):153–161. doi:[10.1016/j.physletb.2012.03.078](https://doi.org/10.1016/j.physletb.2012.03.078). arXiv:[1202.1240](https://arxiv.org/abs/1202.1240) [hep-ex]
71. Ardid M (2013) Dark matter searches with COUPP bubble chambers. Presented at the 21st international conference on supersymmetry and unification of fundamental interactions (SUSY2013), Trieste, Italy, 26–31 Aug 2013. [http://susy2013.ictp.it/lecturenotes/04\\_Thursday/Dark\\_Matter\\_and\\_Cosmology/Ardid.pdf](http://susy2013.ictp.it/lecturenotes/04_Thursday/Dark_Matter_and_Cosmology/Ardid.pdf)
72. Arisaka K (2012) MAX and XAX: dark matter and neutrino observatory based on multi-ton liquid xenon and liquid argon. Presented at the 9th international conference: identification of dark matter (IDM2012), Chicago, IL, US, 23–27 July 2012. <http://kicp-workshops.uchicago.edu/IDM2012/depot/talkarisaka-katsushi.pdf>
73. Arisaka K et al (2009) XAX: a multi-ton, multi-target detection system for dark matter, double beta decay and pp solar neutrinos. *Astropart Phys* 31(2):63–74. doi:[10.1016/j.astropartphys.2008.11.007](https://doi.org/10.1016/j.astropartphys.2008.11.007)
74. Armengaud E [For the EDELWEISS Collaboration] (2012) Searching for WIMPs with EDELWEISS. In: 12th international conference on topics in astroparticle and underground physics (TAUP 2011), special issue. *J Phys Conf Ser* 375(1):012004. doi:[10.1088/1742-6596/375/1/012004](https://doi.org/10.1088/1742-6596/375/1/012004)
75. Armengaud E et al [EDELWEISS Collaboration] (2010) First results of the EDELWEISS-II WIMP search using Ge cryogenic detectors with interleaved electrodes. *Phys Lett B* 687(4–5):294–298. doi:[10.1016/j.physletb.2010.03.057](https://doi.org/10.1016/j.physletb.2010.03.057). arXiv:[0912.0805](https://arxiv.org/abs/0912.0805) [astro-ph.CO]

76. Armengaud E et al [EDELWEISS Collaboration] (2011) Final results of the EDELWEISS-II WIMP search using a 4-kg array of cryogenic germanium detectors with interleaved electrodes. *Phys Lett B* 702(5):329–335. doi:[10.1016/j.physletb.2011.07.034](https://doi.org/10.1016/j.physletb.2011.07.034). arXiv:[1103.4070](https://arxiv.org/abs/1103.4070) [astro-ph.CO]

77. Armengaud E et al [EDELWEISS Collaboration] (2012) Search for low-mass WIMPs with EDELWEISS-II heat-and-ionization detectors. *Phys Rev D* 86(5):051701(R). doi:[10.1103/PhysRevD.86.051701](https://doi.org/10.1103/PhysRevD.86.051701). arXiv:[1207.1815](https://arxiv.org/abs/1207.1815) [astroph.CO]

78. Armengaud E et al [EDELWEISS Collaboration] (2013) Background studies for the EDELWEISS dark matter experiment. *Astropart Phys* 47:1–9. doi:[10.1016/j.astropartphys.2013.05.004](https://doi.org/10.1016/j.astropartphys.2013.05.004). arXiv:[1305.3628](https://arxiv.org/abs/1305.3628) [physics.insdet]

79. Armengaud E et al [EDELWEISS Collaboration] (2013) Axion searches with the EDELWEISS-II experiment. *J Cosmol Astropart Phys* 2013(11):067. doi:[10.1088/1475-7516/2013/11/067](https://doi.org/10.1088/1475-7516/2013/11/067). arXiv:[1307.1488](https://arxiv.org/abs/1307.1488) [astro-ph.CO]

80. Arnaud Q [For the EDELWEISS collaboration] (2014) The EDELWEISS experiment status. In: Augè E, Dumarchez J, Trần Thành Vân J (eds) *Proceedings of the 49th RENCONTRES DE MORIOND. Cosmology*, (La Thuile, Aosta Valley, Italy, 22–29 March 2014. ARISF. pp 175–178. [http://moriond.in2p3.fr/Proceedings/2014/Moriond\\_Cosmo\\_2014.pdf](http://moriond.in2p3.fr/Proceedings/2014/Moriond_Cosmo_2014.pdf)

81. Arnold R et al (2005) Technical design and performance of the NEMO 3 detector. *Nucl Instrum Methods Phys Res Sect A* 536(1–2):79–122. doi:[10.1016/j.nima.2004.07.194](https://doi.org/10.1016/j.nima.2004.07.194)

82. ATLAS, CMS, and LHCb Collaborations (2012) Search for the rare decays  $B_{(s)}^0 \rightarrow \mu^+ \mu^-$  at the LHC with the ATLAS, CMS and LHCb experiments. *Scientific report LHCb-CONF-2012-017, CMS-PAS-BPH-12-009, ATLAS-CONF-2012-061*. European Organization for Nuclear Research. <http://cds.cern.ch/record/1452186/files/LHCb-CONF-2012-017.pdf>

83. ATLAS Collaboration (2012) Search for squarks and gluinos with the ATLAS detector using final states with jets and missing transverse momentum and  $5.8 \text{ fb}^{-1}$  of  $\sqrt{s} = 8 \text{ TeV}$  proton-proton collision data. Presented at the 20th international conference on supersymmetry and unification of fundamental interactions (SUSY2012), Beijing, China, 13–18 Aug 2012. Peking University. <http://cds.cern.ch/record/1472710>. ATLAS-CONF-2012-109

84. Badertscher A et al [ArDM Collaboration] (2013) Status of the ArDM experiment: first results from gaseous argon operation in deep underground environment. arXiv:[1307.0117](https://arxiv.org/abs/1307.0117) [physics.ins-det]

85. Baer H, Barger V, Mustafayev A (2012) Implications of a 125 GeV higgs scalar for the LHC supersymmetry and neutralino dark matter searches. *Phys Rev D* 85(7):075010. doi:[10.1103/PhysRevD.85.075010](https://doi.org/10.1103/PhysRevD.85.075010). arXiv:[1112.3017](https://arxiv.org/abs/1112.3017) [hep-ph]

86. Bahcall JN, Tremaine S (1981) Methods for determining the masses of spherical systems: I - test particles around a point mass. *Astrophys J* 244(1981):805–819. doi:[10.1086/158756](https://doi.org/10.1086/158756). ADS: [1981ApJ...244..805B](https://ui.adsabs.harvard.edu/abs/1981ApJ...244..805B)

87. Barbeau P, Collar J, Whaley P (2007) Design and characterization of a neutron calibration facility for the study of sub-keV nuclear recoils. *Nucl Instrum Methods Phys Res Sect A* 574(2):385–391. doi:[10.1016/j.nima.2007.01.169](https://doi.org/10.1016/j.nima.2007.01.169)

88. Baudis L (2012) Direct dark matter detection: the next decade. In next decade in dark matter and dark energy, special issue. *Phys Dark Universe* 1(1–2):94–108. doi:[10.1016/j.dark.2012.10.006](https://doi.org/10.1016/j.dark.2012.10.006). arXiv:[1211.7222](https://arxiv.org/abs/1211.7222)

89. L. Baudis [DARWIN Consortium] (2012) DARWIN: dark matter WIMP search with noble liquids. *J Phys Conf Ser* 375:012028. doi:[10.1088/1742-6596/375/1/012028](https://doi.org/10.1088/1742-6596/375/1/012028). arXiv:[1201.2402](https://arxiv.org/abs/1201.2402) [astro-ph.IM]

90. Behnke E et al [COUPP Collaboration] (2011) Improved limits on spin-dependent wimp-proton interactions from a two liter CF3I bubble chamber. *Phys Rev Lett* 106(2):021303. doi:[10.1103/PhysRevLett.106.021303](https://doi.org/10.1103/PhysRevLett.106.021303)

91. Behnke E et al (2012) [COUPP Collaboration] First dark matter search results from a 4-kg CF3I bubble chamber operated in a deep underground site. *Phys Rev D* 86(5):052001. doi:[10.1103/PhysRevD.86.052001](https://doi.org/10.1103/PhysRevD.86.052001)

92. Bekenstein J, Milgrom M (1984A) Does the missing mass problem signal the breakdown of Newtonian gravity? *Astrophys J* 286(1984):7–14. doi:[10.1086/162570](https://doi.org/10.1086/162570). ADS: [1984ApJ...286....7B](https://ui.adsabs.harvard.edu/abs/1984ApJ...286....7B)

93. Bekenstein JD (2004) Relativistic gravitation theory for the MOND paradigm. *Phys Rev D* 70(8):083509. doi:[10.1103/PhysRevD.70.083509](https://doi.org/10.1103/PhysRevD.70.083509). arXiv:[astroph/0403694](https://arxiv.org/abs/astro-ph/0403694). As cited in Refs. [95, 156]
94. Bekenstein JD (2006) The modified Newtonian dynamics-MOND and its implications for new physics. *Contemp Phys* 47(6):387–403. doi:[10.1080/00107510701244055](https://doi.org/10.1080/00107510701244055)
95. Bekenstein JD (2009) Relativistic MOND as an alternative to the dark matter paradigm. *Nucl Phys A* 827(1–4):555c–560c. doi:[10.1016/j.nuclphysa.2009.05.122](https://doi.org/10.1016/j.nuclphysa.2009.05.122). arXiv:[0901.1524](https://arxiv.org/abs/0901.1524) [astro-ph]
96. de Bellefon A et al (1996) Dark matter search in the Frejus Underground EDELWEISS experiment. *Nucl Instrum Methods Phys Res Sect A* 370(1):230–232. doi:[10.1016/0168-9002\(95\)01093-9](https://doi.org/10.1016/0168-9002(95)01093-9)
97. Belli P et al (2002) Effect of the galactic halo modeling on the DAMA-NaI annual modulation result: an extended analysis of the data for weakly interacting massive particles with a purely spin-independent coupling. *Phys Rev D* 66(4):043503. doi:[10.1103/PhysRevD.66.043503](https://doi.org/10.1103/PhysRevD.66.043503)
98. Belli P et al (2011) Observations of annual modulation in direct detection of relic particles and light neutralinos. *Phys Rev D* 84(5):055014. doi:[10.1103/PhysRevD.84.055014](https://doi.org/10.1103/PhysRevD.84.055014). arXiv:[1106.4667](https://arxiv.org/abs/1106.4667) [hep-ph]
99. Belokurov V et al (2007) Cats and dogs, hair and a hero: a quintet of new milky way companions. *Astrophys J* 654(2):897–906. doi:[10.1086/509718](https://doi.org/10.1086/509718). arXiv:[astro-ph/0608448v1](https://arxiv.org/abs/astro-ph/0608448v1)
100. Beltrame P [On behalf of the XENON Collaboration] (2013) Direct dark matter search with the XENON program. arXiv:[1305.2719](https://arxiv.org/abs/1305.2719) [astro-ph.CO]
101. Benetti P et al [WARP Collaboration] (2008) First results from a dark matter search with liquid argon at 87 K in the Gran Sasso underground laboratory. *Astropart Phys* 28(6):495–507. doi:[10.1016/j.astropartphys.2007.08.002](https://doi.org/10.1016/j.astropartphys.2007.08.002). arXiv:[astro-ph/0701286](https://arxiv.org/abs/astro-ph/0701286)
102. Bennett GW et al [Muon (g-2) Collaboration] (2006) Final report of the E821 muon anomalous magnetic moment measurement at BNL. *Phys Rev D* 73(7):072003. doi:[10.1103/PhysRevD.73.072003](https://doi.org/10.1103/PhysRevD.73.072003). arXiv:[hep-ex/0602035](https://arxiv.org/abs/hep-ex/0602035). As cited in Ref. [137]
103. Benoit A et al (2000) Event categories in the EDELWEISS WIMP search experiment. *Phys Lett B* 479(1–3):8–14. doi:[10.1016/S0370-2693\(00\)00264-1](https://doi.org/10.1016/S0370-2693(00)00264-1)
104. Benoit A et al [EDELWEISS Collaboration] (2005) Sensitivity of the EDELWEISS WIMP search to spin-dependent interactions. *Phys Lett B* 616(1–2):25–30. doi:[10.1016/j.physletb.2005.04.052](https://doi.org/10.1016/j.physletb.2005.04.052)
105. Benoit A et al [EDELWEISS Collaboration] (2007) Measurement of the response of heat-and-ionization germanium detectors to nuclear recoils. *Nucl Instrum Methods Phys Res, Sect A* 577(3):558–568. doi:[10.1016/j.nima.2007.04.118](https://doi.org/10.1016/j.nima.2007.04.118)
106. Berger C et al [Fréjus Collaboration] (1989) Experimental study of muon bundles observed in the Fréjus detector. *Phys Rev D* 40(7):2163–2171. doi:[10.1103/PhysRevD.40.2163](https://doi.org/10.1103/PhysRevD.40.2163)
107. Bergström L, Edsjo J, Ullio P (1998) Possible indications of a clumpy dark matter halo. *Phys Rev D* 58(8):083507. doi:[10.1103/PhysRevD.58.083507](https://doi.org/10.1103/PhysRevD.58.083507) arXiv:[astro-ph/9804050](https://arxiv.org/abs/astro-ph/9804050)
108. Bergström L et al (2013) New limits on dark matter annihilation from alpha magnetic spectrometer cosmic ray positron data. *Phys Rev Lett* 111(17):171101. doi:[10.1103/PhysRevLett.111.171101](https://doi.org/10.1103/PhysRevLett.111.171101)
109. Bernabei R (2012) Dark matter particles in the galactic halo: DAMA/LIBRA results and perspectives. *Ann Phys* 524(9–10):497–506. doi:[10.1002/andp.201200094](https://doi.org/10.1002/andp.201200094)
110. Bernabei R et al (1998) Searching for WIMPs by the annual modulation signature. *Phys Lett B* 424(1–2):195–201. doi:[10.1016/S0370-2693\(98\)00172-5](https://doi.org/10.1016/S0370-2693(98)00172-5)
111. Bernabei R et al (2003) Dark Matter search. *Rivista Nuovo Cim* 26(1):1–74. arXiv:[astro-ph/0307403](https://arxiv.org/abs/astro-ph/0307403). As cited in Ref. [114]
112. Bernabei R et al (2004) Dark matter particles in the galactic halo: Results and implications from DAMA/NaI. *Int J Mod Phys D* 13(10):2127–2159. doi:[10.1142/S0218271804006619](https://doi.org/10.1142/S0218271804006619) arXiv:[astro-ph/0501412](https://arxiv.org/abs/astro-ph/0501412)
113. Bernabei R et al (2008) Possible implications of the channeling effect in NaI(Tl) crystals. *Eur Phys J C* 53(2):205–213. doi:[10.1140/epjc/s10052-007-0479-0](https://doi.org/10.1140/epjc/s10052-007-0479-0)

114. Bernabei R et al (2008) First results from DAMA/LIBRA and the combined results with DAMA/NaI. *Eur Phys J C* 56(3):333–355. doi:[10.1140/epjc/s10052-008-0662-y](https://doi.org/10.1140/epjc/s10052-008-0662-y)
115. Bernabei R et al (2008) Investigating electron interacting dark matter. *Phys Rev D* 77(2):023506. doi:[10.1103/PhysRevD.77.023506](https://doi.org/10.1103/PhysRevD.77.023506)
116. Bernabei R et al (2010) New results from DAMA/LIBRA. *Eur Phys J C* 67(1–2):39–49. doi:[10.1140/epjc/s10052-010-1303-9](https://doi.org/10.1140/epjc/s10052-010-1303-9)
117. Bernabei R et al (2012) No role for muons in the DAMA annual modulation results. *Eur Phys J C* 72(7):2064. doi:[10.1140/epjc/s10052-012-2064-4](https://doi.org/10.1140/epjc/s10052-012-2064-4)
118. Bernabei R et al (2013) DAMA/LIBRA results and perspectives of the second stage. *Nucl Phys At Energ* 14(2):113–120. [http://jnpae.kinr.kiev.ua/14.2/Articles\\_PDF/jnpae-2013-14-0113-Bernabei.pdf](http://jnpae.kinr.kiev.ua/14.2/Articles_PDF/jnpae-2013-14-0113-Bernabei.pdf)
119. Bernabei R et al (2013) Dark matter investigation by DAMA at Gran Sasso. *Int J Mod Phys A* 28(16):1330022. doi:[10.1142/S0217751X13300226](https://doi.org/10.1142/S0217751X13300226). arXiv:[1306.1411](https://arxiv.org/abs/1306.1411) [astro-ph.GA]
120. Bertone G (ed) (2010) Particle dark matter: observations models and searches. Cambridge University Press, Cambridge
121. Bertone G, Hooper D, Silk J (2005) Particle dark matter: evidence, candidates and constraints. *Phys Rep* 405(5–6):279–390. doi:[10.1016/j.physrep.2004.08.031](https://doi.org/10.1016/j.physrep.2004.08.031)
122. Bettini A (2011) Underground laboratories. *Nucl Instrum Methods Phys Res Sect A* 626–627(Supplement):S64–S68. doi:[10.1016/j.nima.2010.05.017](https://doi.org/10.1016/j.nima.2010.05.017)
123. Billard J, Strigari L, Figueira Feliciano E (2013) Implication of neutrino backgrounds on the reach of next generation dark matter direct detection experiments. arXiv:[1307.5458](https://arxiv.org/abs/1307.5458) [hep-ph]
124. Blumenthal GR et al (1984) Formation of galaxies and large-scale structure with cold dark matter. *Nature* 311:517–525. doi:[10.1038/311517a0](https://doi.org/10.1038/311517a0)
125. de Boer W et al (2005) EGRET excess of diffuse galactic gamma rays as tracer of dark matter. *Astron Astrophys* 444(1):51–67. doi:[10.1051/0004-6361:20053726](https://doi.org/10.1051/0004-6361:20053726). arXiv:[astro-ph/0508617](https://arxiv.org/abs/astro-ph/0508617). As cited in Ref. [264]
126. Bonicalzi R et al (2013) The C-4 dark matter experiment. *Nucl Instrum Methods Phys Res Sect A* 712:27–33. doi:[10.1016/j.nima.2013.02.012](https://doi.org/10.1016/j.nima.2013.02.012)
127. Bottino A, Fornengo N, Scopel S (2012) Phenomenology of light neutralinos in view of recent results at the CERN Large Hadron Collider. *Phys Rev D* 85(9):095013. doi:[10.1103/PhysRevD.85.095013](https://doi.org/10.1103/PhysRevD.85.095013)
128. Boukhira N et al (2000) Suitability of superheated droplet detectors for dark matter search. *Astropart Phys* 14(3):227–237. doi:[10.1016/S0927-6505\(00\)00123-7](https://doi.org/10.1016/S0927-6505(00)00123-7)
129. Boulay MG [For the DEAP Collaboration] (2012) DEAP-3600 dark matter search at SNO-LAB. *J Phys Conf Ser* 375(1):012027. doi:[10.1088/1742-6596/375/1/012027](https://doi.org/10.1088/1742-6596/375/1/012027)
130. Bradač M et al (2008) Revealing the properties of dark matter in the merging cluster MACS j0025.4-1222. *Astrophys J* 687(2):959–967. doi:[10.1086/591246](https://doi.org/10.1086/591246)
131. Brink P et al (2006) First test runs of a dark-matter detector with interleaved ionization electrodes and phonon sensors for surface-event rejection. In proceedings of the 11th international workshop on low temperature detectors (LTD-11), special issue. *Nucl Instrum Methods Phys Res, Sect A* 559(2):414–416. doi:[10.1016/j.nima.2005.12.026](https://doi.org/10.1016/j.nima.2005.12.026)
132. Broniatowski A (2004) A simulation code for the ionization and heat signals in low temperature germanium detectors for Dark Matter research. In proceedings of the 10th international workshop on low temperature detectors, special issue. *Nucl Instrum Methods Phys Res Sect A* 520(1–3):178–181. doi:[10.1016/j.nima.2003.11.287](https://doi.org/10.1016/j.nima.2003.11.287)
133. Broniatowski A et al [EDELWEISS Collaboration] (2008) Cryogenic Ge detectors with interleaved electrodes: Design and modeling. *J Low Temp Phys* 151(3):830–834. doi:[10.1007/s10909-008-9754-1](https://doi.org/10.1007/s10909-008-9754-1)
134. Broniatowski A et al [EDELWEISS Collaboration] (2009) A new high-background-rejection dark matter Ge cryogenic detector. *Phys Lett B* 681(4):305–309. doi:[10.1016/j.physletb.2009.10.036](https://doi.org/10.1016/j.physletb.2009.10.036). arXiv:[0905.0753](https://arxiv.org/abs/0905.0753) [astro-ph.IM]
135. Brown A et al (2012) Extending the CRESST-II commissioning run limits to lower masses. *Phys Rev D* 85(2):021301. doi:[10.1103/PhysRevD.85.021301](https://doi.org/10.1103/PhysRevD.85.021301). arXiv:[1109.2589](https://arxiv.org/abs/1109.2589) [astro-ph.CO]

136. Brown E (2013) Searching for dark matter with XENON100 and XENON1T. In: Presented at the 13th international conference on topics in astroparticle and underground physics (TAUP2013), Asilomar, CA, US, 8–13 Sept 2013. <https://conferences.lbl.gov/event/36/session/11/contribution/86/material/slides/>
137. Buchmueller O et al (2012) The CMSSM and NUHM1 in light of 7 TeV LHC,  $B_s \rightarrow \mu^+ \mu^-$  and XENON100 data. *Eur Phys J C* 72(11):2243. doi:[10.1140/epjc/s10052-012-2243-3](https://doi.org/10.1140/epjc/s10052-012-2243-3)
138. Cao J et al (2012) A SM-like Higgs near 125 GeV in low energy SUSY: a comparative study for MSSM and NMSSM. *J High Energy Phys* 2012(3):1–22. doi:[10.1007/JHEP03\(2012\)086](https://doi.org/10.1007/JHEP03(2012)086)
139. J. Cao et al (2013) A light SUSY dark matter after CDMS-II, LUX and LHC Higgs data. arXiv:[1311.0678](https://arxiv.org/abs/1311.0678) [hep-ph]
140. Carlberg R et al (1996A) Galaxy cluster virial masses and  $\Omega$ . *Astrophys J* 462(1):32–49. doi:[10.1086/177125](https://doi.org/10.1086/177125). ADS: 1996ApJ...462...32C
141. Carr B (1994) Baryonic dark matter. *Ann Rev Astron Astrophys* 32(1):531–590. doi:[10.1146/annurev.aa.32.090194.002531](https://doi.org/10.1146/annurev.aa.32.090194.002531)
142. Cebríán S et al (2001) First results of the ROSEBUD dark matter experiment. *Astropart Phys* 15(1):79–85. doi:[10.1016/S0927-6505\(00\)00138-9](https://doi.org/10.1016/S0927-6505(00)00138-9). arXiv:[astro-ph/0004292](https://arxiv.org/abs/astro-ph/0004292)
143. Censier B [For the EDELWEISS Collaboration] (2006) Final results of the EDELWEISSI dark matter search with cryogenic heat-and-ionization Ge detectors. In: Proceedings of the 11th international workshop on low temperature detectors—LTD-11, special issue. *Nucl Instrum Methods Phys Res Sect A* 559(2):381–383. doi:[10.1016/j.nima.2005.12.171](https://doi.org/10.1016/j.nima.2005.12.171)
144. Censier B [For the EDELWEISS Collaboration] (2006) Erratum to: final results of the EDELWEISS-I dark matter search with cryogenic heat-and-ionization Ge detectors : [Nucl Instrum Methods A 559:381]. *Nucl Instrum Methods Phys Res Sect A* 564(1):614–614. doi:[10.1016/j.nima.2006.04.027](https://doi.org/10.1016/j.nima.2006.04.027)
145. Chang J et al (2008) An excess of cosmic ray electrons at energies of 300–800 GeV. *Nature* 456(7220):362–365. doi:[10.1038/nature07477](https://doi.org/10.1038/nature07477). As cited in Refs. [13,264]
146. Chatrchyan S et al [CMS Collaboration] (2011) Search for supersymmetry at the LHC in events with jets and missing transverse energy. *Phys Rev Lett* 107(22):221804. doi:[10.1103/PhysRevLett.107.221804](https://doi.org/10.1103/PhysRevLett.107.221804). arXiv:[1109.2352](https://arxiv.org/abs/1109.2352) [hep-ex]
147. Chatrchyan S et al [CMS Collaboration] (2012) Observation of a new boson at a mass of 125 GeV with the CMS experiment at the LHC. *Phys Lett B* 716(1):30–61. doi:[10.1016/j.physletb.2012.08.021](https://doi.org/10.1016/j.physletb.2012.08.021). arXiv:[1207.7235](https://arxiv.org/abs/1207.7235) [hep-ex]
148. Chatrchyan S et al [CMS Collaboration] (2013) Search for supersymmetry in events with opposite-sign dileptons and missing transverse energy using an artificial neural network. *Phys Rev D* 87(7):072001. doi:[10.1103/PhysRevD.87.072001](https://doi.org/10.1103/PhysRevD.87.072001). arXiv:[1301.0916](https://arxiv.org/abs/1301.0916) [hep-ex]
149. Chatrchyan S et al [CMS Collaboration] (2013) Search for supersymmetry in events with photons and low missing transverse energy in pp collisions at. *Phys Lett B* 719(1–3):42–61. doi:[10.1016/j.physletb.2012.12.055](https://doi.org/10.1016/j.physletb.2012.12.055). arXiv:[1210.2052](https://arxiv.org/abs/1210.2052) [hep-ex]
150. Chen D-M (2008) Strong lensing probability in TeVeS (tensor-vector-scalar) theory. *J Cosmol Astropart Phys* 2008(1):006. doi:[10.1088/1475-7516/2008/01/006](https://doi.org/10.1088/1475-7516/2008/01/006). As cited in Ref. [95]
151. Chepel V, Araújo H (2013) Liquid noble gas detectors for low energy particle physics. *J Instrum* 8(04):R04001. doi:[10.1088/1748-0221/8/04/R04001](https://doi.org/10.1088/1748-0221/8/04/R04001). arXiv:[1207.2292](https://arxiv.org/abs/1207.2292) [physics.ins-det]
152. Cherwinka J et al (2012) A search for the dark matter annual modulation in South Pole ice. *Astropart Phys* 35(11):749–754. doi:[10.1016/j.astropartphys.2012.03.003](https://doi.org/10.1016/j.astropartphys.2012.03.003). arXiv:[1106.1156](https://arxiv.org/abs/1106.1156) [astro-ph.HE]
153. Chiu H-Y (1966) Symmetry between particle and anti-particle populations in the universe. *Phys Rev Lett* 17:712–714. doi:[10.1103/PhysRevLett.17.712](https://doi.org/10.1103/PhysRevLett.17.712). As cited in Refs. [173, 206]
154. Chiu MC, Tian Y, Ko CM (2008) Necessity of dark matter in modified Newtonian dynamics within galactic scales?—Testing the covariant MOND in elliptical lenses. In: Zhang SN, Li Y, Yu QJ (eds) APRIM 2008: Proceedings of the 10th Asian-Pacific Regional IAU Meeting, Kunming, China, 3–6 Aug 2008. National Observatories of China Press, Beijing, pp 1–2. arXiv:[0812.5011](https://arxiv.org/abs/0812.5011) [astro-ph]. As cited in Ref. [95]

155. Cirelli M et al (2009) Model-independent implications of the, cosmic ray spectra on properties of dark matter. *Nucl Phys B* 813(1–2):1–21. doi:[10.1016/j.nuclphysb.2008.11.031](https://doi.org/10.1016/j.nuclphysb.2008.11.031). As cited in Ref. [30]
156. Clowe D et al (2006) A direct empirical proof of the existence of dark matter. *Astrophys J Lett* 648(2):L109–L113. doi:[10.1086/508162](https://doi.org/10.1086/508162)
157. Collar JI (2010) Light WIMP searches: the effect of the uncertainty in recoil energy scale and quenching factor. arXiv:[1010.5187](https://arxiv.org/abs/1010.5187) [astro-ph.IM]
158. Coron N et al (2011) 2010 update on the ROSEBUD project. In: Identification of dark matter 2010. 8th international workshop on the identification of dark matter (IDM 2010). Proceedings of Science IDM2010, Montpellier, France, 26–30 July 2010. SISSA, Trieste. p 054. [http://pos.sissa.it/archive/conferences/110/054/IDM2010\\_054.pdf](http://pos.sissa.it/archive/conferences/110/054/IDM2010_054.pdf)
159. Crisler MB (2013) PICO 250-liter bubble chamber dark matter experiment. Presented at the SNOLAB future projects workshop, 21 Aug 2013. [http://www.snlab.ca/sites/default/files/Crisler\\_PICO.pdf](http://www.snlab.ca/sites/default/files/Crisler_PICO.pdf)
160. Dawson E et al (2012) Spin-dependent limits from the DRIFT-IIId directional dark matter detector. *Astropart Phys* 35(7):397–401. doi:[10.1016/j.astropartphys.2011.11.003](https://doi.org/10.1016/j.astropartphys.2011.11.003)
161. Defay X (2008) Recherche de matière noire au sein de l’expérience EDELWEISS avec des bolomètres germanium à double composante Ionisation/Chaleur, rejet des événements de surface avec la voie ionisation’ [in French]. PhD dissertation, Université Montpellier II, Sciences et Techniques du Languedoc. <http://tel.archives-ouvertes.fr/tel-00369460/fr/>. As cited in Ref. [133]
162. Defay X et al [EDELWEISS Collaboration] (2008) Cryogenic Ge detectors for dark matter search: surface event rejection with ionization signals. *J Low Temp Phys* 151(3–4):896–901. doi:[10.1007/s10909-008-9762-1](https://doi.org/10.1007/s10909-008-9762-1)
163. Delahaye T et al (2010) Galactic electrons and positrons at the Earth: new estimate of the primary and secondary fluxes. *Astron Astrophys* 524:A51. doi:[10.1051/0004-6361/201014225](https://doi.org/10.1051/0004-6361/201014225). As cited in Ref. [30]
164. Dietrich JP et al (2012) A filament of dark matter between two clusters of galaxies. *Nature* 487:202–204. doi:[10.1038/nature11224](https://doi.org/10.1038/nature11224)
165. DM-Ice homepage. <http://dm-ice.physics.wisc.edu/>
166. D’Onghia E et al (2010) Substructure depletion in the Milky Way halo by the disk. *Astrophys J* 709(2):1138–1147. <http://stacks.iop.org/0004-637X/709/i=2/a=1138>
167. Einasto J, Kaasik A, Saar E (1974) Dynamic evidence on massive coronas of galaxies. *Nature* 250:309–310. doi:[10.1038/250309a0](https://doi.org/10.1038/250309a0)
168. K. Eitel. Private communication, November 2013
169. Fairbairn M, Douce T, Swift J (2013) Quantifying astrophysical uncertainties on dark matter direct detection results. *Astropart Phys* 47:45–53. doi:[10.1016/j.astropartphys.2013.06.003](https://doi.org/10.1016/j.astropartphys.2013.06.003)
170. Feix M, Fedeli C, Bartelmann M (2008) Asymmetric gravitational lenses in TeVeS and application to the bullet cluster. *Astron Astrophys* 480(2):313–325. doi:[10.1051/0004-6361:20078224](https://doi.org/10.1051/0004-6361:20078224). As cited in Ref. [95]
171. Felizardo M et al [SIMPLE Collaboration] (2010) First results of the phase II SIMPLE dark matter search. *Phys Rev Lett* 105(21):211301. doi:[10.1103/PhysRevLett.105.211301](https://doi.org/10.1103/PhysRevLett.105.211301)
172. Felizardo M et al [SIMPLE Collaboration] (2012) Final analysis and results of the phase II SIMPLE dark matter search. *Phys Rev Lett* 108(20):201302. doi:[10.1103/PhysRevLett.108.201302](https://doi.org/10.1103/PhysRevLett.108.201302). arXiv:[1106.3014](https://arxiv.org/abs/1106.3014) [astro-ph.CO]
173. Feng JL (2010) Dark matter candidates from particle physics and methods of detection. *Ann Rev Astron Astrophys* 48(1):495–545. doi:[10.1146/annurev-astro-082708-101659](https://doi.org/10.1146/annurev-astro-082708-101659)
174. Feng JL, Grivaz J-F, Nachtmann J (2010) Searches for supersymmetry at highenergy colliders. *Rev Mod Phys* 82(1):699–727. doi:[10.1103/RevModPhys.82.699](https://doi.org/10.1103/RevModPhys.82.699)
175. Ferrari N [WARP Collaboration] (2006) WARP: a double phase argon programme for dark matter detection. *J Phys Conf Ser* 39(1):111. doi:[10.1088/1742-6596/39/1/022](https://doi.org/10.1088/1742-6596/39/1/022)
176. Ferreras I, Sakellariadou M, Yusaf M (2008) Necessity of dark matter in modified newtonian dynamics within galactic scales. *Phys Rev Lett* 100(3):031302. doi:[10.1103/PhysRevLett.100.031302](https://doi.org/10.1103/PhysRevLett.100.031302)

177. Ferreras I, Saha P, Burles S (2008) Unveiling dark haloes in lensing galaxies. *Mon Not R Astron Soc* 383(3):857–863. doi:[10.1111/j.1365-2966.2007.12606.x](https://doi.org/10.1111/j.1365-2966.2007.12606.x). arXiv:[0710.3159](https://arxiv.org/abs/0710.3159)
178. Ferreras I et al (2012) Confronting MOND and TeVeS with strong gravitational lensing over galactic scales: an extended survey. *Phys Rev D* 86(8):083507. doi:[10.1103/PhysRevD.86.083507](https://doi.org/10.1103/PhysRevD.86.083507). arXiv:[1205.4880](https://arxiv.org/abs/1205.4880) [astro-ph.CO]
179. Figueira-Feliciano E (2011) Direct detection searches for WIMP dark matter. *Prog Part Nucl Phys* 66(3):661–673. doi:[10.1016/j.ppnp.2011.01.003](https://doi.org/10.1016/j.ppnp.2011.01.003)
180. Fiorucci S et al [EDELWEISS Collaboration] (2007) Identification of backgrounds in the EDELWEISS-I dark matter search experiment. *Astropart Phys* 28(1):143–153. doi:[10.1016/j.astropartphys.2007.05.003](https://doi.org/10.1016/j.astropartphys.2007.05.003)
181. Formaggio JA, Martoff CJ (2004) Backgrounds to sensitive experiments underground. *Annu Rev Nucl Part Sci* 54:361–412. doi:[10.1146/annurev.nucl.54.070103.181248](https://doi.org/10.1146/annurev.nucl.54.070103.181248)
182. Fowlie A et al [BayesFITS Group] (2012) Constrained MSSM favoring new territories: the impact of new LHC limits and a 125 GeV Higgs boson. *Phys Rev D* 86(7):075010. doi:[10.1103/PhysRevD.86.075010](https://doi.org/10.1103/PhysRevD.86.075010). arXiv:[1206.0264](https://arxiv.org/abs/1206.0264) [hep-ph]
183. Frandsen MT et al (2013) The unbearable lightness of being: CDMS versus XENON. *J Cosmol Astropart Phys* 2013(7):023. doi:[10.1088/1475-7516/2013/07/023](https://doi.org/10.1088/1475-7516/2013/07/023). arXiv:[1304.6066](https://arxiv.org/abs/1304.6066) [hep-ph]
184. Freeman KC (1970) On the disks of spiral and S0 galaxies. *Astrophys J* 160(1970):811–830. doi:[10.1086/150474](https://doi.org/10.1086/150474). ADS:[1970ApJ...160..811F](https://ui.adsabs.harvard.edu/abs/1970ApJ...160..811F)
185. Freeman KC (1970) Erratum: on the disks of spiral and S0 galaxies. *Astrophys J* 161(1970):802. doi:[10.1086/150583](https://doi.org/10.1086/150583). ADS:[1970ApJ...161..802F](https://ui.adsabs.harvard.edu/abs/1970ApJ...161..802F)
186. Gaitskell RJ (2004) Direct detection of dark matter. *Annu Rev Nucl Part Sci* 54(1):315–359. doi:[10.1146/annurev.nucl.54.070103.181244](https://doi.org/10.1146/annurev.nucl.54.070103.181244)
187. Gavazzi R et al (2007) The Sloan lens ACS survey: IV. The mass density profile of early-type galaxies out to 100 effective radii. *Astrophys J* 667(1):176. doi:[10.1086/519237](https://doi.org/10.1086/519237). ADS:[2007ApJ...667..176G](https://ui.adsabs.harvard.edu/abs/2007ApJ...667..176G)
188. Geha M (2010) Galaxy formation: gone with the wind? *Nature* 463(7278):167–168. doi:[10.1038/463167a](https://doi.org/10.1038/463167a)
189. Gerbier G, Gascon J (2010) Cryogenic detectors. In: Bertone G (ed) Particle dark matter: observations, models and searches. Cambridge University Press, Cambridge (Chap. 20)
190. Giovanetti GK et al (2012) Dark matter sensitivities of the Majorana Demonstrator. *J Phys Conf Ser* 375(1):012014. doi:[10.1088/1742-6596/375/1/012014](https://doi.org/10.1088/1742-6596/375/1/012014)
191. Girard TA et al (2012) Prospects for a phase III SIMPLE measurement. *J Phys Conf Ser* 375(1):012017. doi:[10.1088/1742-6596/375/1/012017](https://doi.org/10.1088/1742-6596/375/1/012017)
192. Giuliani F [DEAP/CLEAN collaboration] (2010) Hunting the dark matter with DEAP/CLEAN. In: Alverson G, Nath P, Nelson B (eds) SUSY09. 7th international conference on supersymmetry and the unification of fundamental interactions. AIP conference proceedings, vol 1200, Boston, MA, USA, 5–10 June 2008. AIP Publishing, Melville, pp 985–988. doi:[10.1063/1.3327779](https://doi.org/10.1063/1.3327779)
193. Gonzalez AH, Zaritsky D, Zabludoff AI (2007) A census of baryons in galaxy clusters and groups. *Astrophys J* 666(1):147–155. doi:[10.1086/519729](https://doi.org/10.1086/519729). arXiv:[0705.1726](https://arxiv.org/abs/0705.1726) [astro-ph]
194. Governato F et al (2010) Bulgeless dwarf galaxies and dark matter cores from supernova-driven outflows. *Nature* 463(7278):203–206. doi:[10.1038/nature08640](https://doi.org/10.1038/nature08640)
195. Grignon C et al (2009) A prototype of a directional detector for non-baryonic dark matter search: MIMAC (Micro-TPC Matrix of Chambers). *J Instrum* 4(11):P11003. arXiv:[0909.0654](https://arxiv.org/abs/0909.0654) [astro-ph.IM]
196. Guedes J et al (2011) Forming realistic late-type spirals in a  $\Lambda$ CDM Universe: the eris simulation. *Astrophys J* 742(2):76. doi:[10.1088/0004-637X/742/2/76](https://doi.org/10.1088/0004-637X/742/2/76). arXiv:[1103.6030](https://arxiv.org/abs/1103.6030) [astro-ph.CO]
197. Gustafsson M [For the Fermi-LAT Collaboration] (2013) Fermi-LAT and the gamma-ray line search. arXiv:[1310.2953](https://arxiv.org/abs/1310.2953) [astro-ph.HE]
198. Harvard-Smithsonian Center for Astrophysics (2006) 1E 0657–56: NASA Finds Direct Proof of Dark Matter. <http://chandra.harvard.edu/photo/2006/1e0657/index.html>

199. Helm RH (1956) Inelastic and elastic scattering of 187-MeV electrons from selected even-even nuclei. *Phys Rev (2nd ser)* 104(5):1466–1475. doi:[10.1103/PhysRev.104.1466](https://doi.org/10.1103/PhysRev.104.1466). As cited in Ref. [42]
200. Hime A (2012) CLEAN detection of dark matter. Presented at the 9th international conference: identification of dark matter, IDM2012, Chicago, IL, USA, July 23–27, 2012. <http://kicp-workshops.uchicago.edu/IDM2012/depot/plenary-talk-hime-andrew.pdf>
201. Hoekstra H, Jain B (2008) Weak gravitational lensing and its cosmological applications. *Annu Rev Nucl Part Sci* 58(1):99–123. doi:[10.1146/annurev.nucl.58.110707.171151](https://doi.org/10.1146/annurev.nucl.58.110707.171151)
202. Horn OM (2007) Simulations of the muon-induced neutron background of the EDELWEISS-II experiment for dark matter search. *Scientific report FZKA 7391*. Forschungszentrum Karlsruhe. <http://bibliothek.fzk.de/zb/berichte/FZKA7391.pdf>. Orig. pub. as PhD dissertation, Universität Karlsruhe (TH), 2007. <http://digibib.ubka.uni-karlsruhe.de/volltexte/1000007402>
203. Hu W, Dodelson S (2002) Cosmic microwave background anisotropies. *Annu Rev Astron Astrophys* 40(1):171–216. doi:[10.1146/annurev.astro.40.060401.093926](https://doi.org/10.1146/annurev.astro.40.060401.093926)
204. Identification of Dark Matter 2010 (2011) 8th international workshop on the identification of dark matter, IDM 2010, Montpellier, France, July 26–30, 2010. *Proceedings of science* IDM2010. SISSA, Trieste. <http://pos.sissa.it/cgi-bin/reader/conf.cgi?confid=110>
205. Jee MJ et al (2007) Discovery of a ringlike dark matter structure in the core of the galaxy cluster Cl 0024+17. *Astrophys J* 661(2):728–749. doi:[10.1086/517498](https://doi.org/10.1086/517498). arXiv:[0705.2171](https://arxiv.org/abs/0705.2171) [astro-ph]
206. Jungman G, Kamionkowski M, Griest K (1996) Supersymmetric dark matter. *Phys Rep* 267(5–6):195–373. doi:[10.1016/0370-1573\(95\)00058-5](https://doi.org/10.1016/0370-1573(95)00058-5)
207. Kamionkowski M, Kinkhabwala A (1998) Galactic halo models and particle dark matter detection. *Phys Rev D* 57(6):3256–3263. doi:[10.1103/PhysRevD.57.3256](https://doi.org/10.1103/PhysRevD.57.3256). arXiv:[hep-ph/9710337](https://arxiv.org/abs/hep-ph/9710337)
208. Kane GL et al (1994) Study of constrained minimal supersymmetry. *Phys Rev D* 49(11):6173–6210. doi:[10.1103/PhysRevD.49.6173](https://doi.org/10.1103/PhysRevD.49.6173). arXiv:[hep-ph/9312272](https://arxiv.org/abs/hep-ph/9312272)
209. Karachentsev I (2005) The local group and other neighboring galaxy groups. *Astron J* 129(1):178–188. doi:[10.1086/426368](https://doi.org/10.1086/426368)
210. Kelso C, Hooper D, Buckley MR (2012) Toward a consistent picture for CRESST, CoGeNT, and DAMA. *Phys Rev D* 85(4):043515. doi:[10.1103/PhysRevD.85.043515](https://doi.org/10.1103/PhysRevD.85.043515). arXiv:[1110.5338](https://arxiv.org/abs/1110.5338) [astro-ph.CO]
211. Khachatryan V et al [CMS Collaboration] (2011) Search for supersymmetry in pp collisions at 7 TeV in events with jets and missing transverse energy. *Phys Lett B* 698(3):196–218. doi:[10.1016/j.physletb.2011.03.021](https://doi.org/10.1016/j.physletb.2011.03.021). arXiv:[1101.1628](https://arxiv.org/abs/1101.1628) [hep-ex]
212. Kim JE, Carosi G (2010) Axions and the strong CP problem. *Rev Mod Phys* 82(1):557–601. doi:[10.1103/RevModPhys.82.557](https://doi.org/10.1103/RevModPhys.82.557)
213. Kim SC et al [KIMS Collaboration] (2012) New limits on interactions between weakly interacting massive particles and nucleons obtained with CsI(Tl) crystal detectors. *Phys Rev Lett* 108(18):181301. doi:[10.1103/PhysRevLett.108.181301](https://doi.org/10.1103/PhysRevLett.108.181301)
214. Klypin A, Zhao H, Somerville RS (2002)  $\Lambda$ CDM-based models for the Milky Way and M31: I. Dynamical models. *Astrophys J* 573(2):597–613. doi:[10.1086/340656](https://doi.org/10.1086/340656)
215. Klypin A et al (1999) Where are the missing galactic satellites? *Astrophys J* 522:82–92. doi:[10.1086/307643](https://doi.org/10.1086/307643)
216. Klypin A et al (2003) Constrained simulations of the real universe: the local supercluster. *Astrophys J* 596(1):19–33. doi:[10.1086/377574](https://doi.org/10.1086/377574)
217. Kopp J, Schwetz T, Zupan J (2012) Light dark matter in the light of CRESST-II. *J Cosmol Astropart Phys* 2012(3):001. doi:[10.1088/1475-7516/2012/03/001](https://doi.org/10.1088/1475-7516/2012/03/001)
218. Kraus H [EURECA Collaboration] (2012) EURECA. Presented at the 9th international conference: identification of dark matter, IDM2012, Chicago, IL, USA, July 23–27, 2012. <http://kicp-workshops.uchicago.edu/IDM2012/depot/talk-kraus-hans.pdf>
219. Kraus H et al (2006) EURECA—the European future of cryogenic dark matter searches. *J Phys Conf Ser* 39(1):139. doi:[10.1088/1742-6596/39/1/031](https://doi.org/10.1088/1742-6596/39/1/031)
220. Kraus H et al (2010) EURECA. In: Identification of dark matter. 8th international workshop on the identification of dark matter, IDM 2010, Montpellier, France, 26–30 July 2010. *Proceedings of science* IDM2010. SISSA, Trieste, p 109. [http://pos.sissa.it/archive/conferences/110/109/IDM2010\\_109.pdf](http://pos.sissa.it/archive/conferences/110/109/IDM2010_109.pdf)

221. Kumar J (2012) Large jet multiplicities and natural supersymmetry at the LHC. In: Limosani A (ed) 36th international conference on high energy physics, ICHEP2012. Melbourne, Australia, 4–11 July 2012. Proceedings of science ICHEP2012. SISSA, Trieste, p 103. arXiv: [1211.6503](https://arxiv.org/abs/1211.6503) [hep-ph]
222. Kuźniak M, Boulay M, Pollmann T (2012) Surface roughness interpretation of 730 kg days CRESST-II results. *Astropart Phys* 36(1):77–82. doi: [10.1016/j.astropartphys.2012.05.005](https://doi.org/10.1016/j.astropartphys.2012.05.005)
223. Lebedenko VN et al (2009) Results from the first science run of the ZEPLIN-III dark matter search experiment. *Phys Rev D* 80(5):052010. doi: [10.1103/PhysRevD.80.052010](https://doi.org/10.1103/PhysRevD.80.052010)
224. Lee HS et al [KIMS Collaboration] (2007) Limits on interactions between weakly interacting massive particles and nucleons obtained with CsI(Tl) crystal detectors. *Phys Rev Lett* 99(9):091301. doi: [10.1103/PhysRevLett.99.091301](https://doi.org/10.1103/PhysRevLett.99.091301). arXiv: [0704.0423](https://arxiv.org/abs/0704.0423) [astro-ph]
225. Lee H et al (2006) [KIMS Collaboration] First limit on WIMP cross section with low background crystal detector. *Phys Lett B* 633(2–3):201–208. doi: [10.1016/j.physletb.2005.12.035](https://doi.org/10.1016/j.physletb.2005.12.035) arXiv: [astro-ph/0509080](https://arxiv.org/abs/astro-ph/0509080)
226. Lesgourgues J et al (2006) Probing neutrino masses with CMB lensing extraction. *Phys Rev D* 73:045021. doi: [10.1103/PhysRevD.73.045021](https://doi.org/10.1103/PhysRevD.73.045021) arXiv: [astro-ph/0511735](https://arxiv.org/abs/astro-ph/0511735)
227. Lewin JD, Smith PF (1996) Review of mathematics, numerical factors, and corrections for dark matter experiments based on elastic nuclear recoil. *Astropart Phys* 6(1):87–112. doi: [10.1016/S0927-6505\(96\)00047-3](https://doi.org/10.1016/S0927-6505(96)00047-3)
228. L'Hour M (1987) *Rev Archeol Ouest* 4:113–131. As cited in Ref. [283]
229. Li HB et al [TEXONO Collaboration] (2013) Limits on spin-independent couplings of WIMP dark matter with a *p*-type point-contact germanium detector. *Phys Rev Lett* 110(26):261301. doi: [10.1103/PhysRevLett.110.261301](https://doi.org/10.1103/PhysRevLett.110.261301). arXiv: [1303.0925](https://arxiv.org/abs/1303.0925) [hep-ex]
230. Li Y-S, White SDM (2008) Masses for the local group and the Milky Way. *Mon Not R Astron Soc* 384(4):1459–1468. doi: [10.1111/j.1365-2966.2007.12748.x](https://doi.org/10.1111/j.1365-2966.2007.12748.x)
231. Li Z et al (2013) The cryogenic system for the Panda-X dark matter search experiment. *J Instrum* 8:P01002. doi: [10.1088/1748-0221/8/01/P01002](https://doi.org/10.1088/1748-0221/8/01/P01002). arXiv: [1207.5100](https://arxiv.org/abs/1207.5100) [astro-ph.IM]
232. Liang H et al (2000) A powerful radio Halo in the hottest known cluster of Galaxies 1E 0657–56. *Astrophys J* 544(2):686. doi: [10.1086/317223](https://doi.org/10.1086/317223). arXiv: [astro-ph/0006072](https://arxiv.org/abs/astro-ph/0006072)
233. Lin ST et al [TEXONO Collaboration] (2009) New limits on spin-independent and spin-dependent couplings of low-mass WIMP dark matter with a germanium detector at a threshold of 220 eV. *Phys Rev D* 79(6):061101. doi: [10.1103/PhysRevD.79.061101](https://doi.org/10.1103/PhysRevD.79.061101). arXiv: [0712.1645](https://arxiv.org/abs/0712.1645) [hep-ex]
234. Lindhard J (1968) Approximation method in classical scattering by screened Coulomb fields. *Mat Fys Medd Dan Vid Selsk* 36(10):1–44. <http://www.sdu.dk/media/bibpdf/Bind%2030-39/Bind/mfm-36-10.pdf>. As cited in Ref. [105]
235. Lindhard J et al (1963) Integral equations governing radiation effects: notes on atomic collisions, III. *Mat Fys Medd Dan Vid Selsk* 33(10):1–44. <http://www.sdu.dk/media/bibpdf/Bind%2030-39/Bind/mfm-33-10.pdf>. As cited in Ref. [105]
236. Luke PN (1988) Voltage-assisted calorimetric ionization detector. *J Appl Phys* 64(12):6858–6860. doi: [10.1063/1.341976](https://doi.org/10.1063/1.341976). As cited in Ref. [77]
237. Luke PN (1995) Unipolar charge sensing with coplanar electrodes-application to semiconductor detectors. *IEEE Trans Nucl Sci* 42(4):207–213. doi: [10.1109/23.467848](https://doi.org/10.1109/23.467848). As cited in Ref. [133]
238. Malling DC et al (2011) After LUX: the LZ program. arXiv: [1110.0103](https://arxiv.org/abs/1110.0103) [astro-ph.IM]
239. Marchionni A et al (2011) ArDM: a ton-scale LAr detector for direct Dark Matter searches. *J Phys Conf Ser* 308(1):012006. doi: [10.1088/1742-6596/308/1/012006](https://doi.org/10.1088/1742-6596/308/1/012006)
240. Martin SP (2008) A supersymmetry primer. arXiv: [hep-ph/9709356](https://arxiv.org/abs/hep-ph/9709356)
241. Martineau O et al [EDELWEISS Collaboration] (2004) Calibration of the EDELWEISS cryogenic heat-and-ionization germanium detectors for dark matter search. *Nucl Instrum Methods Phys Res Sect A* 530(3):426–439. doi: [10.1016/j.nima.2004.04.218](https://doi.org/10.1016/j.nima.2004.04.218)
242. Milgrom M (1983) A modification of the Newtonian dynamics as a possible alternative to the hidden mass hypothesis. *Astrophys J* 270:365–370. doi: [10.1086/161130](https://doi.org/10.1086/161130)

243. Milgrom M (1983) A modification of the Newtonian dynamics—implications for galaxies. *Astrophys J* 270:371–383. doi:[10.1086/161131](https://doi.org/10.1086/161131). ADS:1983ApJ...270..371M

244. Miuchi K et al (2010) First underground results with NEWAGE-0.3a direction-sensitive dark matter detector. *Phys Lett B* 686(1):11–17. doi:[10.1016/j.physletb.2010.02.028](https://doi.org/10.1016/j.physletb.2010.02.028). arXiv:[1002.1794](https://arxiv.org/abs/1002.1794) [astro-ph.CO]

245. Moffat JW (2006) Gravitational lensing in modified gravity and the lensing of merging clusters without dark matter. arXiv:[astro-ph/0608675v1](https://arxiv.org/abs/astro-ph/0608675v1)

246. Monroe J [For the DMTPC Collaboration] (2012) Status and prospects of the DMTPC directional dark matter experiment. In: Steadman SG, Stephans GS, Taylor FE (eds) 19th particles and nuclei international conference, PANIC11, Cambridge, MA, USA, 24–29 July 2011. AIP conference proceedings, vol 1441. AIP Publishing, Melville, pp 515–517. doi:[10.1063/1.3700603](https://doi.org/10.1063/1.3700603). arXiv:[1111.0220](https://arxiv.org/abs/1111.0220) [physics.ins-det]

247. Morgan B [On behalf of the DRIFT and UK Dark Matter collaborations] (2003) DRIFT: a directionally sensitive dark matter detector. In: Proceedings of the 6th international conference on position-sensitive detectors, special issue. *Nucl Instrum Methods Phys Res Sect A* 513 (1–2):226–230. doi:[10.1016/j.nima.2003.08.037](https://doi.org/10.1016/j.nima.2003.08.037)

248. Mulchaey JS (2000) X-ray properties of groups of galaxies. *Annu Rev Astron Astrophys* 38(1):289–335. doi:[10.1146/annurev.astro.38.1.289](https://doi.org/10.1146/annurev.astro.38.1.289)

249. Nakamura K et al (2012) NEWAGE. *J Phys Conf Ser* 375(1):012013. doi:[10.1088/1742-6596/375/1/012013](https://doi.org/10.1088/1742-6596/375/1/012013). arXiv:[1109.3099](https://arxiv.org/abs/1109.3099) [astro-ph.IM]

250. Navarro JF, Frenk CS, White SDM (1996) The structure of cold dark matter halos. *Astrophys J* 462(1996):563–575. doi:[10.1086/177173](https://doi.org/10.1086/177173). ADS:1996ApJ...462..563N

251. Navarro JF, Frenk CS, White SDM (1997) A universal density profile from hierarchical clustering. *Astrophys J* 490:493–508. doi:[10.1086/304888](https://doi.org/10.1086/304888) arXiv:[astro-ph/9611107](https://arxiv.org/abs/astro-ph/9611107)

252. Navarro JF, White SDM (1994) Simulations of dissipative galaxy formation in hierarchically clustering universes: II. Dynamics of the baryonic component in galactic haloes. *Mon Not R Astron Soc* 267:401–412. ADS:1994MNRAS.267..401N

253. Navick X-F [For the EDELWEISS Collaboration] (2009) Status of the development of surface event rejection for ionization-heat detectors in the EDELWEISS collaboration. In: PSD8—proceedings of the 8th international conference on position sensitive detectors, special issue. *Nucl Instrum Methods Phys Res Sect A* 604(1–2):45–47. doi:[10.1016/j.nima.2009.01.199](https://doi.org/10.1016/j.nima.2009.01.199)

254. Navick X-F, L'Hôte D, Tourbot R (2000) Ionization measurement at very low temperature for nuclear and electron recoils discrimination by ionization-heat simultaneous measurement for dark matter research. *Nucl Instrum Methods Phys Res Sect A* 442(1–3):267–274. doi:[10.1016/S0168-9002\(99\)01232-2](https://doi.org/10.1016/S0168-9002(99)01232-2)

255. Navick X-F et al (2004) Fabrication of ultra-low radioactivity detector holders for Edelweiss-II. In: Proceedings of the 10th international workshop on low temperature detectors, special issue. *Nucl Instrum Methods Phys Res Sect A* 520(1–3):189–192. doi:[10.1016/j.nima.2003.11.290](https://doi.org/10.1016/j.nima.2003.11.290)

256. Navick X-F et al [EDELWEISS Collaboration] (2006) Twenty-three ionization heat detectors for the Dark Matter search with EDELWEISS-II. In: Proceedings of the 11th international workshop on low temperature detectors—LTD-11, special issue. *Nucl Instrum Methods Phys Res Sect A* 559(2):483–485. doi:[10.1016/j.nima.2005.12.081](https://doi.org/10.1016/j.nima.2005.12.081)

257. Neganov B, Trofimov V (1985) Otkrytia i izobreteniya 146:215. As cited in Ref. [77]

258. Nones C [On behalf of the Edelweiss Collaboration] (2012) EDELWEISS detectors: from R & D to dark matter search. *J Phys Conf Ser* 375(1):012024. doi:[10.1088/1742-6596/375/1/012024](https://doi.org/10.1088/1742-6596/375/1/012024)

259. Oort JH (1932) The force exerted by the stellar system in the direction perpendicular to the galactic plane and some related problems. *Bull Astron Inst Netherlands* 6:249–287. ADS:1932BAN.....6..249O

260. Ostriker JP, Peebles PJE, Yahil A (1974) The size and mass of galaxies, and the mass of the universe. *Astrophys J* 193:L1–L4. doi:[10.1086/181617](https://doi.org/10.1086/181617). ADS:1974ApJ...193L...1O

261. Peccei RD, Quinn HR (1977) CP conservation in the presence of instantons. *Phys Rev Lett* 38:1440–1443. doi:[10.1103/PhysRevLett.38.1440](https://doi.org/10.1103/PhysRevLett.38.1440). As cited in Ref. [174, 186]

262. Persic M, Salucci P (1991) The universal galaxy rotation curve. *Astrophys J* 368:60–65. doi:[10.1086/169670](https://doi.org/10.1086/169670). ADS:1991ApJ...368...60P

263. Persic M, Salucci P, Stel F (1996) The universal rotation curve of spiral galaxies: I. The dark matter connection. *Mon Not R Astron Soc* 281:27–47. ADS:1996MNRAS.281...27P

264. Porter TA, Johnson RP, Graham PW (2011) Dark matter searches with astroparticle data. *Annu Rev Astron Astrophys* 49(1):155–194. doi:[10.1146/annurev-astro-081710-102528](https://doi.org/10.1146/annurev-astro-081710-102528)

265. E. Previtali [On behalf of the CUORE Collaboration] (2013) Search for neutrinoless double beta decay with CUORE. In: Proceedings of the 12th Pisa meeting on advanced detectors (La Biodola, Isola d’Elba, Italy, 20–26 May 2012), special issue. *Nucl Instrum Methods Phys Res, Sect A* 718:522–523. doi:[10.1016/j.nima.2012.11.141](https://doi.org/10.1016/j.nima.2012.11.141)

266. Profumo S (2012) Dissecting cosmic-ray electron-positron data with Occam’s razor: The role of known pulsars. *Cent Eur J Phys* 10(1):1–31. doi:[10.2478/s11534-011-0099-z](https://doi.org/10.2478/s11534-011-0099-z). arXiv:[0812.4457](https://arxiv.org/abs/0812.4457) [astro-ph]. As cited in Ref. [13]

267. Randall SW et al (2008) Constraints on the self-interaction cross section of dark matter from numerical simulations of the merging galaxy cluster 1E 0657–56. *Astrophys J* 679(2):1173–1180. doi:[10.1086/587859](https://doi.org/10.1086/587859)

268. Rau W [For the CDMS and SuperCDMS collaborations] (2012) CDMS and Super-CDMS. *J Phys Conf Ser* 375(1):012005. doi:[10.1088/1742-6596/375/1](https://doi.org/10.1088/1742-6596/375/1)

269. Rich J (2010) Fundamentals of cosmology, 2nd ed. Springer, Berlin. doi:[10.1007/978-3-642-02800-7](https://doi.org/10.1007/978-3-642-02800-7)

270. Richard M et al (2007) Dark matter maps reveal cosmic scaffolding. *Nature* 445:286–290. doi:[10.1038/nature05497](https://doi.org/10.1038/nature05497)

271. Riffard Q et al (2013) Dark matter directional detection with MIMAC. arXiv:[1306.4173](https://arxiv.org/abs/1306.4173) [astro-ph.IM]

272. Rozov S et al (2010) Monitoring of the thermal neutron flux in the LSM underground laboratory. arXiv:[1001.4383v1](https://arxiv.org/abs/1001.4383v1) [astro-ph.IM]

273. Rubbia A (2006) ArDM: a ton-scale liquid Argon experiment for direct detection of Dark Matter in the Universe. *J Phys Conf Ser* 39(1):129. doi:[10.1088/1742-6596/39/1/028](https://doi.org/10.1088/1742-6596/39/1/028)

274. Rubin VC, Thonnard N, Ford WK Jr (1980) Rotational properties of 21 SC galaxies with a large range of luminosities and radii, from NGC 4605 ( $R = 4$  kpc) to UGC 2885 ( $R = 122$  kpc). *Astrophys J* 238:471–487. doi:[10.1086/158003](https://doi.org/10.1086/158003)

275. Rubin VC et al (1985) Rotation velocities of 16 SA galaxies and a comparison of Sa, Sb, and SC rotation properties. *Astrophys J* 289:81–104. doi:[10.1086/162866](https://doi.org/10.1086/162866)

276. Saldanha RN (2012) Status of darkside. Presented at the 9th international conference: identification of dark matter, IDM2012, Chicago, IL, USA, July 23–27, 2012. <http://kicp-workshops.uchicago.edu/IDM2012/depot/plenary-talk-saldanha-richard.pdf>

277. Samtleben D, Staggs S, Weinstein B (2007) The cosmic microwave background for pedestrians: a review for particle and nuclear physicists. *Annu Rev Nucl Part Sci* 57(1):245–283. doi:[10.1146/annurev.nucl.54.070103.181232](https://doi.org/10.1146/annurev.nucl.54.070103.181232)

278. Sanders RH (1996) The published extended rotation curves of spiral galaxies: confrontation with modified dynamics. *Astrophys J* 473(1):117–129. doi:[10.1086/178131](https://doi.org/10.1086/178131). arXiv:[astro-ph/9606089v1](https://arxiv.org/abs/astro-ph/9606089v1). As cite in Ref. [176]

279. Sanglard V (2005) Recherche de la matière noire non-baryonique à l'aide de détecteurs cryogéniques à double composante ionisation et chaleur: analyse et interprétation des données de l'expérience EDELWEISS-I' [in French]. PhD dissertation, Université Claude Bernard - Lyon I. <http://tel.archives-ouvertes.fr/tel-00178567/fr/>. As cite in Ref. [202]

280. Sanglard V et al [EDELWEISS Collaboration] (2005) Final results of the EDELWEISSI dark matter search with cryogenic heat-and-ionization Ge detectors. *Phys Rev D* 71(12):122002. doi:[10.1103/PhysRevD.71.122002](https://doi.org/10.1103/PhysRevD.71.122002)

281. Savage C, Freese K, Gondolo P (2006) Annual modulation of dark matter in the presence of streams. *Phys Rev D* 74(4):043531. doi:[10.1103/PhysRevD.74.043531](https://doi.org/10.1103/PhysRevD.74.043531)

282. Savage C et al (2009) Compatibility of DAMA/LIBRA dark matter detection with other searches. *J Cosmol Astropart Phys* 2009(4):010. doi:[10.1088/1475-7516/2009/04/010](https://doi.org/10.1088/1475-7516/2009/04/010). arXiv:[0808.3607](https://arxiv.org/abs/0808.3607) [astro-ph]

283. Schmidt B et al [EDELWEISS collaboration] (2013) Muon-induced background in the EDELWEISS dark matter search. *Astropart Phys* 44:28–39. doi:[10.1016/j.astropartphys.2013.01.014](https://doi.org/10.1016/j.astropartphys.2013.01.014). arXiv:[1302.7112](https://arxiv.org/abs/1302.7112) [astro-ph.CO]

284. Schnee RW (2011) Introduction to dark matter experiments. In: Csaki C, Dodelson S (ed) Physics of the large and the small. Proceedings of the theoretical advanced study institute in elementary particle physics, TASI 2009, Boulder, CO, USA, June 1–26, 2009. World Scientific, Singapore, pp 629–681. doi:[10.1142/9789814327183\\_fmatter](https://doi.org/10.1142/9789814327183_fmatter). arXiv:[1101.5205](https://arxiv.org/abs/1101.5205) [astro-ph.CO]

285. Scholl S, Jochum J (2012) Neutron background simulation for the CRESST-II experiment. *J Phys Conf Ser* 375(1):012020. doi:[10.1088/1742-6596/375/1/012020](https://doi.org/10.1088/1742-6596/375/1/012020)

286. Shimwell TW et al (2014) Deep radio observations of the radio halo of the bullet cluster 1E 0657–55.8. *Mon Not R Astron Soc* 440(4):2901–2915. doi:[10.1093/mnras/stu467](https://doi.org/10.1093/mnras/stu467). arXiv:[1403.2393](https://arxiv.org/abs/1403.2393) [astro-ph.CO]

287. Shin-Ted L [TEXONO Collaboration] (2008) Neutrino physics and dark matter physics with ultra-low-energy germanium detector. In: Lee D-S, Lee W, Xue S-S (ed) Relativistic astrophysics. 5th Sino-Italian workshop on relativistic astrophysics, Taipei-Hualien, Taiwan, May 28–June 1, 2008. AIP conference proceedings, vol 1059. AIP Publishing, Melville, pp 164–171. doi:[10.1063/1.3012272](https://doi.org/10.1063/1.3012272)

288. Shutt T et al (2000) A solution to the dead-layer problem in ionization and phonon-based dark matter detectors. *Nucl Instrum Methods Phys Res Sect A* 444(1–2):340–344. doi:[10.1016/S0168-9002\(99\)01379-0](https://doi.org/10.1016/S0168-9002(99)01379-0). As cited in Refs. [134, 253]

289. Simard L [On behalf of the NEMO-3 Collaboration] (2012) The NEMO-3 results after completion of data taking. *J Phys Conf Ser* 375(4):042011. doi:[10.1088/1742-6596/375/1/042011](https://doi.org/10.1088/1742-6596/375/1/042011)

290. Simionescu A et al (2011) Baryons at the edge of the X-ray-brightest galaxy cluster. *Science* 331(6024):1576–1579. doi:[10.1126/science.1200331](https://doi.org/10.1126/science.1200331)

291. Simon JD, Geha M (2007) The kinematics of the ultra-faint Milky Way satellites: solving the missing satellite problem. *Astrophys J* 670(1):313–331. doi:[10.1086/521816](https://doi.org/10.1086/521816)

292. Smith MC et al (2007) The RAVE survey: constraining the local Galactic escape speed. *Mon Not R Astron Soc* 379(2):755–772. doi:[10.1111/j.1365-2966.2007.11964.x](https://doi.org/10.1111/j.1365-2966.2007.11964.x). As cited in Ref. [39, 76]

293. Sofue Y (2012) A grand rotation curve and dark matter halo in the Milky Way galaxy. *Publ Astron Soc Jpn* 64(4):75. arXiv:[1110.4431](https://arxiv.org/abs/1110.4431) [astro-ph.GA]. <http://www.ioa.s.u-tokyo.ac.jp/sofue/htdocs/2012DarkHalo/>

294. Space Telescope Science Institute. Picture album: Einstein ring gravitational lens (SDSS J120540.43+491029.3). <http://hubblesite.org/gallery/album/pr2005032d/>

295. Space Telescope Science Institute. Hubble Finds Ring of Dark Matter. 2007. <http://hubblesite.org/newscenter/archive/releases/2007/17/>. News release STScI-2007-17

296. Spergel DN et al (2003) First-year Wilkinson microwave anisotropy probe (WMAP) observations: determination of cosmological parameters. *Astrophys J Suppl Ser* 148(1):175–194. doi:[10.1086/377226](https://doi.org/10.1086/377226)

297. Spooner NJC (2007) Direct dark matter searches. *J Phys Soc Jpn* 76(11):111016. doi:[10.1143/JPSJ.76.111016](https://doi.org/10.1143/JPSJ.76.111016)

298. Springel V, Frenk CS, White SDM (2006) The large-scale structure of the Universe. *Nature* 440:1137–1144. doi:[10.1038/nature04805](https://doi.org/10.1038/nature04805). arXiv:[astro-ph/0604561](https://arxiv.org/abs/astro-ph/0604561)

299. Steadman SG, Stephans GS, Taylor FE (eds) (2012) 19th particles and nuclei international conference, PANIC11, Cambridge, MA, US, 24–29 July 2011. AIP conference proceedings, vol 1441. AIP Publishing, Melville. <http://scitation.aip.org/content/aip/proceeding/aipcp/1441>

300. Stefano PD et al [EDELWEISS Collaboration] (2001) Background discrimination capabilities of a heat and ionization germanium cryogenic detector. *Astropart Phys* 14(4):329–337. doi:[10.1016/S0927-6505\(00\)00127-4](https://doi.org/10.1016/S0927-6505(00)00127-4)

301. Steigman G (2007) Primordial nucleosynthesis in the precision cosmology era. *Annu Rev Nucl Part Sci* 57(1):463–491. doi:[10.1146/annurev.nucl.56.080805.140437](https://doi.org/10.1146/annurev.nucl.56.080805.140437)

302. Strege C et al (2013) Global fits of the cMSSM and NUHM including the LHC Higgs discovery and new XENON100 constraints. *J Cosmol Astropart Phys* 2013(4):013. doi:[10.1088/1475-7516/2013/04/013](https://doi.org/10.1088/1475-7516/2013/04/013). arXiv:[1212.2636](https://arxiv.org/abs/1212.2636) [hep-ph]

303. Szelc AM [WARP Collaboration] (2009) Current status of the WARP experiment. In: Khalil S (ed) The dark side of the universe. 4th international workshop on the dark side of the universe. Cairo, Egypt, 1–5 June 2008. AIP conference proceedings, vol 1115. AIP Publishing, Melville, pp 105–110. doi:[10.1063/1.3131480](https://doi.org/10.1063/1.3131480)
304. Takahashi R, Chiba T (2007) Weak lensing of galaxy clusters in modified Newtonian dynamics. *Astrophys J* 671(1):45–52. doi:[10.1086/522564](https://doi.org/10.1086/522564)
305. Tegmark M (2005) Cosmological neutrino bounds for non-cosmologists. *Phys Scr* T121:153–155. doi:[10.1088/0031-8949/2005/T121/023](https://doi.org/10.1088/0031-8949/2005/T121/023). arXiv:[hep-ph/0503257](https://arxiv.org/abs/hep-ph/0503257)
306. The XENON100 Collaboration (2010) Reply to the comments on the XENON100 first dark matter results. arXiv:[1005.2615](https://arxiv.org/abs/1005.2615) [astro-ph.CO]
307. Tisserand P et al (2007) [EROS-2 Collaboration] Limits on the macho content of the galactic halo from the EROS-2 survey of the magellanic clouds. *Astron Astrophys* 469:387–404. doi:[10.1051/0004-6361:20066017](https://doi.org/10.1051/0004-6361:20066017). arXiv:[astro-ph/0607207](https://arxiv.org/abs/astro-ph/0607207)
308. Tollerud EJ et al (2008) Hundreds of Milky Way satellites? Luminosity bias in the satellite luminosity function. *Astrophys J* 688(1):277–289. doi:[10.1086/592102](https://doi.org/10.1086/592102)
309. Tomasello V, Robinson M, Kudryavtsev V (2010) Radioactive background in a cryogenic dark matter experiment. *Astropart Phys* 34(2):70–79. doi:[10.1016/j.astropartphys.2010.05.005](https://doi.org/10.1016/j.astropartphys.2010.05.005)
310. Torii S et al (2008) High-energy electron observations by PPB-BETS flight in Antarctica. arXiv:[0809.0760](https://arxiv.org/abs/0809.0760) [astro-ph]. As cited in Ref. [13, 264]
311. Treu T (2010) Strong lensing by galaxies. *Annu Rev Astron Astrophys* 48(1):87–125. doi:[10.1146/annurev-astro-081309-130924](https://doi.org/10.1146/annurev-astro-081309-130924)
312. Trimble V (1987) Existence and nature of dark matter in the universe. *Annu Rev Astron Astrophys* 25:425–472. doi:[10.1146/annurev.aa.25.090187.002233](https://doi.org/10.1146/annurev.aa.25.090187.002233)
313. Vazquez-Jauregui E (2012) COUPP500: a 500kg bubble chamber for dark matter detection. Presented at the 9th international conference: identification of dark matter, IDM2012, Chicago, IL, USA, 23–27 July 2012. [http://kicp-workshops.uchicago.edu/IDM2012/depot/talk-vazquez-jauregui-eric\\_1.pdf](http://kicp-workshops.uchicago.edu/IDM2012/depot/talk-vazquez-jauregui-eric_1.pdf)
314. Vegetti S et al (2012) Gravitational detection of a low-mass dark satellite galaxy at cosmological distance. *Nature* 481:341–343. doi:[10.1038/nature10669](https://doi.org/10.1038/nature10669)
315. Vignati S [On behalf of the CUORE Collaboration] (2012) Direct dark matter and axion detection with CUORE. In: Steadman SG, Stephens GS, Taylor FE (eds) 19th particles and nuclei international conference, PANIC11, Cambridge, MA, USA, 24–29 July 2011. AIP conference proceedings, vol 1441. AIP Publishing, Melville, pp 512–514. doi:[10.1063/1.3700602](https://doi.org/10.1063/1.3700602)
316. Weniger C (2012) A tentative gamma-ray line from dark matter annihilation at the Fermi large area telescope. *J Cosmol Astropart Phys* 2012(8):007. doi:[10.1088/1475-7516/2012/08/007](https://doi.org/10.1088/1475-7516/2012/08/007). arXiv:[1204.2797](https://arxiv.org/abs/1204.2797) [hep-ph]
317. Woods M [For the LUX Collaboration] (2013) Underground commissioning of LUX. arXiv:[1306.0065](https://arxiv.org/abs/1306.0065) [astro-ph.IM]
318. Wright A [For the DarkSide Collaboration] (2011) The DarkSide program at LNGS. arXiv:[1109.2979](https://arxiv.org/abs/1109.2979) [physics.ins-det]
319. Wright A et al (2011) A highly efficient neutron veto for dark matter experiments. *Nucl Instrum Methods Phys Res Sect A* 644(1):18–26. doi:[10.1016/j.nima.2011.04.009](https://doi.org/10.1016/j.nima.2011.04.009). arXiv:[1010.3609](https://arxiv.org/abs/1010.3609) [nucl-ex]
320. Wu Y-C et al (2013) Measurement of cosmic ray flux in China JinPing underground laboratory. arXiv:[1305.0899](https://arxiv.org/abs/1305.0899) [physics.ins-det]
321. Yellin S (2002) Finding an upper limit in the presence of an unknown background. *Phys Rev D* 66(3):032005. doi:[10.1103/PhysRevD.66.032005](https://doi.org/10.1103/PhysRevD.66.032005). As cited in Refs. [39, 76]
322. Yue Q, Wong HT [and the CDEX-Texono Collaboration] (2012) Dark matter search with sub-keV germanium detectors at the China Jinping Underground Laboratory. *J Phys Conf Ser* 375(4):042061. doi:[10.1088/1742-6596/375/1/042061](https://doi.org/10.1088/1742-6596/375/1/042061). arXiv:[1201.5373](https://arxiv.org/abs/1201.5373) [physics.ins-det]
323. Zeldovich YB (1965) Survey of modern cosmology. In: Kopal Z (ed) Advances in astronomy and astrophysics, vol 3. Elsevier, Amsterdam, pp 241–379. doi:[10.1016/B978-1-4831-9921-4.50011-9](https://doi.org/10.1016/B978-1-4831-9921-4.50011-9). As cited in Refs. [173, 206]

324. Zhao W et al [CDEX Collaboration] (2013) First results on low-mass WIMP from the CDEX-1 experiment at the China Jinping underground Laboratory. arXiv:[1306.4135](https://arxiv.org/abs/1306.4135) [hep-ex]
325. Zwicky F (1933) Die Rotverschiebung von extragalaktischen Nebeln [in German]. *Helv Phys Acta* 6(2):110–127. doi:[10.5169/seals-110267](https://doi.org/10.5169/seals-110267)
326. Zwicky F (1937) On the masses of nebulae and of clusters of nebulae. *Astrophys J* 86(1937):217–246. doi:[10.1086/143864](https://doi.org/10.1086/143864). ADS:[1937ApJ....86..217Z](https://ui.adsabs.harvard.edu/abs/1937ApJ....86..217Z)

# Chapter 3

## Review of Muon-Induced Neutron Production at Underground Sites

The main focus of this work is to measure the muon-induced neutron production at the LSM underground laboratory and to assess the ability of Geant4 to reproduce the measurement.

A detailed overview of existing models and measurements of the related physical interactions, like muon propagation and muon spallation, is needed for the assessment of the MC simulations. This is especially true because previous measurements of muon-induced neutrons are not in mutual agreement with MC simulations.

As the muon-induced neutron production is fed by the muon energy loss, both topics are discussed in the following sections: We start with the muon production in the atmosphere and the parametrization of the muon flux at sea level by the Gaisser description in Sect. 3.1. Subsequently, the muon energy loss by electromagnetic and photonuclear interactions is discussed (Sect. 3.2). By folding the muon flux at sea level with the muon energy loss in the rock overburden of the LSM, the local muon flux is introduced in Sect. 3.3. The muon energy loss, both the nuclear and the electromagnetic, feed the production of neutrons at underground sites (Sect. 3.4). Measurements of muon-induced neutrons are discussed and compared to theory and MC driven predictions in Sect. 3.5. In Sect. 3.6 the implementation and systematic uncertainties of MC predictions are discussed for the case of Geant4. Finally, Sect. 3.7 connects this chapter to Chaps. 4 and 5 with a conclusion of literature based suggestions for the measurement and simulation of muon-induced neutrons at underground sites.

The general references in this chapter follow partially the reviews [112, 125, 193] and references therein.

### 3.1 Muon Flux at Sea Level

The muon is a second generation lepton with a rest mass of  $105.7 \text{ MeV}/c^2$  and a lifetime of  $2.2 \mu\text{s}$  [199]. It was first observed by C.D. Anderson and S.H. Neddermeyer [27] as part of the cosmic rays. Atmospheric muons are produced by cosmic rays

incident on the Earth's atmosphere [27]: Inelastic reaction of the primary cosmic ray particle on the nuclei in the atmosphere and fragmentation of the primary particle initiate an air shower, i.e. a cascade of secondary particles like hadrons (the air shower core), electrons/positrons, gammas (the electromagnetic component), and muons (the penetrating component, cf. Sect. 3.3) [104].

The electromagnetic component is fed by the ionisation loss of the hadronic component and the decay of uncharged mesons, like  $\pi^0 \rightarrow 2\gamma$ .

The muonic component is mainly (90 %) [104] produced via the decay of charged mesons, like pions and kaons, and results from the hadronic component. To a lesser extent, muons are produced in electromagnetic showers, mainly via the photo production of charged pions. Production of muon pairs is suppressed by  $m_e^2/m_\mu^2$  compared to electron-positron pair production. Via electron-hadron production only low energy hadrons are produced, therefore their contribution to the number of muons is small [113, p. 245].

The muon flux at sea level (Sect. 3.1.3) is the convolution of the primary cosmic ray spectrum (Sect. 3.1.1) with the production spectrum of muons taking into account the energy loss due to the propagation through the atmosphere, the effect of the atmospheric density profile (Sect. 3.1.2), and particle physical properties like the particle live-time, branching ratios and cross sections [104, 113]. As it will be reported in Sect. 3.3.3 muons need a minimal energy in the range of thousands of GeV (Eq. 3.37) to reach the LSM, allowing to use at sea level the approximative Gaisser parametrization of the muon flux that will be discussed in Sect. 3.1.3.

### 3.1.1 Cosmic Rays as Muon Source

The source of the primary component of cosmic rays (e.g. H, He, C) is partially still unknown. Particles with energies up to  $\approx 1$  PeV mostly originate in our Galaxy and get accelerated by the outer shock boundaries of supernova remnants [132] via 2nd order Fermi acceleration by supernova shock waves [113, p. 149]. Particles above this energy seem to be extragalactic and originate in unknown sources [158]. The secondary component of cosmic rays (e.g. Li, Be, B) is produced via inelastic interaction of the primary component with the interstellar medium.

The cosmic ray flux incident on the earth atmosphere below 15 GeV is modulated by the solar wind [114]. Above, the directions of cosmic rays are randomized by the galactic magnet field, and therefore reach the Earth isotropically. At highest energies, the cosmic rays are again anisotropic [4].

The energy spectrum of each particle species with charge  $Z$  of the cosmic rays is described by a power law [133]

$$\frac{d\dot{\Phi}_Z}{dE} = \dot{\Phi}_{Z,0} E^{\gamma_Z} \left( 1 + \left( \frac{E_0}{E_c} \right)^{\epsilon_c} \right)^{(\gamma_0 - \gamma_Z)/\epsilon_c} \quad (3.1)$$

where  $\gamma_Z$  describes the power law and  $E_c$ ,  $\gamma_0$ ,  $\epsilon_c$  describe the behaviour at the transition between galactic and extragalactic cosmic rays. The net spectrum of cosmic rays is therefore the sum of all individual spectra (see [114, 269, Fig. 24.1]), weighted by the contribution  $\dot{\phi}_{Z,0}$ , where protons are the most abundant species (79 %) [114, p. 269]. This results in an effective power law for the flux [113]

$$\frac{d\dot{\phi}}{dE} \propto E^{-(\gamma+1)} \quad (3.2)$$

where the *integral spectral index*  $\gamma$  is a function of the energy [114], [158, p. 123]:

$$\gamma \approx \begin{cases} 1.7, & E < 1 \text{ PeV} \\ 2, & 1 \text{ PeV} \leq E \leq 1 \text{ EeV} \\ 1.6, & 1 \text{ EeV} \leq E \end{cases} \quad (3.3)$$

As a consequence of the superposition (see Appendix A.2 for more details), air showers initiated by heavy primary particles (e.g. iron) reach their maximum in average at higher altitudes than air showers initiated by light particles (e.g. hydrogen) of the same energy, as the energy per nucleon drops faster below the energy threshold of secondary production.

The important characteristics of cosmic rays as source of atmospheric muons at underground sites are their isotropy, their initial interaction altitude, and the energy spectrum that follows a power law, which affect the muon generation in the simulation, see Sect. 5.3.1.

### 3.1.2 Influence of the Earth's Atmosphere on Muon Production

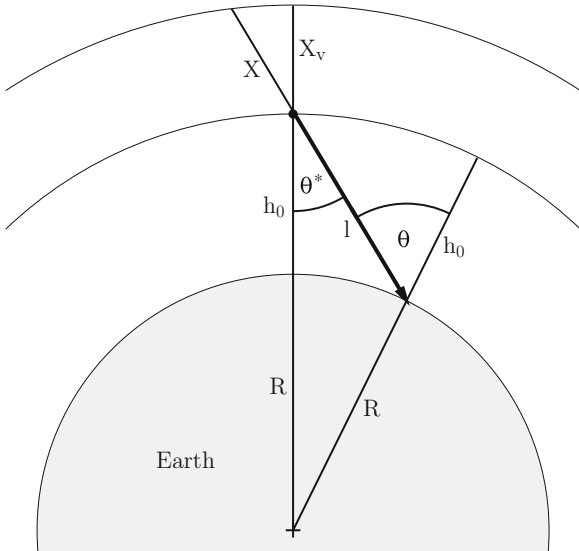
The atmosphere affects the muon flux via the dependency of the macroscopic interaction cross section  $\Sigma$  on the atmospheric density  $\rho$ . The mean tracklength between vertices of inelastic interaction of the particles on the nuclei in the atmosphere is the reciprocal of the macroscopic cross section  $\Sigma$  that is given by [49]:

$$\Sigma = \sigma \cdot \frac{\rho N_A}{A} \quad (3.4)$$

and depends on the molar mass of the target  $A$  and the interaction cross section  $\sigma$ .

Because the atmospheric density  $\rho$  changes with altitude  $h$ , also the macroscopic cross section changes. The *interaction length*  $\lambda_{\text{int}}$  is defined as the reciprocal macroscopic cross section scaled by the density [113, p. 28]

**Fig. 3.1** Illustration of the relation of vertical depth  $X_v$ , slant depth  $X$ , altitude  $h$ , particle track length  $l$ , earth radius  $R$ , zenith angle at production vertex  $\theta^*$ , and zenith angle at sea level  $\theta$ . For details see text. Figure based on [113, Fig. 3.1], [215, Fig. 2.5]



$$\lambda_{\text{int}} = \rho \cdot \frac{1}{\Sigma} \quad (3.5a)$$

$$= \frac{A}{\sigma N_A}, \quad (3.5b)$$

and is hence constant over the altitude.

Similarly, instead of the altitude  $h$  (particle track length  $l$ ) the *vertical atmospheric depth*  $X_v = \int_h^\infty \rho(h') dh'$  (the *slant depth*  $X = \int_l \rho(h(\vec{r})) d\vec{r}$ ), a column density, is used, where the integral is taken along the particle trajectory [104, 113]. Figure 3.1 shows the relation between the column densities/thicknesses  $X_v$ ,  $X$  and the respective lengths  $h$ ,  $l$ .

As for the interaction length, also the *decay lengths*  $\lambda_{\text{dec},i}$  of the particles are scaled by the air density  $\rho(X)$ , and hence by the slant depth  $X$ , [113, pp. 33–35]:

$$\lambda_{\text{dec},i}(E_i, X) = \rho(X) \frac{E}{m_i c^2} c \tau_i \quad (3.6)$$

with the Lorentz factor of the incident particle  $\gamma_i = E/(m_i c^2)$  and the lifetime of the particle  $\tau_i$ . For  $\pi^\pm$  the lifetime is equivalent to  $c\tau_{\pi^\pm} = 7.8$  m and for kaons  $c\tau_K = 3.7$  m, [104].

Therefore, via the scaling of the decay length with the slant depth (Eq. 3.6), the muon generation in Sect. 5.3.1 depends on the Earth's curvature.

### 3.1.3 Gaisser's Parametrization of the Muon Flux at Sea Level

In general atmospheric muons can occur as *muon bundles*, i.e. muons originate in the same cascade of an air shower, resulting in an angular and lateral correlation [112, p. 375], see [113, §14.5] for further details and parametrization.

In this work, only the flux  $\dot{\Phi}_\mu$  of uncorrelated, single muons is considered. The fluxes  $\dot{\Phi}_i$ , ( $i = \mu, \pi, K$ ) of muons and their parent mesons ( $\pi, K$ ) produced by cosmic rays in an air shower at a slant depth  $X$  and energy  $E_i$  is in general described by *coupled cascade equations* [113, p. 33], [178, p. 197], in the one-dimensional case by

$$\frac{d\dot{\Phi}_i(E_i, X)}{dX} = - \left( \frac{1}{\lambda_{\text{int},i}(E_i)} + \frac{1}{\lambda_{\text{dec},i}(X)} \right) \dot{\Phi}_i(E_i, X) + \sum_j S_{ij} \quad (3.7a)$$

$$S_{ij} = \int \frac{\dot{\Phi}_j}{E_j} \frac{F_{ji}(E_i, E_j)}{\lambda_{\text{int},j}} dE_j \quad (3.7b)$$

$$F_{ji}(E_i, E_j) = E_i \frac{dn_i(E_i, E_j)}{dE_i} \quad (3.7c)$$

The sum includes all sources  $S_{ij}$ , i.e. interactions of parent particles  $j$  that produce daughter particles  $i$  of amount  $n_i$  at energy  $E_i$ , where  $F_{ji}$  is the inclusive cross section for this process. The remaining term on the right side in Eq. 3.7a is the sink via particle interaction and particle decay. It is described via the interaction length  $\lambda_{\text{int},i}$  (Eq. 3.5) and decay length  $\lambda_{\text{dec},i}$  (Eq. 3.6), respectively, where the probability for interaction and decay is inversely proportional to the associated length.

The excess of  $\pi^+, K^+$  over  $\pi^-, K^-$  in the air shower and the excess of protons over neutrons in the cosmic rays is reflected by the muon charge ratio  $N_\mu^+/N_\mu^- > 1$ . It increases with muon energy, due to the increasing contribution of kaon decays (see [113, §6.3], [178, §8.1] and references therein). For atmospheric muons with the minimal energy of 2.5 TeV (Eq. 3.37), necessary to reach the LSM, a ratio of

$$\frac{N_\mu^+}{N_\mu^-} \approx 1.37 \quad (3.8)$$

is reported in literature [114]. It also affects the normalization of the simulated data sets, see Sect. 5.3.2.

At sea level, roughly 75 % of the incident particles are muons [112, pp. 374f.] with a flux of  $1 \text{ cm}^{-2} \text{ min}^{-1}$  and a mean energy of 4 GeV [114, p. 270]. They reach an equilibrium and a passage through more atmosphere would not change their abundance [112, pp. 374f.].

In general, the system of coupled cascade equations (Eq. 3.7a) is not analytically solvable and numerical methods or Monte Carlo programs like CORSIKA [129] have to be used (see e.g. [88, 228]). An approximate solution is given by the well known *Gaisser parametrization* [113]

$$\frac{d\dot{\Phi}_{\mu,0}}{dE_{\mu,0}d\Omega_0} = \frac{0.14}{\text{cm}^2 \text{s sr GeV}} \left( \frac{E_{\mu,0}}{\text{GeV}} \right)^{-2.7} \left( \frac{1}{1 + \frac{1.1E_{\mu,0} \cos \theta_0}{\epsilon_\pi}} + \frac{0.054}{1 + \frac{1.1E_{\mu,0} \cos \theta_0}{\epsilon_K}} \right) \quad (3.9a)$$

$$\approx AE^{-\gamma_\mu}, \quad (3.9b)$$

with the critical energies  $\epsilon_K = 850 \text{ GeV}$ ,  $\epsilon_\pi = 115 \text{ GeV}$ , see Eq. A.20. The index 0 indicates quantities at sea level. The energy dependence follows the power law of the primary particle (Eq. 3.2) and the depth dependence of attenuation lengths  $\lambda_{\text{dec},\pi}$ ,  $\lambda_{\text{dec},K}$  (Eq. A.19) leads to the two cosine terms.

Equation 3.9a can be approximate by Eq. 3.9b [24]: For  $E_\mu \ll \epsilon_{K,\pi}$  the slope of the muon spectrum approaches the slope of the primary spectrum:  $\gamma_\mu \rightarrow \gamma + 1$ . For  $E_\mu \gg \epsilon_{K,\pi}$  the muon spectrum gets steeper:  $\gamma_\mu \rightarrow \approx \gamma + 2$ . Measurements of the muon flux performed by several underground experiments (Fréjus [215] at the LSM, LVD [15], MACRO [24]) are in mutual agreement with the high energy limit [15]

$$\gamma = \gamma_\mu - 2 \quad (3.10a)$$

$$= 1.77 \pm 0.02 \quad (3.10b)$$

for single muons. This value is later used for the muon generation in Sect. 5.3.1.

Gaisser's parametrization is based on different approximations (see Appendix A.2 for a detailed review): Among others it neglects the Earth's curvature (Eq. A.19) and assumes stable muons, see approximation 14 in Appendix A.2. Consequently it is only valid for  $\theta \leq 60^\circ$  [113] and  $E_{\mu,0} > 100 \text{ GeV}/\cos \theta$ , respectively. Within this range of application the relative error in the spectral shape is less than 5 % and in the absolute rate with respect to air shower simulations, the error is roughly 20 % for energies between 10 GeV and 100 TeV [112, p. 375].

The lower energy limit is of no concern for the calculations of the muon flux at LSM, as muons need a minimal energy at sea level of 2.5 TeV (Eq. 3.37) to pass through the rock overburden. The limitation on the zenith angle, caused by neglecting the earth curvature, can be compensated by the  $\theta^*$  correction (Eq. A.21). The suitability of the Gaisser parametrization is also shown by its wide usage in literature to model the muon flux at underground sites, e.g. [134, 164, 228].

## 3.2 Muon Energy Loss in Rock

The muon flux at underground sites is the convolution of the muon flux at sea level (see previous Sect. 3.1) with the energy loss of muons along their propagation through the rock overburden mainly via electromagnetic interaction with the atomic electrons and the atomic nucleus, whereas the weak interaction is negligible [6, p. 328]. In this section we give the general parametrization of muon energy loss in Sect. 3.2.1, afterwards we summarize the relevant physical processes (Sects. 3.2.2–3.2.6), and

report the available data compilations in Sect. 3.2.7, following the outline of [6, 65, 125, 126]. The parametrization of the effective energy loss for the LSM rock is given in Sect. 3.2.8 and the muon flux at LSM in Sect. 3.3. The implementation of the physical interactions in Geant4 is discussed in Sect. 3.6.

### 3.2.1 General Parametrization of Energy Loss

The total mean energy loss of the incident muon along its trajectory through a medium with column density  $X$  can be parametrized as [42, 125]<sup>1</sup>:

$$\frac{dE_\mu}{dX} = -a(E_\mu) - b(E_\mu)E_\mu \quad (3.11a)$$

$$b = b_{\text{brems}} + b_{\text{pair}} + b_{\text{nucl}} \quad (3.11b)$$

$$\epsilon = a/b \quad (3.11c)$$

where  $a$  describes the electronic contribution (ionisation, excitation, and knock-on electrons/δ-rays<sup>2</sup>) and  $b$  is the radiative contribution (bremsstrahlung  $b_{\text{brems}}$ , direct electron-positron pair production  $b_{\text{pair}}$ , and muon spallation  $b_{\text{nucl}}$ ). The parameters  $a, b$  vary logarithmically with the muon energy  $E_\mu$  and approach constant values at high energies [125, p. 185]. Their ratio  $\epsilon$ , the muon critical energy, is nearly constant in energy [112, p. 376]. Below the critical energy  $\epsilon$ , the energy loss is predominantly via electronic, above  $\epsilon$  it is predominantly via radiative processes [65, p. 296].

Depending on the amount of interactions needed for a given energy loss, the processes are usually treated either as continuous or as stochastic and discrete [6, 65]: If the energy loss fluctuation within a given volume is small and a mean energy loss can be defined, the process is treated as continuous, which is true for ionisation and excitation. If the energy loss fluctuation is large, a mean energy loss is not well defined. The latter is especially true when the total kinetic energy dissipates in only a few interactions regardless how big the respective volume is [6, p. 329], e.g. due to discrete bursts of knock-on electrons, bremsstrahlung, direct pair production, and muon photonuclear interactions along the muon trajectory [65]. Therefore, the actual energy loss has to be obtained from MC simulations [179], like Geant4 discussed in Sect. 3.6. Their results differ from the mean energy loss Eq. 3.11a by around 5% [112, p. 377].

For a stochastic process, the energy loss  $\Delta E$  within  $dE_\mu$  of a muon with energy  $E_\mu$  can be described by the probability  $P(E_\mu, \nu)$ , where  $\nu$  is the fractional energy loss. It is related to the mean energy loss Eq. 3.11a via [6, p. 330], [32, 42, 126, 154]<sup>3</sup>:

<sup>1</sup>The parametrization is not unique, also  $dE_\mu/dX = a(E_\mu) + E_\mu/b(E_\mu)$  is used [113, p. 76].

<sup>2</sup>Again, the definition is not consistent in the literature: In [42]  $a$  is split into a contribution from the knock-on electrons, and a contribution from ionisation and excitation.

<sup>3</sup>It can be also related to the mean energy loss of a stochastic process to the energy weighted moment  $Z_{ij}$  Eq. A.18 via  $dE = -E_\mu \cdot Z_{\mu\mu'} \sigma \frac{N_A}{A} dX$  as done by T.K. Gaisser [113, p. 75].

$$b(E_\mu) = \int_{\nu_{\min}}^{\nu_{\max}} \frac{dP(E_\mu, \nu)}{d\nu} \nu d\nu \quad (3.12)$$

$$\frac{dP(E_\mu, \nu)}{d\nu} = \frac{N_A}{A} \frac{d\sigma}{d\nu} \quad (3.13)$$

$$\nu = \frac{\Delta E}{E_\mu} \quad (3.14)$$

To take the stochastic character of bremsstrahlung, pair production, and muon spallation into account, MC programs create discrete secondaries (electrons, gammas, etc.) above a threshold  $\nu_{\text{cut}}$  by sampling the probability Eq. 3.12. The energy loss within  $[\nu_{\min}, \nu_{\text{cut}}]$  is treated as continuous energy loss [179]. Several values of  $\nu_{\text{cut}}$  exist in literature as they are a trade off between precision and performance:  $\nu = 10^{-2}$  [179, 228],  $\nu = 10^{-3}$  [32, 164]. For the handling of  $\nu$  in Geant4 [33], see Sect. 3.6.

Exemplary, for a 150 GeV muon in iron, the stochastic energy loss, excluding muon spallation, is dominated in the beginning by pair production  $0.01 \leq \nu \leq 0.03$ , and by knock-on electrons  $0.03 \leq \nu \leq 0.12$ . As the cross section for pair production ( $\propto 1/\nu^2 \dots 1/\nu^3$ ) is steeper than the cross section for bremsstrahlung ( $\propto 1/\nu$ ), the contribution of bremsstrahlung to the muon energy loss exceeds the contribution of pair production and knock-on electrons for  $\nu > 0.12$  [57], [125, p. 196], [65, p. 296]. Figure 3.2a shows these regions of dominance in the  $E_\mu$ - $\nu$ -plane [73]. At low values for  $\nu$ , see Fig. 3.2b, the direct pair production dominates the energy loss and not the bremsstrahlung. Due to the Landau-Pomeranchuk-Migdal effect, see Sect. 3.2.5, the muon energy loss is finally determined at high energy ( $> 10^{20}$  eV) by the remaining muon nuclear interactions [65, p. 293]. At these energies the interactions are characterized by small cross sections, large fluctuations, hard spectra and the production of electromagnetic and hadronic showers [65, p. 296].

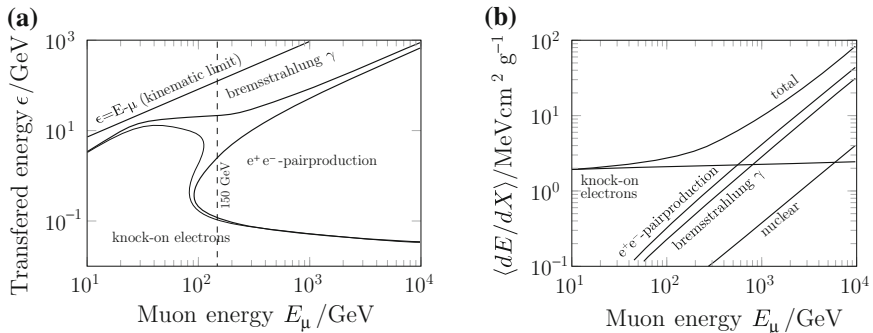


**Fig. 3.2** Process contribution to muon energy loss in iron: **a** The regions of dominance in the  $e$ - $E_\mu$ -plane,  $\epsilon = \nu E_\mu$ . The contours correspond to 50% contribution of the interactions to the combined differential cross section. Also shown is the cut at 150 GeV discussed in the text. **b** The composition of the muon energy loss over muon energy at low  $\nu$  value. Figures adapted from [73]

The shower production associated with the passage through rock is described in Sect. 3.3.

In the following various contributions to the energy loss are discussed, except the muon spallation: It will be described in detail in Sect. 3.4, as it is the main source of muon-induced neutrons. However, also the energy loss via pair production and bremsstrahlung feed the neutron production, in this case via electromagnetic showers, see Sect. 3.4.4.

### 3.2.2 Electronic Contribution to the Energy Loss

The electronic contribution is the sum over all inelastic scatterings of a muon on electrons [125, p. 188]. It reaches a minimum for muons with  $\beta\gamma = 3.0 \dots 3.5$  (i.e. *minimum ionizing particles*) depending on the medium charge  $Z$ , and rises afterwards logarithmically for relativistic muons [125, p. 188], [65, p. 296] (e.g. for electronic energy loss of muons in copper, see [125, Fig. 1]).

For muon kinetic energies above 100 eV ionisation starts to contribute to the energy loss described by J. Lindhard [175, 176], whereas below 100 eV the energy loss is caused by nuclear recoils and is described by J. Lindhard [175, 176] in the same way as the nuclear recoils in the EDELWEISS bolometers (see Sect. 2.3.2).

In the kinetic energy range between several KeV and several 100 KeV, there is no satisfactory theory [125, p. 186], and the energy loss can be described by the phenomenological Anderesen-Ziegler parametrization [26].

Above this intermediate region the average energy loss due to ionisation and excitation is described via the *Bethe equation* [59, 60] in its relativistic form<sup>4</sup> based on first order Born approximation [65, pp. 286, 288]:

$$\left\langle \frac{dE_\mu}{dX} \right\rangle = -Kz^2 \frac{Z}{A} \frac{1}{\beta^2} \left[ \frac{1}{2} \ln \frac{2m_e c^2 \beta^2 \gamma^2 E_{\max}}{I^2} - \beta^2 + \text{corrections} \right] \quad (3.15a)$$

$$E_{\max} = \frac{2m_e c^2 \beta^2 \gamma^2}{1 + 2\gamma m_e / m_\mu + (m_e / m_\mu)} \quad (3.15b)$$

where  $K = 4\pi N_A r_e^2 m_e c^2$ ,  $|z| = 1$  is the charge of the muon,  $m_\mu$  is the mass of the muon, and  $A$ ,  $Z$ ,  $I$  are respectively the atomic weight, charge, and excitation energy of the medium. The maximal kinetic energy transfer in one collision is given by  $E_{\max}$ . The excitation energy  $I$  can be calculated by Barkas' approximation [39], but more precise measured values exist [67, 136]. To Bethe's original formula (Eq. 3.15a) several low energy and high energy extensions exist.

Low energy extensions: For an incident particle with velocities comparable to the velocity of the atomic electrons, the shell correction  $-C/Z$  [180] describes the reduced interaction with K- and higher shells. For the empirical parameter  $C$ , there are

---

<sup>4</sup>For a review of the historical development, see [265], and references therein.

several parametrizations, see [137]. The Barkas effect [40], i.e. the smaller energy loss of negative particles with respect to positive particles, is caused by departure from the validity of first order Born approximation [41]. Its low energetic, distance-collision part is corrected by the Barkas correction  $zL_1(\beta)$ ; references to parametrizations and tabulated values are given in [125, 137]. Higher order terms of the Born development  $z^2L_2(\beta)$  can be added by the Bloch correction, i.e. the difference to Bloch's theory [70], which is not based on first order Born approximation [137]. In high-Z materials the relativistic shell electrons affect the energy loss [173], their effect is equivalent to a decrease of the excitation energy. For muon energies above 100 GeV, it has no effect because the excitation energy approaches the constant plasma energy due to the density correction (see below) [125, p. 189]. These low energetic corrections are described in detail in [137], and are negligible for muon energies above 10 MeV [125, pp. 186, 190]. By including these corrections, the low energy Bethe formula is correct within 1 % [137], [65, p. 288].

High energy corrections: The density correction  $-\delta(\beta\gamma)/2$  describes the truncation of long range interaction by the polarization of the medium. Effectively it replaces the excitation energy  $I$  by the plasma energy  $\hbar\omega_p$ . Values are tabulated and parametrized in a series of papers by R. Sternheimer, M. Berger, and S. Seltzer [236], and references in [65, 125]. They can also be calculated directly from first principles due to increased computer performance [125, pp. 190f.]. Further high energetic corrections [147] consider the part of energy loss via bremsstrahlung on the atomic electrons where the photon is emitted by the electrons, contributing up to 4 % of the energy loss at 100 TeV [66, p. 697], [125, p. 191], see also Sect. 3.2.3. Correction for the muon spin [219] makes up to 0.75 % in iron for  $E_\mu = 670$  GeV, which includes already the correction [141] for the nuclear form factor [125, p. 192]. At *high energies* the close-collision part of the Barkas effect induces a difference in the penetration depth of a few per mil between minimal ionizing  $\mu^+$ ,  $\mu^-$  [125, p. 192]. The associated correction [142] is the *Mott correction*, as it was first proposed by Fermi based on the Mott scattering theory [17]. It must not to be confused with the *low energy Barkas correction* for the distant-collision part of the Barkas effect.

Additional to these continuous processes, high energetic muons produce also *knock-on electrons* (delta-rays) via direct collisions. Albeit the production of knock-on electrons with kinetic energy  $E$  is suppressed like  $d^2N/dEdX \propto 1/E^2$  [65, pp. 288, 290], they have to be considered as they can escape a limited detector volume and therefore reduce the measured energy deposit [234].

Due to the contribution of a few, but high energetic interactions like knock-on electrons, the energy loss  $dE/dX$  strongly fluctuates around the mean energy loss  $\langle dE/dX \rangle$ . In case of thin detectors, i.e. the energy loss is small compared to the particle's initial energy [167], the mean value is not well defined anymore [65, pp. 286, 289]. The energy loss via ionisation is then a stochastic process described by asymmetric straggling functions with a high energy tail, like the *Landau* distribution [167], the more general *Vavilov* distribution [245], and the *Landau-Vavilov-Bichsel* distribution. The *Landau-Vavilov-Bichsel* distribution considers additionally the density correction  $\delta(\beta\gamma)$  [66]. For tick targets, the energy loss distribution approaches

a Gaussian distribution [167]. An overview which straggling function is appropriate for which case is given in [66, 237].

As its physical motivation suggests, the mean value (and higher moments also) of the Landau-Vavilov distribution is not well defined [189], and it is therefore better characterized by the *most probable value* of energy loss  $\Delta_p$  [65]. For the Landau-Vavilov-Bichsel distribution the most probable energy loss is [65]

$$\Delta_p = \xi \left[ \ln \frac{2mc^2\beta^2\gamma^2}{I} + \ln \frac{\xi}{I} + j - \beta^2 - \delta(\beta\gamma) \right] \quad (3.16a)$$

$$\xi = \frac{KZX}{2A\beta^2} \quad (3.16b)$$

with  $j = 0.200$ , and  $K, Z, A, I$  as in Eq. 3.15a. For  $j = 0.37$  and when ignoring the density correction  $\delta$ , it is identical to the most probable energy of the original Landau distribution [167].

For completeness, it should be noted that although the continuous electronic energy loss of the muon contributes little to the neutron production, it causes the muon detection in the muon telescope of the neutron counter, see Sect. 4.2.2.

### 3.2.3 Energy Loss via Bremsstrahlung

The energy loss  $b_{\text{brem}}$  due to *bremsstrahlung*, i.e. real photon production in the Coulomb field of a nucleus, is described for electrons by H. Bethe and W. Heitler [61] in Born approximation. It is adapted for muons by R.F. Christy and S. Kusaka [89], but they missed the screening of the nucleus by the atomic electrons. The screening for atoms with  $Z > 10$  was first consistently added by A. Petrukhin and V. Shestakov [207], but not undisputed [125, p. 193]: I.L. Rozental' [220] proposed its own model, and W.K. Sakumoto et al. [223] reported an overestimation of 10% of the screening by A. Petrukhin and V. Shestakov. S.R. Kel'ner, R.P. Kokoulin, and A.A. Petrukhin [146] suggest that this originates from an erroneous calculation by W.K. Sakumoto et al., as their own results are in agreement with A. Petrukhin and V. Shestakov. The calculation not based on Born approximation by Y.M. Andreev and E.V. Bugaev [29] also agrees with A. Petrukhin and V. Shestakov. Several extensions are applicable to the basic model of A. Petrukhin and V. Shestakov:

S.R. Kel'ner, R.P. Kokoulin, and A.A. Petrukhin [146] approximate the screening for  $Z < 10$ , based on a Thomas-Fermi potential for the atomic electrons. It agrees within 1% with results based on Hartree-Fock calculations [148]. The excitation of the target nucleus is included by Y.M. Andreev, L.B. Bezrukov, and E.V. Bugaev [28]. Further extensions by post Born corrections (i.e. deviation from Coulomb potential for interactions on nuclear scale) are negligible as they nearly cancel each other [29].

Besides the bremsstrahlung production in the nuclear Coulomb field, also the bremsstrahlung production in the field of the atomic electrons contributes to the

energy loss, as shown by S.R. Kel'ner, R.P. Kokoulin, and A.A. Petrukhin [147]. Those bremsstrahlung photons emitted by the electrons are considered as part of the energy loss via ionisation, whereas those emitted by the muons are considered as part of the energy loss via bremsstrahlung [66, p.697], [125, p. 191].

The measured energy loss of a 150 GeV muon beam in iron (CERN RD 34, [57]) further supports the superiority of the model of A. Petrukhin and V. Shestakov [207] in its modification by S.R. Kel'ner, R.P. Kokoulin, and A.A. Petrukhin [147] over the models of I.L. Rozental' and W.K. Sakumoto et al. [125, pp. 197f.].

As it will be shown in Sect. 3.2.8, the question of the correct model for muon bremsstrahlung is relevant for the muon energy loss in the rock overburden over the LSM.

### 3.2.4 Energy Loss via Direct Pair Production

The *direct production* of an electron-positron pair via virtual photons in the nuclear Coulomb field was first calculated by Nishina and Tomonaga, Oppenheimer and Plesset, and Heitler and Sauter in 1933, see references in [135, 198]. The relativistic calculation of the cross section of pair production is based on the work of H. Bethe and W. Heitler [61] using Born approximation. S.R. Kel'ner and Y.D. Kotov [149] include the effect of atomic screening for pair production by muons. Their work is the base for the parametrization described in [156, 201]. The effect of the nuclear form factor is considered by R.P. Kokoulin and A.A. Petrukhin [157]. S.R. Kel'ner [145] describes the influence of the pair production by the atomic electrons (triplet production).

D. Ivanov et al. [140] found that Coulomb correction reduces  $b_{\text{pair}}$  by up to  $-65\%$  at  $\nu \approx 10^{-4}$  for a 86.4 GeV muon incident on a lead target. This may affect the outcome of this work, as the used Geant4 lacks this correction, see Sect. 3.6.1.

### 3.2.5 The Landau-Pomeranchuk-Migdal Effect and the Ter-Mikaelian Effect

Bremsstrahlung and pair production are suppressed if the coherence of the respective process is disturbed along the formation distance. If the formation distance is larger than the atomic radius, also effects of the surrounding atoms have to be considered [65, p.293], e.g. multiple Compton scattering described by the *Landau-Pomeranchuk-Migdal effect* [169, 170, 195] or the polarization of the medium by the *Ter-Mikaelian effect* [243].

The effect on the muon energy loss via bremsstrahlung  $b_{\text{brems}}$  was calculated by S. Polityko et al. [209]. As example for the Landau-Pomeranchuk-Migdal effect they gave a threshold energy of  $E_{\text{LPM}} = 3.02 \times 10^{22}$  eV in lead: Due to this high value,

the effect suppresses the bremsstrahlung emitted by a muon with  $E_\mu = 1 \text{ TeV}$  for  $E_\gamma < 2.2 \text{ KeV}$ . As the neutron photoproduction in lead starts at  $E_\gamma \approx 7 \text{ MeV}$  due to the giant dipole resonance (Sect. 3.4.6), this change of the bremsstrahlung spectrum can be neglected.

The effect on direct pair production  $b_{\text{pair}}$  within  $10^9 \text{ eV} \leq E_\mu \leq 10^{24} \text{ eV}$  was investigated earlier by the same authors [208], but they found no suppression within the given energy range [208, Figs.16-2, 18].

Considering the high threshold energies, these effects are negligible within the applicable energy range of the Gaisser parametrization (Sect. 3.1.3), and hence of the muon generation in Sect. 5.3.1.

### 3.2.6 Energy Loss via Muon Spallation

The energy loss  $b_{\text{nucl}}$  via muon spallation is less well defined theoretically, because it also contains strong interactions. Their handling is avoided by describing the interaction as an exchange of a virtual photon of the electric field of the muon with the nucleus. As the Fourier spectrum of the virtual photon can be calculated precisely, the absorption of the virtual photon can be related to the nuclear photoeffect, well measured at accelerators. Extrapolation of the nuclear photoeffect cross section into ranges of energy transfer and momentum transfer above the accelerator measurements may introduce uncertainties as large as 20 % for the nuclear interaction energy loss  $b_{\text{nucl}}$ , but only 2 % for the total energy loss  $b$  [6, p.333], [112], reflecting the small absolute contribution, cf. Fig. 3.2b.

A detailed discussion of the related cross section and models for photonuclear muon interactions will be given in Sect. 3.4 in the context of muon induced neutrons.

### 3.2.7 References for Total Muon Energy Loss

The total energy loss of muons in various materials can be simulated with MC packages, and it is tabulated by W. Lohmann, R. Kopp, and R. Voss [181] and D.E. Groom, N.V. Mokhov, and S.I. Striganov [125], except the Landau-Pomeranchuk-Migdal effect and the Ter-Mikaelian effect. The compilation of D.E. Groom, N.V. Mokhov, and S.I. Striganov is more accurate than the one of W. Lohmann, R. Kopp, and R. Voss for  $2 \leq Z \leq 10$  as it includes corrections of the ionisation by bremsstrahlung from atomic electrons. At high mass and low energy D.E. Groom, N.V. Mokhov, and S.I. Striganov is less accurate than W. Lohmann, R. Kopp, and R. Voss as it used the Barkas parametrization for shell correction instead of measured values [125, pp. 192f.]. For the radiative regime [125] deviates from [181] as it includes screening of nuclear bremsstrahlung and the recoil of atomic electrons in bremsstrahlung, and pair production [125, p. 196].

Several MC programs are available for the simulation of muon propagation through material: Both dedicated packages (e.g. [179]<sup>5</sup> MUSIC [32, 161]), and general purpose packages (e.g. FLUKA [47, 108], Geant4 [16, 22]).

For this work, we use Geant4 for the muon transport, which relies for the electromagnetic muon interactions on the compilation of D.E. Groom, N.V. Mokhov, and S.I. Striganov [125], see Sect. 3.6.1.

### 3.2.8 Total Energy Loss in LSM Rock

The energy loss parameters  $a$ ,  $b$  (Eq. 3.11a) are both measured and calculated for the LSM rock by W. Rhode [215], based on the results of the Fréjus experiment [55, 56].

For the calculation of the muon energy loss in rock, it is necessary to include the rock composition by weighting the energy loss (Eq. 3.11a) in each constituent via Bragg additivity [77]. This results in [125, p. 203]:

$$\left\langle \frac{dE}{dX} \right\rangle = \sum_j w_j \left. \frac{dE}{dX} \right|_j \quad (3.17a)$$

$$w_j = \frac{n_j A_j}{\sum_k n_k A_k} \quad (3.17b)$$

where  $n_j$ ,  $A_j$  are the amount and the atomic weight respectively of the  $j$ -th constituent. For comparison between different sites commonly the energy loss is expressed with respect to standard rock:  $A = 22$ ,  $Z = 11$ ,  $\rho = 2.65 \text{ g cm}^{-3}$  [114]. Usually the thickness is expressed as the height of a water column with equivalent thickness, expressed as *meter water equivalent* (mwe):  $10^2 \text{ g cm}^{-2} = 1 \text{ mwe}$  [6, p. 328], [113, p. 77].

Based on MC simulations including the stochastic nature of the radiative processes, the energy loss relation Eq. 3.11a for standard rock and  $E_\mu \approx 1 \text{ TeV}$  is fitted with [179]

$$a = 237 \text{ MeV mwe}^{-1} \quad (3.18a)$$

$$b = 3.83 \times 10^{-4} \text{ mwe}^{-1} \quad (3.18b)$$

$$\epsilon = 618 \text{ GeV} \quad (3.18c)$$

$$\gamma_\mu = 3.7 \quad (3.18d)$$

---

<sup>5</sup>Within [179] the simulation code is not named. It is referred as ‘PROP\_MU’ by [215], and as ‘PROP-MU’ by [228].

Neglecting stochastic effects results in [125]

$$a = 268.1 \text{ MeV mwe}^{-1} \quad (3.19a)$$

$$b = 3.934 \times 10^{-4} \text{ mwe}^{-1} \quad (3.19b)$$

These two parametrizations of standard rock have to be considered by comparing different measurements, as it is done in Sect. 3.5.1.

According to [56, p. 2164] the “geological structure [over LSM] is quite homogeneous in a large area”. This conclusion is based on 18 measurements and W. Rhode states that there is only the possibility for local deviations [215, pp. 78, 89]. Despite this statement there exist three published sets for the rock composition [85, 183, 215], see Appendix A.4.2. Furthermore, V.A. Kudryavtsev [166] suggests a modification of the given rock composition to explain the observed depth-intensity-relation, see page 97.

Based on the actual Fréjus rock composition and the models compiled by W. Lohmann, R. Kopp, and R. Voss [181], W. Rhode calculates the energy loss parameters  $a, b$  for the LSM [215]. The value for  $b$  depends on the used screening model for bremsstrahlung and the handling of high energetic interactions [215, pp. 40–49]: Analytical integration of Eq. 3.11a results in  $b = 4.23 \times 10^{-4} \text{ mwe}^{-1}$  for the screening function of A. Petrukhin and V. Shestakov [207] and

$$b = 4.38 \times 10^{-4} \text{ mwe}^{-1} \quad (3.20)$$

for the screening function of I.L. Rozental' [220]. See also Sect. 3.2.3 for a discussion of these functions. MC simulations with discrete processes above  $\nu_{\text{cut}} = 0.01$  with the package PROP\_MU (see Sect. 3.6, [179]) result in  $b = 3.65 \times 10^{-4} \text{ mwe}^{-1}$  [215, pp. 178, 186]. Only the analytically calculated values of the electronic contribution is given [215, pp. 40–49] as

$$a = 217 \text{ MeV mwe}^{-1}, \quad (3.21)$$

which is independent of the bremsstrahlung model. This is expected from the discussion in Sect. 3.2.2, as the contributions of bremsstrahlung and stochastic interaction to the electronic contribution are higher order effects.

W. Rhode reports also measured values for  $a, b$ , based on the results of the Fréjus detector [55, 56]. The measured value of  $a$  is deduced from stopping muons in the Fréjus detector. As they are low energetic, the local spectrum is approximately determined by the electronic energy loss alone (Eq. 3.34), resulting in [215, p. 81]

$$a = 215(4) \text{ MeV mwe}^{-1}. \quad (3.22)$$

From the combined measurement of the remaining local muon flux and the rate of high energy interactions in the detector, the parameters  $\gamma$  and  $b$  can be disentangled [215, pp. 96, 99, 170–172]. The resulting effective values are [215, pp. 170, 173, 177, 186]:

$$b = 4.12(16) \times 10^{-4} \text{ mwe}^{-1} \quad (3.23)$$

$$\gamma + 1 = 2.73 \quad (3.24)$$

Within the uncertainties it is in agreement with the analytically calculated value based on the work of A. Petrukhin and V. Shestakov [207], but not with the work of I.L. Rozental' [220]. Therefore, Rhode's results further strengthening the superiority of the model of [207] (see Sect. 3.2.3).

In the literature values from both approaches, i.e. calculation based on rock composition and measurements, are used: O.M. Horn used in his work [134] the analytically calculated values Eqs. 3.20 and 3.21, the latter based on the screening function of I.L. Rozental' [220]. Contrary, F. Schröder used in his works [228, 229] for  $b$  the measured effective values Eq. 3.23 and for  $a$  the calculated one Eq. 3.21.

We follow the work of O.M. Horn and use also Eqs. 3.20 and 3.21 for the energy loss parameters. However, as discussed in Sect. 3.2.3, the included screening function of I.L. Rozental' [220] seems outdated. Therefore, for future work it may be interesting to investigate the influence of the chosen energy loss parameters.

### 3.3 Muon Flux at LSM

The local muon flux at underground sites as LSM consists of atmospheric muons and neutrino-induced muons. As atmospheric muons dominate over most of the zenith angles, neutrino-induced muons will not be further considered in this work.

The local muon flux (see Sect. 3.3.3) after passage through a given rock overburden (Sect. 3.3.2) is the convolution of the muon flux at sea level (Sect. 3.1) with the survival probability of muons in the rock (Sect. 3.3.1), which depends on the physical processes described in the previous Sect. 3.2.

An exact result is again only possible with the numerical treatment of muon generation and propagation, but an approximation is possible with the Gaisser parametrization (Eq. 3.9a) and the mean energy loss (Eq. 3.11a). The local muon flux at LSM feeds the neutron production mechanism described in the next Sect. 3.4.

#### 3.3.1 Muon Survival Probabilities

Due to the contribution of stochastic processes with a high energy transfer  $\nu$  in a few catastrophic interactions, the survival probability of a muon to pass a rock of thickness  $X$  has to be obtained by MC simulation [179]. As it affects the energy loss of muons, the rock composition has to be considered (see Sect. 3.2). In the literature the survival probability is calculated for several rock compositions, e.g. for standard rock [69, 115, 179] and for modified LSM rock [166].

If the contribution of stochastic process is small, the survival probability can be approximated by the *continuous-slowing-down approximation* (CSDA) [125] based on Eq. 3.11a:

$$\langle X(E_\mu, E_{\mu 0}) \rangle = \int_{E_{\mu 0}}^{E_\mu} \left\langle \frac{dE'}{dX} \right\rangle^{-1} dE' \quad (3.25)$$

where  $\langle X \rangle$  is the average thickness that a muon with energy  $E_{\mu 0}$  can traverse by losing  $E_{\mu 0} - E_\mu$ . Examples of average ranges are given in [125], [114, Table 24.2].

Solving Eq. 3.25 for  $E_\mu$  under the approximation that  $a(E_\mu), b(E_\mu)$  are constant in energy results in [113, Eq. 6.17], [114, §24.4.1]:

$$\langle E_\mu(X, E_{\mu 0}) \rangle = (E_{\mu 0} + \epsilon) e^{-Xb} - \epsilon \quad (3.26)$$

where  $E_{\mu 0}$  is the muon energy before it passes through the rock.

The solution for  $E_\mu = 0$  gives the minimal energy in average  $\langle E_{\mu 0,\min}(X) \rangle$  needed to pass through the rock [113, Eq. 6.18]

$$\langle E_{\mu 0,\min}(X) \rangle = \epsilon (e^{Xb} - 1) \quad (3.27)$$

In the CSDA the survival probability of a muon with energy  $E_{\mu 0}$  is simply a step function [134, p. 72]:

$$P(E_{\mu 0}, X) = \Theta(E_{\mu 0} - \langle E_{\mu 0,\min} \rangle) \quad (3.28)$$

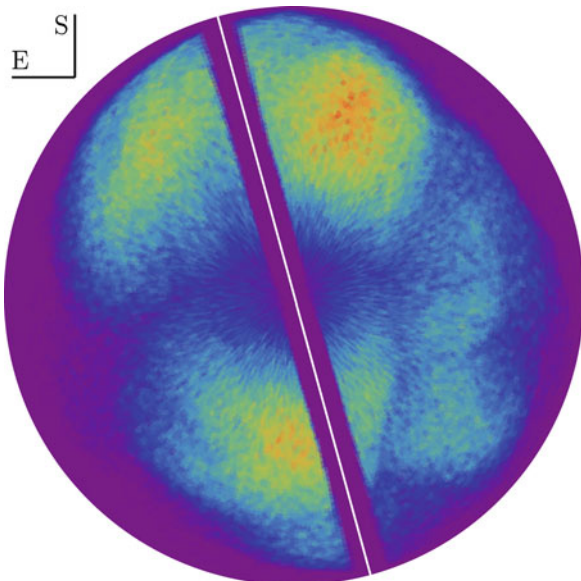
This approximation is usable for a semi-quantitative description of the underground muon flux, as the energy fluctuation due to the broad energy spectrum is bigger than the fluctuation due to the range straggling in the breakdown of the CSDA [113, p. 77]. However, Eq. (3.25) is not fully valid anymore for sites deeper than  $\approx 3$  kmwe, assuming standard rock composition, or muons with energies above  $\approx 1$  TeV. In this energy range the median of the actual muon ranges is less than the one expected from the CSDA Eq. 3.25 [159], [6, p. 335, Fig. 3; p. 338, Fig. 5], [179]. In this case  $a, b$  are effective parameters [196, 215] fitted to the measured energy loss relation via Eq. (3.11a) as done by W. Rhode, see Eqs. 3.22 and 3.23 in Sect. 3.2.8.

Albeit the CSDA may not be valid in full precision for the LSM with its minimal muon energy of  $\approx 2.5$  TeV (Eq. 3.37) it is still suitable as the comparison between the CSDA based muon generator and the Fréjus measurement in Fig. 5.8 will show.

### 3.3.2 Rock Overburden Above LSM

For underground sites located under mountain ranges the rock overburden is not flat. Therefore the depth  $X$  of the underground sites depends on the position and line of sight and has to be considered by measured depth maps  $t(\theta, \phi)$ . As a consequence, the

**Fig. 3.3** Polar plot of the single muon flux measured by the Fréjus experiment [55, 56], based on the data set provided by [166]. The white line indicates the length axis of the Fréjus detector, coincident with low detection efficiency. The plot illustrates the influence of the rock overburden on the local muon flux: Higher flux (red) occurs below thin rock overburden like valleys, and lower flux (blue) occurs below thicker rock overburden like mountain peaks. The angle indicates the south (S) and east (E) direction in agreement with [250]. See text for details



maximum of the remaining muon flux is a convolution of the maximal meson decay probability Eq. A.19 and of the maximal survival probability Eq. (3.28). Therefore, the maximal flux is incident from directions with a maximal zenith angle and a minimal slant depth [113, p. 78]. The influence on the local muon flux at the LSM is illustrated in Fig. 3.3.

The rock overburden at LSM is the mountain range of the Pointe de Fréjus in the French-Italian alps, the lab itself is located at  $45^\circ 8' 32''$  N and  $6^\circ 41' 21''$  E [56, 250]<sup>6</sup> at 1260 m above sea level [215, p. 57]. There are two relief maps of the mountain range, provided by the Fréjus collaboration: One with  $5^\circ \times 5^\circ$  resolution in zenith and azimuth directions used in [56], and a newer one with  $1^\circ \times 1^\circ$  resolution used in [215, 250], which we will call *Wei-Rhode map* afterwards. The latter is also used within the EDELWEISS collaboration (e.g. [134, 166]), see also Appendix A.7.

The Wei-Rhode map is based on relief maps from the space shuttle mission D-1<sup>7</sup> and additional elevation profiles from topographic maps<sup>8</sup> [215, 250]. As the rock

<sup>6</sup>The slightly deviating location of  $45^\circ 8' 22''$  N  $6^\circ 41' 21''$  E in [215] is probably a mistake in writing.

<sup>7</sup>The D-1 mission delivered two relief maps of the mountain range: One with a coverage of  $20\text{ km} \times 20\text{ km}$  and a larger one with  $40\text{ km} \times 40\text{ km}$  coverage, each with  $400 \times 400$  sampling points [215, 250].

<sup>8</sup>Elevation profiles from topographic maps were added to the relief maps, but it is unclear how exactly: According to [215, p. 57], referencing [250], they were added in the outer range. According to [250, pp. 118–120] they were added in the area above LSM to increase the resolution. To contain finally a  $1^\circ \times 1^\circ$  map, the profile was averaged over quarter degree steps in zenith direction and half degree steps in azimuthal direction, and weighted by the expected muon flux at these depth (Eq. B-1 in [250, p. 119]). This is not mentioned by [215]. As usually [215] is given as reference

composition around LSM is mostly homogeneous (see Sect. 3.2.8), the depth map  $X(\theta, \phi)$  for LSM can be constructed from relief map and rock density:

$$X(\theta, \phi) = t(\theta, \phi) \cdot \rho. \quad (3.29)$$

The azimuthal orientation of the LSM length axis coincident with the length axis of the Fréjus detector [55, 56] that is given with respect to the north–south axis precisely as  $74^\circ 43' 34.3''$  [250] clockwise [215, p.57]. Also often the value of  $15.1^\circ$  with respect to the east–west axis is given [56, 166] and rounded to  $16^\circ$  in [134, p. 73].

For a better comparison of underground sites, regardless of the geography of the rock overburden, [193] introduce the equivalent vertical depth  $X_{\text{ved}}$ : It is the thickness of a flat rock overburden resulting in the same muon flux underground as the muon flux obtained from the convolution of the rock profile with the depth-intensity-relation (see page 97). Values for various underground sites are given in [193, p.3], e.g. for the LSM  $X_{\text{ved}} = 4.2(2)$  kmwe.

The equivalent vertical depth  $X_{\text{ved}}$  is up to 20% lower than the average depth [193]:

$$\langle X \rangle = \int \sin(\theta) d\theta \int d\phi X(\theta, \phi) \quad (3.30)$$

For the LSM, the reference value for the average depth is [56]

$$\langle X_{\text{LSM}} \rangle = 4850 \text{ mwe}, \quad (3.31)$$

but also other values exist in the literature: An average thickness for the LSM of 5000 mwe is calculated by [193] using the same relief map as [56]. In contrast, W. Rhode [215] calculates with the Wei-Rhode map an average thickness of 4713 mwe.<sup>9</sup> Also with the Wei-Rhode map [134, p. 71] calculates an average thickness of 4600 mwe.

As it has the highest angular resolution, we chose for this work the Wei-Rhode map with an average depth of 4850 mwe. To be consistent with the work of O.M. Horn [134], we use as azimuthal orientation of the LSM with respect to the east–west axis the value of  $16^\circ$ , see Sect. 5.1.

### 3.3.3 Local Muon Flux at LSM

The local muon flux  $d\dot{\Phi}(E_\mu, X)/dE_\mu$  at an underground site is related to the muon flux at sea level  $d\dot{\Phi}(E_{\mu,0})/dE_{\mu,0}$  via a parameter transformation of the muon energy

---

(Footnote 8 continued)

for the  $1^\circ \times 1^\circ$  depth map (e.g. in [134, 166]), it is not clear if this weighting is included in the Wei-Rhode map.

<sup>9</sup>Given in [215, p.57] as average depth of 1720 m with a density of  $2.74 \text{ g cm}^{-3}$ .

before and after a muon transverses the rock overburden  $X(\theta, \phi)$  [113, p. 78] weighted by the survival probability [178, p. 205]:

$$\frac{d\dot{\Phi}(X)}{dE_\mu} = P(E_\mu, E_{\mu0}, X) \frac{d\dot{\Phi}}{dE_{\mu0}} \frac{dE_{\mu0}}{dE_\mu} \quad (3.32)$$

By using Eq. 3.27 within the CSDA this is:

$$\frac{d\dot{\Phi}(E_\mu, X)}{dE_\mu} = \Theta(E_{\mu0} - \langle E_{\mu0,\min} \rangle) \left. \frac{d\dot{\Phi}(E_{\mu0})}{dE_{\mu0}} \right|_{E_{\mu0} \rightarrow E_\mu} e^{X(\theta, \phi)b} \quad (3.33)$$

As the mountain profile introduces an azimuthal dependence, the calculation has to be three dimensional in general [166].

Approximating the surface muon intensity with a power law (Eq. 3.9b) the local muon intensity is given by [179]

$$\frac{d\dot{\Phi}(E_\mu, X)}{dE_\mu} = A e^{Xb(1-\gamma_\mu)} \left( E_\mu + \epsilon \left( 1 - e^{-Xb} \right) \right)^{\gamma_\mu}. \quad (3.34)$$

Characteristic for this relation is a flat spectrum for  $X \ll 1/b$  and  $E_\mu \ll aX$ , whereas the source spectrum Eq. 3.9a is reflected for  $X \ll 1/b$ ,  $E_\mu \gg aX$ . At  $X \gg 1/b$  the shape of the local spectrum becomes independent from depth [113, p. 79]. An illustration of this effect is shown in [113, Fig. 6.4]. However, at the LSM the local muon spectrum is not in the range  $X \gg 1/b$ , therefore it depends on the slant depth  $X$  and on the rock overburden [215, p. 39] as indicated in Fig. 3.3.

Based on Eq. 3.33, the average local muon energy is given by [24, 193, 262]:

$$\langle E_\mu \rangle = \frac{\epsilon_\mu (1 - e^{-bh})}{\gamma_\mu - 2}. \quad (3.35)$$

Values of  $\langle E_\mu \rangle$  for several underground sites, except LSM, are given in [193, p. 4]. For LSM an analysis of data from the Fréjus detector [55, 56] by W. Rhode [215, 216] results in an average muon energy of

$$\langle E_{\mu, \text{LSM}} \rangle = 255.0(45) \text{ GeV} \quad (3.36)$$

[215]. Only slightly in disagreement with MC simulations indicating an energy range of  $\langle E_\mu \rangle = 260\text{--}290 \text{ GeV}$  [134].

An overview of underground laboratories and the remaining muon flux is given in [112, Fig. 2]. The minimal necessary energy for muons at sea level to reach these sites is given in [113, Table 6.1], e.g. for LSM

$$E_{\mu, \text{min, LSM}} \approx 2.5 \text{ TeV}. \quad (3.37)$$

C. Berger et al. [56] measured for the LSM a single muon flux of

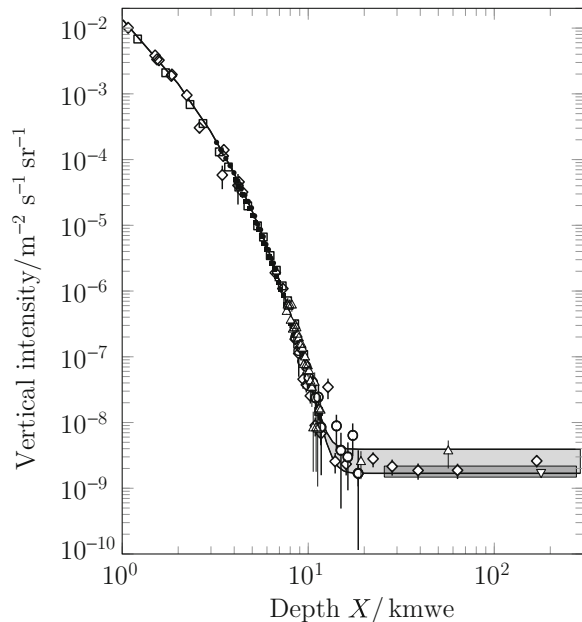
$$\dot{\phi}_{\text{LSM, single}} = 5.47(10) \times 10^{-5} \text{ m}^{-2} \text{ s}^{-1} \quad (3.38)$$

$(5.99 \times 10^{-5} \text{ m}^{-2} \text{ s}^{-1}$  by including also muons from muon bundles) above a zenith angle of  $60^\circ$  and above a threshold 300 MeV [215]. Hence, most probably the threshold excludes secondary muons from the measurement (see page 100). Compared with the muon flux at sea level (see page 81) the local muon flux is suppressed by roughly six orders of magnitude.

Albeit the measurement of C. Berger et al. [56] is the reference for the muon flux at LSM, there exist a confusion about the exact meaning of the given flux, especially how to compare it with MC simulations, see the discussion in Appendix A.7. Parallel to this work, the muon flux was also measured with the EDELWEISS muon veto, resulting in a value of  $(6.25 \pm 0.23_{-1.04}^{+0.58\text{sys}}) \times 10^{-5} \text{ m}^{-2} \text{ s}^{-1}$  [227]. Within the uncertainties it is in agreement with Eq. 3.38. However, for this work we will use the traditional value of C. Berger et al.

The *depth-intensity-relation* (DIR) is the experimentally determined relation between the vertical muon flux Eq. A.32 at a given depth and the slant depth. For the LSM it is investigated in [56, 215]. The compilation of DIR measurements from several underground experiments are shown in Fig. 3.4. The flat spectrum at high depths results from muons induced by neutrinos [113, pp. 78,105] of atmospheric origin [216]. At the LSM the flux of neutrino-induced muons equals the flux of atmospheric muons at a slant depth of roughly 13 kmwe, and dominates above

**Fig. 3.4** Compilation of depth-intensity-relation measurements from various underground experiments [14, 23, 30, 93, 248], including the Fréjus experiment [56], for details see text. Figure adapted from [114], references for the data compilation therein



15 kmwe, equivalent to zenith angles larger than  $80^\circ$  [215, pp. 65, 67]. The average energy of neutrino-induced muons is expected in the range of 10–20 GeV [184, 216]. As it will be reported in Sect. 3.4.1, neutrino induced muons are a source for neutrons via  $\mu^-$  capture even at deep sites. However, we limit this work to the predominant atmospheric muons.

The DIR at LSM is used by V.A. Kudryavtsev [166] to test the rock composition at LSM (see Sect. 3.2.8) and by F. Schröder [228, 229] to test the influence of different MC implementations of muon energy loss processes (see Sect. 3.2) on the local muon flux. The single muon flux data set from W. Rhode [215] is compared by F. Schröder [228, 229] with several implementations: The sea level spectrum, described either by CORSIKA generated surface muons flux or by Gaisser parametrization (Eq. 3.9a), is convolved with muon energy loss described either by muon transport MC<sup>10</sup> or by a CSDA based on Eq. 3.11a with Eqs. 3.21 and 3.23 as values for the energy loss parameter  $a, b$ . In any case a deviation between MC and measurement of the absolute flux in the range of 30–60 % was found. All except one simulation using muon transport codes mismatched the shape of the deep-intensity relation at a level of  $<4\% \text{ kmwe}^{-1}$ , whereas the simulation using CSDA had only a spectral deviation of  $2.8\% \text{ kmwe}^{-1}$ . This was explained by inaccuracies in the cross sections used by the muon transport codes. This conclusion is in disagreement with the findings of V.A. Kudryavtsev [166] for the following reason: A simulation of the DIR using muon transport code MUSUN [162] confirms the disagreement in the absolute flux (about 40 %) and in the spectral shape. However, MUSUN reproduces well the local muon flux at the LNGS underground laboratory measured with the LVD detector, therefore the implemented muon interaction physics in MUSUN seems to be valid. To explain the disagreement between simulations and measurements at LSM, the rock composition may be incorrect or the spectral index has to be increased. The first explanation was excluded by F. Schröder [229, p. 118] as it is in disagreement with the geological findings (see Table A.4). The second explanation is in disagreement with established references.

Therefore the validity and the exact meaning of the existing measurements of the local muon flux at LSM, and the simulation of it are not as undisputed as it seems at the first view. That the CSDA based model has the smallest spectral deviation proofs further its suitability for this work, albeit it is in full strictness not valid anymore for the LSM, see Sect. 3.3.1.

### 3.4 Production Mechanisms for Muon-Induced Neutrons

The muon-induced neutron production is determined by the muon energy loss in the rock overburden, the laboratory structure, and the experimental set-up. Therefore the flux of muon-induced neutrons is the convolution of the local muon flux (see previous Sect. 3.3) and the neutron production in the different materials.

---

<sup>10</sup>PROP\_MU, MUDEX, MUM, MMC, see references in [229].

The neutron production can be divided in direct neutron production, like negative muon capture, quasielastic scattering, muon spallation (Sects. 3.4.1–3.4.3), and indirect neutron production by the showers initiated by the muon via electromagnetic interactions, like photonuclear production and hadronic interactions (Sects. 3.4.4–3.4.5) [35, 112, 187]. As the photonuclear cross section is important for the photonuclear neutron production in electromagnetic showers (Sect. 3.4.4) and for the muon spallation (Sect. 3.4.3), it is discussed separately in Sect. 3.4.6.

The shower development is governed by the same physical interactions like the air shower development (see Sect. 3.1), except for the different material. In case when a hadronic shower is started by a neutron, the neutrons produced in the shower are referred as *secondary neutrons*.

In a fully developed shower, the secondary neutrons outnumber the primary neutrons from muon nuclear interactions: Simulations for the LSM show that only up to 20% of all produced neutrons come from muon nuclear interactions, decreasing towards higher energies, as more energy is transferred to the shower; up to 50% of the neutrons are produced by real photo nuclear interactions in electromagnetic showers, followed by neutron and pion inelastic reactions in hadronic showers [134] (see Fig. 3.5a, b). In total up to 60–75% of all neutrons at high energies are secondary neutrons [112, 187]. This is in agreement with Geant4 simulations [35] for the Boulby Underground Laboratory, which has a similar average muon energy, therefore support the consistency of Geant4 results.

Therefore, a detailed description of the shower development, the electromagnetic energy loss of muons (see Sect. 3.2), and the interaction of neutrons is necessary. Typically, the resulting flux of muon induced neutrons is 2–3 orders of magnitude

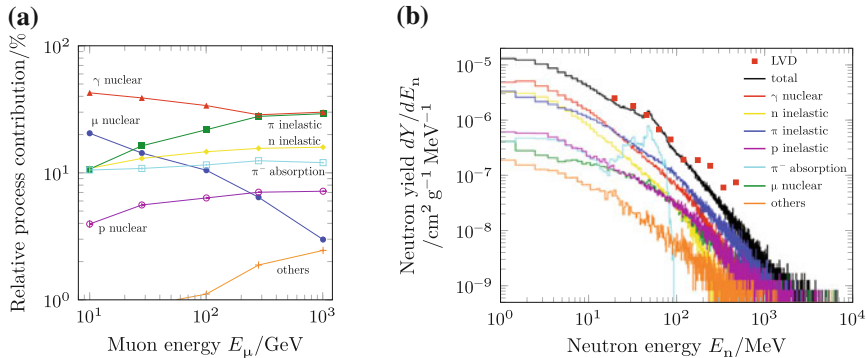


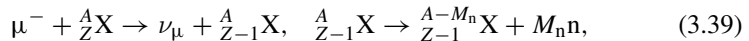
**Fig. 3.5** Relative contribution of the various neutron production channels in hydrocarbon to **a** the amount of muon-induced neutrons as function of muon energy and **b** the resulting neutron energy spectrum, simulated with Geant4 8.2p01, compared to a scaled measurement by LVD [165]. At high energies the contributions from real photonuclear production in bremsstrahlung shower and secondary neutron production dominate over muon photonuclear interactions. For details see text. Figures adapted from [134, Figs. 3.6, 3.8]

smaller than the flux of ambient neutrons from  $(\alpha, n)$  reactions, but with a harder spectrum up to several GeV [193, p.4], and therefore harder to control.

Measurements of the neutron production will be discussed in Sect. 3.5, and actual implementations of the physical interactions in MC models will be discussed in Sect. 3.6.

### 3.4.1 Capture of Negative Muons on Nuclei

In competition to muon decay, slow negative muons become captured by an atomic nucleus  $X$  after forming muonic atoms, resulting in neutron production [112]:



with the neutron multiplicity  $M_n$ . The flux of neutrons  $\dot{\Phi}_n$  from this process is the convolution of the flux of stopped negative muons  $\dot{\Phi}_\mu^-$ , the capture probability  $P_c$ , and the neutron multiplicity  $M_n$  [112]:

$$\dot{\Phi}_n = \dot{\Phi}_\mu^- \times P_c \times M_n \quad (3.40)$$

The flux of stopped negative muons was studied in detail in [68, 81, 84]. Its uncertainty is dominated by the muon photonuclear contribution in muon energy loss and below 1 GeV it depends on the location because of the geomagnetic effect. The fraction of stopped muons in material of thickness  $\Delta X$  at depth  $X \gg \Delta X$  in relation to the total muon flux at the site is given by [113, p.71]

$$\frac{\Delta N}{N} \approx \frac{\gamma_\mu E_{\mu,\min} e^{Xb}}{(e^{Xb} - 1) \epsilon}, \quad (3.41)$$

with  $\epsilon, b$  as defined in Eq. 3.11a. Here  $E_{\mu,\min}$  is the minimal energy needed to pass through the detector, see Eq. 3.27. The rate converges to  $\approx 0.5\%$  for  $X > b$  [113, p.80].

For a 10 cm thick lead target, as it is used in the neutron counter of this work (Sect. 4.2.1), Eq. 3.41 results in  $\Delta N/N \approx 0.0015$  at the LSM as characterized by the measured energy loss parameters Eqs. 3.22 and 3.23, see Sect. 3.2.8, and the depth Eq. 3.31, see Sect. 3.3.2. Based on the muon charge ratio of roughly 1.37 (Eq. 3.8) and the measured muon flux at LSM (Eq. 3.38) a flux of stopped  $\mu^-$  of  $2.9 \times 10^{-3} \text{ m}^{-2} \text{ d}^{-1}$  can be estimated.

This is a lower limit as for a depth greater than 1 kmwe the stopped muons are outnumbered by secondary muons [127]: Slowed down, low energetic  $\pi^-$  of the hadronic shower will decay to secondary muons with  $E_\mu < 500 \text{ MeV}$ . As the interaction length in air is longer than the decay length of pions, the flux of secondary

muons will be increased by air volumes between the rock boundary and the detector [5, pp. 340ff.].

The muon capture probability  $P_c$  [84, 190, 238] is expressed via the muon capture rate  $\Gamma_c$  and muon decay rate  $\Gamma_d$  [112]:

$$P_c = \frac{\Gamma_c}{\Gamma_c + Q\Gamma_d} \quad (3.42)$$

$$\Gamma_d = \frac{1}{\tau_\mu^+} \quad (3.43)$$

where  $Q$  is the Huff factor correcting the muon decay rate for the phase space change via the muonic atom binding. It is listed in [238].

The muon capture rate  $\Gamma_c$  increases with  $Z^4$ , where  $Z$  is the charge of the target. There exist measured values [238] and phenomenological models for low  $Z$  [210], for high  $Z$  the Pauli suppression [124] has to be included.

The expected neutron flux from captured  $\mu^-$  can roughly be estimated by Eq. 3.40: with the Huff factor  $Q = 0.844$  [238], the muon capture rate  $\Gamma_c = 13.45 \times 10^6 \text{ s}^{-1}$  [238], mean lifetime  $\tau_\mu^+ = 75.4 \text{ ns}$  [238], and neutron multiplicity  $M_n = 1.709$  [185]. This results in the neutron flux of  $\approx 2.7 \times 10^{-3} \text{ m}^{-2} \text{ d}^{-1}$ .

The kinetic energy spectrum of the emitted neutrons is parametrized in [190]

$$\frac{dN}{dE_n} = a_{\text{evap}} E_n^{5/11} e^{-E_n/\theta} + a_{\text{direct}} e^{E_n/T}, \quad (3.44)$$

consisting of an evaporation part  $a_{\text{evap}}$ , described with the evaporation temperature  $\theta$  and a direct part  $a_{\text{direct}}$ , described by the effective parameter  $T$ .

In general, up to two neutrons per  $\mu^-$  are expected, with an individual mean energy of  $\approx 8 \text{ MeV}$  for the evaporated neutrons [187]. As this kind of neutron production is proportional to the rate of stopped muons, it is the dominant mechanism for shallow underground sites: it contributes up to 50 % to all neutrons on sites up to 80 mwe, respective 30 GeV muon energy [187]. At depths where low energy neutrino-induced muons dominate (see Sect. 3.3.3), the relative contribution of neutrons from muon capture rises again [187].

### 3.4.2 Quasielastic Scattering on Nuclei

The quasielastic scattering of muons on nuclei produces knock-on neutrons [112] with energies in the order of 100 MeV [97]. The cross section as function of the four-momentum transfer  $Q$  is approximated by D.H. Perkins (as cited in [112, p. 385]) as:

$$\frac{d\sigma}{dQ} = \frac{4\pi\alpha^2}{Q^4} G_M^2 (-Q)^2 \left( \frac{Q^2/4M_n^2}{1 - Q^2/4M_n^2} + \left( \frac{Q^2}{2M_n^2} \right) \tan \frac{\theta^2}{2} \right) \quad (3.45)$$

with the neutron magnetic form factor  $G_M(q^2)$  and the fine structure constant  $\alpha$ . It is expected to be no major contribution of muon-induced neutrons [112].

### 3.4.3 Muon Spallation

The process of muon spallation<sup>11</sup> can be reduced to the inelastic scattering of muons on nucleons with the exchange of a virtual photon [73, p. 513]. The differential cross section for this process depends on the nucleon structure functions [128], and on the energy- and momentum transfer,  $\nu$  and  $q^2$ , respectively [126].

For energy transfers  $\nu < 300$  MeV the muon predominantly interacts with the nucleus, whereas for higher energies the interaction occurs with single nucleons, resulting in the actual muon spallation via photonuclear disintegration [187]. The case of high momentum transfer  $\sqrt{q^2} \gg 800$  MeV is referred as *deep inelastic scattering* in the context of muon nuclear interactions [7]. This interaction results in knock-on nucleons on a time scale of  $10^{-22}$  to  $10^{-21}$  s, and on a longer time scale ( $\approx 10^{-16}$  s) the residual nucleus may de-excite via neutron evaporation [187], see also Sect. 3.4.5.

For the case of muon nucleon interaction within cosmic rays, the transferred momentum is usually small and approximations for  $q^2 \rightarrow 0$  are used. The given quantities are usually integrated over  $dq^2$  [126, p. 141f]. In the limit of  $q^2 \rightarrow 0$  the cross section for longitudinal polarized virtual photons vanishes and the cross section for transverse polarized virtual photons approaches the cross section for real photons [126]. The *equivalent photon approximation* relates the virtual photon cross section  $\sigma_{\mu N}$  to the cross section for the absorption of a real photon (nuclear photoeffect)  $\sigma_{\gamma N}$  by neglecting the longitudinal component of it [126]. It was proposed by E. Fermi [107], developed by C.F. von Weizsäcker and E.J. Williams [251, 253], and an overview is given in [168]. The resulting relation is [112]:

$$\sigma_{\mu N} = \int \frac{n_\gamma(\nu) \sigma_{\gamma N}(\nu)}{\nu} d\nu \quad (3.46)$$

where  $n_\gamma(\nu)$  is the photon spectrum associated with the muon passage. In case of low  $E_\mu$ , the virtuality of the photons is no longer negligible and the equivalent photon approximation breaks down [249].

A classical relativistic electrodynamic model of the photon spectrum  $n_\gamma(\nu)$  is given by the original work of C.F. von Weizsäcker and E.J. Williams [251, 253], a quantum electrodynamic model by D. Kessler and P. Kessler [150, 151], and R.H. Dalitz and D.R. Yennie [96]; the latter consider also the pion production in the photon–nucleon interaction. The nuclear form factor to consider the finite size of the

---

<sup>11</sup>The naming is not unique and varies in the literature: photonuclear muon interaction [65, 73, 125, 193], muon spallation [112, 187], muon hadroproduction [113, p. 75], inelastic muon nucleon scattering [126, 193].

nucleus is included in the model of K. Daiyasu et al. [95]. The method of virtual photon exchange was extended by V.V. Borog and A.A. Petrukhin [74] and L.B. Bezrukov et al. [62, 63] within the framework of Vector Meson Dominance and Generalized Vector Meson Dominance [226], respectively: Here, the photon interacts with the nuclei through transformation in vector mesons [62].

At  $E_\gamma \geq 10 \text{ GeV}$  the photo–nucleon interaction is not completely incoherent anymore [62], and leads to destructive interferences. This nucleon shadowing, or screening, leads to an effective atomic weight of the target  $A_{\text{eff}} < A$  [62, 74, 78]. In the work of V.V. Borog and A.A. petrukhin [74] this is included by a  $q, \nu$  independent parametrization [78], whereas L.B. Bezrukov et al. [62, 63] include the  $q, \nu$  dependence of the screening.

At present, the photon spectrum  $n_\gamma(\nu)$  is commonly parametrized as follows [112]: For collective photon-nuclear interaction at low energy the model of R.H. Dalitz and D.R. Yennie [96] is used, and for interaction above the pion production threshold the model of L.B. Bezrukov et al. [62, 63]. These models are sensitive to their kinematic boundaries, as the integral over  $dq^2$  diverges for large  $q^2$  [126].

As expressed with the equivalent photon approximation, the cross section for muon spallation is mostly affected by the real photonuclear cross sections that will be discussed in Sect. 3.4.6. As a consequence it has a threshold in the 5–10 MeV range, a peak around 30–70 MeV, and remains constant above 1 GeV [187]. Above the threshold of 300 MeV pion photoproduction starts, which leads for  $\nu \geq 10 \text{ GeV}$  to the development of hadronic showers, see Sect. 3.4.5. The neutron multiplicity is nearly constant above 1 GeV, therefore the total contribution of neutron production via muon spallation approaches a stable value, but the relative contribution decreases as the secondary neutron production in showers increases [187], see Fig. 3.5a.

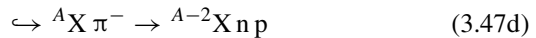
### 3.4.4 Neutron Production in Electromagnetic Showers

Neutrons are produced in electromagnetic showers via real electrons and real photons, unlike virtual photon exchange in muon spallation, see Sect. 3.4.3. At sites deeper than 2000 mwe, like the LSM, the main source for  $\gamma$  and  $e^\pm$  are pair production and bremsstrahlung, respectively [187].

Sources for electromagnetic showers at underground sites are the decay of uncharged mesons, knock-on electrons, pair production, and burst of bremsstrahlung (see [6] and references therein), their interactions follow the description in Sect. 3.2. Therefore, the electromagnetic showers at high energies are dominated by bursts from bremsstrahlung. The production cross section for bremsstrahlung by muons is well known, but the probability distribution governing the production of the cascades of secondary particles is less well known [6, pp. 340ff.], [113, pp. 80f.].

The neutron production occurs mostly via inelastic charge exchange and photoproduction, e.g.  $^{12}\text{C}(\gamma, n)$  in organic scintillators [247]. The photoproduction is similar to the virtual photon exchange of the muon spallation (Sect. 3.4.3) and, as will be discussed in Sect. 3.4.6, is heavily affected by the giant dipole resonance [187].

The inelastic charge exchange reactions



have a threshold of 140 MeV and therefore a small contribution, but can harden the neutron spectrum because of the high neutron energy of  $\approx 60$  MeV gained via pion capture Eq. 3.47d [187]. The total cross section for electromagnetic neutron production is proportional to  $\langle Z^2 \rangle$ , therefore this contribution is more important in high  $Z$ -material like lead [112].

The neutron multiplicity in electromagnetic showers can be related to the shower energy  $E_s$ , and the effective muon energy  $E_\mu$  via [106, 187]

$$M_n \propto E_s^{0.9} \quad (3.48a)$$

$$\propto E_\mu. \quad (3.48b)$$

The index is different from the case of hadronic showers (Eq. 3.49), thus it is possible to distinguish both shower types via the neutron multiplicity [187].

### 3.4.5 Neutron Production in Hadronic Showers

The main source for hadronic showers are pions from muon-induced photonuclear interactions—either via real photon exchange, see Sect. 3.4.4, or virtual photon exchange, see Sect. 3.4.3 [187]. Depending on the energy ranges, the particles in showers can be divided in three types, according to [106, 152, 187]: shower hadrons, cascade nucleons, and evaporating neutrons. The sum of all neutrons make the neutron hadroproduction.

Shower hadrons are mainly charged pions. Above  $\beta = 0.7$  they maintain the shower by generating new particles [106, 152, 187]. Below this threshold they start intranuclear cascades of recoiled nucleons with an energy around 150 meV via pion capture, pion-nuclei scattering [106, 152, 187]. The recoiled nucleon can start further intranuclear cascades at lower energies via nucleon-nuclei collision until their energy drops below the threshold of  $\beta \approx 0.2$  [106, 152, 187]. Below this threshold, equivalent to  $\approx 8$  MeV, the neutrons are referred as evaporated neutrons, which finally decay or get captured [106, 152, 187]. The neutron capture will be discussed in detail in Sect. 4.1.1. The angular correlation of the particles with the incident muon decreases with energy: Whereas shower hadrons are strongly correlated, evaporated neutrons are emitted isotropically [106, 152, 187], see also Sect. 3.5.2.

For interactions above 20 GeV, the neutron production per interaction is nearly constant with a value of 1–2 for nuclei found in rock [187]. The total neutron multiplicity of a hadronic shower can be related to the shower energy  $E_s$  and the effective muon energy  $E_\mu$  via [106, 187, 262]

$$M_n \propto E_s^{0.7} \quad (3.49)$$

$$\propto E_\mu^{0.8}. \quad (3.50)$$

It is therefore possible to estimate the muon energy from the neutron multiplicity [187].

The minimal target thickness needed for a shower to reach equilibrium with the incident muon flux, as investigated via MC simulations is  $800 \text{ g cm}^{-2}$  [134, pp. 57,83], whereas at  $500 \text{ g cm}^{-2}$  thickness the neutron fluence is still rising [163].

### 3.4.6 Photonuclear Cross Section

The cross section for the photonuclear reaction is not only important for the neutron production in electromagnetic showers (see Sect. 3.4.4), but also for the neutron production via muon spallation because of the equivalent photon approximation, see Sect. 3.4.3.

The cross section  $\sigma_{\gamma N}$  for real photons has contributions from various processes (ordered with increasing energy): Giant dipole resonance (GDR) absorption, quasi-deuteron photoabsorption [174], pion resonance [102], and deep-inelastic scattering via photon-parton interactions [62, 63]. The low energetic part, GDR, and quasi-deuteron photoabsorption, contribute 10–30 % to the total neutron rate, therefore they are not negligible.

The GDR describes the collective nuclear oscillation of neutrons against protons. It dominates below 30 MeV, and deexcites mostly through neutron emission. For empirical data the cross section is parametrized by a Lorentzian [112]

$$\sigma_{\gamma N}(E_\gamma) = \sum_i A_i \frac{(E_\gamma \Gamma_i)^2}{(E_\gamma - E_i)^2 + (E_\gamma \Gamma_i)^2} \quad (3.51)$$

with the empirical peak cross section  $A_i$ , peak energy  $E_i$ , and peak width  $\Gamma_i$ . Evaluated parameter sets are provided by the NDS of the IAEA [138, 139]. In lead the threshold for the GDR ranges from 6.47 MeV for  $^{207}\text{Pb}$  to 8.09 MeV for  $^{206}\text{Pb}$ . The most abundant (52.4 %, [218]) lead isotope  $^{208}\text{Pb}$  has a threshold of 7.37 MeV [138].

In the range of  $40 \text{ MeV} \leq E_\gamma \leq 140 \text{ MeV}$ , the quasideuteron model [174] relates the cross section for the nuclear photoeffect  $\sigma_{\gamma N}$  to the photoabsorption cross section of a free deuteron (deuteron photoeffect)  $\sigma_d$  via [112]:

$$\sigma_{\gamma N} = \frac{L}{A} N Z \sigma_d(E_\gamma) f(E_\gamma) \quad (3.52)$$

with the Levinger parameter  $L$  and the Pauli suppression function  $f(E_\gamma)$ . The model agrees well with the data [82].

Above 140 MeV, pion production dominates the cross section [64]. A  $\Delta$  isobar resonance can be produced in the nucleus by photon absorption above the pion production threshold around 300 MeV, which decays to pions and nucleons via  $\Delta \rightarrow \pi N$ ,  $\Delta \rightarrow \pi\pi N$ . Besides the directly produced neutrons, also the stopped pions  $\pi^\pm$  contribute via the pseudo-deuteron capture  $\pi^- + d \rightarrow n + n$ . The contribution of photo-produced pions to the pseudo-deuteron capture is calculated by J. Delorme et al. [102] with and without the equivalent photon approximation, using the cross section functional-forms of G. Chanfray et al. [83].

Above the  $\Delta$  resonance general photon-parton interaction occurs, including Roper resonances [217] in the range  $500 \text{ MeV} \leq E_\gamma \leq 1.2 \text{ GeV}$  [112, 119]. Above 1.2 GeV the cross section is described within the framework of the Regge calculus by Pomeron exchange [92, 119]. This leads to a logarithmic rising of the cross section with energy [134, p. 51].

As it is the case for muon spallation (Sect. 3.4.3), also the photonuclear cross section for real photons in this energy range is described within the generalized vector dominance model by the model of L.B. Bezrukov et al. [62, 63]. More recently, the resulting cross section was parametrized within the formalism of Regge calculus [103] by E.V. Bugaev et al. [79], resulting in [112]:

$$\sigma_{\gamma N} = 67.7 s^{0.0808} + 129 s^{-0.4525} \quad (3.53a)$$

$$s = 2m_n E_\gamma \quad (3.53b)$$

Its integral cross section agrees within statistical uncertainty with experimental data from the MACRO [46, 225] and ATLAS [21] experiments [125, 193].

### 3.5 Measurements of Muon-Induced Neutrons

The local muon-induced neutron production is the effective outcome of all interactions described in Sect. 3.4. Measurements at underground sites are always convolved with the local muon energy spectrum. Therefore they are not directly comparable to accelerator based measurements typically using well defined muon fluxes or even mono-energetic muon beams. Measurements at underground sites are given for averaged muon energies, which in fact highlights the importance of a correct model of the local muon flux (see Sect. 3.3) together with a detailed simulation of the neutron production processes (see Sect. 3.6). In addition, the specific set-up with its materials introduces another important source for systematic differences of measured neutron yields.

In this section we summarize existing measurements of muon-induced neutrons in Sect. 3.5.1, and compare their properties with predictions from recent simulations with the most often used MC packages FLUKA and Geant4 in Sects. 3.5.2–3.5.4. The last Sect. 3.5.5 lists planned and on-going measurements of the neutron production, most of them motivated by the shortcoming of the published MC simulations.

### 3.5.1 Overview of Existing Measurements

The neutron production yield  $Y$  is not only measured by dedicated underground experiments like the work of G.V. Gorshkov and V.A. Zyabkin [120], but also obtained as a byproduct from neutrino experiments based on large liquid scintillator volumes like KamLAND [1], from veto measurements of rare events searches like ZEPLIN-II [35], and from accelerator based experiments like [86]. An overview of measurements relevant for shallow and deep underground sites, i.e. with muon energies  $\gtrsim 5$  GeV, are listed in Table 3.1. References for measurements at lower energies are given in [126].

The most diverse, dedicated measurements at underground sites [120–123] of neutron production in different targets (aluminium, iron, cadmium, lead) and at different slant depths (12–800 mwe) were made by Gorshkov et al. at the *Artemovsk Scientific Station* in Russia, or in its vicinity.

There are eight measurements of the neutron production in organic liquid scintillator [1, 13, 51, 63, 72, 106, 131, 230]: First by L.B. Bezrukov et al. [63] near Artemovsk, Russia, in a gypsum mine at 25 mwe depth and in a salt mine at 316 mwe. The second was done by R.I. Enikeev et al. [106, 187, 222] probably at a deeper level (570 mwe) of the same salt mine, now identified as *Artemovsk Scientific Station*, and the detector identified as *Artemovsk Scintillation Detector* (ASD) [10, 187]. The *Cosmic-ray Underground Background Experiment* (CUBE) measured the neutron production at the shallow *Stanford Underground Facility* [131] (20 mwe).

Deep measurements  $> 1000$  mwe started with the *Large Scintillator Detector* (LSD) at the *Mont Blanc Laboratory* [13], which is up to now also the deepest measurement (5200 mwe). Also at great depth (3650 mwe) were the measurements by the *Large Volume Detector* (LVD) at the *Laboratori Nazionali del Gran Sasso* (LNGS) [165] (LVD1999). Their analysis was several times updated [9–12, 205, 230, 231] to deduce also the neutron production in the iron support structure of the detector. We refer in this work to the latest update given on behalf of the LVD collaboration [230] (LVD2011).

The results of L.B. Bezrukov et al. [63], ASD [106, 187], LSD [13], and LVD [230] are recently re-evaluated by N.Y. Agafonova and A.S. Mal'gin [10]: For the LVD and LSD the neutron yield in the iron support structure is deduced. The author points also out, that the two measurements of L.B. Bezrukov et al. and ASD may contain significant contribution from muon shower, as they were installed near the rock ceiling of the underground laboratory, and correct them by the general MC simulation in [263]. However, we take in this work the values from the original

publications [13, 63, 187, 230], as these re-evaluations were based partly on general, not detector specific MC simulations.

As a byproduct, the neutron production was measured by the *Kamioka Liquid Scintillator Anti-Neutrino Detector* (KamLAND) at 2700 mwe [1], by the solar neutrino experiment Borexino at LNGS [51] at 3800 mwe, and again at a shallow site (32 mwe) by the reactor neutrino experiment *Palo Verde* [72]. Albeit the three neutrino experiments Double Chooz [2, 3] at 150 and 300 mwe depth, DayaBay [25] at 250, 265 and 860 mwe depth, and RENO [18] at 120 and 450 mwe depth have successfully identified muon-induced neutrons in their liquid scintillators, no muon induced neutron production yield is published up to now.

For neutron production in lead there exist the four measurements by Gorshkov et al.: [120] (10 cm target thickness), [121] (16 cm), [123] (10 cm), and [122] (15 cm). Besides these, six additional measurements [35, 52, 53, 94, 214, 232] are reported in literature: M.F. Crouch and R.D. Sard [31, 94] measured the neutron production in a 7.6 cm thick lead target at 20 mwe depth. At the same site the neutron production in iron was studied by M. Annis, H.C. Wilkins, and J.D. Miller [31].

At the *Holborn underground laboratory* ( $\approx$ 60 mwe<sup>12</sup>), A.M. Short [232] measured a neutron yield with low statistical significance and a neutron spectrum using emulsion stack. The neutron spectrum is confirmed by later measurement with a liquid scintillator detector [43, 44], but not quantified in terms of a neutron yield. So the status of these measurements is doubtful. Nevertheless, for the sake of completeness we list the measurement in Table 3.1.

Bergamasco et al. used a 10 cm thick target at two shallow depths (60, 110 mwe) of the *Capuccini Station* [52] near Turin [45], and later a 35 cm thick target at great depth of 4300 mwe at *Mont Blanc Station* [53].

The veto system of the ZEPLIN-II dark matter search at *Boulby Underground Laboratory* was used to measure the neutron production in the lead shield of the experiment [35, 177, 214] at 2850 mwe. Subsequently, the veto system [19] of ZEPLIN-III was used as lead target [213, 214]. The neutron yield from both measurements, ZEPLIN-II and ZEPLIN-III, is scaled via MC simulation to an ideal lead target of  $3200 \text{ g cm}^{-2}$  thickness [214], i.e. 282 cm length, see also Sect. 5.5.2 for a discussion of idealized targets compared with real experiments.

Some additional data of muon-induced neutron yield at shallow sites  $< 60$  mwe may be extractable from measurements of muon-induced neutron *rates* in [91, 233]. However, it is unlikely that they would contribute much to the understanding of the neutron production at current deep underground sites  $> 1000$  mwe, therefore we do not include them.

As these experiments are located at various underground sites with different depths (see Table 3.1), the neutron production yield was therefore measured at different average muon energies. As the neutron production mechanisms depend on the muon energy (see Sect. 3.4) it is therefore necessary to know the average muon energy to

---

<sup>12</sup>In [44] a depth of  $60 \text{ hg m}^{-2}$  is given. This seems to be a mistake in writing, comparing to [43] giving  $60 \text{ hg cm}^{-2} = 60 \text{ mwe}$  and to [232] giving 58 mwe.

**Table 3.1** Measurements of the averaged muon-induced neutron production yield  $\langle Y \rangle$  in different targets and at different averaged muon energies  $\langle E_\mu \rangle$ 

Target	Experiment	Depth (mwe)	$\langle E_\mu \rangle$ (GeV)	$\langle Y \rangle$ ( $\text{cm}^2 \text{ g}^{-1}$ )
Organic liquid scintillator				
	CUBE [131] <sup>a,b</sup>	20	13	$2.0 \times 10^{-5}$
	CUBE [131] <sup>a,c</sup>	20	13	$4.3(3) \times 10^{-5}$
	Bezrukov1973 [63]	25	16.7	$4.7(5) \times 10^{-5}$
	Palo Verde [72] <sup>a,d</sup>	32	16.5	$3.6(3) \times 10^{-5}$
	Bezrukov1973 [63]	316	86	$1.21(12) \times 10^{-4}$
	ASD [10, 106, 187]	570	125	$2.04(24) \times 10^{-4}$
	KamLAND [1]	2700	260(8)	$2.8(3) \times 10^{-4}$
	LVD1999 [165]	3650	270	$1.5(4) \times 10^{-4}$
	LVD,Mei [193]	3650	270	$4.5 \times 10^{-4}$
	LVD2011 [230]	3650	270	$3.0(2) \times 10^{-4}$
	Borexino [51]	3800	280	$3.10(11) \times 10^{-4}$
	LSD [13]	5200	385	$5.30_{-1.02}^{+0.95} \times 10^{-4}$
Aluminium, $\langle A \rangle = 26.98$				
	Gorshkov1971a [123] <sup>e</sup>	40	11	$1.0(8) \times 10^{-4}$
	Gorshkov1971a [123] <sup>e</sup>	80	17.8	$3.6(72) \times 10^{-5}$
	Gorshkov1968 [120] <sup>e,f</sup>	150	30	$2.6(17) \times 10^{-4}$
Iron, $\langle A \rangle = 55.84$				
	Gorshkov1974 [122] <sup>e</sup>	12	6.1	$5.4(42) \times 10^{-5}$
	Annis1954 [31] <sup>e</sup>	20	10	$9.8(13) \times 10^{-5}$
	Gorshkov1971a [123] <sup>e</sup>	40	11	$1.3(3) \times 10^{-4}$
	Gorshkov1971a [123] <sup>e</sup>	80	17.8	$1.7(3) \times 10^{-4}$
	Gorshkov1968 [120] <sup>e,f</sup>	150	30	$3.3(10) \times 10^{-4}$
	LVD2011 [230]	3650	270	$1.6(1) \times 10^{-3}$
Cadmium, $\langle A \rangle = 112.4$				
	Gorshkov1974 [122] <sup>e</sup>	12	6.1	$1.1(6) \times 10^{-4}$
	Gorshkov1971a [123] <sup>e</sup>	40	11	$2.2(4) \times 10^{-4}$
	Gorshkov1971a [123] <sup>e</sup>	80	17.8	$3.3(4) \times 10^{-4}$
	Gorshkov1968 [120] <sup>e,f</sup>	150	30	$1.0(4) \times 10^{-3}$

(continued)

**Table 3.1** (continued)

Target	Experiment	Depth (mwe)	$\langle E_\mu \rangle$ (GeV)	$\langle Y \rangle$ ( $\text{cm}^2 \text{ g}^{-1}$ )
Lead, $\langle A \rangle = 207.2$				
	Gorshkov1974 [122] <sup>e</sup>	12	6.1	$2.3(4) \times 10^{-4}$
	Crouch1952 [31, 94] <sup>e</sup>	20	10	$2.41(12) \times 10^{-4}$
	Gorshkov1971a [123] <sup>e</sup>	40	11	$4.0(4) \times 10^{-4}$
	Holborn [232] <sup>e</sup>	58	21	$0.6_{-0.3}^{+0.6} \times 10^{-4}$
	Bergamasco1970 [52] <sup>g,e,h</sup>	60(15)	9(2)	$4.8(5) \times 10^{-4}$
	Gorshkov1971a [123] <sup>e</sup>	80	17.8	$5.7(4) \times 10^{-4}$
	Bergamasco1970 [52] <sup>g,e,h</sup>	110(28)	16(4)	$6.7(9) \times 10^{-4}$
	Gorshkov1968 [120] <sup>e,f</sup>	150	30	$1.14(12) \times 10^{-3}$
	Gorshkov1971 [121] <sup>e</sup>	800	110	$1.7(3) \times 10^{-3}$
	ZEPLIN-II2008 [35] <sup>i</sup>	2850(20)	260	$1.31(6) \times 10^{-3}$
	ZEPLIN-II2013 [214] <sup>i</sup>	2850(20)	260	$3.4(1) \times 10^{-3}$
	ZEPLIN-III [214] <sup>i</sup>	2850(20)	260	$5.8(2) \times 10^{-3}$
	Bergamasco1973 [53] <sup>e,h</sup>	4300	304(7)	$1.2(4) \times 10^{-2}$

If not stated otherwise the sum over all neutron multiplicities is given, including showering muons (e.g. see [63]). For the elemental targets (aluminium, iron, cadmium, lead) the atomic weight  $\langle A \rangle$  as recommended by the IUPAC [252] is given to four significant decimal places. For details see text<sup>a</sup>

<sup>a</sup>As the average muon energy is not given in the original publication, the value estimated in [193] is listed

<sup>b</sup>Single neutron yield from non-showering muons

<sup>c</sup>Single neutron yield from showering muons

<sup>d</sup>Neutron yield published as  $(3.60 \pm 0.09 \pm 0.31) \times 10^{-5} \text{ cm}^2 \text{ g}^{-1}$  [72], listed is the result with quadratically added statistical and systematic errors

<sup>e</sup>Calculated with Eq. 3.63b,  $N_A$  according to [197]

<sup>f</sup> Averaged muon energy original published as 40 GeV [120], updated to 30 GeV in [122]

<sup>g</sup>Measurement done with inclined muons, the slant depth is given

<sup>h</sup> As no precise muon energy are given in [52, 53], the average muon energy is obtain via Eq. 3.35, see page 106 for details

<sup>i</sup>Scaled per MC to a mono-energetic  $\mu^-$  beam incident on an ideal lead target of 3200 cm thickness [214]

compare the measurements. But for three of the above listed measurement no muon energy is given:

For the measurements with ASD only the depth of 750 mwe is given by R.I. Enikeev et al. in the original publication [106]. Based on this, the corresponding average muon energy is calculated by D. Mei and A. Hime [193] to 120 MeV. Later, A. Mal'gin and O. Ryazhskaya [187] who are coauthors of [106], publish a similar average muon energy of 125 MeV, but a different depth of 570 mwe[!] for this experiment, which is in agreement with the other publications concerning the ASD, e.g. [105, 153]. For the neutron yield, we take the latest update by A. Mal'gin and O. Ryazhskaya [10, 187].

Also for the measurement with CUBE no muon energy is given, we list therefore the calculated value by D. Mei and A. Hime [193]: 13 GeV.

L.B. Bezrukov et al. [52, 53] give no precise muon energy, but energy intervals [53]: 10–20 GeV for 60(15), 110(28) mwe, and 250–300 GeV for 4300 mwe. The same depths are used in [54] with the additional information that they are given with respect to standard rock (see page 90), therefore we calculate the average muon energy via Eqs. 3.9b and 3.35 averaged over both sets of energy loss parameters for standard rock: Eq. 3.18 and Eqs. 3.10b and 3.19. This results in  $\langle E_\mu \rangle = 9(2), 16(4), 304(7)$  GeV for 60(15), 110(28), 4300 mwe respectively; the uncertainties for the shallow sites are dominated by the 25 % uncertainty of the slant depth. Within the uncertainties, all energies are in agreement with the energy intervals given in the original publications, for 4300 mwe it is also in agreement with 310 GeV given in [35] as average muon energy for this measurement.

Beside the underground measurements there are three accelerator based experiments relevant for muon-induced neutron production at underground site:

The CERN NA55 experiment [86] measured the neutron production by a muon beam of 190 GeV in graphite, copper, and lead targets of 75, 25, and 10 cm thickness, respectively. They claim correspondence to underground measurements at 2000 mwe depth, the correctness of this claim is doubted, see Sect. 3.5.4. No values for the integral neutron yield are given, because due to the non-trivial experimental geometry and efficiency, they can not unambiguously deduce the neutron yield from the stated differential cross sections.

The neutrino experiment KARMEN reported the spectrum of neutrons induced by atmospheric muons in their 7000 t iron shield, equivalent to a depth of 3000 mwe [254].

The neutron emission during deexcitation of several targets, including lead, after deep inelastic scattering with 470 GeV muons was measured with the E665 detector at Fermi National Accelerator Laboratory [7, 8].

### 3.5.2 *Angular and Lateral Correlation of Neutrons with Muons*

The angular correlation of the muon-induced neutrons with the parent muon can be characterized by the angle  $\theta$  between the muon and the muon-induced neutron.

The  $\theta$  distribution consists of a forward peaked component from induced showers and cascades, and an isotropically component from neutron evaporation as discussed in Sect. 3.4.5, where the relative contribution of the first component rises with the muon energy [193, 249].

Up to now, only the CERN NA55 experiment [86] measured the muon induced neutron production with respect to the angle between muon beam and neutron. For thin graphite, copper, and lead targets the neutrons were measured at  $45^\circ$ ,  $90^\circ$ ,  $135^\circ$  with respect to the forward direction of the muon beam.

The CERN NA55 experiment is compared to Geant4 8.0 simulations in [188]: For graphite, an agreement in the shape of the angular spectrum is stated, but for the heavier targets the spectrum's shape disagrees. A bugfix for the angular distribution of nucleons in the LEP model of Geant4 9.0 may affect this finding, see Appendix A.3.3. For all targets the absolute values are lower in the simulation as in the measurement, as it will be discussed in Sect. 3.5.4

This theoretical behaviour is quantitatively reproduced, but not compared to measurements, with Geant4 8.2p01 [134], and FLUKA1999 [193, 249]. Based on the latter, the following parametrization is suggested for the angular distribution dependent on the muon energy [193, 249]:

$$\frac{dN}{d \cos \theta} = \frac{A}{(1 - \cos \theta)^{B(E_\mu, a_0, a_1)} + B(E_\mu, a_2, a_3)} \quad (3.54)$$

$$B(E_\mu, a, b) = a E_\mu^b \quad (3.55)$$

with  $a_0 = 0.482$ ,  $a_1 = 0.045$ ,  $a_2 = 0.832$ ,  $a_3 = -0.152$ .

From the development of the hadronic shower, one expects an increase of muon induced neutrons with rising lateral distance to the muon trajectory, before the neutron flux gets attenuated. Measurements of the lateral neutron distribution in liquid scintillator exist from the LVD and Borexino experiments. The attenuation of neutron production over lateral distance to the muon track in the LVD can be described by an exponential attenuation length of 63.4 cm [165], the relative shape is reproduced with FLUKA1999 [162]. Contrary, Borexino used a double exponential with a long (147 cm) and a short (61.2 cm) decay component, the latter in agreement with the LVD result [50, 51].

The lateral distribution is more generally investigated with FLUKA in [193] for different materials: For standard rock, the relative neutron flux starts to drop after 50 cm as neutrons become attenuated, and typically after 3.5 m the flux is attenuated by two orders of magnitude. For Geant4, the lateral distribution is investigated in the context of the shower development in  $C_nH_{2n}$  in [134]: as [134, Fig. 3.10] indicates a drop of the flux of two orders of magnitude is expected at  $150 \text{ g cm}^{-2}$ . None of these two publications compares the simulation to measurements. The attenuation is also relevant for the influence of the target on the neutron yield, discussed in Sect. 5.5.2.

### 3.5.3 Energy and Multiplicity Spectrum

Only few directly measured energy spectra of muon-induced neutrons  $dN/dE_n$  exist from underground experiments and accelerator experiments: At low depths (60 mwe) the spectrum in the range of 7.5–60 MeV was measured at the Holborn underground laboratory [44], at intermediate depths (550 mwe) with the ASD in the range of 18–92 MeV [153, 186]. At 3650 mwe the LVD measured the energy deposit (10–300 MeV) caused by neutrons [165, 194], i.e. it is not the neutron spectrum, but a useful measure for it as emphasized by [187, 193]. This will be further discussed in Sect. 3.5.4. Additionally, the KARMEN neutrino experiment recorded the spectrum of neutrons in the range of 10–80 MeV produced by muons in their iron shield equivalent to 3000 mwe [254]. All these experiments measured the neutron spectrum distantly from the neutron production in the target (e.g. surrounding rock), and it is therefore different from the source spectrum [153, 187]. A measurement more close to the source was done with the CERN NA55 accelerator experiment using various thin targets, including lead, and a 190 GeV muon beam, it is also the experiment with the biggest energy range for the neutrons: 1–1000 MeV [86]. Also the E665 experiment [7, 8] was accelerator based, and measured the low energetic neutron spectrum (0–10 MeV) after deep inelastic muon scattering.

All of these measurements agree qualitative as they show the features expected after the discussion in Sects. 3.4.1, 3.4.3 and 3.4.5: A dominant softer part due to evaporating neutrons from muon capture, or deexcitation after muon spallation, and a harder part due to knock-on neutrons.

Generally, the shape and the slope of the neutron energy spectrum are nearly independent of the muon energy and rise only slowly with the muon energy [112]. Especially the harder part of the spectrum is stable as FLUKA2003 simulations show, whereas the softer part below 1 MeV is also affected by the muon energy. Below 20 MeV, it rises with the average atomic weight of the target [163]. As a consequence, the average neutron energy drops: From 65.3 MeV for hydrocarbon ( $E_\mu = 280$  GeV) to 8.8 MeV for lead ( $E_\mu = 260$  GeV) [177]. The results of the E665 experiment [7, 8] suggest that this drop can be explained as follows: In nuclei with higher mass, like lead, the direct knock-on nucleon would start additional intranuclear cascades during its propagation in the nucleus, and therefore leaving the residual nucleus in a higher state of excitation, leading to more evaporated low energetic neutrons.

However, in a quantitative sense, the directly measured energy spectra are not mutually consistent, and several parametrizations are given in the literature [112, p. 388]:

- The most simple model is a power law

$$\frac{dN}{dE_n} \propto E_n^\beta \quad (3.56)$$

with several values for the hardness  $\beta$  of the spectrum given in literature: Based on theoretical considerations, [44] suggests  $\beta = -1/2$  for 10–50 MeV neutrons, and

flatter above. The experimentally measured spectra of ASD [153, 186] and at Holborn underground laboratory [44] are described by  $\beta = -0.5(1)$  [187]. According to unpublished work of D.H. Perkins (as cited in [112]) the general spectrum is described by  $\beta = -1.6$ . Based on photo-nucleon reaction at accelerators, [153, Fig.4] suggest  $\beta = -1.86$  [112]. Also the neutron energy spectrum measured by LVD [165, 194] follows a power law with  $\beta = (-1.19 \pm 0.02)$  [194].

- More sophisticated models use two components for the softer and harder part of the spectrum: Based on FLUKA simulations, the following values are proposed in [116]:

$$\beta = \begin{cases} -1/2, & 10 \text{ MeV} \lesssim E_n \lesssim 100 \text{ MeV} \\ -2, & 100 \text{ MeV} \lesssim E_n \lesssim 1 \text{ GeV} \end{cases}, \quad (3.57)$$

claiming agreement with the LVD data [162]. Also a two component model was used for the KARMEN data [254] in [112]:

$$\frac{dN}{dE_n} = N_{\text{soft}} e^{-E_n/2.1} + N_{\text{hard}} e^{-E_n/39} \quad (3.58)$$

The energy spectrum of the neutrons evaporated in the E665 experiment during the deexcitation can be also parametrized by a similar two component approach: Each of the component has the form [7, 8]

$$\frac{dM_n}{dE_n} = \frac{M_n}{\theta} E_n e^{-E_n/\theta} \quad (3.59)$$

where  $\theta$  is the nuclear temperature of the residual nucleus. For the lead target the spectrum consists of a preequilibrium part  $\theta_1 = 5(1)$  MeV, and an equilibrium part  $\theta_2 = 0.70(5)$  MeV, where the relative contribution of these two components change with the transferred energy. Simulations with Geant4 6.2 result in  $\theta_1 = 3.7$  MeV,  $\theta_2 = 0.93$  MeV, claimed to be not in conflict with the E665 results [34].

- For a combined description of KARMEN [254] and LVD [162] data, the following function is proposed in [162, 193, 249], based on FLUKA simulations:

$$\frac{dN}{dE_n} = A_\mu \left( \frac{e^{-a_0 E_n}}{E_n} + B_\mu(E_\mu) e^{-a_1 E_n} \right) + a_2 E_n^{-a_3} \quad (3.60a)$$

$$B_\mu(E_\mu) = a_4 - a_5 e^{-a_6 E_\mu} \quad (3.60b)$$

With the parameter  $a_0 = 7$ ,  $a_1 = 2$ ,  $a_2 = 0$ ,  $a_4 = 0.52$ ,  $a_5 = 0.58$ ,  $a_6 = 0.0099$ . It agrees reasonably with the data above 20 MeV, and confirms the physics model used in FLUKA [112]. The same functional form is used in [193] to parametrize the simulated neutron spectra for different underground sites, claiming also agreement with the measured spectrum of CERN NA55 [86].

The results from the CERN NA55 experiment agree in the spectral shape with Geant4 8.0 simulations for the  $45^\circ$ , and  $90^\circ$  positions, whereas for  $135^\circ$  the

simulations produce a significant harder spectrum [188]. Again, the bugfix for the angular distribution of nucleons in the LEP model of Geant4 9.0 may affect this finding, see Appendix A.3.3.

The scaled energy spectrum of the LVD1999 data alone is in agreement with FLUKA1999 [249] and Geant4 6.2 [34] simulations. As it is measured at  $\langle E_\mu \rangle = 270(18)$  GeV it is comparable to the spectrum at LSM expected from simulations with Geant4 8.2p01 [134, p. 63], see Fig. 3.5b.

The neutron multiplicity is the least known quantity [193], but it is a very useful quantity: It is a possibility to distinguish muon-induced neutrons from ambient neutrons [126]. Also the separation of neutrons produced in electromagnetic showers from neutrons produced in hadronic showers is possible, together with an estimation of the shower energy [63, 106, 187], see Sects. 3.4.4 and 3.4.5.

For muon-induced neutrons, the multiplicity was measured at underground by L.B. Bezrukov et al. [63], with the ASD [106], with CUBE [131], with Borexino [51], and with the ZEPLIN-III veto [214]. The E665 experiment [7, 8] measured the multiplicity of evaporated neutrons for deep inelastic scattered 490 GeV muons on thin targets: As the contribution of the soft and hard component of the spectrum Eq. 3.59 change with the transferred energy, also the multiplicity changes from 1.7 for an excitation of 17 MeV to about 6 for 57 MeV in lead [7]. Including shower development in thick targets (Eqs. 3.48a and 3.49), the multiplicity can increase up to  $\approx 100$  [106].

Based on FLUKA simulations, and depending on the target's atomic weight and the muon energy, a parametrization of the multiplicity  $M_n$  as

$$\frac{dN}{dM_n} = A \left( e^{-B(E_\mu)M_n} + C(E_\mu)e^{-D(E_\mu)M_n} \right) \quad (3.61a)$$

$$B(E_\mu) = a_0 E_\mu^{-a_1} \quad (3.61b)$$

$$C(E_\mu) = a_2 e^{-a_3 E_\mu} \quad (3.61c)$$

$$D(E_\mu) = a_4 e^{-a_5 E_\mu} \quad (3.61d)$$

is proposed by [193, 249], with free parameters  $a_0, a_1, a_2, a_3, a_4$ , and  $a_5$ . The averaged multiplicity  $M_{MC}$  obtained from FLUKA simulations [191] is smaller than the measured  $M_n$  in liquid scintillator [63]. Via the correction function

$$\frac{M_n - M_{MC}}{M_n} = 0.64 E_\mu^{0.02} - 0.74 E_\mu^{-0.12} \quad (3.62)$$

[193] could find agreement with the measured multiplicity at KamLAND [191], and also agreement with the measured neutron production yield (see Sect. 3.5.4). For Geant4 9.5p01 it seems that the average multiplicity in lead is *higher* than the one measured by the ZEPLIN-III veto, as the data exceed the simulation especially at low multiplicities [214]: 36% excess for single neutron events, but only up to 20% excess at higher multiplicities. This is in agreement with the comparison of

Geant4 9.6p01 and the measured multiplicity spectrum in the liquid scintillator of Borexino [51], as they find also an excess of single neutron events by 36 %.

For simulations with Geant4 one has to take special care of the correct neutron counting: In inelastic neutron scattering, the final state neutron is treated as different from the incoming neutron. This has to be considered, and corrected for, when compared with other MC packages that treat incoming neutron and final state neutron as identical [34, 134, 214].

In conclusion, we can state that there is no unique parametrization of the measured neutron energy spectra, especially at high energies. In case of the multiplicity spectrum, the simulations seem to systematically overproduce (FLUKA) or underproduce (Geant4) low multiplicities. Discussion of this work in the context of over- and underproduction in comparison with Geant4 will be given in Sect. 6.2.3.

### 3.5.4 Dependence of the Neutron Production Yield on Energy and Target

The neutron production yield  $Y$  is defined as the ratio of the produced neutrons  $N_n$  to incident muons  $N_\mu$  in case of a detected muon, corrected for the neutron detection efficiency  $\epsilon_n$ , and normalized to the thickness of the target along the muon trajectory  $X$  [1, 10, 51, 72, 131, 187].

$$Y = \frac{N_n}{N_\mu \epsilon_n X} \quad (3.63a)$$

$$= \frac{\langle \sigma M_n \rangle}{A} N_A \quad (3.63b)$$

In older works, e.g. [52, 53, 120–123], the expression Eq. 3.63b is often used: Here, the neutron yield is a function of the average product of cross section  $\sigma$  and neutron multiplicity  $M_n$ <sup>13</sup> normalized to the atomic weight of the target  $A$ . It is related to Eq. 3.63a via the expected amount of neutrons [10]

$$N_n = \frac{\langle \sigma M_n \rangle}{A} X N_A \quad (3.64)$$

The dependence of Eq. 3.63a on the muon energy and on the muon trajectory highlights the importance of detailed knowledge of the local muon flux (Sect. 3.3).

The production yield rises with energy (see Fig. 3.6a) of the incident muons, as the production cross sections (Sects. 3.4.3 and 3.4.6), the neutron multiplicities in showers (Sects. 3.4.4 and 3.4.5), and the excitation of the residual nucleus (Sect. 3.5.3) rise with the transferred energy [134]. The general parametrization of

---

<sup>13</sup>The neutron multiplicity is often denoted as  $\nu$  in the original publications.

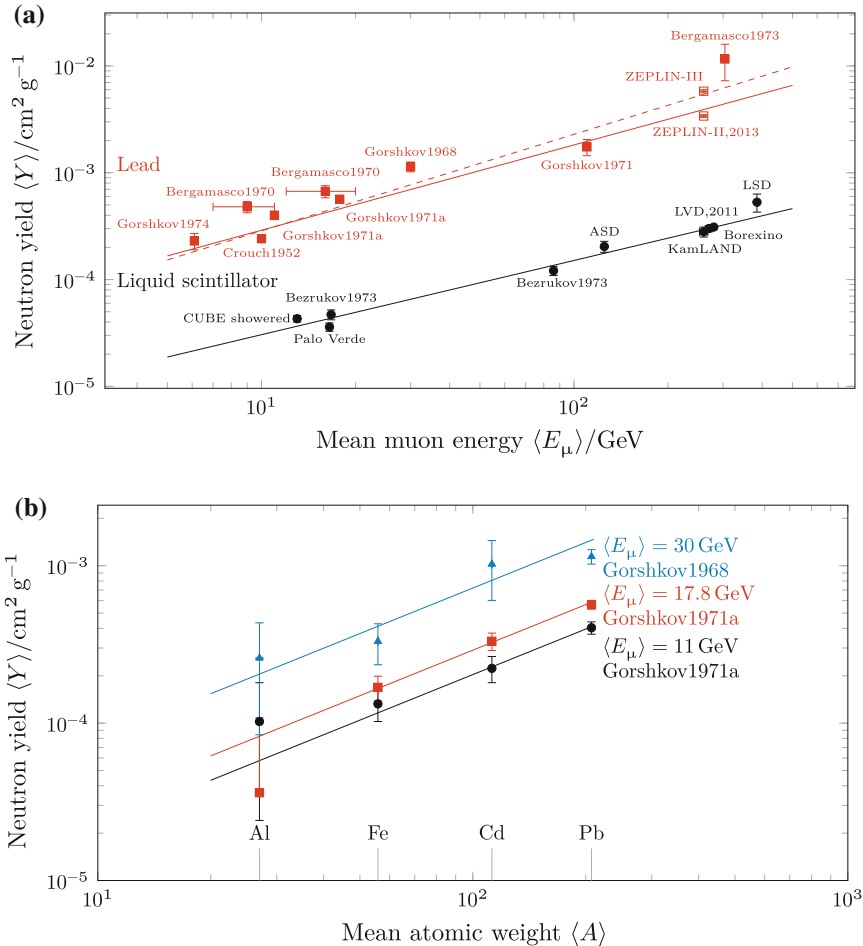


**Fig. 3.6** Dependencies of the average muon-induced neutron yield  $\langle Y \rangle$ : **a** As function of the average muon energy  $\langle E_\mu \rangle$  for liquid scintillator (black circles), and lead (red squares) in thin ( $<400 \text{ g cm}^{-2}$ , filled squares) and thick targets ( $3200 \text{ g cm}^{-2}$ , open squares). The black solid, red solid, red dashed lines are fits of  $\langle Y \rangle(\langle E_\mu \rangle) = c_1 \langle E_\mu \rangle^\alpha$  (Eq. 3.65) to the liquid scintillator data, the combined data of thin and thick lead targets, and only thin lead targets, respectively. **b**  $\langle Y \rangle$  as function of the average atomic weight of the target  $\langle A \rangle$ . The lines are fits of  $\langle Y \rangle(\langle A \rangle) = c_2 \langle A \rangle^\beta$  (Eq. 3.66) to the respective data sets. All fits are done for this work and the fitting parameters are listed in Tables 3.2 and 3.3. For details see text and for references see Table 3.1. Figures based on [112]

the energy dependence by a simple power law was introduced by G.T. Zatsepin and O.G. Razhskaya [262]:

$$Y|_A(\langle E_\mu \rangle) = c_1 \langle E_\mu \rangle^\alpha \quad (3.65)$$

Values for  $c_1$ ,  $\alpha$  from measurements and various MC simulations are listed in Table 3.2.

**Table 3.2** Parameters  $c_1$ ,  $\alpha$  of  $Y|_A$  (Eq. 3.65) for measurements and various MC simulations of the energy dependence of the neutron production yield

$c_1$ ( $10^{-6}$ cm $^2$ g $^{-1}$ )	$\alpha$	Reference	Remark
3.824	0.849	[193]	Fit to liquid scintillator, (LVD1999+Mei) [13, 63, 72, 106, 131, 193]
5.12(62)	0.73(3)	[112]	Fit to liquid scintillator, LVD1999 [13, 63, 72, 106, 131, 165]
6.2(9)	0.69(3)	This work	Fit to liquid scintillator, LVD2011 [1, 13, 51, 63, 72, 106, 131, 230]
–	0.77(3)	[112]	Fit to lead data [53, 120, 121, 123]
–	0.78(2)	[10]	Fit to liquid scintillator, iron, and lead [1, 13, 31, 52, 53, 63, 72, 106, 120, 121, 123, 131, 205] and references in [10]
46(13)	0.80(6)	This work	Fit to lead data, including ZEPLIN data [52, 53, 94, 120–123, 214]
36(14)	0.90(15)	This work	Fit to thin lead data, excluding ZEPLIN data [52, 53, 94, 120–123]
–	0.75	[221]	Based on shower evaluations
4.5	0.73	[193]	MC simulation with FLUKA in C <sub>10</sub> H <sub>20</sub> , version unspecified
4.14	0.74	[249]	MC simulation with FLUKA1999 in C <sub>10</sub> H <sub>22</sub>
3.2(1)	0.79(1)	[162] <sup>a</sup>	MC simulation with FLUKA1999 in C <sub>10</sub> H <sub>20</sub>
3.1	0.79	[34] <sup>b</sup>	MC simulation with FLUKA2003 in C <sub>n</sub> H <sub>2n</sub> of thickness 3200 g/cm <sup>2</sup>
7.5	0.62	[34] <sup>b</sup>	MC simulation with Geant4 6.2 in C <sub>n</sub> H <sub>2n</sub> of thickness 3200 g/cm <sup>2</sup>
4.2(1)	0.70(1)	[134, pp. 57, 59]	MC simulation with Geant4 8.2p01, in C <sub>n</sub> H <sub>2n</sub> of thickness 4000 g/cm <sup>2</sup>

<sup>a</sup>The version of the used MC package is not given in the original publication [162]. Secondary sources state FLUKA1999 [34] or FLUKA2000 [134]

<sup>b</sup>The parameters  $\alpha$ ,  $\beta$  are not given in the original publication [34]. However, they are given by H. Araújo (as cited in [134, pp. 57, 135]). The author of the original publication

The production yield rises with the average atomic weight of the target as discussed in the context of neutron energy spectrum in Sect. 3.5.3, and can be again parametrized by a power law [112, 193]:

$$Y|_{E_\mu}(A) = c_2 A^\beta, \quad (3.66)$$

**Table 3.3** Parameters  $c_2$ ,  $\beta$  of  $Y|_{E_\mu}$  (Eq. 3.66) for measurement and various MC simulations of the target dependence of the average neutron production yield

$c_2$ ( $10^{-5}$ cm $^2$ g $^{-1}$ )	$\beta$	Reference	Remark
–	0.90(23)	[112]	Fit to data [120, 121, 123]
–	0.95	[10]	Fit to data [31, 52, 53, 120, 121] and references in [10]
<sup>a</sup>	0.96(7)	This work	Fit to data [120, 121, 123]
5.33(17)	0.76(1)	[162] <sup>b</sup>	MC with FLUKA1999, $E_\mu = 280$ GeV
4.54	0.81	[193]	MC with FLUKA, version, and $E_\mu$ unspecified
3.0(4)	0.82(3)	[34]	Fit to MC with Geant4, version 6.2., $E_\mu = 280$ GeV
1.61	0.99(1)	[134]	Fit to MC with Geant4, version 8.2p01., $E_\mu = 280$ GeV

<sup>a</sup> $\alpha = 2.4(10) \times 10^{-6}$ ,  $3.5(13) \times 10^{-6}$ ,  $9(3) \times 10^{-6}$  for  $\langle E_\mu \rangle = 11, 17.8, 30$  GeV respectively

<sup>b</sup>The version of the used MC package is not given in the original publication [162]. Secondary sources state FLUKA1999 [34] or FLUKA2000 [134]

Values for  $c_2$ ,  $\beta$  from measurements and various MC simulations are listed in Table 3.3.

N.Y. Agafonova and A.S. Mal'gin [10] proposed a universal parametrization by merging Eqs. 3.65 and 3.66 to

$$Y(\langle E_\mu \rangle, A) = c_3 \langle E_\mu \rangle^\alpha A^\beta \quad (3.67)$$

This form emphasizes the strong dependence on both the target and the muon energy. It allows also a more physical interpretation of the coefficients [10]: Dimensional analysis and fitting to experimental values shows, that the coefficient  $c$  is close to the radiative muon energy loss via nuclear interaction  $b_{\text{nucl}}$  as defined in Eq. 3.11a. Hence, it relates the neutron yield to the muon-induced shower production as such. Via Eqs. 3.48a and 3.49, the indices  $\beta, \gamma$  are related to the contribution of electromagnetic and hadronic neutron production per shower.

Underground measurements providing energy and target dependent neutron yields are listed in Table 3.1, and the respective yields as function of the average muon energy and the average atomic weight are shown in Fig. 3.6a, b respectively. We will first discuss the results from underground measurements for hydrocarbon like organic liquid scintillator, secondly for lead, and then the general dependence of the neutron yield on the atomic weight, each time in comparison with MC simulations. Afterwards the results from the CERN NA55 accelerator experiment [86] will be reported, before possible explanations for the deviation of MC simulations from measurements are discussed. More technical details of the MC simulations will be discussed in Sect. 3.6.

The neutron production in hydrocarbon is important for experiments like KamLAND that use large volumes of liquid scintillator [1], or experiments like EDELWEISS using polyethylene as neutron shield [36]. From Table 3.1, the same *classic* measurements are selected as in [112, 193], i.e. [13, 63, 72, 106, 131], plus the KamLAND [1] and Borexino [51] results, and with the more recent LVD2011 result [230] instead of the LVD1999 result [165]. We do not correct the given values for the neutron contribution of the muon shower to deduce the neutron yield of the target alone: Despite [10], in our opinion a correction for the shower contribution is only possible with detailed, experiment specific MC simulations. As this is highly difficult especially for the older experiments, e.g. [63, 106], we use the results as stated in the original publications. If not stated otherwise, we assume that the original published values include the neutrons from the shower. Therefore, whether the neutron yield is evaluated with neutrons from showers, or without, like in [63, 131], the result including showers is taken.

The mean relative precision of the measurements [1, 13, 51, 63, 72, 106, 131, 230] is 9.8 %, ranging from 3.5 % [51] to 19 % [13]. A fit of  $Y|_A(\langle E_\mu \rangle)$  (Eq. 3.65) to the measurements (Fig. 3.6a, black line) gives

$$c_1 = 6.2(9) \times 10^{-6} \text{ cm}^2 \text{ g}^{-1} \quad (3.68a)$$

$$\alpha = 0.69(3); \quad (3.68b)$$

the value of  $\alpha$  is in the theoretically expected range (Sects. 3.4.4 and 3.4.5). Within the uncertainty it is also in agreement with the fit in [112] to a different data selection, see Table 3.2. The agreement between fit and data, specified as the RMS of the relative residuals [193], is 14 %, slightly better than the 15 % stated in [193], most probably caused by the updated data selection.

Historically, the neutron production in liquid scintillator measured by LVD1999 [165] was below the general trend. D. Mei and A. Hime [193] proposed a correction due to quenching effects (LVD+Mei), resulting in an increased neutron yield in agreement with the general trend. The physical correctness of this correction is disputed by V.A. Kudryavtsev (as cited in [130]) who did the original data analysis. Based on MC simulations (see references in [10]), the recent LVD2011 analysis [230] divides the measured yield into a fraction produced in the liquid scintillator and a fraction produced in the iron support structure. The resulting neutron production in liquid scintillator is now closer to the general trend, thereby removing the previous tension.

With the LVD tension solved, the experimental findings can be compared to the prediction of MC simulations: In Table 3.2 results from Geant4 and FLUKA simulations [34, 134, 162, 193, 249] are listed, constrained to publications that provide at least values for  $\alpha$ . Publications that provide only plots, like [177, 263], are excluded as it is out of scope of this work to reevaluate these plots. Averaging over the listed results [34, 134, 162, 193, 249] gives  $c_1 = 4.4(15) \times 10^{-6} \text{ cm}^2 \text{ g}^{-1}$ ,  $\alpha = 0.73(6)$ , as uncertainty the RMS of the relative residuals is adopted. Therefore, the results of MC vary between different codes and version by 33, 8.0 % for  $c_1$ ,

$\alpha$  respectively. Whereas the spectral index  $\alpha$  is in rather good agreement with the measurement, the absolute scale  $c_1$  is in general underestimated by 28 %. The only exception from this general trend is Geant4 6.2 [34] that overestimated the absolute scale, but produced no agreement in the spectral index.

To specify the deviation between MC and measurements, we evaluate the hydrocarbon data also at  $E_\mu = 280$  MeV, the same energy later used for the lead data. For hydrocarbon, all MC results underestimate the experimental fit at this energy by in average 15 %, ranging from 9.1 % [193] to 28 % [134]. The general underestimation is also recognized in literature [35, 112, 193], ranging from 20 % [112], over 35 % [193] to an often quoted factor two as upper bound, e.g. [34, 35, 130, 134, 163, 177, 187]. However, the qualitative behaviour is well reproduced with MC according to [34, 112]. In Geant4, the neutron production is in general lower than in FLUKA [35], but in detail it depends on the used version and the energy range:

- Geant4 6.2 produces 30 % less neutrons than FLUKA1999,2003 at  $E_\mu > 100$  GeV, but at lower energies it produces more neutrons than FLUKA2003, FLUKA1999 [34].
- FLUKA2003 produces at all energies more neutrons than FLUKA1999. At  $E_\mu = 280$  GeV FLUKA2003 and Geant4 6.2 agree with FLUKA1999 within a factor two, with a higher yield in FLUKA simulations [34].
- FLUKA2008 produces similar neutron yields as FLUKA1999, but less neutrons at low energies than FLUKA2003 [177].
- Geant4 8.2 produces less neutrons than Geant4 6.2, and agrees with FLUKA2008 at low energies and with Geant4 6.2 at high energies [177].
- A. Villano et al. [247] reports good agreement between the newer Geant4 version 9.5 and FLUKA 2011.2p17 for neutron production in liquid scintillator, but still disagreement for the production in lead. This is confirmed by the Borexino collaboration [51] also for Geant4 9.6p01 in liquid scintillator, however they find that Geant4 underproduces  $^{11}\text{C}$ . As  $^{11}\text{C}$  is mostly produced in  $^{12}\text{C}$  (N, Nn)  $^{11}\text{C}$  [118], this would point to an overproduction in some other neutron production channel [51].

Possible explanations for the underestimation and the differences between FLUKA and Geant4 will be discussed later, together with the discussion of the lead data.

The neutron production in lead is important for experiments using a lead shield against gamma background like EDELWEISS-II [36] and ZEPLIN-II/III [19, 35]. For this evaluation the measurements [52, 53, 94, 120–123, 214], listed in Table 3.1, are taken. The mean relative precision is 12 %, ranging from 2.9 % for ZEPLIN-II2013 [214] to 37 % for Bergamasco1973 [53]. We performed a fit of Eq. 3.65 to all the selected measurements (Fig. 3.6a, red line) which gives

$$c_1 = 4.6(13) \times 10^{-5} \text{ cm}^2 \text{ g}^{-1} \quad (3.69a)$$

$$\alpha = 0.80(6). \quad (3.69b)$$

The agreement between fit and data is 32 %, again defined as the RMS of the relative residuals [193]. The fact that the spectral index  $\alpha$  is significantly higher than

in hydrocarbon will be discussed later. The RMS of the residuals is mostly affected by Bergamasco1973 [53], which has the biggest deviation from the trend: It is 1.9 times higher. Therefore it is argued in [259] that Bergamasco1973 [53] is incompatible with the other data, especially Gorshkov1971 [121], whereas [34] suggest a neutron underproduction in the simulations, but pointed out that in the small targets of Bergamasco1973 [53] no shower can develop.

Most of the experimental values for the neutron yield in lead are obtained with thin targets ( $<400 \text{ g cm}^{-2}$ ), except the results for ZEPLIN-II/III [214] ( $3200 \text{ g cm}^{-2}$ ). As the hadron shower within the target needs between 500 and  $800 \text{ g cm}^{-2}$  (Sect. 3.4.5) to reach equilibrium, the ZEPLIN data [214] contains therefore fully developed showers. Therefore they are not compatible with the remaining data and we exclude them.

A fit to the *thin target data set* [52, 53, 94, 120–123] results in

$$c_1 = 3.6(14) \times 10^{-5} \text{ cm}^2 \text{ g}^{-1} \quad (3.70\text{a})$$

$$\alpha = 0.90(15) \quad (3.70\text{b})$$

(Fig. 3.6a, red dashed line). The agreement between fit and data, defined as the RMS of the relative residuals [193], is with 33 % similar.

Comparing now the fits for hydrocarbon data (Eq. 3.68a) with the one for lead data shows a significant higher spectral index for lead, regardless if the ZEPLIN data are included (Eq. 3.69a) or not (Eq. 3.70a). However, based on the parametrisation (Eqs. 3.65 and 3.66) the same spectral index  $\alpha$  is expected for both target materials. As it turns out, especially the measurement Crouch1952 [94] forces the fit in the lead data to the higher spectral index. By excluding Crouch1952 [94], the fit to the thin target data return to

$$c_1 = 8(2) \times 10^{-5} \text{ cm}^2 \text{ g}^{-1} \quad (3.71\text{a})$$

$$\alpha = 0.70(10), \quad (3.71\text{b})$$

in agreement with the hydrocarbon data Eq. 3.68a. Regardless if Crouch1952 [94] is included or not, the fit to the thin target data alone results always in a higher spectral index: Without the precise ZEPLIN measurements [214], the measurement of Bergamasco1973 [53] would force the fit to a higher index. Therefore, the fit is mostly affected by Crouch1952 [94] and Bergamasco1973 [53]. However, both references as such are valid measurements and we can not justify to exclude them from the fitting.

A straight forward comparison to MC simulations, as done for the hydrocarbon measurements, is not possible, as the MC simulations performed so far result in the dependence of the neutron yield on the atomic weight (Eq. 3.66) for a given muon energy<sup>14</sup>  $Y|_{\langle E_\mu \rangle}(A)$ , instead of calculating the dependence on the muon energy for lead targets  $Y|_{A=207.2}(\langle E_\mu \rangle)$  (Eq. 3.65). It is therefore necessary to take the MC

<sup>14</sup>Mostly  $E_\mu = 280 \text{ GeV}$  is used [34, 134, 162], see Table 3.3.

results at the atomic weight of lead  $A = 207.2$  [252] and the fit to the measurements at  $E_\mu = 280$  GeV. Again only publications that state at least  $\beta$  are considered, publications that show only plots like [177] are excluded. The comparison via the fits of Eq. 3.66 are only approximate, as the neutron yield has a systematic, non-statistical fluctuation around this general trend [34].

For the comparison between the MC simulations [34, 134, 162, 193] and the performed fit  $Y|_{A=207.2}((E_\mu))$  (Eq. 3.69a) to the data, we include the ZEPLIN results [214], as also the according MC assumes a muon-induced shower in equilibrium. Historically, the measurement ZEPLIN-II2008 [35, 177] is a factor three smaller than expected based on the fit to the data. It is also smaller than the prediction by detailed, calibrated MC simulations with Geant4 8.2 and FLUKA2008. Therefore it seems that there is some tension between the MC prediction being closer to the general trend expected from previous measurements, and the actual measurement. A recent reevaluation of the neutron yield by the collaboration (ZEPLIN-II2013) results in a higher value [214]. However, the successor experiment ZEPLIN-III at the same site measured an even higher yield. The difference maybe explained by a better solid angle coverage in ZEPLIN-III resulting in a lesser liability to inaccuracy in the angular distribution of the simulated neutrons [214].

As for hydrocarbon, the neutron production is generally underestimated. The average deviation is 28 %, ranging from 18 % [193] over 24 % [134] to 43 % [34].

In the following, we discuss the neutron yield for a given muon energy  $E_\mu$  depending on the atomic mass  $A$ . Concerning  $Y|_{E_\mu}(A)$ , averaging over the MC simulations given in Table 3.3 for  $E_\mu = 280$  GeV results in

$$c_2 = 3.6(39) \times 10^{-5} \text{ cm}^2 \text{ g}^{-1} \quad (3.72a)$$

$$\beta = 0.85(85), \quad (3.72b)$$

i.e. the variation between different MC codes and versions is in the order of 100 %. This can be straightforward compared to the measurements in [120, 121, 123] of the neutron production in the four different targets aluminium, iron, cadmium, and lead, but at the same energies. A fit of  $Y|_{E_\mu}(A)$  (Eq. 3.66) to these measurements results in  $\beta = 0.96(7)$  (see Fig. 3.6b), reproducing the result in [112]. The agreement between data and fit is 30 %. As the measurements happen at different muon energies than the simulations, only the spectral index  $\beta$  can be compared, not the scale  $c_2$  [112]. Given the spread of the MC results, they are not contradicted by the measurements [112].

Comparing the average neutron underproduction in hydrocarbon (14 %) with the one in lead (28 %), the increased deviation with atomic weight is recognized in literature [35, 188]: Again a factor two is quoted as upper limit of the deviation for lead in [34], for complex composite materials like rock, an upper limit of three is given in [134]. Among the MC packages, Geant4 has a lower neutron yield than FLUKA, e.g. Geant4 8.2, Geant4 9.5 versus FLUKA 1999, FLUKA2011 [177, 247].

The differences between FLUKA and Geant4 are possibly caused by the different total interaction cross sections, neutron production cross sections, final state

multiplicities of secondary neutrons, and contributions from electromagnetic (neutron photoproduction) and hadronic cascades (neutron hadroproduction) to the total neutron yield [34, 163]: In FLUKA the relative contribution of neutron hadroproduction is predominant over neutron photoproduction at higher energies. For light targets, this is nearly compensated by an absolute underproduction of neutron hadroproduction, therefore resulting in similar high energy behaviour of FLUKA and Geant4 [34]. However, it seems that Geant4 has a systematic deficit with respect to FLUKA in neutron photoproduction for heavy targets, and generally in neutron hadroproduction [34]. The higher neutron yield in hadronic cascades in FLUKA is possibly caused by a missing fast fragmentation of highly excited, heavy nuclei in FLUKA, leaving more energy for neutron evaporation [34]. This is in agreement with the findings in [206], that FLUKA has, especially below neutron energies of 3 MeV, a higher neutron production than Geant4.

A general, systematic underproduction of neutrons in cascades in both Geant4 and FLUKA is suggested by D.-M. Mei [191], as also the neutron multiplicity measurements of Bezrukov 1973 [63] is above simulation results [193, 214], see Sect. 3.5.3. By correcting the simulated neutron multiplicity to the measured one via Eq. 3.62, D.-M. Mei claims to reduce the difference of the total yield between FLUKA and the measurements to 15 %, the same deviation as between a fit of Eq. 3.65 to the data and the data.

However, for recent Geant4 versions the situation may have changed, as the cascade models were improved since version 9.1, leading to an expected 10–15 % higher neutron yield (see Appendix A.3.3). Additionally, L. Reichhart et al. [214] find an increase of  $\approx 38\%$  for the inelastic neutron scattering between Geant4 9.4 and Geant4 9.5. Furthermore, comparison of Geant4 9.5p01 simulations with measurements [51, 214] finds a more complex behaviour: Whereas the complete neutron yield is still underestimated by the simulation, this is especially the case for events with a low neutron multiplicity and in a lesser extent at higher multiplicities, see also Sect. 3.5.3. This emphasise the strong influence of the used MC code version on the results.

Beside in underground experiments, the neutron production yield was also measured in the NA55 experiment [86] at CERN. CERN NA55 uses thin targets, so it maybe comparable to the thin target data set. However, as pointed out in [163], at underground sites the muon induces also fully developed showers in the rock overburden around the laboratory. Therefore, measurements at underground sites may have neutron contributions from the environment that are missing in the CERN NA55 data. Nevertheless, the neutron production in the thin graphite target of CERN NA55 is a factor 2.1 higher than predicted by Geant4 8.0 [188], similar to the factor 2 found in [34] for thick hydrocarbon targets, and Geant4 6.2; therefore it seems that the shower development is consistent for light targets [188]. The finding for the heavy target lead is contrary: Here an underprediction by a factor of 5.9 is found<sup>15</sup> in Geant4 8.0 [188], where for thick lead targets the usual factor two is quoted. Possible reasons are investigated in [34, 188]: Under the assumption that no shower

---

<sup>15</sup>The agreement between CERN NA55 and a detailed MC simulation within 15 % stated in [112] could not be verified, as no reference for the mentioned MC simulation is given.

can develop in the thin targets of CERN NA55, H. Araújo et al. [34] simulate only the direct muon spallation with FLUKA2003 and Geant4 6.2; both MC packages agree with each other but underpredict the measurements. Allowing shower development as second stage in the simulations reduces the disagreement with CERN NA55, therefore a possible contamination of the CERN NA55 results with neutrons from showers is postulated [34, 112]. A slightly different explanation is suggested in [177]: By replacing the standard G4MuNuclear model for the muon spallation with a new CHIPS based in Geant4, the neutron yield increases. Again, by including neutrons from showers it even reaches agreement for the graphite target, but still underpredicts the heavier targets (copper, lead) [177]. Therefore also the initial neutron production via muon spallation seems to play an important role. As in Geant4 9.5 the handling of the muon spallation changed (see Appendix A.3.3), these results may also change.

One can summarize the explanations discussed in the literature for the general underestimation of neutron production in both Geant4 and FLUKA with respect to experimental data to five possible reasons:

- An underestimation of the initial neutron production by muon spallation, as a new CHIPS based model instead of the standard G4MuNuclear model [74] reduces the differences between Geant4 and CERN NA55 [177]. However, it should be one explanation for both MC packages, as both Geant4 and FLUKA underestimate the neutron production, albeit FLUKA uses a different model for muon spallation [62].

A possible explanation could be a break down of the equivalent photon approximation at low energy transfers, see Sect. 3.4.3, as the virtuality of the exchanged photons is no longer negligible [34, 177, 249]. FLUKA1999 predicts an increase of the neutron yield by a factor two to three [249] when the lower bound of the muon spallation model is decreased from the default threshold 140–10 MeV, similar in Geant4 6.2 when the default threshold of 200 MeV is lowered. But at this energy regime the used parametrization in FLUKA, and Geant4 overestimate the ‘more rigorous’ theoretical models [34, 249], therefore the stated factor two to three is an upper bound for this effect. This maybe affected by the new handling of muon spallation introduced in Geant4 9.5, see Appendix A.3.3 .

- An underestimation of neutron production in electromagnetic and hadronic cascades, with different extents in Geant4 and FLUKA [34, 163, 193]. A contamination with cascade neutrons may also be the explanation [34, 112, 188] for the differences between MC simulation and the thin target data of Bergamasco1973 [53] and CERN NA55 [86]. For Geant4 the improved cascade models since version 9.1 (see Appendix A.3.3) could change this finding.
- M. Marino et al. report a stronger attenuation of neutrons in Geant4 8.1 compared to experimental data [241] by a factor four. This may affect modelling experiments using thick targets.
- The loss of details from earlier experiment, like Bergamasco1973 [53] or Gorshkov1974 [122], resulting in an inexact MC model as suggested in [35, 134,

[163, 177]. This stresses the importance of new measurements with detailed documentations like ZEPLIN-II/III [35, 177, 214].

- K. Zbiri [263] suggested that simulations typically ignore the hadronic shower development in the rock surrounding the detector and take into account shower development only inside the detector. By including the shower outside the detector he claims a better agreement with the measurements, but gives no quantitative details. Also in [231] the importance of the full simulation and tracking of all shower products is noted.

All those findings highlight the strong influence of the used MC package, its version, and the implemented physics. In any case, one has to keep in mind that a successful MC model of an existing measurement has to include, besides the neutron production, also the neutron moderation, transport, and diffusion, together with the detector geometry, and hardware/software cuts [163, 187], as well as a high statistics sample [177].

For the LSM, the contribution of neutrons produced by muons in the rock to the background of the EDELWEISS experiment is estimated in [134], but the neutron yield itself is not stated. Based on the measured average muon energy at LSM of 255 GeV [215], and on the general trend one can interpolate the neutron yield for LSM in hydrocarbon to  $2.9(6) \times 10^{-4} \text{ cm}^2 \text{ g}^{-1}$  (Eq. 3.68a) and in lead to

$$Y = 5(5) \times 10^{-3} \text{ cm}^2 \text{ g}^{-1} \quad (3.73)$$

for only the thin target data (Eq. 3.70a). The great uncertainty of the interpolation highlights the necessity of a dedicated measurement at site.

### 3.5.5 Currently Running and Future Experiments

As it was indicated in the previous subsections, a deviation exists of up to a factor 2 between measurements of the neutron yield and MC simulations. To assess the accuracy of the simulation packages, further measurements are needed, supported by the argument that possibly not all details of earlier measurements are available for implementations in MC simulations. This subsection lists currently running and planned detectors dedicated to the investigation of muon-induced neutrons at underground sites.

C. Galbiati and J.F. Beacom [116, 117] suggest the deduction of the muon-induced neutron spectrum from neutron induced isotope production in large liquid scintillators, which is measured by KamLAND [1] and Borexino [50, 51]. For liquid scintillators they propose to use the reaction  $^{12}\text{C}(\text{n}, \text{p})^{12}\text{B}$  to probe the neutron spectrum at intermediate energies, as the reaction cross section has a threshold of  $\approx 10$  MeV, and drops above  $\approx 100$  MeV. Also the neutrino experiments Double Chooz [2, 3], DayaBay [25], and RENO [18] should be able to calculate the neutron yield from their measurements of muon-induced neutron events.

Besides using already existing experiments, also dedicated detectors for muon-induced neutrons are planned or already running. As a tool for the measurement of secondary neutron production by muon-induced neutrons at underground sites, R. Hennings-Yeomans and D. Akerib [130] proposed a neutron multiplicity meter based on gadolinium loaded liquid scintillator similar to earlier detectors (e.g. [63]). In the following years several proposals were made that are currently in different stages of realization:

The *Neutron Multiplicity Meter* (NMM) [239] follows in most parts the design of R. Hennings-Yeomans and D. Akerib [130], except that it uses a gadolinium doped water Cherenkov detector [240] instead of a gadolinium loaded liquid scintillator. It is assembled at the *Soudan Underground Laboratory* and used the muon veto system of the *Low Background Counting Facility* (LBCF) at 2100 mwe [203, 246]. The operation of the NMM is accompanied by simulations of the detector response with Geant4 version 9.4.p01 [239]. According to [75] it takes data on muon-induced neutrons at the moment.

Also for the planned *Deep Underground Science and Engineering Laboratory* (DUSEL) at the Homestake mine a dedicated neutron counter is projected. Albeit the NMM at Soudan is also a DUSEL R&D project [239], the design of the planned DUSEL detector [192, 204] is completely different. It is based on a complete enclosure of a lead target with gadolinium loaded liquid scintillator cells and gadolinium doped water Cherenkov cells in association with a muon tracker. As the funding of DUSEL is doubtful at the moment [224], also the planned start-up of the detector in 2016 [193] is uncertain.

At the *Sanford Underground Research Facility* (SURF), the site of the *Large Underground Xenon* (LUX) dark matter experiment, a detector for fast neutrons is in its prototype stage. It uses liquid scintillator on a hydrocarbon base and pulse shape analysis to select neutron events [264].

The *Aberdeen Tunnel Experiment* at Hong Kong is a neutron detector and part of the *Daya Bay Neutrino experiment* at 611 mwe [71, 98]. It consists of a gadolinium loaded liquid scintillator in association with a muon tracker [87, 90]. Currently it is still in R&D stage [71].

A second China based experiment using gadolinium loaded liquid scintillator seems to be planned at the *China JinPing Underground Laboratory* (CJPL) at 6720 mwe [144, 258, 260, 261], the location of the *China Darkmatter EXperiment* (CDEX) [143].

Contrary to the experiments above, the *UMD-NIST Fast Neutron Spectrometer* at the 1450 mwe deep *Kimballton Underground Research Facility* (KURF) does not use gadolinium to detect neutrons underground, but  $^3\text{He}$  proportional counter tubes: Albeit they have a smaller volume, and hence smaller counting rate, their energy resolution is better than that of large volume liquid scintillators. This provides the possibility to measure the neutron energy spectrum. However, currently it is background limited [171].

For the two sites of the Double Chooze neutrino oscillation experiment, measurements with the time projection chamber *DCTPC* are planned to resolve energy and angular distribution of muon-induced neutrons at 114, and 300 mwe. A first

generation detector was already built and tested. It is installed at the far site of Double Chooz (300 mwe), but no data are published yet. At the next stage bigger detectors should be installed at each site [182].

The NMM [239] and the DCTCP [182] seem currently to be the only operational detectors. However, they are located at shallower sites, compared to this work, hence they measure the neutron yields at lower average muon energies.

### 3.6 Implementation of Muon Interactions in Geant4

To simulate the physical interactions leading to muon energy loss (see Sect. 3.2), and to muon-induced neutron production (see Sect. 3.4) the mostly used MC packages are FLUKA [47, 108] and Geant4 [16, 22], e.g. in [34, 35, 48, 134, 163, 177, 188].

We will focus on Geant4 in this section for the following reason: For FLUKA2003 it is reported [34, pp. 2, 12–13], [48] that nuclear recoils are modelled with fixed ‘KERMA’ factors instead of using the actual kinematic distribution, as it is done in Geant4. The different handling of elastic neutron scattering leads to differences of at most 30 % in the detection of nuclear recoils by neutrons, as stated in [34]. The handling seems to be improved in the current version FLUKA2011 [109], at least for recoiling protons and neutrons, but not for all nuclei. As most of the running and planned experiments aiming to measure the neutron production yield (Sect. 3.5.5) rely on a precise moderation and capture of neutrons as event signature, Geant4 seems more suitable.

The current Geant4 version is 9.6, see Appendix A.3.2 for a short explanation of Geant4 specific terminology. This section describes the implementation of the different physical interactions related to muon energy loss (Sects. 3.6.1–3.6.4) and neutron production, and discusses possible sources for systematic errors. An overview of the changes in the implementation of the interaction models described below between different Geant4 releases is given in Appendix A.3.3.

Besides a correct model of the physical interactions, the implemented geometry is important too: To ensure that a shower development in a MC simulation reaches equilibrium between muon and neutrons, the thickness of rock has to be sufficient. V.A. Kudryavtsev [166] recommended 5 m of rock and up to 10 m above the detector. A rock thickness of 7 m is recommended in [193]. In [134], 2 m of rock below the detector and anywhere else 5 m is used. The thinner rock below is justified by the strong correlation between muon-induced neutrons and muons (see Sect. 3.5.2). The recommended thicknesses are rather conservative values compared to the necessary thickness to reach equilibrium based on simulation [134, pp. 57, 83] (see Sect. 3.4.5):  $800 \text{ g cm}^{-2}$  is roughly equivalent to 3 m of Fréjus rock.

#### 3.6.1 Electromagnetic Interactions

In Geant4 the energy loss by a given process is handled as continuous loss along the particle track if the kinetic energy of the secondary particles (knock-on electrons,

bremsstrahlung photons, electron-positron pairs) is below the specified production threshold. Above the threshold, the energy loss causes the creation and tracking of the secondary particles [33].

The production threshold energy is calculated internally by Geant4, based on the user specified range cut and the actual material (see Appendix A.3.2). For example, in [134, p. 55] a cut for gamma rays of  $\approx 2.7$  MeV in lead is used, resulting in  $\nu_{cut} \approx 3 \times 10^{-6}$  for a 1 TeV muon. A lower production threshold (a few 10 KeV for gammas, and a few MeV for  $e^\pm$ ) is recommended in [177] as the photoproduction by bremsstrahlung is an important source of neutrons at low energies, see Sect. 3.4.

The models of muon interactions in Geant4 is identical to the one recommended by D.E. Groom, N.V. Mokhov, and S.I. Striganov [125], except the muon spallation interactions which will be discussed in Sect. 3.6.2.

The electronic energy loss for muons (Sect. 3.2.2) is implemented in the Geant4 class G4MuIonisation by using different model classes appropriate for three ranges of muon kinetic energy  $E_\mu$  [119, pp. 202–208, 219–220]:

- The G4BraggModel for  $E_\mu < 200$  KeV calculates the energy loss by using a parametrization of evaluated data. Depending on the material, either [137] or [58] is used.
- The G4BetheBlochModel for  $200 \text{ KeV} < E_\mu < 1 \text{ GeV}$  implements the Bethe formula Eq. 3.15a. The excitation energies are taken from [136]. It includes the following corrections:
  - The shell correction  $C/Z$ , with  $C$  parametrized according to [137].
  - The density correction  $\delta(\beta\gamma)$  as parametrized in [235].
  - The Barkas correction  $zL_1(\beta)$  as parametrized in [137].
  - The Bloch correction  $z^2L_2(\beta)$  as parametrized in [137].
  - The Mott correction [17].
- The G4MuBetheBlochModel for  $E_\mu > 1 \text{ GeV}$  includes the correction of S.R. Kel'ner, R.P. Kokoulin, and A.A. Petrukhin [147] for bremsstrahlung on the atomic electrons. The correction for the muon spin [125, 219] is not included.

In cases the energy loss exceeds the production threshold, knock-on electrons are created and tracked. It seems, that this modelling is unchanged since Geant4 9.0, see Appendix A.3.3.

For muon energy loss due to bremsstrahlung (Sect. 3.2.3) only the ultra relativistic case ( $E_\mu \gg m_\mu c^2$ ) is implemented in G4MuBremsstrahlung. It is based on the models of [28, 146, 147]. Therefore it includes nuclear screening, nuclear excitation, and the contribution of bremsstrahlung on the atomic electrons, but not the Ter-Mikaelian effect (Sect. 3.2.5), limiting its applicability to  $\nu \geq 10^{-6}$  [119, pp. 221–224].

The muon energy loss via direct pair production (Sect. 3.2.4) is handled by G4-MuPairProduction, again only in the ultra relativistic case ( $E_\mu \gg m_\mu c^2$ ). It is based on [156] and considers the nuclear form factor [157] and the triple production in the field of the atomic electrons [145]. Not included is the Coulomb correction, which is important for  $Z > 50$  [119, pp. 226–232], see Sect. 3.2.4. This may affect

this work, as its objective is the measurement and simulation of the neutron yield in lead.

The applicability for both Bremsstrahlung and direct pair production is limited to  $E_\mu \leq 10^{20}$  eV as the Landau-Pomeranchuk-Migdal effect (Sect. 3.2.5) is not included [119], in contrast to FLUKA [47]. Considering the used muon generator in this work, which application range is given by the Gaisser parametrization (Sect. 3.1.3), the Landau-Pomeranchuk-Migdal effect can be omitted.

For the modelling of the subsequent electron, positron, and gamma interactions caused by muon interactions in Geant4 the usage of the *low energy* extensions is recommended by [34, 134, 177]. Since Geant4 version 9.3 these packages are included in the standard packages (see Appendix A.3.3). The systematic uncertainty of these interactions is stated as within 5 %, see references in [202].

The deviation between implementation and theoretical model of electromagnetic muon interactions is investigated for Geant4 6.2p01 in the range of 1 GeV to 1 PeV to be at most 2 % [73]. Therefore, the implementation of the models in Geant4 is in agreement with the theoretical models and data by D.E. Groom, N.V. Mokhov, and S.I. Striganov [125]. In addition, recent versions of Geant4 claimed an improvement in the accuracy in the muon bremsstrahlung production (version 9.1), and in the multiple scattering of muons (version 9.3), see Appendix A.3.3.

### 3.6.2 Muon Spallation

For the simulation of muon spallation (Sect. 3.4.3), the parametrization of L.B. Bezrukov and É.V. Bugaev [62] is most widely used [125, pp. 194f.], also in FLUKA.

However, Geant4 uses a different approach [73, 119]: The implementation in G4MuNuclear takes the virtual photon spectrum as parametrized by the model of V.V. Borog and A.A. Petrukhin [74], the nuclear shadowing is included by parametrization [78], and the real photonuclear cross section is based on parametrized experimental data [80]. For the hadronic interaction the virtual photon is transformed to charged pions which interaction is governed by the LEP model [119, p. 323], see Sect. 3.6.4.

The agreement between the models of L.B. Bezrukov and É.V. Bugaev [62], K. Kobayakawa [154], and V.V. Borog and A.A. Petrukhin [74] in terms of cross section is within 30 % [181]. Much better is the agreement between the models of L.B. Bezrukov and É.V. Bugaev, and V.V. Borog and A.A. Petrukhin with 10 % in terms of cross section and 5 % in terms of energy loss  $b_{\text{nucl}}$  [119, p. 233].

Whereas the used interaction model has a 5 % effect, the use of precise experimental cross sections [37, 38] for photo absorption instead of the model of L.B. Bezrukov and É.V. Bugaev [62] does not change  $b_{\text{nucl}}$  appreciably [125, p. 196].

G4MuNuclear is applicable for  $1 \text{ GeV} \leq E_\mu \leq 1 \text{ EeV}$ , and  $\nu > 200 \text{ MeV}$  [119, p. 233]. The choice of the threshold in  $E_\mu$  varies in the literature: In [34] a threshold of 1 GeV is used. A higher threshold of  $E_\gamma \geq 3 \text{ GeV}$  is used in [134]. Below this threshold, the contribution of muon spallation to the muon energy loss

is low and possible secondary particles are below the Geant4 production threshold [134]. Below the lower boundary on  $\nu$ , the equivalent photon approximation breaks down, see Sect. 3.4.3. Therefore, the actual lower boundary may affect the deviation between the simulated and measured neutron yield, as suggested in [34, 177, 249] (Sect. 3.5.4).

By using a CHIPS based model (see Sect. 3.6.4) for the interaction between the virtual photon and the nucleus a neutron yield increased by a factor 1.6 and better agreement to the CERN NA55 [86] experiment is reported in [177]. However the new model results in a larger energy loss of muons compared to FLUKA2007 and MUSIC, causing an increase of low energetic muons in muon propagation simulations [177]. The average muon energy after propagating 2 TeV through 3 kmwe deviates by  $\approx 17$  GeV between Geant4 8.2 (G4MuNuclear), FLUKA2007, and MUSIC [177].

The even newer G4MuonVDNuclearModel<sup>16</sup> splits at 10 GeV the handling of the virtual photons in a low and high energy part [255]: Above, the virtual photon is transformed to a  $\pi^0$  for the hadronic interaction, below it interacts directly via the Bertini cascade, see [33] and references therein. As the Bertini cascade produces more neutrons than the LEP model, this also increases the neutron yield [214].

As it is not clear that the implemented models of the muon spallation cause the observed deviation between measured and simulated neutron yield, see Sect. 3.5.4, we see no disadvantage in using the classic G4MuNuclear model in this work.

### 3.6.3 Photo-Nuclear and Electron-/Positron-Nuclear Interactions

The modelling of the (real) photo-nuclear interaction, e.g. by bremsstrahlung, is uniformly described in [34, 134] and based on the Geant4 provided QGSP\_BIC\_HP physics list.

In the high energy range  $3 \text{ GeV} \leq E_\gamma \leq 100 \text{ TeV}$  a theoretical quark-gluon string model (QGS) [111, 257] is used [134]. It selects the collision partner of the incident particle within a 3D model of the target nucleus, and creates quark-gluon strings in the selected particles. Afterwards, the final state fragments form into an excited nucleus and excited strings. The strings de-excite via hadronization in secondary particles, which can interact inelastically with the nucleus and start nuclear cascades. The interactions of the secondaries with the excited nucleus are treated by a cascade model (see Fig. 3.7) [119, p. 385], [33]. We follow in this work [134] and use the CHIPS model (see later) as cascade model [134], hence it is a QGSC model [177].

At intermediate energies  $E_\gamma \leq 3.5 \text{ GeV}$  [134] a chiral invariant phase space decay model is used: It computes the fragmentation on a quark-level based on a nonperturbative three-dimensional chiral invariant phase space (CHIPS) model [99–101], including only massless partons (only u-, d-, s-quarks) [119, p. 395], [33]. The photonuclear cross section in Geant4 starts at the hadron production threshold and

---

<sup>16</sup>Previously called G4VDMuonNuclearModel in Geant4 9.4.

Shielding	HP	BERT		FTFP		
QGSP_BIC_HP	HP	PC	BiC	LEP	QGSP	
[Horn]	HP	PC	BiC	LEP	QGSP	
[Lindote et al.]	HP	PC	BiC		QGSP	

10 MeV 100 MeV 1 GeV 10 GeV 100 GeV 1 TeV 10 TeV

**Fig. 3.7** Models for inelastic neutron scattering according to Geant4 Shielding, Geant4 QGSP\_BIC\_HP version 1.0, O. M. Horn [134], and A. Lindote et al. [177]: Data driven high precision model (HP), Bertini cascade (BERT), FriToF string model (FTF) using the Precompound (PC) model for deexcitation (FTFP), Binary Cascade (BiC), LEP model, quark-gluon string model (QGS) using the Precompound model to fragment (QGSP). In QGSP\_BIC\_HP and [177], the PC is called implicitly via the BiC at its low energy end, whereas in [134] it is explicitly called. For details see text

is implemented for all energies upward in `G4PhotoNuclearCrossSection`, covering all five models discussed in Sect. 3.4.6. It is parametrized as function of photon energy and atomic mass, based on measured cross sections for 14 nuclei [119, p. 326].

The electron/positron-nuclear reaction is entirely based on a CHIPS model for  $E_{e^\pm} \leq 100$  TeV. It is related via the equivalent photon approximation to the photo-nuclear interaction [119, p. 239].

### 3.6.4 Hadronic Interactions

The modelling of the hadronic interactions is strongly user dependent [33, 257]: Not only the interaction cross sections affect the simulation, but also the subsequent intra-nuclear reactions of the excited nucleus, its fragmentation, and deexcitation [134, p. 51].

Within the literature there are mainly three suggested Geant4 physics lists: The first two are based on the QGSP\_BIC\_HP reference physics list provided within the Geant4 packages. As third one the Shielding physics list [155, 256] is provided by recent Geant4 versions and is based on the FTFP\_BERT reference physics list.

The first physics list is described in detail and used with Geant4 8.2p01 by O.M. Horn [134] for simulating muon-induced neutron background in the EDELWEISS experiment. The similar, but not identical, second physics list is shortly described by H. Araújo et al. [34] for Geant4 6.2 and later reused with Geant4 8.2 [35, 177] and Geant4 9.0p02 [263]. The Shielding physics list is up to now only used by L. Reichhart et al. [214] with Geant4 9.5p01.

The physics list shortly described and used with Geant4 8.0 in [188] is closely related to the one of O.M. Horn, the same seems to be true for *model III* used by Borexino [51] with Geant4 9.6p01. Whereas *model II* of Borexino [51] seems more

close to the `Shielding` physics list. The physics list used in [48, 202] seems to be more closely related to the one of H. Araújo et al. Figure 3.7 illustrates the differences between the five main physics lists on the example of the neutron inelastic scattering.

In the following, we will illustrate the implementation of hadronic interactions via Horn's physics list and later discuss the differences to the ones of H. Araújo et al. and L. Reichhart et al.

The reactions of the excited nuclei are governed by different models:

For the inelastic nucleon scattering in the high energy range ( $12 \text{ GeV} \leq E_N \leq 100 \text{ TeV}$ ) a theoretical quark-gluon string model (QGS) [111, 257] is used, it is linked to a `G4PreCompound` model (see later) to handle the fragmentation of the excited nucleus (QGSP). In the intermediate energy range ( $6 \text{ GeV} \leq E_N \leq 12.1 \text{ GeV}$ ) the inelastic nucleon scattering is parametrized by a low energy model (LEP). It is based on the GEISHA models of Geant3 [119, p. 369]. They consider the recoil of the nucleon, the scattering of the incident hadron, and the secondary production.

Each of the above models can generate secondaries that start an intra-nuclear cascade. For the energy range  $65 \text{ MeV} \leq E_N \leq 6.1 \text{ GeV}$  the `G4BinaryCascade` (BiC) [110] is used, describing the binary interaction between an incident hadron, and a single nucleon of the target nucleus. It reproduces well the cross sections for secondary neutron production by protons [33]. The cascade terminates when the average energy and the maximum energy of all secondaries drop below the production threshold [119, p. 457].

After terminating of the intra-nuclear cascades, the `G4PreCompound` model is applied below 70 MeV. It provides a smooth transition to the equilibrium stage via emission of fragments and photons [119, p. 490]. The remaining nucleus deexcites via fission [119, p. 506],  $\gamma$ -evaporation [119, p. 496], Fermi breakup [119, p. 511], and multi-fragmentation [119, p. 515] before reaching equilibrium. An bugfix in `G4PreCompound` in Geant4 9.1 increases the neutron yield by 10–15 %, see Appendix A.3.3.

For the whole energy range, the elastic scattering of nucleons is based on the GEISHA model. For neutrons below 20 MeV the transportation, elastic/inelastic scattering, capture, and fission are described by data driven low energy models `G4NeutronHP` based on ENDF/B-VI data [119, p. 531]. The influence of the interpolation between the tabulated cross sections on the neutron propagation is at most 1 % [119], and the influence of the chosen cross section library (ENDF in Geant4, JENDL in MCNPX) is at most 20 % in the energy range 0.01–5 MeV [172]. The accuracy of neutron tracking at the higher energy range of 100–300 MeV is assumed to be less than 20 %, see references in [202].

The model used in [51, 188] is very similar to the one by O.M. Horn described above, except that the change between LEP and BiC happens at 10 GeV.

As main difference to the model of O.M. Horn, the model used by H. Araújo et al. does not use LEP to bridge QGSP and BiC; instead the QGS model starts already at 6 GeV. The direct connection between QGSP, BiC is also used in [202], but at 10 GeV. The variety of combinations is caused by a missing, officially approved connection between BiC and QGSP [177]: BiC is recommended below 3 GeV [257], QGS aimed above 20 GeV. The often used LEP model to bridge this gap is not

generally approved, as it conserves energy only in average, not event by event [257]. The influence on the neutron yield of the energy threshold at 6, 10 GeV in case of a direct connection BiC/QGS, and for 20 GeV in case of bridging BiC/LEP/QGS is within 3 % [214] to 10 % [177], less than the change between Geant4 6.2 and Geant4 8.2 [177]. A similar comparison, but investigating also the influence of BiC and G4NeutronHP, found a variation of 25 % in neutron yield between different physics lists [48]. As in the more recent simulations [34, 134], the usage of BiC and G4NeutronHP is not disputed, we take the estimation of 10 % [177] for the systematic uncertainty.

Whereas the approaches of O.M. Horn and H. Araújo et al. are similar to each others as they both are based on the QGSP\_BIC\_HP reference physics list, L. Reichhart et al. [214] uses the Shielding list [155, 256] based on FTFP\_BERT\_HP: Here the high energy part down to 5 GeV is covered by a FriToF string (FTF) model [244], using the Precompound model for deexcitation (hence FTFP). In the low energy range the Bertini cascade (see [33] and references therein) ( $\leq 5$  GeV) and G4NeutronHP ( $\leq 20$  MeV) is used. Additional to the reference Shielding list, the chemical bounds of the atoms are considered for  $\leq 4$  eV [214].

Comparison of the Shielding physics list with QGSP\_BIC\_HP in Geant4 9.5p01 shows an increased muon-induced neutron yield in lead by  $\approx 15$  %, where the change from Binary cascade to Bertini cascade contributes  $\approx 9$  % [214]. However, this behaviour seems strongly target dependent. In liquid scintillator, the influence of the Bertini cascade on QGSP based physics list is smaller, only  $\approx 1$  % [51]. Moreover, in this target the FTFP based physics list is underproducing neutrons by up to 15 % compared to a QGSP based physics list [51], contrary to the behaviour in lead. Therefore the systematic uncertainty associated with selecting Shielding/FTFP\_BERT\_HP or QGSP\_BIC\_HP has the same order of magnitude as the uncertainty by selecting between different QGSP\_BIC\_HP based physics lists.

By quadratically adding all the systematic uncertainties discussed in this subsection, as proposed in [202], the uncertainty on the neutron production yield is 76 %, see Table 3.4. The main contribution is from the new CHIPS based model for the muon spallation reported in [177]. Without this, the uncertainty is 47 %. This is similar to, but not comparable with the 45 % in [202], as there are also systematic uncertainties of the primary muon spectrum included, which are not related to Geant4. Therefore the systematic uncertainties in Geant4 physics lists discussed in literature can account for the differences between Geant4 simulations of muon induced neutron production in lead and the expectation on the fitted data, see Sect. 3.5.4.

We adopt for this work Horn's physics list [134], see Sect. 5.2, as it is based on the well tested QGSP\_BIC\_HP reference list and to be consistent to earlier simulations for the EDELWEISS experiment [134]. Based on the investigation of the release notes of Geant4 versions since version 8.2p01 [134] (see Appendix A.3.3), the physics list should be applicable up to the most recent Geant4 version 9.6. Due to improvements and fixes in the intra-nuclear cascade models, the neutron production as implemented in the lastest Geant4 version in lead most likely will increase compared to the one used here.

**Table 3.4** Individual contributions to and the derived total value of the systematic uncertainties of the muon-induced neutron yield simulated in Geant4

Contribution	Uncertainty (%)
Electron/Positron/Gamma interactions [202]	5
Muon electromagnetic interactions [73]	2
Muon spallation [181]	30
Muon spallation, G4MuNuclear/CHIPS model [177]	60
Neutron cascade, bugfix in Geant4 9.1, see Appendix A.3.3	15
Neutron propagation low energy, interpolation [119]	1
Neutron propagation low energy, cross sections [172]	20
Neutron propagation high energy [202]	20
Selecting physics list and bridging [177, 214]	15
Total systematic uncertainty	76

For details see text

## 3.7 Conclusion

As it was discussed in Sect. 3.5, the results of MC simulations, both Geant4 and FLUKA, at least for light targets like hydrocarbon, agree quantitatively with the measurements of the neutron energy spectrum, the angular distribution except backscattering, and the neutron production yield. However, for heavier targets like lead the disagreement increases. Also for the absolute scale of the neutron yield there is some tension, especially in lead, as it is generally underestimated by up to 28 %, see Sect. 3.5.4.

In literature, mainly two explanations are proposed, a physical and a technical one: First, mainly based on comparison of the CERN NA55 experiment [86] to MC simulations [34], an underproduction of neutrons in hadronic cascades in thick targets, possibly combined with an initial underproduction in the muon spallation, is assumed, see Sect. 3.5.4. Second, it is proposed that most MCs are not precise enough with respect to details of the experimental set-up like detection threshold and efficiency.

The first issue maybe solved by the continuous improvement of the MC packages, as the systematic uncertainties in the neutron yield for Geant4 alone is estimated to be within 45–75 %, depending on the choosen model implementation (see Sect. 3.6). Only due to the change of Geant4 to version 9.1, an increase of the neutron yield in the order of 10 % is expected. But a continuous validation is necessary as the case of the new CHIPS based muon spallation model [177] shows: Albeit it removes some tension with the CERN NA55 data, it may produce new tension with respect to the muon propagation.

To solve the second issue, newer and well documented measurements are proposed (Sect. 3.5.4, [35, 134, 163]). Therefore the solution of this second issue provides further data to validate the models and contributes to the solution of the first issue. To compare results with respect to neutron energy spectrum, neutron multiplicity spectrum, and neutron yield, accepted parametrizations exist, e.g. Eqs. 3.60a, 3.65 and 3.66.

Several attempts to measure the neutron production at different underground sites are currently running or are planned, see Sect. 3.5.5. Most of them based on neutron multiplicity meters with gadolinium loaded liquid scintillator, as proposed in [130], and already used in the 1970s, e.g. [63].

As it was discussed in Sect. 3.6 the selection of the actual physics model in the MC is very important for a reliable model. As most of the proposed new experiments (Sect. 3.5.5) rely on neutron detection via moderation and subsequent capture, the more detailed implementation of neutron recoil in Geant4 over FLUKA [34] has to be considered. As actual physics model for Geant4 simulation of muon-induced neutron production, two cases are described in literature [34, 134], the difference between each other is expected to be in the order of 10%, see Sect. 3.6.4.

The modelling of the detector response has also to include the technical details of the detector like threshold, cuts, and efficiencies [163, 187], as highlighted by the controversy [130, 193] about the possible influence of quenching on the LVD1999 data [165]. Beside the actual detector, the MC model has also to include the surrounding [263]: As it is important to guarantee a correct development of muon induced showers, leading to shower neutrons [163].

Suggestions for sufficient thickness of the underground laboratory walls needed for shower development are given in [134, 166, 193]. To model the incident muon flux at underground site, feeding the neutron production, there is a well tested method [134, 164, 228] with the Gaisser model folded with the energy loss of the muons in the actual rock around the laboratory, see Sects. 3.1–3.3. For the LSM, besides a full MC simulation of the muon energy loss [166], there is also a parametrization of the energy loss based on the CSDA approximation (Sect. 3.3.1), describing various distributions of rock, see [215], Sects. 3.2.8 and 3.3.2.

Based on the measured average muon energy at LSM of 255 GeV [215] and on the general trend of the neutron yield (Eq. 3.70a), a neutron yield of  $5(5) \times 10^{-3} \text{ cm}^2 \text{ g}^{-1}$  in thin lead targets can be expected. For the neutron counter used in this work with a 10 cm thick lead target, this is equivalent to a neutron flux of  $3(3) \text{ m}^{-2} \text{ d}^{-1}$ . As the contribution of captured muons in lead is negligible  $\approx 2.7 \times 10^{-3} \text{ m}^{-2} \text{ d}^{-1}$  (Sect. 3.4.1), simulations predict mainly neutrons from hadronic and electromagnetic showers, cf. Fig. 3.5a.

As the muon energy at LSM (255 GeV [215]) is close to the average muon energy at the Boulby underground laboratory (260 GeV [35]), measurements at LSM can be compared to the ZEPLIN-II/III results [35, 214].

## References

1. Abe S et al [KamLAND Collaboration] (2010) Study of the production of radioactive isotopes through cosmic muon spallation in KamLAND. *Phys Rev C* 81(2):025807. doi:[10.1103/PhysRevC.81.025807](https://doi.org/10.1103/PhysRevC.81.025807). arXiv:[0907.0066](https://arxiv.org/abs/0907.0066) [hep-ex]
2. Abe Y et al [Double Chooz Collaboration] (2012) Reactor  $\bar{\nu}_e$  disappearance in the Double Chooz experiment. *Phys Rev D* 86(5):052008. doi:[10.1103/PhysRevD.86.052008](https://doi.org/10.1103/PhysRevD.86.052008)
3. Abe Y et al [Double Chooz Collaboration] (2013) Direct measurement of backgrounds using reactor-off data in Double Chooz. *Phys Rev D* 87(1):011102. doi:[10.1103/PhysRevD.87.011102](https://doi.org/10.1103/PhysRevD.87.011102)
4. Abreu P et al (2010) Update on the correlation of the highest energy cosmic rays with nearby extragalactic matter. *Astropart Phys* 34(5):314–326. doi:[10.1016/j.astropartphys.2010.08.010](https://doi.org/10.1016/j.astropartphys.2010.08.010)
5. Adair RK (1971) Origins of muons which stop underground. *Lett Nuovo Cim* 2(17):891–894. doi:[10.1007/BF02774124](https://doi.org/10.1007/BF02774124). Cited in Ref. [6], however with an incorrect year: 1970[!] instead of 1971
6. Adair RK, Kasha H (1977) Cosmic-ray muons. In: Hughes VW, Wu CS (eds) *Muon physics. Volume 1: Electromagnetic interactions*. Academic Press, New York. Chap. 4
7. Adams MR et al [E665 Collaboration] (1995) Nuclear decay following deep inelastic scattering of 470 GeV muons. *Phys Rev Lett* 74(26):5198–5201. doi:[10.1103/PhysRevLett.74.5198](https://doi.org/10.1103/PhysRevLett.74.5198)
8. Adams MR et al [E665 Collaboration] (1998) Erratum: Nuclear decay following deep inelastic scattering of 470 GeV muons [Phys. Rev. Lett. 74, 5198 (1995)]. *Phys Rev Lett* 80(9):2020–2021. doi:[10.1103/PhysRevLett.80.2020](https://doi.org/10.1103/PhysRevLett.80.2020)
9. Agafonova NY [LVD Collaboration] (2005) Measurement of specific yield of neutrons produced by muons, using underground LVD detector. *Bull Russ Acad Sci Phys Ser* 69(3):459–461. As cited in Ref. [10]
10. Agafonova NY, Mal'gin AS (2013) Universal formula for the muon-induced neutron yield. arXiv:[1304.0919](https://arxiv.org/abs/1304.0919) [nucl-ex]
11. Agafonova NY et al [LVD Collaboration] (2011) Single and multiple muons and the generation of neutrons in the LVD experiment. *Bull Russ Acad Sci Phys Ser* 75(3):408–410. doi:[10.3103/S1062873811030038](https://doi.org/10.3103/S1062873811030038)
12. Agafonova N et al [LVD collaboration] (2005) The measurement of the total specific muon-generated neutron yield using LVD. In: Acharya BS et al (eds) *Proceedings of the 29th international cosmic ray conference, Pune, India, 3–10 Aug 2005, vol 9*. Tata Institute of Fundamental Research, Mumbai, pp 239–242. ADS: 2005ICRC....9..239A
13. Aglietta M et al (1989) Neutron flux generated by cosmic-ray mouns at 5200 hg/cm<sup>2</sup> s.r. underground. Depth-neutron intensity curve. *Nuovo Cim C* 12(4):467–477. doi:[10.1007/BF02525079](https://doi.org/10.1007/BF02525079)
14. Aglietta M et al (1995) Neutrino-induced and atmospheric single-muon fluxes measured over five decades of intensity by LVD at Gran Sasso Laboratory. *Astropart Phys* 3(4):311–320. doi:[10.1016/0927-6505\(95\)00012-6](https://doi.org/10.1016/0927-6505(95)00012-6). As cited in Ref. [114]
15. Aglietta M et al [LVD Collaboration] (1998) Muon “depth-intensity” relation measured by LVD underground experiment and cosmic-ray muon spectrum at sea level. *Phys Rev D* 58(9):092005. doi:[10.1103/PhysRevD.58.092005](https://doi.org/10.1103/PhysRevD.58.092005). arXiv:[hep-ex/9806001](https://arxiv.org/abs/hep-ex/9806001)
16. Agostinelli S et al [GEANT4 Collaboration] (2003) GEANT4—a simulation toolkit. *Nucl Instrum Methods Phys Res Sect A* 506(3):250–303. doi:[10.1016/S0168-9002\(03\)01368-8](https://doi.org/10.1016/S0168-9002(03)01368-8)
17. Ahlen SP (1980) Theoretical and experimental aspects of the energy loss of relativistic heavily ionizing particles. *Rev Mod Phys* 52(1):121–173. doi:[10.1103/RevModPhys.52.121](https://doi.org/10.1103/RevModPhys.52.121)
18. Ahn JK et al [RENO Collaboration] (2012) Observation of reactor electron antineutrinos disappearance in the RENO experiment. *Phys Rev Lett* 108(19):191802. doi:[10.1103/PhysRevLett.108.191802](https://doi.org/10.1103/PhysRevLett.108.191802)
19. Akimov D et al (2010) The ZEPLIN-III anti-coincidence veto detector. *Astropart Phys* 34(3):151–163. doi:[10.1016/j.astropartphys.2010.06.010](https://doi.org/10.1016/j.astropartphys.2010.06.010)

20. Albrow M, Raja R (eds) (2006) Hadronic shower simulation workshop, Batavia, IL, US, 6–8 Sept 2006. AIP conference proceedings, vol 896. AIP Publishing, Melville
21. Alexa C [TileCal System of the ATLAS Collaboration] (2003) A measurement of the photonuclear interactions of 180 GeV muons in iron. *Eur Phys J C* 28(3):297–304. doi:[10.1140/epjc/s2003-01176-6](https://doi.org/10.1140/epjc/s2003-01176-6). As cited in Ref. [193]
22. Allison J et al (2006) Geant4 developments and applications. *IEEE Trans Nucl Sci* 53(1):270–278. doi:[10.1109/TNS.2006.869826](https://doi.org/10.1109/TNS.2006.869826)
23. Ambrosio M et al [MACRO Collaboration] (1995) Vertical muon intensity measured with MACRO at the Gran Sasso laboratory. *Phys Rev D* 52(7):3793–3802. doi:[10.1103/PhysRevD.52.3793](https://doi.org/10.1103/PhysRevD.52.3793). As cited in Refs. [112, 114, 193]
24. Ambrosio M et al [MACRO Collaboration] (2003) Measurement of the residual energy of muons in the Gran Sasso underground laboratories. *Astropart Phys* 19(3):313–328. doi:[10.1016/S0927-6505\(02\)00217-7](https://doi.org/10.1016/S0927-6505(02)00217-7). arXiv:[hepex/0207043](https://arxiv.org/abs/hepex/0207043). As cited in Refs. [134, 193]
25. An FP et al (2012) Observation of electron-antineutrino disappearance at Daya Bay. *Phys Rev Lett* 108(17):171803. doi:[10.1103/PhysRevLett.108.171803](https://doi.org/10.1103/PhysRevLett.108.171803)
26. Andersen HH, Ziegler JF (1977) Hydrogen: stopping powers and ranges in all elements. The stopping and ranges of ions in matter 3. Pergamon Press, Oxford. As cited in Ref. [65]
27. Anderson CD, Neddermeyer SH (1936) Cloud chamber observations of cosmic rays at 4300 meters elevation and near sea-level. *Phys Rev* (2nd ser) 50(4):263–271. doi:[10.1103/PhysRev.50.263](https://doi.org/10.1103/PhysRev.50.263)
28. Andreev YM, Bezrukov LB, Bugaev EV (1994) Excitation of a target in muon bremsstrahlung. *Phys At Nucl* 57(12):2066–2074. Orig. pub. as *Yad Fiz* 57(12):2146–2154 [in Russian]. As cited in Refs. [65, 119]
29. Andreev YM, Bugaev EV (1997) Muon bremsstrahlung on heavy atoms. *Phys Rev D* 55(3):1233–1243. doi:[10.1103/PhysRevD.55.1233](https://doi.org/10.1103/PhysRevD.55.1233). As cited in Refs. [119, 125]
30. Andreyev YM, Gurentsov VI, Kogai IM (1987) Muon intensity from the Baksan Underground Scintillation Telescope. In: Kozyarivsky et al (eds) Proceedings of the 20th international cosmic ray conference, Moscow, USSR, 2–15 Aug 1987, vol 6. International union of pure and applied physics. Nauka, Moscow, pp 200–203. ADS: 1987ICRC....6..200A. As cited in Refs. [112, 114]
31. Annis M, Wilkins HC, Miller JD (1954) Nuclear interaction of fast  $\mu$  mesons. *Phys Rev* 2nd ser 94(4):1038–1045. doi:[10.1103/PhysRev.94.1038](https://doi.org/10.1103/PhysRev.94.1038)
32. Antonioli P et al (1997) A three-dimensional code for muon propagation through the rock: MUSIC. *Astropart Phys* 7(4):357–368. doi:[10.1016/S0927-6505\(97\)00035-2](https://doi.org/10.1016/S0927-6505(97)00035-2). arXiv:[hep-ph/9705408v2](https://arxiv.org/abs/hep-ph/9705408v2)
33. Apostolakis J et al (2009) Geometry and physics of the Geant4 toolkit for high and medium energy applications. *Radiat Phys Chem* 78(10):859–873. doi:[10.1016/j.radphyschem.2009.04.026](https://doi.org/10.1016/j.radphyschem.2009.04.026)
34. Araújo H et al (2005) Muon-induced neutron production and detection with GEANT4 and FLUKA. *Nucl Instrum Methods Phys Res Sect A* 545(1–2):398–411. doi:[10.1016/j.nima.2005.02.004](https://doi.org/10.1016/j.nima.2005.02.004). arXiv:[hep-ex/0411026](https://arxiv.org/abs/hep-ex/0411026)
35. Araújo H et al (2008) Measurements of neutrons produced by high-energy muons at the Boulby Underground Laboratory. *Astropart Phys* 29(6):471–481. doi:[10.1016/j.astropartphys.2008.05.004](https://doi.org/10.1016/j.astropartphys.2008.05.004)
36. Armengaud E et al [EDELWEISS Collaboration] (2010) First results of the EDELWEISS-II WIMP search using Ge cryogenic detectors with interleaved electrodes. *Phys Lett B* 687(4–5):294–298. doi:[10.1016/j.physletb.2010.03.057](https://doi.org/10.1016/j.physletb.2010.03.057). arXiv:[0912.0805](https://arxiv.org/abs/0912.0805) [astro-ph.CO]
37. Armstrong TA et al (1972) Total hadronic cross section of  $\gamma$  rays in hydrogen in the energy range 0.265–4.215 GeV. *Phys Rev D* 5(7):1640–1652. doi:[10.1103/PhysRevD.5.1640](https://doi.org/10.1103/PhysRevD.5.1640). As cited in Ref. [125]
38. Armstrong T et al (1972) The total photon deuteron hadronic cross section in the energy range 0.265–4.215 GeV. *Nucl Phys B* 41(2):445–473. doi:[10.1016/0550-3213\(72\)90403-8](https://doi.org/10.1016/0550-3213(72)90403-8). As cited in Ref. [125]

39. Barkas WH, Berger MJ (1964) Tables of energy losses and ranges of heavy charged particles. Scientific report NASA-SP-3013. National Aeronautic and Space Administration. [http://ntrs.nasa.gov/archive/nasa/casi.ntrs.nasa.gov/19650002906\\_1965002906.pdf](http://ntrs.nasa.gov/archive/nasa/casi.ntrs.nasa.gov/19650002906_1965002906.pdf). As cited in Refs. [65, 125]
40. Barkas WH, Birnbaum W, Smith FM (1956) Mass-ratio method applied to the measurement of  $L$ -meson masses and the energy balance in pion decay. *Phys Rev* (2nd ser) 101(2):778–795. doi:[10.1103/PhysRev.101.778](https://doi.org/10.1103/PhysRev.101.778). As cited in Refs. [65, 125]
41. Barkas WH, Dyer JN, Heckman HH (1963) Resolution of the  $\Sigma$ -mass anomaly. *Phys Rev Lett* 11(1):26–28. doi:[10.1103/PhysRevLett.11.26](https://doi.org/10.1103/PhysRevLett.11.26). As cited in Ref. [125]
42. Barrett PH et al (1952) Interpretation of cosmic-ray measurements far underground. *Rev Mod Phys* 24(3):133–178. doi:[10.1103/RevModPhys.24.133](https://doi.org/10.1103/RevModPhys.24.133). As cited in Refs. [6, 65, 178]
43. Barton JC (1983) The flux of neutrons in underground laboratories. In: Durgaprasad N et al (eds) Proceedings from the 18th international cosmic ray conference, Bangalore, India, 22 Aug–3 Sept 1983, vol 11. Tata Institute of Fundamental Research, Bombay, pp 462–465. ADS: 1983ICRC...11..462B
44. Barton JC (1985) The spectrum of neutrons at  $60 \text{ hg m}^{-2}$ . In: 19th international cosmic ray conference. Conference Papers, La Jolla, CA, US, 11–23 Aug 1985, vol 9. NASA conference publication, vol 2376. University of California, Scientific, Technical Information Branch, National Aeronautics, and Space Administration, Hampton, pp 98–101. ADS: 1985ICRC....8...98B
45. Baschiera B et al (1970) Experimental results on muons stopping underground ((60  $\div$  4500) m w.e.). *Lett Nuovo Cim* 4(4):121–123. doi:[10.1007/BF02755395](https://doi.org/10.1007/BF02755395). As cited in Ref. [6]
46. Battistoni G et al [MACRO Collaboration] (1998) Study of photo-nuclear interaction of muons in rock with the MACRO experiment. In: Giovannelli F, Mannocchi G (eds) Proceedings of the Vulcano workshop on frontier objects in astrophysics and particle physics, Vulcano, Italy, 25–30 May 1998. Italian Physical Society, Bologna. arXiv:[hep-ex/9809006](https://arxiv.org/abs/hep-ex/9809006). As cited in Ref. [193]
47. Battistoni G et al (2006) The FLUKA code: description and benchmarking. In: Albrow M, Raja R (eds) Hadronic shower simulation workshop, Batavia, IL, US, 6–8 Sept 2006. AIP conference proceedings, vol 896. AIP Publishing, Melville, pp 31–49. doi:[10.1063/1.2720455](https://doi.org/10.1063/1.2720455)
48. Bauer M, Jochum J, Scholl S (2005) Simulations of muon-induced neutron background with GEANT4. In: Spooner NJC, Kudryavtsev V (eds) The identification of dark matter. Proceedings of the fifth international workshop (IDM 2004), Edinburgh, UK, 6–10 Sept 2004. World Scientific, Singapore, pp 494–498. doi:[10.1142/9789812701848\\_0075](https://doi.org/10.1142/9789812701848_0075)
49. Beckurts KH, Wirtz K (1964) Neutron physics. Springer, Berlin
50. Bellini G et al [Borexino Collaboration] (2011) Muon and cosmogenic neutron detection in Borexino. *J Instrum* 6(05):P05005. doi:[10.1088/1748-0221/6/05/P05005](https://doi.org/10.1088/1748-0221/6/05/P05005)
51. Bellini G et al [Borexino Collaboration] (2013) Cosmogenic backgrounds in Borexino at 3800 m water-equivalent depth. *J Cosmol Astropart Phys* 2013(08):049. doi:[10.1088/1475-7516/2013/08/049](https://doi.org/10.1088/1475-7516/2013/08/049). arXiv:[1304.7381](https://arxiv.org/abs/1304.7381) [physics.ins-det]
52. Bergamasco L (1970) Experimental results on the pion and neutron production by muons at 60 and 110 m w.e. *Nuovo Cim B* 66(1):120–128. doi:[10.1007/BF02710194](https://doi.org/10.1007/BF02710194)
53. Bergamasco L, Costa S, Picchi P (1973) Experimental results on neutron production by muons at 4300 m w.e. *Nuovo Cim. A* 13:403–412. doi:[10.1007/BF02827344](https://doi.org/10.1007/BF02827344)
54. Bergamasco L, Piazzoli B, Picchi P (1971) Muon intensities underground ((50/4300) m w.e.) and the S. L. energy spectrum. *Nuovo Cim B* 4(1):59–67. doi:[10.1007/BF02737564](https://doi.org/10.1007/BF02737564)
55. Berger C et al [Fréjus Collaboration] (1987) The fréjus nucleon decay detector. *Nucl Instrum Methods Phys Res Sect A* 262:463–495. doi:[10.1016/0168-9002\(87\)90890-4](https://doi.org/10.1016/0168-9002(87)90890-4)
56. Berger C et al [Fréjus Collaboration] (1989) Experimental study of muon bundles observed in the Fréjus detector. *Phys Rev D* 40(7):2163–2171. doi:[10.1103/PhysRevD.40.2163](https://doi.org/10.1103/PhysRevD.40.2163)
57. Berger E [RD 34 Collaboration] (1997) A measurement of the energy loss spectrum of 150 GeV muons in iron. *Z Phys C* 73(3):455–463. doi:[10.1007/s002880050335](https://doi.org/10.1007/s002880050335). As cited in Ref. [125]
58. Berger MJ (2012) Radiation dosimetry data—stopping-power and range tables for electrons, protons, and helium ions. National Institute of Standards and Technology. <http://www.nist.gov/pml/data/radiation.cfm>

59. Bethe H (1930) Zur Theorie des Durchgangs schneller Korpuskularstrahlen durch Materie [in German]. *Ann Phys* 397(3):325–400. doi:[10.1002/andp.3970303](https://doi.org/10.1002/andp.3970303). As cited in Ref. [65]
60. Bethe H (1932) Bremsformel für Elektronen relativistischer Geschwindigkeit' [in German]. *Z Phys* 76(5):293–299. doi:[10.1007/BF01342532](https://doi.org/10.1007/BF01342532). As cited in Ref. [200]
61. Bethe H, Heitler W (1934) On the stopping of fast particles and on the creation of positive electrons. *Proc R Soc Lond Ser A* 146(856):83–112. <http://www.jstor.org/stable/2935479>. As cited in Refs. [65, 125, 126]
62. Bezrukov LB, Bugaev ÉV (1981) Nucleon shadowing effects in photonuclear interactions (trans: Toker G). *Sov J Nucl Phys* 33(5):635–641. Orig. pub. as *Yad Fiz* 33:1195–1207 [in Russian]. As cited in Refs. [65, 112, 119, 125]
63. Bezrukov LB et al (1973) Investigation of the depth-intensity curve of the nuclear events induced by cosmic-ray muons (trans: Adashko JG). *Sov J Nucl Phys* 17(1):51–53. Orig. pub. as *Yad Fiz* 17:98–103 [in Russian]
64. Bianchi N et al (1996) Total hadronic photoabsorption cross-section on nuclei in the nucleon resonance region. *Phys Rev C* 54:1688–1699. doi:[10.1103/PhysRevC.54.1688](https://doi.org/10.1103/PhysRevC.54.1688). As cited in Ref. [134]
65. Bichsel H, Groom DE, Klein SR (2010) Passage of particles through matter. In Chap. 24. In: Nakamura K et al [Particle Data Group] (eds) Review of particle physics. *J Phys G: Nucl Part Phys* 37(7A):075021. doi:[10.1088/0954-3899/37/7A/075021](https://doi.org/10.1088/0954-3899/37/7A/075021)
66. Bichsel H (1988) Straggling in thin silicon detectors. *Rev Mod Phys* 60(3):663–699. doi:[10.1103/RevModPhys.60.663](https://doi.org/10.1103/RevModPhys.60.663). As cited in Ref. [65]
67. Bichsel H (1992) Stopping power and ranges of fast ions in heavy elements. *Phys Rev A* 46(9):5761–5773. doi:[10.1103/PhysRevA.46.5761](https://doi.org/10.1103/PhysRevA.46.5761). As cited in Refs. [65, 125]
68. Bilokon H et al (1989) Flux of the vertical negative muons stopping at depths 0.35–1000 hg/cm<sup>2</sup>. *J Geophys Res: Solid Earth* 94(B9):12145–12152. doi:[10.1029/JB094iB09p12145](https://doi.org/10.1029/JB094iB09p12145). As cited in Refs. [112, 215]
69. Bilokon H et al (1991) Underground survival probabilities of high energy muons in the depth range 3100–10 100 hg/cm<sup>2</sup> of standard rock. *Nucl Instrum Methods Phys Res Sect A* 303(2):381–392. doi:[10.1016/0168-9002\(91\)90805-Z](https://doi.org/10.1016/0168-9002(91)90805-Z). As cited in Ref. [215]
70. Bloch F (1933) Zur Bremsung rasch bewegter Teilchen beim Durchgang durch Materie [in German]. *Ann Phys* 408(3):1521–3889. doi:[10.1002/andp.19334080303](https://doi.org/10.1002/andp.19334080303)
71. Blyth S et al (2013) An apparatus for studying spallation neutrons in the Aberdeen Tunnel laboratory. *Nucl Instrum Methods Phys Res Sect A* 723:67–82. doi:[10.1016/j.nima.2013.04.035](https://doi.org/10.1016/j.nima.2013.04.035)
72. Boehm F et al (2000) Neutron production by cosmic-ray muons at shallow depth. *Phys Rev D* 62:092005. doi:[10.1103/PhysRevD.62.092005](https://doi.org/10.1103/PhysRevD.62.092005). arXiv:[hep-ex/0006014](https://arxiv.org/abs/hep-ex/0006014)
73. Bogdanov A et al (2006) Geant4 simulation of production and interaction of muons. *IEEE Trans Nucl Sci* 53(2):513–519. doi:[10.1109/TNS.2006.872633](https://doi.org/10.1109/TNS.2006.872633)
74. Borog VV, Petrukhin AA (1975) The cross-section of the nuclear interaction of high energy muons. In: Pinkau K (ed) Proceedings from the 14th international cosmic ray conference, Munich, Germany, 15–29 Aug 1975, vol 6. Max-Planck-Institut für extraterrestrische Physik, Munich, pp 1949–1954. ADS: 1975ICRC...6.1949B. As cited in Ref. [119]
75. Bowden N, Sweany M, Dazeley S (2012) A note on neutron capture correlation signals, backgrounds, and efficiencies. *Nucl Instrum Methods Phys Res Sect A* 693:209–214. doi:[10.1016/j.nima.2012.07.005](https://doi.org/10.1016/j.nima.2012.07.005)
76. Bozóki G et al (eds) (1969) Proceedings of the 11th international conference on cosmic rays: invited papers and rapporteur talks, Budapest, Hungary, 25 Aug–4 Sept 1969, vol 4. *Acta Phys Acad Sci Hung* 29 Suppl. Central Research Institute for Physics. 1970. ADS: 1970ICRC....5....B
77. Bragg WH, Kleeman R (1905) XXXIX. On the  $\alpha$  particles of radium, and their loss of range in passing through various atoms and molecules. *Philos Mag* (6th ser) 10(57):318–340. doi:[10.1080/14786440509463378](https://doi.org/10.1080/14786440509463378). As cited in Ref. [125]
78. Brodsky SJ, Close FE, Gunion JF (1972) Phenomenology of photon processes, vector dominance, and crucial tests for parton models. *Phys Rev D* 6(1):177–189. doi:[10.1103/PhysRevD.6.177](https://doi.org/10.1103/PhysRevD.6.177). As cited in Ref. [119]

79. Bugaev EV et al (1998) Atmospheric muon flux at sea level, underground and underwater. *Phys Rev D* 58:054001. doi:[10.1103/PhysRevD.58.054001](https://doi.org/10.1103/PhysRevD.58.054001) arXiv: [hep-ph/9803488](https://arxiv.org/abs/hep-ph/9803488). As cited in Ref. [112]
80. Caldwell DO et al (1979) Measurement of shadowing in photon-nucleus total cross sections from 20 to 185 GeV. *Phys Rev Lett* 42(9):553–556. doi:[10.1103/PhysRevLett.42.553](https://doi.org/10.1103/PhysRevLett.42.553). As cited in Ref. [119]
81. Cassiday GL, Keuffel JW, Thompson JA (1973) Calculation of the stoppingmuon rate underground. *Phys Rev D* 7:2022–2031. doi:[10.1103/PhysRevD.7.2022](https://doi.org/10.1103/PhysRevD.7.2022). As cited in Refs. [113, 192]
82. Chadwick MB et al (1991) Pauli-blocking in the quasideuteron model of photoabsorption. *Phys Rev C* 44(2):814–823. doi:[10.1103/PhysRevC.44.814](https://doi.org/10.1103/PhysRevC.44.814). As cited in Ref. [112]
83. Chanfray G et al (1993) Quasi-elastic delta excitation in the charge response of the nucleus. *Nucl Phys A* 556(3):439–452. doi:[10.1016/0375-9474\(93\)90371-4](https://doi.org/10.1016/0375-9474(93)90371-4). As cited in Ref. [112]
84. Charalambus S (1971) Nuclear transmutation by negative stopped muons and the activity induced by the cosmic-ray muons. *Nucl Phys A* 166(2):145–161. doi:[10.1016/0375-9474\(71\)90419-2](https://doi.org/10.1016/0375-9474(71)90419-2). As cited in Ref. [112]
85. Chazal V et al (1998) Neutron background measurements in the underground laboratory of Modane. *Astropart Phys* 9(2):163–172. doi:[10.1016/S0927-6505\(98\)00012-7](https://doi.org/10.1016/S0927-6505(98)00012-7)
86. Chazal V et al (2002) Investigations of fast neutron production by 190 GeV/c muon interactions on graphite target. *Nucl Instrum Methods Phys Res Sect A* 490:334–343. doi:[10.1016/S0168-9002\(02\)01006-9](https://doi.org/10.1016/S0168-9002(02)01006-9). arXiv:[hep-ex/0102028](https://arxiv.org/abs/hep-ex/0102028)
87. Cheung H, Tsoi T (2012) The Aberdeen tunnel experiment. <http://www.phy.cuhk.edu.hk/gee/mctalks/aberdeen.pdf>. Accessed 09 July 2012
88. Chirkin D (2007) Fluxes of atmospheric leptons at 600 GeV - 60 TeV. arXiv: [hep-ph/0407078](https://arxiv.org/abs/hep-ph/0407078)
89. Christy RF, Kusaka S (1941) The interaction of  $\gamma$ -rays with mesotrons. *Phys Rev* (2nd ser) 59(5):405–414. doi:[10.1103/PhysRev.59.405](https://doi.org/10.1103/PhysRev.59.405)
90. Chu M (2011) The Aberdeen tunnel experiment. [http://dayabay.physics.hku.hk/underground/talks/Aberdeen\\_tunnel\\_experiment.pdf](http://dayabay.physics.hku.hk/underground/talks/Aberdeen_tunnel_experiment.pdf). Accessed 27 May 2011
91. Cocconi G, Tongiorgi VC (1951) Nuclear disintegrations induced by  $\mu$ -mesons. *Phys Rev* (2nd ser) 84(1):29–36. doi:[10.1103/PhysRev.84.29](https://doi.org/10.1103/PhysRev.84.29)
92. Collins PDB (1977) An introduction to Regge theory and high energy physics. Cambridge monographs on mathematical physics 4. Cambridge University Press, Cambridge. doi:[10.1017/CBO9780511897603](https://doi.org/10.1017/CBO9780511897603). As cited in Ref. [134]
93. Crouch M (1987) An improved world survey expression for cosmic ray vertical intensity vs. depth in standard rock. In: Kozyarivsky VA et al (eds) Proceedings of the 20th international cosmic ray conference, Moscow, USSR, 2–15 Aug 1987, vol 6. International Union of Pure and Applied Physics. Nauka, Moscow, pp 165–168. ADS: 1987ICRC....6.165C. As cited in refs. [112, 113]
94. Crouch MF, Sard RD (1952) The distribution of multiplicities of neutrons produced by cosmic-ray  $\mu$ -mesons captured in lead. *Phys Rev* (2nd ser) 85(1):120–129. doi:[10.1103/PhysRev.85.120](https://doi.org/10.1103/PhysRev.85.120)
95. Daiyasu K et al (1962) On hard showers produced by  $\mu$ -mesons'. In: Maeda K, Minakawa O (eds) Proceedings of the international cosmic ray conference 1961 and the earth storm, Kyoto, Japan, 4–15 Sept 1961, vol 3. Journal of the Physical Society of Japan: Supplement 17/A/3. Physical Society of Japan, Tokyo, pp 344–347. As cited in Ref. [126]
96. Dalitz RH, Yennie DR (1957) Pion production in electron-proton collisions. *Phys Rev* (2nd ser) 105(5):1598–1615. doi:[10.1103/PhysRev.105.1598](https://doi.org/10.1103/PhysRev.105.1598). As cited in Ref. [112]
97. Day D (2011) Electromagnetic nuclear interactions at GeV energies—can electron cattering data contribute to an understanding of the backgrounds? Presented at the cosmogenic activity and backgrounds workshop, Berkeley, CA, US, 13–15 April 2011. <https://docs.sanfordlab.org/docushare/dsweb/View/Wiki-141/Agenda/DD-Cosmogenic.pdf>
98. Daya Bay reactor neutrino experiment and Aberdeen tunnel underground cosmic ray experiment: the detector. <http://dayabay.physics.hku.hk/lab.html#detector>. Accessed 09 July 2012. Homepage > Aberdeen > The Detector

99. Degtyarenko P, Kossov M, Wellisch H-P (2000) Chiral invariant phase space event generator: I. Nucleon-antinucleon annihilation at rest. *Eur Phys J A* 8(2):217–222. doi:[10.1007/s100500070108](https://doi.org/10.1007/s100500070108). As cited in Ref. [257]
100. Degtyarenko P, Kossov M, Wellisch H-P (2000) Chiral invariant phase space event generator: II. Nuclear pion capture at rest and photonuclear reactions below the (3, 3) resonance. *Eur Phys J A* 9(3):411–420. doi:[10.1007/s100500070025](https://doi.org/10.1007/s100500070025). As cited in Ref. [257]
101. Degtyarenko P, Kossov M, Wellisch H-P (2000) Chiral invariant phase space event generator: III. Modeling of real and virtual photon interactions with nuclei below pion production threshold. *Eur Phys J A* 9(3):421–424. doi:[10.1007/s100500070026](https://doi.org/10.1007/s100500070026). As cited in Ref. [257]
102. Delorme J et al (1995) Pion and neutron production by cosmic ray muons underground. *Phys Rev C* 52(4):2222–2230. doi:[10.1103/PhysRevC.52.2222](https://doi.org/10.1103/PhysRevC.52.2222). arXiv:[hep-ph/9504331](https://arxiv.org/abs/hep-ph/9504331). As cited in Ref. [112]
103. Donnachie A, Landshoff P (1992) Total cross sections. *Phys Lett B* 296(1–2):227–232. doi:[10.1016/0370-2693\(92\)90832-O](https://doi.org/10.1016/0370-2693(92)90832-O). As cited in Ref. [112]
104. Engel R, Heck D, Pierog T (2011) Extensive air showers and hadronic interactions at high energy. *Annu Rev Nucl Part Sci* 61(1):467–489. doi:[10.1146/annurev.nucl.012809.104544](https://doi.org/10.1146/annurev.nucl.012809.104544)
105. Enikeev RI et al (1981) Investigation of muon inelastic scattering with energy up to  $5 \cdot 10^{12}$  eV. In: Auger P et al (eds) 17th international cosmic ray conference. Proceedings of a conference held at Paris, France, 13–25 July 1981, by the Commissariat à l’Energie Atomique and the International Union of Pure and Applied Physics, Paris, France, 13–25 July 1981, vol 10. Commissariat à l’Energie Atomique, the International Union of Pure, and Applied Physics. Centre d’Etudes Nucléaires de Saclay, Gif-sur-Yvette, pp 359–362. ADS: 1981ICRC...10..359E
106. Enikeev RI et al (1987) Hadrons generated by cosmic-ray muons underground (trans: Robinson CS). *Sov J Nucl Phys* 46(5):883–889. Orig. pub. as *Yad Fiz* 46:1492–1501 [in Russian]. As cited in Refs. [112, 193]
107. Fermi E (1924) Über die Theorie des Stoßes zwischen Atomen und elektrisch geladenen Teilchen [in German]. *Phys Z* 29(1):315–327. doi:[10.1007/BF03184853](https://doi.org/10.1007/BF03184853). As cited in Ref. [112]
108. Ferrari A et al (2005) FLUKA: a multi-particle transport code. <http://cdsweb.cern.ch/record/898301/files/CERN-2005-010.pdf>
109. FLUKA homepage: Low-energy neutrons in FLUKA. [http://www.fluka.org/fluka.php?id=man\\_onl&sub=96](http://www.fluka.org/fluka.php?id=man_onl&sub=96). Accessed 11 Sept 2012. FLUKA homepage > Documentation > Manuals > Online Manual > 10 Low-energy neutrons in FLUKA
110. Folger G, Ivanchenko V, Wellisch J (2004) The binary cascade. *Eur Phys J A* 21(3):407–417. doi:[10.1140/epja/i2003-10219-7](https://doi.org/10.1140/epja/i2003-10219-7). As cited in Ref. [257]
111. Folger G, Wellisch JP (2007) String parton models in Geant4. arXiv:[nucl-th/0306007](https://arxiv.org/abs/nucl-th/0306007). As cited in Ref. [257]
112. Formaggio JA, Martoff CJ (2004) Backgrounds to sensitive experiments underground. *Annu Rev Nucl Part Sci* 54:361–412. doi:[10.1146/annurev.nucl.54.070103.181248](https://doi.org/10.1146/annurev.nucl.54.070103.181248)
113. Gaisser TK (1991) Cosmic rays and particle physics. 1. publ., repr. ed. Cambridge University Press, Cambridge
114. Gaisser T, Stanev T (2010) Cosmic rays. In Chap. 24. In: Nakamura K et al [Particle Data Group] (eds) Review of particle physics. *J Phys G Nucl Part Phys* 37(7A):075021. doi:[10.1088/0954-3899/37/7A/075021](https://doi.org/10.1088/0954-3899/37/7A/075021)
115. Gaisser T, Stanev T (1985) Muon bundles in underground detectors. *Nucl Instrum Methods Phys Res Sect A* 235(1):183–192. doi:[10.1016/0168-9002\(85\)90260-8](https://doi.org/10.1016/0168-9002(85)90260-8). As cited in Ref. [215]
116. Galbiati C, Beacom JF (2005) Measuring the cosmic ray muon-induced fast neutron spectrum by  $(n, p)$  isotope production reactions in underground detectors. *Phys Rev C* 72(2):025807. doi:[10.1103/PhysRevC.72.025807](https://doi.org/10.1103/PhysRevC.72.025807)
117. Galbiati C, Beacom JF (2006) Erratum: Measuring the cosmic ray muon-induced fast neutron spectrum by  $(n, p)$  isotope production reactions in underground detectors [Phys. Rev. C 72, 025807 (2005)]. *Phys Rev C* 73(4):049906. doi:[10.1103/PhysRevC.73.049906](https://doi.org/10.1103/PhysRevC.73.049906)

118. Galbiati C et al (2005) Cosmogenic  $^{11}\text{C}$  production and sensitivity of organic scintillator detectors to pep and CNO neutrinos. *Phys Rev C* 71(5):055805. doi:[10.1103/PhysRevC.71.055805](https://doi.org/10.1103/PhysRevC.71.055805)
119. Geant4 Collaboration (2009) Physics reference manual. Version: geant4 9.3. 2009. <http://geant4.web.cern.ch/geant4/UserDocumentation/UsersGuides/PhysicsReferenceManual/BackupVersions/V9.3/fo/PhysicsReferenceManual.pdf>
120. Gorshkov GV, Zyabkin VA (1968) Production of neutrons in Pb, Cd, Fe, and Al under the influence of cosmic-ray muons at a depth of 150 in water equivalent (trans: Adashko JG). *Sov J Nucl Phys.* 7(4):470–474. Orig. pub. As *Yad Fiz* 7:770–777 [in Russian]
121. Gorshkov GV, Zyabkin VA (1970) Neutron production in Pb at a depth of 150 m w.e. under the influence of cosmic-radiation mesons traveling at large zenith angles (trans: Adashko JG). *Sov J Nucl Phys* 12(2):187–190 (1971). Orig. pub. as *Yad Fiz* 12:340–346 [in Russian]
122. Gorshkov GV, Zyabkin VA, Yakovlev RM (1974) Production of neutrons in Pb, Cd, Fe, and Al by high energy muons (trans: Adashko JG). *Sov J Nucl Phys* 18(1):57–61. Orig. pub. as *Yad Fiz* 18:109–117 [in Russian]
123. Gorshkov GV, Zyabkin VA, Yakovlev RM (1971) Production of neutrons in Pb, Cd, Fe, and Al and fission of Pb nuclei by cosmic rays in the depth range 0–1000 m water equiv (trans: Robinson CS). *Sov J Nucl Phys* 13(4):450–452. Orig. pub. as *Yad Fiz* 13:791–796 [in Russian]
124. Goulard B, Primakoff H (1974) Nuclear muon-capture sum rules and mean nuclear excitation energies. *Phys Rev C* 10(5):2034–2044. doi:[10.1103/PhysRevC.10.2034](https://doi.org/10.1103/PhysRevC.10.2034). As cited in Ref. [112]
125. Groom DE, Mokhov NV, Striganov SI (2001) Muon stopping power and range tables 10 MeV–100 TeV. *At Data Nucl Data Tables* 78(2):183–356. doi:[10.1006/adnd.2001.0861](https://doi.org/10.1006/adnd.2001.0861)
126. Grupen C (1976) Electromagnetic interactions of high energy cosmic ray muons. *Fort Phys* 23(3):127–209. doi:[10.1002/prop.19760240302](https://doi.org/10.1002/prop.19760240302). As cited in Ref. [215]
127. Grupen C, Wolfendale A, Young E (1972) Stopping particles underground. *Nuovo Cim B* 10(1):144–154. doi:[10.1007/BF02911416](https://doi.org/10.1007/BF02911416). As cited in Refs. [10, 215]
128. Hand LN (1963) Experimental investigation of pion electroproduction. *Phys Rev* (2nd ser) 129(4):1834–1846. doi:[10.1103/PhysRev.129.1834](https://doi.org/10.1103/PhysRev.129.1834). As cited in Refs. [119, 126]
129. Heck D et al (1998) CORSIKA: A Monte Carlo code to simulate extensive air showers. Scientific report FZKA 6019, Forschungszentrum Karlsruhe. <http://bibliothek.fzk.de/zb/berichte/FZKA6019.pdf>
130. Hennings-Yeomans R, Akerib D (2007) A neutron multiplicity meter for deep underground muon-induced high-energy neutron measurements. *Nucl Instrum Methods Phys Res Sect A* 574(1):89–97. doi:[10.1016/j.nima.2007.01.137](https://doi.org/10.1016/j.nima.2007.01.137)
131. Hertenberger R, Chen M, Dougherty BL (1995) Muon induced neutron and pion production in an organic liquid scintillator at a shallow depth. *Phys Rev C* 52:3449–3459. doi:[10.1103/PhysRevC.52.3449](https://doi.org/10.1103/PhysRevC.52.3449)
132. Hillas AM (2006) Cosmic rays: recent progress and some current questions. In: Klöckner H-R et al (eds) Cosmology, galaxy formation and astroparticle physics on the pathway to the SKA. Proceedings of the conference held in Oxford on the 10–12 April 2006, Oxford. ASTRON, Dwingeloo. arXiv:[astro-ph/0607109](https://arxiv.org/abs/astro-ph/0607109)
133. Hörandel JR (2003) On the knee in the energy spectrum of cosmic rays. *Astropart Phys* 19(2):193–220. doi:[10.1016/S0927-6505\(02\)00198-6](https://doi.org/10.1016/S0927-6505(02)00198-6)
134. Horn OM (2007) Simulations of the muon-induced neutron background of the EDELWEISS-II experiment for Dark Matter search. Scientific report FZKA 7391, Forschungszentrum Karlsruhe. <http://bibliothek.fzk.de/zb/berichte/FZKA7391.pdf>. Orig. pub. as PhD dissertation, Universität Karlsruhe (TH). <http://digibib.ubka.uni-karlsruhe.de/volltexte/1000007402>
135. Hubbell J (2006) Electron-positron pair production by photons: a historical overview. *Radiat Phys Chem* 75(6):614–623. doi:[10.1016/j.radphyschem.2005.10.008](https://doi.org/10.1016/j.radphyschem.2005.10.008). Pair Production
136. International Commission on Radiation (1984) Stopping powers for electrons and positrons. ICRU Report 37, International Commission on Radiation, Bethesda, MD. As cited in Ref. [65]
137. International Commission on Radiation (1993) Stopping powers and ranges for proton and alpha particles. ICRU Report 49, International Commission on Radiation, Bethesda, MD. As cited in Ref. [65]

138. International Atomic Energy Agency (1999) Handbook of photonuclear data for applications: Cross sections and spectra. Technical report IAEA-TECDOC-1178. International Atomic Energy Agency, Vienna. <http://www-pub.iaea.org/books/iaeabooks/6043/Handbook-on-Photonuclear-Data-for-Applications-Cross-sections-and-Spectra>. See also Ref. [139]
139. International Atomic Energy Agency (2012) IAEA photonuclear data library. <http://www-nds.iaea.org/photonuclear/>
140. Ivanov D et al (1998) Production of  $e^+e^-$  pairs to all orders in  $Z\alpha$  for collisions of highenergy muons with heavy nuclei. *Phys Lett B* 442(1–4):453–458. doi:[10.1016/S0370-2693\(98\)01278-7](https://doi.org/10.1016/S0370-2693(98)01278-7). As cited in Ref. [65]
141. Jackson JD (1998) Electromagnetic form factor corrections to collisional energy loss of pions and protons, and spin correction for muons. *Phys Rev D* 59(1):017301. doi:[10.1103/PhysRevD.59.017301](https://doi.org/10.1103/PhysRevD.59.017301). As cited in Ref. [125]
142. Jackson JD, McCarthy RL (1972)  $z3$  corrections to energy loss and range. *Phys Rev B* 6(11):4131–4141. doi:[10.1103/PhysRevB.6.4131](https://doi.org/10.1103/PhysRevB.6.4131)
143. Kang K-J et al [CDEX Collaboration] (2013) Introduction of the CDEX experiment. [arXiv:1303.0601](https://arxiv.org/abs/1303.0601) [physics.ins-det]
144. Kang KJ et al (2010) Status and prospects of a deep underground laboratory in China. *J Phys Conf Ser* 203(1):012028. doi:[10.1088/1742-6596/203/1/012028](https://doi.org/10.1088/1742-6596/203/1/012028)
145. Kel'ner SR (1998) Pair production in collisions between muons and atomic electrons (trans: Isaakyan A). *Phys At Nucl* 61:448–456. Orig. pub. as *Yad Fiz* 61(3):511–519 [in Russian]. As cited in Refs. [119, 125]
146. Kel'ner SR, Kokoulin RP, Petrukhin AA (1995) About cross section for high-energy muon bremsstrahlung. Scientific report MEPhI 024–95, State Committee of the Russian Federation in Higher Education—Moscow State Engineering Physics Institute (Technical University), Moscow. <http://cdsweb.cern.ch/record/288828/files/MEPHI-024-95.pdf>. As cited in Refs. [119, 125]
147. Kel'ner SR, Kokoulin RP, Petrukhin AA (1997) Bremsstrahlung from muons scattered by atomic electrons (trans: Rogalyov R). *Phys At Nucl* 60(4):576–583. Orig. pub. as *Yad Fiz* 60(4):657–665 [in Russian]. As cited in Refs. [119, 125]
148. Kel'ner SR, Kokoulin RP, Petrukhin AA (1999) Radiation logarithm in the hartree-fock model (trans: Kobrinsky M). *Phys At Nucl* 62:1894–1898. Orig. pub. as *Yad Fiz* 62(11):2042–2048 [in Russian]. As cited in Ref. [125]
149. Kel'ner SR, Kotov YD (1968) Pair production by muons in the field of nuclei. *Can J Phys* 46(10):S387–S390. doi:[10.1139/p68-253](https://doi.org/10.1139/p68-253). As cited in Ref. [6]
150. Kessler D, Kessler P (1956) On the validity of the Williams-Weizsäcker method and the problem of the nuclear interactions of relativistic  $\mu$ -mesons. *Nuovo Cim* 4(3):601–609. doi:[10.1007/BF02745385](https://doi.org/10.1007/BF02745385). As cited in Ref. [126]
151. Kessler P (1960) Sur une méthode simplifiée de calcul pour les processus relativistes en électrodynamique quantique [in French]. *Nuovo Cim* 17(6):809–829. doi:[10.1007/BF02732124](https://doi.org/10.1007/BF02732124). As cited in Ref. [126]
152. Khal'chukov FF et al (1995) Hadrons and other secondaries generated by cosmic ray muons underground. *Nuovo Cim C* 18(5):517–529. doi:[10.1007/BF02506782](https://doi.org/10.1007/BF02506782)
153. Khal'chukov F et al (1983) High-energy hadron background in proton decay experiments. *Nuovo Cim C* 6(3):320–326. doi:[10.1007/BF02507819](https://doi.org/10.1007/BF02507819)
154. Kobayakawa K (1967) Fluctuations and nuclear interactions in the energy loss of cosmic-ray muons. *Nuovo Cim B* 47(2):156–184. doi:[10.1007/BF02710720](https://doi.org/10.1007/BF02710720). As cited in Ref. [6]
155. Koi T (2014) A Geant4 physics list for shielding calculations. In: Shielding aspects of accelerators, targets and irradiation facilities—SATIF 10: workshop proceedings, Geneva, Switzerland, 2–4 June 2010. OECD/Nuclear Energy Agency. OECD Publishing, Paris, pp 407–412. doi:[10.1787/9789264096509-en](https://doi.org/10.1787/9789264096509-en). As cited in Ref. [214]
156. Kokoulin RP, Petrukhin AA (1969) Analysis of the cross-section of direct pair production by fast muons. In: Bozóki G et al (eds) Proceedings of the 11th international conference on cosmic rays. Invited papers and rapporteur talks, Budapest, Hungary, 25 Aug–4 Sept 1969, vol 4. *Acta Phys Acad Sci Hung* 29 (Suppl). Central Research Institute for Physics, pp 277–284. ADS: 1970ICRC....4..277K. As cited in Ref. [119]

157. Kokoulin RP, Petrukhin AA (1971) Influence of the nuclear formfactor on the cross-section of electron pair production by high energy muons. In: Cosmic ray conference papers: 12th international conference on cosmic rays, Hobart, Tasmania, Australia, 16–25 Aug 1971, vol 4. University of Tasmania, Tasmania, Australia, p 1446. ADS: 1971ICRC....4.1446K. As cited in Ref. [65]
158. Kotera K, Olinto AV (2011) The astrophysics of ultrahigh-energy cosmic rays. *Annu Rev Astron Astrophys* 49(1):119–153. doi:[10.1146/annurevastro-081710-102620](https://doi.org/10.1146/annurevastro-081710-102620)
159. Kotov YD, Logunov VM (1969) Energy losses and the absorption curve of muons. In: Somogyi A (ed) Proceedings of the 11th international conference on cosmic rays. Invited papers and rapporteur talks, Budapest, Hungary, 25 Aug–4 Sept 1969, vol 4. Acta Phys Acad Sci Hung 29(Suppl). Central Research Institute for Physics, pp 73–79. ADS: 1970ICRC....5.....B. As cited in Ref. [6]
160. Kozyarivsky VA et al (eds) (1987) Proceedings of the 20th international cosmic ray conference, Moscow, USSR, 2–15 Aug 1987. International union of pure and applied physics. Nauka, Moscow. ADS: 1987ICRC...20.....K
161. Kudryavtsev VA, Korol'kova EV, Spooner NJC (1999) Narrow muon bundles from muon pair production in rock. *Phys Lett B* 471(2–3):251–256. doi:[10.1016/S0370-2693\(99\)01378-7](https://doi.org/10.1016/S0370-2693(99)01378-7) arXiv:[hep-ph/9911493v1](https://arxiv.org/abs/hep-ph/9911493v1)
162. Kudryavtsev VA, Spooner NJC, McMillan JE (2003) Simulations of muoninduced neutron flux at large depths underground. *Nucl Instrum Methods Phys Res Sect A* 505(3):688–698. doi:[10.1016/S0168-9002\(03\)00983-5](https://doi.org/10.1016/S0168-9002(03)00983-5). arXiv:[hep-ex/0303007](https://arxiv.org/abs/hep-ex/0303007)
163. Kudryavtsev V, Pandola L, Tomasello V (2008) Neutron- and muon-induced background in underground physics experiments. *Eur Phys J A* 36(2):171–180. doi:[10.1140/epja/i2007-10539-6](https://doi.org/10.1140/epja/i2007-10539-6)
164. Kudryavtsev V (2009) Muon simulation codes MUSIC and MUSUN for underground physics. *Comput Phys Commun* 180(3):339–346. doi:[10.1016/j.cpc.2008.10.013](https://doi.org/10.1016/j.cpc.2008.10.013)
165. Kudryavtsev V [For the LVD Collaboration] (1999) Measurement of the neutron flux produced by cosmic-ray muons with LVD at Gran Sasso. In: Kieda D, Salamon M, Dingus B (eds) Proceedings of the 26th international cosmic ray conference, Salt Lake City, UT, US, 17–25 Aug 1999, vol 2. University of Utah/American Institute of Physics, Salt Lake City (UT), USA, pp 44–48. arXiv:[hep-ex/9905047](https://arxiv.org/abs/hep-ex/9905047)
166. Kudryavtsev VA Simulation of muons at LSM. Internal note for the EDELWEISS collaboration
167. Landau LD (1944) On the energy loss of fast particles by ionization. In: Ter Haar D (ed) Collected papers of L. D. Landau. Pergamon Press, Oxford. Chap. 56. Orig. pub. as *Zh Eksp Teor Fiz* 8:201 [in Russian]
168. Landau LD, Lifshitz EM (1971) Relativistic quantum theory. Course of theoretical physics, vol 4. Pergamon Press, Oxford, p 351. As cited in Ref. [112]
169. Landau LD, Pomeranchuk I (1953) Electron-cascade processes at ultra-high energies. In: Ter Haar D (ed) Collected papers of L. D. Landau. Pergamon Press, Oxford. Chap. 76. Orig. pub. as *Dokl Akad Nauk SSSR* 92(4):735–738 [in Russian]
170. Landau LD, Pomeranchuk I (1965) The limits of applicability of the theory of Bremsstrahlung by electrons and of the creation of pairs at large energies. In: Ter Haar D (eds) Collected papers of L. D. Landau. Pergamon Press, Oxford. Chap. 75. Orig. pub. as *Dokl Akad Nauk SSSR* 92(3):535–536 [in Russian]
171. Langford T et al (2011) The UMD- NIST fast neutron spectrometer. Presented at the cosmogenic activity and backgrounds workshop, Berkeley, CA, US, 13–15 April 2011. <https://docs.sanfordlab.org/docushare/dsweb/View/Wiki-141/Agenda/040511-Berkeley-TJL-v6.pdf>
172. Lemrani R et al (2006) Low energy neutron propagation in MCNPX and GEANT4. *Nucl Instrum Methods Phys Res Sect A* 560(2):454–459. doi:[10.1016/j.nima.2005.12.238](https://doi.org/10.1016/j.nima.2005.12.238). arXiv:[hep-ex/0601030](https://arxiv.org/abs/hep-ex/0601030)
173. Leung PT (1989) Bethe stopping-power theory for heavy-target atoms. *Phys Rev A* 40(9):5417–5419. doi:[10.1103/PhysRevA.40.5417](https://doi.org/10.1103/PhysRevA.40.5417)

174. Levinger JS (1951) The high energy nuclear photoeffect. *Phys Rev* (2nd ser) 84(1):43–51. doi:[10.1103/PhysRev.84.43](https://doi.org/10.1103/PhysRev.84.43). As cited in Ref. [112]
175. Lindhard J (1954) On the properties of a gas of charged particles. *Mat Fys Medd Dan Vid Selsk* 28(8):1–57. <http://www.sdu.dk/media/bibpdf/Bind%2020-29/Bind/mfm-28-8.pdf>. As cited in Ref. [65]
176. Lindhard J, Scharff M, Schiøtt HE (1963) Range concepts and heavy ion ranges: notes on atomic collisions, II. *Mat Fys Medd Dan Vid Selsk* 33(14):1–44. <http://www.sdu.dk/media/bibpdf/Bind%2030-39/Bind/mfm-33-14.pdf>. As cited in Ref. [125]
177. Lindote A et al (2009) Simulation of neutrons produced by high-energy muons underground. *Astropart Phys* 31:366–375. doi:[10.1016/j.astropartphys.03.008](https://doi.org/10.1016/j.astropartphys.03.008). arXiv:[0810.1682](https://arxiv.org/abs/0810.1682) [hep-ex]
178. Lipari P (1993) Lepton spectra in the earth's atmosphere. *Astropart Phys* 1(2):195–227. doi:[10.1016/0927-6505\(93\)90022-6](https://doi.org/10.1016/0927-6505(93)90022-6)
179. Lipari P, Stanev T (1991) Propagation of multi-TeV muons. *Phys Rev D* 44(11):3543–3554. doi:[10.1103/PhysRevD.44.3543](https://doi.org/10.1103/PhysRevD.44.3543)
180. Livingston MS, Bethe HA (1937) Nuclear physics C: Nuclear dynamics, experimental. *Rev Mod Phys* 9(3):245–390. doi:[10.1103/RevModPhys.9.245](https://doi.org/10.1103/RevModPhys.9.245). As cited in Ref. [125]
181. Lohmann W, Kopp R, Voss R (1985) Energy loss of muons in the energy range 1–10000 GeV. Scientific report CERN-85-03, European Organization for Nuclear Research. <http://cdsweb.cern.ch/record/158706>
182. Lopez J et al (2012) A prototype detector for directional measurement of the cosmogenic neutron flux. *Nucl Instrum Methods Phys Res Sect A* 673:22–31. doi:[10.1016/j.nima.2012.01.021](https://doi.org/10.1016/j.nima.2012.01.021)
183. Lubashevsky A E-mail message to V. A. Kudryavtsev, as cited in Ref. [166]
184. LVD Collaboration (1997) An energy signature for very deep underground muons observed by the LVD experiment. In: Potgieter MS, Raubenheimer C, van der Walt DJ (eds) *Proceedings of the 25th international cosmic ray conference*, Durban, South Africa, 30 July–6 Aug 1997, vol 6. Potchefstroom University, Transvaal, p 337. ADS: 1997ICRC....6..337L
185. Macdonald B et al (1965) Neutrons from negative-muon capture. *Phys Rev* (2nd ser) 139(5B):B1253–B1263. doi:[10.1103/PhysRev.139.B1253](https://doi.org/10.1103/PhysRev.139.B1253). As cited in Ref. [112]
186. Mal'gin AS et al (1982) High-energy hadrons produced by cosmic-ray muons in the earth as a source of background in proton-decay experiments (trans: Parsons D, Ed: Amoretti SJ). *JETP Lett* 36:376–379. Orig. pub. as Pis'ma Zh Eksp Teor Fiz 36(8):308–310 [in Russian]
187. Mal'gin A, Ryazhskaya O (2008) Neutrons from muons underground. *Phys At Nucl* 71(10):1769–1781. doi:[10.1134/S1063778808100116](https://doi.org/10.1134/S1063778808100116)
188. Marino M et al (2007) Validation of spallation neutron production and propagation within Geant4. *Nucl Instrum Methods Phys Res Sect A* 582:611–620. doi:[10.1016/j.nima.2007.08.170](https://doi.org/10.1016/j.nima.2007.08.170). arXiv:[0708.0848](https://arxiv.org/abs/0708.0848) [nucl-ex]
189. Marucho M, Canal CAG, Fanchiotti H (2006) The Landau distribution for charged particles traversing thin films. *Int J Mod Phys C* 17(10):1461–1476. doi:[10.1142/S0129183106009928](https://doi.org/10.1142/S0129183106009928)
190. Measday D (2001) The nuclear physics of muon capture. *Phys Rep* 354(4–5):243–409. doi:[10.1016/S0370-1573\(01\)00012-6](https://doi.org/10.1016/S0370-1573(01)00012-6). As cited in Ref. [112]
191. Mei D-M (2003) Measurement of cosmic-ray muon-induced processes at the KamLAND neutrino experiment. PhD dissertation, The University of Alabama. ADS: 2003PhDT.....199M. UMI-31-15062, as cited in Ref. [193]
192. Mei D (2011) What we don't know well in the simulation of the muon-induced processes. Presented at the cosmogenic activity and backgrounds workshop, Berkeley, CA, US, 13–15 April 2011. <https://docs.sanfordlab.org/docushare/dsweb/View/Wiki-141/Agenda/CosmogenicWorkshopMei1.pdf>
193. Mei D, Hime A (2006) Muon-induced background study for underground laboratories. *Phys Rev D* 73:053004. doi:[10.1103/PhysRevD.73.053004](https://doi.org/10.1103/PhysRevD.73.053004). arXiv:[astro-ph/0512125](https://arxiv.org/abs/astro-ph/0512125)
194. Menghetti H, Selvi M [On behalf of the LVD Collaboration] (2004) Study of the muon-induced neutron background with the LVD detector. In: Cleveland B, Ford R, Chen M (eds) *Topical workshop on low radioactivity techniques (LRT2004)*, Sudbury, ON, Canada, 12–14 Dec 2004. AIP conference proceedings, vol 785. AIP Publishing, Melville, pp 259–262. doi:[10.1063/1.2060478](https://doi.org/10.1063/1.2060478)

195. Migdal AB (1956) Bremsstrahlung and pair production in condensed media at high energies. *Phys Rev* (2nd ser) 103(6):1811–1820. doi:[10.1103/PhysRev.103.1811](https://doi.org/10.1103/PhysRev.103.1811). As cited in Ref. [65]
196. Mitsui K (1992) Muon energy-loss distribution and its applications to muon energy determination. *Phys Rev D* 45(9):3051–3060. doi:[10.1103/PhysRevD.45.3051](https://doi.org/10.1103/PhysRevD.45.3051). As cited in Ref. [215]
197. Mohr PJ, Taylor BN, Newell DB (2010) CODATA recommended values of the fundamental physical constants: 2010. Scientific report, National Institute of Standards and Technology. <http://physics.nist.gov/cuu/Constants/Preprints/Isa2010.pdf>
198. Motz JW, Olsen HA, Koch HW (1969) Pair production by photons. *Rev Mod Phys* 41(4):581–639. doi:[10.1103/RevModPhys.41.581](https://doi.org/10.1103/RevModPhys.41.581)
199. Nakamura K et al [Particle Data Group] (2010) Review of particle physics. *J Phys G Nucl Part Phys* 37(7A):075021. doi:[10.1088/0954-3899/37/7A/075021](https://doi.org/10.1088/0954-3899/37/7A/075021)
200. Nankov N (2002) Untersuchung der Abbremsung von Schwerionen in Materie im Energiebereich (40–400) MeV/u. PhD dissertation, Justus-Liebig-Universität Gießen
201. Nikishov AI (1978) Energy spectrum of  $e^+e^-$  pairs produced in the collision of a muon with an atom (trans: Adashko JG). *Sov J Nucl Phys* 27(5):677–681. Orig. pub. as *Yad Fiz* 27:1281–1289. As cited in Ref. [125]
202. Pandola L et al (2007) Monte Carlo evaluation of the muon-induced background in the GERDA double beta decay experiment. *Nucl Instrum Methods Phys Res Sect A* 570(1):149–158. doi:[10.1016/j.nima.2006.10.103](https://doi.org/10.1016/j.nima.2006.10.103)
203. Pastika NJ (2010) Muon-shielded counting facility at Soudan. Presented at the topical workshop on low radioactivity techniques (LRT 2010), Sudbury, ON, Canada, 28–29 Aug 2010. <http://www.snlab.ca/lrt2010/talks/Session3/PastikaLRT2010.pdf>
204. Perevozchikov O et al (2011) Measurement of cosmogenics at homestake. Presented at the cosmogenic activity and backgrounds workshop, Berkeley, CA, US, 13–15 April 2011. <https://docs.sanfordlab.org/docushare/dsweb/View/Wiki-141/Agenda/Measurement%20of%20cosmogenics%20at%20Homestake.pdf>
205. Persiani R (2011) Measurement of the muon-induced neutron flux at LNGS with the LVD experiment. PhD dissertation, Università di Bologna. [http://www.bo.infn.it/lvd/pubdocs/phdThesis\\_PersianiRino.pdf](http://www.bo.infn.it/lvd/pubdocs/phdThesis_PersianiRino.pdf)
206. Persiani R et al (2011) Monte Carlo simulation study of the muon-induced neutron flux at LNGS. In: Mezzetto M (ed) Fourteenth international workshop on neutrino telescopes, Venezia, Italy, 15–18 March 2011. Istituto Veneto di scienze, lettere ed arti, Venice, pp 429–431
207. Petrukhan A, Shestakov V (1968) The influence of the nuclear and atomic form factors on the muon bremsstrahlung cross section. *Can J Phys* 46(10):S377–S380. doi:[10.1139/p68-251](https://doi.org/10.1139/p68-251). As cited in Refs. [65, 119, 125]
208. Polityko S et al (1999) Muon's behaviors under bremsstrahlung with both the LPM effect and the Ter-Mikaelian effect and direct pair production with the LPM effect. [arXiv:hep-ph/9911330v1](https://arxiv.org/abs/hep-ph/9911330v1)
209. Polityko S et al (2001) The bremsstrahlung of muons at extremely high energies with LPM and dielectric suppression effect. *Nucl Instrum Methods Phys Res Sect B* 173(1–2):30–36. doi:[10.1016/S0168-583X\(00\)00114-2](https://doi.org/10.1016/S0168-583X(00)00114-2)
210. Primakoff H (1959) Theory of muon capture. *Rev Mod Phys* 31(3):802–822. doi:[10.1103/RevModPhys.31.802](https://doi.org/10.1103/RevModPhys.31.802). As cited in Ref. [112]
211. (2001) In: Proceedings of the 27th international cosmic ray conference, Hamburg, Germany, 7–15 Aug 2001. Copernicus Gesellschaft, Göttingen
212. (1966) In: Proceedings of the 9th international cosmic ray conference, London, UK. Institute of Physics and the Physical Society, London
213. Reichhart L [On behalf of the ZEPLIN-III Collaboration] (2011) ZEPLIN-III: VETO performance and backgrounds. Presented at the cosmogenic activity and backgrounds workshop, Berkeley, CA, US, 13–15 April 2011. [https://docs.sanfordlab.org/docushare/dsweb/Get/Document-69734/CAB\\_ZEPLIN-III.pdf](https://docs.sanfordlab.org/docushare/dsweb/Get/Document-69734/CAB_ZEPLIN-III.pdf)

214. Reichhart L et al (2013) Measurement and simulation of the muon-induced neutron yield in lead. *Astropart Phys* 47:67–76. doi:[10.1016/j.astropartphys.2013.06.002](https://doi.org/10.1016/j.astropartphys.2013.06.002). arXiv:[1302.4275](https://arxiv.org/abs/1302.4275) [physics.ins-det]

215. Rhode W (1993) Study of ultra high energy muons with the Fréjus detector. PhD dissertation, Bergische Universität Gesamthochschule Wuppertal. <http://hdl.handle.net/10068/260384>. WUB-DIS 93-11

216. Rhode W et al [Frejus Collaboration] (1996) Limits on the flux of very high-energetic neutrinos with the Frejus detector. *Astropart Phys* 4:217–225. doi:[10.1016/0927-6505\(95\)00038-0](https://doi.org/10.1016/0927-6505(95)00038-0)

217. Roper LD (1964) Evidence for a  $P_{11}$  pion-nucleon resonance at 556 MeV. *Phys Rev Lett* 12:340–342. doi:[10.1103/PhysRevLett.12.340](https://doi.org/10.1103/PhysRevLett.12.340). As cited in Ref. [134]

218. Rosman KJR, Taylor PDP (1998) Isotopic compositions of the elements 1997 (Technical report). *Pure Appl Chem* 70(1):217–235. doi:[10.1351/pac199870010217](https://doi.org/10.1351/pac199870010217)

219. Rossi B (1952) High-energy particles. Prentice-Hall physics series. Prentice-Hall, Upper Saddle River. As cited in Refs. [65, 125]

220. Rozental' IL (1968) Interaction of cosmic muons of high energy (trans: Adashko JG). Sov Phys Usp 11:49–65. doi:[10.1070/PU1968v01n01ABEH003724](https://doi.org/10.1070/PU1968v01n01ABEH003724). Orig. pub. as Usp Fiz Nauk 94:91–125 [in Russian]. As cited in Refs. [125, 215]

221. Ryajskaya OG, Zatsepin GT (1965) Depth-intensity curve of nuclear events induced by muons. In: Proceedings of the 9th international cosmic ray conference, London, UK, vol 1. Institute of Physics and the Physical Society, London, pp 987–988. ADS: 1965ICRC....2.987R. As cited in Ref. [112]

222. Ryazhskaya OG (1986) Pronikaûsie izlucenîâ pod zemlej i issledovanie ih harakteristik s pomos û scintillâcionnyh detektorov bol šogo ob ema [in Russian]. PhD dissertation, Institute for Nuclear Research of the Russian Academy of Sciences. As cited in Ref. [10]

223. Sakumoto WK et al (1992) Measurement of TeV muon energy loss in iron. *Phys Rev D* 45(9):3042–3050. doi:[10.1103/PhysRevD.45.3042](https://doi.org/10.1103/PhysRevD.45.3042). As cited in Refs. [125, 192]

224. Sanford Underground Research Facility: DUSEL Project status fact sheet. <http://www.dusel.org>. Accessed 09 July 2012. Sanford Underground Research Facility homepage > DUSEL Project status fact sheet

225. Scapparone E (1999) Study of photonuclear interaction of muons in rock with the MACRO experiment. *Nucl Phys B Proc Suppl* 75(1–2):397–399. doi:[10.1016/S0920-5632\(99\)00304-7](https://doi.org/10.1016/S0920-5632(99)00304-7). As cited in Ref. [125]

226. Schildknecht D (2005) Vector meson dominance. In: Ajduk Z, Krawczyk M, Wroblewski AK (eds) The photon, its first hundred years and the future, the centenary of the photon. PHOTON2005, International conference on the structure and interactions of the photon including the 16th international workshop on photon-photon collisions, Warsaw, Poland, 30 Aug–4 Sept 2005. *Acta Physica Polonica B* 3, Warsaw, pp 595–608. arXiv:[hep-ph/0511090](https://arxiv.org/abs/hep-ph/0511090) [hep-ph]

227. Schmidt B et al [EDELWEISS collaboration] (2013) Muon-induced background in the EDELWEISS dark matter search. *Astropart Phys* 44:28–39. doi:[10.1016/j.astropartphys.2013.01.014](https://doi.org/10.1016/j.astropartphys.2013.01.014). arXiv:[1302.7112](https://arxiv.org/abs/1302.7112) [astro-ph.CO]

228. Schröder F, Rhode W, Meyer H (2001) Muon flux simulation and comparison with Frejus measurements. In: Proceedings of the 27th international cosmic ray conference, Hamburg, Germany, 7–15 Aug 2001. Copernicus Gesellschaft, Göttingen, pp 1013–1016. ADS: 2001ICRC....3.1013S

229. Schröder F (2001) Simulation und beobachtung von Luftschauern unter großen Zenitwinkeln [in German]. PhD dissertation, Bergische Universität Gesamthochschule Wuppertal. WUB-DIS 2001–17

230. Selvi M [On behalf of the LVD Collaboration] (2011) Measurement of the muon-induced neutron yield with LVD. Presented at the cosmogenic activity and backgrounds workshop, Berkeley, CA, US, 13–15 April 2011. <https://docs.sanfordlab.org/docushare/dsweb/View/Wiki-141/Agenda/LVD-MuonInducedNeutrons-Cosmog2011.ppt>

231. Selvi M (2013) Review of Monte Carlo simulations and muon-induced neutrons. Presented at the low radioactivity techniques 2013 (LRT2013), Assergi (AQ), Italy, 10–12 April 2013. <https://agenda.infn.it/getFile.py/access?contribId=75&sessionId=9&resId=0&materialId=slides&confId=5248>

232. Short AM (1965) Fast neutron production by muons underground. In: Proceedings of the 9th international cosmic ray conference, London, UK, vol 1. Institute of Physics and the Physical Society, London, pp 1009–1011. ADS: 1965IC RC....2.1009S

233. Silva AD et al (1995) Neutron background for a dark matter experiment at a shallow depth site. *Nucl Instrum Methods Phys Res Sect A* 354(2–3):553–559. doi:[10.1016/0168-9002\(94\)01049-8](https://doi.org/10.1016/0168-9002(94)01049-8)

234. Spencer LV (1959) Energy dissipation by fast electrons. U.S. National Bureau of Standards Monograph 1. Washington: U.S. Dept. of Commerce, National Bureau of Standards. <http://hdl.handle.net/2027/mdp.39015017252027>. As cited in Ref. [65]

235. Sternheimer RM, Peierls RF (1971) General expression for the density effect for the ionization loss of charged particles. *Phys Rev B* 3(11):3681–3692. doi:[10.1103/PhysRevB.3.3681](https://doi.org/10.1103/PhysRevB.3.3681). As cited in Ref. [125]

236. Sternheimer R, Berger M, Seltzer S (1984) Density effect for the ionization loss of charged particles in various substances. *At Data Nucl Data Tables* 30(2):261–271. doi:[10.1016/0092-640X\(84\)90002-0](https://doi.org/10.1016/0092-640X(84)90002-0). As cited in Refs. [65, 125]

237. Striganov S (1996) Evaluation of approaches in muon transport simulation. *Nucl Phys B Proc Suppl* 51A(1):172–178. doi:[10.1016/0920-5632\(96\)00429-X](https://doi.org/10.1016/0920-5632(96)00429-X)

238. Suzuki T, Measday DF, Roalsvig JP (1987) Total nuclear capture rates for negative muons. *Phys Rev C* 35(6):2212–2224. doi:[10.1103/PhysRevC.35.2212](https://doi.org/10.1103/PhysRevC.35.2212). As cited in Ref. [112]

239. Sweany M (2011) Neutron multiplicity counter. Presented at the cosmogenic activity and backgrounds workshop, Berkeley, CA, US, 13–15 April 2011. <https://docs.sanfordlab.org/docushare/dsweb/View/Wiki-141/Agenda/BerkeleyMeeting.pdf>

240. Sweany M et al (2011) Large-scale gadolinium-doped water Cherenkov detector for nonproliferation. *Nucl Instrum Methods Phys Res Sect A* 654(1):377–382. doi:[10.1016/j.nima.2011.06.049](https://doi.org/10.1016/j.nima.2011.06.049)

241. Taniguchi S et al (2003) Neutron energy and time-of-flight spectra behind the lateral shield of a high energy electron accelerator beam dump: Part I: Measurements. *Nucl Instrum Methods Phys Res Sect A* 503(3):595–605. doi:[10.1016/S0168-9002\(03\)01002-7](https://doi.org/10.1016/S0168-9002(03)01002-7)

242. Ter Haar D (ed) (1965) Collected papers of L. D. Landau. Pergamon Press, Oxford

243. Ter-Mikaelian ML (1954) [in Russian]. *Dokl Akad Nauk SSSR* 94(6):1033–1036. As cited in Refs. [208, 209]

244. Uzhinsky V [On behalf of the Geant4 Hadronics Working Group] (2010) Development of the Fritiof Model in Geant4. Presented at the joint international conference on supercomputing in nuclear applications and Monte Carlo 2010 (SNA + MC2010), Tokyo, Japan, 17–21 Oct 2010. <http://geant4.web.cern.ch/geant4/results/papers/Fritiof-MC2010.pdf>

245. Vavilov PV (1957) Ionization losses of high-energy heavy particles. *Sov Phys JETP* 5(4):749–751. Orig. pub. as *Zh Eksp Teor Fiz* 32:920–923 [in Russian]

246. Villano A (2011) Soudan muon shower detector. Presented at the cosmogenic activity and backgrounds workshop, Berkeley, CA, US, 13–15 April 2011. [https://docs.sanfordlab.org/docushare/dsweb/View/Wiki-141/Agenda/SoudanMuonShower\\_AVillano.ppt](https://docs.sanfordlab.org/docushare/dsweb/View/Wiki-141/Agenda/SoudanMuonShower_AVillano.ppt)

247. Villano A et al (2013) A comprehensive comparison for simulations of cosmic ray muons underground. Presented at the low radioactivity techniques 2013 (LRT2013), Assergi (AQ), Italy, 10–12 April 2013. <https://agenda.infn.it/getFile.py/access?contribId=42&sessionId=9&resId=0&materialId=slides&confId=5248>

248. Waltham C et al [For the SNO Collaboration] (2001) Through-going muons in the Sudbury Neutrino Observatory. In: Proceedings of the 27th international cosmic ray conference, Hamburg, Germany, 7–15 Aug 2001. Copernicus Gesellschaft, Göttingen, pp 991–994. ADS: 2001ICRC....3.991W. As cited in Ref. [114]

249. Wang Y-F et al (2001) Predicting neutron production from cosmic-ray muons. *Phys Rev D* 64:013012. doi:[10.1103/PhysRevD.64.013012](https://doi.org/10.1103/PhysRevD.64.013012). arXiv:[hepex/0101049](https://arxiv.org/abs/hepex/0101049)

250. Wei Y (1993) Untersuchung der neutrinoinduzierten Myonen im Fréjus-Untergrunddetektor [in German]. PhD dissertation, Bergische Universität Gesamthochschule Wuppertal. WUB-DIS 93–8

251. von Weizsäcker CF (1934) Ausstrahlung bei Stößen sehr schneller Elektronen [in German]. *Z Phys* 88(9–10):612–625. doi:[10.1007/BF01333110](https://doi.org/10.1007/BF01333110). As cited in Refs. [112, 126]
252. Wieser ME (2006) Atomic weights of the elements 2005 (IUPAC technical report). *Pure Appl Chem* 78(11):2051–2066. doi:[10.1351/pac200678112051](https://doi.org/10.1351/pac200678112051)
253. Williams EJ (1935) Correlation of certain collision problems with radiation theory. *Mat Fys Medd Dan Vid Selsk* 13(4):1–50. <http://www.sdu.dk/media/bibpdf/Bind%2010-19/Bind/mfm-13-4.pdf>. As cited in Refs. [112, 126]
254. Wolf J (2003) Measurement of muon-induced neutron background at shallow sites. In: Spooner N, Kudryavtsev V (eds) *Proceedings of 4th international workshop on the identification of dark matter* (IDM 2002), New York, UK, 2–6 Sept 2002. World Scientific, Singapore, pp 458–464. doi:[10.1142/9789812791313\\_fmatter](https://doi.org/10.1142/9789812791313_fmatter). arXiv:[hep-ex/0211032](https://arxiv.org/abs/hep-ex/0211032)
255. Wright D (2011) Hadronic improvements for release 9.5. Presented at the 32nd Geant4 Technical Forum, CERN, 8 Nov 2011. <https://hep.kisti.re.kr/indico/getFile.py/access?resId=0&materialId=slides&confId=51>
256. Wright D (2013) Shielding physics list description. Geant4. [https://www.slac.stanford.edu/comp/physics/geant4/slac\\_physics\\_lists/shielding/physlistdoc.html](https://www.slac.stanford.edu/comp/physics/geant4/slac_physics_lists/shielding/physlistdoc.html). Accessed 18 May 2013
257. Wright DH et al (2007) Low and high energy modeling in Geant4. In: Albrow M, Raja R (eds) *Hadronic shower simulation workshop*, Batavia, IL, US, 6–8 Sept 2006. AIP conference proceedings, vol 896. AIP Publishing, Melville, pp 11–20. doi:[10.1063/1.2720453](https://doi.org/10.1063/1.2720453)
258. Wu Y-C et al (2013) Measurement of cosmic ray flux in China JinPing Underground Laboratory. arXiv:[1305.0899](https://arxiv.org/abs/1305.0899) [physics.ins-det]
259. Wulandari et al H (2004) Neutron background studies for the CRESST dark matter experiment. arXiv:[hep-ex/0401032v1](https://arxiv.org/abs/hep-ex/0401032v1)
260. Xing H (2013) Progress of fast neutron flux measurement in CJPL. Presented at the symposium of the Sino-German GDT Cooperation, Tübingen, Germany, 8–12 April 2013. <https://indico.mpp.mpg.de/getFile.py/access?contribId=64&sessionId=6&resId=0&materialId=slides&confId=2117>
261. Yue Q [On behalf of CDEX Collaboration] (2011) China JinPing Underground Laboratory (CJPL) and cosmogenic background measurement. Presented at the cosmogenic activity and backgrounds workshop, Berkeley, CA, US, 13–15 April 2011. [https://docs.sanfordlab.org/docushare/dsweb/View/Wiki-141/Agenda/YueQian-20110413\\_CJPL%20and%20DM%20Exps%20in%20China.pdf](https://docs.sanfordlab.org/docushare/dsweb/View/Wiki-141/Agenda/YueQian-20110413_CJPL%20and%20DM%20Exps%20in%20China.pdf)
262. Zatsepin GT, Razhskaya OG (1965) Calculation of neutron production by muons at different depths underground. *Bull Acad Sci USSR Phys Ser* 29(10):1779–1782. Orig. pub. as *Izv Akad Nauk SSSR* 29(10):1946 [in Russian]. As cited in Ref. [116]
263. Zbiri K (2010) Remark on the studies of the muon-induced neutron background in the liquid scintillator detectors. *Nucl Instrum Methods Phys Res Sect A* 615(2):220–222. doi:[10.1016/j.nima.2010.01.035](https://doi.org/10.1016/j.nima.2010.01.035)
264. Zhang C et al (2013) Measuring fast neutrons with large liquid scintillation detector for ultra-low background experiments. *Nucl Instrum Methods Phys Res Sect A* 729:138–146. doi:[10.1016/j.nima.2013.07.012](https://doi.org/10.1016/j.nima.2013.07.012)
265. Ziegler JF (1999) Stopping of energetic light ions in elemental matter. *J Appl Phys* 85(3):1249–1272. doi:[10.1063/1.369844](https://doi.org/10.1063/1.369844)

# Chapter 4

## Long Term Measurement of Muon-Induced Neutrons at LSM

As it was discussed in Sect. 3.7, the reliability of MC simulations of neutron production via atmospheric muons at underground sites has an uncertainty of up to a factor two. The actual agreement between simulation and measurement depends on the location of the measurement and the precision of the detector model. To reduce this uncertainty and to provide data for possible improvements of the MC models, new, well documented measurements are requested [1, 27, 45].

The installation of a dedicated counter for muon-induced neutrons at LSM in 2008 until 2012 [44] is part of a greater group of experiments, see Sect. 3.5.5, to provide these data. In addition at medium-term, this work also allows the EDELWEISS collaboration to calibrate their existing MC models to the neutron production at the site of the experiment.

The detector in question was a multi-component *neutron counter* mainly based on a gadolinium loaded *neutron multiplicity meter* (NMM) in coincident with a *muon telescope*. It included also slow control systems and a light pulser to monitor the detector stability. The principle of an NMM as core component of the neutron counter will be explained in Sect. 4.1, followed by the documentation of the neutron counter at the LSM in Sect. 4.2. Based on the the actual detector, the event definitions used for the detection of muon-induced neutrons are given in Sect. 4.3. Having defined the event signature, the performance of the detector in terms of live-time and stability is described in Sect. 4.4. Finally, the measured events will be discussed in Sect. 4.5.

The interpretation of the measurements, with respect to the Geant4 simulations described in detail in Chap. 5, will be given in Chap. 6.

### 4.1 Functionality of a Neutron Multiplicity Meter

For the detection of muon-induced neutrons this works relies mainly on a neutron multiplicity meter based on a gadolinium loaded liquid scintillator as its core element and extended by a muon telescope. The design is similar to the proposal of R. Henning-Yeomans and D. Akerib [26].

However, R. Hennings-Yeomans and D. Akerib proposed an NMM in *anticoincidence* with a muon veto to study the production of secondary neutrons produced by high energetic, muon-induced neutrons. The focus of this work is the investigation of the muon-induced neutrons. Therefore, the apparatus consists of an NMM in *coincidence* with a muon telescope based on two modules. As muon telescopes<sup>1</sup> are well known in the context of investigation of cosmic ray related phenomena at underground sites, e.g. [58], this section focuses in the following on the principle of NMM.

This section starts with the basic principle of a neutron multiplicity meter classified by the physical processes involved in Sect. 4.1.1. Section 4.1.2 will list possible background sources and Sect. 4.1.3 will consider the general influence of these processes on the detection efficiency.

For illustration purposes these subsections refer to the actual set-up of the detector that is given in Sect. 4.2.

#### 4.1.1 Neutron Detection via Capture on Gadolinium

Albeit the term NMM is used more in the context of accelerator based neutron studies [33, 75], the basic principle was already applied by L.B. Bezrukov et al. [9] to study muon-induced neutron production. But it seems that R. Hennings-Yeomans and D. Akerib [26] firstly called the detectors NMM within this context.

The NMM consists of an *active volume*, often filled with organic liquid scintillator loaded with gadolinium and instrumented with photomultiplier tubes (PMTs) near the target of neutron production. For this work, a lead target below the liquid scintillator is used. Depending on the geometrical coverage of the target by the NMM, a fraction of the produced neutrons enters the liquid scintillator and after moderation gets radiatively captured on the nuclei in the scintillator. The absorbed gamma rays finally lead to scintillation light, detected after propagation through the scintillator by the PMTs.

The placement of the lead target below the active volume results in a generally higher detection efficiency, as especially low energetic neutrons become reflected by the lead contrary to their incident direction [26] which is expected to be highly correlated with the direction of the incoming muon [27] and therefore pointing downwards. Already for a target thickness of  $\approx 10$  cm an effect in the order of a few percent is expected [26].

After transportation to the active volume, the neutrons enter the liquid scintillator and are moderated through mainly elastic scattering on hydrogen and carbon. This causes the so called *prompt* signal, see also Sect. 4.2.1. For neutron energies  $E_n > 4.813$  MeV also inelastic scattering  $^{12}\text{C}(n, n')^{12}\text{C}^*$  occurs, leading to the first excited state of carbon [75]. The neutron finally reaches thermal equilibrium with the liquid

---

<sup>1</sup>For the following text, a muon telescope is defined as two muon counters in coincidence with each other and separated by a given distance.

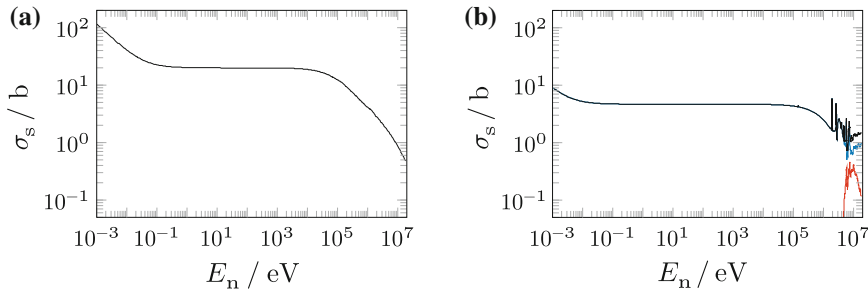


**Fig. 4.1** Neutron scattering cross sections  $\sigma_s$  for **a**  $^1\text{H}$  and **b**  $^{12}\text{C}$ . Shown are the total (black), the elastic (blue), and the inelastic (red) cross sections as function of the kinetic neutron energy  $E_n$ . For details see text. Data from the *Evaluated Nuclear Data File* (ENDF) database [32] via the *Nuclear Data Services* (NDS) of the IAEA

scintillator at a standard temperature of  $20.4^\circ\text{C}$  on a time scale of nanoseconds. Afterwards it diffuses in the scintillator for several microseconds before it is captured by one of the nuclei [33].

The mean path length  $\lambda_s$  between scatterings<sup>2</sup> is the inverse of the macroscopic scattering cross sections  $\Sigma_s$ , which is for a target of density  $\rho$  and molar mass  $A$  defined as [5]:

$$\Sigma_s = \frac{\rho}{A} N_A \sum_i n_i \sigma_{s,i} \quad (4.1a)$$

$$\lambda_s = \frac{1}{\Sigma_s} \quad (4.1b)$$

where the sum goes over all constituents of the target material with scattering cross section  $\sigma_s$  and stoichiometric fraction  $n_i$ . The cross section for direct elastic neutron scattering on hydrogen ( $^1\text{H}$ ) and carbon ( $^{12}\text{C}$ ) is shown in Fig. 4.1: Whereas hydrogen features only direct elastic scattering on the nuclear potential [5], carbon features also compound elastic scattering on resonances above 1 MeV and inelastic reactions begin for  $E_n > 4.813 \text{ MeV}$  [5].

In case the neutron energy is above the energy regime of the chemical bounds in the molecule, the scattering is described by a gas of free nuclei. If the incident neutron has the same or less energy than the chemical bounds, it can also lose energy by molecular excitations, leading to an increased cross section [5]. In hydrocarbons mainly vibrational modes are excited [21].

As the scattering cross section  $\sigma_s$  depends on the kinetic energy of the incident neutron and therefore also on the incoming direction relative to the target molecule and on the boundary conditions of a finite moderator volume, the complete

<sup>2</sup>Albeit the physical meaning is similar to the interaction length  $\lambda_{\text{int}}$  defined by Eq. 3.5 in the context of shower development, the actual definition is slightly different, as  $\lambda_s$  is not scaled by the medium's density  $\rho$ .

moderation process is in general not solvable [5]. But, as an approximation, the case of a non-absorbing medium, with space independent neutron flux and energy loss only via elastic collisions, is useful. In this case the average number of scatterings  $n_s$  needed to moderate a neutron from energy  $E_0$  to energy  $E$  depends only on the average logarithmic energy decrement  $\xi$ , which is a function of the atomic weight  $A$  [5]:

$$n_s = \frac{\ln(E_0/E)}{\xi} \quad (4.2a)$$

$$\xi = 1 + \frac{\alpha}{1 - \alpha} \ln \alpha \quad (4.2b)$$

$$\alpha = \left( \frac{A - 1}{A + 1} \right)^2 \quad (4.2c)$$

To ensure an efficient moderation of neutrons, the moderator must be big enough to contain the needed scatterings. Under the same assumptions as applied for Eq. 4.2b, the average squared distance needed for a neutron with initial energy  $E_0$  to pass below the energy  $E$  is [5]:

$$\langle r_E^2 \rangle = 2\lambda_s^2(E_0) + \frac{2}{\xi \left( 1 - \frac{2}{3A} \right)} \int_E^{E_0} \frac{\lambda_s^2(E')}{E'} dE' \quad (4.3)$$

with  $\xi$ ,  $\lambda_s$  as defined in Eqs. 4.2b and 4.1b.

The moderation stops when the neutrons reach thermal equilibrium with the liquid scintillator. For the standard temperature of  $T = 20.4$  °C the thermal energy is  $E_{\text{th}} = k_B T = 25.3$  meV. In an ideal case without neutron leakage through boundaries and without neutron absorption, the number density  $n_n$  of neutrons with kinetic energy  $E_n$  follows a Maxwell distribution [5]

$$\frac{dn_n}{dE_n} = \frac{2n_n}{\sqrt{\pi} E_{\text{th}}} e^{-E_n/E_{\text{th}}} \sqrt{\frac{E_n}{E_{\text{th}}}} \quad (4.4a)$$

$$\langle E_n \rangle = \frac{3E_{\text{th}}}{2} \quad (4.4b)$$

$$\langle v \rangle = 2 \sqrt{\frac{2E_{\text{th}}}{\pi m_n}} \quad (4.4c)$$

with the average energy  $\langle E_n \rangle$  (Eq. 4.4b) and the average velocity  $\langle v \rangle$  (Eq. 4.4c). As the NMM has a finite volume and is loaded with strongly absorbing gadolinium, the above formulae are only an approximation and the MC simulation in Sect. 5.4.1 based on the detector geometry and scintillator composition has to be used to calculate  $n_s$ ,  $\xi$ , and  $\langle r_E^2 \rangle$ .

Capturing of an incident neutron by a nucleus  ${}^A X$  occurs either via the formation of an excited compound nucleus  ${}^{A+1} X^*$  [11], or via direct capture [49, 50]. The latter

is dominant for  $24 \leq A \leq 62$  and  $130 \leq A \leq 142$  [60]. The highest capture cross section is expected for thermal neutrons by the gadolinium in the liquid scintillator, see Table 4.1. As the average atomic weight of gadolinium  $\langle A \rangle = 157.25$  [79] is well outside the ranges where direct capture predominates, this subsection has to focus on the resonant capture via compound nuclei.

For the formation of a compound nucleus, the kinetic energy of the incident neutron  $E_n$  plus the neutron binding energy  $S_n$  must match the energy level  $E_R$  of the compound nucleus. After formation, the compound nucleus can de-excite via several decay channels: On one hand, the deexcitation by emission of charged particles ( $p, \alpha, \dots$ ) and multiple neutrons is only possible above specific energy thresholds [5]. On the other hand the deexcitation via gamma ray emission  ${}^A X(n, \gamma) {}^{A+1} X$ , i.e. *radiative capture*, and via emission of a neutron with the same energy as the incident one  ${}^A X(n, n) {}^A X$ , i.e. *elastic compound scattering*, is possible for any compound nucleus [5].

The cross section  $\sigma_{n\gamma}$  for radiative capture is in general described by the R-matrix formalism, relating it to the level structure of the excited nuclei [73]. For the case of capture in a single, isolated energy level, the cross section is described by the *Breit and Wigner single level* approximation [73], which takes for a s-wave capture<sup>3</sup> the form [5, 13]:

$$\sigma_{n\gamma}(E_n) = \pi \lambda^2 \frac{\Gamma_n \Gamma_\gamma}{(E_n - E_R)^2 + (\Gamma/2)^2} \quad (4.5a)$$

$$\Gamma = \Gamma_n + \Gamma_\gamma \quad (4.5b)$$

$$\Gamma_i = \frac{\hbar}{\tau_i} \quad (4.5c)$$

with the reduced deBroglie wavelength of the incident neutron  $\lambda = \hbar/m_n v$ . The probabilities of neutron capture and gamma ray emission are characterized by their respective partial decay widths  $\Gamma_n, \Gamma_\gamma$ . They are related to the lifetimes  $\tau_n, \tau_\gamma$  of the excited state  ${}^{A+1} X^*$  against the respective decay channels  ${}^{A+1} X^*(, n) {}^A X, {}^{A+1} X^*(, \gamma) {}^{A+1} X$ . For light nuclei with  $A < 25$ , like carbon, the elastic compound scattering predominates because of  $\Gamma_n \approx 1 \text{ keV} \gg \Gamma_\gamma \approx 1 \text{ eV}$  [5]. In contrast, for heavy nuclei with  $A > 80$ , like gadolinium and low energetic neutrons, radiative capture is more likely [5]. The macroscopic absorption cross section  $\Sigma_a$  is defined in analogy to the macroscopic scattering cross section Eq. 4.1a as the weighted sum over the cross section of all constituents:

$$\Sigma_a = \frac{\rho}{A} N_A \sum_i n_i \sigma_{n\gamma,i} \quad (4.6)$$

The Breit and Wigner single level approximation is valid for most resonances below 500 keV [5] and shows two maxima: One at the resonance energy  $E_n = E_R$

---

<sup>3</sup>That is, no orbital angular momentum is transferred from the incident neutron to the compound nucleus [5].

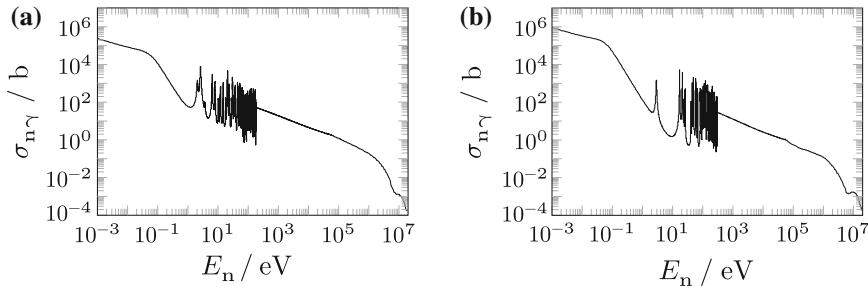


**Fig. 4.2** Radiative capture cross section  $\sigma_{n\gamma}$  of **a**  $^{155}\text{Gd}$  and **b**  $^{157}\text{Gd}$  versus the kinetic energy  $E_n$  of the incident neutron. Data from ENDF [32]

and one at  $E_n = 0$  [13]. For s-wave capture  $\Gamma_n \propto \sqrt{E_n}$ , and for  $E_R \gg \Gamma$  the cross section for thermal neutrons follows  $1/v$  [5, 13], i.e. it increases with decreasing neutron energy. Figure 4.2 shows this for the example of  $^{157}\text{Gd}$ .

Thermal neutrons ( $E_n = E_{\text{th}}$ ) become captured on gadolinium in the resonance region of the cross sections, mostly in the  $J^\pi = 2^-$  capture state at 26.8 meV (31.4 meV) for  $^{155}\text{Gd}$  ( $^{157}\text{Gd}$ ) [3, 59, 75]. As the resonance is near the thermal energy regime  $E_R \approx E_{\text{th}}$  the region of the  $1/v$  law is shifted to subthermal energies [13], see Fig. 4.2. The increasing capture cross section at low neutron energies highlights the necessity to properly moderate the neutrons. As another consequence, the thermal cross section  $\sigma_{n\gamma, \text{th}} = \sigma_{n\gamma}(E_n = E_{\text{th}})$  is normally used to characterize the capture [5, 59].

Table 4.1 lists the thermal cross sections for the isotopes contained in the applied gadolinium loaded liquid scintillator. The reason for the loading is obviously, as the thermal cross section for  $^{157}\text{Gd}$  is  $2.10 \times 10^5 \text{ b}$  and therefore six orders of magnitude higher than the thermal cross section for hydrogen  $^1\text{H}$ , which would be otherwise the isotope with the biggest thermal cross section in an unloaded organic liquid

**Table 4.1** The natural abundance, the thermal cross section for radiative neutron capture  $\sigma_{n\gamma, \text{th}}$ , and neutron binding energy  $S_n$  for the stable isotopes in the used liquid scintillator. Data from [31]

Isotope	Abundance (%)	$\sigma_{n\gamma, \text{th}}$ (b)	$S_n$ (keV)
$^1\text{H}$	99.9885	$3.326 \times 10^{-1}$	2224.576
$^2\text{H}$	0.0115	$4.92 \times 10^{-4}$	6257.2482
$^{12}\text{C}$	98.93	$3.89 \times 10^{-3}$	4946.311
$^{13}\text{C}$	1.07	$1.22 \times 10^{-3}$	8176.61
$^{152}\text{Gd}$	0.20	$>3.7 \times 10^2$	6247.48
$^{154}\text{Gd}$	2.18	85	6435.29
$^{155}\text{Gd}$	14.80	$5.17 \times 10^4$	8536.04
$^{156}\text{Gd}$	20.47	1.8	6360.05
$^{157}\text{Gd}$	15.65	$2.10 \times 10^5$	7937.39
$^{158}\text{Gd}$	24.84	2.2	5943.29
$^{160}\text{Gd}$	21.86	1.4	5635.4

scintillator. Also the released neutron binding energy with up to 8.5 MeV is well above the regime of natural gamma radioactivity of up to  $\approx 3$  MeV (Sect. 4.1.2), enabling a clear signal detection. Figure 5.19 shows the simulated spectrum of energy deposit via neutron capture in the liquid scintillator (red histogram), compared with calibration measurements (red data points).

The mean time  $\tau_{\text{cap}}$  between the subsequent capture of thermalized neutrons depends on the neutron velocity  $v$  and the macroscopic cross section (Eq. 4.6) averaged over the neutron energy distribution [64], which may be approximated as Maxwellian (Eq. 4.4a) [5, 64]:

$$\tau_{\text{cap}} = \frac{1}{v \langle \Sigma_a \rangle} \quad (4.7a)$$

$$\langle \Sigma_a \rangle = \frac{\sqrt{\pi}}{2} \Sigma_a(E_{\text{th}}) \quad (4.7b)$$

In case the neutrons are already thermal, the pure capture probability is:

$$P(\Delta t) = C_0 + A_0 e^{-\Delta t/\tau_{\text{cap}}} \quad (4.8)$$

The original equation [4, 64] is extended by a free parameter  $C_0$  to accommodate for a flat contribution of random coincidences and by a free normalization constant  $A_0$ .

The distribution of time  $\Delta t$  elapsed between the entrance of a neutron in the liquid scintillator and the capture of the neutron includes in addition the time needed by the neutrons to thermalize. A parametrization to take this offset into account is the convolution of the probabilities to moderate and get captured within  $(\Delta t, \Delta t + dt)$  [4, 64]

$$P(\Delta t) = C_1 + A_1 \left( e^{-\Delta t/\tau_{\text{mod}}} \left( \Delta t \left( \tau_{\text{cap}}^{-1} - \tau_{\text{mod}}^{-1} \right) - 1 \right) + e^{-\Delta t/\tau_{\text{cap}}} \right) \quad (4.9)$$

where  $2/\tau_{\text{mod}}$  is the mean time needed to moderate the incident neutrons [64]. A fit of Eq. 4.9 to experimental data is shown in Fig. 4.12 in red. During moderation, the energy and velocity of the neutrons decrease with time, therefore the capture cross section Eq. 4.6 increases. This results in a low value cut [12], visible in Fig. 4.12. For  $\tau_{\text{cap}} \gg \tau_{\text{mod}}$ , Eq. 4.9 can be approximated by a term similar to Eq. 4.8 but with effective values  $C_{\text{eff}}$ ,  $A_{\text{eff}}$ , and  $\tau_{\text{cap,eff}}$  as shown in Fig. 4.12 (blue). As the effective approach fits the data better, it will be used in this work.

The gadolinium nuclei de-excite by transitions from the capture state through the continuous and discrete part of the level structure to the ground state, resulting in gamma cascades, e.g. for  $^{157}\text{Gd}(n, \gamma)^{158}\text{Gd}$  with a mean multiplicity of roughly 4.5 [75]. For details of the level structure of gadolinium see references in [75]. The gamma cascade causes the so-called *delayed* signals in the NMM, which will be further defined in Sect. 4.2.1.

The emitted gamma quanta degrade and lose energy by multiple processes to the electrons of the surrounding material: Incoherent Compton scattering and electron-positron pair production before the gamma quantum is terminated by photoelectric absorption; the associated cross sections are  $\sigma_C$ ,  $\sigma_{pp}$ , and  $\sigma_{pe}$ , respectively [17, 29, 52]. The single cross sections are combined to a macroscopic cross section, called the *linear attenuation coefficient*  $\mu$ . Therefore the intensity  $I$  of a beam of gamma rays changes according to [29]

$$I = I_0 \exp(-\mu X) \quad (4.10)$$

$$\mu = \frac{\rho N_A}{A} (\sigma_C + \sigma_{pp} + \sigma_{pe}) \quad (4.11)$$

when propagating through a material of molar mass  $A$ , density  $\rho$ , and thickness  $X$ . Additional, also photo-nuclear absorption as discussed in Sect. 3.4.4 in the context of neutron production, is possible, but normally not included in the definition of  $\mu$  [17, 29]. Based on the data in [29], the biggest contribution is expected from gadolinium in the gadolinium loaded scintillator. In the relevant energy range up to  $E_\gamma \approx 8$  MeV for  $\text{Gd}(n, \gamma)$ , the contribution of photo-nuclear absorption to  $\mu$  is at most 0.3 %. The linear attenuation coefficient for compounds is the weighted sum of the linear attenuation coefficients of the constituents, similar to Eq. 3.11a. Figure 4.3 shows the *mass attenuation coefficient*  $\mu/\rho$  of the liquid scintillator used in the NMM, calculated via the data base XCOM [7], based on the composition of the liquid scintillator, see Table A.5.

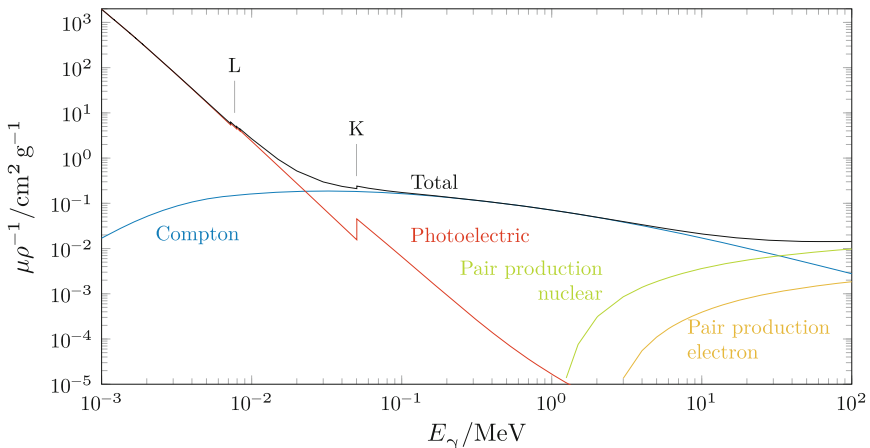


**Fig. 4.3** Mass attenuation coefficient  $\mu/\rho$  (black) as function of the gamma energy  $E_\gamma$  for 99.8 % w/w  $\text{C}_{100}\text{H}_{156}$ , 0.2 % w/w Gd. Additionally shown are also the contribution from compton scattering (blue), photoelectric effect (red), and pair production in the nuclear (green) and in the electron (orange) field. Also indicated are the peaks in the photoelectric contribution due to the L- and K-shells of gadolinium. Data from XCOM [7]

The average energy loss of the gamma quanta is [52]:

$$\frac{dE_\gamma}{dX} = -E_\gamma \mu(E_\gamma) \quad (4.12)$$

For an infinite absorber volume this is also the energy deposit. For a finite volume, like the active volume of the NMM, a fraction of the energy is lost by two circumstances: First, because not all energy is transferred to the electrons, as the gamma quantum or the positron from pair production escape before they get finally terminated. Second, the energy is not locally deposited because of fluorescence, knock-on electrons, or bremsstrahlung by high energetic electrons [28]. Therefore the energy loss calculated via Eq. 4.12 is in a finite absorber only an upper limit, the correct value has to be obtained by detailed MC simulations, as they will be presented in Sect. 5.4.1.

These electronic excitations of the scintillator atoms by the gamma quanta lead finally to the emission of scintillation light via the excitation and ionisation of the electrons in the molecular  $\pi$ -bounds. Excitation and ionisation of other electrons dissipate thermally [10]. The deposited energy  $E_{\text{dep}}$  in a material of thickness  $X$  along the particle path is

$$E_{\text{dep}} = \int_X \frac{dE}{dX} dX \quad (4.13)$$

Besides the gamma quanta, also nuclear recoils induced by scattering neutrons lead to electronic excitation of the scintillator atoms. Incident gamma quanta and neutrons differ in their energy loss density  $dE/dX$  along their path and in the light yield of the scintillation. This phenomenon is called *ionization quenching*. According to J.B. Birks [10] the ionization quenching is caused by the different extent of ionisation  $BdE/dX$ , leading to a different degree of temporary damaged molecules that recombine non-radiatively, further suppressed by a quenching parameter  $k$ . This leads to the empirical parametrization of the amount of emitted photons  $N_{\text{ph}}$  as [10]:

$$N_{\text{ph}} = \frac{S}{1 + kB \frac{dE}{dX}} E_{\text{dep}} \quad (4.14a)$$

$$= Sq E_{\text{dep}} \quad (4.14b)$$

$$= SE_{\text{vis}} \quad (4.14c)$$

where  $q$  is the *quenching factor* and  $S$  is the light yield. Hereafter  $N_{\text{ph}}/S$  is referred as the *visible energy* deposit  $E_{\text{vis}}$ . Therefore, the number of scintillation photons is not a unique measure of the deposited energy, but depends on the incident particle type. The importance to consider the ionization quenching in context of neutron yield measurements is highlighted by the discussion of the corrected interpretation of the LVD1999 [46] results in [26, 57], see Sect. 3.5.4.

At the end of this chain of physical processes the scintillation photons are absorbed by the photocathodes of the *photomultiplier tubes* (PMTs) [75].

The implementation of all these processes in the detector response model of the actual NMM is discussed in Sect. 5.4.

### 4.1.2 Possible Sources for Background

Together with the basic detection principle discussed in the previous Sect. 4.1.1, possible background sources affect the event signature that will be defined in Sect. 4.3. Besides a review of background sources, this section also discusses whether the influence of the particular background source can be estimated from measurements, see Sect. 4.5, or whether it has to be assessed by MC simulations (Sect. 5.5.5).

Possible sources for background are ambient gamma rays from natural radioactivity and ambient neutrons mostly from the rock and concrete walls of the underground site. The neutrons originate by spontaneous fission of  $^{238}\text{U}$  and by  $(\alpha, n)$  reactions on light nuclei [26]. For the resulting neutron yield in various materials see [56].

The ambient neutron production via  $(\alpha, n)$  reactions is similar to the neutron production in AmBe sources, see Appendix A.6. The review of underground sites by A. Bettini [8] lists for the LSM a neutron flux of  $5.6 \times 10^{-6} \text{ cm}^{-2} \text{ s}^{-1}$ , without giving further details. Therefore, in this work we will use the more detailed study for the LSM by S. Rozov et al. [70]. Using a  $^3\text{He}$  counter, the measured values for the thermal neutron flux range from  $2.0 \times 10^{-6} \text{ cm}^{-2} \text{ s}^{-1}$  to  $6.2 \times 10^{-6} \text{ cm}^{-2} \text{ s}^{-1}$ , depending on the position. At the latter position of the neutron counter,<sup>4</sup> a thermal neutron flux of  $2.0(2) \times 10^{-6} \text{ cm}^{-2} \text{ s}^{-1}$  was measured. Therefore, the neutron counter is placed at the position with the lowest background of ambient neutrons. Taken into account the systematic uncertainties, the work of S. Rozov et al. [70] is in agreement with the lower value of  $1.6(1) \times 10^{-6} \text{ cm}^{-2} \text{ s}^{-1}$  found earlier by V. Chazal et al. [15] for the thermal neutron flux. It is also in reasonable agreement with  $4(2) \times 10^{-6} \text{ cm}^{-2} \text{ s}^{-1}$  [62], estimated on the gamma ray flux of captured ambient neutrons.

Based on MC simulations, the measurements of S. Rozov et al. [70] are extrapolated to a total neutron flux of  $9.6 \times 10^{-6} \text{ cm}^{-2} \text{ s}^{-1}$ , out of which 16% of the flux are fast neutrons at  $E_n > 1 \text{ MeV}$  [18]. This fraction is in agreement with the work of V. Chazal et al. [15, 20], which measured<sup>5</sup> a fast neutron flux of  $(1.06 \pm 0.10^{\text{stat}} \pm 0.59^{\text{syst}}) \times 10^{-6} \text{ cm}^{-2} \text{ s}^{-1}$ .

The expected energy spectrum of ambient neutrons from the rock and concrete at LSM is investigated in [45, 54, 74] using MC simulations with Geant4 and SOURCES4A [80]. The neutron energy can go up to  $\approx 10 \text{ MeV}$  [45], but its average is 1.9 MeV [74] at production, which is further reduced along the propagation through the rock and concrete [54].

---

<sup>4</sup>Position 4 in [70, table2]. The neutron counter was installed after the  $^3\text{He}$  measurement.

<sup>5</sup>This measurement was analysed four times, resulting in different values for the fast neutron ( $E_n > 1 \text{ MeV}$ ) flux:  $4 \times 10^{-6} \text{ cm}^{-2} \text{ s}^{-1}$  [15],  $1.6 \times 10^{-6} \text{ cm}^{-2} \text{ s}^{-1}$  [14],  $1.1 \times 10^{-6} \text{ cm}^{-2} \text{ s}^{-1}$  [53],  $1.06 \times 10^{-6} \text{ cm}^{-2} \text{ s}^{-1}$  [20].

The gamma background at the LSM is studied by H. Ohsumi et al. [62]: Gamma rays from capture of ambient neutrons are the predominant contribution to the ambient gamma background at the LSM for  $6 \text{ MeV} \leq E_\gamma \leq 10 \text{ MeV}$  [62]. Below 4 MeV the dominant source is natural radioactivity, and above 10 MeV the gamma quanta originate from muon bremsstrahlung (see also Sect. 3.2.3) [62]. Contamination of the detector with uranium, thorium, and progenies may be dominant in the energy range of 4–6 MeV [62]. Below 4 MeV, only partial gamma ray fluxes are given in [62] for LSM:  $4 \times 10^{-2} \text{ cm}^{-2} \text{ s}^{-1}$  from  $^{208}\text{Tl}$  (2.61 MeV) and  $10^{-1} \text{ cm}^{-2} \text{ s}^{-1}$  from  $^{40}\text{K}$  (1.46 MeV). For energies above 4 MeV a total gamma ray flux of  $7.03 \times 10^{-6} \text{ cm}^{-2} \text{ s}^{-1}$  is stated [62]. As results, the ambient gamma ray flux and its contribution as background to the neutron counter depends not only on the natural gamma radioactivity, but also on the local field of thermal neutrons, the muon flux, and the details of the used detector.

In principle, the gamma background can be suppressed in two ways; requiring a higher threshold energy to trigger an event and demanding  $n$ -folded coincidences between several, optical separated PMTs [33]. Because the detector used in this work had only one optical volume, we rely mainly on the first method. As the sum energy of the gamma cascade for neutron capture on gadolinium is of the order of 8 MeV, an energy threshold well above the energy regime of the natural radioactivity [26] can be applied. For the actual set-up, the used thresholds are given in Sects. 4.2.4 and 4.2.5.

The ambient neutron background can be distinguished from the muon-induced neutron signal by its multiplicity: Whereas muon-induced neutron cascades have multiplicities up to 100 (Sect. 3.5.3),  $(\alpha, n)$  reactions lead to only one neutron. Contrary, the spontaneous fission of  $^{238}\text{U}$  can produce correlated neutrons with multiplicities larger than 2, but its rate is typically up to six orders of magnitude lower than the gamma rate [26]. Several correlated neutrons can be also mimicked by one high energetic ( $\approx 10 \text{ MeV}$ ) neutron that causes several nuclear recoils during moderation in the liquid scintillator, which may lead to several energy deposits above the trigger threshold. However, these energies are only available at the extreme end of the energy spectrum.

In conclusion, the expected background from ambient neutrons and gamma rays depends not only on the local natural radioactivity, but also on the muon flux, the detector, and the used trigger thresholds. Within this work the background of ambient neutrons from  $(\alpha, n)$  reactions and from contamination of the used liquid scintillator are explicitly investigated by Geant4 simulations in Sect. 5.5.5. As for all simulations, the same Geant4 physics list is used, including neutron capture and bremsstrahlung production, the contribution of gamma rays from neutron capture and muon bremsstrahlung are implicitly included. The latter is treated in the simulation of muon-induced neutrons described in Sect. 5.5. Not simulated is the correlation of neutrons from  $^{238}\text{U}$  due to their expected low rate and the contribution of natural gamma radioactivity. As we will see in the following, this work relies on the background suppression by the used trigger threshold ( $\approx 3 \text{ MeV}$ , see Sect. 4.2.5).

### 4.1.3 Assessing the Neutron Detection Efficiency

The neutron detection efficiency of an NMM is affected by the free detector parameters (dimensions, gadolinium content, etc.) via the slowing down length, the neutron capture cross section, the gamma absorption length, the ionisation quenching, and the light collection efficiency taking into account the detector geometry. Furthermore, it depends on the details of the event building process and relies therefore on a full model of the detector response, which will be presented in Sect. 5.4.

This subsection shortly summarizes the aspects of the detection efficiency with respect to the actual detector geometry and motivates the actual technical realisation documented in Sect. 4.2. It will not optimize these parameters of the actual set-up, as this was already done during the prototype stage [39].

As a first order approximation we use the fraction  $\epsilon_{\text{cap}}$  of captured neutrons with a visible energy deposit (Eq. 4.14a) of  $E_{\text{dep}} \geq 3 \text{ MeV}$  relative to the amount of incident neutrons, therefore above the expected gamma background (Sect. 4.1.2). As neutron source, an AmBe source in the centre of the top surface of the NMM is assumed. Again, this is only an approximation as the muon-induced neutrons will emerge over the full surface of the lead target. The actual detection efficiency for muon-induced neutrons will be given at the end of Sect. 5.5.3.

The detection efficiency of an NMM with a finite active volume decreases with  $E_n$  because the slowing down length increase, see Eq. 4.3. Therefore the NMM acts as a low pass filter for neutrons. Also the capture cross section (Eq. 4.5a) decreases with rising kinetic energy. Therefore non-thermalized, non-captured neutrons will be lost by leaking out of the scintillator. To reduce the neutron loss, the iron walls of the support structure of the actual NMM is designed to act as neutron mirror, scattering back at least the thermalized neutrons in the active volume. The 2 cm thick iron plates on the side result in a relative increase of the detection efficiency by 5 % [39].

For an efficient detection of the gamma quanta after a neutron capture, the gamma trajectory within the active volume must be long enough, so that at least 3 MeV energy is deposited. Assuming a maximal energy of a single gamma quantum of 8 MeV, integration of Eq. 4.12 with the data shown in Fig. 4.3 results in a minimal track length of  $\approx 27 \text{ cm}$ , in agreement with MC simulations performed in [39].

Therefore the requirements for an efficient gamma quanta absorption are inconsistent with the requirements of an efficient neutron absorption [26, 39]: On one side an effective neutron absorption needs a strong moderation and hence a short penetration in the active volume. On the other side an effective gamma absorption needs a deep penetration of the neutron before it gets captured, so that the path length of the subsequent emitted gamma quanta is sufficiently long to deposit 3 MeV before they leave the active volume.

The combination of both effects can be seen in Fig. 4.4. It shows the influence of the thickness of the liquid scintillator on the neutron capture efficiency  $\epsilon_{\text{cap}}$  for neutrons with 0.5, 2.0, 5.0, 20 and 50 MeV kinetic energy. The neutrons started isotropic and equally distributed at the boundary between a  $200 \text{ cm} \times 100 \text{ cm} \times 10 \text{ cm}$  lead layer and an adjacent volume of liquid scintillator of thickness  $d_{\text{LS}}$ , which is loaded

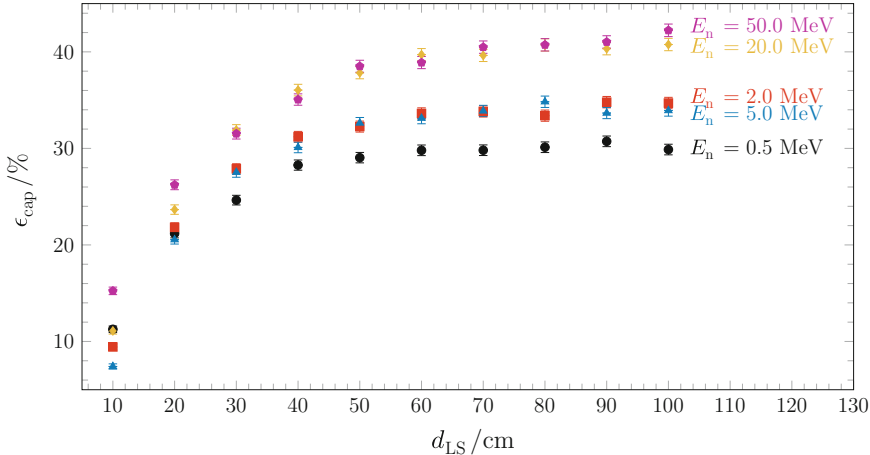


**Fig. 4.4** Neutron capture efficiency  $\epsilon_{cap}$ , i.e. number of captured neutrons with an energy deposit of  $\geq 3$  MeV relative to  $N = 10^4$  started neutrons, as function of scintillator thickness  $d_{LS}$  for different neutron energies  $E_n$ . Error bars indicating 68 % CL. For details see text. A similar figure is already published by the author in [44]

with 0.2 % w/w gadolinium. First the three lowest energies will be discussed and the remaining two later on. At  $d_{LS} = 10$  cm the detector has the highest detection efficiency for 0.5 MeV, as more of the higher energetic neutrons leak out of the active volume before they thermalize and get captured. After reaching the plateau at  $\approx 50$  cm for  $E_n \geq 5$  MeV, the 2 MeV and 5 MeV neutrons have higher detection efficiencies than the 0.5 MeV neutrons: They penetrate deeper before getting captured and they allow therefore a sufficient energy deposit by the gamma quanta. As a fraction of gamma quanta still leaks out of the active volume, the spectrum of energy deposits is a continuous distribution instead of discrete gamma lines, see Fig. 5.17.

Another trade off exists between the coverage of large targets and high moderation efficiency on one hand and a high efficiency of scintillation light collection on the PMTs on the other hand, as the latter is degraded in large volume detectors by internal absorption in the liquid scintillator and increased light trajectories due to multiple reflections on the detector walls. It can be further degraded by a chemical long term instability of the scintillator, leading to an increased light absorption. For the actually used liquid scintillator this is further discussed in Sects. 4.2.1, 4.3 and 4.4.3.

The efficiency may further decrease by the finite time resolution of the NMM, resulting in pile up of delayed signals, the *dead time* [23] of the NMM, resulting in missed signals, and the ionization quenching (Eq. 4.14a), suppressing the prompt signals from proton recoils. This is further discussed in Sect. 4.2.6. Also the measured multiplicity can get further distorted by secondary neutron production in the liquid scintillator via  $^{12}\text{C}(n, x n)$ ,  $x > 1$  [33, 75]. A selection of the related cross sections are shown in Fig. 4.1b. This effect is also evident in Fig. 4.4 for the two lines of 20 and 50 MeV neutrons: The increased detection efficiency with respect to the three lower

energetic neutrons is caused by the neutron multiplication via inelastic scatterings, not only on the carbon in the scintillator but also on the lead target.

As the detection efficiency for all investigated neutron energies reaches a plateau at  $d_{LS} \approx 50$  cm, this is the optimal thickness for the active volume with respect to the neutron detection. Here a neutron detection efficiency of  $\epsilon_{cap} = \approx 40\%$  can be expected for this configuration.

As all these effects are energy dependent, measurements of poly-energetic neutrons, like muon-induced neutrons, are not easily to correct for detection efficiencies. It is more appropriate to convolve simulated results with the detector efficiency and compare it afterwards with the measurements [33]. For this reason the next Sect. 4.2 will document in detail the detector properties, serving as input for the model of detector response in Sect. 5.4, which is then folded by the simulated neutron production in Sect. 5.5 and finally compared in Chap. 6 with the measurements in Sect. 4.5.

## 4.2 Experimental Set-Up of the Neutron Counter

As it was pointed out in Sect. 3.5.4 a detailed documentation of the experimental set-up is necessary for the development of a reliable model of the detector response in view of not only the MC model that will be presented in Sect. 5.4, but also for possible future works. Therefore, this section documents the actual experimental set-up of the neutron counter and its characteristics based on the basic principles discussed in Sect. 4.1. The actual detector was based on a prototype study [39] and a short description was already published in [44]. The documentation starts with the NMM as the central part of the multi component set-up in Sect. 4.2.1, continue with peripheral subsystems like the muon telescope in Sect. 4.2.2 and the light pulser (Sect. 4.2.3). Then the data acquisition electronics (Sect. 4.2.4), adjustment of high tension (Sect. 4.2.5), and data processing (Sect. 4.2.6) are described as they are common to all subsystems.

### 4.2.1 Neutron Multiplicity Meter (NMM)

The NMM was based on a gadolinium loaded liquid scintillator for the neutron detection placed on top of a lead target for the neutron production by through-going muons. The scintillation light was received by 16 PMTs, split in two groups of 8 PMTs one on the north and one on the south side of the NMM. The NMM was placed near the lower part of the muon veto of EDELWEISS at the LSM. On top of it, module 50 of the muon telescope (see Sect. 4.2.2) was placed. Figure 4.5a shows the actual set-up at LSM. For a better overview see also the geometry implemented in Geant4, shown in Figs. 5.1 and 5.2. A selection of detailed construction schemes are placed in Appendix A.5.1. The principal capability of the NMM to detect neutrons was verified as a side product by monitoring measurements with an AmBe source

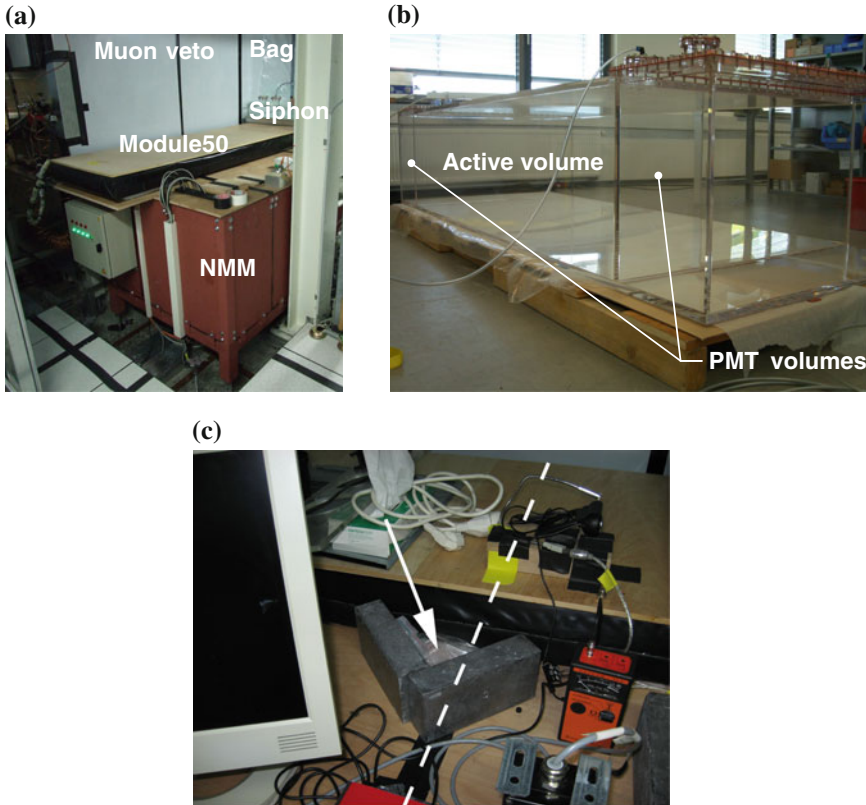


**Fig. 4.5** **a** The NMM at LSM, on *top* module 50 of the muon telescope, the siphon, and the extension bag. Seen on the *left* side are the lower part of the EDELWEISS muon veto, i.e. ‘niveau 0’. **b** The acrylic glass body of the NMM with three chambers prior to the detector assembly: In the middle the active volume for the liquid scintillator and on the outside the two volumes for the PMTs. **c** Position of the AmBe source (*white arrow*) on the top surface of the NMM beside muon module 50. The AmBe source inside its lead castle (here open for taking the photography) was regularly placed at half-length of the NMM (*dashed white line*). For details see text. Pictures provided by V.Y. Kozlov [40]

as neutrons source, described in more details in Sect. 4.4.2. This subsection starts with a general overview of the NMM and continues with a detailed description of its functional parts.

The NMM takes advantage of the otherwise unfavourable low interaction rate between the neutrons and the detector compared to charged particles for example: The long time of diffusion in liquid scintillator after moderation and before the neutron gets captured on the nuclei in the liquid scintillator delivered a sequence of neutron captures well separated in time and hence a measure of the neutron multiplicity [33]. One distinguishes therefore two signal categories in an NMM: The *prompt signal* from the quenched nuclear recoils within the first nanoseconds and the *delayed*

*signals* from the neutron capture after some microseconds. Contrary to the neutron multiplicity, the neutron energy is not directly measurable with an NMM [33]. For a neutron captured on the solved gadolinium a maximal energy deposit of 8.5 MeV is expected in case all emitted gamma quanta get absorbed. To distinguish neutron signals from background (random coincidences and ambient gamma, see Sect. 4.1.2) one can use an appropriate threshold (Sect. 4.2.5) and the high gamma multiplicity of a neutron capture by demanding a coincidence between signals from several PMTs.

The body of the NMM consisted of an acrylic glass box with three chambers (Fig. 4.5b), the inner chamber was the active volume of length  $\times$  width  $\times$  height = 200 cm  $\times$  100 cm  $\times$  51 cm filled with 1 m<sup>3</sup> of gadolinium loaded liquid scintillator. The filling level was therefore 50 cm, the values estimated previously for an optimal neutron detection (see Sect. 4.1.3). The chambers to both sides had the identical dimensions of 32.5 cm  $\times$  100 cm  $\times$  51 cm and contained PMTs optically coupled to the active volume via paraffin, filled to the same level as the liquid scintillator. The body was wrapped with aluminium foil to increase the light collection.

For the case of leakage of the liquid scintillation, especially critical in the environment of an underground laboratory, the body was placed in an aluminium safety container. Below the safety container was a lead target for muon-induced neutron production. Its measured dimension<sup>6</sup> was 272 cm  $\times$  106 cm  $\times$  10 cm, consisting of multiple lead bricks with individual dimensions of 20 cm  $\times$  10 cm  $\times$  5 cm.

Both safety container and lead target were enclosed by an iron<sup>7</sup> support structure. As already discussed in Sect. 4.1.3, the iron side plates were increased to 2 cm to act as mirror for thermal neutrons. To compensate pressure changes in the active volume due to thermal expansion of the liquid scintillator, it was connected via a siphon to an argon filled expansion bag. Besides the PMTs the NMM was also instrumented with an LED based light pulser to monitor the optical stability of the liquid scintillator (see Sect. 4.4.3) and a slow control system.

The pseudocumene<sup>8</sup> based liquid scintillator BC-525<sup>9</sup> is loaded with 0.2 % w/w gadolinium [44]. The scintillator properties are listed in Table A.5, and Fig. 5.14 shows the emission spectrum with an emission peak at 425 nm. As it is obvious from the hydrogen to carbon ratio (Table A.5) the empirical formula of the hydrocarbon is C<sub>100</sub>H<sub>156</sub>, which was used to calculate the mass attenuation coefficient of the scintillator shown in Fig. 4.3.

The manufacturer states an attenuation length of more than 4.5 m, but gives no detailed information about the absorption spectra or chemical formulation. Such information is essential for the MC model of the detector response in Sect. 5.4, as the effective attenuation and the light collection efficiency depends on the attenuation spectrum integrated along the light paths, within the individual geometry of the active volume. As a dedicated photometric measurement of the absorption spectrum was beyond the scope of this work, we tried to find a published absorption spectrum of

<sup>6</sup>This is equivalent to a perpendicular column density of  $X = 113.42 \text{ g cm}^{-2}$ .

<sup>7</sup>Steel of type S 235 JR, standardized in DIN EN 10 025.

<sup>8</sup>1,2,4-trimethylbenzene.

<sup>9</sup>BC-525 (Saint-Gobain Crystals, 104 Route de Larchant, BP 521, 77794 Nemours Cedex, France).

a chemically similar scintillator. To do this, first the chemical formulation has to be identified<sup>10</sup>: The BC-525 is based on the scintillator BC-521C developed for the Palo Verde experiment [66]: Gadolinium complexed by carboxylic acid<sup>11</sup> and solved in pseudocumene. Additional components are a primary fluorescent (emission peak at 365 nm), a spectrum shifter (emission peak at 425 nm), an antioxidant and two additional solvents to keep the gadolinium compound in solution. As pseudocumene is aggressive towards acrylic glass the scintillator is diluted with mineral oil [66]. The chemical similarity between BC-525 and BC-521C is also highlighted by the same wavelength of the emission peak, therefore the formulation of BC-521C should be a suitable approximation for the formulation of BC-525. However, the absorption spectrum of BC-521C is also not published, but with the approximate formulation it is possible to choose a published spectrum from a chemically similar scintillator. In this work the absorption spectrum [81, Fig.3], shown in Fig. A.2, is used.<sup>12</sup>

Liquid scintillators in general are sensitive for a reduced light yield by oxygen quenching [10]. To remove solved oxygen the liquid scintillator was bubbled with argon<sup>13</sup> after filling the active volume and the remaining volume was filled with argon. Further deterioration of the light yield and the chemical stability of the liquid scintillator can be caused by slow chemical reaction like hydrolysis or polymerization, leading to the formation of cloudy suspension, colour, gels, or precipitation of the gadolinium. Also impurities from aggression towards acrylic glass can lead to such effects [81]. As a scintillator degeneration would cause a shift in the detection efficiency via reduced transparency and reduction of solved gadolinium, the long term behaviour of the scintillator is monitored with two methods: An LED based light pulser was used to monitor the transparency (see Sect. 4.4.3) and regular reference measurements with an AmBe source allowed the deduction of the gadolinium content via the measured capture time  $\tau_{\text{cap}}$ , see Sect. 4.4.2.

---

<sup>10</sup>The chemical formulation of an organic liquid scintillator loaded with gadolinium is complicated: The metal must form an organo-metallic complex via ligands (complexing agents) like carboxylic acids. Carboxylic acids with long carbon chains are more organic-like and thus their organo-complex are easier to solve in the solvent. However, increasing the weight percent of the organo-metallic complex in this way reduces the weight percentage of the organic solvent that determines the light yield [81]. According to [81, p. 331] the best compromise between an easy solubility of gadolinium in pseudocumene on one hand and a high light yield on the other hand is 2-methylvaleric acid. Also, care must be taken to stabilize the scintillator: The synthesis of the organo-metallic complex from gadolinium oxide, opposite to the synthesis from gadolinium nitrate, increase the stability against solid-liquid phase separation when the scintillator is exposed to air [66, 81]. According to [81, p. 330] the oxidation of the organic liquid by the used  $\text{Gd}(\text{NO}_3)_3$  likely caused the degeneracy of the scintillator in the CHOOZ experiment.

<sup>11</sup>Gadolinium 2-ethylhexanoate  $[\text{Gd}(\text{CH}_3(\text{CH}_2)_3\text{CH}(\text{C}_2\text{H}_5)\text{CO}_2)_3 \cdot x\text{H}_2\text{O}]$ , synthesised from gadolinium oxide  $\text{Gd}_2\text{O}_3$ .

<sup>12</sup>The chemical formulation used in [66] ([81]) is: 0.1 % w/w (0.2 % w/w) of gadolinium complexed by carboxylic acid, solved in pseudocumene, diluted by 60 % v/v of mineral oil (80 % v/v of dodecane).

<sup>13</sup>It is also common to bubble liquid scintillators with nitrogen, but by gadolinium loaded liquid scintillators it can cause the precipitation of the gadolinium compound out of the solution [66, p. 394].

The liquid scintillator was viewed by 16 PMTs of 8 inch diameter,<sup>14</sup> optically coupled via paraffin to the acrylic glass wall of the active volume. The PMTs were originally bought for a never realized water Cherenkov detector as the second stage of the KARMEN experiment [61]. To increase the light collection, the acrylic glass body was wrapped with crumpled aluminium foil, using two effects: The total internal reflection on the boundary air–acrylic glass and the high reflectivity of the aluminium for a light ray incident under an angle smaller than the critical angle. Again the optical properties of the used materials for the MC model are based on literature values and will be given in Sect. 5.4.2 and Appendix A.4.3.

The high tension for the PMTs was provided by the PC controlled high tension generator<sup>15</sup> of the nearby EDELWEISS muon veto system, see [24] for details. As the high tension generator provides only negative polarity, but the original voltage divider of the PMTs described in [61] was designed for positive polarity, it had to be replaced with a dedicated one. This was developed by the electronic workshop of the Institute for Nuclear Physics (IKP) at KIT. The circuit design follows common guidelines for fast response PMTs operated in pulse mode [25, 65] and is described in Appendix A.5.3. The high tension adjustment is described in Sect. 4.2.5 and is based on the PMT gain as function of the high tension (Eq. A.47) and on the after-pulse rate (Eq. A.49). For each PMT the gain function was measured (Appendix A.5.3) and the actual parameters of the gain function are listed in Table A.7. The after-pulse rate was spot-checked (Appendix A.5.3) and, as expected, increased after illumination of the PMT with light flashes. Kozlov [40] found empirically that the PMTs need a *recovery time* [23] of 200 ns (1  $\mu$ s) after receiving the scintillation light flash of a neutron capture (through-going muon) before the after-pulse rate decreases again.

The 8 inch PMTs are called hereafter *neutron PMTs*, identified as  $\text{PMT}_{i,j}^N$ ,  $i = 1, \dots, 8$ ,  $j = 1, 2$ , where  $i$  indicates the later defined PMT group and  $j$  the PMT within the group  $i$ . Figure 4.6 shows their positions with respect to the active volume. Due to the high gamma multiplicity of the neutron capture reaction on gadolinium, a signal in several PMT is expected.

To enhance the light collection, two neighbouring PMTs build a *PMT group*, operated on individual high tensions, but the anode signals of the two PMTs within a group are connected in parallel to the same signal channel. For the naming scheme of these PMT groups ( $\text{PMTG}_i^N$ ,  $i = 1, \dots, 8$ ) see again Fig. 4.6. This results in a combined output impedance of  $50 \Omega$  for each of the eight signal channels ( $S_i^N$ ,  $i = 1, \dots, 8$ ), matching the input impedance of the following data acquisition electronics (Sect. 4.2.4). A signal on one of the signal channels above the discriminator threshold (Sect. 4.2.5) of the following data acquisition will be defined as *NMM hit*.

To avoid great differences in the high tensions for a given PMT group, the PMTs in the group are matched for similar gain parameters, see Table A.7. Via setting of the high tension the gain of these PMT groups is tuned for an agreement between the

<sup>14</sup>Hamamatsu Photomultiplier Tube R5912 (HAMAMATSU PHOTONICS K.K., Electoron Tube centre 314-5, Shimokanzo, Toyooka-village, Iwata-gun, Shizuoka-ken, 438-0193, Japan).

<sup>15</sup>LeCroy 1440, (LeCroy Research Systems SA, Avenue Louis-Casa 81, case postale 43, 1216 Cointrin-Geneva, Switzerland), out of production.

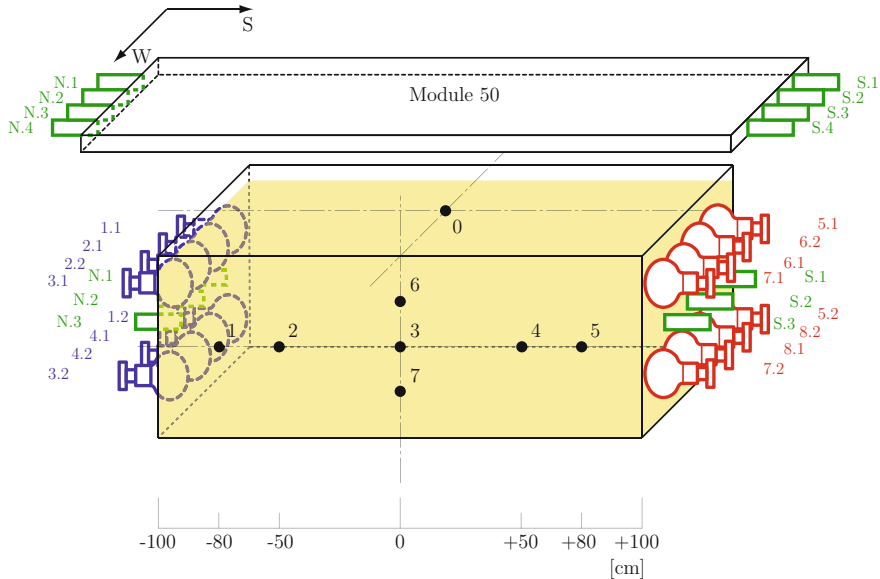


**Fig. 4.6** Simplified, not to scale illustration of the position and naming of the PMTs relative to the scintillator (yellow) filled active volume of the NMM and module 50. 16 neutron PMTs  $\text{PMT}_{i,j}^N$  are combined in 8 PMT groups  $\text{PMTG}_i^N$  and distributed to the north (blue) and to the south (red) of the active volume. The 14 muon PMTs  $\text{PMT}_{i,j}^M$  are combined in 4 PMT groups  $\text{PMTG}_i^M$ . The position of the eight LEDs of the light pulser (black dots) are also shown. Dash-dotted lines indicate the symmetry axes of the active volume. The arrows indicate the south (S) and west (W) directions

dynamic range of the NMM and the energy deposit spectrum of the captured neutrons as reference, see Sect. 4.2.5. To expand the dynamic range of the NMM, the PMT groups are further divided in so called *low-gain* and *high-gain* PMT groups: From the four PMT groups on each side two PMT groups are operated on a lower high tension and hence on a lower gain (low-gain PMTs,  $i = 3, 4, 7, 8$ ) in comparison with the remaining PMT groups (high-gain PMTs,  $i = 1, 2, 5, 6$ ). The low-gain PMTs are suitable for signals that are already in saturation on the high-gain PMTs.

The slow control system of the NMM served in first instance the safety of the laboratory and controlled the leak tightness of the active volume, as pseudocumene vapour is hazardous for the human health, especially in small and closed environments like underground laboratories. The monitoring was based on three redundant subsystems, operated by a LabView based control software [43]: To prevent leaks caused by overpressure due to expanding liquid scintillator heated by the PMTs, the active volume is connected to an argon filled siphon. Both the temperature of the scintillator and its level in the siphon were continuously monitored. In case of a breach of the active volume, two level meters would have detected the liquid scintillator in the aluminium safety container. As third subsystem two vapour sensors, one inside the NMM support structure and one outside, were continuously scanning the

air for evaporated pseudocumene. In case of a detection, an alarm signal was to be delivered to the global safety system of the LSM and notification emails were sent to the operators. Fortunately, during the total operational life of the neutron counter all notifications were false alarms and the active volume never leaked.

### 4.2.2 Muon Telescope

The muon telescope consisted of two optical and spatially separated counters, each independently handled by the data acquisition electronics, described in the next Sect. 4.2.4. To reduce random coincidences, a coincidence between several PMTs is demanded by the data acquisitioning electronics, see Sect. 4.2.4. The functionality of the muon telescope, i.e. selecting particles that cross both counters, is achieved in the offline data analysis by searching for events where the data acquisition in both counters was triggered, see Sect. 4.3.

The first counter was a dedicated muon module [68] of the EDELWEISS muon veto [24], placed on top of the NMM. The muon module is integrated as module 50 in the muon veto of the EDELWEISS,<sup>16</sup> for its spatial relation to the NMM and the muon veto see Fig. 4.5a. As a standard muon module it consists of a polyvinyltoluene based plastic scintillator<sup>17</sup> body of  $365\text{ cm} \times 65\text{ cm} \times 5\text{ cm}$ , viewed by four fast response PMTs with 2 inch diameter<sup>18</sup> on each side of 65 cm width. According to its direction a side is named north (N), or south (S). The PMT position on these sides are optimized for high and uniform light collection [68]. Figure 4.6 shows a simplified illustration of their position. For further details, e.g. the light guides between plastic scintillator and PMTs, see [24, 68].

The manufacturer states an attenuation length of  $\alpha^{-1} = 4\text{ m}$  [71] for the used plastic scintillator, see also Table A.6. On actual muon modules, an effective attenuation length  $\Lambda(\alpha^{-1})$ , see Eq. 5.35b for its definition, of

$$\Lambda_{\text{M50}} = 3.24\text{ m} \quad (4.15)$$

was measured.<sup>19</sup> This value is later included in the MC model of the neutron counter in Sect. 5.4.2.

The PMTs were originally used for the muon veto of the KARMEN experiment [68], since 2004 some of them are re-used for the muon veto of EDELWEISS [24]. In both cases the suitability for muon detection of these PMTs, including the voltage divider design, were shown. These PMTs are called *muon PMTs* ( $\text{PMT}_{i,j}^{\text{M50}}$ ,  $i = \text{N, S}$ ,

<sup>16</sup>Modules 1 to 22 and 25 to 48 constitute the actual muon veto, the modules 50 and 51 were the muon telescope; no modules 23, 24, and 49 exist.

<sup>17</sup>BC-412 (Saint-Gobain Crystals).

<sup>18</sup>Photonis XP2262 (PHOTONIS France S.A.S, Avenue Roger Roncier, 19100 Brive La Gaillarde, France).

<sup>19</sup>The measurement was performed by a student during a summer internship.

$j = 1, \dots, 4$ ) in the following. To enhance the light collection the PMT anode pulses of each side are summed, resulting in one signal channel ( $S_i^{M50}$ ,  $i = N, S$ ) of  $50 \Omega$  output impedance for each PMT group ( $PMTG_i^{M50}$ ,  $i = N, S$ ). A signal on one of the signal channels above the discriminator threshold (Sect. 4.2.5) of the following data acquisition electronics (Sect. 4.2.4) will be defined as *muon telescope hit*. To reduce the number of needed high tension channels, the gain of the PMTs on each side are matched and can therefore be operated on the same high tension. The gain parameters were already measured for each single PMT by the KARMEN experiment.

Based on the energy loss (see Sect. 3.2.1) of relativistic muons in plastic scintillator of  $\approx 2 \text{ MeV cm}^{-1}$  [22], an averaged energy deposit of  $\approx 10 \text{ MeV}$  due to ionisation is expected for a muon passing through the module along the  $z$ -axis, causing hits at both opposite sides of the module.

The second counter has a similar design, but uses instead of a separate plastic scintillator the active volume of the NMM: Three 2 inch muon PMTs viewed the liquid scintillator from each chambers on both sides of the active volume ( $PMT_{i,j}^{M51}$ ,  $PMTG_i^{M51}$ ,  $S_i^{M51}$ ,  $i = N, S$ ,  $j = 1, \dots, 3$ ), see Fig. 4.6 for their positions. Again the output impedance of each group summed up to  $50 \Omega$  and each group was operated on the same high tension line. As the design of this counter with respect to high tension input and signal output was similar to a muon module it was integrated as module 51 in the EDELWEISS muon veto. Since the level of liquid scintillator in the active volume is 50 cm, an energy deposit of  $\approx 100 \text{ MeV}$  for muons passing along the  $z$ -axis is expected.

The high tension adjustment is described in Sect. 4.2.5 and the actual used values are listed in Table A.8a.

As the muon telescope was in principle a subset of the muon veto, which has proven its well understood functionality over the last years, no technical difficulties occurred during its run time.

### 4.2.3 Light Pulser

Light pulser based on LEDs are a well proven and accepted reference light source for monitoring the detector stability, see e.g. [2, 37, 55]. Therefore, the NMM was equipped with such a light pulser to monitor the time development of the transparency and chemical stability of the liquid scintillator (see Sect. 4.2.1).

In total 8 LEDs<sup>20</sup> were fixed on the outer surface of the acrylic glass body of the NMM, their positions are shown in Fig. 4.6 and their properties according to the data sheet [69] are listed in Table A.15. Each LED was oriented perpendicular to the vessel surface. The LED was fixed by putting it in a hole drilled in a small block of acrylic glass that is glued on the acrylic glass body. Optical grease coupled all parts together. As receiver for the light pulses the neutron PMTs of the NMM were used.

<sup>20</sup>RLT420-3-30 (Roithner Lasertechnik, Schönbrunner Straße 7, 1040 Vienna, Austria).

To mimic the scintillation light, the used LEDs have an emission peak at 423 nm matching the peak of the emission spectrum of the liquid scintillator at 425 nm (see Table A.5). In addition, the width of the light pulse of 10 ns is of the same magnitude as the width of a scintillation pulse [44].

The LED driver was two parted: The actual driver was soldered directly to the LED. It is based on a variation of the Kapustinsky design [37] developed for the calibration of the surface detectors of the Pierre Auger observatory [2, 38], adapted to the LEDs used on the NMM. For the PC based control of all eight drivers, a VME based module was developed within this work in close cooperation with the electronic workshop of the IKP [36]. The supply voltages of each of the eight LEDs were individually adjusted, see Table A.16 for the actual values. This ensured that the light pulses caused signals in the dynamic range of the data acquisition electronics (see Sect. 4.2.4). This two parted design avoids the difficulties in propagating current pulses of nanosecond length over long distances, as they were produced in the drivers close to the LEDs, still requiring only one control module.

Every 8 hours, a *LED sequence* was started: Each of the eight LEDs was flashed 501 times with a frequency of 1 Hz. Between consecutive LEDs the control software waited for 1 min for the stabilization of the supply voltage. Figure 4.15 shows the ADC values of the opposite  $\text{PMTG}_1^N$  and  $\text{PMTG}_5^N$  caused by such an LED sequence: The time periods where the different LEDs were light up are visible, clearly separated by the 1 min break. The begin and end of each LED sequence was logged in a text file, together with the ID of the used LED (0, …, 7) and the number of light ups. This log file and the recorded data files from the NMM, were analysed by a ROOT based program, developed within this work. To distinguish signals from the light pulser from physical signals, a flag signal  $F_{\text{LED}}$  was delivered to the data acquisition electronics for each LED light up (Sect. 4.2.4).

In every run, until the 29 September 2010, an error in the LED control board caused randomly a flashing up of all 8 LEDs instead of the selected one via cross talk between the LED channels. This is visible in Fig. 4.15 as a less dense population of data points shifted to higher ADC values. An improved version of the VME module fixed this problem. In this final version, the light pulser proved to be well suited for monitoring the scintillator transparency [48], as it is discussed in Sect. 4.4.3. Due to the successful monitoring of the liquid scintillator, a second LED pulser system was installed to monitor the transparency and gain of the newest EDELWEISS muon veto modules.<sup>21</sup> The analysis of the light pulser data in context of detector stability will be discussed in Sect. 4.4.3.

#### 4.2.4 Data Acquisition Electronics

The signals generated by the neutron counter, i.e. NMM (see Sect. 4.2.1) and muon telescope (Sect. 4.2.2), are recorded by a shared *data acquisition system* (DAQ). As

<sup>21</sup> Modules 7, 8, 15, and 16.

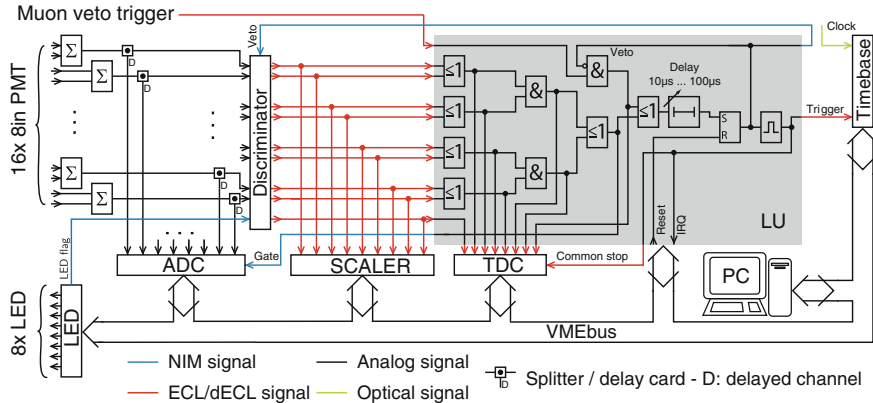


**Fig. 4.7** Scheme of the DAQ electronics of the NMM. For details see text. An earlier version was already published by the author in [44]

the space is limited in an underground laboratory, this DAQ participates on the VMEbus<sup>22</sup> and CAMAC<sup>23</sup> based DAQ of the EDELWEISS muon veto where possible. This is obviously true for the muon telescope that is, from the technical point of view, a part of the muon veto system. It is also true for the NMM that extends the necessary hardware and software, but keeps it as close as possible to the muon veto system. However, both systems operate their own trigger logic.

As the muon veto DAQ is also of concern for this work we start with a summary of it. Based on this, the NMM extension of the DAQ is documented. For a better overview of this section, a scheme of the NMM DAQ is shown in Fig. 4.7. For a scheme of the muon telescope DAQ, we refer to the scheme of the muon veto DAQ in [24]. For the meaning of common abbreviations like ADC and TDC and the related functionality, see for example [23].

The muon veto is designed for a high detection efficiency of muons, therefore the condition for the muon veto DAQ to trigger the data recording is conservative: It only requires a coincidence between hits on the N and S channel [24] of a given module to reduce random coincidences. As this is the same requirement needed for the muon telescope (see Sect. 4.2.2) the two muon modules 50, 51 of the muon telescope are completely integrated in the muon veto, i.e. muon telescope and EDELWEISS muon veto share the same electronic components.

The electronic modules of the DAQ are housed in a VMEbus crate<sup>24</sup> and a CAMAC crate, installed in a rack near the NMM. The CAMAC bus is driven by

<sup>22</sup>Standardized in ANSI/IEEE 1014-1987, for an overview see e.g. [78].

<sup>23</sup>Standardized in ANSI/IEEE 583-1982, for an overview see e.g. [30].

<sup>24</sup>UEV 6023 9U bin, UEL 6020 LX-Fan tray, Modulare VHF switcher Stromversorgung UEP 6021 (wiener—Plein & Baus GmbH, Müllersbaum 20, 51399 Burscheid, Germany).

a VME-to-CAMAC interface<sup>25,26</sup>. Finally a Linux based PC controls the VME electronics via an interface module.<sup>27</sup> The module allocation for both crates is given in Tables A.10 and A.11 and the mapping of the PMTs to the modules is given in Table A.12.

For each of the 46 muon modules of the muon veto, including the muon telescope, the N and S channels are split in a logical branch and an analog branch. The analog branch delivers the signals to an ADC, whereas the logical branch passes the signal through a leading edge discriminator and distributes it subsequently to a logical unit, a scaler, and a TDC. From the logical unit the signal is fed to a so called veto card that generates the trigger signal  $T_M$  of the muon veto system. Based on this trigger the following data of the signals are stored: The energy proportional to the charge via the ADC, the relative time between signals via the TDC and the absolute time via a time base. Additional three scaler modules<sup>28</sup> store the signal rate for each channel (identified as  $SCA_i^M$ ,  $i = 1, \dots, 3$  in Table A.10). To avoid different signal propagation times between different channels, care was taken to ensure that cables of the same length were used for all channels.

The incoming channels from the muon modules are delivered via coaxial cables, terminated to  $50 \Omega$ , and connected via BNC connectors to splitter/delay cards<sup>29</sup>: The incoming signal is split and amplified, so that the amplitude of the outgoing signal agrees with the incoming signal amplitude within better than 2 % below 1.7 V [24]. Above this voltage the integrated amplifier breaks down. To compensate the processing time within the logical branch and to adjust the interval between the trigger signal and the analog signal to the ADC, the analog signals are delayed by 100 ns.

The logical branch is fed via LEMO cables to six leading edge discriminator modules<sup>30</sup> ( $DISC_i^M$ ,  $i = 1, \dots, 6$ ). For the adjustment of the discriminator threshold see Sect. 4.2.5. The resulting ECL output channels are divided in three branches: One is connected to the TDC, another branch is connected to one of the scaler units, and the last branch is connected to one of the logic units.

Three logical units<sup>31</sup> ( $LU_i^M$ ,  $i = 1, \dots, 3$ ) are used to test the input signals on coincident hits between the N and S channel of any of the muon modules. In case of a coincidence a NIM output signal<sup>32</sup> is propagated to the veto card.

---

<sup>25</sup>CCA-2 Type A-2 Crate Controller (Hytec Electronics Ltd., 5 Cradock Road, Reading, Berkshire, RG2 0JT, England).

<sup>26</sup>CBD 8210 CAMAC Branch Driver (Creative Electronic Systems, 70, Route du Pont-Butin, P.O. Box 107, CH-1213 PETIT-LANCY 1, Switzerland).

<sup>27</sup>PCI to VME Interface (wiener).

<sup>28</sup>CAMAC Model 4434—32-Channel, 24-Bit Scaler (LeCroy), out of production.

<sup>29</sup>Development of the Institute for Data Processing and Electronics (IPE) at the KIT, for a detailed description see [24].

<sup>30</sup>Model 4413—16-Channel CAMAC Discriminator (LeCroy), out of production.

<sup>31</sup>Mod.V512—8 Ch 4 Fold Programmable Logic Unit (CAEN).

<sup>32</sup>For the definition of the signal levels used in Nuclear Instrumentation Modules see [76].

After the veto card<sup>33</sup> receives any input signal from the three logical units it gets in a pre-triggered state for 100 ns before it generates the muon veto trigger  $T_M$ . The trigger condition for the muon veto, including the muon telescope, is therefore a logical AND between N and S channel of each module  $m$ . The modules themselves are OR connected:

$$T_M = \bigvee_m S_S^m \wedge S_N^m \quad (4.16)$$

The 100 ns time interval (or *DAQ window*) ensures that all information of the ongoing interactions in the muon modules are recorded. As the DAQ was designed for the muon veto, the DAQ window is adapted for the time a muon needs to travel along the largest distance within the volume of the muon veto ( $\leq 60$  ns [24]) and for the time of the light propagation in the muon modules ( $\leq 30$  ns [24]). This interval is also suitable for the muon telescope, as the maximal spatial extension of the muon telescope is smaller than the maximal extension of the muon veto.

After the veto card triggered, it reacts four-folded: First it sends a NIM veto signal to the discriminators to block the acquisition of further input signals. Second it issues an interrupt request (IRQ) on the VMEbus. As third and fourth actions it sends a NIM gate signal of 100 ns length to the ADC and distributes the trigger as ECL signal to the TDC, the logic module of the NMM, and the time module. As the triggered veto card locked any further data acquisition, it is necessary to unlock it via VME command again when the data read out by the control software is finished.

The TDC module<sup>34</sup> (TDC<sup>M</sup>) has a 20 bit resolution, i.e. 1,048,575 TDC units,<sup>35</sup> the maximal time interval between the input signals and the trigger signal  $T_M$  is 838.86 ms. These time intervals are stored for all input signals within a window starting 125 ns before the  $T_M$  signal arrives and lasts for 250 ns [24]. Additionally, the trigger signal is stored on input channel 128. The accuracy for time intervals between any input signal and the trigger signal on channel 128 is 800 ps. A reconstruction of the event location along the module axis is possible by the precise TDC data. In case two modules have triggered the DAQ, it is therefore possible to reconstruct the trajectory of the through-going particle, most likely a muon [72].

As the EDELWEISS experiment consists of several detector systems (e.g. cryogenic bolometer, muon veto) a general clock signal with a resolution of 10  $\mu$ s is distributed via optical fibres to all detectors. Based on this clock signal, the time base generates time stamps for the muon veto DAQ. To allow an independent time stamp for the NMM, the original time base [51] was replaced by a completely new version, developed and tested within this work in cooperation with the electronic workshop of the IKP [35]. The clock signal is duplicated and continuously stored in two internal registers: One register for the NMM and one for the muon veto. After receiving the

<sup>33</sup>Development of the IPE at the KIT, for a detailed description see [24].

<sup>34</sup>Mod.V767—128 Ch. General Purpose Multihit TDC (CAEN S.p.A., Via Vetreria, 11, 55049—Viareggio, Italy).

<sup>35</sup>Often the TDC units are called *TDC channels*, this naming is rejected in this work to prevent confusion with the input channels of the TDC.

associated trigger signal the register content gets locked and is ready for read out via VMEbus. Therefore it is necessary to unlock the register after the data transfer is finished.

Three charge integrating ADC (QDC) modules<sup>36</sup> ( $\text{QDC}_i^M$ ,  $i = 1, \dots, 3$ ) are connected to the analog branch of the splitter/delay output channels. The QDC measured an input range of 0–400 pC with 12 bit, i.e. up to 4095 ADC units,<sup>37</sup> starting 15 ns after receiving the gate signal. The *pedestal*, i.e. the measured value of the input baseline without any signal, is listed in Table A.13 for the QDCs connected to module 50, 51. To reduce the amount of recorded data, values below the so called *software threshold* are not recorded, as they most likely are not caused by muons. This threshold is individually adapted for each ADC channel and their values are given in Appendix A.5.4. As one expects only one prompt interaction of the muon within one module the rather long dead time of the QDCs of 6.9  $\mu\text{s}$  is of no concern.

The triggering scheme of the NMM DAQ was similar to the one of the muon veto: At least one coincident hit between channels from the opposite sides (Fig. 4.6) was needed to start the data acquisition. This scheme uses the high gamma multiplicity of a neutron capture to reduce the gamma background and random coincidences as discussed in Sects. 4.1.2 and 4.2.1.

The DAQ of the NMM was an extension to the muon veto DAQ, based purely on VME modules. Each of the eight signal channels from the neutron PMTs were terminated to  $50 \Omega$  and divided by a splitter/delay card in an analog branch and a logical branch. The logical branch passed the signals through a leading edge discriminator and delivered them to a scaler and to the logical unit of the NMM. Independently of the muon veto, the generator of the NMM trigger signal  $T_N$  was integrated in the logical unit, schematically shown in Fig. 4.7 (gray shade). In case of an NMM trigger the following data of the incoming signals were stored: The energy equivalent charge via an ADC, the relative time between signals via a TDC and the absolute time via the time base. The flag  $F_{\text{LED}}$  sent by the LED light pulser during its activation to the NMM DAQ (see Sect. 4.2.3) was stored together with the NMM data. Furthermore, the scaler<sup>38</sup> ( $\text{SCA}^N$ ) stored the signal rate for each channel. The NMM DAQ was controlled by the same software as the muon veto DAQ (see Sect. 4.2.6).

The used splitter/delay cards differ from the one of the muon veto in the delay of the analog branch: As the processing time in the logical branch of the NMM was shorter, a delay of 70 ns was sufficient.

After dividing, the logical branches were led to a leading edge discriminator unit<sup>39</sup> ( $\text{DISC}^N$ ) operating in non updating mode with a maximal input frequency of 80 MHz. This defines the time resolution of the DAQ electronics for the NMM, i.e. two signals must be separated by at least 12.5 ns to produce two hits. The adjustment of the discriminator thresholds are described in Sect. 4.2.5. The ECL output channels

<sup>36</sup>Mod.V792N—32 Ch QDCs (CAEN).

<sup>37</sup>Again, the naming *ADC channels* is rejected to prevent confusion with the input channels of the ADC.

<sup>38</sup>Mod. V830 series—32 Channel Latching Scalers (CAEN).

<sup>39</sup>Mod.V895B—16 Channel Leading Edge Discriminators (CAEN).

of the discriminator were divided into two branches: One was connected to the logic unit and the second branch was connected to the scaler. Additional to the incoming signals from the NMM PMT groups, also the flag from the LED light pulser was put on the discriminator. Besides serving as input for the logic unit, the LED flashing rate could thus be monitored via the scaler.

The in-house made logical unit of the NMM ( $LUN^N$ ) provides a functionality similar to the ones of the logical units and veto card of the muon veto DAQ, but integrated within a programmable FPGA [34]. It was developed and tested within this work in close cooperation with the electronic workshop of the IKP. The trigger decision is based on three levels:

First, the signals from the two high gain PMT groups on each side are combined via an OR circuit, similar the two low gain PMT groups on each side are combined. This reduced the number of signal channels from eight to four.

In the second level the logical units tested the signals of the reduced channels for a coincident hit between signals from opposite PMT groups, but same gain type (high gain PMT or low gain PMT). The coincident window of 44 ns was the width of the incoming signals from the discriminator. It is equal to a difference of 13 m in the light paths. As the maximal extension of the active volume is only 2.3 m this value is a conservative approach to include also the case of increasing light paths due to multiple reflection.

The third level combined the outcome of the second level via an OR connection to a pre-trigger signal of the NMM. The pre-trigger signal was also caused by any trigger signal from the muon veto  $T_M$ . The muon veto trigger signal was also sent to the TDC unit ( $TDC^N$ , see Fig. 4.7) and serves in the data as the *muon veto flag*. This allowed the search for muon-induced NMM signals, like muon-induced neutrons. The outgoing ECL signals of each trigger level were further delivered to the TDC unit. The LED flag signal was not part of the trigger decision, but was directly passed through to the TDC unit. As the LED light flashes were tuned to be well above the discriminator threshold, it was in any case recorded.

The pre-trigger caused three actions: It was immediately propagated to the ADC of the NMM as NIM gate signal. It started a DAQ window of  $\Delta t_{DAQ} = 60 \mu s$  nominal length [44], and it prevented any further pre-trigger generation by locking the logical unit, i.e. the pre-trigger state could not be extended. Besides the recording of prompt signals from recoiling neutrons, the long DAQ window allowed also to record delayed signals from captured neutrons, see Sect. 4.2.1. Shifts of  $\Delta t_{DAQ}$  are investigated in Sect. 4.4.4.

After the window was closed the trigger signal of the NMM  $T_N$  was generated. The trigger condition for the NMM was:

$$T_N = T_M \vee \left( \left( S_1^N \vee S_2^N \right) \wedge \left( S_5^N \vee S_6^N \right) \right) \vee \left( \left( S_3^N \vee S_4^N \right) \wedge \left( S_7^N \vee S_8^N \right) \right) \quad (4.17)$$

The  $T_N$  was delivered as ECL signal to the time base to generate a time stamp for the NMM and to the TDC as common stop signal. As NIM veto signal it was delivered to the discriminator to lock the data acquisition and it issued an IRQ on the VMEbus.

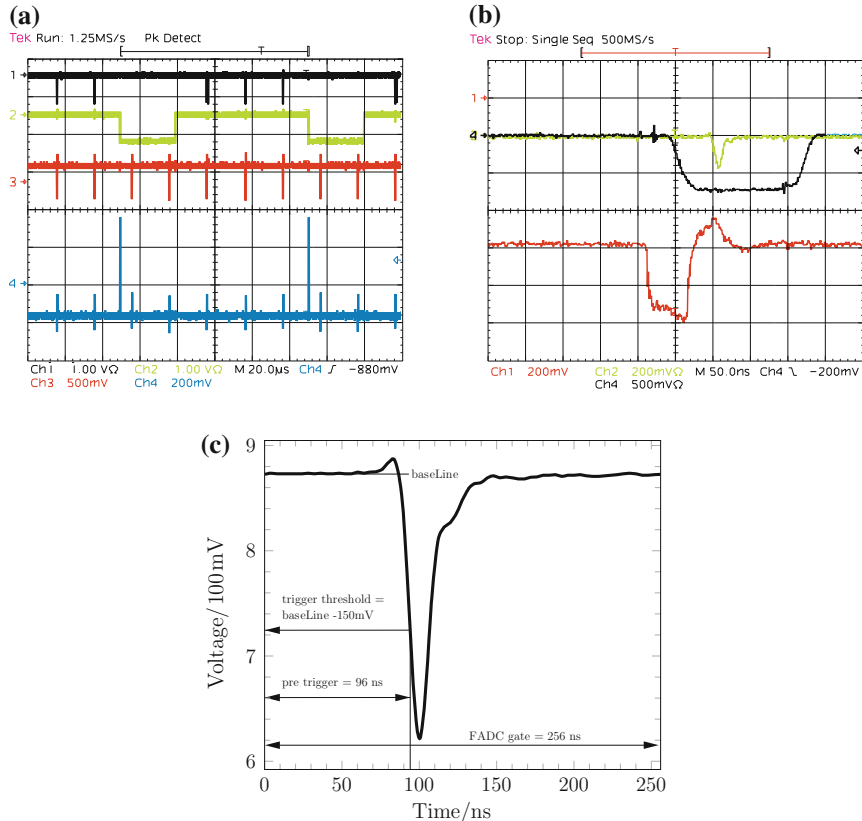


**Fig. 4.8** Timing of NMM signals: **a** Event building of LU<sup>N</sup> operated by internal 12.6 kHz test pulse generator. Channel 1 (black) ADC gate, NIM signal; channel 2 (green) discriminator veto, NIM signal; channel 3 (red) first trigger level signal to TDC, ECL signal; channel 4 (blue) TDC common stop, ECL signal. **b** Positioning of the ADC gate signal (black) relative to the delayed input signal for the first used QDC (green) and the output of the discriminator (red, ECL signal) after installation. Pulses recorded with Tektronix TDC 784C oscilloscope and afterwards modified for better readability. **c** Illustration of the gate relative to the trigger threshold in the used FADC, based on actual physics data. For more details see text, lines are to guide the eye

Similar to the muon veto DAQ, the NMM DAQ needed to be unlocked again, after the control software completed the data read out.

Additionally, the LU<sup>N</sup> is equipped with two internal test pulse generators of 12.6 and 50 kHz frequency. Figure 4.8a illustrates the above described signal generation by using the 12.6 kHz test pulse generator<sup>40</sup> and an external C programme that unlocked the NMM DAQ as soon as an IRQ on the VMEbus was detected, without reading any data. Therefore, the interval between the setting of the discriminator

<sup>40</sup> As an *internal* test pulser is used, the veto signals (green) shown in Fig. 4.8a have obviously no effect on the signals from the first trigger level (red).

veto signal (green, falling edge) and the resetting (rising edge) of  $\approx 30 \mu\text{s}$  is a lower bound to the dead time caused by  $\text{LU}^N$ , VMEbus and the interrupt handling within a C based programme running on a standard Linux PC. The dead time of the total DAQ system is given in Sect. 4.2.6.

The outgoing channels of each trigger level of the logical unit were delivered to the TDC unit<sup>41</sup> ( $\text{TDC}^N$ ) with 16 bit resolution, i.e. maximal 65,535 TDC units. The maximal time interval between any of the input channels and the common stop signal is  $65.535 \mu\text{s}$ . It was therefore suitable to measure all time intervals possible in the DAQ window of the logical unit. After receiving the common stop signal, the time intervals were stored for any of the input channels within the last  $\Delta t_{\text{DAQ}}$ .

The TDC was a central component of the DAQ electronics of the NMM: The recorded data of the first trigger level allowed the reconstruction of the number of delayed signals within a DAQ window, i.e. this is a measure for the captured neutrons. There is also the possibility for a limited reconstruction of the location of a light flash (scintillation light or LED flash) in the active volume: As there is no possibility to relate the recorded signals to a single PMT, due to the grouping of the PMTs and the OR circuit in the first trigger level, it is not possible to reconstruct the position within the plane perpendicular to the N–S-axis. But as the time delays between the PMTs from N and S side are recorded, a limited reconstruction of the location along the N–S-axis is possible. As the position is not part of the event signature, see Sect. 4.3, the limited reconstruction capabilities are no drawback. It was rather used as an additional possibility to test the DAQ function by reconstructing the position of an AmBe source placed at different positions along the N–S-axis.

In the beginning a charge integrating ADC (QDC) was used.<sup>42</sup> As the gate signal had a slow falling time and it had to precede the input signal by at least 20 ns, an additional delay line of 62.5 ns was inserted between the already delayed splitter card output and the input to the QDC. Figure 4.8b shows the resulting position of the delayed signal within the ADC gate. As the QDC *dead time* [23] of  $16 \mu\text{s}$  was in the same order of magnitude as the DAQ window, this resulted in loss of energy information of the delayed signals. Albeit the energy information is not necessary, as the event signature is based on the hit timing and multiplicity, it offers additional discrimination power against background. Therefore on 9 September 2009 the QDC was replaced with a dead time less flash ADC (FADC)<sup>43</sup> ( $\text{ADC}^N$ ). Pulses within the input range of  $-1$  to  $1 \text{ V}$  were digitized by the FADC with 12 bit resolution and with a sampling rate<sup>44</sup> of  $250 \text{ MSs}^{-1}$ . The sampled pulse trace is stored in a ring buffer of  $1.25 \text{ MS}$  length per input channel. After the end of the DAQ window the ring buffer was read and afterwards reset. The dead time is equivalent to the sampling rate, which is orders of magnitude lower than the dead time of the QDC. The integration

---

<sup>41</sup> Model 1176—16 Channel VME TDC (LeCroy), out of production.

<sup>42</sup> Model 1182—VME Multiple Input Charge ADC (LeCroy), out of production.

<sup>43</sup> Mod.VX1720—8 Channel 12 bit 250MS/s Digitizer (CAEN).

<sup>44</sup> Given in samples (S) per second, i.e.  $\text{S s}^{-1}$ .

of the signals was performed offline on the stored data, see Sect. 4.2.6. With the given voltage and time resolution the least significant charge values are

$$\text{ADCunit} := 4 \text{ ns} \cdot \frac{2V}{2^{12} - 1} \approx 2 \text{ pC} \quad (4.18)$$

The resolution is lower than the one of the muon veto QDC ( $\approx 0.1$  pC). However, as previously stated, for the NMM the timing data is more important than the energy data.

The FADC input range is equivalent to the dynamic range of the NMM. To optimize the usage of this range the baseline of the incoming signal was shifted: As the neutron PMTs are operated on high tension with negative polarity, a positive bias voltage is applied by the FADC. The resulting pedestals for each FADC channel are listed in Appendix A.5.4 and possible shifts are investigated in Sect. 4.4.4. Contrary to a QDC, the gate actually applied by the FADC was independent of the width of the gate signal, therefore the additional delay lines were removed again. The FADC gate was a fixed time window starting 24 S (96 ns) before the gate signal occurs and lasted for 64 S (256 ns). As shown in Fig. 4.8c, this resulted in a gate well containing the signal pulse. Together with the sampled pulse trace the FADC also stored the time when the gate signal arrived. This enables the reconstruction of the temporal arrangement of the single pulse traces within a DAQ window as shown in Fig. 4.10. As result of the chosen gate length and the size of the ring buffer, up to 19,531 gates per FADC input channel could be stored before the first samples would be erased by a new sample. This is well above the maximal number of 14 hits per NMM event observed during the run of the NMM, see Sect. 4.5. Therefore it was no limiting factor for the measurement. It would have been even possible to record the full DAQ window, but in this case an extended offline analysis would be necessary to identify the pulses within the trace. The chosen solution used instead the already generated gate signal as a more straight forward approach without loss of information on the signal as shown in Sect. 4.5.

#### 4.2.5 Adjustment of High Tension and Discriminator Threshold

The previously described DAQ electronics has free parameters like the coincident window width, the delay time of the analog branch to the logical one, the discriminator threshold, and the PMT supply voltage. Whereas the coincident window and the delay time was already determined by the size of the detector and the design of the electronics, the discriminator threshold and the PMT supply voltage had to be adjusted with respect to the expected signals.

In case of the muon telescope, the signal is the energy deposited by muons passing through the muon telescope. One expects a Landau distribution with a well defined peak as signal, see also Eq. 3.16a, and a background due to ambient gamma

radioactivity rising towards lower energy. For the muon module like module 50 the Landau peak is expected at  $\approx 10$  MeV, for the thicker module 51 at 100 MeV (see Sect. 4.2.2), whereas the gamma background is expected at an energy regime below  $\approx 3$  MeV (Sect. 4.1.2).

A high tension setting is regarded as optimal if the Landau peak is placed in the middle of the dynamic range of the associated QDC, i.e. at 2048 ADCunit (see page 176). On one hand this uses most of the available dynamic range of the QDCs, but on the other hand it leaves enough safety margin to both lower and higher values in case of signal or detector fluctuations. In case of module 50, the high tension was already pre-adjusted at sea level, using atmospheric muons as reference source, following the description in [24].

As module 51 was first operational after filling the active volume with liquid scintillator at LSM, the complete high tension adjustment was made during the commissioning stage. As it relies on the local muon flux, reduced  $\approx 10^6$  times with respect to the sea level (Sect. 3.1.3), no rapid correction was possible. At the same time also the pre-adjusted voltage supply of module 50 was checked and finally set. Follow-up checks during the run of the detector led to some voltage changes to compensate ageing effects in the modules, the history of the high tension values are listed in Table A.8b.

As the muon telescope used the same discriminators as the muon veto, also the same discriminator thresholds of 150 mV were applied. It was originally optimized to minimize the gamma background while at the same time maximizing the muon signal as described in [24]. However, the originally reported threshold voltage of 60 mV [24] had to be increased to 150 mV to reduce the overall event rate and hence the total dead time of the muon veto. The possible loss of muons is no constrain for the neutron counter to measure the neutron production yield, as it is defined with respect to the detected muons (see Eq. 3.64a).

The adjustment of the high tension for the NMM was similar to the one for the muon telescope, but instead of the atmospheric muons, an AmBe source as signal source was placed at the centre of the top surface of the NMM. Figure 4.5c shows the used position, and the properties of the AmBe source are given in Appendix A.6. The adjustment was individual for each PMT in a given PMT group, as the PMTs were alternately switched off. Therefore, the signal from each individual PMT is at one half of the dynamical range of the NMM. An upper limit on the high tension was placed as the fraction of afterpulse reaches a level in the order of  $10^{-2}$  at 1300 V (Table A.9), therefore decreasing the noise to signal ratio. Consequently most high tensions are below this value (Table A.8a). The gains of the low gain PMTs were adjusted to a lower value as mentioned in Sect. 4.2.1. Again, the high tension was empirically determined, the resulting values are listed in Table A.8a. Figure 4.9 shows the resulting clear separation of these two PMT groups in terms of signal amplitude. As this plot shows *any* first hit, i.e. primary hits in context of the event signatures defined in Sect. 4.3, in *all* recorded events, most of them are probably captured neutrons from ambient background and *not* passing muons.

The resulting PMT pulses are exemplified in Fig. 4.10, now demanding also a high multiplicity of hits: The delayed signals from the neutron capture (Fig. 4.10c)

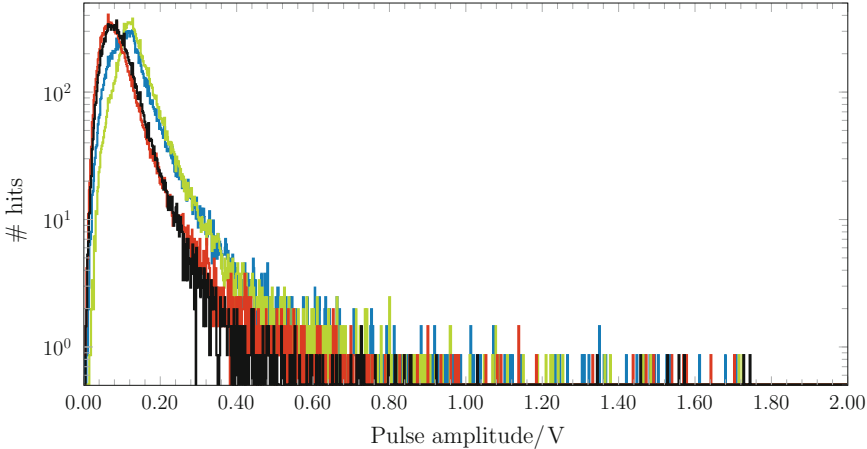


**Fig. 4.9** Distribution of  $N = 10^5$  pulse amplitudes for primary hits viewed by high gain PMTG<sub>1,2</sub><sup>N</sup> (blue, green) and low gain PMTG<sub>3,4</sub><sup>N</sup> (red, black). The respective mean amplitudes are 120, 133, 83, and 89 mV with an uncertainty of less than 1 mV

are well within the dynamic range of the FADC and also within the linear range (up to 1.7 V) of the splitter cards, whereas the prompt signal from a through-going muon (Fig. 4.10b) drive the PMTs in saturation. It is also above the linear range of the delay/splitter card resulting in the measurement of a smaller signal by the FADC. But as the muon signal was only needed for triggering, the resulting distortion in the energy values did not affect the neutron counter. Also in average the prompt signals are within the linear range, as Fig. 4.9 shows.

The high tension for the neutron PMTs was regularly checked and adjusted to compensate for ageing effects, especially of the liquid scintillator, as it will be described in Sect. 4.4.2.

Contrary to the muon telescope where the Landau distributed muon energy deposits have a pronounced peak, the energy deposits from captured neutrons have a continuous spectrum, caused by the leakage of gamma quanta out of the active volume (Sect. 4.1.3). Therefore on one hand every non-zero threshold will cut into the signal and will reduce the neutron detection efficiency. On the other hand, a very low threshold voltage will be well within the gamma background, decreasing the signal-to-noise ratio and will increase the count rate of the NMM. Via the increased dead time this would also decrease the neutron detection efficiency. As the muon veto DAQ and the NMM DAQ are connected, this will also affect the muon veto, reducing the efficiency of the EDELWEISS experiment. Test measurements with an AmBe source by varying the threshold values resulted in the adoption of the threshold voltage of the muon veto (150 mV) also for the NMM as best compromise between a low threshold and a low dead time. The resulting threshold is roughly 3 MeV, as the peak from  $^1\text{H}$  ( $n, \gamma$ )  $^2\text{H}$  at 2.1 MeV is not visible, but the 4.4 MeV gamma ray peak from AmBe, see Fig. 5.19 (blue curve).

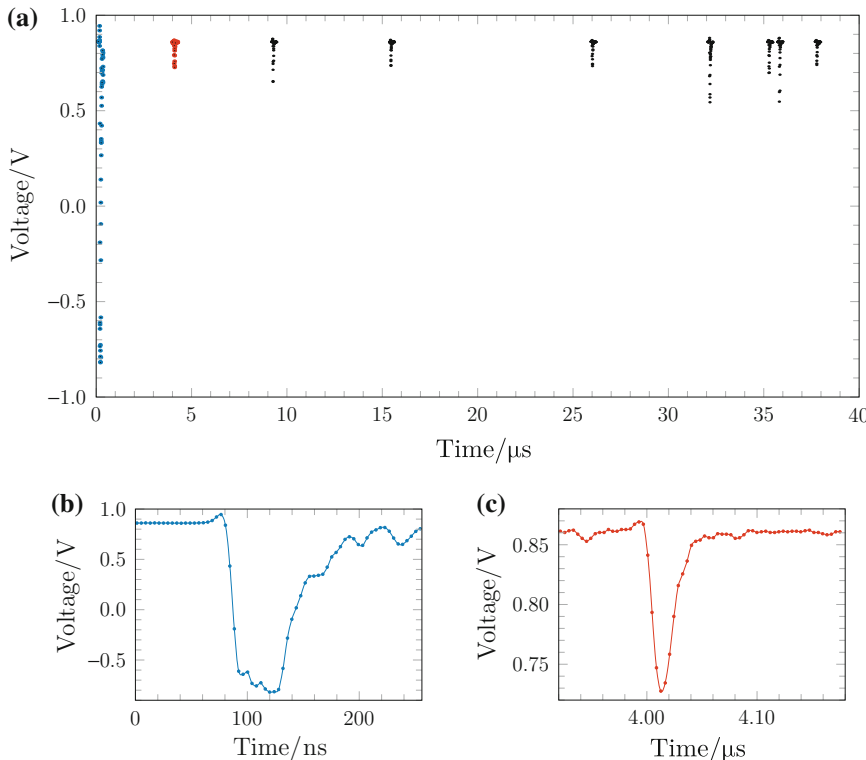


**Fig. 4.10** Exemplary pulse traces of physical data, viewed by  $\text{PMTG}_1^N$  and recorded by  $\text{ADC}^N$  channel 0: **a** Full trace of a candidate for a muon-induced neutron cascade containing 9 hits, **b** magnification of the primary hit (blue), **c** magnification of the first secondary hit (red). Notice the different scales. Lines are to guide the eye

A more detailed threshold calibration is not needed, because the threshold behaviour is in detail included in the Geant4 detector model in Sect. 5.4, which is calibrated against AmBe measurements. Furthermore the energy calibration of the threshold, as any energy calibration, is highly arbitrary, because it depends on the type of particle (neutron, gamma ray) and the location of the interaction due to the quenching and leakage of gamma rays out of the detector (Sect. 4.1.3). As the event signature used in this work is based on the multiplicity and not on an absolute energy scale this is no drawback. Important is the relative energy scale, i.e. the relation between deposited energies and threshold, which is included in the calibrated detector model. The simulation of muon-induced neutron production, which will be discussed in Sect. 5.5, can therefore directly be compared to the measurements with respect to the loss of muon-induced neutrons due to the discriminator threshold. Consequently, in this work the energy scales for both experimental and simulated data will be given in ADC units Eq. 4.18.

#### 4.2.6 Data Acquisition Software and Dead Time

For the control of the muon veto DAQ and the NMM DAQ a combined software was developed within this work. It is based on the software for the muon veto DAQ presented in [24] and was mainly changed by the update for the new time base and extension to control the completely new electronics of the NMM DAQ. It is written in C and directly communicates with the VME/CAMAC electronic modules, handles the transfer of the data from the electronic modules to the hard disk, handles the event creation, and unlocks the modules after the transfer is accomplished.

The used algorithm for event creation was based on the event signature that will be defined in Sect. 4.3. The handling of scaler data is distinct from the handling of the TDC, ADC, and time base data, which is as follows:

The software is based on two POSIX threads<sup>45</sup>. One thread is polling for IRQs on the VMEbus and reads the data from the electronic modules, the second thread stores the data to hard disk. According to the IRQ priority, the two detectors are differenced by the software: The processing of muon veto IRQs has a higher priority than the processing of NMM IRQs, avoiding affection of the muon veto efficiency, important for the overall EDELWEISS performance. An IRQ from each of the two DAQs defines a new event of the respective detector. In case the first thread detected an IRQ the data from TDC, ADC, and the time stamp from the time base get read. Afterwards the second thread stores the data together with a continuous event number in a user defined binary format to hard disk. For the muon veto, including the muon telescope, the data format in [24] is used, for the NMM a similar format was developed. Both data streams are stored in the run based directory structure of the muon veto [24]. After the data are stored to disk, the time base, the veto card of the muon veto, and the logical unit of the NMM are unlocked, i.e. the veto signal to the discriminators is reset and the first threat polls again for IRQs.

Contrary, the scaler data of the muon veto and the NMM are not stored on an event basis, but read every 15 min, the scaler storage is cleared afterwards. Therefore already in their raw form, the read data allow a quick check of the stability of the signal rate.

The software runs on a dedicated Linux based PC at LSM and is remotely controlled via SSH from IKP. The acquired data are automatically transferred on a daily base to the TESLA computer cluster of the IKP. After transfer, the binary data are automatically converted into ROOT files. For the NMM data, dedicated conversion programs were created in this work. Using these ROOT files, the event selection, based on the event signatures in Sect. 4.3, is done by user defined ROOT scripts semi-automatically.

For the NMM data the conversion programme integrated the pulse traces from the FADC using the 2-point closed Newton-Cotes formulae, i.e. the trapezoidal rule [67]. The difference between the FADC data and QDC data, i.e. the difference between a

---

<sup>45</sup>Standardized in IEEE 1003.1c-1995.

numerical and analytical integrated PMT pulse was evaluated according to [63]: A PMT anode pulse, recorded with  $1 \text{ GS s}^{-1}$ , served as reference template and is fitted with [63]

$$V(t) = \begin{cases} -V_0 \exp\left(-\left(\frac{t-t_0}{\tau_r}\right)^2\right), & t \leq t_0 \\ -V_0 \exp\left(-\left(\frac{t-t_0}{\tau_f}\right)^2\right), & \text{otherwise} \end{cases} \quad (4.19)$$

where  $V_0$ ,  $t_0$ ,  $\tau_r$ ,  $\tau_f$  are the amplitude, the peak position, the rising time, and the falling time, respectively. The fitted function is randomly placed within the ADC gate, then the whole pulse trace is on one hand analytically integrated and on the other hand numerically integrated taking into account the voltage resolution and the sampling rate. For pulses with an amplitude of up to 2 V, i.e. using the complete FADC input range, the difference between FADC and QDC is less than 0.017 %. As the reference template is recorded with a sampling rate higher than the one of the FADC, the systematic uncertainty is assumed to be smaller than the stated difference.

In case of interesting events, the user can configure the conversion programme to store also the pulse traces in the ROOT file. Up to now, the possibilities of this feature are not widely used, examples are shown in Figs. 4.9 and 4.10.

The dead time of the complete DAQ system, i.e. hardware and software, was measured with a pulse generator directly connected to the input channels of the NMM discriminator. The electronic branch of the system remains in the state described in Sect. 4.2.4. The measured value [44] of

$$\Delta T_{\text{dead}} = 6.76(8) \text{ ms} \quad (4.20)$$

is significantly higher than the previously measured values of  $48.7(57) \mu\text{s}$  [24] for the muon veto alone. For the neutron counter alone one would expect a dead time in the order of  $\approx 100 \mu\text{s}$ , based on the  $30 \mu\text{s}$  for VME IRQ handling (Sect. 4.2.4) and the additional time for the data transfer, which should be in the same order of magnitude.

A possible reason for the high value of  $\Delta T_{\text{dead}}$  may be the integration of the two triggering processes of NMM and muon veto in one existing DAQ system: The integration of hardware and software had to be done during the running of the EDELWEISS experiment at LSM. Only the hardware extensions for the NMM could be tested at IKP, but because no duplicate of the muon veto DAQ was available at IKP the complete DAQ could not be tested previously to the integration under running condition. This is especially true for the control software, which had to control also the existing muon veto electronic modules. Albeit the total dead time of the combined DAQ is high, it does not affect the neutron counter capability to measure the neutron production yield: As this is the dead time between acquiring of consecutive events, it only affects the detection of muons, but not the detection of neutrons produced by a detected muon, as they are defined by the number of consecutive, delayed signals within an event of the NMM. For comparison with MC simulations in Chap. 6, the measured rates have obviously to be corrected for the dead time.

### 4.3 Signatures for Muon-Induced Neutrons

Besides the definition of the neutron production yield in Eq. 3.64a, the measurement of muon-induced neutrons needs also a dedicated signature to distinguish between the signal, i.e. muon-induced neutrons, and background, i.e. ambient gamma and neutron background as described in Sect. 4.1.2.

Based on the previously explained functionality of the NMM (Sect. 4.2.1), the muon telescope (Sect. 4.2.2) and DAQ electronics (Sect. 4.2.4), this section contains the definition of muon induced events used in this work, both in the measurement (Sect. 4.5) and the simulation (Chap. 5).

Within the selected data, the following two signatures based on the prompt and delayed signals (Sect. 4.2.1) are applied to search for candidates of muon-induced neutrons: the *multiple hit signature* and the *coincident hit signature*. The definition of a *hit* is given in the description of the respective detector (Sects. 4.2.1 and 4.2.2).

The multiple hit signature is similar to the definition proposed in [26] to detect cascades of secondary neutrons produced by a primary muon-induced neutron: Once the NMM starts a DAQ window of length  $\Delta t_{\text{DAQ}} = 60 \mu\text{s}$  it is sensitive for the subsequent hits. The 60  $\mu\text{s}$  long DAQ window (or *sensitive time* [23]) of the NMM is no limitation to the detection of muon-induced neutrons: The expected interval between consecutive muons at LSM is much longer, typically being 2.5 h.<sup>46</sup> Thus, no relevant pile-up of muon-induced neutron cascades is expected.

In this dissertation the following terminology will be used: The hit that starts the DAQ window is called the *primary hit*, the subsequent hits within the DAQ window are *secondary hits*. The primary hit together with secondary hits constitutes the *NMM event*. The primary hit can be caused by a prompt high energetic muon induced neutron as proposed in [26], but also the muon induced shower, or the muon passing through the NMM. The secondary hits are most likely delayed signals from neutrons captured on gadolinium. This can be also checked by the energy deposit. An NMM event with at least one secondary hit constitutes a *neutron cascade candidate*.

To remove the ambiguity of the physical reason of the primary hit and to only select neutron cascades induced by a muon, the *coincident hit signature* is defined. It extends the multiple hit signatures to include also the muon telescope: A hit coincidence between the two muon modules 50 and 51 defines a *muon telescope event*. The coincidence is most likely caused by a muon penetrating both modules, therefore the muon telescope event is also a *muon candidate*. The coincidence between module 50 and 51 is not demanded during data recording, but during the offline analysis. The coincident hit signature is therefore a coincidence of a neutron cascade candidate with a muon candidate within the 10  $\mu\text{s}$  accuracy of the global clock, used to synchronize NMM and muon telescope (Sect. 4.2.4). Consequently, the coincident hit signature

---

<sup>46</sup>Based on the single muon flux of  $5.47(10) \times 10^{-5} \text{ m}^{-2} \text{s}^{-1}$  [6] and a perpendicular detector cross section of  $2 \text{ m}^2$ .

defined a subgroup of neutron cascade candidates. This coincidence is likely caused by a muon passing through the muon telescope, producing neutrons in the lead target of the NMM, which initiates a cascade of secondary neutrons detected by the NMM.

Together with these signatures, also the following *cuts* were applied to the recorded data set to selected periods of pure physics data: Quality cuts exclude periods when monitor measurements with LEDs (Sect. 4.4.3) or AmBe (see later and in Sect. 4.4.2) were ongoing.

As next step, two time cuts are applied to exclude afterpulses as a technical artefact of a neutron PMT within its *recovery time* [23]: As empirically found by Kozlov [40] a minimal interval of 200 ns between consecutive hits is needed, as within this interval the afterpulse rate is increased due to a previous flash of scintillation light. Consequently this interval is not updated.<sup>47</sup> The interval required between the primary hit, which may be caused by a muon, and the first secondary hit is increased to 1  $\mu$ s, as with a higher light intensity of the primary hit a longer recovery time of the PMTs is needed. These cuts define the time resolution of the measurements, as they are longer than the time resolution of the DAQ electronics of 12.5 ns.

These time cuts are applied to the TDC data only and affect the multiplicity, but they are not applied to the ADC data. As one ADC gate could contain several hits (*pile up effect*) the removal of afterpulses from the ADC data would be based on a pulse trace analysis. Albeit a pulse trace analysis is possible, up to now it was not used, and raw ADC values are shown in respective plots [40], e.g. Fig. 4.19. The inclusion of pile-ups and afterpulses may slightly change the energy of events, but they are still valid for the data quality check and not critical for the measurements of muon-induced neutrons as it is based on the hit multiplicity.

An AmBe source was used to test the detection of muon-induced neutron events as defined by the multiple hit signature and for monitoring the detection efficiency: It was placed on top of the NMM near the muon telescope, see Fig. 4.5c. In 57.5 % of the cases the emitted neutron is accompanied with a 4.4 MeV gamma quantum (Eq. A.53), that gives the prompt signal, and the capture of the neutron produces the delayed signal.

The multiplicity of secondary hits is a measure of the produced neutrons in the lead target, but its interpretation is not straight forward: Contribution from  $(n, 2n)$  reactions in the liquid scintillator (Sect. 4.1.2) and the muon-induced shower distort the multiplicity. Therefore, the measurements had to be compared with MC simulations of the neutron production process (Chap. 5), taken into account the  $(n, 2n)$  reactions and given event signatures within their model of detector response (Sect. 5.4). This work is focused on the more restricted coincident hit signature as it provides a better suppression of ambient neutron background as will be shown in Sect. 5.5.5.

---

<sup>47</sup>For example, if a sequence of three hits occurs at times 10, 200 and 220 ns the last two hits are removed, even if the third hit is separated from the first by more than 200 ns.

## 4.4 Detector Live-Time and Stability

For a successful *long term* measurement of muon-induced neutron production, the neutron detector had to be operated under stable conditions during its live-time, planned to last three years [44]. The neutron detection efficiency is directly affected by three effects: Reduced neutron capture due to precipitation of gadolinium out of the liquid scintillator, reduced scintillation light collection due to colouring of the liquid scintillator (for a physical explanation of both effects see Sect. 4.2.1), and shifts of the parameters of the DAQ electronics (Sect. 4.2.4).

The overall live-time of the neutron counter, based on its chronological performance, is given in Sect. 4.4.1. Thereafter, the stability of the gadolinium content, of the scintillator transparency, and of the electronic properties are investigated in Sects. 4.4.2–4.4.4, respectively.

### 4.4.1 Live-Time and Chronological Performance of the Experiment

The live-time of the neutron counter equals the interval between the end of its commissioning phase and its dismantling, corrected for all times when it was not sensitive for muon-induced neutrons. The obvious cases are when the detector was powered off due to maintenance issues, but also in case of monitoring measurements. Also the dead time due to DAQ has to be taken into account, see Sect. 4.2.6.

The detector was running for nearly three years: The installation at LSM was finished on 19 September 2008, and after a commissioning stage, data was taken from Apr 2009 on until its dismantling started on 16 October 2012, i.e. it was installed for 1488 days. Within this interval, the DAQ electronics was improved three times in the following aspects, see also Sect. 4.2.4:

- A new IKP-made time board was installed on 9 September 2009 and provided dedicated time stamps for the neutron counter. Even before the installation, coincident events in NMM and muon telescope events were marked via the muon veto flag in the NMM data. But with a time stamp for both sub-detectors further information could be retrieved from the muon telescope.
- The replacement of the NMM QDC with a FADC also on 9 September 2009 enabled the measurement of the energy deposit per hit. This allowed further testing of the signal by comparison of the measured energy spectrum with the prediction from simulations.
- On 29 September 2010, a new version of the light pulser control module was installed. It removed the cross talk problem described in Sect. 4.2.3.

This work is based on the recorded data from April 2009 to September 2012 [40], i.e. roughly 1249 days. Subtracting monitoring measurements with the AmBe source (see Sect. 4.4.2 for details), any test period or malfunctioning DAQ, a total

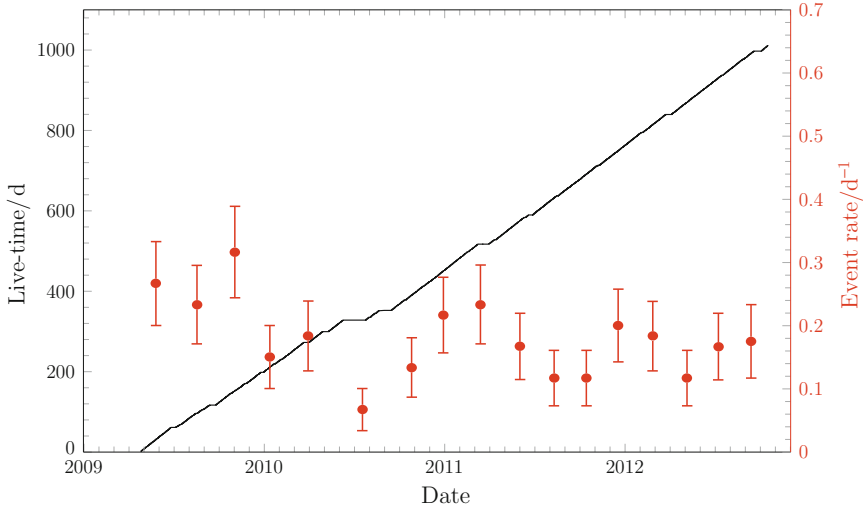


**Fig. 4.11** Accumulated live-time of the detector as a function of time (black, left scale), corrected for AmBe monitoring measurements. Red data points show the rate of events according to the coincident event signature over time (right scale). Figure provided by V.Y. Kozlov [40]

live-time of 1012 d [40] for the NMM was recorded. This is equivalent to a duty cycle of  $\approx 81\%$ . The live-time of 964.5 days for the whole neutron counter is shorter, as the muon telescope was not running during the whole NMM live-time [40]. The development of the cumulative live-time of the NMM is shown in Fig. 4.11. The periods where the NMM was powered off due to maintenance are clearly visible as horizontal sections. The remaining live-time has to be further corrected for the time of LED based monitoring and the dead time: The latter is 6.8 ms (Eq. 4.20) between consecutive events and is equivalent to 75 days for the period of 964.5 days [40]. However, more detailed studies of the dead time are ongoing [40], and hereafter the estimate is handled as systematic uncertainty.

The overall stability of the neutron counter during its running can be assessed also with Fig. 4.11: In red it shows the rate of events passing the coincident event signature over time. Its constancy since beginning of 2010 together with the high duty cycle indicates the stable running of the neutron counter. The decrease of the event rate within 2009 maybe related to precipitation of gadolinium out of the liquid scintillators, see Sect. 4.4.2.

The neutron counter reached its planned running time of 3 years under stable conditions allowing a satisfactory statistical accuracy of its measurements. However, due to the nonreversible degradation of the liquid scintillator via gadolinium precipitation (Sect. 4.4.2) and decreasing of transparency (Sect. 4.4.3), a longer running time would have led to limited better statistics, but significantly higher systematic uncertainties and risks of hardware failure.

#### 4.4.2 Precipitation of the Gadolinium Out of the Liquid Scintillator

As discussed in Sect. 4.1.1, the neutron capture efficiency depends mostly on the gadolinium content of the liquid scintillator, as gadolinium has the biggest cross section for the capture of thermalized neutrons. Since the solution of gadolinium in liquid scintillator tends to be chemically unstable, the precipitation of the gadolinium out of the liquid scintillator is a prominent threat, see Sect. 4.2.1. As this work aimed to assess the capability of Geant4 to reproduce the neutron production and detection, it is necessary to include such shifts of the neutron capture efficiency in the detector model. Therefore, the neutron capture was regularly monitored with an AmBe neutron source, placed on top of the NMM. Figure 4.5c shows the position of the source. Besides the monitoring of the gadolinium content, these measurements with the AmBe source also prove the principal capability of the NMM to detect neutrons. For details of the used AmBe source, see Appendix A.6.

As measure for the gadolinium content  $n_{\text{Gd}}$  of the liquid scintillator, the neutron capture time  $\tau_{\text{cap}}$  was used: The capture time depends on the capture times of the individual scintillator components weighted by their abundance (Eq. 4.7a). Therefore a change in the capture time indicates a change in the composition of the liquid scintillator. The empirical capture time was obtained from a fit of the effective Eq. 4.8 to the *capture time distribution*, see exemplary Fig. 4.12. This is the distribution of time intervals between the primary hit and any secondary hit within an NMM event, see Sect. 4.3 for the definition. The secondary hits are most likely the delayed signals

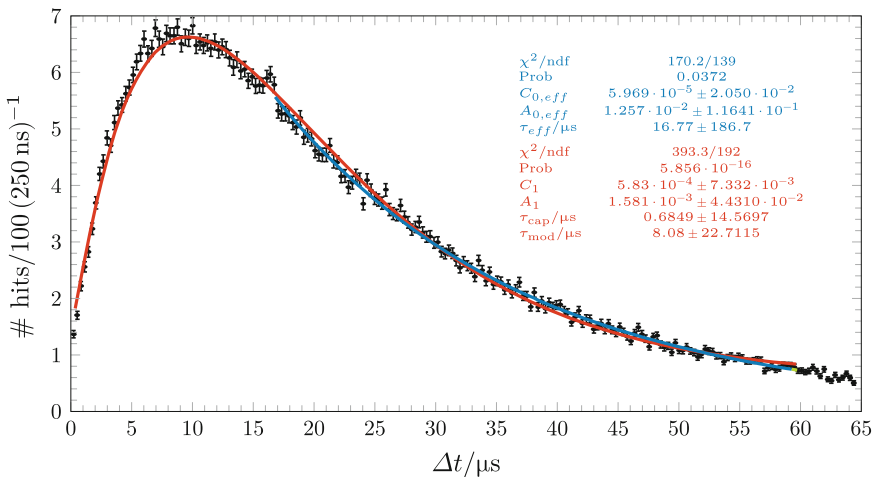


**Fig. 4.12** Distribution of time intervals  $\Delta t$  between primary hit and any secondary hit, for  $N = 210,791$  events recorded in an AmBe measurement. The error bars indicate 68 % CL. Fitted with an effective capture time (Eq. 4.8, blue) and a full description of moderation and capture (Eq. 4.9, red). For details see text

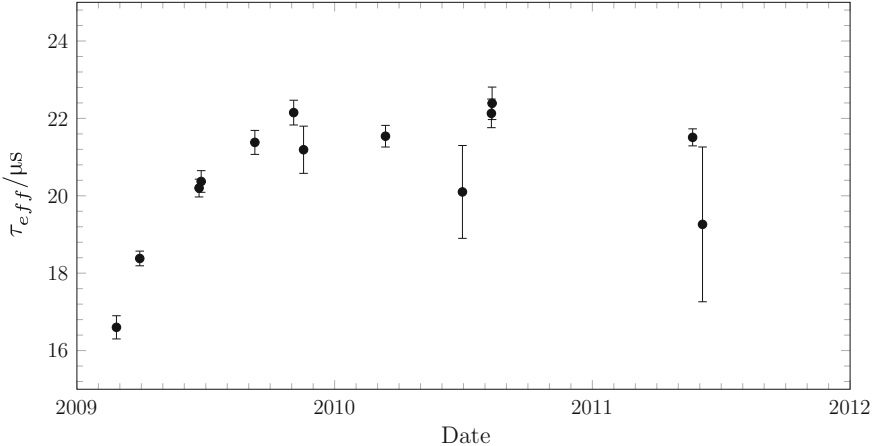


**Fig. 4.13** Time series of effective neutron capture time  $\tau_{eff}$  in the NMM. Each data point is based on mostly a 1-day measurement with an AmBe source of  $20\text{ s}^{-1}$  neutron activity. Error bars indicate 68% CL. Data provided by V.Y. Kozlov [42]

from captured neutrons on gadolinium with respect to the 4.4 MeV gamma rays of AmBe as primary hit. Its variation over time is shown in Fig. 4.13: The capture time increased after the installation of the neutron counter and reached a somewhat stable plateau at the beginning of 2010. This coincides with the decrease of the event rate in Fig. 4.11 and thus could be attributed to the rate reduction.

The relation of the effective capture time to the gadolinium content is not straightforward (Sect. 5.4.1). It was determined via Geant4 simulations:

In a first stage, the shift  $\delta n_{Gd}$  was deduced from the shift  $\delta \tau_{cap}$  by modelling the AmBe monitor measurements. Here, the same AmBe source configuration was implemented as used for the measurement, taking into account the branching ratio of the neutron emission only, and the neutron and gamma decay channel, see Appendix A.6. The simulations contain the detailed geometry implementation, physics list, and detector response model with the best fitting model parameter that will be described in Sects. 5.1, 5.2 and 5.4, respectively. The TDC distribution of the simulated NMM events as a function of  $n_{Gd}$  was fitted with the effective Eq. 4.8:  $P(\Delta t) = C_{eff} + A_{eff} e^{-\Delta t/\tau_{eff}}$ , i.e. replacing  $\tau_{cap}$  with  $\tau_{eff}$ . As the simulation contains no background, the free parameter  $C_{eff}$  is in agreement with 0. To increase the degrees of freedom, the final fits were done with  $C_{eff} \equiv 0$ .

Figure 4.14 shows the resulting curve  $\tau_{eff}(n_{Gd})$  in black. For AmBe as source, the detection efficiency  $\epsilon_{AmBe}$ , i.e. number of started neutrons to number of secondaries within the NMM events (Sect. 4.3), is shown in black.

For the first measurement in Fig. 4.13, i.e. on 26 February 2009, one obtained  $\tau_{eff} = 16.6(3)\text{ }\mu s$ . Together with the  $\tau_{eff}(n_{Gd})$  curve shown in Fig. 4.14, this results in  $n_{Gd} = 0.203(9)\text{ \% w/w}$ . This is in excellent agreement with the specification of 0.20% w/w as given in the data sheet as nominal loading (Table A.5). It also proves

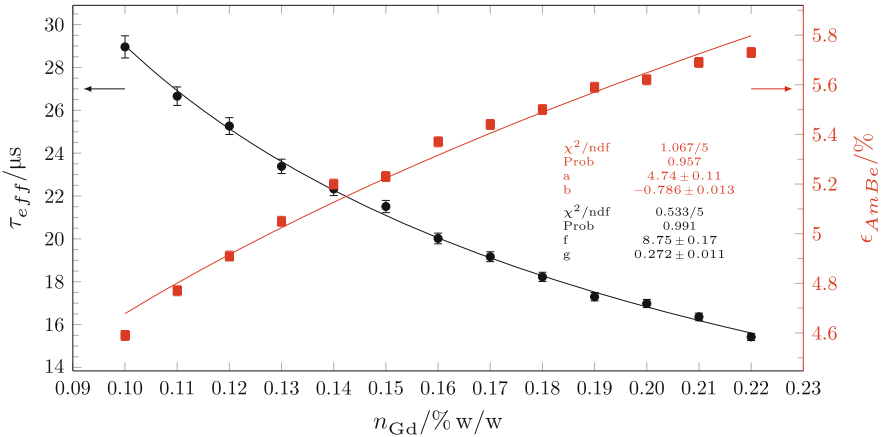


**Fig. 4.14** Simulated dependence of the effective neutron capture time  $\tau_{\text{eff}}$  (black circles, left scale) and neutron capture efficiency  $\epsilon_{\text{AmBe}}$  (red boxes, right scale) on the gadolinium content  $n_{\text{Gd}}$  of the liquid scintillator.  $N = 2 \times 10^6$  neutrons are started from an AmBe source for each data point. Error bars indicate 68 % CL, which is smaller than the marker for  $\epsilon_{\text{AmBe}}$ . The individual points are fitted by empirical functions:  $\tau_{\text{eff}} = a \times n_{\text{Gd}}^b$ ,  $\epsilon_{\text{AmBe}} = f \times n_{\text{Gd}}^g$ . For details see text

the capability of the neutron counter to detect neutrons and distinguish them from the background, as well as the ability of Geant4 to model neutron capture on gadolinium.

For the nominal loading, the simulation gives a detection efficiency of

$$\epsilon_{\text{AmBe, MC}}(0.203(9)\% \text{ w/w}) = 5.67(16)\%. \quad (4.21)$$

In the following measurements the capture time increased up to 22.4(4)  $\mu\text{s}$  on 12 August 2010. If this is interpreted as a decrease of the gadolinium content, then it drops to

$$n_{\text{Gd}} = 0.139(7)\% \text{ w/w} \quad (4.22)$$

for this measurement, resulting in

$$\epsilon_{\text{AmBe, MC}}(0.139(7)\% \text{ w/w}) = 5.11(16)\%, \quad (4.23)$$

i.e. the detection efficiency shifts by

$$\frac{\epsilon_{\text{AmBe, MC}}(22.4(4)\mu\text{s}) - \epsilon_{\text{AmBe, MC}}(16.6(3)\mu\text{s})}{\epsilon_{\text{AmBe, MC}}(16.6(3)\mu\text{s})} = -10(4)\%. \quad (4.24)$$

This may contribute to the shift in the detection rate shown in Fig. 4.11.

The hypothesis of a decreased gadolinium content is also supported by the observation of a white powder at the bottom of the active volume during the dismantling of the NMM [41], which was possibly gadolinium-oxide precipitated out of the liquid scintillator.

The *absolute* efficiency determined from AmBe measurements is not applicable for muon-induced neutrons, as the source geometry is different, e.g. a point like AmBe source instead of extended neutron emission from the lead target. However, we assume that the *relative* shift of the efficiency due to precipitation of gadolinium is the same. Therefore, it is taken into account as systematic uncertainty in Sect. 5.5.4 for the detection efficiency for muon-induced neutrons that will be given in Sect. 5.5.3.

#### 4.4.3 Deterioration of the Transparency of the Liquid Scintillator

The detection efficiency of the neutron counter is also affected by the light collection efficiency, i.e. the ratio of light finally collected by the PMTs to the total amount of light emitted in scintillation. A long term shift of the light collection efficiency can be likely caused by the decreased transparency of the liquid scintillator via colouring, see Sect. 4.2.1. The transparency of the liquid scintillator can be determined by comparing the emitted light intensity of a reference source with the collected light after passing through the active volume. As the reference source, the LED based light pulser described in Sect. 4.2.3 was used.

Albeit the absolute light output of the LEDs is not calibrated, a relative measurement is possible due to the symmetric positions of the LEDs to each other, see Fig. 4.6. In the following, the high gain neutron PMT groups  $\text{PMTG}_1^N$  ( $\text{PMTG}_5^N$ ) connected to ADC<sup>N</sup> channel 0 (channel 2) are used as light receiver.

As they are symmetric with respect to LED0 they should receive the same light intensity from LED0, thus any deviation of the ADC0/ADC2 ratio from unity indicates a difference in the gain of the respective PMT groups. Therefore, after subtraction of the pedestals  $P$  (Appendix A.5.4), the measured ADC values are normalized to the ADC value caused by LED0.

For an LED at a position that is not symmetric with respect to  $\text{PMTG}_{1,5}^N$ , e.g. LED2, the received signals are different, due to the different light absorption along the light paths of different length. Exemplary Fig. 4.15 shows a full sequence of all 8 LEDs of the light pulser. As this particular sequence was recorded with the first, malfunctioning LED control board, also cross talk between the LED channels is visible. As LEDs 0, 3, 6, and 7 are symmetric with respect to  $\text{PMTG}_{1,5}^N$ , these PMTs receive the same amount of light, resulting in roughly the same ADC signals. LEDs 1 and 2 are closer to  $\text{PMTG}_1^N$  than to  $\text{PMTG}_5^N$ , therefore the signals on ADC0 (blue) are higher than on ADC2 (red). For LEDs 4 and 5 the opposite is true.

The gain and pedestal corrected ratio  $\eta_{1,5,2}$  of the received light by  $\text{PMTG}_{1,5}^N$  from LED2 is therefore:

$$\eta_{1,5,2} = \frac{\text{ADC0(LED2)} - P0}{\text{ADC0(LED0)} - P0} \Big/ \frac{\text{ADC2(LED2)} - P2}{\text{ADC2(LED0)} - P2} \quad (4.25)$$

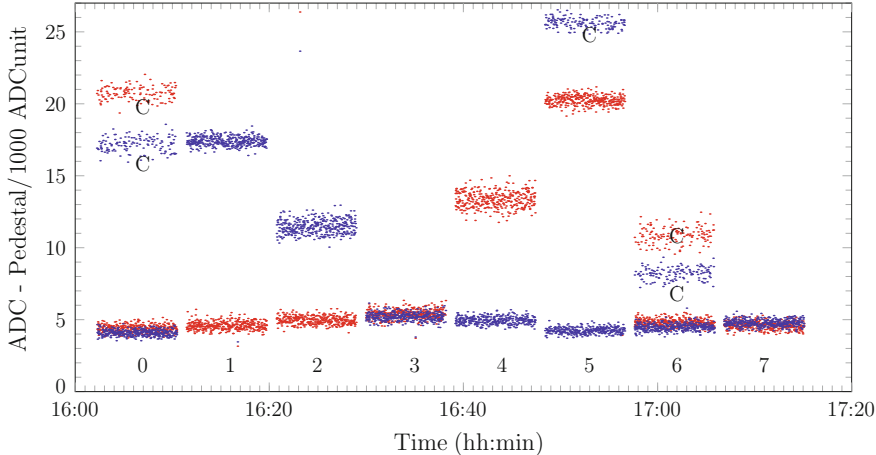


**Fig. 4.15** A sequence of all eight LEDs viewed from  $\text{PMTG}_1^N$  (blue) and  $\text{PMTG}_5^N$  (red). Starting with LED0 and ending with LED7. Above the signal region, noise due to cross talk is visible for LED0, LED5, and LED6 and marked with C. For details see text

Within this work, a programme was developed to automatically select the regular started LED sequences out of the recorded data, remove the cross talk noise by applying appropriate cuts and to calculate  $\eta_{1,5,2}$ .

In case of a long, but infinitely thin active volume, the light paths are identical to the distances  $l_{1,2}$  ( $l_{5,2}$ ) between  $\text{PMTG}_1^N$  ( $\text{PMTG}_5^N$ ) and LED2. Therefore  $\eta_{1,5,2}$  can be expressed using the *Beer-Lambert law* [77] by:

$$\eta_{1,5,2}(\alpha^{-1}) = e^{-(l_{1,2}-l_{5,2})\alpha} \quad (4.26)$$

where  $\alpha^{-1}$  is the absorption length of the scintillator.

As the NMM uses a large active volume, the light paths are longer than the distances between PMTs and LED2 due to reflections at the boundaries and  $\alpha^{-1}$  in Eq. 4.26 has to be replaced with the effective attenuation length  $\Lambda(\alpha^{-1})$ , containing the information about the actual light paths caused by the geometry of the active volume and by the given placement of PMTs and LEDs.

The detector geometry of the active volume of the NMM is not trivial, therefore a relation between  $\eta_{1,5,2}$  and  $\alpha^{-1}$  has to be based on MC simulations of the light propagation. Besides an implementation of the optical properties of the materials coupled to the active volume, the MC detector model in Sect. 5.1 also contains a correct implementation of the position and aperture angle of the LEDs.

Based on this model, F. Laible [48, Fig. 5.1] obtained the function  $\eta_{1,5,2}(\alpha^{-1})$ . Together with an improved analysis of the empirical  $\eta_{1,5,2}$  time series [48, Fig. 4.10], obtained via the light pulser, the time series of  $\alpha^{-1}$  can be fitted by [48, Fig. 5.2], [47]:

$$\alpha^{-1}(t) = (3.56 \pm 0.29) + (2.90 \pm 0.59)e^{-t/0.58(28)\text{yr}} \quad (4.27)$$

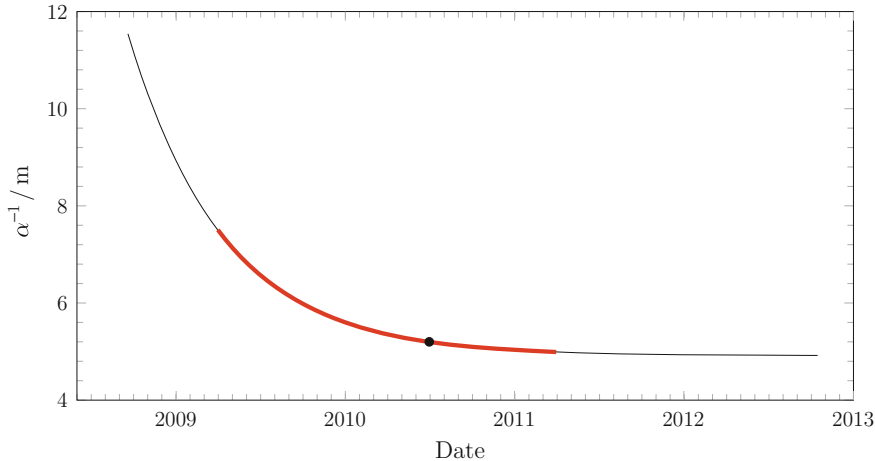


**Fig. 4.16** Long term shift of the absorption length  $\alpha^{-1}$ . Based on the LED light pulser measurement for the period April 2009—April 2011 as parametrized by Eq. 4.27 [48, Fig. 5.2] (thick red curve) and extrapolated to the complete running period of the neutron counter (thin black curve). Absolute value normalised to 5.2 m on 1 July 2010 (black point), based on Geant4 simulation of an AmBe reference measurement in this work

As even a small misalignment of the LEDs results in great changes of the light propagation [44], this investigation does not reveal the absolute value of the absorption length. However, we can scale  $\alpha^{-1}(t)$  by a factor of 1.38(15) to the absorption length of 5.2(1) m obtained in Sect. 5.4.4 for an AmBe reference measurement at 1 July 2010, see Fig. 4.16.

With this normalisation the attenuation length of  $\alpha^{-1} = 12(2)$  m is extrapolated for 19 September 2008 when the liquid scintillator was filled in the NMM. As the used BC-525 is based on the scintillator described in [66], which had an average attenuation length of 11.4 m, this value seems plausible. At the dismantling of the neutron counter on 20 October 2012 the attenuation length dropped to 4.9(7) m, still above the lower bound of 4.5 m specified in the data sheet, see Table A.5.

The average shift is therefore  $-0.44(15)$  cm d $^{-1}$ . This is smaller than the published shift of  $-1.3$  cm d $^{-1}$  to  $-2.2$  cm d $^{-1}$  for the similar scintillator [66]. Taken the exponential decay into account (Eq. 4.27), the smaller value in this work compared to [66] can be explained by the longer time period of 1488 d in this work compared to 255 d in [66]. Taken the same 255 d as reference period after filling of the scintillator, this work gives a shift of  $-1.8(10)$  cm d $^{-1}$ , in agreement with [66].

As it will be shown in Sect. 5.4, the decrease of the effective attenuation length is anti-correlated to the increase of the PMT gain with respect to the detection efficiency. This proves that a decreasing absorption length can be compensated with increased gain of the detector that is controlled via the high tension of the PMTs. As mentioned in Sect. 4.2.5 this was performed regularly. Therefore, the change of attenuation length does not need to be included in the Geant4 model of the detector in Sect. 5.5.

#### 4.4.4 Long Term Shifts in the DAQ Electronics

As discussed in Sect. 4.3, the signatures of muon induced neutrons used in this work are based on the multiplicity of signals above threshold within the DAQ window. Therefore shifts in the DAQ electronics may affect the measurements if they change the effective threshold or if they change the length of the DAQ window.

For the discriminator threshold itself no time stability is specified in the discriminator manual. But as the threshold voltage is specified with 8 bit resolution value a stability equal to the last significant bit, i.e. a relative stability of 0.4 %, is assumed within this work.

A change in the pedestals as measured by the ADC can indicate a change on the baseline of the input channel that can change therefore the effective threshold. As at least a part of the pedestals are generated within the ADC itself, changes of the pedestals are only an upper limit in the change of the effective threshold. The method of pedestal measurement and the resulting values are given in Appendix A.5.4, the largest variation is 1.05 %. By linearly adding of the discriminator threshold shift and the pedestal shift one obtains a shift of the effective threshold in the order of 1.5 %.

Albeit the width of the DAQ window was set to a nominal value of  $\Delta t_{\text{DAQ}} = 60 \mu\text{s}$  it varied over time: Fig. 4.17a shows the TDC value of the primary hit within an event over roughly one year. Although we analysed only a part of the whole live-time of the detector, we assume that it is typical for all recorded data. As the primary hit starts the DAQ window and the TDC value is given with reference to the end of the DAQ window, it is equal to the width of the DAQ window  $\Delta t_{\text{DAQ}}$ . The distribution of the DAQ window for the analysed time period is shown in Fig. 4.17b: The mean

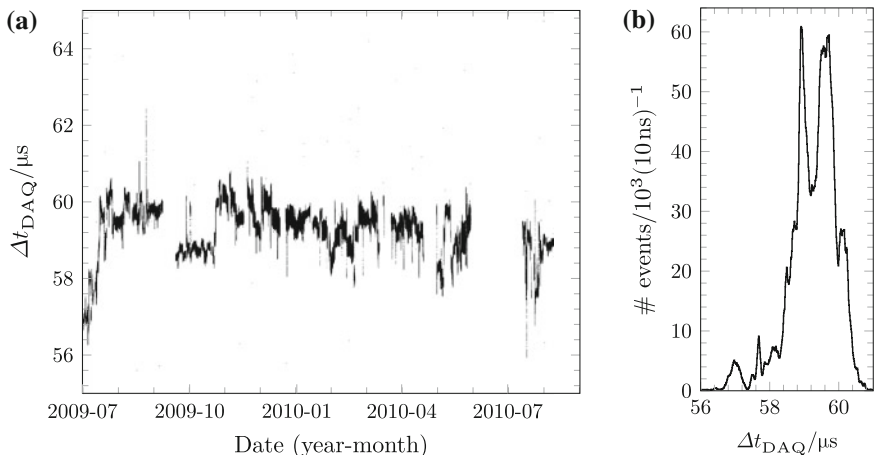


**Fig. 4.17** DAQ window width  $\Delta t_{\text{DAQ}}$  for  $N \approx 1.4 \times 10^7$  events: **a**  $\Delta t_{\text{DAQ}}$  as a function of time. **b** Distribution of  $\Delta t_{\text{DAQ}}$ : mean  $59.25 \mu\text{s}$ , RMS  $723.7 \text{ ns}$

value of  $59.25 \mu\text{s}$  is shifted by  $-1.3\%$  with respect to the nominal value of  $60 \mu\text{s}$ . Based on the RMS the DAQ window  $\Delta t_{\text{DAQ}}$  varied by  $1.2\%$  relative to the mean value.

Therefore we considered a small systematic uncertainty in the effective threshold and in the DAQ window when the complete set of measured data is compared with the prediction of the Geant4 simulation, see Sect. 5.5.4.

## 4.5 Measured Muon-Induced Neutrons

As pointed out in Sect. 4.4, the neutron counter, i.e. the NMM and the muon telescope, was running for roughly three years under stable conditions and up to 964.5 days live-time of data were taken. In Sect. 4.5.1 we will confirm that the measured data set contains muon-induced neutrons and in Sect. 4.5.2 the corresponding rate of neutron candidates will be calculated.

### 4.5.1 Particle Identification

The analysis of the physical data discussed in this work was provided by V.Y. Kozlov [40]: For data recorded with the high gain PMTs of the NMM (Sect. 4.2.1) the coincident hit signature was used and for the data recorded by the low gain PMTs, the multiple hit signature was used. The demanded coincidence with a through-going muon strongly suppresses background from ambient neutrons and gamma quanta. Contrary, the multiple hit signature has less discrimination power, and thus it is only applied to the data recorded with the low gain PMTs, i.e. with a higher effective threshold. Nevertheless, the data analysed with the multiple hit signatures still contain significant contamination from ambient neutrons, more than the data analysed with the coincident hit signature, as Geant4 simulations will show in Sect. 5.5.5. Therefore this work will focus on the coincident hit signature.

The monitoring measurements with the AmBe source described in Sect. 4.4.2 verifies that the chosen detector systems, electronics, and event selection were clearly able to identify neutron signals and separate them from background. However, it remains the question if the same procedure is also able to detect muon-induced neutrons in the *physics data*, i.e. the recorded data without the AmBe and light pulser monitor measurements, which is quantified in Table 4.2. The answer to this question is the particle identity that causes the primary and secondary hits.

The identity of the secondary hits was investigated via a comparison of the recorded TDC values: Fig. 4.18 shows a distribution of the measured time differences  $\Delta t$  between any secondary hit and the primary hit within an event according to the coincident hit signature, see Sect. 4.3 for the relevant definitions. If the secondary hits in the physics data are also caused by captured neutrons, then the distribution should be in agreement with the one from AmBe monitoring data. This hypothesis

**Table 4.2** Properties of the measured data set. Data provided by V.Y. Kozlov [40]

Property	Value
Live-time NMM in days	1012
Live-time neutron counter in days	964.5
Dead time in days	$\approx 75$
Number of events	181
Number of secondaries	313
Number of muons	5583

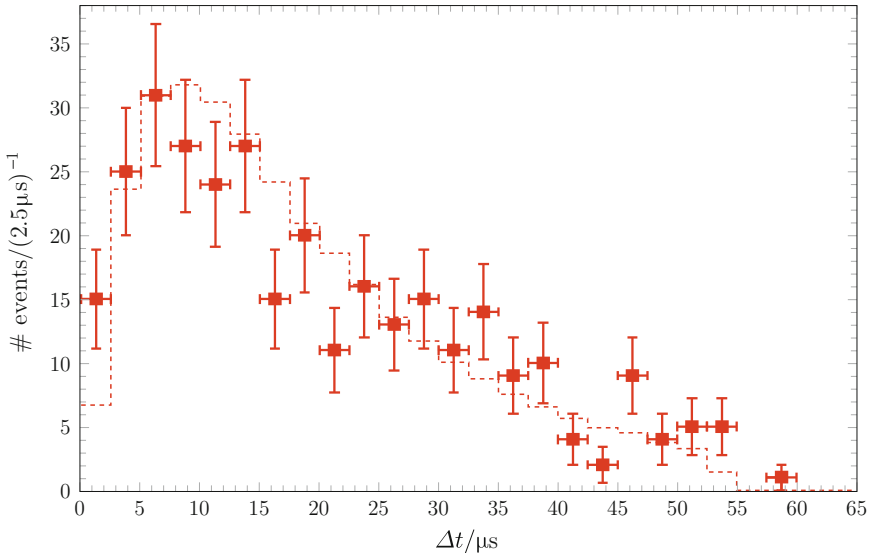


**Fig. 4.18** Distribution of time intervals  $\Delta t$  between any secondary hit and the primary hit (data points) for the multiple hit signature, containing 313 secondary hits over a live-time of 964.5 d. Compared to AmBe data (histogram) scaled to the same live-time. Figure adapted from [40]

was investigated via a Kolmogorov-Smirnov test, comparing the complete set of physics data with AmBe measurements from 4 dates. For 3 out of 4 cases the test does not reject the hypothesis [40]. The rejection of one sample may be caused by the progressing decrease of the gadolinium content in the scintillator, see Sect. 4.4.2. Therefore, the hypothesis that the secondary hits within the physics data are caused by captured neutrons is well justified.

As discussed in Sect. 4.3 the primary hits should be caused by through-going muons, i.e. they constitute a muon candidate. Indeed, the ADC distribution of the primary hits as shown in Fig. 4.19 follows a Landau distribution as expected for muons in a thin target. A more detailed test is the comparison between the measured ADC and TDC distributions and the results from Geant4 simulations in Chap. 6.

The TDC and ADC spectra by themselves are useful as checks of the data quality and our understanding of the detector, but the information about the production yield

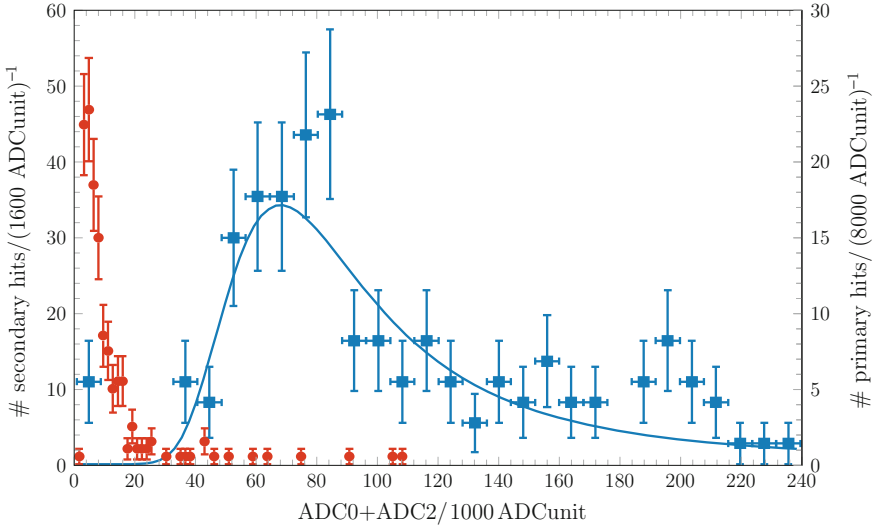
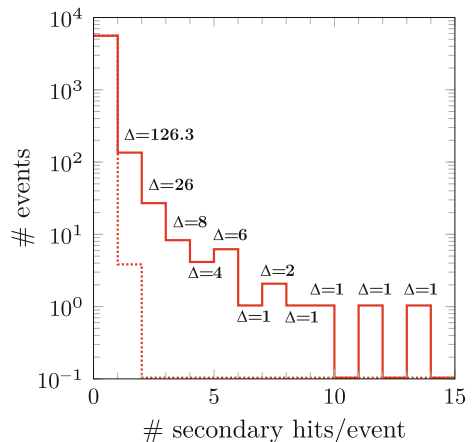


**Fig. 4.19** Accumulated sum spectra  $\text{ADC0} + \text{ADC2}$  for the coincident hit signature viewed by  $\text{PMTG}_{1,5}^N$ . Subset of 853.7 d live-time with installed flash ADC. For each value, the pedestal from the corresponding pedestal measurement is subtracted. Red circles (left scale) show the spectrum of 255 secondary hits, blue squares (right scale) show the spectrum of 151 primary hits. Error bars indicate 68 % CL. A Landau function is fitted to the primary hits ( $\chi^2/\text{ndf} = 27.34/23$ ) with most probable value of  $\mu = 71(3) \times 10^3 \text{ ADCunit}$ . Figure adapted from [40]

of muon-induced neutrons as defined in Sect. 3.5.4 is extracted from the multiplicity spectrum of secondary hits within an event: The ratio of secondary hits to primary hits is a measure of the ratio of produced neutrons per muon. Figure 4.20 shows these spectra for the 964.5 d live-time of the coincident hit signature.

**Fig. 4.20** Accumulated multiplicity spectrum for the coincident hit signature over 964.5 d live-time. The numbers give the measured excess over the expected background of random coincidences, which is indicated by the dashed line. Figure adapted from [40]



The measured multiplicity spectrum has to be also compared to the expected background of accidental coincidences. Random coincidences between  $n$  not correlated secondary hits and a primary hit would follow a Poisson distribution [16]:

$$P(n; \nu) = \frac{\nu^n e^{-\nu}}{n!} \quad (4.28a)$$

$$\nu = \frac{n_{\text{event}}}{T_{\text{run}}} T_{\text{DAQ}} \quad (4.28b)$$

with the averaged event rate per run  $n_{\text{event}}/T_{\text{run}}$ , i.e. number of events  $n_{\text{event}}$  within a run of length  $T_{\text{run}}$ . The average DAQ window width  $T_{\text{DAQ}}$  was determined from the TDC data per run [40] and is therefore not identical to the nominal window width of  $\Delta t_{\text{DAQ}}$ . The resulting expectation for uncorrelated events is shown in Fig. 4.20 as dashed histogram. As every event has per definition at least one hit, the *primary* hit that caused the event generation, the Poisson distribution was normalized to the experimental data for no *secondary* hit. The measured event numbers with at least one secondary are clearly in excess over the expectation of Poisson distributed uncorrelated coincidences and listed in Table 4.3.

In summary, the measured physics data contains clearly events caused by multiple neutrons correlated with through-going muons, i.e. candidates for muon-induced neutrons. The corresponding candidate rate will be calculated in the following Sect. 4.5.2.

**Table 4.3** Rate  $R_{n,\text{can},\text{exp}}$  of measured neutron candidates, i.e. excess of measured events  $n_{n,\text{can},\text{exp}}$  over expected Poisson background  $n_{\text{acc}}$ , classified for the multiplicity of neutron candidates  $M_{n,\text{can}}$

$M_{n,\text{can}}$	$n_{n,\text{can}}$	$n_{\text{acc}}$	$R_{n,\text{can},\text{exp}} (\text{d}^{-1})$
1	130	3.7	$(1.31^{+0.12\text{stat}}_{-0.12} {}^{+0.11\text{sys}}_{-0.09}) \times 10^{-1}$
2	26	$1.3 \times 10^{-3}$	$(2.70^{+0.53\text{stat}}_{-0.53} {}^{+0.23\text{sys}}) \times 10^{-2}$
3	8	$3.4 \times 10^{-7}$	$(8.29^{+3.44\text{stat}}_{-2.80} {}^{+0.70\text{sys}}) \times 10^{-3}$
4	4	$7.0 \times 10^{-11}$	$(4.15^{+2.88\text{stat}}_{-1.72} {}^{+0.35\text{sys}}) \times 10^{-3}$
5	6	$1.2 \times 10^{-14}$	$(6.22^{+3.40\text{stat}}_{-2.26} {}^{+0.52\text{sys}}) \times 10^{-3}$
6	1	$1.7 \times 10^{-18}$	$(1.04^{+1.81\text{stat}}_{-0.65} {}^{+0.09\text{sys}}) \times 10^{-3}$
7	2	$2.3 \times 10^{-22}$	$(2.07^{+2.33\text{stat}}_{-1.31} {}^{+0.17\text{sys}}) \times 10^{-3}$
8	1	$2.6 \times 10^{-26}$	$(1.04^{+1.81\text{stat}}_{-0.65} {}^{+0.09\text{sys}}) \times 10^{-3}$
9	1	$2.8 \times 10^{-30}$	$(1.04^{+1.81\text{stat}}_{-0.65} {}^{+0.09\text{sys}}) \times 10^{-3}$
10	0	$2.7 \times 10^{-34}$	$(0.00^{+1.34\text{stat}}_{-0.00} {}^{+0.00\text{sys}}) \times 10^{-3}$
11	1	$2.4 \times 10^{-38}$	$(1.04^{+1.81\text{stat}}_{-0.65} {}^{+0.09\text{sys}}) \times 10^{-3}$
12	0	$1.9 \times 10^{-42}$	$(0.00^{+1.34\text{stat}}_{-0.00} {}^{+0.00\text{sys}}) \times 10^{-3}$
13	1	$1.5 \times 10^{-46}$	$(1.04^{+1.81\text{stat}}_{-0.65} {}^{+0.09\text{sys}}) \times 10^{-3}$

The statistical uncertainty indicates 68 % CL. For details see text

### 4.5.2 Rate of Muon-Induced Neutron Candidates

As the previous section confirmed, the data set recorded over  $T_{\text{exp}} = 964.5$  d contains candidates for muon-induced neutrons. Based on Table 4.2, this section will give the candidate rate and the associated uncertainties as listed in Sect. 4.5.2.

The rates of measured candidates for  $x = \text{muons, neutron cascades, and neutrons}$  are straightforward defined as ratio of the measured excess  $n_x - n_{\text{acc},x}$  of quantity  $x$  over the accidental background  $n_{\text{acc},x}$  to the experimental live-time  $T_{\text{exp}}$ :

$$R_{x,\text{exp}} = \frac{n_x - n_{\text{acc},x}}{T_{\text{exp}}} \quad \text{for } x = \mu, \text{cas, n} \quad (4.29)$$

$$\delta R_{x,\text{exp}}^{\text{stat}} = \left| \frac{\sqrt{n_x}}{T_{\text{exp}}} \right| \quad (4.30)$$

An insight into the physics of muon-induced neutron production is obtained via the ratios  $\eta_{n,x,\text{exp}}$ :

$$\eta_{n,x,\text{exp}} = \frac{R_{n,\text{exp}}}{R_{x,\text{exp}}} \quad \text{for } x = \mu, \text{cas} \quad (4.31)$$

$$\delta \eta_{n,x,\text{exp}}^{\text{stat}} = \sqrt{\frac{R_{x,\text{exp}}^2 (\delta R_{n,\text{exp}}^{\text{stat}})^2 + R_{n,\text{exp}}^2 (\delta R_{x,\text{exp}}^{\text{stat}})^2}{R_{x,\text{exp}}^4}} \quad (4.32)$$

The ratios  $\eta_{n,\mu,\text{exp}}$ ,  $\eta_{n,\text{cas},\text{exp}}$  are a measure for the neutron yield per muon and per neutron cascade, respectively. They will be further discussed in Chap. 6 in comparison with corresponding Geant4 simulations.

As the neutron counter is a counting experiment, we assume that the  $n_x$  follow a Poisson distribution. Therefore we take the Poissonian standard deviation in its Gaussian limit  $\sqrt{n_x}$  as statistical uncertainty on the  $n_x$ . We assume a positive correlation between the  $n_x$  and overestimate the uncertainty by using the equations Eqs. 4.30 and 4.32 for the uncorrelated case.

The possibility of up to  $T_{\text{dead}} = 75$  d of dead time adds a positive systematic uncertainty of 8.43 % to the absolute rates  $R_{x,\text{meas}}$  (Eq. 4.29) via:

$$\delta R_{x,\text{meas}}^{\text{sys}}(T_{\text{dead}}) = \frac{n_x - n_{\text{acc},x}}{T_{\text{exp}} - T_{\text{dead}}} - R_{x,\text{meas}} \quad (4.33)$$

As the live-time is cancelled in the ratios  $\eta_{n,x}$  (Eq. 4.31), they are not affected by this systematics.

Another source for systematic uncertainty is the expected correlated background due to ambient neutrons as discussed in Sect. 4.1.2: Up to 8.8 neutron cascade candidates with one neutron due to ambient neutrons can be derived from MC. As this is correlated background, it is not included in the already considered background of

accidental coincidences. Therefore, it contributes as negative systematic uncertainty to the  $R_{x,\text{meas}}$  via

$$\delta R_{x,\text{meas}}^{\text{sys}}(n_{\text{bckgrnd}}) = \frac{n_x - n_{\text{acc},x} - n_{\text{ambient}}}{T_{\text{exp}}} - R_{x,\text{meas}} \quad (4.34)$$

and subsequently to the  $\eta_{n,x}$  via the modified rates  $R_{x,\text{meas}} + \delta R_{x,\text{meas}}^{\text{sys}}(n_{\text{bckgrnd}})$ . Only the results for a neutron candidate multiplicity  $M_{n,\text{can}} = 1$  are affected by the possible background from ambient neutrons. This results in a systematic uncertainty of  $-9 \times 10^{-3} \text{d}^{-1}$ , smaller than the corresponding statistical uncertainty.

Table 4.3 classifies the measurements according to their neutron candidate multiplicity  $M_{n,\text{can}}$ , i.e. the number of neutron candidates per neutron cascade candidate. For low multiplicities and more than 20 counts we use the Poissonian standard deviation in its Gaussian limit as statistical uncertainty. At higher multiplicities and lower counts, we take the approach by G.J. Feldman and R.D. Cousins [19] to calculate the 68 % CL. As the expected background from accidental coincidences is seven orders of magnitude lower than the signal, we take a background of 0 for the approach by G.J. Feldman and R.D. Cousins.

Finally, the measured rates and their ratios are:

$$R_{n,\text{exp}} = (3.21 \pm 0.18^{\text{stat}} {}^{+0.27^{\text{sys}}}_{-0.09}) \times 10^{-1} \text{d}^{-1} \quad (4.35)$$

$$R_{\text{cas},\text{exp}} = (1.84 \pm 0.14^{\text{stat}} {}^{+0.15^{\text{sys}}}_{-0.09}) \times 10^{-1} \text{d}^{-1} \quad (4.36)$$

$$R_{\mu,\text{exp}} = (5.79 \pm 0.08^{\text{stat}} {}^{+0.49^{\text{sys}}}) \text{d}^{-1} \quad (4.37)$$

$$\eta_{n,\text{cas},\text{exp}} = 1.75 \pm 0.17^{\text{stat}} {}^{+0.04^{\text{sys}}} \quad (4.38)$$

$$\eta_{n,\mu,\text{exp}} = (5.54 \pm 0.33^{\text{stat}} {}^{-0.16^{\text{sys}}}) \times 10^{-2}, \quad (4.39)$$

with a linearly combined uncertainty of at most 16 % for  $R_{\text{cas},\text{exp}}$ , which is dominated by the limited statistics of the measurement.

The final relation between the measured secondary to primary relation and the neutron production yield is given in Chap. 6 using the Geant4 simulations of Chap. 5.

## References

1. Araújo H et al (2008) Measurements of neutrons produced by high-energy muons at the Boulby underground laboratory. *Astropart Phys* 29(6):471–481. doi:[10.1016/j.astropartphys.2008.05.004](https://doi.org/10.1016/j.astropartphys.2008.05.004)
2. Ayunutdinov VM et al [Pierre Auger Collaboration] (2003) The Pierre Auger surface detector LED flashers and their use for monitoring and calibration. In: Kajita T et al (eds) Proceedings of the 28th international cosmic ray conference, Trukuba, Japan, 31 July–7 Aug 2003. Frontiers science series, vol 41. Universal Academy Press, Tokyo, pp 825–828. ADS: 2003ICRC....2..28A
3. Bäcklin A et al (1982) Levels in 156Gd studied in the  $(n, \gamma)$  reaction. *Nucl Phys A* 380(2):189–260. doi:[10.1016/0375-9474\(82\)90104-X](https://doi.org/10.1016/0375-9474(82)90104-X). As cited in Ref. [75]

4. Banerjee K et al (2007) Characteristics of Gd-loaded liquid scintillators BC521 and BC525. *Nucl Instrum Methods Phys Res Sect A* 580(3):1383–1389. doi:[10.1016/j.nima.2007.06.019](https://doi.org/10.1016/j.nima.2007.06.019)
5. Beckerts KH, Wirtz K (1964) Neutron physics. Springer, Berlin
6. Berger C et al [Fréjus Collaboration] (1989) Experimental study of muon bundles observed in the Fréjus detector. *Phys Rev D* 40(7):2163–2171. doi:[10.1103/PhysRevD.40.2163](https://doi.org/10.1103/PhysRevD.40.2163)
7. Berger MJ et al (2012) XCOM: Photon cross sections database 1.5. Scientific report NBSIR 87–3597. National Institute of Standards and Technology. <http://www.nist.gov/pml/data/xcom/index.cfm>. NIST homepage > physical reference data > X-ray and gamma-ray data >. XCOM: Photon Cross Sections Database
8. Bettini A (2011) Underground laboratories. *Nucl Instrum Methods Phys Res Sect A* 626–627(Suppl):S64–S68. doi:[10.1016/j.nima.2010.05.017](https://doi.org/10.1016/j.nima.2010.05.017)
9. Bezrukov LB et al (1973) Investigation of the depth-intensity curve of the nuclear events induced by cosmic-ray muons (trans: Adashko JG). *Sov J Nucl Phys* 17(1):51–53. Orig. Pub. as *Yad Fiz* 17: 98–103 [in Russian]
10. Birks JB (1964) The theory and practice of scintillation counting. International series of monographs on electronics and instrumentation, vol 27. Pergamon Press, Oxford
11. Bohr N (1936) Neutron capture and nuclear constitution. *Nature* 137(3461):344–348. doi:[10.1038/137344a0](https://doi.org/10.1038/137344a0)
12. Bowden N, Sweany M, Dazeley S (2012) A note on neutron capture correlation signals, backgrounds, and efficiencies. *Nucl Instrum Methods Phys Res Sect A* 693:209–214. doi:[10.1016/j.nima.2012.07.005](https://doi.org/10.1016/j.nima.2012.07.005)
13. Breit G, Wigner E (1936) Capture of slow neutrons. *Phys Rev (2nd Ser)* 49(7):519–531. doi:[10.1103/PhysRev.49.519](https://doi.org/10.1103/PhysRev.49.519)
14. Chardin G, Gerbier G (2003) Neutron background studies for the EDELWEISS WIMP search. In: Spooner N, Kudryavtsev V (eds) Proceedings of 4th international workshop on the identification of dark matter, IDM 2002, New York, UK, 2–6 Sept 2002. World Scientific, Singapore, pp 470–476. doi:[10.1142/9789812791313\\_fmatter](https://doi.org/10.1142/9789812791313_fmatter). As cited in Refs. [20, 53]
15. Chazal V et al (1998) Neutron background measurements in the underground laboratory of Modane. *Astropart Phys* 9(2):163–172. doi:[10.1016/S0927-6505\(98\)00012-7](https://doi.org/10.1016/S0927-6505(98)00012-7)
16. Cowan G (1998) Statistical data analysis. Clarendon Press, Oxford. <http://www.gbv.de/dms/goettingen/241026571.pdf>
17. Davission CM, Evans RD (1952) Gamma-ray absorption coefficients. *Rev Mod Phys* 24(2):79–107. doi:[10.1103/RevModPhys.24.79](https://doi.org/10.1103/RevModPhys.24.79)
18. Eitel K [For the EDELWEISS Collaboration] (2012) Measurements of neutron fluxes in the LSM underground laboratory. *J Phys Conf Ser* 375(1):012016. doi:[10.1088/1742-6596/375/1/012016](https://doi.org/10.1088/1742-6596/375/1/012016)
19. Feldman GJ, Cousins RD (1998) Unified approach to the classical statistical analysis of small signals. *Phys Rev D* 57(7):3873–3889. doi:[10.1103/PhysRevD.57.3873](https://doi.org/10.1103/PhysRevD.57.3873)
20. Fiorucci S et al [EDELWEISS Collaboration] (2007) Identification of backgrounds in the EDELWEISS-I dark matter search experiment. *Astropart Phys* 28(1):143–153. doi:[10.1016/j.astropartphys.2007.05.003](https://doi.org/10.1016/j.astropartphys.2007.05.003)
21. Garmy S et al (2009) GEANT4 transport calculations for neutrons and photons below 15 MeV. *IEEE Trans Nucl Sci* 56(4):2392–2396. doi:[10.1109/TNS.2023904](https://doi.org/10.1109/TNS.2023904)
22. Groom DE, Mokhov NV, Striganov SI (2001) Muon stopping power and range tables 10 MeV–100 TeV. *At Data Nucl Data Tables* 78(2):183–356. doi:[10.1006/adnd.2001.0861](https://doi.org/10.1006/adnd.2001.0861)
23. Grupen C, Shwartz BA (2008) Particle detectors, 2nd edn. Cambridge monographs on particle physics, nuclear physics, and cosmology, vol 26. Cambridge University Press, Cambridge
24. Habermehl F (2004) Entwicklung der Datenaufnahme und Tests der VetoModule für das EDELWEISS II  $\mu$ -Vetozählersystem [in German]. Master's thesis, Universität Karlsruhe (TH)
25. Hamamatsu Photonics (2006) In: Hakamata T et al (eds) Photomultiplier tubes: basics and applications, 3rd edn. Hamamatsu Photonics KK Electron Tube Division, Hamamatsu
26. Hennings-Yeomans R, Akerib D (2007) A neutron multiplicity meter for deep underground muon-induced high-energy neutron measurements. *Nucl Instrum Methods Phys Res Sect A* 574(1):89–97. doi:[10.1016/j.nima.2007.01.137](https://doi.org/10.1016/j.nima.2007.01.137)

27. Horn OM (2007) Simulations of the muon-induced neutron background of the EDELWEISS-II experiment for dark matter search. Scientific report FZKA 7391. Forschungszentrum Karlsruhe. <http://bibliothek.fzk.de/zb/berichte/FZKA7391.pdf>. Orig. Pub. as PhD Dissertation, Universität Karlsruhe (TH). <http://digibib.ubka.uni-karlsruhe.de/volltexte/1000007402>
28. Hubbell JH, Seltzer SM (2004) Tables of x-ray mass attenuation coefficients and mass energy-absorption coefficients from 1 keV to 20 MeV for elements Z = 1 to 92 and 48 additional substances of dosimetric interest. Scientific report NISTIR 5632. National Institute of Standards and Technology. <http://www.nist.gov/pml/data/xraycoef/index.cfm>. NIST homepage > PML > physical reference data > X-ray mass attenuation coefficients
29. Hubbell J (1982) Photon mass attenuation and energy-absorption coefficients. *Int J Appl Radiat Isot* 33(11):1269–1290. doi: [10.1016/0020-708X\(82\)90248-4](https://doi.org/10.1016/0020-708X(82)90248-4)
30. Institute of Electrical and Electronics Engineers (1976) CAMAC instrumentation and interface standards: modular instrumentation and digital interface system; serial high way interface system; parallel highway interface system; block transfers in CAMAC systems. Institute of Electrical and Electronics Engineers/Wiley-Interscience, New York
31. International Atomic Energy Agency (ed) (2007) Database of prompt gamma rays from slow neutron capture for elemental analysis. International Atomic Energy Agency, Vienna
32. International Atomic Energy Agency (2012) Nuclear data services: evaluated nuclear data files. <http://www-nds.iaea.org/exfor/endf.htm>
33. Jahnke U et al (2003) A combination of two  $4\pi$  detectors for neutrons and charged particles: part I. The Berlin neutron ball-a neutron multiplicity meter and a reaction detector. *Nucl Instrum Methods Phys Res Sect A* 508(3):295–314. doi: [10.1016/S0168-9002\(03\)01652-8](https://doi.org/10.1016/S0168-9002(03)01652-8)
34. Jokisch S (2009) Neutrondetector-Logical card version 2.0. Internal manual for the EDELWEISS collaboration
35. Jokisch S (2009) Time-base for the muon-veto electronic system version 1.0. Internal manual for the EDELWEISS collaboration
36. Jokisch S (2010) Neutrondetector-VME-LED-Module version 1.0. Internal manual for the EDELWEISS collaboration
37. Kapustinsky J et al (1985) A fast timing light pulser for scintillation detectors. *Nucl Instrum Methods Phys Res Sect A* 241(2–3):612–613. doi: [10.1016/0168-9002\(85\)90622-9](https://doi.org/10.1016/0168-9002(85)90622-9)
38. Kleifges M (2012) LED-controller of the SED of the Pierre Auger observatory. E-mail message to author, September 11
39. Kluck H (2007) Aufbau und Test eines Prototyp-Neutronendetektors für das EDELWEISS Experiment [in German]. Master's thesis, Universität Karlsruhe (TH)
40. Kozlov VY (2013) Analysis of neutron counter data and dead time. E-mail messages to author, 1–9 Oct 2012 and 3 July 2013
41. Kozlov VY (2012) Precipitation of gadolinium out of the liquid scintillator. E-mail message to author, 08 Dec 2012
42. Kozlov VY (2012) Time series of neutron capture time. E-mail message to author, 11 Sept 2012
43. Kozlov VY [For the EDELWEISS Collaboration] (2008) Studies of the muon-induced neutron background in LSM: detector concept and status of the installation. In: Identification of dark matter 2008, Stockholm, Sweden, 18–22 Aug. Proceedings of science IDM2008. SISSA, Trieste, p 86. arXiv: [0902.4858v1](https://arxiv.org/abs/0902.4858v1) [astro-ph.IM]
44. Kozlov VY et al (2010) A detection system to measure muon-induced neutrons for direct dark matter searches. *Astropart Phys* 34(2):97–105. doi: [10.1016/j.astropartphys.2010.06.001](https://doi.org/10.1016/j.astropartphys.2010.06.001). arXiv: [1006.3098](https://arxiv.org/abs/1006.3098) [astro-ph.IM]
45. Kudryavtsev V, Pandola L, Tomasello V (2008) Neutron- and muon-induced background in underground physics experiments. *Eur Phys J A* 36(2):171–180. doi: [10.1140/epja/i2007-10539-6](https://doi.org/10.1140/epja/i2007-10539-6)
46. Kudryavtsev V [For the LVD Collaboration] (1999) Measurement of the neutron flux produced by cosmic-ray muons with LVD at Gran Sasso. In: Kieda D, Salamon M, Dingus B (eds) Proceedings of the 26th international cosmic ray conference, Salt Lake City, UT, USA, 17–25 Aug 1999, vol 2. University of Utah/American Institute of Physics, Salt Lake City, pp 44–48. [hep-ex/9905047](https://arxiv.org/abs/hep-ex/9905047)

47. Laible F (2012) Relative decrease of the transparency of the liquid scintillator. E-mail message to author, 11 Sept 2012
48. Laible F (2012) Untersuchung der Langzeitstabilität eines Flüssigszintillators im Untergrundlabor von Modane [in German]. Bachelor's thesis, Karlsruher Institut für Technologie (KIT)
49. Lane A, Lynn J (1960) Anomalous radiative capture in the neutron resonance region: analysis of the experimental data on electric dipole transitions. *Nucl Phys* 17:586–608. doi:[10.1016/0029-5582\(60\)90147-4](https://doi.org/10.1016/0029-5582(60)90147-4)
50. Lane A, Lynn J (1960) Theory of radiative capture in the resonance region. *Nucl Phys* 17:563–585. doi:[10.1016/0029-5582\(60\)90146-2](https://doi.org/10.1016/0029-5582(60)90146-2)
51. Launay S Time-base for the muon-veto electronics system—User manual. Internal manual for the EDELWEISS collaboration
52. Leipunskii OI, Novozhilov BV, Sakharov VN (1965) The propagation of gamma quanta in matter. International series of monographs on nuclear energy-Division X: reactor design physics, vol 6. Pergamon Press, Oxford
53. Lemrani R, Gerbier G [For the EDELWEISS Collaboration] (2006) Update of neutron studies in EDELWEISS. *J Phys Conf Ser* 39(1):145. doi:[10.1088/1742-6596/39/1/033](https://doi.org/10.1088/1742-6596/39/1/033)
54. Lemrani R et al (2006) Low energy neutron propagation in MCNPX and GEANT4. *Nucl Instrum Methods Phys Res Sect A* 560(2):454–459. doi:[10.1016/j.nima.2005.12.238](https://doi.org/10.1016/j.nima.2005.12.238). [hep-ex/0601030](https://arxiv.org/abs/hep-ex/0601030)
55. Lubsandorzhiev B et al (2006) Photoelectron backscattering in vacuum phototubes. In: Proceedings of the 4th international conference on new developments in photodetection-BEAUNE 2005, special issue. *Nucl Instrum Methods Phys Res Sect A* 567(1):12–16. doi:[10.1016/j.nima.2006.05.047](https://doi.org/10.1016/j.nima.2006.05.047)
56. Mei D-M, Zhang C, Hime A (2009) Evaluation of induced neutrons as a background for dark matter experiments. *Nucl Instrum Methods Phys Res Sect A* 606(3):651–660. doi:[10.1016/j.nima.2009.04.032](https://doi.org/10.1016/j.nima.2009.04.032)
57. Mei D, Hime A (2006) Muon-induced background study for underground laboratories. *Phys Rev D* 73:053004. doi:[10.1103/PhysRevD.73.053004](https://doi.org/10.1103/PhysRevD.73.053004). arXiv:[astro-ph/0512125](https://arxiv.org/abs/astro-ph/0512125)
58. Miyake S, Narasimham V, Ramana Murthy P (1964) Cosmic-ray intensity measurements deep underground at depths of (800–8400) m w.e. *Nuovo Cim* 32(6):1505–1523. doi:[10.1007/BF02732788](https://doi.org/10.1007/BF02732788)
59. Mughabghab SF (2006) Atlas of neutron resonances: resonance parameters and thermal cross sections Z=1–100, 5th edn. Elsevier, Amsterdam
60. Mughabghab S (1979) Verification of the Lane-Lynn theory of direct neutron capture. *Phys Lett B* 81(2):93–97. doi:[10.1016/0370-2693\(79\)90496-9](https://doi.org/10.1016/0370-2693(79)90496-9)
61. Oehler C (1996) Untersuchung der Eigenschaften hemisphärischer 8-inch Photomultiplier für einen großvolumigen Wasser-Čerenkov-Detektor [in German]. Scientific report FZKA 5695. Forschungszentrum Karlsruhe. Orig. pub. as master's thesis, Universität Karlsruhe (TH) [in German]
62. Ohsumi H et al (2002) Gamma-ray flux in the Fréjus underground laboratory measured with NaI detector. *Nucl Instrum Methods Phys Res Sect A* 482(3):832–839. doi:[10.1016/S0168-9002\(01\)01866-6](https://doi.org/10.1016/S0168-9002(01)01866-6)
63. O'Neill D (2001) PMT pulse digitization simulations for Hall D. [http://argus.phys.uregina.ca/gluex/DocDB/0004/000425/001/O'Neill\\_PMT.pdf](http://argus.phys.uregina.ca/gluex/DocDB/0004/000425/001/O'Neill_PMT.pdf)
64. Parker J et al (1968) Monte Carlo studies of scintillator efficiencies and scatter corrections for (n,2n) cross section measurements. *Nucl Instrum Methods* 60(1):7–23. doi:[10.1016/0029-554X\(68\)90083-9](https://doi.org/10.1016/0029-554X(68)90083-9)
65. Photonis (2002) In: Flyckt S-O, Marmonier C (eds) Photomultiplier tubes: principles and application, Rev edition. Photonis, Brive
66. Piepke AG, Moser SW, Novikov VM (1999) Development of a Gd loaded liquid scintillator for electron anti-neutrino spectroscopy. *Nucl Instrum Methods Phys Res Sect A* 432(2–3):392–398. doi:[10.1016/S0168-9002\(99\)00530-6](https://doi.org/10.1016/S0168-9002(99)00530-6). arXiv:[nucl-ex/9904002v1](https://arxiv.org/abs/nucl-ex/9904002v1)
67. Press WH et al (2007) Numerical recipes: the art of scientific computing, 3rd edn. Cambridge University Press, Cambridge

68. Reichenbacher J (1998) Untersuchung der optischen Eigenschaften grossflächiger Plastiksintillatoren für den KARMEN-Upgrade [in German]. Scientific report FZKA 6202. Forschungszentrum Karlsruhe. Orig. pub. as master's thesis, Universität Karlsruhe (TH) [in German]
69. Roithner Lasertechnik. RLT420-3-30-Violet LED Lamp. Roithner Lasertechnik, Vienna
70. Rozov S et al (2010) Monitoring of the thermal neutron flux in the LSM underground laboratory. arXiv:[1001.4383v1](https://arxiv.org/abs/1001.4383v1) [astro-ph.IM]
71. Saint-Gobain Crystals (2005) BC400, BC-404, BC-408, BC-412, BC-416: premium plastic scintillators. Saint-Gobain Crystals, Nemours
72. Schmidt B et al [EDELWEISS collaboration] (2013) Muon-induced background in the EDELWEISS dark matter search. *Astropart Phys* 44:28–39. doi:[10.1016/j.astropartphys.2013.01.014](https://doi.org/10.1016/j.astropartphys.2013.01.014). arXiv:[1302.7112](https://arxiv.org/abs/1302.7112) [astro-ph.CO]
73. Sukhoruchkin SI et al (2009) Introduction. In: Schopper H (ed) Landolt-Börnstein-group I elementary particles, nuclei and atoms-numerical data and functional relationships in science and technology, vol I/24. Neutron resonance parameters, Chap 1. Springer, Berlin. doi:[10.1007/978-3-540-87866-7\\_1](https://doi.org/10.1007/978-3-540-87866-7_1)
74. Tomasello V, Kudryavtsev V, Robinson M (2008) Calculation of neutron background for underground room experiments. *Nucl Instrum Methods Phys Res Sect A* 595(2):431–438. doi:[10.1016/j.nima.2008.07.071](https://doi.org/10.1016/j.nima.2008.07.071)
75. Trzciński A et al (1999) A monte-carlo code for neutron efficiency calculations for large volume Gd-loaded liquid scintillation detectors. *J Neutron Res* 8(2):85–117. doi:[10.1080/10238169908200048](https://doi.org/10.1080/10238169908200048)
76. US NIM Committee (1990) Standard NIM instrumentation system. Tech rep DOE/ER-0457T. US Department of Energy-Office of Energy Research. <http://www.osti.gov/energycitations/servlets/purl/7120327-MV8wop/7120327.pdf>
77. Verhoeven JW (1996) Glossary of terms used in photochemistry: IUPAC Recommendations 1996. *Pure Appl Chem* 68(12):2223–2286. doi:[10.1351/pac199668122223](https://doi.org/10.1351/pac199668122223)
78. VMEbus International Trade Association. VME Technology FAQ. <http://www.vita.com/home/Learn/vmefaq/vmefaq.html>. VITA homepage > Learn > Frequently Asked Questions (FAQ) > VMEbus
79. Wieser ME (2006) Atomic weights of the elements 2005 (IUPAC Technical Report). *Pure Appl Chem* 78(11):2051–2066. doi:[10.1351/pac200678112051](https://doi.org/10.1351/pac200678112051)
80. Wilson WB et al (1999) SOURCES 4A: A code for calculating  $(\alpha, n)$ , spontaneous fission, and delayed neutron sources and spectra. Tech rep LA-13639-MS. Los Alamos National Laboratory. <https://www.fas.org/sgp/othergov/doe/lanl/docs1/00460139.pdf>
81. Yeh M, Garnov A, Hahn R (2007) Gadolinium-loaded liquid scintillator for highprecision measurements of antineutrino oscillations and the mixing angle,  $\theta_{13}$ . *Nucl Instrum Methods Phys Res Sect A* 578(1):329–339. doi:[10.1016/j.nima.2007.03.029](https://doi.org/10.1016/j.nima.2007.03.029)

# Chapter 5

## Simulation of Muon-Induced Neutrons at LSM with Geant4

For a better understanding of the experimental results in Chap. 4, the measurement was accompanied with a detailed simulation of the production and detection of muon-induced neutrons. In a detailed implementation of the detector geometry and its surrounding (see Sect. 5.1), the chosen physics models were applied (Sect. 5.2).

Within an end-to-end approach, starting with the muon generation (Sect. 5.3) and including a calibrated detector response model (Sect. 5.4), the muon-induced neutron production and detection are simulated (Sect. 5.5). The resulting count rates serve as reference values for the assessment of the reliability of Geant4 to simulated muon-induced neutrons in Chap. 6.

### 5.1 Implementation of the Detector Set-Up and Its Environment

As it was pointed out in [4, 36, 44, 51, 71] (see Sect. 3.5.4) measurements of muon induced neutrons are affected not only by the detector response, but also by the surrounding of the detector. An inadequate consideration of the surrounding may be one of the reasons for the observed discrepancy between measurements and simulation of muon-induced neutrons.

Therefore, a detailed model of the neutron counter, i.e. the NMM (Sect. 4.2.1) and the muon telescope (Sect. 4.2.2), and its surrounding, i.e. the LSM including the EDELWEISS-II set-up and the NEMO 3 set-up, was used in this work. This section documents the implemented geometry and the used materials. The name of their Geant4 implementations are given in typewriter style. The compositions are listed in Appendix A.4.2, in all cases a natural isotope composition is assumed. The implemented optical properties of the active volume of the NMM and its surrounding are discussed in context of the simulated light propagation in Sect. 5.4.2.

A unified geometry implementation is used for all Geant4 simulations throughout this work: simulations of the detector response including light propagation

(Sect. 5.4.2), simulation of reference measurements with an AmBe source (Sect. 5.4.4), simulations of muon-induced neutrons (Sect. 5.5.1), and finally simulations of background contributions (Sect. 5.5.5). This unified model ensures that all simulations are mutually consistent with respect to the used geometry and material compositions.

The model for the LSM and the EDELWEISS set-up used in this work are based on a modified version of the implementation used by O. M. Horn [36]. The modification results from an effort to unify the geometry and material definitions used by the several working groups within the EDELWEISS collaboration.

Detailed models were used for the neutron counter and the nearby EDELWEISS set-up, but the more distant NEMO 3 and the LSM cavern were implemented in a very simple way, as a reduced influence on the neutron counter is expected due to the larger distance. Figure 5.1a shows an overview of the implemented LSM cavern with the models of the contained neutron counter, EDELWEISS, and NEMO 3.

As outlined in [36], the LSM cavern is implemented with an air (pre-defined as `Air` in Geant4) filled box of dimensions  $10.6\text{ m} \times 19.8\text{ m} \times 10.8\text{ m}$  along the  $x$ -,  $y$ -, and  $z$ -axis, see Fig. 5.1a. The positive  $x$ - and  $y$ -half-axes are oriented towards south and east with an angle of  $16^\circ$  between the east and the  $y$ -axis.

The concrete walls of the cavern are represented by a layer of `FrejusConcrete2` with 30 cm thickness. This value is increased with respect to the one used by O. M. Horn [36] as suggested by V. A. Kudryavtsev [41]. As consequence of the mentioned unification effort the material composition of the concrete is now based on [18] instead of [57].

After the concrete, a layer of homogeneous Fréjus rock is implemented with a thickness of 30 m at all sides, except at the floor. There, only 2 m are taken [36], because it is unlikely that muon-induced shower products produced deep inside the bottom layer will reach the cavern due to its strong angular correlation, see Sect. 3.5.2. As discussed in Sect. 3.3.3, the material composition and homogeneity of the Fréjus rock is debated in the literature. Whereas O. M. Horn [36] uses the composition given in [57], this work uses a composition (`FrejusRock3`,  $\rho = 2.65\text{ g cm}^{-3}$ ) based on the more recent measurement [18] as consequence of the unification effort, see also Table A.4. Except for the bottom, the effective rock in muon simulation has a minimal thickness of  $1325\text{ g cm}^{-2}$ , enough for the shower development to reach equilibrium, see Sect. 3.4.5 for a discussion of the needed thickness.

Technically, the whole geometry is placed in a vacuum (`G4_Galactic`) filled box with dimensions of  $200\text{ m} \times 200\text{ m} \times 200\text{ m}$ , as such a world volume is demanded by Geant4 (Appendix A.3.2). The centre of the world volume, coincident with the point of origin of the coordinate system, is placed in the centre of the neutron counter to ensure its homogeneous illumination with muons, as it will be discussed in Sect. 5.3.1.

Due to its higher mass, the implemented rock serves as main target for the neutron production by muons and accompanied muon-induced showers (Sect. 5.5.1). Contrary, most of the ambient neutrons from the  $(\alpha, n)$  reactions originate in the concrete layer, as ambient neutrons from the underlying rock are mostly absorbed in the concrete, see Sect. 5.5.5. The air inside the cavern is important by its own:

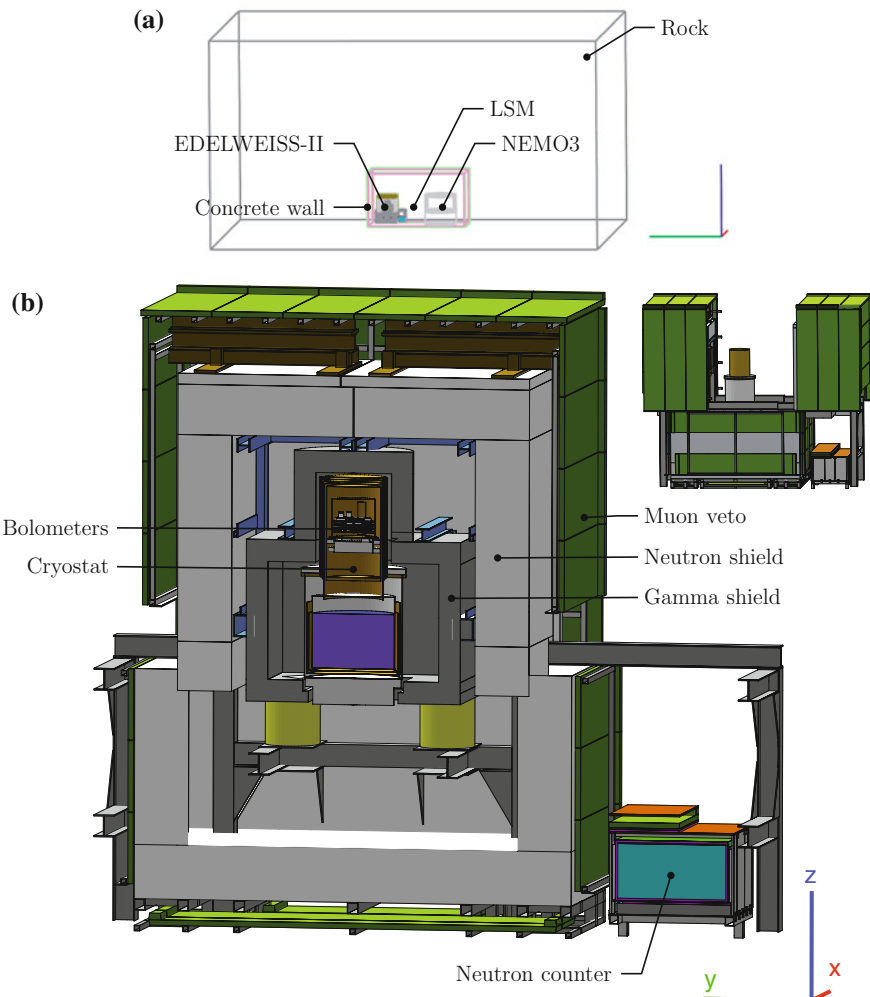


**Fig. 5.1** Geant4 implemented geometry, as visualized by DAWN: **a** the LSM cavern surrounded by concrete and rock, including NEMO 3 and EDELWEISS-II. The axis-cross is 15 m along each axis. **b** A zoom on EDELWEISS-II with closed niveau 1 configuration, nearby the neutron counter. Cut parallel to the  $y$ - $z$ -plane, the several shields and the cryostat of EDELWEISS-II are visible. The axis-cross is 1 m along each axis. The *inset* shows an uncut version with open niveau 1 configuration

The lower pion half life in the air filled cavern results in the production of low energetic, secondary muons (Sect. 3.4.1). That must be considered for the definition of the simulated muon flux, see Sect. 5.3.3.

During most of its run time the neutron counter shared the LSM not only with the EDELWEISS experiment, but also with the NEMO 3 experiment. Therefore a simplified model of NEMO 3 is implemented in the Geant4 simulation, based on its

technical documentation from [5]. Albeit NEMO 3 contains several materials with a high neutron capture cross section, e.g.  $^{150}\text{Nd}$ ,  $^{96}\text{Zr}$ , their mass and hence their macroscopic cross section is small. The biggest influence on the local neutron field at LSM is expected from the volumes with the biggest masses: the neutron shield, via neutron absorption, and the iron gamma shield, via neutron mirroring and production. Two parts build the implemented neutron shield: one paraffin part at the floor below NEMO 3 and one part around the outer wall of NEMO 3 as described in [5]. The implemented dimensions are taken from [5], whereas the implemented material composition is simplified: instead of a complex mixture of paraffin, wood, and borated water for the neutron shield, uniformly distributed polyethylene (PolyEthylene) was used. Since NEMO 3 is rather far away from the neutron counter, it is assumed that the differences are negligible. The gamma shield is implemented as an air filled steel tube (Steel) inside the upper part of the neutron shield with the dimension taken from [5]. The relative position of NEMO 3 with respect to EDELWEISS-II was estimated via perspective analysis of Fig. 2.12.

The detailed model of the EDELWEISS-II set-up (Sect. 2.3.1), see Fig. 5.1b, and its position relative to the LSM cavern is taken from [36]. It consists of the underlying steel structure (Steel) that supports the helium filled cryostat and the three shields against background. The innermost gamma shield consists of lead (Lead), followed by the neutron shield made of polyethylene (PolyEthylene), and as outermost shield the active muon veto. The latter is implemented as 42 individual muon modules, i.e. without a recent extension of additional four modules above the gap between east and west side of niveau 1. To further increase the accordance between model and reality, the following three modifications were done with respect to [36]:

- The gamma shield was originally implemented as a monolithic volume, unable to simulate the opening/closing of the EDELWEISS niveau 1 (Sect. 2.3.1). Therefore, it was replaced by a two volume model that can be opened and closed. The inset in Fig. 5.1b shows an open configuration, the shift of the parts is based on actual measured data from the laser distant monitoring system of the muon veto, see Sect. 2.3.1.
- A more accurate material composition of the steel parts was implemented, mild steel is used instead of stainless steel as suggested by V. A. Kudryavtsev [42].
- The allocation of the bolometers in the cryostat was updated to the configuration of the cryogenic run 12 as consequence of the unification effort.

The basic influence of the EDELWEISS set-up on the neutron counter is expected to be similar to the one of the NEMO 3 set-up, albeit stronger because it is closer: The steel infrastructure and the lead shield act as source for the muon-induced neutrons and as mirror for thermal neutrons. The polyethylene and the plastic scintillators of the muon modules act as neutron sink.

In the short periods ( $\approx 1$  d) with an open configuration of niveau 1, the upper parts of the gamma and neutron shields are usually moved such that one half is directly above the neutron counter. In such a case the polyethylene reduces the ambient neutron background of the neutron counter by 68 %, see Sect. 4.1.2. In principle, also the muon-induced neutron production increased due to the EDELWEISS lead

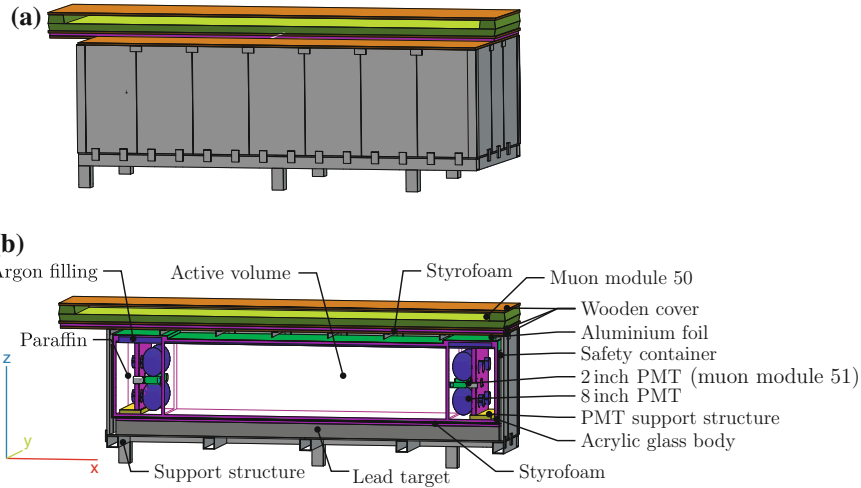


**Fig. 5.2** Geant4 implemented geometry of the neutron counter as visualized by DAWN: **a** uncut and **b** cut parallel to the  $x$ - $z$ -plane. Symmetric structures are labelled only once, for details see text. The axis-cross is 1 m along each axis. The figure was modified for better clarity

shield if located above the neutron counter. As the periods with open configurations contribute only little to the total live-time of the neutron counter, the geometry was simulated in closed configuration for the data sets listed in Sect. 5.3.2.

The descriptions of the neutron counter in Geant4, i.e. the NMM and the muon telescope are based on the technical drawings used for construction, see Appendix A.5.1, simplified by omitting screws and screw holes. Figure 5.2 shows the resulting implementation.

As stated in Sect. 4.2.1 the main parts of the neutron counter are the acrylic glass body of the NMM, containing the active volume and the PMTs, an aluminium safety container, the iron support structure, and the lead target. On top of the NMM the plastic scintillator of the module 50 of the muon telescope is placed.

The acrylic glass body follows the technical drawings except that for simplification the four filler caps and the syphon are not implemented. It is implemented as box of dimension 273 cm  $\times$  104 cm  $\times$  57.2 cm made of Plexiglass and containing three daughter boxes: The middle one with dimensions 200 cm  $\times$  100 cm  $\times$  51 cm implements the active volume, the two outer ones with dimensions of 32.5 cm  $\times$  100 cm  $\times$  51 cm contain the PMTs. The active volume is filled with 1 m<sup>3</sup> of liquid scintillator (liquid scintillator), i.e. up to a level height of 50 cm.

The liquid scintillator BC-525 is implemented as a mixture of hydrogen, carbon, and gadolinium. To simulate the effect of different gadolinium loadings (see e.g. Fig. 4.14), the amount of the individual components and the resulting density of the mixture are calculated by Eq. A.38. The user can choose different loadings via a macro command, the default value used mostly in this work is the nominal loading of

$$n_{\text{Gd}} = 0.2 \% \text{ W/W} \quad (5.1)$$

as given in the data sheet [61] of the liquid scintillator, see also Table A.5.

The outer boxes are filled with paraffin (`Paraffin`) to the same level as the middle volume is filled with scintillator. The remaining volumes of all three boxes are filled with argon gas (`G4_Ar`). The PMTs are placed in the outer chamber of the acrylic container together with their support structure made of acrylic glass with an iron foot (`G4_Fe`). This support structure holds simplified models of both PMT types,<sup>1</sup> the 8 in. PMT<sup>N</sup>s of the NMM and the 2 in. PMT<sup>M</sup>s of module 51 of the muon telescope. The PMT models consist of glass bulbs (`borosilicateGlass` for 8 in. PMTs and `limeGlass` for 2 in. PMTs) with a geometry according to the data sheets, coated with a 20 nm thick layer of `BiAlkali` as photocathode on the inner front side. The PMT models are simplified as the stack of dynodes is omitted and the whole interior is filled with vacuum.

The positions of the LEDs of the light pulser are not hard coded, but provided in a macro file controlling the `G4GeneralParticleSource` interface of Geant4: this enables the user to start optical photons with an aperture angle and emission spectrum matching the specification of the LED data sheet [58], see also Table A.15.

As described in Sect. 4.2.1, the acrylic glass body is wrapped in an aluminium foil to increase the light collection. With respect to the detector geometry, the foil is implemented as actual volume of `G4_A1` and not as an optical property of the acrylic glass–air boundary: it is a layer of 0.5 mm thickness and it is separated from the acrylic glass container by an air gap of 0.1 mm at the bottom and 1 mm everywhere else. We decided to implement the foil as actual volume, to include its influence on the neutron transport, see Fig. 5.29.

The aluminium foil is placed inside the aluminium safety container (`G4_A1`), a box of 2 mm thickness and an inner dimension of 275 cm × 108 cm × 51.2 cm.

Between the acrylic glass body and the aluminium safety container, a styrofoam layer (`Polystyrol`) of 5 mm thickness is placed, and between the safety container and the lead target is a layer of 17.9 mm thickness.

The lead target is implemented as a solid lead (`G4_Pb`) block of 272 cm × 106 cm × 10 cm, its dimensions and position relative to the support structure were measured during assembling of the neutron counter. The real lead target consists of 5 cm × 10 cm × 20 cm lead bricks. A comparison of the total volumes in both approaches indicates that the simulation overestimates the mass of lead by 0.11 % because it neglects the air gaps between the bricks. However, this is negligible compared to the other sources of systematic uncertainties, which will be discussed in Sect. 5.5.4.

The individual parts of the iron support structure (e.g. iron plates, L-sections) were implemented according to the technical drawings and the iron `S235JR` was implemented according to the material composition stated in standard DIN EN 10 025. The upper surface of the implemented NMM is a wooden board of 1.5 cm

---

<sup>1</sup>The models of the PMT geometries were implemented by a student during a summer internship, based on the data sheets.

thickness, in reality used as protective cover. The material wood was modelled according to beech wood.<sup>2</sup>

The plastic scintillator of module 50 of the muon telescope is placed on top of the wooden board, separated by 2 cm of styrofoam. It consists of a main part of 365 cm  $\times$  65 cm  $\times$  5 cm, and one trapezoid light guide of  $\approx$  115 cm  $\times$  65 cm  $\times$  6 cm on each edge of 65 cm width. The used plastic scintillator BC-412 is implemented as PVT for all three parts according to its data sheet [60]. On top and below the plastic scintillator protective wooden boards are placed, each 1.5 cm thick. Again, they are implemented as beech wood. The 2 in. muon PMTs of muon module 50 are not implemented. This is also the case for all muon modules of the EDELWEISS muon veto.

The position of the neutron counter relative to the EDELWEISS set-up is specified according to measurements at site. As it was stated above, the centre of the neutron counter, i.e. NMM and muon telescope, coincides with the point of origin of the used coordinate system. This does not coincide with the centre of mass of the active volume of the NMM, because module 50 is shifted askew with respect to the NMM, see Fig. 5.2. This is the reason for the asymmetric scales on Fig. 5.15.

The neutron counter itself is a source and a sink for the muon-induced neutrons (Sect. 5.5.1): neutrons are produced mainly in the lead target, but also in the iron of the support structure, the liquid scintillator, and the aluminium of the safety container. As it was mentioned in Sect. 4.1.3, the iron plates of the support structure serve as mirror for thermal neutrons. This further supports the importance of a detailed implementation of the detector geometry.

## 5.2 Physics List for Modelling Interactions

Besides the measurement of muon-induced neutrons, the objective of this work is also to assess the capability of Geant4 to correctly simulate the neutron production at LSM. Such a modelling depends on the used physics interaction models, as discussed in Sect. 3.6. Therefore, it is important to choose a suitable physics list. The physics list used in this work is based on the one developed by O. M. Horn [36], which was chosen with the aim of great accuracy for muon induced neutron production at LSM. A further development with respect to neutron production was not the objective of this thesis, as there was no obvious need for such modifications. Only extensions for a better detector model were added, allowing to assess the implementation of the neutron production. We first describe the technical properties of the used list, then its expected influence on the muon-induced neutron production.

As it is the case for the material and geometry implementations, also the same unified physics list is used for all simulations done in this work. This ensures that the results of individual simulations are mutually consistent.

---

<sup>2</sup>We equal the chemical composition of the wood to cellulose C<sub>6</sub>H<sub>10</sub>O<sub>5</sub> and use the density of beech wood of 0.8 g cm<sup>-3</sup> [22].

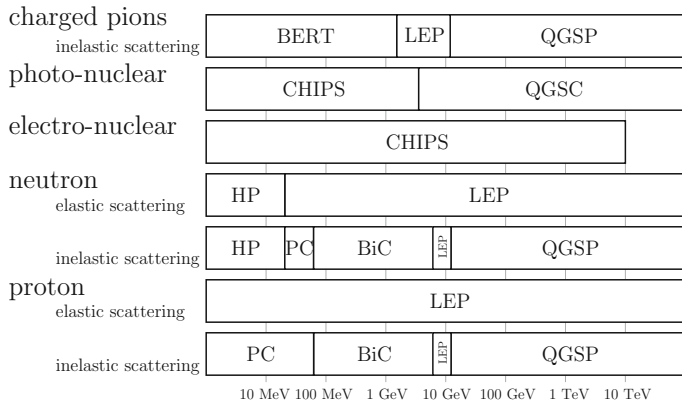


**Fig. 5.3** Application range of models for photo-nuclear interaction, electron-nuclear interaction, pion inelastic scattering, and elastic/inelastic nucleon scattering according to [36]: data driven high precision model (HP), pre-compound model (PC), binary cascade (BiC), Bertini cascade (BERT), LEP model, chiral invariant phase space model (CHIPS), quark-gluon string model (QGS) using pre-compound (QGSP) or CHIPS (QGSC) to fragment. For details see text

The physics list used for this work within Geant4 version 9.2p01 is based on the one developed in [36] for Geant4 8.2p01 that is based itself on QGSP\_BIC\_HP version 1.0. Compared to QGSP\_BIC\_HP the default behaviour was changed in [36] as following:

- For the inelastic scattering of nucleons, charged pions, kaons and ions, a different model composition and different energy boundaries between the models are used. The actual application ranges are listed in Table A.2. Figure 5.3 shows the used composition for the processes most relevant for neutron production and propagation. As discussed in Sect. 3.6.4, the chosen models are comparable to those proposed in literature.
- Contrary to the Geant4 standard settings, muon nuclear spallation via G4Mu-Nuclear is used throughout the entire simulation. See Sect. 3.6.2 for further details.
- The photo-nuclear interaction above 3 GeV is implemented as a QGSC model, again in agreement with the literature, see Sect. 3.6.3.
- The range of application of electromagnetic interactions is extended down to 250 eV by using the low energy package [17], as proposed in literature, see Sect. 3.6.1. Contrary to the standard implementation, this includes Rayleigh scattering, X-ray fluorescence, and the emission of Auger electrons.
- For anti-proton and anti-neutron also the annihilation at rest is included.
- For elastic scattering, the LEP parametrization is used, extended to  ${}^3\text{He}$  and  $\alpha$ .
- The Fermi break-up is also enabled for  $A < 12$ ,  $Z < 6$ .
- Multi fragmentation above 3 MeV is enabled. Together with the extended application range of the Fermi break-up, they aim to improve the neutron production at low energies.

**Table 5.1** Energy threshold for secondary gamma, electron and positron production in materials as calculated by Geant4, based on the chosen default production cut

Material	Production threshold of		
	Gamma (keV)	Electron (keV)	Positron (keV)
Lead	100.91	1378.14	1280.02
Liquid scintillator	2.25	326.42	318.48
Concrete	6.55	575.45	554.20
Steel S235JR	20.65	1280.02	1218.51
Acrylic glass	2.77	387.81	373.75

- For the absorption of pions and kaons at rest, the data driven G4PiMinus-AbsorptionAtRest, G4KaonMinusAbsorptionAtRest models [27, p. 365] are used instead of the theory driven CHIPS based G4QCaptureAtRest [28] used in QGSP\_BIC\_HP.
- The default production cut for electrons, positrons and gamma quanta is slightly increased from 0.7 to 1.0 mm.
- No G4TripathiLightCrossSection for detailed elastic scattering of d, t,  $^3\text{He}$  and  $\alpha$  in hydrogen and helium is applied.

Most of the changes extend the functionality of the physics list, aiming for a more precise simulation, except the last two changes. We do not expect that these changes affect the simulation. The last one concerns materials not even present in the NMM.

The energy thresholds for the five materials that contribute most to the detected neutrons, see Fig. 5.28, are listed in Table 5.1. They are based on the default production cut we chose. Albeit the energy threshold for secondary electron, positron and gamma quanta production, which is equivalent to the default cut, is increased with respect to QGSP\_BIC\_HP, it is still below the start of electromagnetic neutron production in lead via the GDR ( $\approx 7$  MeV, see Sect. 3.4.6). In liquid scintillator, it is also below the expected trigger threshold of the NMM ( $\approx 3$  MeV, see Sect. 4.2.5). Therefore, the chosen production cut is suitable. No cut on the simulation time was used, i.e. all processes were simulated until all particles left the world volume or end otherwise, e.g. by capture.

As the physics list was defined with respect to Geant4 8.2p01, the following four changes in the *model selection* in Geant4 9.2p01 are consequently not included:

- A dedicated handling of quasi elastic interactions for neutrons, protons, pions and kaons.
- A dedicated model (G4eMultipleScattering) for multiple scattering of electrons and positrons.
- Pair production for pions and protons via G4hPairProduction.
- Bremsstrahlung for pions and protons via G4hBremsstrahlung.

Despite the lack of these changes, the simulations in this work profit from all improvements in the *models* and tabulated cross sections introduced between Geant4 8.2p01

and Geant4 9.2p01. For example, Geant4 9.1 and 9.2 introduce some bugfixes in the pre-compound model, leading to an increase of the neutron production. See Appendix A.3.3 for a summary of those improvements.

In addition to the models that govern the neutron production and neutron propagation, for a better detector description the following models were added:

- G4Decay and G4RadioactiveDecay allow the decay of potentially produced radioisotopes and the decay of  $^{214}\text{Bi}$  as background source in Sect. 5.5.5.
- For a better description of the gamma cascade emitted after a neutron capture on gadolinium, GdNeutronHPCapture [53, 70] from the Double Chooz collaboration is used instead of the default G4NeutronHPCapture. It will be discussed in more detail in Sect. 5.4.1.
- To include the propagation of the scintillation light in the liquid scintillator, optical models are included. They will be described in Sect. 5.4.2.

The detector model will be discussed in detail in Sect. 5.4.

With respect to the possible background sources discussed in Sect. 4.1.2, this physics list provides the production of ambient gamma background via muon bremsstrahlung and radiative neutron capture in the simulation of muon-induced neutron production (Sect. 5.5.1). In dedicated simulations (Sect. 5.5.5), also the ambient gamma ray and neutron production via radioactive decay are included.

The above described physics list covers the neutron production via  $\mu^-$  capture (Sect. 3.4.1), muon spallation (see Sect. 3.4.3), photo nuclear and electron/positron nuclear interactions in electromagnetic showers (Sect. 3.4.4), and hadron inelastic scattering in hadronic showers and cascades (Sect. 3.4.5). The contribution of pion absorption in the nucleus (Sect. 3.4.6) is taken into account. Not included is neutron production via quasielastic muon nuclear scattering (Sect. 3.4.2) and charge exchange reaction in electromagnetic showers (Sect. 3.4.4), but they are expected to contribute much fewer neutrons than the implemented interactions. For a precise simulation of the detector response to these muon-induced neutrons, also radioactive decays, optical interactions, and a precise model of the neutron capture on gadolinium was included. Therefore, the physics list should be suitable for the simulation of muon-induced neutrons, background contributions and the subsequent detector response to them.

### 5.3 Muon Generation in Geant4

Before we discuss the simulation of muon-induced neutron production in Sect. 5.5, this section will summarize the used muon generator.

Albeit the simulation of the local muon flux at underground sites is a well established and mature field (see the discussion in Sect. 3.2.7), there exists no general ‘out of the box’ solution. For each underground site, the chosen muon generator has to consider the specific site characteristics like rock overburden and geometry. The

carefully chosen muon generator used in this work and its modification are described in Sect. 5.3.1.

The data sets of muon-induced energy deposits within the neutron counter, including the signals from muon-induced neutrons and their corresponding muon fluence are characterized in Sect. 5.3.2.

Also the time normalization (Sect. 5.3.3) of the simulated muon fluence to reference measurements has to be done with care, to ensure that the used definitions of fluence, live-time, and detector efficiency are comparable.

### 5.3.1 Muon Generator

The muon generator has to provide starting position  $\vec{r}_s$ , direction  $\hat{\omega}_s$ , and energy  $E_s$  of a primary muon within a Geant4 event. This information is based on the local flux of atmospheric muons at LSM, as discussed in Sect. 3.3.

First, the parametrization of the local muon flux used in this implementation is given. Second, the *probability density function* (pdf) associated with the local muon flux is constructed and sampled. In a third step, the actual starting parameters are randomly chosen from the pdf. Finally, the correctness of the implementation will be proven by comparing the simulated muon flux to reference measurements.

Within this work, the muon generator developed by O. M. Horn [36] is improved and called *muon generator* afterwards. It has for the specific research objective of this work two technical advantages against more general generators, e.g. MUSUN [45]:

First, it increases the simulation performance by using a sophisticated sampling algorithm that considers the strong angular correlation between the incident, high relativistic muon and the produced shower (see Sect. 3.5.2). As this work analyses muon-induced neutrons in coincidence with the muon, it is not necessary to illuminate the complete LSM volume with muons. It is sufficient to illuminate a sphere centred on the neutron counter. As it will be shown in Sect. 5.5.1, all simulated neutrons that are ‘detected’ by the neutron counter have their origin well within this sphere, therefore the limited illumination does not introduce a significant bias and is suitable for this work.

Second, the complete integration of the C++ implementation of the muon generator in Geant4 provides an easier handling than the usage of an additional program to Geant4.

The muon generator used in this work has two improvements compared to the original one of O. M. Horn [36]: a more consequent calculation of the element of solid angle and a more precise description of the rock overburden. The details of the improvements will be given later. As the detailed functioning of the muon generator was often unclear to the EDLEWEISS collaboration, this section outlines the functionality of the muon generator in detail. Considering the muon flux, we use the same terminology and symbols as introduced in Chap. 3.

The muon generator starts with the atmospheric flux of single muons  $d\dot{\Phi}_{\mu,0}/dE_{\mu,0}$   $d\Omega_0$  from direction  $\hat{\omega}_0 = (\theta_0, \phi_0)$  and transforms it to the flux in the rock near the LSM  $d\dot{\Phi}_{r,\mu}/dE_{r,\mu}$   $d\Omega$ ,  $\hat{\omega} = (\theta, \phi)$  by considering the energy loss in the rock overburden and the angular distortion by the earth curvature. Afterwards Geant4 starts muons within the implemented rock shell around LSM (Sect. 5.1) and handles the subsequent propagation through the rock and the secondary production in showers. Consequently, the index  $r$  indicates quantities taken when the muon start in the rock, because they are different from the local quantities at the LSM. This is obviously true for the muon energy  $E_\mu$ , see also Sect. 5.3.2. However, we expect only a negligible deflection of the mostly relativistic muons during their propagation, and therefore assume that the muon direction at the LSM is approximately the same as the start direction.

The atmospheric flux  $d\dot{\Phi}_{\mu,0}/dE_{\mu,0} d\Omega_0$  is parameterized according to Gaisser [24], see Eq. 3.9a in Sect. 3.1.3 and Appendix A.2. The earth curvature is taken into account via the  $\theta^*$  correction (Eq. A.21), depending on the earth radius  $R = 6600$  km and the production height of muons  $H = 18.6$  km [57], see Sect. 3.1.2. Consequently, this implementation includes the correction also in the element of the solid angle, i.e.  $d\Omega_0 = \sin \theta_0 d\theta_0 d\phi$ , which was missing in [36].

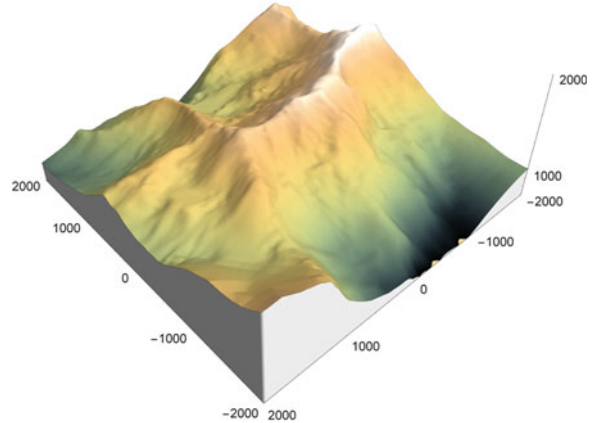
By applying the CSDA (Sect. 3.3.1), the energy loss of muons along their propagation through the rock overburden of thickness  $X$  is described by Eq. 3.26 and the local muon flux by Eq. 3.33. The suitability of the CSDA will be proven by comparison with experimental data in Fig. 5.6. As only atmospheric muons above 2.5 TeV (Eq. 3.37) can reach the LSM, corrections due to the energy loss in the atmosphere or to the finite muon lifetime are not necessary, because these corrections are only significant at lower energies, see Appendix A.2.

The influence of the chemical composition of the rock on the energy loss is considered by the energy loss parameters  $a$ ,  $b$ , see Eq. 3.11a and Sect. 3.2.1. As discussed in Sect. 3.2.8, the chemical composition of the Fréjus rock, and hence the values of the energy loss parameters, is debatable, see also Table A.4. In this work we follow [36] and adopt for the standard analysis the values in Eqs. 3.20 and 3.21 given by W. Rhode [57] and calculated from the chemical composition of the Fréjus rock. Additionally, the spectral index Eq. 3.10b is chosen. These are listed as *standard parameters* in Table 5.2.

In Sect. 5.5.4 we will estimate the influence of the chosen parameter set as theoretical uncertainty by evaluating also an alternative parameter set: W. Rhode [57] gives also effective values for  $a$ ,  $b$ ,  $\gamma$  (Eqs. 3.22–3.24) from fitting the Fréjus measurement. They are listed as *alternative parameters* in Table 5.2.

As the Fréjus rock is homogeneous [14, 57] (Appendix A.4.2), the thickness is related to the mountain profile  $h(\theta, \phi)$ , as given by the Wei-Rhode map [57, 66] (Sect. 3.3.2), and to the rock density  $\rho$  via Eq. 3.29. The value of  $\rho = 2.74 \text{ g cm}^{-3}$  is adopted to be consistent with the chosen energy loss parameters, both values are taken from [57]. However, we note that the adopted  $\rho$  is slightly different from the value used for the material composition in the geometry implementation in Sect. 5.1, which is based on the more recent work [18]. As the Wei-Rhode map gives the mountain

**Fig. 5.4** The innermost  $4 \times 4$  km of the implemented mountain range around the LSM at the centre. The height scale is increased by a factor ten with respect to the lateral scale for better visibility. Based on the data set of the Wei-Rhode map [57, 66]



profile with respect to the centre of the LSM, see Fig. 5.4, it is corrected by the distance  $h_0$  for the muon start position in the Geant4 simulation. Since the muons are started outside the LSM cavern in the simulation, omission of this correction would double count the energy loss along  $h_0$  as it is the case in the original implementation [36]: The calculated  $d\dot{\Phi}_{r,\mu}/dE_{r,\mu}d\Omega$  would already correspond to the muon energy at LSM centre, but the propagation of muons in Geant4 includes again the energy loss of the muon along  $h_0$  towards LSM centre.

In summary, the differential muon flux  $d\dot{\Phi}_{r,\mu}/dE_{r,\mu}d\Omega$  is obtained from the atmospheric muon flux  $d\dot{\Phi}_{\mu,0}/dE_{\mu,0}d\Omega_0$  via a set of coordinate transformations

$$\frac{d\dot{\Phi}_{r,\mu}}{dE_{r,\mu}d\Omega} = \frac{d\dot{\Phi}_{\mu,0}}{dE_{\mu,0}d\Omega_0} \frac{dE_{\mu,0}}{dE_{r,\mu}} \frac{d\Omega_0}{d\Omega} \quad (5.2)$$

$$E_{\mu,0}(E_{r,\mu}) = (E_{r,\mu} + \epsilon) e^{b\rho(h(\theta,\phi) - h_0)} - \epsilon, \quad \epsilon = a/b$$

$$dE_{\mu,0} = e^{b\rho(h(\theta,\phi) - h_0)} dE_{\mu}$$

$$\theta_0(\theta) = \arcsin\left(\frac{R}{R+H} \sin \theta\right)$$

$$d\Omega_0 = \left(\frac{R}{R+H}\right)^2 \frac{\cos \theta}{\sqrt{1 - \left(\frac{R}{R+H}\right)^2 \sin^2 \theta}} d\Omega \quad (5.3)$$

and the parameters listed in Table 5.2.

To construct a volume in the simulation that is homogeneously illuminated by muons, the four integral boundaries have to be chosen. Figure 5.5 shows a scheme of the following definitions:

**Table 5.2** Standard and alternative parameter sets used in the muon generator for the LSM and the surrounding Fréjus rock as given in [57]

Parameter	Value
Earth radius $R$ (km)	6600
Muon production height $H$ (km)	18.6
Rock density $\rho$ (g cm $^{-3}$ )	2.74
Standard parameters	
Spectral index $\gamma + 1$	2.77
Energy loss, electronic contribution $a$ (MeV mwe $^{-1}$ )	217
Energy loss, radiative contribution $b$ (mwe $^{-1}$ )	$4.38 \times 10^{-4}$
Muon critical energy $\epsilon$ (GeV)	495
Alternative parameters	
Spectral index $\gamma + 1$	2.73
Energy loss, electronic contribution $a$ (MeV mwe $^{-1}$ )	215
Energy loss, radiative contribution $b$ (mwe $^{-1}$ )	$4.12 \times 10^{-4}$
Muon critical energy $\epsilon$ (GeV)	522

For details see text

The boundary  $\Omega_0$  for the integration over the solid angle is reduced: generally, the integral would go over the total solid angle of  $4\pi$ . As Eq. 5.2 considers only downward going atmospheric muons and no upward going neutrino-induced muons, the integral over the lower hemisphere always vanishes. Therefore, the sphere can be reduced to the upper hemisphere Eq. 5.8.

Based on the relativistic boost of the muon shower, the position  $\vec{s}(s, \theta', \phi')$  (Eq. 5.12) where the muons pass through a given surface inside the LSM and the direction  $\hat{\omega}(\theta, \phi)$  (Eq. 5.13) of the incidence are strongly correlated. As this work is interested in the energy deposit in the neutron counter by the muon shower, especially by muon-induced neutrons, the correlation is used to increase the simulation performance. As it will be shown in Fig. 5.27, muon-induced showers that deposit energy in the neutron counter pass by closer than  $s = 5$  m in more than 99 % of the cases. Therefore, it is possible to restrict the volume that is homogeneously illuminated by the incident muons from the whole LSM cavern to a ball  $\mathcal{B}$  with radius  $s$  around the neutron counter without introducing a significant bias.

In a first attempt the surface integral has to be taken over the surface of  $\mathcal{B}$ , i.e. the sphere  $\partial\mathcal{B}$ , as it is the minimal surface enclosing all the homogeneously illuminated volume. As only *incoming* muons are considered, the actual boundary  $S_0$  of the

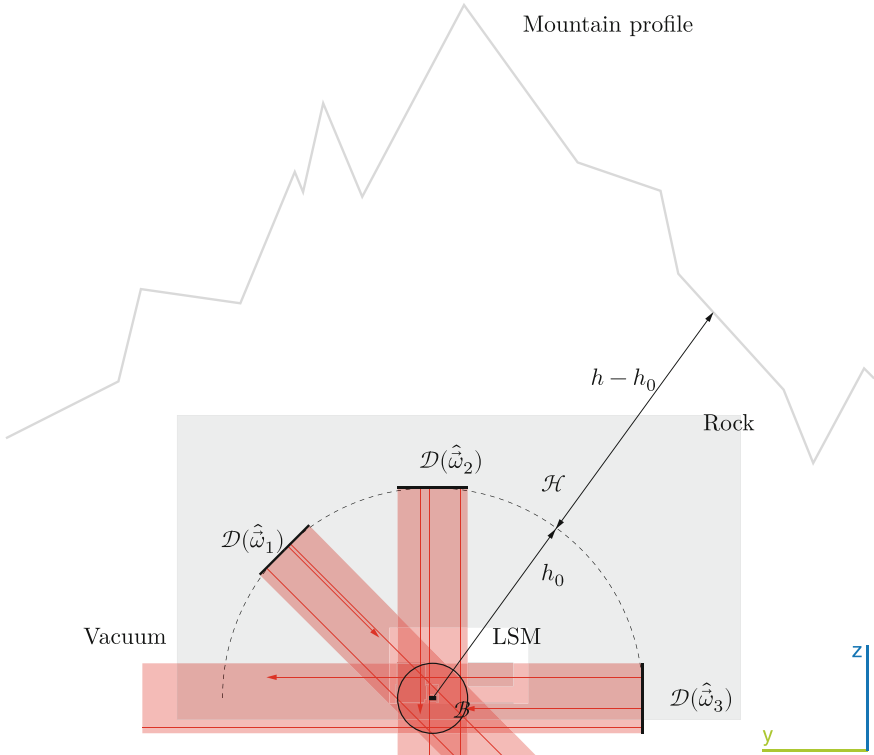


**Fig. 5.5** Illustration of the muon generator in the  $y$ - $z$ -plane: shown in light gray are the implemented rock and the LSM inventory, the active volume of the neutron counter is indicated as black box. Exemplary shown are three incident muons (red solid lines) for three directions  $\hat{\omega}_1, \hat{\omega}_2, \hat{\omega}_3$  (light red). The muons are started in Geant4 on plane disks  $\mathcal{D}$  with radius  $d$  laying on a hemisphere  $\mathcal{H}$  with radius  $h_0$  (dashed black line) from the active volume. Finally, they end in the surrounded vacuum of the Geant4 world volume. The remaining distance  $h - h_0$  to the mountain surface is considered in the muon generator. The intersections of all muons illuminate homogeneously a ball  $\mathcal{B}$  of radius  $d$  around the active volume. Except for the illustrative mountain profile, the dimensions are to scale. The axis cross is 15 m along each axes. For details see text

surface integral has to be restricted to the hemisphere of  $\partial\mathcal{B}$  oriented towards the given direction  $\hat{\omega}$ , see Eq. 5.6.<sup>3</sup>

Albeit the differential muon flux drops as  $E^{-(\gamma+1)}$  (Eq. 3.9a), it never vanishes. Therefore the upper limit of the energy boundary Eq. 5.7<sup>4</sup> is set to infinity.

<sup>3</sup>It is important to restrict to *incoming* muons, hence to the hemisphere  $\mathcal{S}_0$ . As the net muon number, i.e. the integral over the total sphere  $\partial\mathcal{B}$ , includes also the outgoing muons leaving through the opposite hemisphere. Therefore reducing the number nearly to zero, as only a few muons stop within the ball.

<sup>4</sup>Here,  $[a, b)$  denotes a set with an open upper limit. Albeit there is no difference to a closed upper limit with respect to integration, it is relevant later on when the integral is approximated by a sum.

As Eq. 5.2 does not depend on time, the time boundary  $\mathbf{T}_0$  can be freely chosen, here Eq. 5.5.

In summary, the total number  $N_{\text{tot}}$  of *incoming* muons illuminating the ball  $\mathcal{B}$  can be calculated from Eqs. 5.2 by 5.4a:

$$\begin{aligned} N_{\text{tot}} &= \int_{\mathbf{T}_0} \int_{\mathbf{E}_0} \int_{\mathbf{S}_0} \int_{T_0} \frac{d\dot{\Phi}_{r,\mu}}{dE_{r,\mu} d\Omega} (E_{r,\mu}, \vec{\omega}, \vec{r}) dt d\vec{S} dE_{r,\mu} d\vec{\Omega} \\ &= \Delta t \int_{\mathbf{T}_0} \int_{\mathbf{E}_0} \int_{\mathbf{S}_0} \frac{d\dot{\Phi}_{r,\mu}}{dE_{r,\mu} d\Omega} (E_{r,\mu}, \vec{\omega}, \vec{r}) d\vec{S} dE_{r,\mu} d\vec{\Omega} \\ &= \Delta t \sum_{t=0}^{90} \sum_{p=0}^{359} \int_{\mathbf{E}_0} \int_{\mathbf{S}_0} \frac{d\dot{\Phi}_{r,\mu}}{dE_{r,\mu} d\Omega} (E_{r,\mu}, t\delta_\theta, p\delta_\phi, \vec{r}) d\vec{S} dE_{r,\mu} \hat{\hat{\omega}}(t\delta_\theta, p\delta_\phi) \sin t\delta_\theta \end{aligned} \quad (5.4a)$$

$$\approx \Delta t \sum_{t=0}^{90} \sum_{p=0}^{359} \int_{\mathbf{E}_0} \frac{d\dot{\Phi}_{r,\mu}}{dE_{r,\mu} d\Omega} (E_{r,\mu}, t\delta_\theta, p\delta_\phi) \int_{\mathbf{S}_0} d\vec{S} dE_{r,\mu} \hat{\hat{\omega}}(t\delta_\theta, p\delta_\phi) \sin t\delta_\theta \quad (5.4b)$$

$$= \Delta t S_0 \sum_{t=0}^{90} \sum_{p=0}^{359} \int_{\mathbf{E}_0} \frac{d\dot{\Phi}_{r,\mu}}{dE_{r,\mu} d\Omega} (E_{r,\mu}, t\delta_\theta, p\delta_\phi) dE_{r,\mu} \sin t\delta_\theta \quad (5.4c)$$

$$\mathbf{T}_0 = [t_0, t_0 + \Delta t) \quad (5.5)$$

$$\begin{aligned} \mathbf{S}_0 = \{ &\vec{r} \in \mathbb{R}^3 \mid (|\vec{r}| = d) \wedge (\theta' \in [0, \pi/2]) \\ &\wedge (\phi' \in [0, 2\pi]) \} \text{ with } d = 5 \text{ m} \end{aligned} \quad (5.6)$$

$$\mathbf{E}_0 = [0, \infty) \quad (5.7)$$

$$\mathbf{\Omega}_0 = [0, \pi/2] \times [0, 2\pi) \quad (5.8)$$

$$d\vec{S} = r^2 \sin \theta' \hat{\hat{s}}(\theta', \phi') d\theta' d\phi' \quad (5.9)$$

$$d\vec{\Omega} = \sin \theta \hat{\hat{\omega}}(\theta, \phi) d\theta d\phi \quad (5.10)$$

$$\hat{\hat{s}}(\theta', \phi') = (\sin \theta' \cos \phi', \sin \theta' \sin \phi', \cos \theta')^T \quad (5.11)$$

$$= \vec{s}/s \quad (5.12)$$

$$\hat{\hat{\omega}}(\theta, \phi) = (\sin \theta \cos \phi, \sin \theta \sin \phi, \cos \theta)^T \quad (5.13)$$

Here the element of surface  $d\vec{S}$  (Eq. 5.9) and the element of solid angle  $d\vec{\Omega}$  (Eq. 5.10) are expressed in polar coordinates and point in directions  $\hat{\hat{s}}$  (Eq. 5.12),  $\hat{\hat{\omega}}$  (Eq. 5.13), respectively.

As the used Wei-Rhode map is discrete with an angular resolution of  $\delta_\theta \times \delta_\phi = 1^\circ \times 1^\circ$ , the integral over the solid angle reduces to a double sum over the zenith and azimuth angles (Eq. 5.4a) with the indices  $t$  and  $p$ .

In general,  $N_{\text{tot}}$  depends via the mountain profile  $h$  on the position  $\vec{s}$ . In this work, it is neglected because the maximal shifting of  $\vec{s}$  is smaller than the lateral resolution of the Wei-Rhode map used for the mountain profile.<sup>5</sup> Therefore, the integral over  $d\dot{\phi}_{r,\mu}/dE_{r,\mu} d\Omega$  can be approximated by Eq. 5.4b and  $S_0 = \pi s^2$  is the cross section of the ball  $\mathcal{B}$ , i.e. a plane disk with radius  $s$  (Eq. 5.4b).

The above given considerations fix only the incoming direction of the muon, not its starting position within the simulation. To ensure the shower development, at least 5 m rock around the implemented LSM cavern is needed (Sect. 3.4.5). As the maximal extension of the cavern is 25 m, the muons are started  $h_0 = 30$  m away from the cavern centre. As already mentioned, the mountain profile has to be subtracted by  $h_0$  to avoid double counting.

As a consequence of Eq. 5.4b, the muons starting positions  $\vec{r}_s$  for a given direction  $\hat{\omega}_s$  lie within a disk  $\mathcal{D}(\hat{\omega})$  at distant  $h_0$  that is the projection of the ball's  $\mathcal{B}$  cross section. Considering all directions, the disks themselves lie on a hemisphere  $\mathcal{H}$  of radius  $h_0$  with respect to the cavern centre. Consequently, muons propagate through all the inside of the hemisphere  $\mathcal{H}$ , but only the ball  $\mathcal{B}$  is homogeneously illuminated. We want to point out, that this hemisphere  $\mathcal{H}$  is *not* the surface boundary  $S_0$  needed in Eq. 5.4a to calculate  $N_{\text{tot}}$ , it is purely an artefact of the construction; highlighted by the fact that the muon flux passing through the hemisphere is inhomogeneous.

The probability  $P$  to have a muon within the energy range  $\mathbf{E}$  (Eq. 5.14b) is calculated in a frequentist approach as ratio of the partial muon number  $N_{\text{part}}$  to the total muon number  $N_{\text{tot}}$ . Approximating  $N_{\text{tot}}$  with Eq. 5.4c and express  $N_{\text{part}}$  in a similar way by adapting the boundary, the probability is:

$$P(E_i, E_f) = \frac{N_{\text{part}}}{N_{\text{tot}}} \approx \frac{\sum_{t=0}^{90} \sum_{p=0}^{359} \int_E \frac{d\dot{\phi}_{r,\mu}}{dE_{r,\mu} d\Omega} (E_{r,\mu}, t\delta_\theta, p\delta_\phi) dE_{r,\mu} \sin t\delta_\theta}{\sum_{t'=0}^{90} \sum_{p'=0}^{359} \int_{E_0} \frac{d\dot{\phi}_{r,\mu}}{dE_{r,\mu} d\Omega} (E_{r,\mu}, t'\delta_\theta, p'\delta_\phi) dE_{r,\mu} \sin t'\delta_\theta} \quad (5.14a)$$

$$\mathbf{E} = [E_i, E_f] \subset \mathbf{E}_0 \quad (5.14b)$$

To obtain the start information  $(E_s, \vec{\omega}_s, \vec{r}_s)$  for a muon in Geant4, the probability Eq. 5.14a has to be sampled (Eq. 5.15a):

$$P(E_i, E_f) \approx \frac{\sum_{t=0}^{90} \sum_{p=0}^{359} \sum_{j=0}^{J-1} \frac{d\dot{\phi}_{r,\mu}}{dE_{r,\mu} d\Omega} (E_j, t\delta_\theta, p\delta_\phi) \Delta E_j \sin t\delta_\theta}{\sum_{t'=0}^{90} \sum_{p'=0}^{359} \int_{E_0} \frac{d\dot{\phi}_{r,\mu}}{dE_{r,\mu} d\Omega} (E, t'\delta_\theta, p'\delta_\phi) dE \sin t'\delta_\theta} = w(E_i, E_f) \cdot \sum_{t=0}^{90} \sum_{p=0}^{360} \sum_{j=0}^{J-1} P_{tpj} \quad (5.15a)$$

<sup>5</sup>The maximal shifting of  $\vec{s}$  is limited to the ball  $\mathcal{B}$  with 10 m diameter. The used Wei-Rhode map has an angular resolution of 1° and an average depth of the rock overburden of 1720 m, see Sect. 3.3.2, resulting in an average lateral resolution of  $\approx 30$  m.

$$w(E_i, E_f) = \frac{\sum_{t=0}^{90} \sum_{p=0}^{359} \sum_{j=0}^{J-1} \frac{d\dot{\phi}_{r,\mu}}{dE_{r,\mu} d\Omega} (E_j, t\delta_\theta, p\delta_\phi) \Delta E_j \sin t\delta_\theta}{\sum_{t=0}^{90} \sum_{p=0}^{359} \int_{E_0} \frac{d\dot{\phi}_{r,\mu}}{dE_{r,\mu} d\Omega} (E_{r,\mu}, t\delta_\theta, p\delta_\phi) dE_{r,\mu} \sin t\delta_\theta} \quad (5.15b)$$

$$P_{tpj} = \frac{\frac{d\dot{\phi}_{r,\mu}}{dE_{r,\mu} d\Omega} (E_j, t\delta_\theta, p\delta_\phi) \Delta E_j \sin t\delta_\theta}{\sum_{t'=0}^{90} \sum_{p'=0}^{359} \sum_{j'=0}^{J-1} \frac{d\dot{\phi}_{r,\mu}}{dE_{r,\mu} d\Omega} (E_{j'}, t'\delta_\theta, p'\delta_\phi) \Delta E_{j'} \sin t'\delta_\theta} \quad (5.15c)$$

$$E_j = 10^{\log E_i + j \Delta E} \quad (5.15d)$$

$$\Delta E_j = \frac{10^{\log E_i + (j+1) \Delta J} - 10^{\log E_i + j \Delta J}}{2}$$

$$\Delta J = \frac{\log E_f - \log E_i}{J}$$

Here, the  $P_{tpj}$  (Eq. 5.15c) are the sampling points of the pdf that a muon from direction  $\hat{\omega}(t\delta_\theta, p\delta_\phi)$  and energy  $E_j$  crosses the reference surface  $S_0$ .

Because of the rapid drop of the muon flux with energy, Eq. 5.15d samples the energy logarithmically as proposed in [36] and  $J = 100$  sampling points are used.<sup>6</sup> The weight  $w$  (Eq. 5.15b), needed to merge simulations of different energy ranges  $E$ , is calculated in Sect. 5.3.2.

The actual start direction  $\hat{\omega}_s$  and energy  $E_s$  for a Geant4 event are chosen from the *cumulative distribution function* (cdf) (Eq. 5.16a) of the sampled pdf (Eq. 5.15c) via the *inverse transform sampling* for discrete distributions [21, p. 85] and a uniformly distributed random number  $x_0$ :

$$F(t, p, j) = \sum_{t'=0}^t \sum_{p'=0}^p \sum_{j'=0}^j P_{t'p'j'} \quad (5.16a)$$

$$\{t_s, p_s, j_s\} = F^{-1}(x_0) \quad x_0 \in [0, 1] \quad (5.16b)$$

$$\hat{\omega}_s = \hat{\omega}(t_s \delta_\theta, p_s \delta_\phi) \quad (5.16c)$$

$$E_s = E_{j_s} \quad (5.16d)$$

as done in [36].<sup>7</sup>

As one can see from Eq. 5.14a, the probability is independent from time and position. Therefore, the muon starting position for a given direction  $\hat{\omega}_s$  can be obtained from two independent uniformly distributed random numbers  $x_1, x_2$ , restricted to

<sup>6</sup> The sum over  $j$  has the upper limit  $J - 1$  to consider the open upper limit of the set  $E$ . Otherwise, merging two simulated data sets over  $[E_1, E_2), [E_2, E_3)$  would double count the sampling point at  $E_2$ , which is significant.

<sup>7</sup> Albeit it is not explicitly mentioned in [36], it is evident from the source code.

the disk  $\mathcal{D}(\hat{\vec{\omega}}_s)$ . By approximating the plane disks  $\mathcal{D}$  with spherical caps on  $\mathcal{H}$  of the same radius<sup>8</sup>  $s$ , one gets:

$$\vec{r}_s = h_0 (\sin \theta \cos \phi, \sin \theta \sin \phi, \cos \theta)^T \Big|_{|\vec{r} - h_0 \hat{\vec{\omega}}_s| \leq s} \quad (5.17)$$

$$\theta = \arccos x_1 \quad x_1 \in [0, 1]$$

$$\phi = 2\pi \cdot x_2 \quad x_2 \in [0, 1]$$

To verify the correctness of the muon generator, it has to be compared to experimental data. Hereafter, it will be compared with the high statistics data set of the Fréjus experiment, which is described together with its normalization in Appendix A.7. B. Schmidt et al. [62] compared this implementation also with the lower statistics data set of the EDELWEISS muon veto.

Here, the merged data sets from Sect. 5.3.2 are compared to the Fréjus data set; Fig. 3.3 shows a map of the measured muon flux. We calculate the *local* muon flux at LSM by counting the number of simulated muons  $N_{\text{MC}}$  passing through the upper surface  $S_{\text{nc}} = 2 \text{ m}^2$  of the neutron counter from direction  $(\theta, \phi)$ . To be comparable with Fréjus data set, we normalize the simulation by the same method<sup>9</sup> and convolved them with the detector efficiency  $\epsilon_{\text{Frejus}}$  of the Fréjus experiment:

$$\frac{d\dot{\Phi}_{\text{MC}}}{d\Omega} = \frac{N_{\text{MC}}(\theta, \phi)\epsilon_{\text{Frejus}}(\theta, \phi)}{T_{\text{MC}}S_{\text{nc}} \cos \theta} \quad (5.18)$$

$$\frac{d\dot{\Phi}_{\text{MC}}}{d\theta} = \int_0^{2\pi} \frac{d\dot{\Phi}_{\text{MC}}}{d\Omega} d\phi \quad (5.19)$$

$$\frac{d\dot{\Phi}_{\text{MC}}}{d\phi} = \int_0^{\pi/2} \frac{d\dot{\Phi}_{\text{MC}}}{d\Omega} d\theta \quad (5.20)$$

with the live-time of the simulations  $T_{\text{MC}}$  from Sect. 5.3.3. The simulated marginalised distributions Eqs. 5.19 and 5.20 along the zenith and azimuth angle, respectively, agree both with the Fréjus data, as shown in Fig. 5.6.

Whereas the agreement in azimuth direction was already achieved in the original work of O. M. Horn [36], this work shows for the first time that this particular muon generator agrees also in the zenith direction. The difference to [36] is a correct normalization of the simulated data to the solid angle when muons pass through the upper surface of the neutron counter, making them comparable to the Fréjus data set.

---

<sup>8</sup>The probability is distorted by the deviation between plane disk and spherical cap. Here, this distortion is less than  $(1 - S_{\text{cap}})/S_{\text{disk}} = 1\%$ , based on the surfaces  $S_{\text{cap}} = \pi(2h_0^2 - 2h_0\sqrt{h_0^2 - s^2})$ ,  $S_{\text{disk}} = \pi s^2$ . Compared with the other systematic uncertainties, see Sect. 5.5.4, this is negligible.

<sup>9</sup>Whereas most of this subsection handles the correct calculation of the number of muons from the given differential muon flux, for the comparison of simulation and measurement the opposite is needed: the deduction of the differential muon flux from a *simulated measurement*. Therefore, we have to include the detection efficiency.

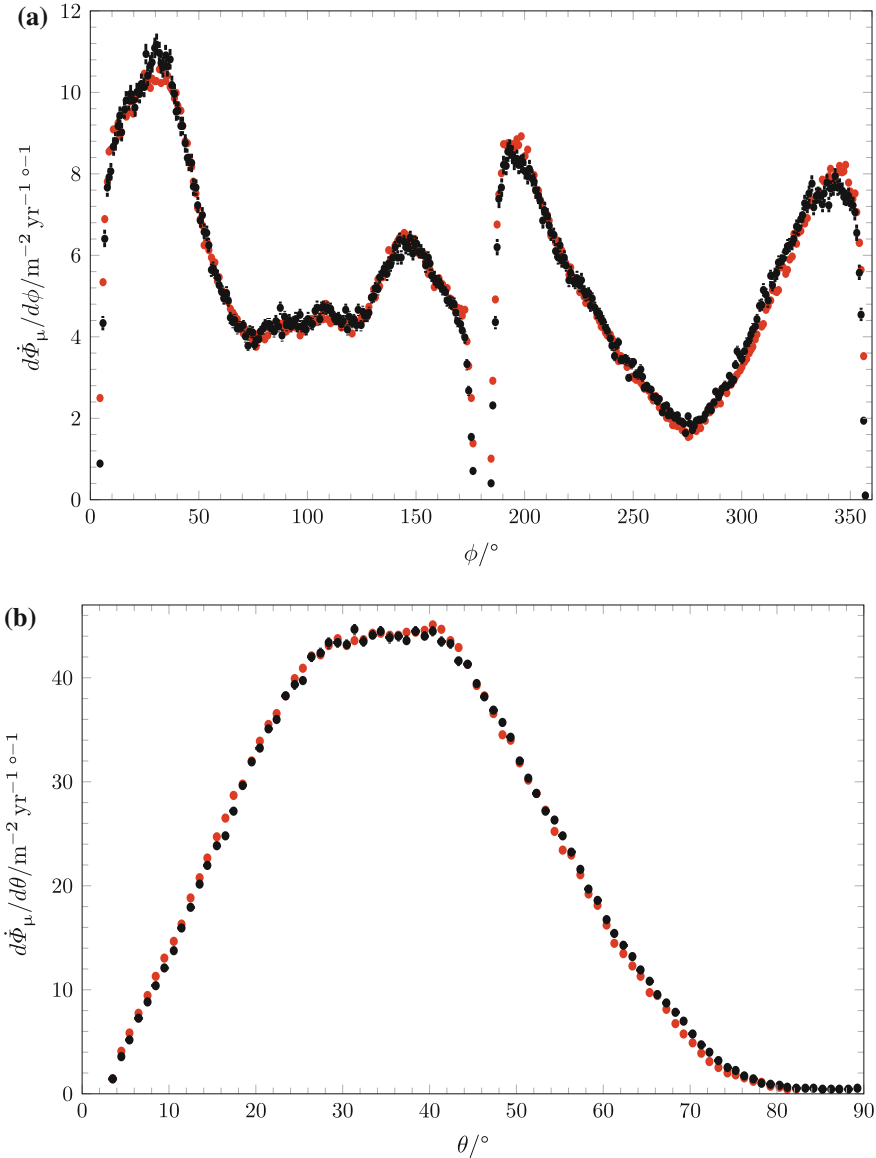


**Fig. 5.6** Differential muon flux  $d\dot{\Phi}_\mu/d\theta$  versus **a** the azimuth angle  $\phi$  and **b** zenith angle  $\theta$  as simulated with Geant4 (red) and measured in the Fréjus experiment [14, 57] (black). For most data points the statistical uncertainties are smaller than the markers. The peaks and dips in the azimuth distribution are caused by valleys and mountain tops in the mountain profile, respectively. For details see text

B. Schmidt et al. [62] found also agreement with the EDELWEISS muon veto data set, taken into account the specific detector response.

In conclusion, for a given energy range  $E$  the muon generator starts a muon with a direction  $\hat{\omega}_s$  (Eq. 5.16c) and energy  $E_s$  (Eq. 5.16d) taken from  $P_{ijk}$  (Eq. 5.15c) and at a position  $\vec{r}_s$  (Eq. 5.17) uniformly sampled from the disk  $\mathcal{D}(\hat{\omega}_s)$ . This results in a ball  $\mathcal{B}$  of 5 m radius around the neutron counter homogeneously illuminated by muons and their accompanied showers developed in at least 5 m of rock. The simulated data sets used in this work are based on different energy ranges  $E$ . Their merging using the corresponding weights  $w$  are discussed in Sect. 5.3.2.

The successful validation against two independent experimental data sets proves the suitability of the muon generator for detailed muon flux simulations at LSM, as it is needed for the simulation of muon-induced neutron production. It highlights also the necessity of a careful implementation and a correct normalization of the simulated data.

### 5.3.2 Simulating the Local Muon Spectrum at LSM

It is necessary to cover most of the muon spectrum at the LSM cavern for a precise simulation of muon-induced neutrons, including low energy effects like neutrons from  $\mu^-$  capture (see Sect. 3.4.1) together with high energy effects like muon spallation (Sect. 3.4.3).

To ensure high statistics throughout the muon flux spectrum, despite its steep falling, the whole energy range  $E_0 = [0, \infty)$  (Eq. 5.7) is partitioned in six ranges  $E_{r,i} = [E_{\min,i}, E_{\max,i}]$ ,  $i = 1, \dots, 6$ , see Table 5.3. The energies correspond to energies of muons starting at  $h_0 = 30$  m away from the LSM centre in the implemented Fréjus rock (Sect. 5.3.1). As discussed later, the first energy range does not contribute to the muon flux in the LSM cavern. It is not possible to simulate the last energy range due to its infinite upper limit. However, the contribution of the last range to the muon flux is the smallest one, two magnitudes lower than the second smallest one. Therefore we assume it is negligible. For each of the remaining four energy ranges ( $i = 2, \dots, 5$ ) a data set with  $\mu^-$  and a data set with  $\mu^+$  was simulated, as the muon capture on nuclei obviously depends on the charge. The resulting eight data sets are listed in Table 5.5 and contain in total  $\approx 55 \times 10^6$  muons of both charges.

To estimate the theoretical uncertainties of the neutron counter rates caused by muon-induced neutrons (Sect. 5.5.4), in the following all values are calculated for the standard and for the alternative muon flux parameter set, listed in Table 5.2. Albeit sources for systematic uncertainties are noted, their influence will be discussed later on in Sect. 5.5.4.

In each data set, the relative uncertainty from Poisson counting statistic on the fluence  $\Phi$  is less than 1 %, see Table 5.5. Each data set is weighted by the contribution of the specific energy range to the whole spectrum via  $w_i$ , and by the contribution of the  $\mu^-/\mu^+$  via  $w_c$  with  $c = +, -$ :

**Table 5.3** Partition of the muon spectrum in distinct energy ranges  
 $E_{r,i} = [E_{\min,i}, E_{\max,i})$  used in this work

$i$	$E_{\min,i}$ (GeV)	$E_{\max,i}$ (GeV)
1	0	2
2	2	20
3	20	200
4	200	2000
5	2000	20,000
6	20,000	$\infty$

$$w_c = \begin{cases} 57.8(9)\%, & c = + \\ 42.2(9)\%, & c = - \end{cases} \quad (5.21)$$

The  $w_c$  are based on the expected muon charge ratio of  $w_+/w_- \approx 1.37$  (Eq. 3.8) at the depth of LSM. That is similar to the 1.38 used by the Borexino collaboration for their simulations in [11], therefore it seems a suitable value for muons at underground sites. We assume its uncertainty to be  $\pm 0.05$ , and handle it in the following as systematic uncertainty, correlated with each other via the condition  $w_+ + w_- = 100\%$ .

The  $w_i$  (Eq. 5.15b) are defined with respect to Eqs. 5.15a and 5.15c and the used parameters are listed in Table 5.2. The actual values of  $w_i$  depends on  $\int d\dot{\Phi}_\mu/dE_\mu d\Omega dE$  which is calculated in *Wolfram MATHEMATICA* via

$$\begin{aligned} & \int \frac{d\dot{\Phi}_\mu}{dE_\mu d\Omega} (E, \theta, \phi) dE \\ &= \zeta^2 \frac{\cos \theta}{f(\theta)} g(\theta, \phi) (G_{1.1/115}(E, \theta, \phi) + 0.054 G_{1.1/850}(E, \theta, \phi)) + C \end{aligned} \quad (5.22)$$

$$G_\delta(E, \theta, \phi) = -\frac{{}_2F_1(\gamma, \gamma; 1 + \gamma; H(E, \theta, \phi))}{\gamma \delta g(\theta, \phi) f(\theta)} \left( \frac{1 - H_\delta(E, \theta, \phi)}{h(E, \theta, \phi)} \right)^\gamma \quad (5.23a)$$

$$H_\delta(E, \theta, \phi) = \frac{1}{1 + \delta f(\theta) h(E, \theta, \phi)} \quad (5.23b)$$

$$h(E, \theta, \phi) = ((E + \epsilon) g(\theta, \phi) - \epsilon) \quad (5.23c)$$

$$f(\theta) = \sqrt{1 - \zeta^2 \sin^2 \theta} \quad (5.23d)$$

$$g(\theta, \phi) = e^{b\rho(h(\theta, \phi) - h_0)} \quad (5.23e)$$

$$\zeta = \frac{R}{R + H} \quad (5.23f)$$

where  ${}_2F_1$  is the hypergeometric function<sup>10</sup> and  $C$  is the integration constant.

As systematic uncertainty we quote the difference between the numerical evaluation of the numerator of Eq. 5.15b as implemented in Geant4 and an analytical integration via Eq. 5.22 in MATHEMATICA. The biggest deviation between both is 0.24 %. For the alternative parameters no Geant4 simulation was run, therefore no numerical results were obtained to estimate this uncertainty. We assume that it is the same as for the standard parameter set. The systematic uncertainties on  $w_c$  and  $w_i$  and their influence on the simulated rate of muon-induced neutron counter events are discussed in Sect. 5.5.4.

During the MC propagation through the rock layer muons get lost by capture and decay (see Sect. 3.4.1). The remaining muons lose energy, therefore the muon spectrum in the LSM cavern potentially starts at 0 eV certainly well below  $E_{\min,2} = 2 \text{ GeV}$ , as shown in Fig. 5.8. The influence of the muon loss can be considered by multiplying the weights  $w_i$  with a transmission probability  $\eta_i$  and subsequent normalizing them to unity:

$$w'_i = \frac{\eta_i w_i}{\sum_i \eta_i w_i} \quad (5.24a)$$

$$\delta w'_i^{\text{stat}} = \sqrt{\left( \frac{w_i \delta \eta_i}{\sum_j w_j \eta_j} - \frac{w_i^2 \eta_i \delta \eta_i}{\left( \sum_j w_j \eta_j \right)^2} \right)^2 + \frac{w_i^2 \eta_i^2 \sum_{k \neq i} (w_k \delta \eta_k)^2}{\left( \sum_j w_j \eta_j \right)^4}} \quad (5.24b)$$

The  $\eta_i$  are obtained from the simulated data sets and have an associated statistical uncertainty due to the limited statistic.

As the data sets are normalized to the Fréjus data in Sect. 5.3.3, the detection threshold of 300 MeV [57] of this experiment has to be taken into account in calculation of  $\eta_i$ . A rough estimation of  $\eta_i$  is the ratio of simulated events where at least one muon above threshold reaches the LSM cavern to all simulated events. This gives a lower bound, as discussed later. The resulting values are given in Table 5.4 where the statistical uncertainties on  $\eta_i$  are given assuming Poisson distribution.

For energy range 6 it is assumed that  $\eta_6 \approx \eta_5$ . The low transmission probability  $\eta_2$  compared to  $\eta_3, \eta_4, \eta_5$  indicates that the minimal energy needed to pass the rock layer is within the energy range  $E_2 = [2 \text{ GeV}, 20 \text{ GeV}]$ . Consequently the weight  $w'_2$  drops strongly compared to  $w'_3, w'_4$ . Because of these indications, we did not simulate  $\eta_1$ , but extrapolate it from  $\eta_2$ :

Figure 5.7 shows the transmission probability  $\eta_2$  for those started primary muons that reach the LSM caverns and have there a kinetic energy above the detection threshold of the Fréjus experiment. Based on Sect. 3.3.1, we expect a smeared step function, i.e. the convolution of a normal distribution  $P_N$  and a Heaviside step function  $\Theta$ ,

---

<sup>10</sup> ${}_2F_1(a, b; c; z) = \sum_{k=0}^{\infty} (a)_k (b)_k / (c)_k z^k / k!$

**Table 5.4** Weights  $w_i$  of various energy ranges  $i$ ,  $i = 1, \dots, 6$ 

$i$	$w_i$ (%)	$\eta_i$ (%)	$w'_i$ (%)
<i>Standard parameters</i>			
1	1.25	0	0
2	10.3(11)	$39.64 \pm 0.03^{\text{stat}} + 6.32^{\text{sys}}$	4.716(4)
3	53.0(2)	$93.76 \pm 0.04^{\text{stat}} + 6.24^{\text{sys}}$	57.118(16)
4	34.6(3)	$93.70 \pm 0.05^{\text{stat}} + 6.30^{\text{sys}}$	37.225(15)
5	0.87(2)	$93.58 \pm 0.13^{\text{stat}} + 6.42^{\text{sys}}$	0.9383(13)
6	0.0020	$93.58 \pm 0.13^{\text{stat}} + 6.42^{\text{sys}}$	$(2.619 \pm 0.004) \times 10^{-3}$
<i>Alternative parameters</i>			
1	1.19	0	0
2	9.87(11)	$39.64 \pm 0.03^{\text{stat}} + 6.32^{\text{sys}}$	4.482(4)
3	51.8(2)	$93.76 \pm 0.04^{\text{stat}} + 6.24^{\text{sys}}$	55.693(16)
4	36.1(3)	$93.70 \pm 0.05^{\text{stat}} + 6.30^{\text{sys}}$	38.734(16)
5	1.02(2)	$93.58 \pm 0.13^{\text{stat}} + 6.42^{\text{sys}}$	1.0884(16)
6	0.0031	$93.58 \pm 0.13^{\text{stat}} + 6.42^{\text{sys}}$	$(3.365 \pm 0.005) \times 10^{-3}$

The uncertainties on the  $w_i$  are systematic uncertainties. The uncertainties on the muon transmission probabilities  $\eta_i$  are statistical and systematic. For illustration purposes also the expected  $w'_i = w_i \eta_i$  are listed with statistical uncertainties only. For details see text

$$f(x; a, \mu, \sigma) = (P_N * \Theta)(x) \quad (5.25a)$$

$$= \frac{a}{2} \left( 1 + \text{erf} \left( \frac{x - \mu}{\sqrt{2}\sigma} \right) \right) \quad (5.25b)$$

for a rock overburden with unique thickness. Here,  $\mu$  is the threshold energy needed to pass through the rock overburden,  $\sigma$  defines the steepness of the threshold, and  $\text{erf}(x)$  is the *error function*.<sup>11</sup> However, the rock thickness between the muon start vertex, situated on the hemisphere  $\mathcal{H}$  around the LSM, see Fig. 5.5, and the cuboid LSM cavern varies continuously over the muon direction. Therefore, an infinite sum of Eq. 5.25b seems more appropriate. We approximate this by the sum of two step functions, which is fitted to the simulated data (red lines in Fig. 5.7). Albeit this oversimplified fit features a bad  $\chi^2/\text{ndf}$  value, this is acceptable as the fit overestimates the simulated data. Consequently, we obtained as average transmission probability of the fit  $\eta_2 = 0.41$ , which is slightly higher than the previously stated  $\eta_2 = 0.40$  in Table 5.4. As this proves the consistency, the fit is used to extrapolate the average transmission probability  $\eta_1 = 6.1 \times 10^{-10}$ . As this is nine orders of magnitude lower than the  $\eta_2$ , we set it in the following to 0.

<sup>11</sup>  $\text{erf}(x) = 2 \int_0^x e^{-t^2} dt / \sqrt{\pi}$ .

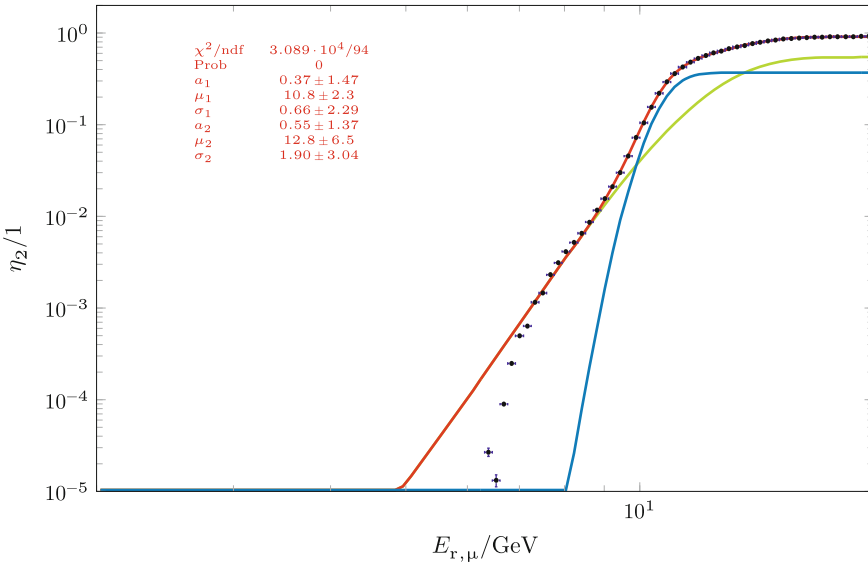


**Fig. 5.7** Simulated muon transmission probability  $\eta_2$  (data points) as function of the muon energy at start  $E_{r,\mu}$ , based on  $N \approx 1.59 \times 10^7$  started  $\mu^-$ . The data are fitted with the sum (red line) of two smeared step functions (Eq. 5.25b)  $f_1(E_{r,\mu}; a_1, \mu_1, \sigma_1)$  (blue line),  $f_2(E_{r,\mu}; a_2, \mu_2, \sigma_2)$  (green line). For most data points the error bars are smaller than the markers. For details see text

One would expect that high energy muons, i.e. in the energy ranges 3, 4, and 5 are not lost in the rock. We assign the difference of  $\approx 6\%$  from  $\eta_i$  to 100 % to not corrected geometric effects and add it as systematic uncertainty. Therefore the  $\eta_i$  are lower bounds on the transmission probability.

Based on this estimation, a lower boundary on the coverage of the muon spectrum in the LSM cavern can be given to 99.997 %, i.e. the sum of  $w'_2$  up to  $w'_5$ . Except the highest energetic interaction above 20 TeV, this work considers most of the muon-induced interactions with a statistical uncertainty on the muon fluence of less than 1 %.

### 5.3.3 Absolute Normalization of the Simulated Muon Flux

For the direct comparison between the simulated event rate and the measured event rate in Sect. 6.1, it is necessary to calculate the equivalent live-time  $T_{\text{MC}}$  of the simulation. As a MC simulation does not provide a time scale per se, it is necessary to relate the simulated fluence  $\Phi_\mu$  [38] to a measured muon flux<sup>12</sup>  $\dot{\Phi}_\mu = \Phi_\mu / T_{\text{MC}}$  to

<sup>12</sup>According to the ICRU [38], we assign the symbol  $\Phi$  to the *fluence*. In [38] the quantity corresponding to the unit  $\text{m}^{-2} \text{s}^{-1}$  is called *fluence rate*. In this work we will use the more common

obtain the live-time  $T_{MC}$ . The normalization relies on the measured reference value and the definition of the reference value. After discussing the proper flux definition, the live-time of the simulated data sets is given and its consistency is illustrated on the simulated muon energy spectrum.

As reported in Sect. 3.3.3, the Fréjus experiment [14] provided high statistic reference values of the muon flux at LSM. The values are based on the rate of events measured by the Fréjus detector with a given muon multiplicity per event and for a zenith angle of  $\theta \leq 60^\circ$ : in total there are  $4.98 \text{ m}^{-2} \text{ d}^{-1}$  events, containing all multiplicities. In contrast, the often cited value, e.g. [46], of  $4.73(9) \text{ m}^{-2} \text{ d}^{-1}$  (Eq. 3.38) contains only events with one muon. Multiplying the events per multiplicity with the multiplicity results in  $5.31 \text{ m}^{-2} \text{ d}^{-1}$  muons in total.

As only one muon is started in a Geant4 event, it seems to be obvious to normalize the simulation to the single muon flux of  $4.73(9) \text{ m}^{-2} \text{ d}^{-1}$  [14]. However, by propagating the muons through the implemented rock layer around the LSM cavern, secondary muons at lower energies can be produced by pion decay, see Sect. 3.4.1. On the other hand, one has also to consider the trigger threshold of 300 MeV [57] for the Fréjus detector, and thus mostly only the primary muons pass the threshold.

The highest contribution of multiple secondary muons passing the threshold occurs for the data set  $\mu^+, E_\mu \in [2 \text{ TeV}, 20 \text{ TeV}]$  with 878,830 events in total: here, there are 7 events with in total 16 muons entering the neutron counter above threshold. Relative to the 878,830 events, this is three magnitudes less than the statistical uncertainty of the fluence for this data set. Therefore, we assume the contamination with multiple secondary muons as negligible. Anyhow, for the calculation of the fluence we count in the simulation only those events where only one muon enters the NC. Therefore, we will use in the following the single muon flux as reference.

While the simulation has to be compared to the single muon flux, the neutron counter can not distinguish between single and multiple muon events. Therefore, a deviation of  $0.25 \text{ m}^{-2} \text{ d}^{-1}$ , the difference between single and multiple muon flux from [14], can be expected between the simulated muon rate and the rate measured by the neutron counter. We consider it as additional uncertainty and add it quadratically:

$$\dot{\Phi}_{\text{ref}} = 4.73_{-0.09}^{+0.27} \text{ m}^{-2} \text{ d}^{-1} \quad (5.26)$$

This uncertainty on the reference flux will be considered as systematic uncertainty in Sect. 5.5.4.

The definition of the flux used by C. Berger et al. [14], or more precisely the definition of the fluence, is unfortunately not clearly stated. The ICRU [38] proposes as definition the number of particles crossing a reference surface perpendicular to the direction of the particles divided by the area of this surface. Based on the discussion in Appendix A.7, we assume in the following that the fluence given in [14] is defined in

---

term *flux* in accordance with [24], but adopt the symbol  $\dot{\Phi}$  proposed by [38] to indicate the relation between fluence and flux.

agreement with [38]. For the simulations in this chapter, the rectangular top surface of the active volume of the NMM is used as reference surface, projected towards the incident muon Eq. 5.27a. Its area is  $2\text{ m} \times 1\text{ m}$ , and its normal is parallel to the  $z$ -direction. Therefore the fluence of  $N_{\mu,ic}$  incident muons with charge  $c = +, -$  and within the energy range  $E_i$  from the direction  $\hat{\omega}(\theta, \phi)$  through the projected area is

$$\Phi_{\mu,ic} = \sum_{t=0}^{\leq 60} \sum_{p=0}^{359} \sum_{E_{\mu} \in E_i} \frac{N_{\mu,c}(t\delta_{\theta}, p\delta_{\phi}, E_{\mu})}{2\text{ m}^2 \cos \theta} \quad (5.27a)$$

$$\delta\Phi_{\mu,ic}^{\text{stat}} = \frac{1}{2\text{ m}^2} \sqrt{\sum_{t=0}^{\leq 60} \sum_{p=0}^{359} \sum_{E_{\mu} \in E_i} \frac{N_{\mu,c}(t\delta_{\theta}, p\delta_{\phi}, E_{\mu})}{\cos^2 \theta}} \quad (5.27b)$$

with an angular resolution of  $\delta_{\theta} \times \delta_{\phi} = 1^\circ \times 1^\circ$  and considering the  $60^\circ$  cut in the zenith angle of the Fréjus experiment [14].

The limited statistic of the simulation introduces a statistical uncertainty on the fluence. Together with the reference flux Eq. 5.26, the live-time  $T_{\text{MC},ic}$  of a data set is therefore:

$$T_{\text{MC},ic} = \frac{1}{w'_i w_c} \frac{\Phi_{\mu,ic}}{\dot{\Phi}_{\text{ref}}} \quad (5.28a)$$

$$\delta T_{\text{MC},ic}^{\text{stat}} = \sqrt{\left( \frac{\delta\Phi_{\mu,ic}^{\text{stat}}}{w'_i w_c \dot{\Phi}_{\text{ref}}} \right)^2 + \left( \frac{\Phi_{\mu,ic} w_c \dot{\Phi}_{\text{ref}} \delta w'_i^{\text{stat}}}{(w'_i w_c \dot{\Phi}_{\text{ref}})^2} \right)^2} \quad (5.28b)$$

with the weights  $w'_i$  (Eq. 5.24a) and  $w_c$  (Eq. 5.21). The statistical uncertainty results from the limited statistic. It is propagated via  $\delta w'_i^{\text{stat}}$  Eq. 5.24b and  $\delta\Phi_{\mu,ic}^{\text{stat}}$  Eq. 5.27b. Table 5.5 lists the resulting live-times for the simulated data sets  $i, c$ , which are defined in Table 5.3. The theoretical uncertainty on the live-time due to the model of the incident muon flux is expressed by the live-times for the alternative parameter set for the muon flux model (Table 5.2). The theoretical and systematic uncertainties on the live-times will be needed in Sect. 5.5.4 and are discussed there.

Consequently, Fig. 5.8 shows the differential muon spectrum of the eight simulated data sets, normalized to the live-time: The filled gray histogram is the spectrum of the primary muons as they are started in the implemented rock,  $h_0 = 30\text{ m}$  away from the LSM center. Therefore, it is a function of the muon energy at start  $E_{\text{r},\mu}$ . It is normalized also to the cross section  $S_0$  (Eq. 5.4b) of the ball  $\mathcal{B}$ . The open red histogram shows the *local* spectrum at LSM, when muons pass through the upper surface of the liquid scintillator in the NMM. It is a function of the local muon energy  $E_{\mu}$ . Here, the reference surface normalization is the same as in Eq. 5.27a.

**Table 5.5** Overview of the number of started muons  $\tilde{N}_\mu$ , the combined weight  $w'_{ic} = w'_i \cdot w_c$ , the resulting fluence  $\Phi_{\mu,ic}$  and the live-time  $T_{MC,ic}$  is given, for each data set  $ic$

Data set $i, c$	$\tilde{N}_\mu$ ( $10^6$ )	$w'_{ic}$ (%)	$\Phi_{\mu,ic}$ ( $\text{m}^{-2}$ )	$T_{MC,ic}$ (yr)	
				SPS	APS
$\mu^-$					
2, –	9.08	1.9901(16)	47,388(171)	$1380 \pm 5^{\text{stat}} {}^{+56}_{-223} \text{ sys}$	1452
3, –	10.09	24.104(7)	120,571(276)	$290.0 \pm 0.7^{\text{stat}} {}^{+13.0}_{-22.9} \text{ sys}$	297.4
4, –	7.668	15.709(7)	91,499(241)	$337.7 \pm 0.9^{\text{stat}} {}^{+17.9}_{-24.9} \text{ sys}$	324.5
5, –	1.009	0.3961(6)	12,035(88)	$1761 \pm 13^{\text{stat}} {}^{+122}_{-130} \text{ sys}$	1519
$\mu^+$					
2, +	9.08	2.726(2)	46,891(170)	$997 \pm 4^{\text{stat}} {}^{+34}_{-155} \text{ sys}$	1049
3, +	10.09	33.014(9)	121,066(277)	$212.6 \pm 0.5^{\text{stat}} {}^{+8.2}_{-15.6} \text{ sys}$	218
4, +	7.43796	21.516(9)	88,686(237)	$238.9 \pm 0.6^{\text{stat}} {}^{+11.2}_{-16.3} \text{ sys}$	229.6
5, +	0.87883	0.5425(8)	10,460(82)	$1118 \pm 9^{\text{stat}} {}^{+71}_{-76} \text{ sys}$	964

For  $w'_{ic}$ ,  $\Phi_{\mu,ic}$  the statistical uncertainty is given. The live-time  $T_{MC,ic}$  is given with statistical and systematic uncertainty for the standard parameter set (SPS) of the muon generator, and calculated for the alternative parameter set (APS)

As a consequence of the slowing down of primary muons and the production of secondary muons, the local spectrum  $d\Phi/dE_\mu$  already starts at 0 eV. The smooth curve, based on the merged individual data sets, indicates the consistency of the used normalization method.

Based on the normalization to the single muon flux measured by the Fréjus experiment (Eq. 5.26), the local integral flux<sup>13</sup> above the Fréjus threshold of 300 MeV is  $4.73 \text{ m}^{-2} \text{ d}^{-1}$ , confirming the self-consistency of the normalization. However, we note that the total integral flux, including the low energetic part of the spectrum, is  $5.36 \text{ m}^{-2} \text{ d}^{-1}$ .

In conclusion, the equivalent live-times for the simulated data sets can be calculated by normalizing their fluences to the muon flux measured by the Fréjus experiment. This enables the continuous merging of the data sets, reproducing the flux value measured by Fréjus, therefore proving the consistency of the method. The normalization enables an absolute comparison of the simulated events with the measured event rate in Sect. 6.1. The equivalent live-times range up to roughly 1600 years. This ensures, that the accuracy of simulation results is not limited by statistic.

<sup>13</sup>Note that Fig. 5.8 gives the flux per year.

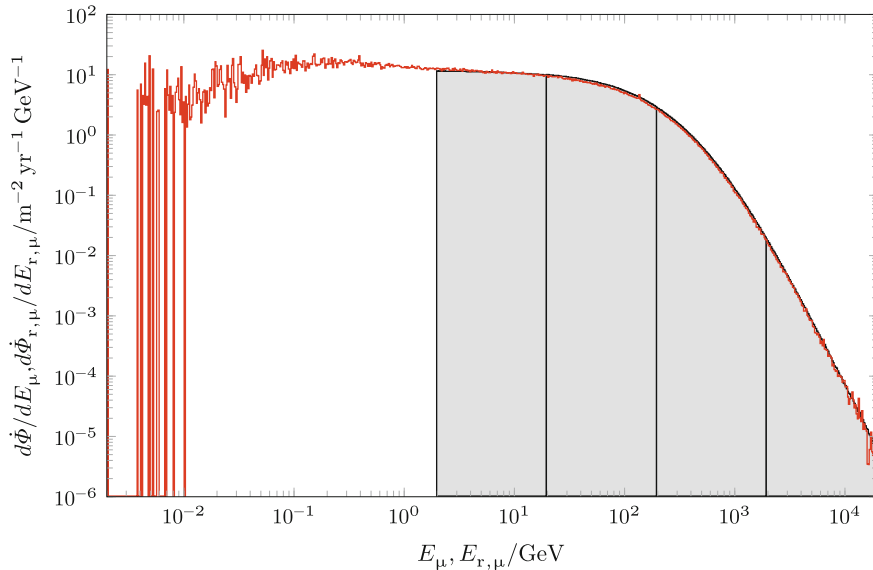


**Fig. 5.8** The *filled gray* histogram shows the spectrum  $d\dot{\Phi}_{r,\mu}/dE_{r,-}$  of the primary muon in Geant4, started 30 m away from the LSM centre in the rock. The four energy ranges are indicated. The *open red* histogram shows the spectrum  $d\dot{\Phi}/dE_\mu$  for muon entering the neutron counter, including secondary muons produced in the rock. For details see text

## 5.4 MC Model of the Detector Response

The signatures for muon-induced neutrons (see Sect. 4.3) depend on the multiplicity of the secondary hits within one event. Therefore, they depend on individual signals relative to the trigger threshold and on the interval between these hits. For the assessment of Geant4 and for a determination of the detection efficiency of muon-induced neutrons, a detailed understanding of the detector response is needed. As the NMM has a non-unique relation between the incoming neutron flux and the multiplicity of secondary hits (Sect. 4.1), a detailed MC model of the detector response is essential and will be given in this section.

Whereas the physical processes included in this model were discussed in detail in Sect. 4.1, this section focuses on the technical aspects: implementation and validation of the model.

The model is split in four stages: The first stage is the simulation of the primary particle<sup>14</sup> and its interaction within the geometry implemented in Geant4 (Sect. 5.4.1). This stage includes the tracking of the primary particle until it terminates or leaves the world volume, but also the production and interaction of secondary particles,

<sup>14</sup>For the simulation of muon-induced neutrons, the primary particle is the muon, whereas for simulations of calibration measurements, based on AmBe as neutron reference source, the primary particles are neutrons and gamma rays.

e.g. neutrons in hadronic cascades, gamma quanta from neutron capture, or knock-on electrons from Compton scattering. The energies, which these particles deposit within the volumes of the muon telescope and the NMM are stored in ROOT files for each Geant4 event.<sup>15</sup> Besides the energy, each deposit is specified by its time, its three-dimensional position, and the step length<sup>16</sup> along which it happened.

In the next stage (Sect. 5.4.2) each energy deposit is quenched and the equivalent number of scintillation photons is calculated. After applying a light propagation model, this stage stores the number of absorbed photons per PMT, binned in time. In the last stage (Sect. 5.4.3), the same trigger conditions as used experimentally are applied. When a trigger is issued, a DAQ window is opened and NMM- and muon telescope events are built from the simulated data. Finally, the signatures are searched in these data to decide if they contain candidates for muon-induced neutrons.

This work flow has the advantage that with increasing stage the amount of data is reduced, therefore changes on higher stages are rather fast and do not need a repetition of time consuming simulations, e.g. of the neutron transport in stage one. This performance gain was used when determining the free model parameters (Sect. 5.4.4) by fitting the model to reference measurements of AmBe neutrons via parameter variation. The systematic uncertainties on the simulated detector response, which are caused by the uncertainties in the parameter determination, are discussed in Sect. 5.5.4.

The calibrated detector response model is used in Sect. 5.5.3 to investigate the expected rate of muon-induced neutron candidates and the detection efficiency, and in Sect. 5.5.5 to investigate the expected event rate from background sources.

### 5.4.1 Simulation of Energy Deposits

The important interactions that have to be considered for the model of a neutron detector response are scattering of neutrons during their transport and moderation, and capture or decay as the processes that terminate their tracks. Energy is deposited in the active volume of the NMM directly via nuclear recoils during the moderation stage and mainly indirectly via the absorption of the emitted gamma quanta from the final capture. These energy deposits are non-local in two ways: first, the thermalized neutrons diffuse before they get captured, therefore their capture position may be distant to their production position. Second, the gamma quanta and tertiary particles like knock-on electrons can deposit the emitted energy distantly from the location of gamma emission. For a more detailed discussion see Sect. 4.1.1. Consequently,

---

<sup>15</sup>Depending on the context *event* has two meanings: a *Geant4 event* is defined as the amount of all interactions caused by a primary particle in the simulation. Based on the simulated data the detector model builds *NMM- and muon telescope events*, which correspond to the experimentally measured ones.

<sup>16</sup>For the definition of step length in context of Geant4 simulations see Appendix A.3.2.

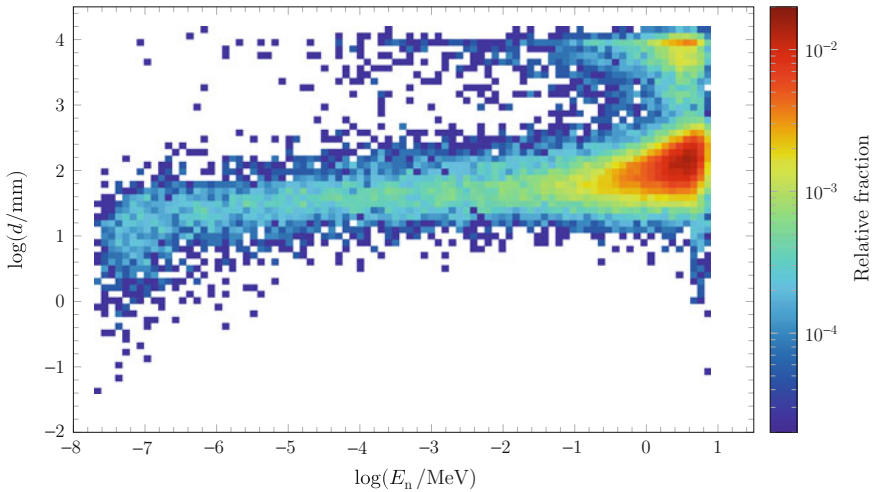
a detailed, three dimensional simulation within the fully implemented geometry is needed to obtain correct results.

The model benefits from the unified approach discussed before: the implemented geometry of the detector and its surrounding (see Sect. 5.1) enables a realistic decision whether an energy deposit occurs in the active volume, and the used physics list (Sect. 5.2) considers not only the neutron transport, but also the non-locality of the energy deposits. Due to the unified approach, the simulation contains also the ‘contamination’ of the energy deposits with muon induced electromagnetic showers and bremsstrahlung, as in the real experiment.

The neutron transport and moderation is an important part of the detector model: first, the diffusion of the thermalized neutrons contribute to the non-local energy deposits. Second, the moderation affects the capture cross section as it rises with decreasing neutron energy (Fig. 4.1). Therefore, a realistic implementation of the neutron transport is necessary. The neutron transport in Geant4, based on elastic and inelastic scatterings, is governed by several theory- and data-driven implementations. The set of models used in this work is shown in Fig. 5.3 and the energy bounds of the individual models are listed in Appendix A.4.1. The accuracy of the implementation for the energy range  $10\text{ keV} \leq E_n \leq 5\text{ MeV}$  is in agreement with MCNPX, a dedicated MC package for neutron transport simulations [49].

For thermalized neutrons, Geant4 can consider the chemical bounds and the thermal motion of the nuclei via extended cross sections for  $E_n \leq 4\text{ eV}$  [25, 40]. This, however, is not used in our work, since it depends on the chemical composition of the used material and for most materials used in this work no data sets are pre-defined in Geant4, especially not for the liquid scintillator that is the main moderator of neutrons produced in the lead target of the NMM. As discussed in Sect. 4.1.1, the consideration of chemical bounds increases the scattering cross section, hence decreases the mean free path. As a consequence, a Geant4 model without thermal cross section data underestimates the moderation [25], and the neutron detection efficiency deduced via the detector response model in Sect. 5.5.3 is only a lower bound.

Due to the dependence on the material composition and detector geometry it is difficult to verify the accuracy of the moderation and thermalization without dedicated measurements. However, as plausibility check an AmBe neutron source installed at the centre of the top surface of the NMM was implemented. The obtained characteristics were compared to literature values of similar material. Within this model, averaged over the neutron energy spectrum reaching up to 10 MeV (see Appendix A.6), the neutron needs 50 ns to pass below 10 keV and 7  $\mu\text{s}$  to pass below the thermal energy  $E_{\text{th}} = 23.5\text{ meV}$  in agreement with [39] that gives an order of magnitude of 100 ns and 10  $\mu\text{s}$ , respectively. Figure 5.9 shows the distance between the position where the neutron passes below  $E_{\text{th}}$  and the position where it enters the liquid scintillator, as function of the kinetic neutron energy  $E_n$  when it enters the liquid scintillator. The main population is at distances less than 1 m, since the maximal distance of the active volume is its diagonal of 2.3 m. About 21 % of all neutrons thermalize not in the liquid scintillator, but in the lab cavern, due to their larger kinetic energy. In



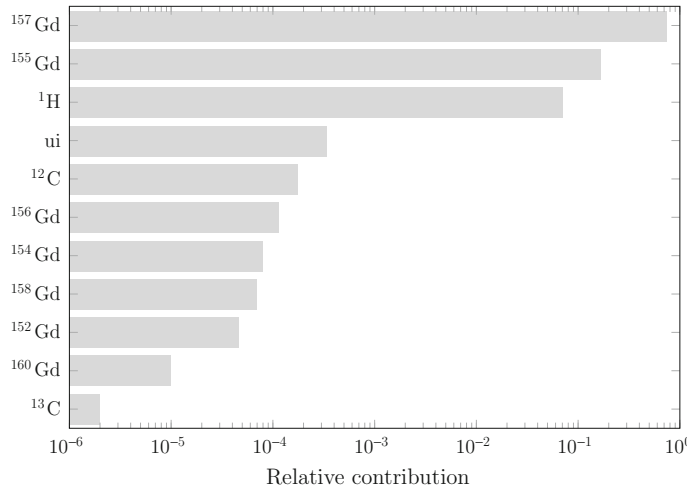
**Fig. 5.9** Distance  $d$  between the point where a neutron energy becomes smaller than 25.3 meV and the point where the neutron enters the scintillator as function of neutron initial kinetic energy  $E_n$ . Bin contents are normalized to the total number of  $N = 38,178$  started neutrons, note the logarithmic scales. For details see text

Fig. 5.9 this corresponds to the second population with  $d > 1$  m and  $E_n > 1$  MeV. Overall, the quadratic mean distance needed to thermalize (Eq. 4.3) is  $\sqrt{\langle r_E^2 \rangle} = 4$  m.

Limiting the sample to the neutrons that stay within the liquid scintillator, the moderation process can be characterized by a logarithmic energy decrement (Eq. 4.2b) of  $\xi = 0.728$ , and an average number of collisions (Eq. 4.2a) before thermalization of  $n = 26.0$ . As the scintillator is mostly a hydrocarbon, one would expect a moderation capability between the one of hydrogen ( $\xi = 1.000$ ,  $n = 18$  [10]) and carbon ( $\xi = 0.158$ ,  $n = 114$  [10]). In fact, it is only slightly worse than hydrogen and closer to deuterium ( $\xi = 0.725$ ,  $n = 25$  [10]).

In summary, the implementation of the moderation seems plausible as the obtained parameters are close to literature values. Furthermore, this test highlights the necessity of a detailed geometry implementation via the position dependence of the neutron moderation.

After moderation, the next step is the capture of thermal neutrons, not only in the liquid scintillator, but also by the materials in its surrounding. Figure 5.10 shows the relative contribution of nucleus X in the neutron capture reaction  ${}^A\text{X}(\text{n}, \gamma) {}^{A+1}\text{X}$ . As expected from the discussion of the neutron capture cross section in Sect. 4.1.1, most of neutrons are captured by the gadolinium isotopes  ${}^{157}\text{Gd}$  and  ${}^{155}\text{Gd}$ , followed by hydrogen  ${}^1\text{H}$ . The ‘unidentified nucleus’ (ui) is a technical artefact: for some reactions Geant4 does not list the produced nucleus  ${}^{A+1}\text{X}$  as secondary particle of the reaction, therefore an identification of  ${}^A\text{X}$  is not directly possible. However, an identification is possible via the spectrum of the emitted gamma rays: Fig. 5.11 shows the simulated gamma spectrum, classified according to  ${}^A\text{X}$ . The gamma spectrum



**Fig. 5.10** Relative contribution of different nuclei  $^A\text{X}$  ( $ui$  unidentified nucleus) to the radiative neutron capture  $^A\text{X}(\text{n}, \gamma)^{A+1}\text{X}$ . Extracted from  $10^6$  capture events normalized to  $N = 10^6$  started neutrons. For details see text

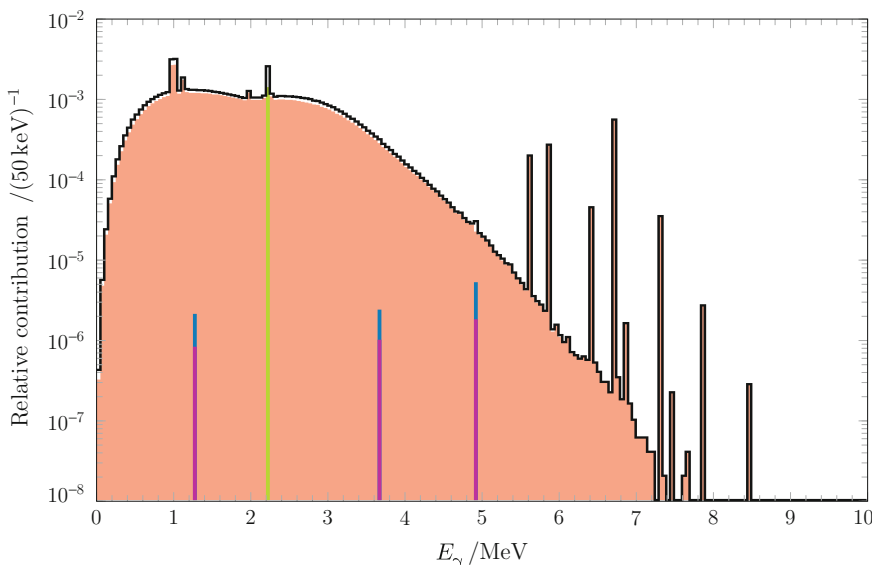


**Fig. 5.11** Gamma spectrum for radiative neutron capture  $^A\text{X}(\text{n}, \gamma)$  as function of the gamma energy  $E_\gamma$ , classified for different  $\text{X}$ : Gadolinium (red), hydrogen (green), carbon (blue), and unidentified nuclei (violet). The sum spectrum of all gamma rays is shown in black. In total, 3,803,308 gamma rays are normalized to  $N = 10^6$  started neutrons. For details see text

from the ‘unidentified nucleus’ clearly agrees with the spectrum from neutron capture on carbon.

The implemented neutron capture model was experimentally tested: as discussed in Sect. 4.1.1 the falling edge of a capture time distribution (Fig. 4.12) is related to the neutron capture cross section and can be parametrized via the capture time  $\tau_{\text{cap}}$  (Eq. 4.8). Based on the detector response model, capture time distributions for different loadings of the liquid scintillator with gadolinium  $n_{\text{Gd}}$  were simulated and the obtained capture times were compared with the values measured with AmBe neutron source. Figure 4.14 shows the expected increase of  $\tau_{\text{cap}}$  with decreasing  $n_{\text{Gd}}$ . As already discussed in Sect. 4.4.2, simulated and experimental values agree for the first measurement and the nominal gadolinium loading of  $n_{\text{Gd}} = 0.2\% \text{ W/W}$ , but for latter measurements the experimental  $\tau_{\text{cap}}$  values increase, most probably caused by the precipitation of the gadolinium out of the liquid scintillator. In the following, a nominal loading is assumed in simulations and the influence of the gadolinium precipitation is included as systematic uncertainty in Sect. 5.5.4.

As discussed in Sect. 4.1.3, not only the neutron capture efficiency contributes to the total neutron detection efficiency, but also the absorption efficiency of the emitted gamma rays. The simulated absorption efficiency is affected by the precision of the implemented gamma cascade, because high energetic gammas have a higher probability to escape the scintillator as those with less energy. For  ${}^{\text{A}}\text{Gd} (n, \gamma) {}^{\text{A}+1}\text{Gd}$ , the correctness of the gamma cascade implemented in Geant4 is debatable [4]. It is especially stated that the Geant4 standard model G4NeutronHPCapture misses discrete gamma lines in the higher energy part of the spectrum [37]. Therefore, in this work a dedicated implementation of the capture reaction on gadolinium, Gd-NeutronHPCapture [53], developed by the Double Chooz collaboration and provided by K. Zbiri [70] was used. It is regarded as a more precise implementation [37]. Unfortunately, no comparison between G4NeutronHPCapture, GdNeutronHPCapture, and experimental data is published to test the correctness and validity of claims in [37, 53].

In Fig. 5.12a, c we compare the two MC models with each other and the experimental gamma energy spectrum published by L. Groshev et al. [33]<sup>17</sup> in 1968. Despite its age, this publication seems up to date to be the only one containing besides the discrete gamma lines also the continuum part of the gamma cascade [65]. Also simulated  $\gamma$ -multiplicity is compared to the data of L. V. Pikelner and G. P. Georgiev (as cited in [65]), see Fig. 5.12b. This comparison suggests that the gamma multiplicity distribution is better modelled in GdNeutronHPCapture, both in terms of spectral shape and mean value. Also the experimental gamma spectrum seems to agree more with GdNeutronHPCapture than with G4NeutronHPCapture (Fig. 5.12c): ignoring that the MC data sets miss the obvious resolution effects of

<sup>17</sup>The experimental data were digitized from [33, p. 180] and their efficiency curve from [33, p. 16], both via the program *GetData GRAPH DIGITIZER*. Subsequently a linear spline interpolation was applied and the interpolation was integrated over the bin size via *MATHEMATICA* to obtain the binned histogram in Fig. 5.12c. For a better comparison, the MC data sets are convolved with the experimental efficiency curve, which is published for  $E_{\gamma} > 500 \text{ keV}$ , below this value the MC data are set to zero.

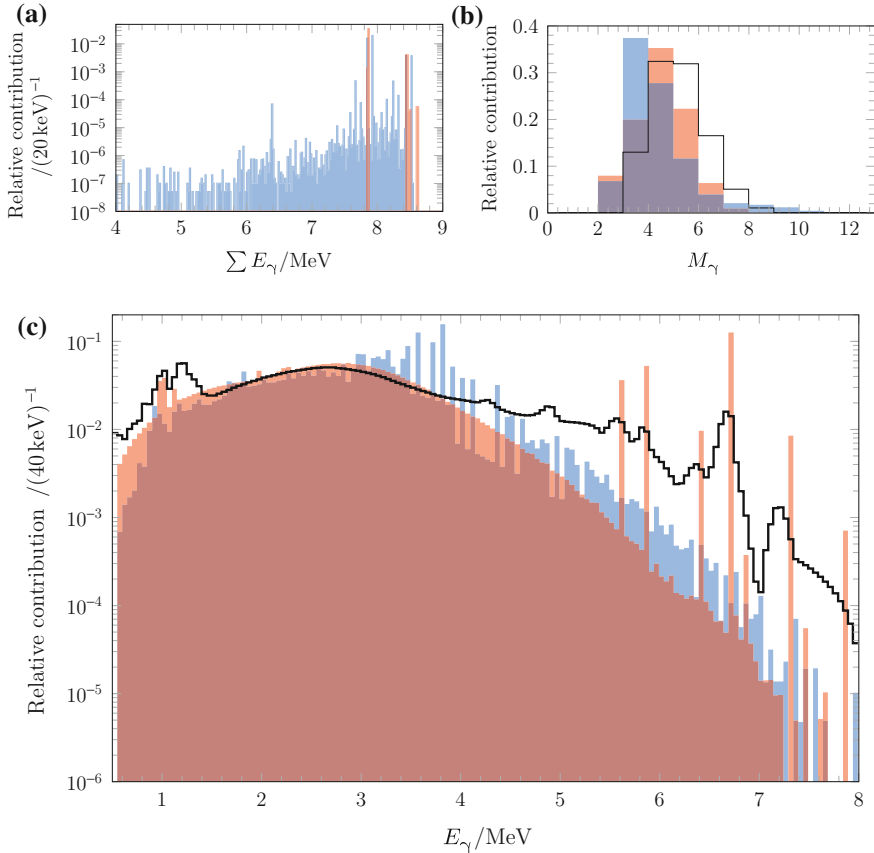


**Fig. 5.12** Comparison of MC models G4NeutronHPCapture (blue), GdNeutronHPCapture (red) for the gamma cascade Gd(n,  $\gamma$ ) with each other and with experimental data (black). Each MC simulation contains  $N = 10^6$  started neutrons, resulting in 927,045 events for G4NeutronHPCapture and 927,599 events for GdNeutronHPCapture. **a** Distribution of summed energy of all gamma rays  $\sum E_\gamma$  per event, normalized to  $N$ . **b** Gamma multiplicity  $M_\gamma$  (mean values: GdNeutronHPCapture  $\bar{M}_\gamma = 4.022$ , G4NeutronHPCapture  $\bar{M}_\gamma = 3.883$ ) compared with data [65, fig. 6] ( $\bar{M}_\gamma = 5.21$ ), normalized to  $N$ . **c** Distribution of the gamma ray energy  $E_\gamma$ , compared with and scaled to experimental data [33]. For details see text

the experimental data [33], the most prominent difference is, as stated by [37, 53], the missing of discrete, high energetic gamma lines in G4NeutronHPCapture, which are included in GdNeutronHPCapture. But GdNeutronHPCapture has also disadvantages: contrary to G4NeutronHPCapture, only the capture on  $^{155}\text{Gd}$ ,  $^{157}\text{Gd}$  is implemented and the recoil of the de-excited nucleus is neglected, which can be seen in Fig. 5.12a: for GdNeutronHPCapture the complete neutron binding energy goes in gamma rays, resulting in the discrete lines in the sum energy spectrum, whereas G4NeutronHPCapture produces a continuous sum energy

spectrum, indicating the split of the neutron binding energy between the gamma rays and the nucleus. Nevertheless, for this work `GdNeutronHPCapture` was used as  $^{155}\text{Gd}$ ,  $^{157}\text{Gd}$  are the gadolinium isotopes that contributed most to the capture (Fig. 5.10) and nuclear recoils produce only a strongly quenched signal in the neutron detector as discussed in Sects. 4.1.1 and 5.4.2. The influence of the chosen model for the gamma cascade on the detection efficiency will be investigated in Sect. 5.5.4 as a theoretical uncertainty.

The emitted gamma rays finally deposit their energy via Compton scattering, pair production, and the photoelectric effect (Sect. 4.1.1, especially Fig. 4.3). In this work the low energy package G4EMLOW version 6.2 [17] of Geant4 is used, which is data driven and based on the *Livermore data libraries*, for references see [27].

Recoils of charged hadrons and ions deposit energy via ionisation. The implemented individual processes and models are the same as discussed in Sect. 3.2.2 and 3.6.1 in the context of ionization caused by muons, albeit the energy ranges are adapted, see [17, 27] for more details.

For each Geant4 event all simulated energy deposits within the active volumes of the NMM (i.e. the liquid scintillator) and of muon module 50 (i.e. the plastic scintillator) are stored in objects of the dedicated ROOT event class. The ROOT event class was developed for this work and stores besides the energy  $E_{\text{dep}}$ , also the time  $t$ , the three-dimensional position  $\vec{r}$ , and the step length  $l$  along which the energy deposit happens. The importance of this information on an event-by-event base is illustrated in the next section. It provides detailed, localized energy deposits within the actual detector geometry for the next stage of the detector response model.

### 5.4.2 Scintillation Light Production, Propagation, and Absorption

The signature of a muon-induced neutron event depends on a coincidence between spatially separated PMTs. Since the light propagation within the detector is position dependent, it is necessary to take this dependence into account.

As discussed in Sect. 4.2.5 the energy deposition of muons follows a Landau distribution, thus in the experiment the discriminator threshold is adjusted to a value well below the Landau peak. Therefore, the generation of a *muon telescope event* (Sect. 4.3) is rather unaffected by the detailed shape of the energy spectrum. On the other hand, the spectrum of energy deposits caused by neutron capture is continuous down to low energies and the discriminator threshold always cuts part of the spectrum. Hence, the effect of the scintillation is only included in the detector response model of the NMM and not in the detector response model for the muon telescope.

The actual light tracking is applied to the simulated energy deposition in two steps: first, the fraction of the deposited energy  $E_{\text{dep}}$  that is available for scintillation is calculated, called the *visible energy*  $E_{\text{vis}}$ . Second, the equivalent amount of photons is convolved with the collection efficiency to obtain a number of photons absorbed on

each neutron PMT ( $\text{PMT}_{i,j}^N$ ) within the neutron PMT groups ( $\text{PMTG}_i^N$ ), see Sect. 4.2.1 for their definition. The results of the light tracking for the NMM and the raw energy deposits for the muon telescope are binned according to the time resolution of PMTs and stored in ROOT files for the next stage of the detector response model. The  $k$ -th *time bin*  $T_k$ :

$$T_k = [t_k, t_k + \Delta t_{\text{bin}}] \quad (5.29\text{a})$$

$$\Delta t_{\text{bin}} = 10 \text{ ns} \quad (5.29\text{b})$$

starts at time  $t_k$  and lasts for  $\Delta t_{\text{bin}}$ . The actual value of  $\Delta t_{\text{bin}} = 10 \text{ ns}$  will be motivated later on page 248.

Each energy deposit  $l$  is characterized by the tuple  $\{E_{\text{dep},l}, t_l, \vec{r}_l, l_l\}$ . The mean amount of scintillation photons  $\bar{N}_{\text{ph},l}$  caused by the energy deposit  $E_{\text{dep},l}$  along the step length  $l_l$  is calculated according to Eq. 4.14a:

$$\bar{N}_{\text{ph},l} = \frac{S}{1 + \frac{kB}{\rho} \frac{E_{\text{dep},l}}{l_l}} E_{\text{dep},l} \quad (5.30)$$

The scintillator density  $\rho$  and the scintillation light yield  $S$  are taken from the data sheet of the used liquid scintillator, which is listed in Table A.5. The two quenching parameters  $k \cdot B$  [15] are effectively one free parameter. It was determined in Sect. 5.4.4 as  $kB = 0.016(4) \text{ g MeV}^{-1} \text{ cm}^{-2}$  by fitting the detector response model to reference measurements with AmBe. This value is in agreement with published results for other pseudocumene based liquid scintillators:  $0.0094\text{--}0.035 \text{ g MeV}^{-1} \text{ cm}^{-2}$ , depending on the actual chemical composition [64].

The resulting *effective quenching factor*  $Q_k$  of a time bin  $T_k$  is defined similar to Eq. 4.14b as ratio of the visible energy  $E_{\text{vis}} = N_{\text{ph}}/S$  to deposit energy  $E_{\text{dep}}$ :

$$Q_k = \frac{\sum_{\substack{l \\ t_l \in T_k}} N_{\text{ph},l}}{S E_{\text{dep},k}} \quad (5.31)$$

$$E_{\text{dep},k} = \sum_{\substack{l \\ t_l \in T_k}} E_{\text{dep},l} \quad (5.32)$$

Figure 5.13 shows  $Q_k$  as function of  $E_{\text{dep},k}$ : Electromagnetic interactions caused by the gamma rays from deexcitation and neutron capture are associated with  $Q_k \lesssim 1$ , whereas nuclear recoils caused by thermalizing of neutrons have a lower quenching factor of  $Q_k \approx 0.1$ .<sup>18</sup> The effect of the binning in time is well visible for

<sup>18</sup>The reader may note that Fig. 5.13 looks similar to the q-plots of the EDELWEISS experiment, e.g. Fig. 2.14. The similarity is caused by the same processes of energy loss  $dE/dX$ , i.e. Compton scattering and nuclear recoils, for gamma rays and neutrons. However, the material constants are obviously different between liquid hydrocarbons, as the used gadolinium loaded scintillator, and crystalline germanium, as used for the EDELWEISS bolometers.

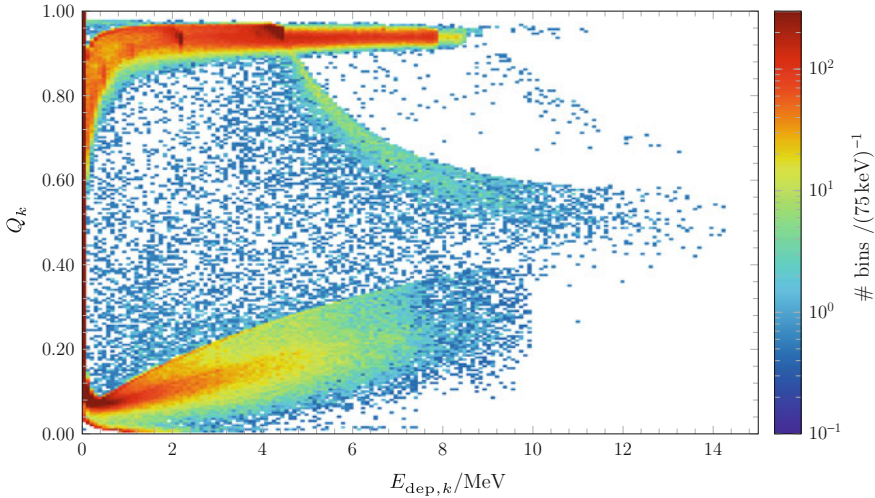


**Fig. 5.13** The effective quenching factor  $Q_k$  of the liquid scintillator as a function of the total deposited energy  $E_{\text{dep},k}$  per time bin  $k$  as simulated for an AmBe source placed on top of the NMM. Clearly seen in the electromagnetic band ( $Q_k \lesssim 1$ ) are the peaks from  ${}^1\text{H}(\text{n}, \gamma) {}^2\text{H}$  (2.2 MeV),  ${}^{12}\text{C}^*(\text{n}, \gamma) {}^{12}\text{C}$  (4.4 MeV), and the continuum from  ${}^1\text{Gd}(\text{n}, \gamma) {}^{A+1}\text{Gd}$  up to 8.5 MeV. The nuclear recoil band starts at  $Q_k \approx 0.1$  for  $E_{\text{dep},k} = 0$  MeV. The mixing of electromagnetic interactions and nuclear recoils due to the binning in time results in a third population between both bands, starting at  $E_{\text{dep},k} \geq 4.4$  MeV. The plot contains  $N = 2,310,988$  bins. For details see text

$E_{\text{dep},k} \geq 4.4$  MeV where the prompt gamma rays of 4.4 MeV from AmBe are summed up with the fastest and highest energetic nuclear recoils in the same bin  $T_k$ . As the electromagnetic interactions have a quenching near 1, but the quenching of the nuclear recoils is significantly smaller, the effective quenching in these bins is lower than the pure electromagnetic ones, but higher than the bins with pure nuclear recoils. This results in the dropping band.

To obtain the mean numbers of scintillation photons absorbed on the photocathode of the  $\text{PMT}_{i,j}^N$  one has to apply the collection efficiency  $e_{i,j}(\vec{r}_l)$ . It is a function of three parameters: First, the light path  $l(\vec{r}_{i,j}, \vec{r}_l)$  is defined as the path between the position  $\vec{r}_l$  where the scintillation photons are emitted and the position  $\vec{r}_{i,j}$  of the PMT photocathode. Due to the multiple reflections on the boundaries of the optical transparent volumes in the NMM (liquid scintillator, argon filling, aluminium foil, PMT window etc.) it is not identical to the geometric distance, i.e.  $l(\vec{r}_{i,j}, \vec{r}_l) \geq |\vec{r}_{i,j} - \vec{r}_l|$ . It depends on the detector geometry and the reflection indices of the materials. The average length of the light path in various materials for an exemplary pair of start and end positions are listed in Table 5.6. It confirms that the total light path is, with 513 cm, by far longer than the geometrical distance of 88.4 cm. The second parameter is the light transmittance along the light path in the various optical volumes. Finally the light absorbance in the photocathode is the third parameter. For the used definitions see Appendix A.4.3.

**Table 5.6** Mean light path in various materials

Material	Mean path length (mm)
Liquid scintillator	3376
Paraffin	958
PMMA	496
PMT vacuum	156
Argon	74
Borosilicate glass	52
Air	10
Lime glass	10
Sum	5132

In Geant4,  $N = 10^6$  photons were started at the centre of the neutron counter at (0, 0, 0) mm and collected on  $\text{PMT}_{2,1}^N$ . The centre of the photocathode is at (-862, 103, 170) mm

Because of these strong geometry dependencies, the collection efficiencies  $e_{i,j,l}$  have to be obtained from Geant4 simulation of the light propagation within the NMM, consisting of the emission of the scintillator light, its tracking through the geometry, and its absorption on the PMT photocathodes. In the Geant4 simulation, the *UNIFIED* optical model [26, 50] was chosen. For all volumes the surfaces were treated as rough surfaces made of micro facets. A value of  $0.1^\circ$  is assumed for the roughness, characterized as the standard deviation of the angle between the normal of a micro facet and the mean surface [50]. All boundaries were treated as dielectric–dielectric boundaries, i.e. an optical photon can be transmitted or reflected [27, 50] according to the refraction indices of the adjacent materials.

To ensure a sufficient statistic of tracked photons, the active volume was not homogeneously sampled, but *binned* in 1000 cubes  $o$  of 10 cm length of the edge, centered at  $\vec{r}_o$ . At the centre of each cube,  $N_o = 10^5$  optical photons were isotropically started by the *General Particle Source* (GPS) of Geant4, their wavelengths were sampled from the emission spectrum of the liquid scintillator (Fig. 5.14) [61].<sup>19</sup> For each cube the ratio of photons  $N_{i,j}$  absorbed in the photocathode of  $\text{PMT}_{i,j}^N$  to the started photons  $N_o$

$$e_{i,j,o} = \frac{N_{i,j}}{N_o} \quad (5.33)$$

was calculated. The actual collection efficiency  $e_{i,j,l}$  is approximated by  $e_{i,j,o}$  if the position of the scintillation  $\vec{r}_l$  falls within the cube  $o$ , i.e.

$$e_{i,j}(\vec{r}_l) = e_{i,j,o} \Leftrightarrow |\vec{r}_l - \vec{r}_o| \leq 5 \text{ cm} \quad (5.34)$$

For the light tracking the same geometry implementation as described in Sect. 5.1 was used to ensure consistency in this work. The optical processes of reflection and refraction at the material boundaries, and absorption in the materials are included in

<sup>19</sup>Again, digitized with *GRAPH DIGITIZER* and processed with *MATHEMATICA*.

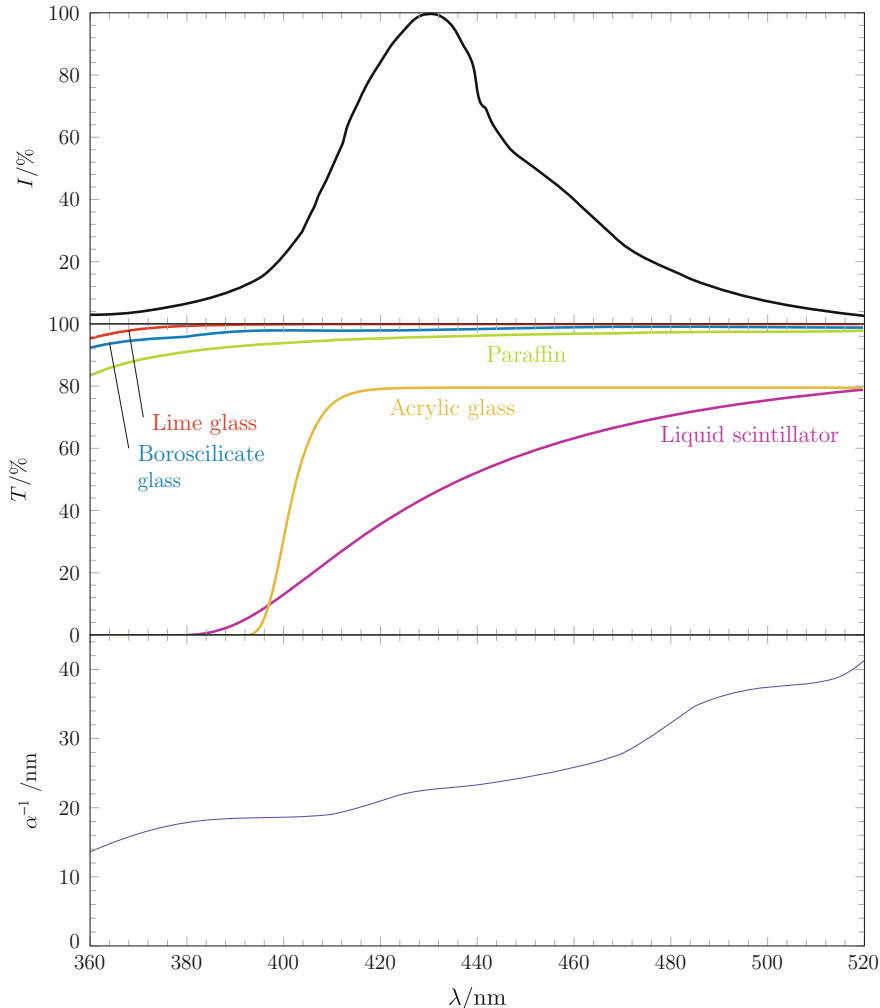


**Fig. 5.14** Optical characterization of the NMM: transmission, specified by the transmittances  $T(\lambda)$  (middle figure), along the mean photon path between the scintillation in the liquid scintillator (relative emission intensity  $I(\lambda)$ , top figure) and absorption on the photocathode (absorption length  $\alpha^{-1}(\lambda)$ , bottom figure). For details see text

the simulation for the following volumes: the active volume of the NMM filled with liquid scintillator and argon, the acrylic glass body, the paraffin and argon filling of the PMT chambers, the air gap between the acrylic glass body and the aluminium foil, the aluminium foil, the support structure of the PMTs made of acrylic glass and its iron footer, the vacuum within the PMTs, and the PMT windows. The latter are made of borosilicate glass for the neutron PMTs and of lime glass for the muon PMTs. Table 5.6 shows that most of the light path is contained in the biggest volume,

the liquid scintillator. Therefore it is assumed in this work that the optical properties of the liquid scintillator are of predominate influence on the light absorption. Indeed, at the wavelength of maximum scintillation emission, the liquid scintillator has the lowest transmittance of all materials which are considered in the optical model, see Fig. 5.14. The absorption together with the reflection on the volume boundaries determine the collection efficiencies  $e_{i,j,l}$ .

Unfortunately, no absorption spectrum of the used liquid scintillator could be found in literature (Sect. 4.2.1), despite its importance for the simulation. A dedicated measurement is out of the scope of this work, thus the absorption is implemented as follows: the shape of the absorption spectrum was taken from a chemically similar scintillator [69], but the absolute value of the absorption length at 440 nm was treated as free parameter; it will be determined in Sect. 5.4.4 to  $\alpha_{440}^{-1} = 5.2(2)$  m. As already discussed in Sect. 4.4.3, this value seems plausible. The absorption and reflectance parameter of the remaining optical materials are taken from literature. They are given together with more details about the used absorption spectrum of the liquid scintillator in Appendix A.4.3. The resulting effective transmission spectrum of the optical materials is shown in Fig. 5.14.

Finally the photocathode was implemented as 20 nm thin layer of K<sub>2</sub>CsSb, Fig. 5.14 shows its absorption spectrum according to [52].

Figure 5.15a shows the collection efficiency  $e_{i,j,o}$  for an exemplary plane in the active volume parallel to the  $x$ - $y$ -plane. The resulting *light curve*  $e_i(x)$  parallel to the longitudinal axis of the active volume, i.e. the  $x$ -axis, is shown in Fig. 5.15b. It features the expected symmetric behaviour for opposite PMTs (see Fig. 4.6 for a scheme of their positions). Usually the light curve is specified by an *effective attenuation length*  $\Lambda$ :

$$e_i(x) = \int \int e_{i,j,o} dy dz \quad (5.35a)$$

$$= e^{-x/\Lambda} \quad (5.35b)$$

However, as the fit of Eq. 5.35b to the simulated data in Fig. 5.15b shows, the parametrization breaks down near the boundary of the active volume as the local geometry, and hence the light propagation, changes near the boundary compared to the bulk of the active volume. Nevertheless, comparing the effective attenuation length (Fig. 5.15, e.g.  $\Lambda_1 = 0.85$  m) with the absorption length ( $\alpha_{440}^{-1} = 5.2$  m) confirms, additional to Table 5.6, that the average light path is longer than the geometrical distance. As the deterioration of the transparency was experimentally compensated with increased PMT gain (Sects. 4.2.5 and 4.4.3), the attenuation length of the liquid scintillator is fixed to  $\alpha_{440}^{-1} = 5.2$  m in the simulation.

In conclusion, the mean number of scintillation photons absorbed in the photocathode of PMT <sub>$i,j$</sub> <sup>N</sup> within the time bin  $T_k$  is:

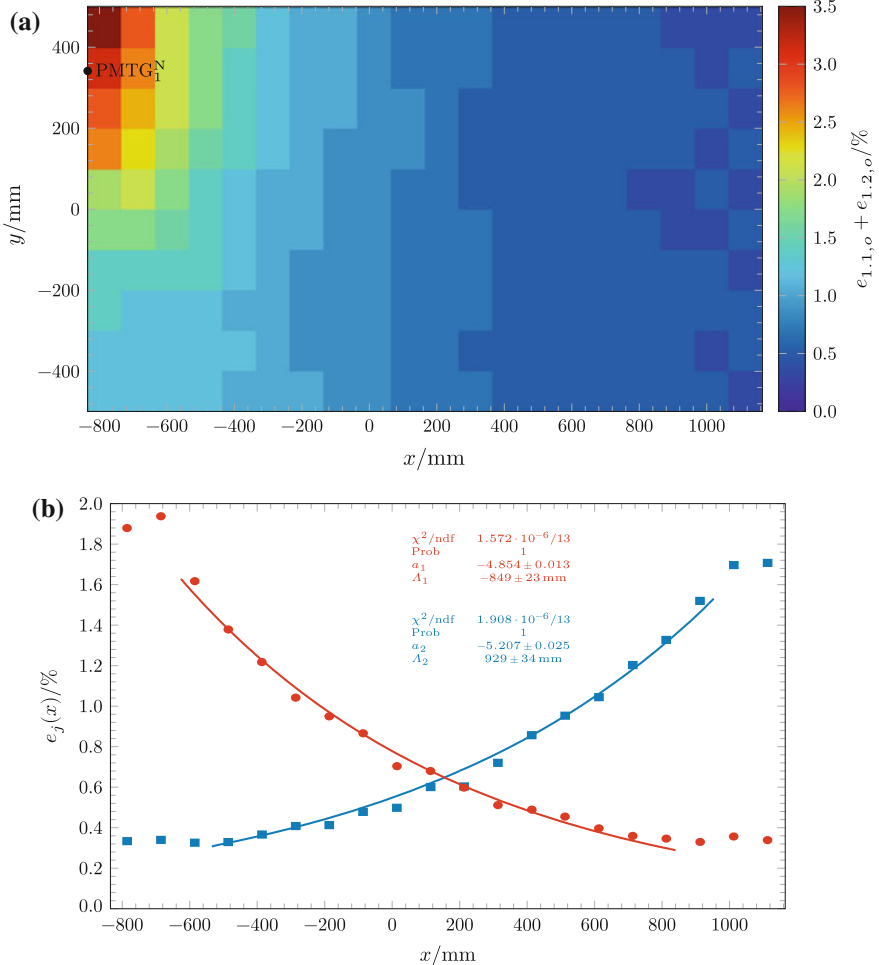


**Fig. 5.15** **a** Light collection efficiency  $e_{1,1,o} + e_{1,2,o}$  for all starting positions  $\vec{r}_o$  in the  $x$ - $y$ -plane parallel to  $z = -36$  mm, viewed by PMTG<sub>1</sub><sup>N</sup>, normalized to  $N = 10^5$  started photons at each position. The black dot indicates the PMTG position on the  $y$ -axis. **b** Light collection efficiency  $e_{1,1}(x) + e_{1,2}(x)$  integrate along the  $y$ -,  $z$ -axis viewed by PMTG<sub>1</sub><sup>N</sup> (red circles) and PMTG<sub>5</sub><sup>N</sup> (blue boxes). Normalized to  $N$  and fitted with  $f(x; a_1, \Lambda_1)$  (red),  $f(x; a_2, \Lambda_2)$  (blue) of type  $f(x; a, \Lambda) = e^{a+x/\Lambda}$ . For details see text

$$\bar{N}_{\text{ph},i,j,k} = \sum_{l \in T_k} e_{i,j}(\vec{r}_l; \alpha_{440}^{-1}) \frac{S}{1 + k B \frac{E_{\text{dep},l}}{\rho l}} E_{\text{dep},l} \quad (5.36)$$

To take into account the stochastic nature of photon emission and absorption, the actual number of scintillation photons is normally distributed around  $\bar{N}_{\text{ph},i,j,k}$ :

$$P_N \left( N_{\text{ph},i,j,k}; \bar{N}_{\text{ph},i,j,k}, \sqrt{\bar{N}_{\text{ph},i,j,k}} \right) \quad (5.37)$$

For the next stage of the detector model, the sum  $N_{\text{ph},ik}$  of absorbed photons for each PMT group is stored:

$$N_{\text{ph},ik} = \sum_j N_{\text{ph},i,j,k} \quad (5.38)$$

For the modules 50 and 51 of the muon telescope the time binned energy deposits in the plastic scintillator of module 50 and the active volume are stored, similar to Eq. 5.32. For module 50, the light absorption along the long axis of the module is considered via the measured effective attenuation length Eq. 4.15.

Additional to the collection efficiency, the simulation of the light propagation returns the distribution  $P(t)$  of the time between emission and absorption of the optical photons. It can be parametrized by the convolution of a normal distribution  $P_N$ , to consider the time resolution  $\sigma$ , and two exponential decays  $\tau_1, \tau_2$ , to consider the light absorption<sup>20</sup>.

$$P(t) = \frac{\sqrt{\pi}}{2} \exp \left( -t \left( \frac{1}{\tau_1} + \frac{1}{\tau_2} \right) \right) \left( a_1 \exp \left( \frac{\sigma^2}{2\tau_1^2} + \frac{t}{\tau_2} \right) \operatorname{erfc} \left( \frac{\sigma^2 + (t_0 - t)\tau_1}{\sqrt{2}\sigma\tau_1} \right) \right. \\ \left. + a_2 \exp \left( \frac{\sigma^2}{2\tau_2^2} + \frac{t}{\tau_1} \right) \operatorname{erfc} \left( \frac{\sigma^2 + (t_0 - t)\tau_2}{\sqrt{2}\sigma\tau_2} \right) \right) \quad (5.39)$$

with the *complementary error function*<sup>21</sup>  $\operatorname{erfc}(x)$ . Figure 5.16 shows one example of two time distributions for a near and a distant emission position, relative to the same neutron PMT. The contribution of the offset of the light propagation to the time resolution of the NMM is therefore up to  $\approx 7$  ns. In addition, the *response pulse width* of the PMTs contributes to the total time resolution of the NMM. For the neutron PMTs it is about 2.4 ns (Eq. A.48). Therefore, in the detector response model a total time resolution of  $\Delta t_{\text{bin}} = 10$  ns was included by applying the time binning  $T_k$ .

The time resolution directly affects the energy scale, which by itself affects the event rate: via the bin  $T_k$ , the bin width  $\Delta t_{\text{bin}}$  affects the number of collected photons in Eq. 5.36, which will be compared to the threshold in Eq. 5.40a and hence the decision if a hit is produced. However, the time resolution of the model is dominated by the recovery time cuts, see Sects. 4.3 and 5.4.3, which are with  $\leq 250$  ns larger than  $\Delta t_{\text{bin}}$ . The uncertainty of the actual value for  $\Delta t_{\text{bin}}$  will be taken into account as systematic uncertainty in Sect. 5.5.4.

<sup>20</sup>As photons that need longer time to reach the photocathode have a longer light path, they are also stronger absorbed than fast photons, hence the photon arrival distribution has a similar exponential decay as the light absorption curve. Two exponential decays are used for a better fitting of the parametrization near the boundary of the active volume.

<sup>21</sup> $\operatorname{erfc}(x) = 2 \int_x^\infty e^{-t^2} dt / \sqrt{\pi}$ .

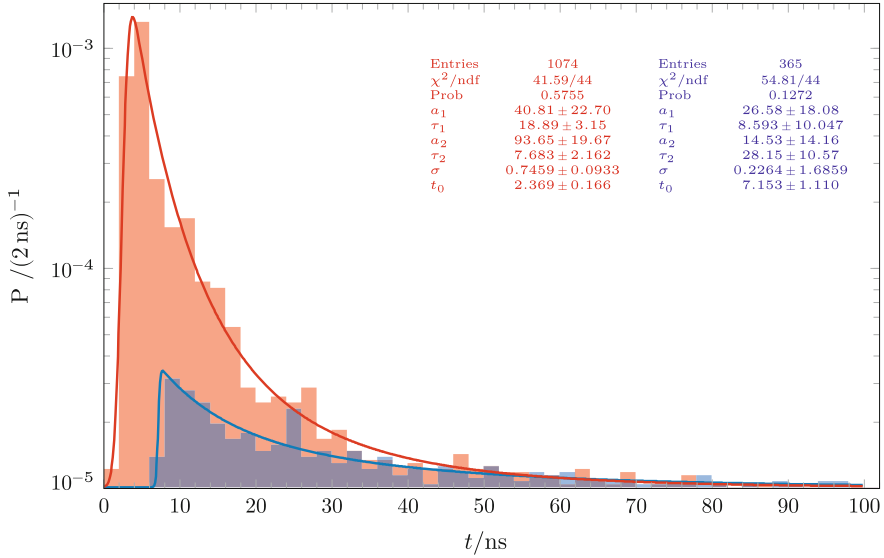


**Fig. 5.16** Distribution  $P(t)$  of photon arrival time  $t$  on  $\text{PMTG}_1^N$ . Each distribution normalized to  $N = 10^5$  started photons. Started near (red, distance of 50 mm), and far away (blue, distance of 950 mm) from  $\text{PMTG}_1^N$ . Fitted with Eq. 5.39. For details see text

The influence of the quenching and the light propagation on the shape of the signal spectrum is shown in Fig. 5.17. The black curve shows the spectrum of energy deposits caused by the AmBe source on top of the neutron counter as simulated by Geant4 (Sect. 5.4.1). Clearly visible are the peaks from  ${}^1\text{H}(\text{n}, \gamma){}^2\text{H}$ ,  ${}^{12}\text{C}^*(\gamma, \gamma){}^{12}\text{C}$ , and the falling edge due to high energy neutron scattered off nuclei. The blue curve shows the quenched spectrum, i.e. the visible energy. Here, the nuclear recoils are shifted to lower energies, reducing the chance to create hits within an NMM event (Sect. 4.3). Finally, the red curve shows the sum spectrum of photons absorbed on the photocathodes of all high gain neutron PMTs (Sect. 4.2.1). The peaks in the photon spectrum are scaled to the peaks of the deposited energy. The light tracking reduces the features of the spectrum, especially the step-like structure of the neutron capture on gadolinium. Additionally, the light tracking introduces a position dependence of the overall detection efficiency via the light collection efficiencies  $e_{ij}$ .

This model of light propagation is also used by F. Laible [47] to investigate the long term monitoring of the LED light pulser (Sect. 4.2.3). Based on his investigations, an agreement between the monitored deterioration of the scintillator transparency and literature findings can be stated, as discussed in Sect. 4.4.3. This agreement indicates that the model gives a correct description of the light propagation in the NMM and is therefore reliable for the detector response model.

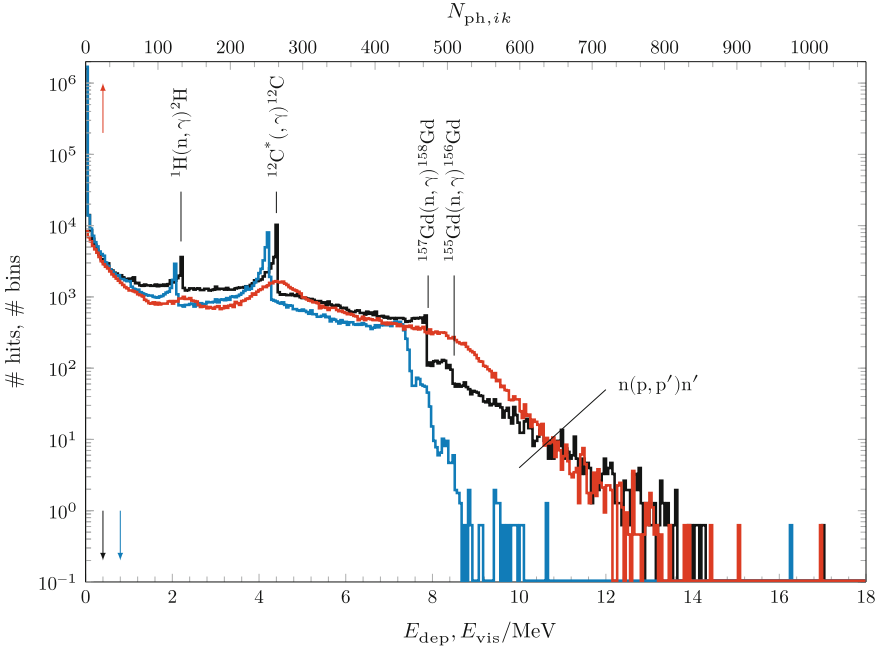


**Fig. 5.17** Simulated response of the NMM to the AmBe source placed on top. Shown are the distributions of hits as a function of the deposited energy  $E_{\text{dep}}$  (black), the distribution of bins as function of the visible energy  $E_{\text{vis}}$  (blue) and as function of the equivalent number of photons  $N_{\text{ph},ik}$  (red). The photon scale is scaled to the scale of energy deposits via the  $^1\text{H}(\text{n}, \gamma)^2\text{H}$ ,  $^{12}\text{C}^*(\gamma)$ ,  $^{157}\text{Gd}(\text{n}, \gamma)^{156}\text{Gd}$  peaks at 2.2 MeV, 4.4 MeV, respectively. For details see text

### 5.4.3 Event Building

The final stage of the detector response model is the building of NMM- and muon telescope events from the simulated data sets and to select the signatures of muon-induced neutron candidates (see Sect. 4.3). To be consistent with the experimental DAQ, the simulation use the hit topology in the same way, i.e. demanding the coincidence based trigger requirements Eqs. 4.16 and 4.17.

The event building consists of four stages, following closely the DAQ electronics (Sect. 4.2.4): the pre-trigger generation, the opening of the DAQ window, and the generation of the TDC and ADC data. The number of simulated candidates for muon-induced neutrons is determined via the TDC data matching the signature of muon-induced neutrons. The handling of the muon telescope data is a simplified version of the handling of the NMM data. Therefore, first the NMM event building is discussed, and then the muon telescope event building.

The NMM event building starts with the actual number of absorbed photons  $N_{\text{ph},ik}$  at each neutron PMT group  $\text{PMTG}_i^N$  within the time bin  $T_k$ . By scaling  $N_{\text{ph},ik}$  with an effective gain parameter  $G_N$ , the scale is transformed to ADC units. As the

experimental neutron PMT gains are adjusted to the same value via the high tension settings (Sect. 4.2.5), also the detector response model uses the same gain parameter for all neutron PMTs. The simulated NMM hit  $S_{ik}^N$  of a neutron PMT group is defined as

$$S_{ik}^N = \begin{cases} \text{true,} & N_{\text{ph},ik} \cdot G_N \geq T_N \\ \text{false,} & \text{otherwise} \end{cases} \quad (5.40\text{a})$$

$$t_{ik} = t_k + \frac{\Delta t_{\text{bin}}}{2} \quad (5.40\text{b})$$

where  $T_N$  is the threshold parameter. As in the DAQ of the NMM the same experimental threshold value is applied to all input channels, also the simulation uses one threshold parameter for all PMT groups. The time  $t_{ik}$  (Eq. 5.40b) assigned to the hit  $S_{ik}^N$  is the mean time of the corresponding time bin  $T_k$ .

With this definition, the detector response model can apply the same trigger condition (Eq. 4.17) to the simulated data as used in the experiment: The first signal  $S_{ik}^N$  that fulfill the trigger conditions opens as pre-trigger a time window of

$$\Delta t_{\text{DAQ,MC}} = 56 \mu\text{s} \quad (5.41)$$

length. The start time  $t_{\text{trig}}$  of the windows is set to the time  $t_{ik}$  assigned to the pre-trigger. The deviation from the experimental measured window length discussed in Sect. 4.4.4 is applied as systematic uncertainties in Sect. 5.5.4.

Since the experimental dead time of the neutron counter is with 6.76(8) ms (Eq. 4.20) two orders of magnitude longer than the event window, it is assumed that all simulated physical interactions occur either within the event window or in the subsequent dead time and do not start another event. Therefore, the event window in the detector response model is not updatable. Consequently, the energy deposits simulated in one Geant4 event lead at most to one simulated NMM event.

Each hit, that fulfils the trigger conditions and occurs within the event window, is stored as TDC data. It therefore corresponds to the TDC data from the third level of the NMM logical unit in the DAQ electronics, described in Sect. 4.2.4. In accordance to the definitions in Sect. 4.3, the first hit within the event is the primary hit and any subsequent hits are secondary hits.

Pre-trigger signals within the event window open an ADC gate  $g$  of  $\Delta t_{\text{ADC}}$  length at time  $t_g$ . In the electronic DAQ (Sect. 4.2.4), a value of 256 ns was used with an offset of 96 ns to cover also the rising edge of the pulse before it crosses the discriminator threshold. This offset is not necessary in the detector response model, as no pulse shapes are simulated. Therefore, the simulated ADC gate is set to

$$\Delta t_{\text{ADC,MC}} = 160 \text{ ns.} \quad (5.42)$$

As in the real experiment, the simulated ADC gate is not updatable. Therefore, the simulation includes, as the real DAQ electronics, the possibility of a *pile-up*, i.e. several trigger signals, and hence TDC data, could fall within the same ADC gate.

The ADC value  $A_{ng}$  of a given channel  $n$  within the ADC gate  $g$  is the sum  $N_{nk}$  of all photons absorbed by the connected neutron PMT group in the time bins  $k$  scaled by the gain  $G_N$ . The mapping of PMT group  $i$  to ADC channel  $n$  is the same as used in the experiment (Table A.12) and can be expressed via a matrix ( $M_{in}$ ) (Eq. A.51)

$$N_{nk} = \sum_i M_{in} N_{\text{ph},ik} G_N. \quad (5.43)$$

Additionally to the gain, the PMT influence on the data is taken into account by a free parameter  $R^N$ : it is the resolution of a normal distribution (Eq. 5.44a) that smears the scaled number of absorbed photons:

$$P_N \left( A_{nk}; N_{nk}, R^N \sqrt{N_{nk}} \right) \quad (5.44a)$$

$$A_{ng} = \sum_k_{T_k \in [t_g, t_g + \Delta t_{\text{ADC,MC}}]} A_{nk} \quad (5.44b)$$

As the resolution  $R_N$  is applied *after* the hit generation (Eq. 5.40a) it affects only the simulated ADC spectrum and not the simulated rate of muon-induced neutrons and their multiplicities. However,  $R_N$  has to be considered as it may be correlated with the remaining parameters of the detector response model ( $G_N, T_N, k_B, \alpha_{440}^{-1}$ ). Indeed, the fitting of the detector response model to reference measurements in Sect. 5.4.4 will show a small correlation to the attenuation length  $\alpha_{440}^{-1}$ , see Fig. 5.18. Therefore, the resolution has to be considered in this context.

For the muon telescope, the time-binned energy deposits  $E_{\text{dep},k}$  in the plastic and liquid scintillator are the base for the hit generation for muon module 50 and 51, respectively. The hit definition is similar to Eq. 5.40a if  $N_{\text{ph},ik}$  is replaced with  $E_{\text{dep},k}$ , and the gain and threshold parameters defined as  $G_{M50}, T_{M50}, R_{M50}$  and  $G_{M51}, T_{M51}, R_{M51}$ , respectively. A coincidence between hits in module 50 and 51 within the same time bin  $T_k$  creates a muon telescope event.

The coincident hit signature of muon-induced neutrons is searched for in the simulated data as follows: a Geant4 event containing a muon telescope event and an NMM event with at least one secondary is identified as candidate for muon-induced neutrons. The evaluation of the event topology, i.e. the number of secondary hits, also considers the recovery time cuts given in Sect. 4.3, which determine the time resolution. After determination of the free parameters  $G_N, T_N, G_M$ , and  $T_M$  in Sect. 5.4.4, it is possible to compare directly the simulated ADC and TDC data to the measured ones.

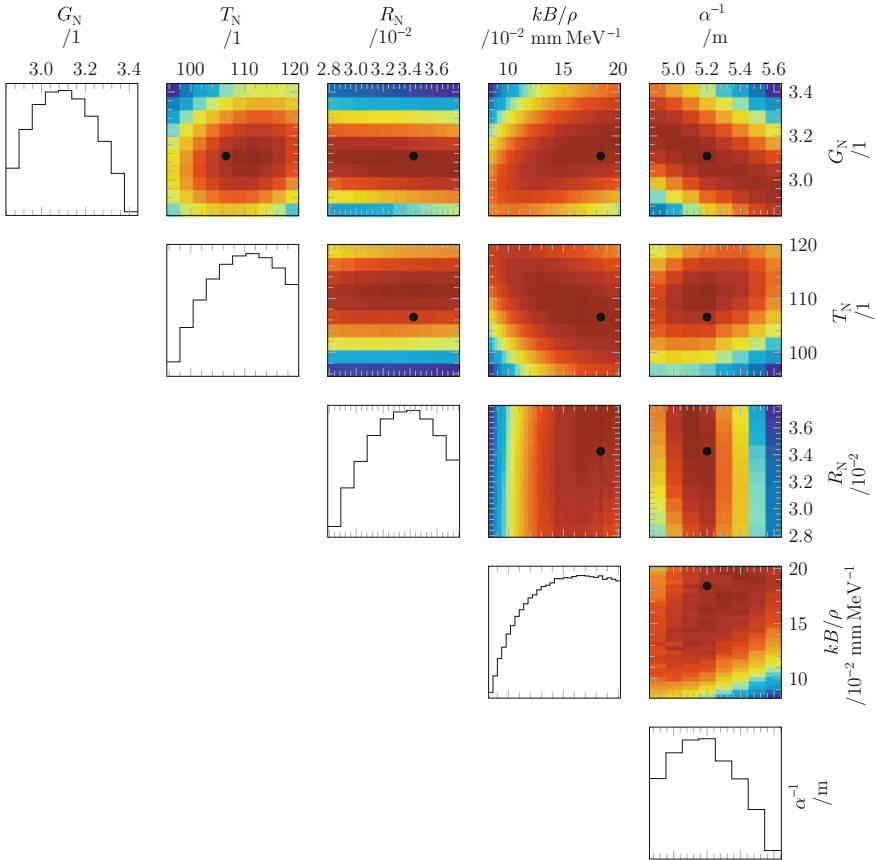


**Fig. 5.18** One- and two-dimensional marginal distributions of the log likelihood in the five-dimensional parameter space of the detector response model of the NMM. The parameter space  $kB \times \alpha_{440}^{-1} \times G_N \times T_N \times R_N$  is sampled at  $30 \times 8 \times 10 \times 10 \times 10 = 240,000$  points. Within the five times five grid of the plot, the one-dimensional marginal distributions are located on the diagonal, the two-dimensional ones are located off diagonal. The log likelihood within each marginal distribution is given in arbitrary units, the *black dots* show the position of the maximum likelihood value. For details see text

#### 5.4.4 Calibration of the Model

The model of detector response described in the previous Sects. 5.4.1–5.4.3 is characterized by three independent parameter sets:  $\{kB, \alpha_{440}^{-1}, G_N, T_N, R_N\}$  for the NMM and  $\{G_{M50}, T_{M50}, R_{M50}\}, \{G_{M51}, T_{M51}, R_{M51}\}$  for the modules 50, 51 of the muon telescope, respectively. The values of a parameter set are determined by matching the ADC spectrum of a reference measurement with the corresponding simulation of this measurement convolved with the detector response model.

Due to the multiple stage design of the detector response model, this approach is rather fast: it is not necessary to repeat the most time consuming first stage, i.e. the Geant4 simulation of particle transport and energy deposition for every parameter set, but only the faster higher stages that runs on a reduced input data set. The method is exemplified on the NMM, before it is repeated for the modules of the muon telescope.

For the NMM, an AmBe source is used as reference for the detector response model, therefore the matching is independent from the measurements of muon-induced neutrons. The reference measurement was recorded on 1 July 2010 by placing an uncollimated AmBe within a lead castle on top of the NMM, see Fig. 4.5c. Corrected by the dead time (Eq. 4.20), the live-time is 62,322 s, with a neutron activity of 20 Bq (Eq. A.54). The source is implemented as isotropic point source in Geant4 via the general particle source, considering the branching ratio between pure neutron emission and the emission of a neutron accompanied with a gamma ray (Eq. A.53). The simulation contains 180,000 started neutrons for each branching and was normalized to the experimental neutron activity given above. See Appendix A.6 for details of the AmBe source and its modelling in Geant4. For this calibration we assume a complete experimental compensation of the deterioration of the scintillator transparency by the adjusted high tension and a nominal loading of  $n_{\text{Gd}} = 0.2\% \text{ W/W}$ . The shift of  $n_{\text{Gd}}$  will be handled in Sect. 5.5.4 as systematic uncertainty. Contrary to the simulation of muon-induced neutrons in Sect. 5.5, the calibration uses the multiple hit signature and not the coincident hit signature, as obviously no muon source for calibration is available.

The ADC spectrum is chosen as reference quantity because it is sensitive to all the above mentioned parameters:

- The effective gain  $G_N$  can be deduced from the position of the 4.4 MeV  $\gamma$ -peak  $^{12}\text{C}^*(, \text{n}\gamma)^{12}\text{C}$  in the ADC spectrum of primary hits.
- The threshold parameter  $T_N$  affects the position of the low energy cut in this spectrum.
- To distinguish the effect of the quenching parameter  $k_B$  from the scaling of  $G_N$ , also the ADC spectrum of the secondary hits is used. Whereas the scaling of  $G_N$  is for both spectra the same, the quenching is different, as the secondary hits are from purely electromagnetic interactions, but the primary hits contain also nuclear recoils. See also Fig. 5.20 and its discussion later on.
- To distinguish the scaling from the effect of the light attenuation with an attenuation length  $\alpha_{440}^{-1}$ , also a reference measurement with AmBe at a position out of centre is needed, so that the different length of the light paths compared with the measurements at the centre position can be used.
- The effective resolution  $R_N$  can be deduced from the width of the 4.4 MeV peak after all the previous effects are taken into account.

Since the neutron field of the muon-induced neutrons is different from the AmBe source, AmBe is only used to tune the detector response model and to estimate the *simulation efficiencies*, i.e. how accurate the simulations can reproduce reference measurements. The important *detection efficiency* for muon-induced neutrons will be given in Sect. 5.5.3.

In a technical sense, the matching is done by an *extended binned log likelihood* comparison between the histogram  $\mathbf{D}$ , containing the measured ADC spectrum, and the histogram  $\mathbf{M}$ , containing the simulated spectrum. The simulated histogram  $\mathbf{M}$  is sampled over the parameter space of the detector response model. Then the extended binned log likelihood of  $\mathbf{M}$  with respect to  $\mathbf{D}$  is according to:

$$\log L(\mathbf{M}, \mathbf{D}) = \sum_{i=0}^N |d_i| \log n_D \frac{|m_i|}{n_M}, \quad (5.45)$$

for equal binning:  $N := N_D = N_M$ . Where  $n_X$  is the sum over the  $N_x$  bins  $x_i$  of a given histogram  $X$ :

$$X = \{x_i\}_{i \in [0, N_x - 1]} \quad (5.46)$$

$$n_X = \sum_{x_i \in X} x_i. \quad (5.47)$$

Let be

$$\mathbf{P}_N = k_B \times \alpha_{440}^{-1} \times G_N \times T_N \times R_N \quad (5.48)$$

the five-dimensional parameter space of the NMM detector response model. For this work it is sampled at 240,000 discrete points

$$\mathbf{p}_{ijklm} = \{k_B i, \alpha_{440, j}^{-1}, G_{N, k}, T_{N, l}, R_{N, m}\}. \quad (5.49)$$

As already discussed above, three histograms are needed to determine the model parameter and to distinguish the light attenuation and quenching from the scaling: the primary hit (p) and secondary hit (s) caused by the AmBe source at centre (c) and the primary hit caused by the AmBe source out of centre (oc).<sup>22</sup> Therefore, in total six histograms are compared for each  $\mathbf{p}_{ijklm}$ , i.e. the measured and the simulated ADC spectra for these three cases. The total log likelihood is the sum of the log likelihood of each of these cases [19].

The simulation matches the measurement for the best fitting parameter values  $\hat{\mathbf{p}}$  that corresponds to the maximum log likelihood:

$$\begin{aligned} \log L(\mathbf{p}_{ijklm}) &= \log L(\mathbf{M}(\mathbf{p}_{ijklm})_{p,c}, \mathbf{D}_{p,c}) + \log L(\mathbf{M}(\mathbf{p}_{ijklm})_{s,c}, \mathbf{D}_{s,c}) \\ &\quad + \log L(\mathbf{M}(\mathbf{p}_{ijklm})_{p,oc}, \mathbf{D}_{p,oc}) \end{aligned} \quad (5.50)$$

$$\log L(\hat{\mathbf{p}}) = \max\{\log L(\mathbf{p}_{ijklm})\}_{ijklm} \quad (5.51)$$

---

<sup>22</sup>In this work we chose the comparison of the primary hits at center and out of centre to determine the attenuation length. In principle, one is free to choose instead the secondary hits at centre and out of centre for the determination. However, a comparison of both, primary and secondary hits, is not necessary.

Figure 5.18 shows  $\log L(\mathbf{p}_{ijklm})$  as one and two dimensional projections, or *marginal distributions* [19]. The best fitting parameter set  $\hat{\mathbf{p}}$  is marked by black dots. It is well within the sampled region of parameter space, so that there should be no boundary effects.

As the projection in the  $G_N - \alpha_{440}^{-1}$  plane confirms, a decreasing liquid scintillator transparency can be compensated by an increased gain, i.e. by increasing the high tension of the neutron PMTs, as done during the run of the neutron counter (Sect. 4.2.5). To assess the uncertainty of the matched parameter values, the RMS of the one-dimensional projection along the respected parameter is taken, the final results are listed at the end of this section in Table 5.7.

For  $\hat{\mathbf{p}}$ , Fig. 5.19 compares the simulated ADC spectra of primary and secondary hits with the measured ones. The efficiency of the model is expressed as ratio between the simulated ( $R_{\text{event,MC}}$ ) and measured ( $R_{\text{event,data}}$ ) NMM event rate for the best fitting parameter set  $\hat{\mathbf{p}}$ :

$$\epsilon_{\text{NMM}} = \frac{R_{\text{event,MC}}}{R_{\text{event,data}}} \quad (5.52\text{a})$$

$$= 0.949 \pm 0.013^{\text{stat}} {}^{+0.205^{\text{sys}}}_{-0.145} \quad (5.52\text{b})$$

Here, we assume an uncertainty of  $\sqrt{N_{\text{event}}}$  on the counted event number  $N_{\text{event}}$  due to limited statistics and use uncorrelated error propagation. The systematic influence of the uncertainties in the model parameter is evaluated by the *shift method* [35]. The estimation of both statistical and systematic uncertainties closely follows the discussion in Sect. 5.5.4. The systematic uncertainty of the function  $\epsilon_{\text{NMM}}(\mathbf{p})$  is likely to depend on the actual source configuration. Contrary to the point like AmBe source, muon-induced neutrons are produced throughout the lead target, hence the contribution of boundary effects to the detection efficiency is different. Therefore, the systematic uncertainties have to be re-evaluated for the case of muon-induced neutrons, see Sect. 5.5.4. Based on the response model, the detection efficiency for the neutrons from the AmBe source is derived to 5.7 % (Eq. 4.21).

Compared to the event rate of the AmBe reference measurement, the simulation is in good agreement within the uncertainties. This emphasises the suitability of the detector response model. Figure 5.19 shows the measured and simulated ADC spectra for the best fitting parameter set. Within the uncertainties of the model parameter (Table 5.7), we can find also parameter sets that provide a better spectral agreement but at the cost of a worse log likelihood value.

The suitability of the ADC spectra of primary and secondary hits to disentangle the quenching from scaling is shown in Fig. 5.20: it shows the reduced  $\chi^2$  profile between the simulated and measured ADC spectra for primary and secondary hits as function of  $kB/\rho$ , the remaining four parameters are set to  $\hat{\mathbf{p}}$ . There is no significant influence of the quenching on the pure electromagnetic secondary hits, i.e.  $\chi^2/\text{ndf}(kB/\rho)$  agrees with a constant. However, it clearly affects the primary hits due to the contribution of nuclear recoils. Therefore, the secondary hits are a suitable fixed point to specify the variation of the primary hits due to quenching.

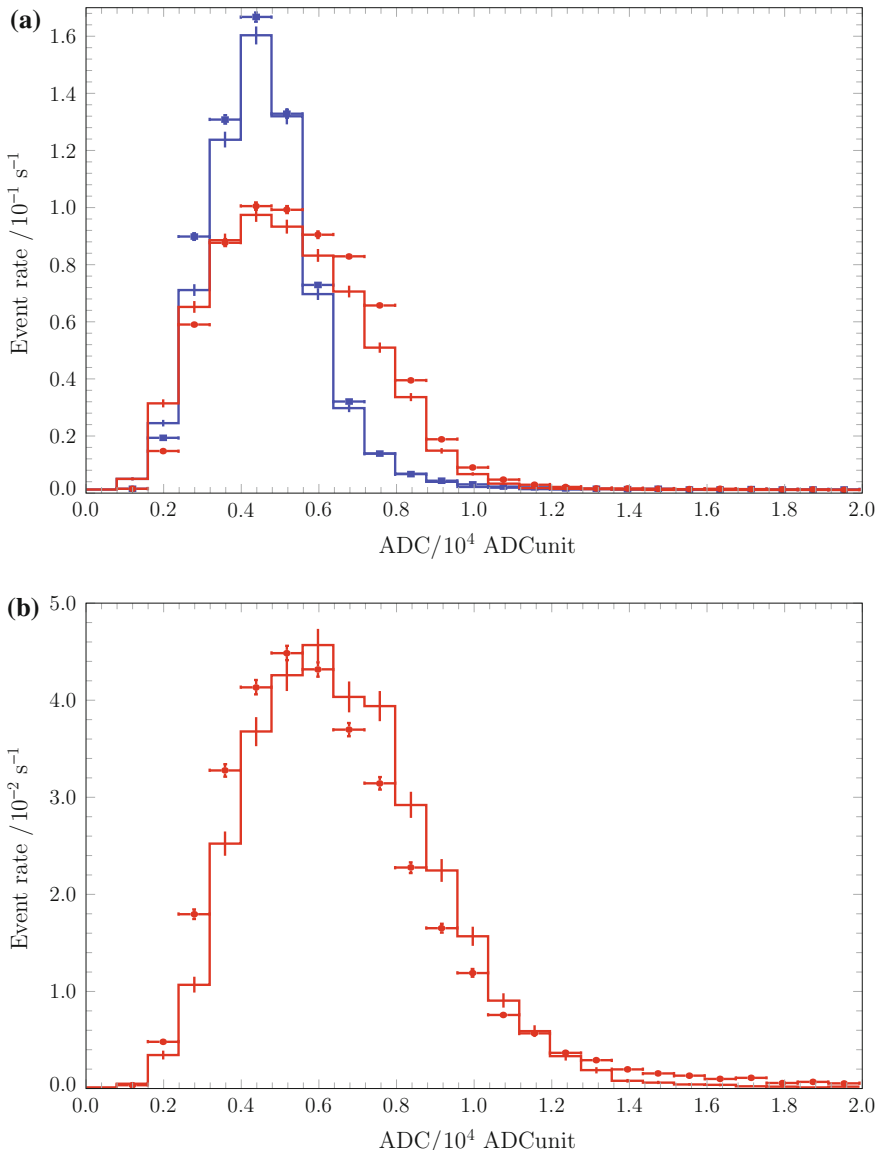
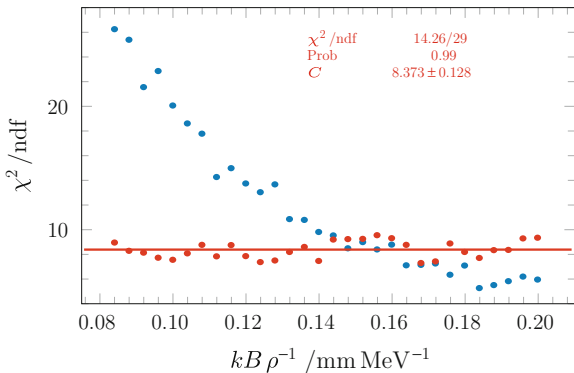


**Fig. 5.19** Comparison of the ADC spectrum measured with the NMM (data points) with the simulated one (solid histograms): **a** For primary hits (blue) and secondary hits (red) in case the AmBe source is placed in the centre of the NMM top surface. Here, 1000 ADC units are roughly 1 MeV. **b** For secondary hits in case the AmBe source is placed off center. For details see text

Module 50 is used to detect passing muons due to their energy via ionisation (Sect. 4.2.2). Consequently, no quenching is included in the detector response model

**Fig. 5.20** Reduced  $\chi^2$  profile of the comparison between detector response model and measurement for primary (blue) and secondary (red) hits over a set of  $kB/\rho$  values when the remaining parameters are set to their best fitting values. The influence of  $kB/\rho$  on the secondary hits is in agreement with a constant  $C$ . For details see text



of module 50. As the light attenuation is included via the measured effective attenuation length (Sect. 5.4.2), only three free model parameter remain. Gain  $G_{M50}$ , threshold  $T_{M50}$ , and resolution  $R_{M50}$  for muon module 50 are determined again by matching a simulated ADC sum spectrum to the measured ADC sum spectrum of north (N) and south (S) channel, for the channel definition see Sect. 4.2.2. We use the same AmBe measurement as reference, as the AmBe location is also near the middle of module 50. Contrary to the PMT<sup>N</sup>, the gains of the muon PMTs of module 50 can not be adjusted via individual high tension, but only via its initial matching to similar gain parameters, see Sect. 4.2.2. In principle, this can be considered in the detector model by individual gain parameters for each channel at the cost to increase the dimensionality of the parameter space. Therefore, differences in the gain between N and S channel were experimentally corrected: events originate in the middle of the module, hence having the same light path to N and S end, were used as reference to determine the gain difference and correct it.

As it is not necessary to determine quenching and light attenuation via the calibration, it is sufficient to match one ADC spectrum. In the following, we chose the spectrum of primary hits. The resulting log likelihood distribution is shown in Fig. 5.21 and the matching parameter set  $\hat{p}_{M50}$  is listed in Table 5.7. Again it is well within the sampled region of parameter space.

Comparison between the simulated and measured ADC spectrum is shown in Fig. 5.22. The spectral shapes are not in perfect agreement, but the simulated and measured rates agree within the uncertainties:

$$\epsilon_{M50, \text{event}} = 1.040 \pm 0.016^{\text{stat}} {}^{+ 0.623^{\text{sys}}}_{- 0.490} \quad (5.53)$$

It is not possible to calibrate the detector model of muon module 51 with a reference measurement of AmBe due to the module's high threshold above the 4.4 MeV  $\gamma$ -peak of AmBe (see Sect. 4.2.5). Here, a dead time corrected subset of the recorded muon telescope events is used as reference data, i.e. coincidence between muon module 50 and 51, see Sects. 4.2.2 and 4.3. In total it contains 2429 muon candidates, recorded between May 2010 and September 2011. Again, gain differences between

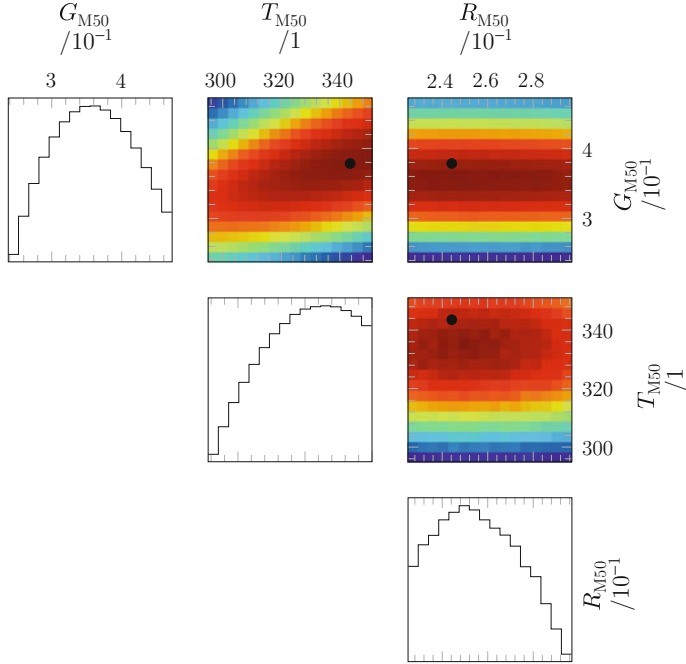


**Fig. 5.21** One- and two-dimensional marginal distribution of the log likelihood in the three-dimensional parameter space of the detector response model for the muon module 50. The parameter space  $G_{M50} \times T_{M50} \times R_{M50}$  is sampled at  $16 \times 16 \times 16 = 4096$  points. Within the three times three grid of the plot, the one-dimensional marginal distributions are located on the diagonal, the two-dimensional ones are located off diagonal. The log likelihood within each marginal distribution is given in arbitrary units. The black dots show the position of the maximum likelihood value. For details see text

N and S channel are experimentally corrected. The ADC spectrum for the sum of N and S channels is compared to the simulation of muon telescope events, based on the best fitting parameter for muon module 50 and the standard settings of the muon generator as defined in Sect. 5.3.1.

Except the different reference source, the matching of muon module 51 is the same as the matching of muon module 50. The distributions of the log likelihood are shown in Fig. 5.23 and the matching parameter set  $\hat{p}_{M51}$  is listed in Table 5.7.

The simulation efficiency is

$$\epsilon_{MT} = 0.88 \pm 0.02^{\text{stat}} {}^{+0.04^{\text{sys}}}_{-0.04}. \quad (5.54)$$

As the matching is based on muon telescope events, it is the simulation efficiency for the muon telescope and not for the individual muon module 51.

The situation for module 51 is unsatisfying: the simulated spectrum strongly disagrees with the measured one, as shown in Fig. 5.24. Also the central value of the

**Table 5.7** Parameters of the detector response model as obtained from calibration

Parameter	Value	RMS	RMS/value (%)
<i>NMM</i>			
$kB\rho^{-1}$ (cm MeV $^{-1}$ )	0.18	0.04	22
$\alpha_{440}^{-1}$ (m)	5.2	0.2	3.8
$G_N$ (ADCunit/photon)	3.11	0.17	5.5
$T_N$ (ADCunit)	107	7	6.5
$R_N$ (ADCunit $^{1/2}$ )	0.034	0.003	8.8
<i>Muon telescope module 50</i>			
$G_{M50}$ (ADCunit MeV $^{-1}$ )	0.38	0.07	18
$T_{M50}$ (ADCunit)	344	17	4.9
$R_{M50}$ (ADCunit $^{1/2}$ )	0.24	0.02	8.3
<i>Muon telescope module 51</i>			
$G_{M51}$ (ADCunit MeV $^{-1}$ )	27.0	1.9	7.0
$T_{M51}$ (ADCunit)	1000	313	31
$R_{M51}$ (ADCunit $^{1/2}$ )	0.092	0.006	6.5

For details see text

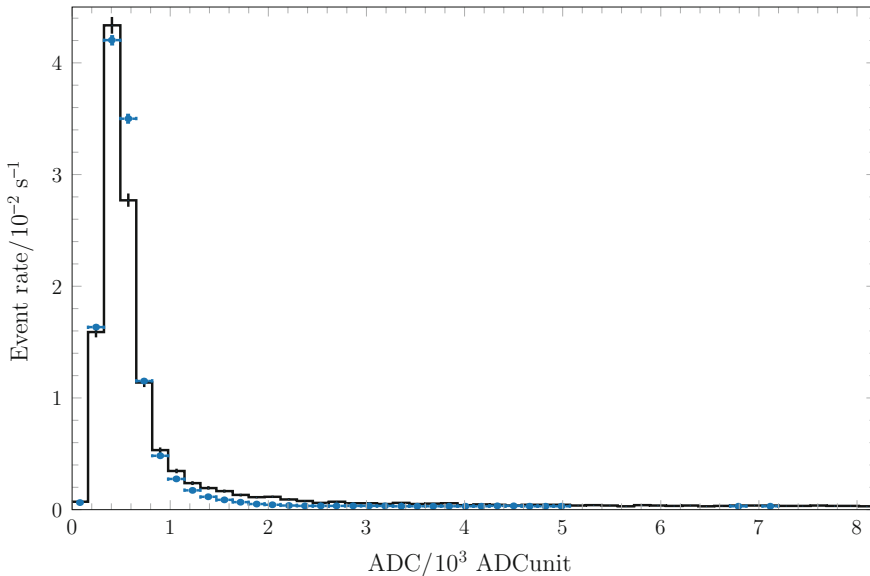


**Fig. 5.22** Comparison of the ADC spectrum measured with muon module 50 (blue data points) with the simulated one (black solid histogram) for primary hits

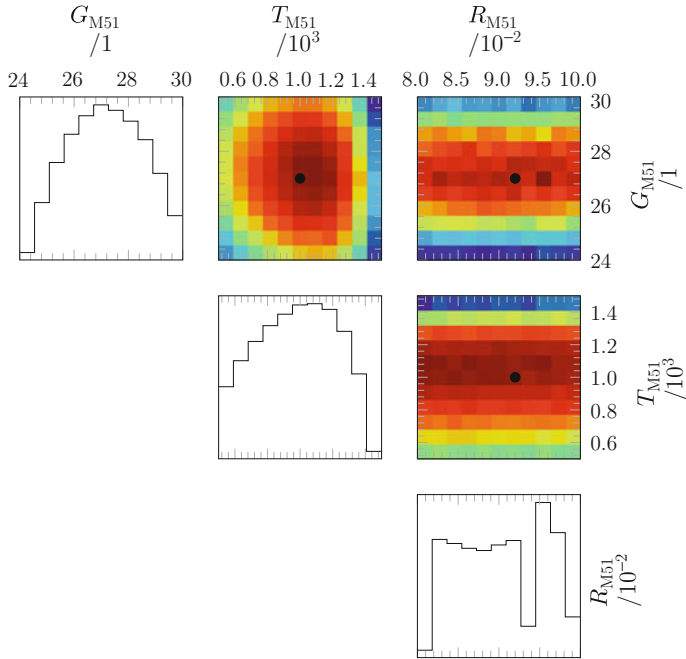


**Fig. 5.23** One- and two-dimensional marginal distributions of the log likelihood in the three-dimensional parameter space of the detector response model for the muon module 51. The parameter space  $\mathbf{G}_{\text{M51}} \times \mathbf{T}_{\text{M51}} \times \mathbf{R}_{\text{M51}}$  is sampled at  $11 \times 11 \times 11 = 1331$  points. Within the three times three grid of the plot, the one-dimensional marginal distributions are located on the diagonal, the two-dimensional ones are located off diagonal. The log likelihood within each marginal distribution is given in arbitrary units. The *black dots* show the position of the maximum likelihood values. For details see text

simulation efficiency is considerably lower compared to the case of the NMM and M50 and it does not include the measured count rate within the uncertainties. The low simulation efficiency can be explained by the disagreement in the spectral shape: whereas the simulation shows the expected Landau distribution, the measurement shows a more symmetric distribution. Albeit it is expected that in thick absorbers the energy deposits approach a Gaussian distribution instead of a Landau distribution, this is not the case for module 51: The average energy loss of muons in the liquid scintillator is with  $\approx 100$  MeV still small compared to the average muon energy of 267 GeV (Eq. 5.74). Therefore, the target can be considered as thin according to L. D. Landau [48], see also Sect. 3.2.2. As a result of the spectral disagreement, the matching process selects a parameter set with a low gain  $G_{\text{M51}}$  and a high threshold  $T_{\text{M51}}$  to cut in the rising part of the simulated spectrum. Consequently, the simulated spectrum contains less events than the measured one, which contains most of its entries in the overflow of Fig. 5.24, resulting in the low central value of  $\epsilon_{\text{MT, event}}$ .

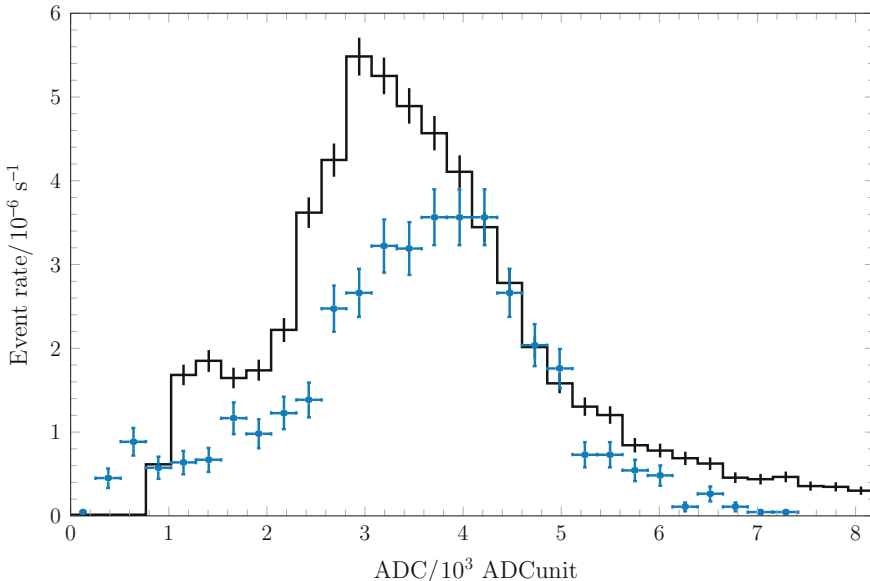


**Fig. 5.24** Comparison of the ADC spectrum measured with muon module 51 (blue data points) with the simulated one (black solid histogram) for primary hits

One possible explanation is that, the spectral disagreement is caused by deviation in gain between N and S channel that is enhanced by the bigger volume of module 51 compared to the small volume of module 50. This could be checked in future simulations by providing individual gain, threshold, and resolution parameters for the N and S channel of module 51 and by comparing the individual ADC spectra instead of the sum spectrum. For this work, the disagreement is considered via the inclusion of  $\epsilon_{\text{MT}}$  as systematic uncertainty in Sect. 5.5.4.

For a comparison between measurement and simulation of muon-induced neutron candidates a decent detector response model is necessary. As the candidate signature is based on the event topology where the numbers of sequences and hits is the decision criterion, a good agreement in the individual event rate is of special importance. For NMM and module 50 of the muon telescope, an excellent agreement is achieved by matching reference AmBe measurements. As discussed in Sect. 5.4.2 the parameters  $kB$  and  $\alpha_{440}^{-1}$  are in good agreement with literature values and monitoring measurements, respectively. For module 51 the event rate is considerably underestimated, leading to a systematic uncertainty in the simulation of muon-induced neutrons.

## 5.5 MC Modelling of Muon-Induced Neutron Production and Detection

With the high statistics data set of simulated muons (see Sect. 5.3.2), the amount of muon-induced events in the neutron counter can be determined.

First, in Sect. 5.5.1 we discuss the neutrons produced in the implemented geometry (Sect. 5.1) via the processes specified in the physics list (Sect. 5.2). We discuss and chose the used definition of the neutron yield in Sect. 5.5.2.

Second, by applying the detector response model (Sect. 5.4) and using the absolute time normalization (Sect. 5.3.3), it is possible to simulate the rate and topology of events detected by the neutron counter and hence deduce the detection efficiency in Sect. 5.5.3. Systematic uncertainties caused by uncertainties in model parameters and time normalization are discussed in Sect. 5.5.4. These are necessary preparations for a direct comparison to the measurements of the neutron detector in Sect. 6.1 and for the calculation of the measured neutron yield in Sect. 6.2. We discuss possible background sources and their contribution to the measured event rates in Sect. 5.5.5.

Finally in Sect. 5.5.6, the prospects to deconvolve the detector response and the measured energy and multiplicity spectra of neutron candidates are studied.

### 5.5.1 Muon-Induced Neutron Production

Before we build events out of the simulated muon data sets and to compare them to the measurement in Sect. 6.1, we first have to confirm that they contain muon induced neutrons.

Figure 5.25 shows the production vertices of neutrons projected on the  $x$ - $y$ -,  $x$ - $z$ -, and  $y$ - $z$ -plane.<sup>23</sup> It contains all Geant4 events of the complete data set as given in Sect. 5.3.2, where the muon is detected by the neutron counter. The high statistics of  $\approx 11 \times 10^6$  neutrons makes a fine binning of  $5\text{ cm} \times 5\text{ cm}$  possible. This allows the differentiation of the individual parts of the neutron counter and its surroundings like EDELWEISS by pure visible inspection, cf. Fig. 5.1 to identify the different parts. The contrast clearly indicates the high neutron production yield of materials with high atomic mass, like the iron of the support structure and the lead shields. Despite the high statistics, muons with highest energies are still identifiable by the increased neutron production along their track. These tracks demonstrate the operational principle of the used muon generator (Sect. 5.3.1): they clearly point inwards, homogeneously illuminating the ball  $\mathcal{B}$  of 5 m radius around the neutron counter and diluting further away. As later shown, this does not introduce a significant bias in the simulation of *detectable* muon induced neutrons.

---

<sup>23</sup>Given the used definitions of the axes, the projections are viewed from the *inside* of the LSM cavern. If one would view it from the *outside*, the EDELWEISS set-up appeared in a wrong location. This effect is visible in the top view, e.g. parallel to the  $x$ - $y$ -plane.

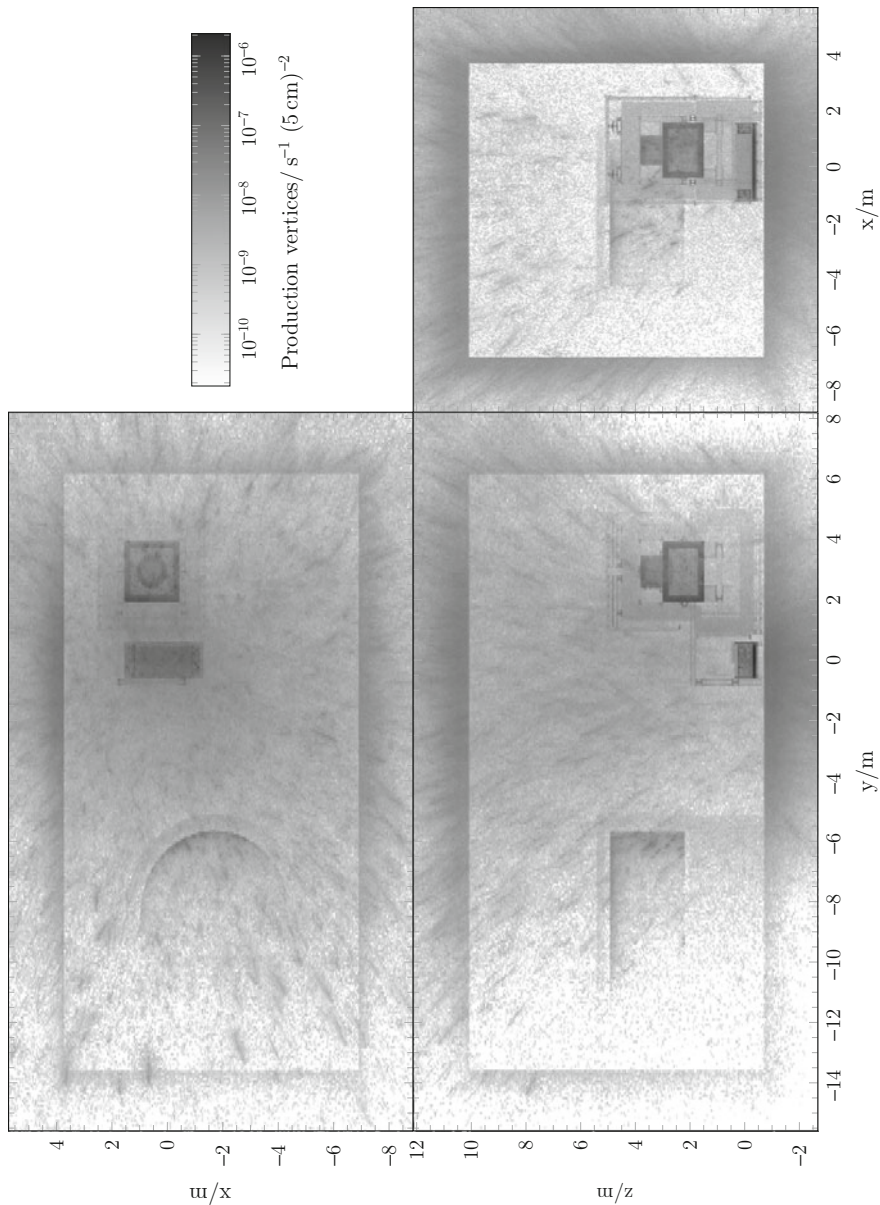


**Fig. 5.25** Projections parallel to the  $x$ - $y$ -,  $x$ - $z$ -, and  $y$ - $z$ -plane of the production vertices of muon-induced neutrons ( $N = 10,648,170$ ) for muons detected by the neutron detector. For details see text

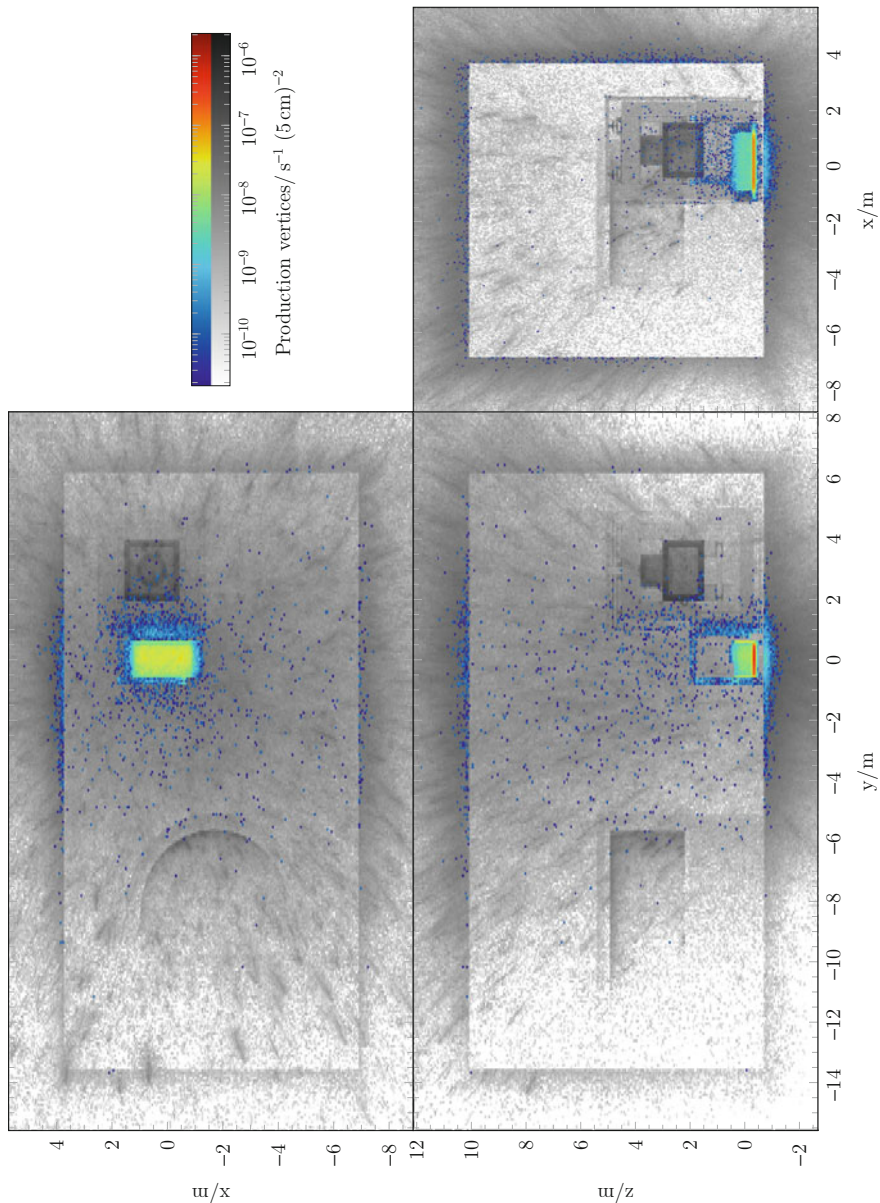
A subset of those neutrons that are terminated by capture and inelastic scattering in the liquid scintillator of the NMM is shown in colour in Fig. 5.26, the gray scaled plot shows again all neutrons for better comparison. It once again shows the importance of a detailed implementation of the surrounding for the simulation of muon-induced neutrons. Albeit most of the implemented volume is cut away as neutron producer, there is still a contribution, e.g. from the iron support structure of nearby EDELWEISS and from the ceiling of the LSM cavern.

Figure 5.27 (*top panel*, black histogram) shows the distance between the neutron production vertex and the centre of the neutron counter for all neutrons produced in coincidence with a detected muon, cf. Fig. 5.25. The red histogram shows the distance for those neutrons terminated in the liquid scintillator, cf. Fig. 5.26. The peak at around 10 m is due to neutrons produced in the concrete ceiling above the neutron counter. Over 95.5 % of all detected neutrons are produced within a sphere of 1.19 m, cf. Fig. 5.27 (*bottom panel*). Therefore, the muon generator (Sect. 5.3.1) does not introduce significant direct boundary effects as the homogeneous illuminated volume  $\mathcal{B}$  is with a radius of 5 m four times larger. However, this leaves still the possibility of indirect boundary effects, e.g. a bias on tertiary neutrons produced well within the ball by muon secondaries from outside the ball. We neglect them in this work, but we note that a future investigation seems interesting, especially as they may contribute to the environmental factor defined and discussed in Sect. 5.5.2.

Whereas in total most of the neutrons are produced in the rock, only few of them reach the neutron counter. The Fig. 5.28 quantifies the contribution of different volumes to the neutrons terminated in the liquid scintillator: the most important neutron source is the lead target (relative contribution 78.2 %), followed by the liquid scintillator (8.23 %) and the iron support structure (7.93 %). By implementing only the lead target in the model, one would therefore underestimate the incident neutron by roughly 21.8 %. The concrete walls of the laboratory are the biggest contributors (1.63 %) that are not part of the detector itself. Therefore, the environment has an influence on the measurement. However, its importance decreases with increasing distance.

The high contribution of the liquid scintillator is probably due to inelastic scattering ( $n, n'$ ): One has to keep in mind, that Geant4 considers an inelastic scattered neutron  $n'$  as different from its predecessor  $n$ . In the general use, the  $n$  and  $n'$  are considered as identical and this specific Geant4 approach is considered as *double counting*. This problem will be discussed in more detail in Sect. 5.5.2. Hereafter, it will be avoided by demanding that the neutrons cross a reference surface. As we are investigating the neutron production in lead and not in liquid scintillator, a suitable method is the requirement on the neutrons to be produced in lead and to be terminated somewhere else, e.g. in the liquid scintillator. This removes all double counting by demanding a crossing of the lead targets surface.

This method is applied to Fig. 5.29: it shows the volumes where neutrons terminate that are produced in lead. The liquid scintillator is with 26.3 % already the second most frequent volume, only 6.5 % less than the concrete below the lead target. Therefore, the placement of the liquid scintillator above the lead target, caused by the mechanical requirements at site, only slightly reduced the detection efficiency



**Fig. 5.26** Projections parallel to the  $x$ - $y$ -,  $x$ - $z$ -, and  $y$ - $z$ -plane of the production vertices of the muon-induced neutrons for muons detected by the neutron counter. Shown in grayscale are all production vertices ( $N = 10,648,170$ ), shown in color scale is the production rate of the neutrons terminated in the active volume of the NMM ( $N = 131,098$ ). For details see text

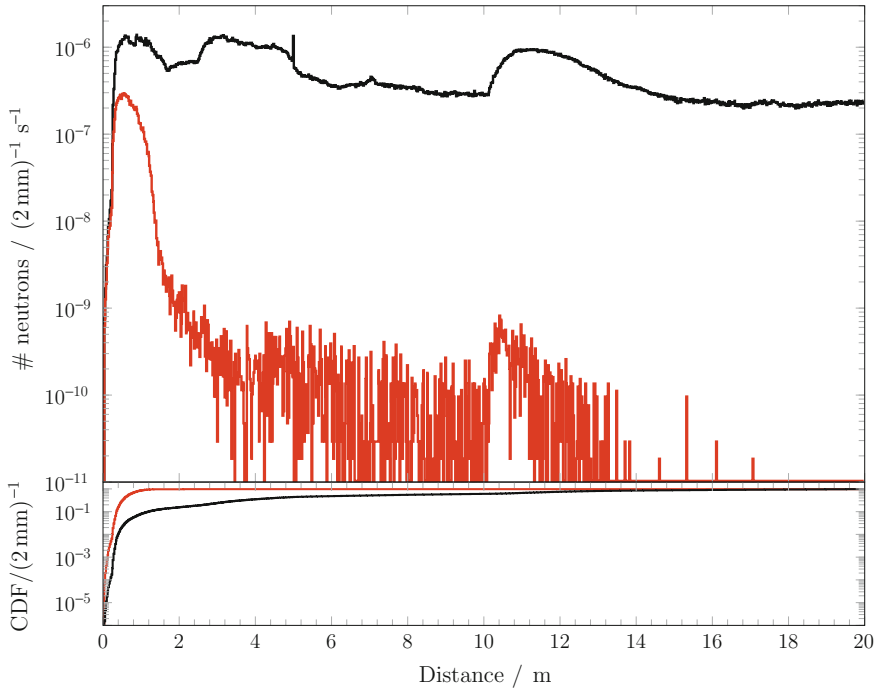


**Fig. 5.27** *Top* Distance between muon-induced neutron production vertices and the centre of the neutron counter in case the parent muon is detected; *bottom*, the corresponding cumulative distribution function (CDF). From  $N = 10,648,170$  produced neutrons (black),  $131,098$  neutron terminated in the liquid scintillator of the neutron counter (red)

compared to a placement below the target. The stated 26.3 % are *neither* identical to the detection efficiency nor to the total efficiency to transport neutrons from the target to the detector. The latter efficiency has to include also indirect effects, e.g. a neutron that leaves the lead target, inelastically scatters in the concrete, and finally enters the liquid scintillator. A suitable detection efficiency to include such effects is defined in Sect. 5.5.3.

Whereas the previous discussions confirm the importance of a precisely implemented geometry of the detector and its surrounding, Fig. 5.30 highlights the importance of the various neutron production processes, both at high and at low energies: Most of the neutron production in the lead is caused by neutron inelastic scattering (relative contribution of 47.1 %) and  $\gamma$  nuclear reactions (41.8 %) as expected for hadronic and electromagnetic cascades (Sects. 3.4.4 and 3.4.5); also pion inelastic scattering contributes prominently with combined 6.03 %. The muons contribute directly via the high energy muon spallation (1.25 %, Sect. 3.4.3) of primary muons and the capture of stopped  $\mu^-$  (0.141 %, Sect. 3.4.1). These reaction composition is expected for poly-energetic incident muons with a high, average energy of  $\langle E \rangle_\mu = 266.5 \text{ GeV}$  (Eq. 5.74), see Sect. 3.4.

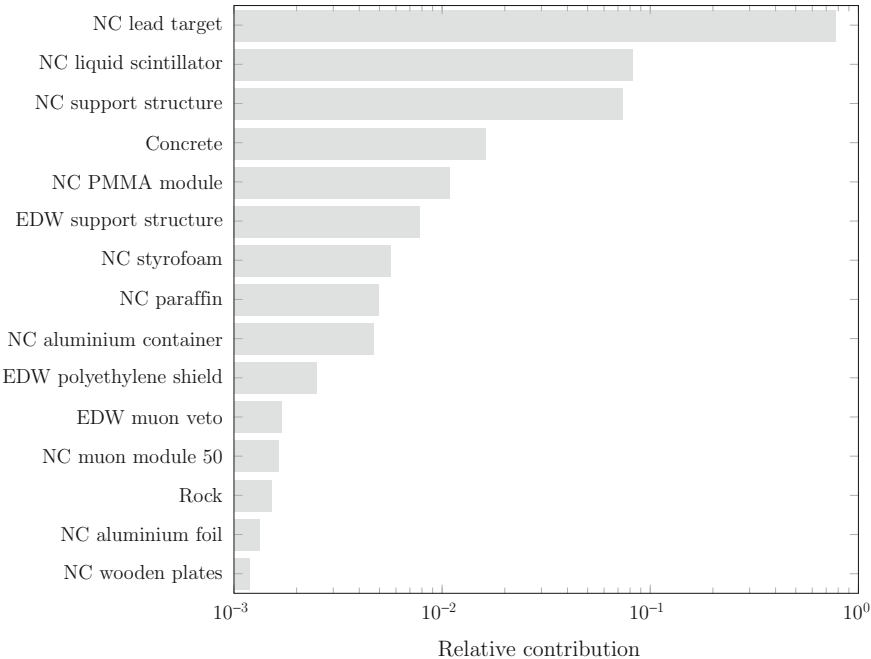


**Fig. 5.28** Production volumes for  $N = 131,096$  muon-induced neutrons that terminated in the liquid scintillator of the NMM: most prominently, parts of the neutron counter (NC) or EDELWEISS (EDW) contribute. Shown are volumes with a relative contribution of  $\geq 10^{-3}$

The energy spectrum of the neutrons emitted from the lead target is shown in Fig. 5.31, reaching up to 30 GeV. Below  $\approx 10$  MeV the influence of the propagation within the target leads to a softer spectrum.

In summary, the simulations contain a high statistics sample of 131,096 muon induced neutrons detected by the implemented neutron counter, see Table 5.5 for the equivalent live-time. The simulations cover, via the detailed implementation of geometry and processes, a variety of neutron producers, which show the expected behaviours: The increased neutron production in heavy materials, the increased detection of neutrons from near producers and the predominance of hadronic and electromagnetic cascades to the total neutron production. But it also shows the contribution of the more distant source volumes like the concrete walls and the low energy processes like the  $\mu^-$  capture. The simulated direct and indirect muon-induced neutrons, but also other secondary products, induced by the incident muon, generate neutron counter events, as it will be shown in Sect. 5.5.3.

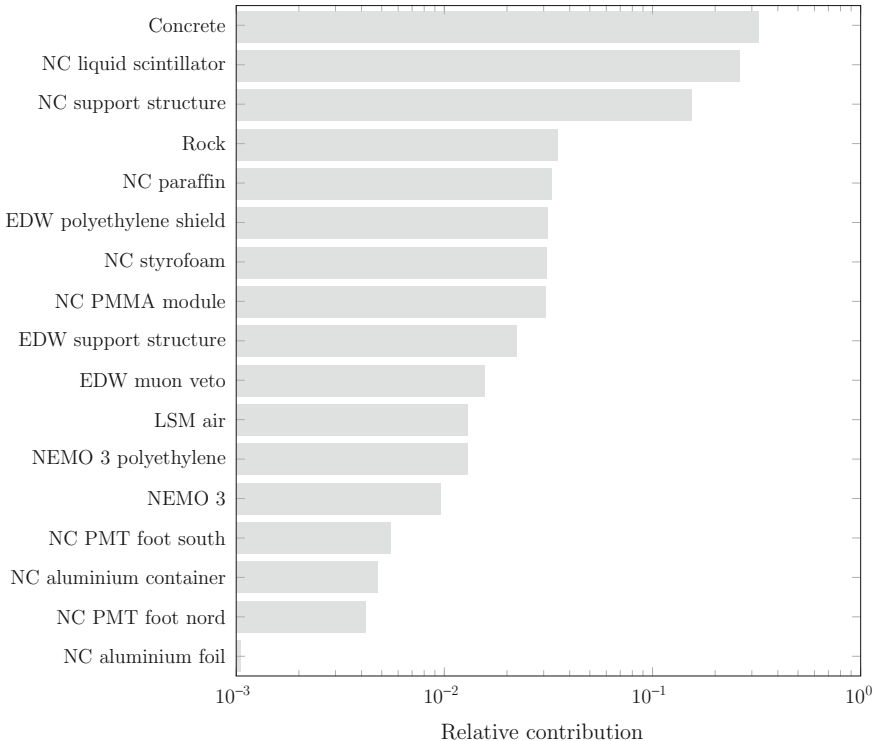


**Fig. 5.29** Final volumes for  $N = 402,829$  neutrons produced in the lead target by muons: mainly subvolumes from the neutron counter (NC) or EDELWEISS (EDW) contribute. Shown are volumes with a relative contribution of  $\geq 10^{-3}$

### 5.5.2 Definition of the Neutron Yield

In this section we will first review the possible definitions of the neutron yield, their suitability with respect to experimental and MC data, and their relation to each other. Afterwards we will discuss the physical reasons for various definitions in terms of target thickness, the environment, the relative process contribution, and the differential production rate along the muon track. Finally, we try to estimate the influence of the used Geant4 version in terms of implemented physics on the neutron yield. We will have a special focus on the comparison of our definition and the one used by L. Reichhart et al. for the ZEPLIN-II and ZEPLIN-III experiments installed at the Boulby underground lab [56]. These results are of special interest, because a mean muon energy of 260 GeV at Boulby is very close to the value of 266.5 GeV used in this work which will be deduced later (Eq. 5.74).

The widely used definition (Eq. 3.64a) of the neutron yield, see the discussion in Sect. 3.5.4, does not define how to count the number of produced neutrons  $N_n$ . This is especially important in the context of MC simulations: as it is pointed out in e.g.

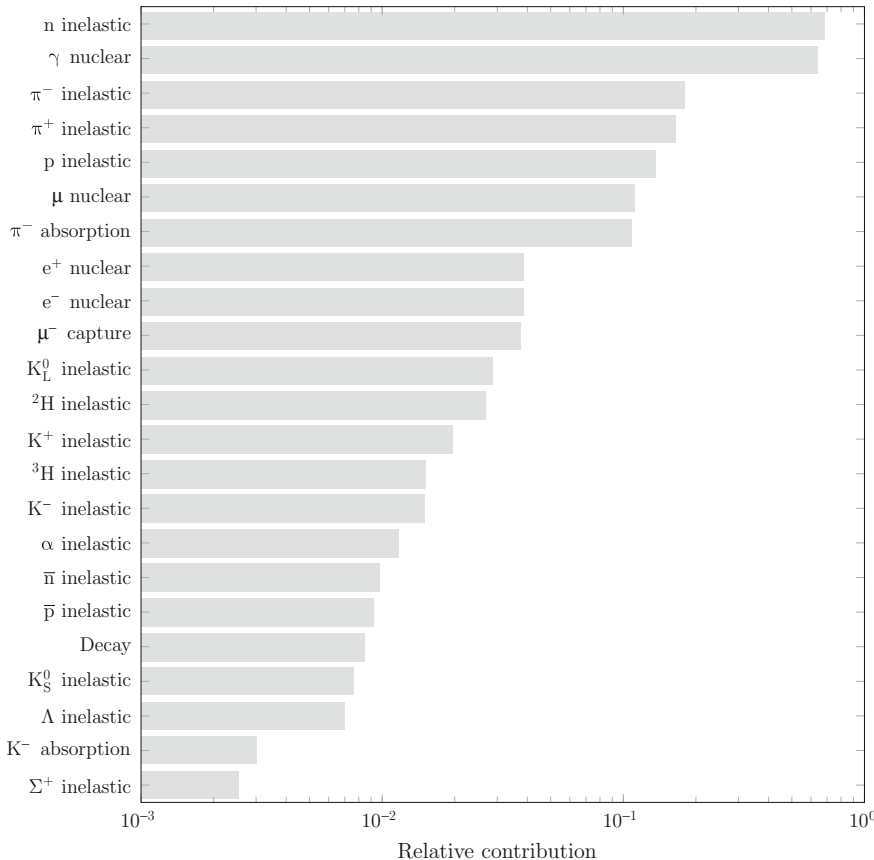


**Fig. 5.30** Relative contribution of creation processes for  $N = 402,829$  muon-induced neutrons produced within the lead target at primary muon energy  $\langle \hat{E}_\mu \rangle = 260.5$  GeV for the primary muons and with the standard muon parameter set: mainly inelastic scattering (inelastic) on various hadrons contributes to neutron production

[3, 36, 56], in an inelastic neutron scattering ( $n_1, n_2$ ) Geant4 treats the neutrons  $n_1, n_2$  as completely independent entities and assign them different *trackIDs*. However, from a physical point of view these neutrons are identical, i.e.  $n_1 = n_2$ . Counting only the *trackIDs* of the simulated neutrons would therefore overestimate  $N_n$ , a problem known as *double counting* [56]. Figure 5.32 illustrates a simulated neutron cascade as tree graph: The lines represent individual neutron tracks and the nodes interactions. Open nodes are inelastic neutron scatterings, filled nodes are other interactions. Only the neutron tracks that end in later interactions represent physical neutrons.<sup>24</sup>

To solve the double counting problem the following method is proposed in [3, 36, 56]: count the reaction multiplicity  $x \geq 1$  of neutron-producing reactions ( $X, x n_i$ )

<sup>24</sup>In the terminology of graph theory, these nodes are the leaves of the tree.

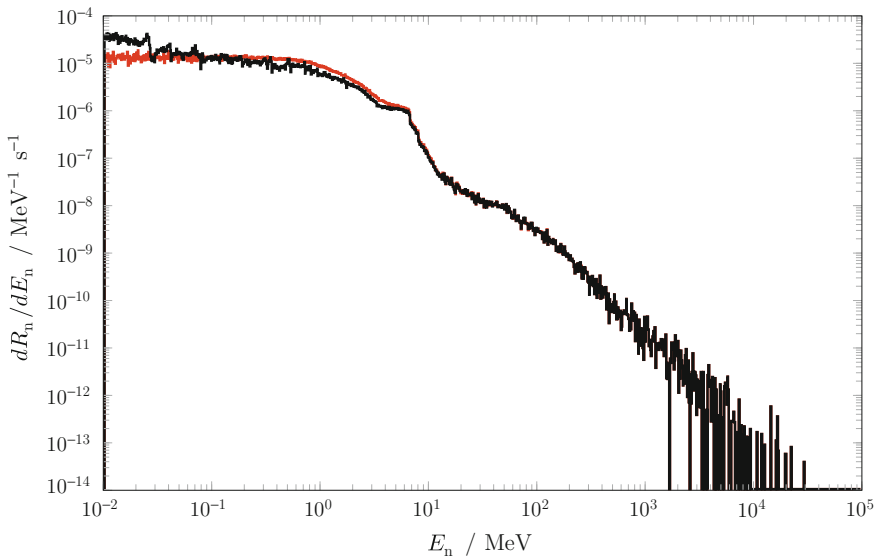
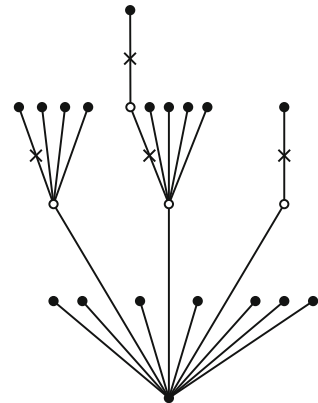


**Fig. 5.31** Differential rate spectrum  $dR_n/dE_n$  of the emitted neutrons, reaching up to  $\approx 30$  GeV. At production, the mean energy is 432 keV (red), reduced to 285 keV when they cross the lead target boundary (black,  $N = 402,829$ )

**Fig. 5.32** Tree graph representing the topology of a simulated neutron cascade consisting of 21 neutron tracks (edges), connected via 4 inelastic scatterings (open nodes) and terminated in 17 other reactions (filled nodes). Neutron tracks removed via double counting correction are marked with a cross. For details see text



instead of the trackID. By counting  $x - 1$  for the case of neutron inelastic scatterings ( $n, x n_i$ ) the identity of the incident neutron with one of the outgoing neutrons is considered.

We will call the neutron yield corrected for double counting *internal neutron yield* for the following reason: it represents the total of all produced neutrons *inside* a given target without relation to any reference surface the neutrons have to cross. Consequently, the neutron propagation in the target and the neutron self-absorption in the target are not taken into account. However, it is still affected by the target thickness

that the muon-induced shower needs to reach equilibrium, as we will discuss later. To exclude this influence we define the *equilibrium neutron yield*  $Y_{\text{equi}}$  by restricting the internal neutron yield  $Y_{\text{int}}$  to the equilibrium stage [36, 56], here defined as the central half length of the target as proposed in [56]. Consequently, in case of a lead target, this internal equilibrium neutron yield is not measurable, not even by an ideal neutron detector, which would be placed in any case outside the target boundary. Hence, this definition is only suitable for MC simulations like [3, 36, 56].

Contrary, experimental works like [2, 12, 13, 29–32] state the neutron yield based on the measured neutrons in the respective detectors. The measured yields are comparable to each other with respect to their similar target thicknesses, see Sect. 3.5.1. Albeit these measurements are corrected for the detection efficiency of the used detectors, they measure only the number of neutrons *emitted* from the target, which is also true for the neutron counter used in this work. Thus, to obtain a direct comparison between experiment and simulation, we define the *external neutron yield*  $Y_{\text{ext}}$ :

The rate of emitted neutrons is defined as the *effective* rate through the surface of the target (lead in our case), i.e. the difference between the number of outgoing neutrons  $N_{\text{out}}$  and the number of ingoing neutrons  $N_{\text{in}}$ . Outgoing neutrons are all neutrons that are produced within the target, but are terminated outside. Hence, they cross the target boundary at least once. Even if the effective neutron rate is used, the neutron rate maybe still affected by incoming neutrons: The effective rate is only corrected for the number of *direct*, incoming neutrons that cross the reference boundary. However, the incoming neutron may start a neutron cascade inside the target and thus the incoming neutrons may also contribute, leading to additional *indirect* neutrons.<sup>25</sup> This definition is free of the double counting problem, as the definition requires that the outgoing neutron must remain outside the target, only one of the neutron tracks  $n_1, n_2$  in  $(n_1, n_2)$  is counted.

Both definitions have their advantages:  $Y_{\text{equi}}$  is independent from the target geometry and hence closer to a general definition of the neutron yield for a given material, but it is *not* directly comparable to experimental results [12, 13, 20, 29–32].  $Y_{\text{ext}}$  is compatible to these results, but it is not a general quantity as it depends on the target geometry.

It is proposed in [4, 43, 51, 56] to use MC simulation to scale the measured external neutron yield  $Y_{\text{ext,exp}}$  to the equilibrium neutron yield  $Y_{\text{equi}}$  via

$$\frac{Y_{\text{ext,exp}}}{Y_{\text{ext,MC}}} = \frac{Y_{\text{equi}}}{Y_{\text{equi,MC}}} \quad (5.55)$$

---

<sup>25</sup>For a complete correction of this kind of contamination, it would be necessary to build a forest graph out of the individual neutron tracks. In such a graph primary neutrons would be the roots of the trees. By cutting the roots that are produced outside the target, not only the primary neutrons, but also all subsequent secondary neutrons, i.e. the nodes of the trees, would be removed. As such an implementation within the Geant4 simulation would be complicated, we chose the approximative correction for this work.

under the assumption that for the simulation of  $Y_{\text{equi}}$ ,  $Y_{\text{equi,MC}}$  the same physics list and Geant4 version is used, in our work Geant4 9.2p01 and the physics list described in Sect. 5.2. Here,  $Y_{\text{ext,MC}}$  is the MC prediction of the measured neutron yield, based on a detailed model of the detector, its surrounding, and the incoming muon flux. For our detector,  $Y_{\text{ext,MC}}$  is based on the simulation described in Sect. 5.5.1 and will be given by Eq. 5.73b.

Contrary,  $Y_{\text{equi,MC}}$  is based on the simulation of an idealized set-up to exclude the environmental effects. We used the following set-up, similar to the one described in [36, 43, 56]: a beam of  $N_{\mu} = 105,000$  mono-energetic  $\mu^-$  at 266.5 GeV strikes a block of lead, placed in vacuum implemented as G4\_Galactic. The muon energy is the same as the average muon energy for the main simulation (Eq. 5.74). The target has the same cross section as the neutron counter, i.e.  $272.2 \text{ cm} \times 105.5 \text{ cm}$  (Sect. 5.1). However, we adopted the higher thickness of  $d_z = 282 \text{ cm}$  along the muon beam and parallel to the  $z$ -axis as it is used in [56]. With a column density  $X \approx 3200 \text{ g cm}^{-2}$  the muon-induced shower reaches the equilibrium stage, see Sect. 3.4.5, and we obtain an equilibrium neutron yield of

$$Y_{\text{equi,MC}} = 3.618(13) \times 10^{-3} \text{ cm}^2 \text{ g}^{-1}. \quad (5.56)$$

To study the influence of the target thickness, the target surrounding (via  $Y_{\text{equi,MC}}$ ), as well as of the used Geant4 version in the relation Eq. 5.55, we simulate the neutron yield also for the following variations of the idealized set-up: For 10 cm thickness ( $X = 113 \text{ g cm}^{-2}$ ) the target is the same as in the main simulation in Sect. 5.5.1 and the muon-induced shower in the target is still in pre-equilibrium stage. The target is also placed in the otherwise empty LSM cavern, starting the muon beam in the rock, to study the influence of muon showers. In this case, the muon energy at start was increased, so that they had again  $\approx 266 \text{ GeV}$  when they entered the target. We run the simulation also with Geant4 9.5p01 (Shielding physics list with activated muon spallation) to compare to [56]. For a comparison with [36], we used a thickness of 352 cm ( $X \approx 4000 \text{ g cm}^{-2}$ ). O. M. Horn [36] used a physics list similar to ours, see Sect. 5.2, but with Geant4 8.2p01 instead of Geant4 9.2p01. All the resulting neutron yields are listed in Table 5.8, the given uncertainties are statistical only, based on propagation of  $\delta N_{\mu}^{\text{stat}} = \sqrt{N_{\mu}}$ ,  $\delta N_{\text{n}}^{\text{stat}} = \sqrt{N_{\text{n}}}$ .

Based on these studies, we introduce an environmental factor  $\eta_{\text{env}}$ , a build-up factor  $B$ , and the neutron self-absorption  $\alpha_{\text{Pb}}$  in the target, and express the ratio  $Y_{\text{equi,MC}}/Y_{\text{ext,MC}}$  of Eq. 5.55 via these factors.

The environmental factor represents the fact that the external neutron yield in the main simulation is with  $3.2(3) \times 10^{-3} \text{ cm}^2 \text{ g}^{-1}$  (Eq. 5.73b, linearly combined uncertainties) significantly higher than the external yield in the idealized 10 cm thick target in vacuum with  $1.462(12) \times 10^{-3} \text{ cm}^2 \text{ g}^{-1}$ . It is suggested in [71] that idealized simulations miss the contribution of neutrons produced in the target by muon-induced showers in the rock overburden. According to [55], an additional contribution may be the neutron cascades inside the target that are started by the earlier discussed incoming neutrons. By comparing the neutron yields in case of the LSM as surrounding and a vacuum as surrounding (Table 5.8), it shows that this effect decreases with the

**Table 5.8** External neutron yield  $Y_{\text{ext,MC}}$  and equilibrium neutron yield  $Y_{\text{equi,MC}}$  for a lead target of  $272.2 \text{ cm} \times 105.5 \text{ cm}$  cross section and a thickness of 10 cm, 282 cm, 352 cm along the muon track, placed in vacuum or in the empty LSM cavern. Simulations were performed with both Geant4 9.2p01 and Geant4 9.5p01

		$Y_{\text{ext,MC}}(10^{-3} \text{ cm}^2 \text{ g}^{-1})$			$Y_{\text{equi,MC}}(10^{-3} \text{ cm}^2 \text{ g}^{-1})$	
		10 cm	282 cm	352 cm	282 cm	352 cm
Geant4 9.2p01, target in ...						
	vacuum, $\mu^+$ beam	1.641(13)	3.033(10)	3.011(10)	3.606(12)	3.683(12)
	vacuum, $\mu^-$ beam	1.462(12)	2.988(10)	2.859(9)	3.618(13)	3.400(11)
	LSM, $\mu^-$ beam	2.382(16)	2.970(10)	2.927(9)	3.592(12)	3.596(12)
Geant4 9.5p01, target in ...						
	vacuum, $\mu^-$ beam	1.864(14)	3.363(11)	3.261(10)	4.576(15)	4.384(14)
	LSM, $\mu^-$ beam	2.598(17)	3.555(11)	3.348(11)	4.789(16)	4.536(15)

For details see text

target thickness: it drops from 63 % for the 10 cm target to 2.4 % for the 352 cm target. A comparison of the relative process contribution for both surroundings in Fig. 5.33a shows an increase of pion inelastic scatterings in case the target is placed in LSM, which may be caused by additional pions from the muon-induced shower. Consequently, the hadronic cascade in the target may reach equilibrium earlier compared to the case the target is placed in vacuum, as indicated by the steeper rising of the differential neutron production inside the target placed in LSM (Fig. 5.34a, red) compared to the target in vacuum (black). Even with the idealized target placed in the empty LSM the neutron yield is with  $2.382(16) \text{ cm}^2 \text{ g}^{-1}$  still lower than the  $3.2(3) \text{ cm}^2 \text{ g}^{-1}$  from the main simulation. As the external neutron yield based on the net rate of emitted neutrons, this may be caused by hadronic, non-neutron cascades produced in the neutron counter support structure that enhance neutron production in the target.

We study also the influence of the charge on the external neutron yield, as the incident muons are of mixed charges in the main simulation: it increases by 9.4 % when the  $\mu^-$  beam was replaced with  $\mu^+$ , possibly due to an increased contribution of pion inelastic scatterings, see Fig. 5.33b.

In summary, Geant4 9.2p01 predicts an environmental factor of

$$\eta_{\text{env}} = \frac{Y_{\text{ext,MC}}(d_z = 10 \text{ cm})|_{\text{Full MC in LSM}}}{Y_{\text{ext,MC}}(d_z = 10 \text{ cm})|_{\text{MC in vacuum}}} \quad (5.57\text{a})$$

$$= 2.207(19) \quad (5.57\text{b})$$

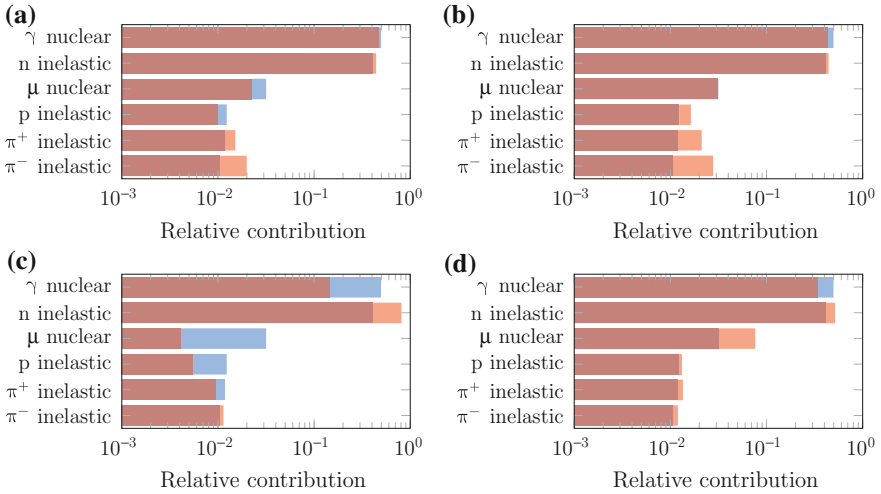


**Fig. 5.33** Comparison of relative contributions of the five most abundant production processes for outgoing neutrons. The numbers are given relative to a 10 cm target ( $X = 113 \text{ g cm}^{-2}$ ) with incident  $\mu^-$  started in vacuum and simulated with Geant4 9.2p01 (light blue histogram,  $N = 17,413$ ): **a** the target placed in the empty LSM cavern (light red,  $N = 28,659$ ). **b** incident  $\mu^+$  (light red,  $N = 19,548$ ). **c** a thick target of 282 cm ( $3200 \text{ g cm}^{-2}$ ) (light red,  $N = 860,209$ ). **d** Simulated with Geant4 9.5p01 (light red,  $N = 22,200$ ). For details see text

with only statistical uncertainties. It takes into account that the full simulation was performed with a detailed LSM geometry and incoming  $\mu^+$ ,  $\mu^-$  showers, whereas the idealized simulations were done in vacuum with an incoming  $\mu^-$ -beam.

The influence of the build-up of the muon-induced shower on the internal neutron yield is shown in Fig. 5.34b: At  $X \approx 347 \text{ g cm}^{-2}$ , the yield reaches equilibrium in Geant4 9.2p01 (black) and at  $X \approx 519 \text{ g cm}^{-2}$  in Geant4 9.5p01 (red). These numbers justify correctness of our decision to base the rock thickness in the main simulation on the higher limit of  $X = 800 \text{ g cm}^{-2}$  [36] instead of the lower value of  $X = 500 \text{ g cm}^{-2}$  [44], see Sect. 3.4.5. The increased neutron yield in equilibrium is associated with an increased contribution of inelastic neutron scattering, see Fig. 5.33c, as expected from Sect. 3.4.5. Albeit the build-up is most clear when defined with the internal neutron yield, for the parametrization of  $Y_{\text{equi,MC}}/Y_{\text{ext,MC}}$  we need the *effective build-up factor*, defined with the external yield:

$$B = \frac{Y_{\text{ext,MC}}(d_z = 282 \text{ cm})}{Y_{\text{ext,MC}}(d_z = 10 \text{ cm})} \quad (5.58a)$$

$$= 2.044(18) \quad (5.58b)$$

where the value is given for Geant4 9.2p01, uncertainties are statistical only. For Geant4 9.5p01, the effective build-up factor is lower ( $B = 1.804(15)$ ), as it reaches already at 10 cm a higher yield than Geant4 9.2p01, see Table 5.8.

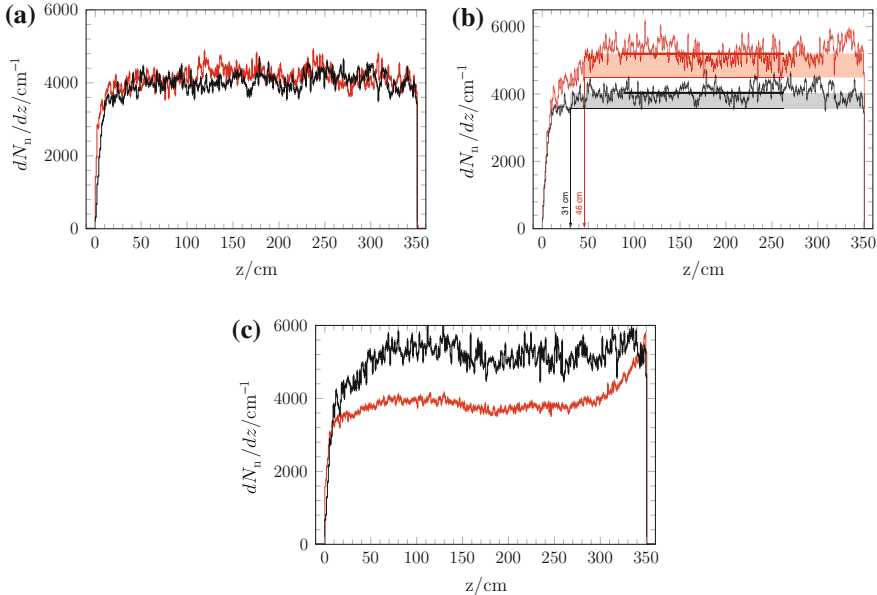


**Fig. 5.34** The differential neutron production  $dN_n/dz$  for 105,000 muons along the muon track for a lead target of 352 cm ( $X \approx 4000 \text{ g cm}^{-2}$ ) thickness. Neutron counting follows the definitions of: **a** the internal neutron yield for the target in vacuum (black) and in the empty LSM (red), both simulated with Geant4 9.2p01. **b** The internal neutron yield for the target in vacuum, simulated with Geant4 9.2 (black) and Geant4 9.5 (red). The thick lines represent the average over the inner half length of the target  $\langle dN/dz \rangle$ , the filled areas represent the maximum lower residual  $\langle dN/dz \rangle - dN/dz$ . The arrows indicate the thickness when the differential neutron yield enters finally the range  $\max(\langle dN/dz \rangle - dN/dz)$ . **c** The internal neutron yield (black) compared with the external neutron yield (red), both for Geant4 9.5p01 and a target placed in vacuum. For most data points the error bars are smaller than the markers

The *target selfabsorption* describes the difference between  $Y_{\text{ext}}$  and  $Y_{\text{equi}}$ , in case of Geant4 9.2p01:

$$\alpha_{\text{Pb}} = \frac{Y_{\text{ext,MC}}(d_z = 282 \text{ cm})}{Y_{\text{equi,MC}}(d_z = 282 \text{ cm})} \quad (5.59a)$$

$$= 0.826(4), \quad (5.59b)$$

The effect of the self absorption on the differential neutron production is clearly visible in Fig. 5.34c, with a stronger effect and hence a smaller value  $\alpha_{\text{Pb}} = 0.735(3)$  for Geant4 9.5p01: The external yield (red) matches the internal yield (black) when the muon beam enters the top of the target ( $z \approx 0 \text{ cm}$ ) and leaves at bottom ( $z \approx 350 \text{ cm}$ ), but drops clearly in the middle of the target. This can be explained by the self absorption in the middle of the target: there, the distance to the top and bottom surface is greater than near the entrance and exit point, whereas the distance to the sides is independent from the position along the  $z$ -axis.

To cross check the consistency of the used definitions, we compare the results of the idealized set-up to [36, 56]: The equilibrium neutron yield for the 352 cm target is with  $3.400(11) \times 10^{-3} \text{ cm}^2 \text{ g}^{-1}$  significantly higher than the  $3.180 \times 10^{-3} \text{ cm}^2 \text{ g}^{-1}$  calculated<sup>26</sup> in [36] for Geant4 8.2p01 with a similar physics list. The increased yield by 6.9 % is within the expected range due to improvements in Geant4, see also the discussion in Sect. 3.6.4 and Appendix A.3.3. For the 282 cm thick target, the equilibrium neutron yield of  $4.576(15) \text{ cm}^2 \text{ g}^{-1}$  for Geant4 9.5p01 is in perfect agreement with the  $4.594(4) \text{ cm}^2 \text{ g}^{-1}$  published in [56, Table 4]. Hence, the boundary conditions of the idealized simulations and the correction for double counting used in this work are compatible with the one in [4, 36, 56].

As a result, we can scale our measurement of  $Y_{\text{ext}}$  for a real 10 cm thick target in LSM (Sect. 6.2) to  $Y_{\text{equi}}$  for an idealized 282 cm thick target in vacuum, to be compared with the results of ZEPLIN-II, ZEPLIN-III [56], via Eq. 5.55 with the following scaling factor:

$$\frac{Y_{\text{equi}}}{Y_{\text{ext,exp}}} = \frac{Y_{\text{equi,MC}}}{Y_{\text{ext,MC}}} \quad (5.60\text{a})$$

$$= \frac{B}{\alpha_{\text{Pb}} \eta_{\text{env}}} \quad (5.60\text{b})$$

$$= 1.122(15), \quad (5.60\text{c})$$

based on Eqs. 5.57a, 5.58a and 5.59a. As it turns out, the increase in the neutron yield, expected by the increased target thickness ( $B = 2.044$  (Eq. 5.58b)), is nearly completely canceled by the environmental factor in Geant4 9.2p01 ( $\eta_{\text{env}} = 2.207$  (Eq. 5.57b)). This demonstrates once again the importance of a careful handling of boundary conditions for this kind of comparisons.

The estimation of the influence of the used Geant4 version on the scaling of the neutron yield is not straightforward: In absolute terms one expects an increase by

$$\frac{Y_{\text{equi,MC}}|_{\text{Geant49.5p01}}}{Y_{\text{equi,MC}}|_{\text{Geant49.2p01}}} = 1.265(6) \quad (5.61)$$

for the equilibrium neutron yield in the 282 cm target in vacuum between Geant4 9.2p01 and Geant4 9.5p01, see Table 5.8. The rise is mainly caused by improvements in the muon spallation and hadronic interactions (Sects. 3.4.3 and 3.6.4). The simulated neutron yield enters in the calculation of  $Y_{\text{equi}}$  via Eq. 5.55 by  $B$ ,  $\alpha_{\text{Pb}}$ ,  $\eta$  (Eq. 5.60b). As the ratio  $B/\alpha_{\text{Pb}}$  stays within  $\approx 1\%$  the same between Geant4 9.2p01 and 9.5p01, the environmental factor  $\eta$  might be the main cause for a possible change in scaling (Eq. 5.60b). As especially the physics of muon energy loss seems to be updated, see Appendix A.3.3, an influence on the shower contribution to the neutron yield, and hence a change in  $\eta$ , seems possible. Therefore, the scaling of the measured  $Y_{\text{ext}}$  to  $Y_{\text{equi}}$  also depends on the used Geant4 version.

<sup>26</sup>Based on the fit to  $Y_{\text{equi}}(A)$  [36, fig. 3.7] for  $A = 207.2$ .

As shown in this section, the definition of the neutron yields is not unambiguous. Also the surrounding of the target has a significant influence on the neutron yield. Therefore, one has to take care to chose the definition of the neutron yield that is most suitable: To reproduce experimental values, the *external* neutron yield is a suitable definition. However, it is detector specific. A more physical approach is the *equilibrium* neutron yield, but it has an increased dependence on MC simulations.

### 5.5.3 Neutron Production Rate and Detection Efficiency

As Sect. 5.5.1 shows, the simulated data sets contain muon-induced neutrons. To be compared to the measurement, these *produced neutrons* have to be related to the *detected neutron candidates*<sup>27</sup> via the neutron detection efficiency and by defining quantities corresponding to the experimental ones.

This section starts with simulated rates of neutron candidates and neutrons, and then defines the neutron detection efficiency. The definitions in this section will be given with respect to the *standard configuration*, i.e. the standard parameter set for the muon generator (Sect. 5.3.1), the GdNeutronHPCapture model for the neutron capture on gadolinium (Sect. 5.4.1), the best fitting parameter for the detector response model (Sect. 5.4.4), and a nominal loading of 0.2 % W/W gadolinium. In the following we denote values obtained for the standard configuration with a hat, e.g.  $\hat{x}$ .

The influence of deviating configurations and the calculation of statistical, systematic, and theoretical uncertainties will be discussed in Sect. 5.5.4. It also contains the calculation of the *average values*, e.g.  $\bar{x}$ , as they are affected also by changes in the configurations. Section 6.1 discusses the differences to the measured values.

The amount of simulated muon candidates  $n_{\mu,ic}$ , neutron candidates  $n_{n,ic}$ , and neutron cascade candidates  $n_{cas,ic}$  within the data set  $ic$  depends on the amount of the simulated neutron counter events that match the respective signature: within the coincident hit signature (see Sect. 4.3) any coincidence between the muon module 50 and 51 is a muon candidate, any NMM event coincident with a muon candidate is a candidate for muon-induced neutron cascade, the secondary hits within the cascade are neutron candidates. The number of secondary hits also defines the multiplicity of the neutron cascade candidate  $M_{n,can}$ . Here the index *can* indicates the *candidate* multiplicity, to be distinguished from the later defined multiplicity of neutrons  $M_n$ .

The amounts of candidates  $n_{x,ic}$  are summed up over the data sets  $ic$  (Sect. 5.3.2) after applying the calibrated detector response model (Sect. 5.4), normalized to the live-time  $T_{MC,ic}$  of the simulation (Table 5.5), and stated as rates  $R_{\mu,MC}$ ,  $R_{cas,MC}$ , and  $R_{n,MC}$ :

$$R_{x,MC} = \sum_{c=+,-} \sum_i \frac{n_{x,ic}}{T_{MC,ic}} \text{ for } x = \mu, n, \text{cas} \quad (5.62)$$

---

<sup>27</sup>A neutron candidate is a simulated NMM event that matches the neutron signature, see Sect. 4.3.

The muon charge ratio  $\mu^-/\mu^+$  is considered via the live-time  $T_{MC,ic}$ , see Table 5.5. Hence, the defined rates are analog to the ones used for the measurements (Eq. 4.29) and ensure the compatibility between measurement and simulation.

Based on the individual  $\hat{n}_{x,MC,ic}$  listed in Table 5.9, the rates  $\hat{R}_{x,MC}$  are calculated.

$$\bar{R}_{\mu,MC} = (5.728 \pm 0.010_{-0.471}^{stat} \pm 1.486_{-0.471}^{sys} \pm 0.012^{theo}) \text{ d}^{-1} \quad (5.63)$$

$$\bar{R}_{cas,MC} = (1.549 \pm 0.012_{-0.378}^{stat} \pm 0.554_{-0.378}^{sys} \pm 0.034^{theo}) \times 10^{-1} \text{ d}^{-1} \quad (5.64)$$

$$\bar{R}_{n,MC} = (3.753 \pm 0.019_{-1.019}^{stat} \pm 1.472_{-1.019}^{sys} \pm 0.107^{theo}) \times 10^{-1} \text{ d}^{-1} \quad (5.65)$$

The uncertainties are defined and discussed in Sect. 5.5.4, especially in Eqs. 5.78, 5.79a and 5.84. The differential rates per multiplicity are discussed in Sect. 6.1 in comparison with the measurements.

Besides the absolute count rates  $R_{x,MC}$ , also the ratios as defined in Eq. 4.31, i.e.

$$\bar{\eta}_{n,cas} = 2.433 \pm 0.023_{-0.597}^{stat} \pm 0.388_{-0.597}^{sys} \pm 0.017^{theo} \quad (5.66)$$

$$\bar{\eta}_{n,\mu} = (6.56 \pm 0.04_{-1.83}^{stat} \pm 1.49_{-1.83}^{sys} \pm 0.17^{theo}) \times 10^{-2} \quad (5.67)$$

are interesting quantities:  $\eta_{n,\mu}$  is needed to calculate the *simulated* neutron production yield (Eq. 3.64a) in Sect. 6.2 and  $\eta_{n,cas}$  gives a measure for the neutron multiplicity per cascade, discussed further in Sect. 6.1 in context of the assessment of Geant4. As we will show in Sect. 5.5.4, they are also more precise as the individual rates  $R_{x,MC}$  because of correlations between the individual sources of systematic uncertainties.

For a better comparison with the measured rates, we introduce the scaled rates  $\tilde{R}_{x,MC}$  relative to the measured rate of muon candidates  $R_{\mu,meas}$  as an extension of the just defined ratios  $\eta_{n,x}$ :

$$\tilde{R}_{x,MC} = \frac{R_{\mu,meas}}{R_{\mu,MC}} R_{x,MC} \text{ for } x=cas, n \quad (5.68)$$

As already mentioned, the systematic uncertainties of the rates are correlated. Consequently, the systematic uncertainty of the scaled rate drops and compensates the increased statistical uncertainty. Therefore, the resulting values

$$\bar{\tilde{R}}_{cas,MC} = (1.57 \pm 0.02_{-0.37}^{stat} \pm 0.28_{-0.37}^{sys} \pm 0.03^{theo}) \times 10^{-1} \text{ d}^{-1} \quad (5.69)$$

$$\bar{\tilde{R}}_{n,MC} = (3.79 \pm 0.05_{-1.06}^{stat} \pm 0.86_{-1.06}^{sys} \pm 0.10^{theo}) \times 10^{-1} \text{ d}^{-1} \quad (5.70)$$

show a reduced combined uncertainty.

Whereas the comparisons of these simulated candidate rates and their ratios to the measured ones are a sufficient method to assess Geant4's reliability in Sect. 6.1, we are also interested in the neutron production rate for the estimation of the neutron production yield in Sect. 6.2.

As discussed in Sect. 5.5.2, we choose the external neutron yield as a suitable quantity to compare to the majority of existing measurements. As the neutron yield is defined in relation to the rate of *detected* muons (see Sect. 3.5.4), we define the rate of produced neutrons as the effective rate through the surface of the lead target in case the through-going muon is detected, i.e. the simulated Geant4 event contains a muon candidate. The *effective* rate is the number of outgoing neutrons  $n_{n,out,ic}$  reduced by the number of ingoing neutrons  $n_{n,in,ic}$ , both defined with respect to the target boundary, again summed up over all data sets  $ic$  and normalized to the live-time  $T_{MC,ic}$ :

$$R_{n,eff} = \sum_{c=+,-} \sum_{i=2}^5 \frac{n_{n,out,ic} - n_{n,in,ic}}{T_{MC,ic}} \quad (5.71)$$

Table 5.9 lists  $n_{n,in,ic}$ ,  $n_{n,out,ic}$  for the standard configuration. By relying on the target boundary, we avoid double counting of neutrons from  $(n, n')$  reactions as discussed in Sect. 5.5.2. Similar to the definition for the cascade candidate, the number of effective neutrons per neutron cascade is the multiplicity  $M_n$  of the cascade.

With this definition, the simulated data sample contains a neutron rate of

$$\bar{R}_{n,eff} = (2.498 \pm 0.006^{stat} \pm 0.597^{sys} \pm 0.057^{theo}) \text{ d}^{-1}, \quad (5.72)$$

where the individual contributions per data set are listed in Table 5.9. The corresponding external neutron yield is

$$\bar{Y}_{ext,MC} = \frac{\bar{R}_{n,eff}}{\bar{R}_{\mu,MC} \langle X \rangle} \quad (5.73a)$$

$$= (3.226 \pm 0.010^{stat} \pm 0.191^{sys} \pm 0.067^{theo}) \times 10^{-3} \text{ cm}^2 \text{ g}^{-1} \quad (5.73b)$$

**Table 5.9** Number of outgoing neutrons  $\hat{n}_{out,ic}$ , incoming neutrons  $\hat{n}_{in,ic}$ , muon candidates  $\hat{n}_{\mu,MC,ic}$ , neutron cascade candidates  $\hat{n}_{cas,MC,ic}$ , and neutron candidates  $\hat{n}_{n,MC,ic}$  as obtained from the Geant4 simulations in standard configuration, classified for each data set  $ic$

	Data set $i, c$	$\hat{n}_{n,out,ic}$	$\hat{n}_{n,in,ic}$	$\hat{n}_{\mu,MC,ic}$	$\hat{n}_{cas,MC,ic}$	$\hat{n}_{n,MC,ic}$
$\mu^-$						
	2, -	2221(47)	65(8)	49,769(223)	805(28)	876(30)
	3, -	19,780(141)	574(24)	136,073(369)	1848(43)	3326(58)
	4, -	87,934(297)	2722(52)	121,678(349)	5246(72)	13,075(114)
	5, -	93,529(693)	3163(22)	27,500(166)	3162(56)	10,985(105)
$\mu^+$						
	2, +	693(26)	22(5)	49,117(222)	445(21)	471(22)
	3, +	19,713(140)	617(25)	136,651(370)	1832(43)	3298(57)
	4, +	85,950(293)	2632(51)	117,541(343)	4846(70)	12,735(113)
	5, +	93,009(305)	3238(57)	23,793(154)	2724(52)	10,146(101)

The statistical uncertainties on the numbers are Poissonian standard deviations  $\sqrt{\hat{n}_x}$ . For details and definitions of the quantities see text

based on Eqs. 5.63, 5.72 and 5.75b. It represents the *simulated* external neutron yield for the given geometry in case of an NMM with 100 % detection efficiency. Hence, it can be compared with the *measured*, efficiency corrected external neutron yield in Sect. 6.2.1.

In the following, we show that these neutrons are produced in the *thin* lead target at *high* muon energies: Fig. 5.35a shows the energy distribution of the muons when they enter the target and cause valid neutron cascade candidates. In case of several muons passing the target, i.e. having secondary muons, only the primary one is considered to assign an energy, as it starts the shower. As muon energy we take the distribution mean.<sup>28</sup> For the standard configuration this is  $\langle \hat{E}_\mu \rangle = 260.5(7)$  GeV, see Fig. 5.35a. Finally, considering various configurations of the muon flux model, see Sect. 5.5.4, we state

$$\overline{\langle E_\mu \rangle} = (266.5 \pm 0.7_{-3.9}^{+1.1\text{sys}} \pm 6.0^{\text{theo}}) \text{ GeV} \quad (5.74)$$

as muon energy.

Within its uncertainties, this value agrees with the 255.0(45) GeV measured by W. Rhode [57], see as well Sect. 3.3.3.

The track length  $l$  of primary muons in lead, again for valid neutron cascade candidates, is shown in Fig. 5.35. Its average value is  $\langle \hat{l} \rangle = 119.18(4)$  mm. With a lead density of  $\rho_{\text{Pb}} = 11.342 \text{ g cm}^{-3}$ , the average target thickness along the track for primary muons is

$$\overline{\langle X \rangle} = \rho_{\text{Pb}} \overline{\langle l \rangle} \quad (5.75a)$$

$$= (135.189 \pm 0.049_{-0.284}^{+0.230\text{sys}} \pm 0.015^{\text{theo}}) \text{ g cm}^{-2}. \quad (5.75b)$$

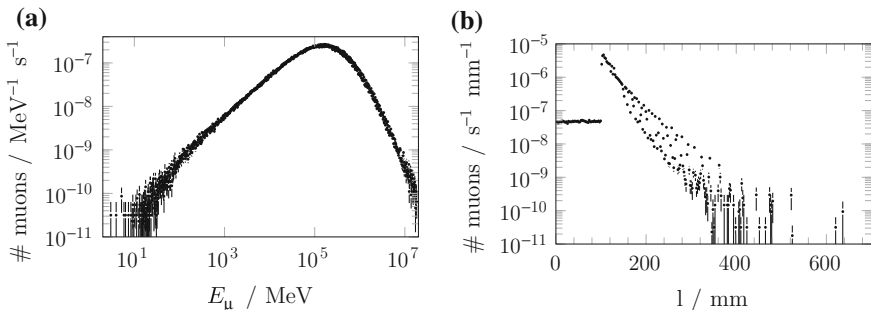


**Fig. 5.35** **a** Muon energy  $E_\mu$  and **b** muon track length  $l$  in the lead target for neutron cascade candidates with the coincident hit signature. Error bars indicate 68 % CL. Shown are only primary muons ( $N = 506,435$ ), obtained from Geant4 simulation using the standard configuration. For detail see text

<sup>28</sup>We denote the mean of a distribution of a quantity  $x$  as  $\langle x \rangle$  and the arithmetic mean of a quantity  $x$  as  $\bar{x}$ , i.e.  $\langle \bar{x} \rangle$  is the arithmetic mean over several distributions of  $x$ .

As the lead target has a perpendicular thickness of  $X_{\perp} = 113.42 \text{ g cm}^{-2}$  (Sect. 4.2.1), this is equivalent to an average muon zenith angle of  $\arccos(X_{\perp}/X) \approx 33^\circ$  in agreement with the muon zenith spectrum Fig. 5.6b. Including all muons would result in a slightly higher incident angle, because few incident muons pass nearly parallel through the 2 m lead target, see Fig. 5.35b. As discussed in Sect. 3.4.5, the neutron cascade needs  $\approx 800 \text{ g cm}^{-2}$  to reach equilibrium, therefore this work simulates and measures the neutron yield in the pre-equilibrium stage, i.e. in a thin target. This has to be considered when the results are compared to other works in Chap. 6.

The efficiency  $\epsilon_n$  to detect muon-induced neutrons produced in the lead target has to consider two factors: the efficiency to detect any neutrons incident on the NMM and the fraction of this incoming neutrons that were produced in the lead target. Based on the discussion in Sect. 5.5.2, we define  $\epsilon_n$  as ratio of the rate  $R_{n,MC}$  of neutron candidates (Eq. 5.62) to the rate  $R_{n,eff}$  of effective neutrons (Eq. 5.71) produced in the lead target:

$$\epsilon_n = \frac{R_{n,MC}}{R_{n,eff}} \quad (5.76)$$

The resulting neutron detection efficiency

$$\bar{\epsilon}_n = \left( 15.14 \pm 0.08^{\text{stat}} {}^{+2.71^{\text{sys}}}_{-3.50} \pm 0.06^{\text{theo}} \right) \% \quad (5.77)$$

is therefore already restricted to the neutron emitted from the lead target. Hence, the efficiency to detect muon-induced neutrons from other materials may be different.

As expected,  $\bar{\epsilon}_n$  is significantly lower than the capture efficiency of 40 % in Sect. 4.1.3, because it also includes the detector response. It is higher than the neutron detection efficiency of 5.7 % for AmBe (Eq. 4.21), probably due to the different source geometries: the plain lead target as source for the muon-induced neutrons versus the point-like AmBe source.

Based on a detailed simulation including neutron production, propagation, and detection in coincidence with muon detection, we specified the expected detector performance in LSM in terms of muon-induced neutrons and neutron candidates. As the detector response is included, the simulated rates can be directly compared to the measured ones (Sect. 6.1) and the deduced neutron detection efficiency of  $\approx 15\%$  can be used to calculate the neutron yield in Sect. 6.2.

#### 5.5.4 Estimation of Systematic Uncertainties in the Simulation

To give a convincing assessment in Sect. 6.1 of the Geant4 capability to reproduce the measured rate of muon-induced neutrons, this section discusses the statistical, systematic and theoretical uncertainties on the simulated values. Also possible ways to reduce these uncertainties in future works are discussed. The resulting values for the uncertainties were already given with the central values in Sect. 5.5.3, and their individual origins are classified in Tables 5.10 and 5.11.

**Table 5.10** Statistical, systematic, and theoretical uncertainties for  $R_{\mu,MC}$ ,  $R_{cas,MC}$ ,  $R_{n,MC}$ ,  $\tilde{R}_{cas,MC}$ ,  $\tilde{R}_{n,MC}$ , and  $E_{\mu}$  relative to the respective average value

	$\delta R_{\mu,MC}$ (%)	$\delta R_{cas,MC}$ (%)	$\delta R_{n,MC}$ (%)	$\delta \tilde{R}_{cas,MC}$ (%)	$\delta \tilde{R}_{n,MC}$ (%)	$\delta E_{\mu}$ (%)
Statistical uncertainty						
	$\pm 0.18$	$\pm 0.80$	$\pm 0.52$	$\pm 1.56$	$\pm 1.43$	$\pm 0.27$
Systematic uncertainties						
Flux normalization						
Numerical	-0.08	-0.59	<b>-0.77</b>	-0.51	-0.69	-0.86
$\eta + \delta$	-0.05	-0.22	-0.30	-0.17	-0.25	-0.32
$w_c \pm \delta$	$\pm 0.00$	$\pm 0.04$	$\pm 0.00$	$\pm 0.04$	$\mp 0.00$	$\pm 0.00$
$\dot{\phi}_{\text{ref}} \pm \delta$	$\begin{array}{c} +5.59 \\ -1.82 \end{array}$	$\begin{array}{c} +5.55 \\ -1.81 \end{array}$	$\begin{array}{c} +5.53 \\ -1.81 \end{array}$	$\pm 0.00$	$\pm 0.00$	$\pm 0.00$
Sum	+5.59	+5.59	+5.54	+0.04	+0.00	+0.00
	-1.96	-2.67	-2.88	-0.72	-0.94	-1.18
NMM						
$\alpha_{440}^{-1} \pm \delta$	-0.04 -0.02	<b>+0.96</b> <b>-1.38</b>	<b>+1.44</b> <b>-1.92</b>	+1.00 -1.36	<b>+1.48</b> <b>-1.91</b>	+0.02 +0.01
$kB \pm \delta$	-0.08 +0.09	-0.60 +0.21	<b>-0.91</b> <b>+0.65</b>	-0.52 +0.13	-0.83 +0.56	+0.03 -0.03
$G_N \pm \delta$	$\pm 0.00$	$\begin{array}{c} +2.29 \\ -2.66 \end{array}$	$\begin{array}{c} +3.16 \\ -3.76 \end{array}$	$\begin{array}{c} +2.29 \\ -2.67 \end{array}$	$\begin{array}{c} +3.16 \\ -3.77 \end{array}$	$\pm 0.00$
$T_N \pm \delta$	$\pm 0.00$	$\begin{array}{c} -3.02 \\ +3.61 \end{array}$	$\begin{array}{c} -4.28 \\ +4.96 \end{array}$	$\begin{array}{c} -3.03 \\ +3.61 \end{array}$	$\begin{array}{c} -4.28 \\ +4.97 \end{array}$	$\pm 0.00$
$\Delta t_{\text{bin}} \pm \delta$	+0.02 <b>-0.25</b>	-0.11 <b>-0.88</b>	+0.36 <b>-0.91</b>	-0.13 -0.63	+0.34 -0.66	+0.03 -0.07
$n_{\text{Gd}} - \delta$	0.00	<b>-9.92</b>	<b>-9.89</b>	<b>-9.93</b>	<b>-9.90</b>	-
$\Delta t_{\text{DAQ}} + \delta$	0.00	<b>+0.99</b>	<b>+1.70</b>	+0.99	<b>+1.70</b>	0.00
$1/\epsilon_{\text{NMM}}$	0.00	<b>+5.33</b>	<b>+5.31</b>	<b>+5.34</b>	<b>+5.32</b>	-
Sum	+0.10 -0.39	+13.39 -18.57	+17.59 -21.67	+13.36 -18.26	+17.55 -21.35	+0.12 -0.07
MT						
$G_{M50} \pm \delta$	<b>+0.51</b> <b>-0.62</b>	<b>+1.12</b> <b>-1.12</b>	<b>+1.23</b> <b>-1.30</b>	+0.61 -0.50	+0.72 -0.69	+0.15 -0.18
$T_{M50} \pm \delta$	-0.15 +0.16	-0.28 +0.35	-0.26 +0.45	-0.13 +0.19	-0.12 +0.29	-0.04 +0.05
$G_{M51} \pm \delta$	<b>+0.94</b> <b>-1.02</b>	+0.30 -0.36	+0.16 -0.21	-0.63 +0.66	-0.77 +0.82	+0.01 +0.01
$T_{M51} \pm \delta$	<b>-4.09</b> <b>+5.03</b>	<b>-1.39</b> <b>+1.48</b>	<b>-0.84</b> <b>+0.79</b>	<b>+2.78</b> <b>-3.36</b>	<b>+3.35</b> <b>-4.00</b>	-0.01 +0.06
$1/\epsilon_{\text{MT}}$	<b>+13.61</b>	<b>+13.53</b>	<b>+13.48</b>	+0.00	+0.00	-
Sum	+20.25 -5.88	+16.78 -3.15	+16.11 -2.61	+4.25 -4.62	+5.18 -5.58	+0.28 -0.22
Sum	+25.94 -8.22	+35.77 -24.38	+39.23 -27.15	+17.65 -23.60	+22.73 -27.87	+0.40 -1.47
Theoretical uncertainties						
Standard configuration	<b>+0.20</b>	<b>+0.81</b>	<b>+1.13</b>	+0.67	+0.99	<b>+2.24</b>
APS	<b>-0.20</b>	<b>-2.21</b>	<b>-2.85</b>	<b>-1.93</b>	<b>-2.58</b>	<b>-2.24</b>
GCM	-	<b>+1.40</b>	<b>+1.72</b>	+1.26	<b>+1.58</b>	-
Sum	$\pm 0.20$	$\pm 2.21$	$\pm 2.85$	$\pm 1.93$	$\pm 2.58$	$\pm 2.24$
Sum	+26.32 -8.61	+38.77 -27.39	+42.60 -30.51	+21.15 -27.10	+26.74 -31.88	+2.92 -3.99

The alternative muon parameter set is denoted as APS and the alternative gamma cascade model as GCM. Statistically significant deviations are printed in bold. For details see text

**Table 5.11** Statistical, systematic, and theoretical uncertainties for  $X$ ,  $R_{n,\text{eff}}$ ,  $\epsilon_n$ ,  $\eta_{n,\text{cas}}$ ,  $\eta_{n,\mu}$ , and  $Y_{\text{ext}}$  relative to the respective average value

	$\delta X$ (%)	$\delta R_{n,\text{eff}}$ (%)	$\delta \epsilon_n$ (%)	$\delta \eta_{n,\text{cas}}$ (%)	$\delta \eta_{n,\mu}$ (%)	$\delta Y_{\text{ext}}$ (%)
Statistical uncertainty						
	$\pm 0.04$	$\pm 0.25$	$\pm 0.54$	$\pm 0.95$	$\pm 0.55$	$\pm 0.30$
Systematic uncertainties						
Flux normalization						
Numerical	-0.01	<b>-0.81</b>	+0.05	-0.18	<b>-0.69</b>	<b>-0.72</b>
$\eta + \delta$	-0.01	<b>-0.28</b>	-0.02	-0.08	-0.25	-0.22
$w_c \pm \delta$	$\pm 0.00$	+0.04 +0.08	-0.04 -0.07	-0.04 +0.04	$\pm 0.00$	+0.04 +0.08
$\dot{\phi}_{\text{ref}} \pm \delta$	$\pm 0.00$	<b>+5.53</b> <b>-1.73</b>	-0.06	$\pm 0.00$	$\pm 0.00$	+0.06 +0.06
Sum	+0.00	+5.64	+0.05	+0.04	+0.00	+0.23
	-0.02	-2.81	-0.25	-0.30	<b>-0.94</b>	<b>-0.94</b>
NMM						
$\alpha_{440}^{-1} \pm \delta$	$\pm 0.00$	+0.12 +0.10	<b>+1.35</b> <b>-2.05</b>	+0.48 -0.56	<b>+1.48</b> <b>-1.91</b>	+0.16 +0.12
$kB \pm \delta$	$\pm 0.00$	+0.10 <b>+0.26</b>	<b>-1.03</b> +0.39	-0.31 +0.44	<b>-0.83</b> <b>+0.56</b>	+0.18 +0.18
$G_N \pm \delta$	$\pm 0.00$	$\pm 0.06$	<b>+3.14</b> <b>-3.88</b>	+0.86 -1.14	<b>+3.16</b> <b>-3.77</b>	+0.06 +0.06
$T_N \pm \delta$	$\pm 0.00$	$\pm 0.06$	<b>-4.40</b> <b>+4.98</b>	<b>-1.31</b> +1.33	<b>-4.28</b> <b>+4.97</b>	+0.06 +0.06
$\Delta t_{\text{bin}} \pm \delta$	$\pm 0.00$ -0.01	<b>+0.65</b> <b>-0.64</b>	-0.30 -0.27	+0.47 -0.04	+0.34 <b>-0.66</b>	+0.63 <b>-0.39</b>
$n_{\text{Gd}} - \delta$	-	-	<b>-10.04</b>	<b>-19.86</b>	<b>-9.90</b>	-
$\Delta t_{\text{DAQ}} + \delta$	0.00	+0.06	<b>+1.67</b>	-0.71	<b>+1.70</b>	-
$1/\epsilon_{\text{NMM}}$	-	-	<b>+5.40</b>	<b>+10.67</b>	<b>+5.32</b>	+0.06
Sum	+0.01	+1.51 -0.64	+16.92 -21.96	+14.96 -23.22	+17.55 -21.35	+1.55 -0.39
MT						
$G_{M50} \pm \delta$	<b>+0.06</b> <b>-0.06</b>	<b>+1.28</b> <b>-1.27</b>	-0.07 -0.01	+0.11 -0.19	<b>+0.72</b> <b>-0.69</b>	<b>+0.73</b> <b>-0.61</b>
$T_{M50} \pm \delta$	-0.02	-0.20	-0.06	+0.01	-0.12	-0.04
$G_{M51} \pm \delta$	+0.02	<b>+0.49</b>	-0.04	+0.10	+0.29	<b>+0.31</b>
$G_{M51} \pm \delta$	-0.02	<b>+0.28</b>	-0.12	-0.14	<b>-0.77</b>	<b>-0.63</b>
$T_{M51} \pm \delta$	<b>+0.07</b> <b>-0.09</b>	<b>-1.62</b> <b>+1.37</b>	<b>+0.83</b> <b>-0.60</b>	+0.56 -0.68	<b>+3.35</b> <b>-4.00</b>	<b>+2.42</b> <b>-3.31</b>
$1/\epsilon_{\text{MT}}$	-	<b>+13.32</b>	-	$\pm 0.00$	$\pm 0.00$	$\pm 0.00$
Sum	+0.16 -0.18	+16.74 -3.40	+0.94 -0.91	+0.94 -1.01	+5.18 -5.58	+4.14 -4.59
Sum	+0.17 -0.21	+23.90 -6.86	+17.91 -23.12	+15.94 -24.53	+22.73 -27.87	+5.92 -5.92
Theoretical uncertainties						
Standard configuration	+0.01	<b>+2.30</b>	-0.42	+0.71	<b>+0.99</b>	<b>+2.08</b>
APS	-0.01	<b>-2.30</b>	+0.24	-0.24	<b>-2.58</b>	<b>-2.08</b>
GCM	-	-	+0.18	-0.48	<b>+1.58</b>	-
Sum	$\pm 0.01$	$\pm 2.30$	$\pm 0.42$	$\pm 0.71$	$\pm 2.58$	$\pm 2.08$
Sum	+0.22 -0.26	+26.44 -9.41	+18.87 -24.08	+17.61 -26.20	+25.86 -30.99	+8.31 -8.31

The alternative muon parameter set is denoted as APS and the alternative gamma cascade model as GCM. Statistically significant deviations are printed in bold. For details see text

We introduce the used method of error estimation first with the rates  $R_{x,MC}$  (Eq. 5.62), then it is applied also to the ratios  $\eta_{h,x}$  (Eq. 4.31), scaled rates  $\tilde{R}_{x,MC}$  (Eq. 5.68),  $R_{n,eff}$  (Eq. 5.72),  $Y_{ext}$  (Eq. 5.73b),  $\langle E_\mu \rangle$  (Eq. 5.74),  $\langle X \rangle$  (Eq. 5.75b), and  $\epsilon_n$  (Eq. 5.76).

As defined in Eq. 5.62, the rates  $R_{x,MC}$  depend only on the candidates  $n_{x,ic}$  and the live-times  $T_{MC,ic}$ . Based on the definitions in Sects. 4.3 and 5.3.3, we expect that the  $n_{x,ic}$  are positively correlated with the  $T_{MC,ic}$ , albeit the determination of the actual correlation coefficient is a task for future work. In this work, we approximate the uncertainty as uncorrelated, therefore overestimate it [19]:

$$\delta \hat{R}_{x,MC}^{\text{stat}} \leq \sqrt{\sum_{c=+,-} \sum_{i=0}^3 \frac{\hat{n}_{x,ic}(\hat{T}_{MC,ic}^2 + \hat{n}_{x,ic}(\delta \hat{T}_{MC,ic}^{\text{stat}})^2)}{\hat{T}_{MC,ic}^4}} \quad (5.78)$$

This approximation is justified, as the statistical uncertainty is a minor contribution to the combined uncertainty, as will be shown later. We calculate the  $\delta \hat{R}_{x,MC}^{\text{stat}}$  with respect to the standard configuration: The statistical uncertainties  $\delta \hat{T}_{ic}^{\text{stat}}$  on the live-time are listed in Table 5.5, and for the counted candidates  $n_{ic}$  we take the Poissonian standard deviation as statistical uncertainty, i.e.  $\delta \hat{n}^{\text{stat}} = \sqrt{\hat{n}}$  listed in Table 5.9.

The systematic uncertainties considered in this work are associated with the chosen values for the 14 nuisance parameters of the simulation, the numerical accuracy of the weights  $w_i$  (Eq. 5.15b), and the deviation between detector response model and reference measurement. Tables 5.10 and 5.11 list the resulting uncertainties.

The considered nuisance parameters  $\mathbf{p} = \{p_j\}_{j=0,\dots,13}$  are: The parameters of the detector response model  $G_N$ ,  $T_N$ ,  $kB$ ,  $\alpha_{440}^{-1}$  for the NMM,  $G_{M50}$ ,  $T_{M50}$  for the muon module 50,  $G_{M51}$ ,  $T_{M51}$  for the muon module 51 (Table 5.7), the DAQ window width  $\Delta t_{\text{DAQ}}$  (Eq. 5.41), the time binning  $\Delta t_{\text{bin}}$  (Eq. 5.29b), the muon transmission probabilities  $\eta_i$  (Table 5.4), the charge ratio  $w_+/w_-$  of the incident muons (Table 5.4), the reference muon flux  $\dot{\phi}_{\text{ref}}$  (Eq. 5.26), and the gadolinium content  $n_{\text{Gd}}$  (Eq. 5.1). As explained in Sect. 5.4.3, the effective resolutions  $R_N$ ,  $R_{M50}$ , and  $R_{M51}$  of the detector response model do not affect the event rate. We assume that the experimental shift in the attenuation length  $\alpha_{440}^{-1}$  was already compensated by the increased PMT gain (Sect. 4.4.3) in the experiment. Therefore, it is omitted in this consideration.

We calculate the upper and lower limit of the systematic uncertainty of a given quantity  $n(\mathbf{p})$  separately via the *shift method* as proposed by J. Heinrich and L. Lyons [35] and add the individual contribution  $\delta R_{x,ic}^{\text{sys}}$  linearly:

$$\delta R_{x,MC}^{\text{sys}} = \sum_j \sum_{i,c} \delta R_{x,ic}^{\text{sys}}(p_j) \quad (5.79a)$$

$$\delta R_{x,ic}^{\text{sys}}(p_j) = \frac{\partial n_{x,ic}(\mathbf{p})}{\partial p_j} \delta p_j \frac{1}{T_{MC,ic}} \text{ for } x = \mu, \text{ cas, n} \quad (5.79b)$$

$$\frac{\partial n_{ic}(\mathbf{p})}{\partial p_j} \delta p_j \approx n_{ic}(\hat{p}_0, \dots, \hat{p}_j \pm \delta p_j, \dots, \hat{p}_{13}) - n_{ic}(\hat{\mathbf{p}}) \quad (5.79c)$$

J. Heinrich and L. Lyons proposed to add the  $\delta R_{x,ic}^{\text{sys}}$  quadratically, but mentioned that this is not correct in case of asymmetric uncertainties. R. Barlow indicates in [8, 9] that a quadratic summation in this case underestimates the combined error. As Tables 5.10 and 5.11 shows the  $\delta R_{x,ic}^{\text{sys}}$  are asymmetric due to the non-linearity of  $n_{x,ic}(\mathbf{p})$ . We approximate the detailed calculation of R. Barlow with a linear summation under consideration of the algebraic sign and overestimate therefore the uncertainty.

The best fitting parameters  $\hat{p}_j$  for the detector response models are listed in Table 5.7, together with their RMS values, which we take as measure of the shifts  $\delta p_j$ . Additionally, the lower shift of the threshold parameter  $T_N$  is increased by 1.5 % to consider the experimental shift, as discussed in Sect. 4.4.4.

For the DAQ window width  $\Delta t_{\text{DAQ}}$  we take as shift the difference of 3.97  $\mu\text{s}$  between the 56  $\mu\text{s}$  used in the simulations and the upper limit of the experimental measured 59.97  $\mu\text{s}$ , see Sect. 4.4.4.

We do not have an estimator for the uncertainty of the standard time binning (10 ns, Sect. 5.4.2). Here we assume a maximal variation of  $\pm 50\%$ .

Each of the above discussed uncertainties  $\partial n_{ic}(\mathbf{p})/\partial p_j$  is evaluated from the data sets of muon-induced neutrons, by repeating the light propagation and event building stage of the simulation with the shifted parameter  $\hat{p}_j \pm \delta p_j$  instead of the best fitting parameter  $\hat{p}_j$ .

The influence of the muon transmission probabilities  $\eta_i$ , the charge ratio  $w_c$  of the incident muons, and the reference muon flux  $\dot{\Phi}_{\text{ref}}$  are again estimated by repeating the normalization of the data sets, as described in Sects. 5.3.2 and 5.3.3, with shifts according to the systematic uncertainties of the individual parameters. For the charge ratio the correlation  $w_+ + w_- = 100\%$  is considered.

To estimate the influence of the numerical accuracy of the weights  $w_i$  (Eq. 5.15b) the normalization was repeated with the weights analytically calculated in MATHEMATICA instead of the numerical evaluation, see Sect. 5.3.2. The difference between both sets of values are linearly added as contribution to Eq. 5.79a.

The uncertainty introduced by the gadolinium content  $n_{\text{Gd}}$  is estimated by the experimental shift in the capture time  $\tau_{\text{cap}}$  (Eq. 4.8): as discussed in Sect. 4.4.2, the measured shift in  $\tau_{\text{cap}}$  is equivalent to a shift in  $n_{\text{Gd}}$ . A calculation of the resulting uncertainty in  $R_{x,MC}$  via the shift method would require a repetition of the time consuming neutron production, transport, and capture in the first stage of the simulation with shifted gadolinium content  $n_{\text{Gd}} \pm \delta n_{\text{Gd}}$ . To save time, we assume that the *relative* shift in the detection efficiency of muon-induced neutrons is approximately the same as the relative shift of the detection efficiency for AmBe,  $\delta \epsilon_{\text{AmBe}} = -10\%$  (Eq. 4.24).

The influence of the reduced detection efficiency on  $R_{n,MC}$  and  $R_{\text{cas},MC}$  depends on the probability to detect  $M_{n,\text{can}}$  neutron candidates for  $M_n$  incident neutrons per Geant4 event. In general this has to be obtained from simulations. However, it is reasonable to assume, that the probability for a constant  $M_n$  is binomially distributed  $P = P_B(m_{n,\text{can}}; m_n, \epsilon_n)$  with a detection efficiency  $\epsilon_n$ . Within this ansatz, the total amount of detected neutron candidates is proportional to the expectation value  $m_n \epsilon_n$  and hence linear in  $\epsilon$ . Assuming that this behaviour remains the same for variable  $n$ ,

we use:

$$\delta R_{n,MC}^{\text{sys}}(\hat{n}_{\text{Gd}} - \delta n_{\text{Gd}}) \approx \delta \epsilon_{\text{AmBe}} \hat{R}_{n,MC} \quad (5.80)$$

As a neutron cascade candidate has to have at least one neutron candidate,  $R_{n,MC}$  is proportional to  $1 - P_B(0; m_n, \epsilon_n) = 1 - (1 - \epsilon_n)^{m_n}$ . The dependencies of  $R_{n,MC}$ ,  $R_{\text{cas},MC}$  on  $\epsilon$  are therefore not identical in general, and simulations are needed. We overestimate the influence of  $\epsilon_{\text{AmBe}}$  on  $R_{\text{cas},MC}$  with a linear approximation and use:

$$\delta R_{\text{can},MC}^{\text{sys}}(\hat{n}_{\text{Gd}} - \delta n_{\text{Gd}}) \lesssim \delta \epsilon_{\text{AmBe}} \hat{R}_{\text{can},MC} \quad (5.81)$$

Contrary to  $R_{n,MC}$ ,  $R_{\text{cas},MC}$ , the rate of simulated muon candidates  $R_{\mu,MC}$  is independent from  $n_{\text{Gd}}$ , as it is only determined from the simulated muon telescope events based on the energy deposits on modules 50, 51 via ionization.

The remaining difference between the detector response model and the corresponding reference measurements (Sect. 5.4.4) is considered via the simulation efficiencies  $\epsilon_{\text{NMM}}$  (Eq. 5.52b) and  $\epsilon_{\text{MT}}$  (Eq. 5.54) as additional linear contribution

$$\delta R_{x,MC}^{\text{sys}}(\epsilon_y) = \left( \frac{1}{\epsilon_y} - 1 \right) \hat{R}_{x,MC} \quad \text{with } x = \mu, \text{ cas, n; y=NMM, MT} \quad (5.82)$$

to the systematic uncertainty Eq. 5.79a.

All rates  $R_{n,MC}$ ,  $R_{\text{cas},MC}$ , and  $R_{\mu,MC}$  depend on  $\epsilon_{\text{MT}}$ , as a neutron candidate or a neutron cascade candidate requires a coincidence with a muon candidate, see Sect. 4.3. Contrary, the definition of a muon candidate is independent from the NMM. Hence only the rates  $R_{n,MC}$  and  $R_{\text{cas},MC}$  depend on  $\epsilon_{\text{NMM}}$ .<sup>29</sup>

We introduce theoretical uncertainties as uncertainties in the theoretical models used for the incident flux of atmospheric muons and for the neutron capture on gadolinium. To study this uncertainties we consider the *alternative parameter set* (APS) of the incident flux of atmospheric muons, see Sect. 5.3.2, and an alternative *gamma cascade model* (GCM) for the neutron capture on gadolinium, see Sect. 5.4.1.

As proposed by J. Heinrich and L. Lyons [35], as final central value the average  $\bar{R}_{x,MC}$  over the standard configuration and the alternative models is stated:

$$\bar{R}_{x,MC} = \frac{\hat{R}_{x,MC} + R_{x,MC}^{\text{APS}} + R_{x,MC}^{\text{GCM}}}{3} \quad (5.83)$$

---

<sup>29</sup> We note, that  $\epsilon_{\text{NMM}}$  and  $\epsilon_{\text{MT}}$  were determined by calibrating the MC simulation to *independent* measurements of neutrons and muons in Sect. 5.4.4. However, neutrons are clearly *correlated* with muons in case of muon-induced neutrons. This raises the question, whether the independent calibration of the MC model to muons and neutrons is suitable in this case. However, no ‘out of the box’ calibration source for muon-induced neutrons exists. Furthermore, one can interpret the main objective of this work as to establish the neutron production in lead by atmospheric muons as such a calibration source, at least for simulations concerning the LSM. Therefore, the agreement within the combined uncertainty between the simulated and measured neutron yield in Fig. 6.1 will show the suitability of this approach, at least as an approximation.

The theoretical uncertainty is given as the linear sum of the deviation towards the average under consideration of the algebraic sign, leading to:

$$\delta R_{x,MC}^{\text{theo}} = |\hat{R}_{x,MC} - \bar{R}_{x,MC}| + |R_{x,MC}^{\text{APS}} - \bar{R}_{x,MC}| + |R_{x,MC}^{\text{GCM}} - \bar{R}_{x,MC}| \quad (5.84)$$

As statistical and systematic uncertainties we assume  $\delta \bar{R}^{\text{stat}} = \delta \hat{R}^{\text{stat}}$  and  $\delta \bar{R}^{\text{sys}} = \delta \hat{R}^{\text{sys}}$ .

For the muon flux, the weights  $w_i$  (Eq. 5.15b) and live-times  $T_{MC,ic}$  are also calculated for the alternative parameter set, listed in Tables 5.4 and 5.5, respectively. By using these alternative weights for the normalization of the data sets, the influence of the alternative parameter set is expressed via the live-time whereas the amounts of candidates  $n_{x,ic}$  are still obtained from the simulation in standard configuration, i.e.

$$R_{x,MC}^{\text{APS}} = \sum_{ic} \frac{\hat{n}_{x,ic}}{T_{MC,ic}^{\text{APS}}} \text{ for } x = \mu, n, \text{cas}, \quad (5.85)$$

cf. Eq. 5.62. This approach is only an approximation, as only the weighting between the energy ranges of the individual data sets is varied. For a refined evaluation, also the simulation of the individual data sets has to be repeated to cover the change in the muon spectrum over the energy range of the particular data set, which is the subject for future improvements.

The difference between the two models G4NeutronHPCapture [27] and GdNeutronHPCapture [53, 70] (Sect. 5.4.1) for the gamma ray cascade of the Gd ( $n, \gamma$ ) reaction was evaluated by comparing the amount of simulated NMM events, each caused by  $10^6$  neutrons from an AmBe source:  $N_{\text{event,G4}} = 51,693$ ,  $N_{\text{event,Gd}} = 51,999$ . For both cases we take Poissonian standard deviations as statistical uncertainty on  $N_{\text{event,G4}}$ ,  $N_{\text{event,Gd}}$ . Albeit the difference between both models

$$\epsilon_{\text{GCM}} = \frac{N_{\text{event,Gd}} - N_{\text{event,G4}}}{N_{\text{event,Gd}}} \quad (5.86a)$$

$$= 0.6(6) \% \quad (5.86b)$$

is not significant, we consider it as:

$$R_{x,MC}^{\text{GCM}} = (1 - \epsilon_{\text{GCM}}) \hat{R}_{x,MC} \quad (5.87)$$

The theoretical uncertainty of the correct gamma cascade model affects only the detection of neutrons. Therefore this uncertainty is only considered for  $R_{n,MC}$ ,  $R_{\text{cas},MC}$  and not for  $R_{\mu,MC}$ .

The obtained rates of muon candidates  $R_{\mu,MC}$ , neutron cascade candidates  $R_{\text{cas},MC}$ , and neutron candidates  $R_{n,MC}$  were already given in Eqs. 5.63–5.65, respectively. Tables 5.10 and 5.11 list the individual contribution to the uncertainties relative

to the respective central values.<sup>30</sup> Due to the asymmetric nature of systematic uncertainties, we linearly combine the uncertainties and obtain at most 26, 39, and 43 % for  $\bar{R}_{\mu,MC}$ ,  $\bar{R}_{cas,MC}$ , and  $\bar{R}_{n,MC}$ , respectively.

In each case the uncertainties are dominated by the systematics with a major influence from the muon reference flux  $\dot{\Phi}_{ref}$  and the simulation efficiency of the muon telescope  $\epsilon_{MT}$ . They cancel each other in the ratios  $\eta_{n,\mu}$  (Eq. 4.31), i.e. the rates of neutron candidates relative to the rate of muon candidates. Similar, also the ratio of neutron candidates to candidates for neutron cascades  $\eta_{n,cas}$  profits from the cancellation of quantities affected with systematic uncertainties.

The statistical uncertainty on  $\eta_{n,x}$  is:

$$\delta\eta_{n,x}^{\text{stat}} = \sqrt{\left(\frac{\delta R_{n,MC}^{\text{stat}}}{R_{x,MC}}\right)^2 + \left(\frac{R_{n,MC}\delta R_{x,MC}^{\text{stat}}}{R_{x,MC}^2}\right)^2} \text{ for } x = \mu, \text{ cas} \quad (5.88)$$

By replacing  $\delta R_{x,ic}^{\text{sys}}$  with

$$\delta\eta_{n,x,ic}^{\text{sys}}(p_j) = \eta_{n,x}(p_j) - \hat{\eta}_{n,x} \text{ for } x = \mu, \text{ cas}, \quad (5.89)$$

the systematic uncertainty is calculated via Eq. 5.79a. Similarly, the theoretical uncertainty is calculated via Eq. 5.84 by replacing  $\hat{R}_{x,MC}$ ,  $\bar{R}_{x,MC}$ ,  $R_{x,MC}^{\text{APS}}$ ,  $R_{x,MC}^{\text{GCM}}$  with  $\hat{\eta}_{n,x}$ ,  $\bar{\eta}_{n,x}$ ,  $\eta_{n,x}^{\text{APS}}$ ,  $\eta_{n,x}^{\text{GCM}}$ .

Although we defined the ratios  $\eta_{n,x}$  to profit from the cancellation in the quotient, we consider three cases where we assume the cancellation would underestimate the uncertainty. In these cases we apply the following exception from the general definition of  $\delta\eta_{n,x,ic}^{\text{sys}}$ ,  $\delta\eta_{n,x}^{\text{theo}}$  given above.

As we stated above,  $\delta R_{n,MC}^{\text{sys}}$ ,  $\delta R_{cas,MC}^{\text{sys}}$  are not equally dependent on  $\delta n_{Gd}$ ,  $\epsilon_{NMM}$  (Eqs. 5.80 and 5.81); we used only the same expression  $\delta\epsilon_{AmBe}\hat{R}_{n,MC}$  to approximate an upper limit of these dependencies. Therefore we assume that the cancellation in Eq. 5.89 would underestimate the uncertainty. For  $\delta n_{Gd}$  and  $\epsilon_{NMM}$  we used instead:

$$\delta\eta_{n,cas}^{\text{sys}}(\delta n_{Gd}) = \left| \frac{\partial\eta_{n,cas}}{\partial R_{n,MC}} \delta R_{n,MC}^{\text{sys}} \right|_{p=\hat{p}} + \left| \frac{\partial\eta_{n,cas}}{\partial R_{cas,MC}} \delta R_{cas,MC}^{\text{sys}} \right|_{p=\hat{p}} \quad (5.90a)$$

$$= \left| \frac{\partial\eta_{n,cas}}{\partial R_{n,MC}} R_{n,MC} \epsilon_{AmBe} \right|_{p=\hat{p}} + \left| \frac{\partial\eta_{n,cas}}{\partial R_{cas,MC}} R_{cas,MC} \epsilon_{AmBe} \right|_{p=\hat{p}} \quad (5.90b)$$

$$= 2\hat{\eta}_{n,cas} |\delta\epsilon_{AmBe}(\delta n_{Gd})| \quad (5.90c)$$

<sup>30</sup>Please note the different meaning of *standard configuration* and *average value*, i.e. the average over the standard configuration and the alternative configurations. For example, the shift in the gadolinium content causes a decrease of  $R_{cas,MC}$  by  $-10\%$  relative to the standard configuration, but results in a decrease of  $\approx 9.9\%$  relative to the average value as listed in Table 5.10.

$$\delta\eta_{n,cas}^{sys}(\epsilon_{NMM}) = 2\hat{\eta}_{n,cas} \left| \frac{1}{\epsilon_{NMM}} - 1 \right| \quad (5.91)$$

Similar, for the contribution of the gamma cascade model, we use

$$\delta\eta_{n,cas}^{theo,GCM} = 2\hat{\eta}_{n,cas}\epsilon_{GCM} \quad (5.92)$$

based on Eq. 5.87.

The resulting uncertainties for  $\bar{\eta}_{n,x}$  are given by Eqs. 5.66 and 5.67. For  $\eta_{n,cas}$ , their linear combination is at most 26 %. It is dominated by the shift in  $n_{Gd}$ , which contributes 20 %. For  $\bar{\eta}_{n,\mu}$  the linearly combined uncertainty is at most 31 %. The correlation between the individual rates  $R_{n,MC}$ ,  $R_{cas,MC}$ , and  $R_{\mu,MC}$  causes a reduction of the ratios' systematic uncertainties. This indicates that the comparison of the simulated ratios to the measured ones is a more precise way to asses Geant4 than of the comparison of the rates alone.

Derived from the  $\eta_{n,x}$ , the statistical uncertainty on the scaled rates  $\tilde{R}_{x,MC}$  (Eq. 5.68) is:

$$\begin{aligned} \left( \delta\tilde{R}_{x,MC}^{stat} \right)^2 &= \left( \frac{\delta R_{\mu,meas}^{stat}}{R_{\mu,MC}} R_{x,MC} \right)^2 + \left( \frac{R_{\mu,meas} \delta R_{x,MC}^{stat}}{R_{\mu,MC}} \right)^2 \\ &+ \left( \frac{R_{\mu,meas} \delta R_{\mu,MC}^{stat}}{R_{\mu,MC}^2} R_{x,MC} \right)^2 \end{aligned} \quad (5.93)$$

The theoretical and systematic uncertainties are estimated in the same way as previously for the unscaled quantities, where Eq. 5.79a is modified by replacing  $\delta R_{x,MC}^{sys}$  with

$$\delta\tilde{R}_{x,ic}^{sys}(p_j) = \tilde{R}_{x,MC}(p_j) - \hat{\tilde{R}}_{x,MC}, \quad (5.94)$$

except that  $\epsilon_{MT}$  and  $\delta\dot{\phi}_{ref}$  do not contribute due to their cancellation.

As expected, the resulting values (Eqs. 5.69 and 5.70) show the reduced systematic uncertainties known from the  $\eta_{n,x}$ , whereas the statistical uncertainty is slightly increased due to the contribution from measured rate of muon candidates  $R_{\mu,meas}$ . The linearly combined uncertainty is at most 27 % for  $\bar{R}_{cas,MC}$  and at most 32 % for  $\bar{R}_{n,MC}$ . Hence, the scaled rates are in total about 1.3 times more precise than the unscaled ones, even if the statistical uncertainty is increased.

The handling of  $\langle E_{\mu} \rangle$ ,  $\langle X \rangle$ ,  $\bar{R}_{n,eff}$ , and  $\bar{Y}_{ext}$  is similar to the handling of  $\bar{R}_{x,MC}$ , except that we assume no dependence on the gadolinium content  $n_{Gd}$  and on the NMM simulation efficiency  $\epsilon_{NMM}$ . We assume also that  $\epsilon_{MT}$  is constant over the muon spectrum and therefore does not affect  $\langle E_{\mu} \rangle$ ,  $\langle X \rangle$ . The handling of  $\bar{\epsilon}_n$  is similar to the handling of  $\bar{\eta}_{n,\mu}$ .

For the effective neutron rate  $R_{n,\text{eff}}$  (Eq. 5.71) the statistical uncertainty is

$$\delta R_{n,\text{eff}}^{\text{stat}} = \sqrt{\sum_{c=+,-} \sum_{i=0}^3 \frac{T_{\text{MC},ic}^2 (N_{\text{in},ic} + N_{\text{out},ic}) + \delta T_{\text{MC},ic}^{\text{stat}} {}^2 (N_{\text{out},ic} - N_{\text{in},ic})}{T_{\text{MC},ic}^4}}, \quad (5.95)$$

with the Poissonian standard deviations as statistical uncertainties on  $N_{\text{out},ic}$  and  $N_{\text{in},ic}$ . Again we approximate the statistical uncertainty as uncorrelated. As  $R_{n,\text{eff}}$  is defined for the cases when a muon is detected, its systematic uncertainty is not independent from the nuisance parameters of the detector response model. Indeed, it depends significantly on the detector response model for the modules 50 and 51, the model of the muon flux and its normalization. Because muon module 51 uses the liquid scintillator of the NMM as its active volume, it depends also on the attenuation length and the quenching factor. The biggest contribution to the systematic uncertainty is the simulation efficiency  $\epsilon_{\text{MT}}$ . In total, the linearly combined uncertainty of Eq. 5.72 is at most 26 %, similar to the one of the muon candidate rate  $R_{\mu,\text{MC}}$ .

Similar to  $R_{n,\text{eff}}$ , also the external neutron yield  $Y_{\text{ext}}$  depends on the detector response model. Albeit it represents the yield in case of an ideal NMM, it is affected by the response model for the muon telescope, as its influence on  $R_{n,\text{eff}}$  and  $R_{\mu,\text{MC}}$  is not canceled completely. Also the energy of the detected muon candidates is affected by the uncertainty in the response model of the muon telescope. Consequently, Eq. 5.73b has a combined linear uncertainty of 8.3 %.

To describe the statistical uncertainties of  $\overline{\langle E_{\mu} \rangle}$  and  $\overline{\langle X \rangle}$  we take the standard deviation of the distributions mean. Their systematic uncertainties are far less affected by the detector response model: For the average muon energy  $\overline{\langle E_{\mu} \rangle}$  the combined uncertainty of Eq. 5.74 is 4.0 %. The most significant contributions are uncertainties in the muon flux parameters and normalization, as they affect the muon energy spectrum directly.

The average target thickness  $\overline{\langle X \rangle}$  along the muon track is nearly independent from the considered nuisance parameters, except for  $G_{\text{M50}}$  and  $T_{\text{M51}}$ . This parameter combination affects the muon detection in both muon modules and hence the minimal muon track length measurable by the muon telescope. The combined uncertainty of Eq. 5.75b is only 0.26 %.

For the neutron detection efficiency  $\epsilon_n$  (Eq. 5.76), the statistical uncertainty is

$$\begin{aligned} (\delta \epsilon_n^{\text{stat}})^2 = & \frac{1}{R_{n,\text{eff}}^4} \left( \sum_{c=+,-} \sum_{i=0}^3 \frac{R_{n,\text{eff}}^2 n_{n,\text{MC},ic}}{T_{\text{MC},ic}^2} \right. \\ & + \frac{(R_{n,\text{eff}} n_{n,\text{MC},ic} - R_{n,\text{MC}} (N_{\text{out},ic} - N_{\text{in},ic}))^2 (\delta T_{\text{MC},ic}^{\text{stat}})^2}{T_{\text{MC},ic}^4} \\ & \left. + \frac{R_{n,\text{MC}}^2 (N_{\text{out},ic} + N_{\text{in},ic})}{T_{\text{MC},ic}^2} \right) \end{aligned} \quad (5.96)$$

As  $\epsilon_n$  is the ratio of  $R_{n,MC}$  to  $R_{n,eff}$  (Eq. 5.76), its systematic uncertainties are well described by the difference between them. This is especially clear for  $G_{M50}$  where both contributions nearly cancel each other. Consequently, the biggest single contribution is due to  $n_{Gd}$ , which only affects  $R_{n,MC}$ . This results in a linearly combined uncertainty of at most 24 % (Eq. 5.77).

As a future work, a further reduction of the uncertainty of the simulated quantities could be envisaged. Several approaches are possible: The statistical uncertainties can be reduced by considering the positive correlation between  $n_{x,ic}$  and  $T_{ic}$ . However, this would not affect significantly the combined uncertainty, as it is dominated by the systematic uncertainties.

One of the biggest individual contribution to the systematic uncertainty, up to 20 % for  $\eta_{n,cas}$ , is the shift in the gadolinium content of the liquid scintillator. A further increase in the precision seems feasible by correcting the efficiency based on the AmBe monitoring data. As shown in Sect. 4.4.2, the gadolinium content can be determined from the AmBe monitor measurements. Hence, the shift in  $n_{Gd}$  as function of the measurement time can be deduced and consequently also the shift in the detection efficiency over time. Multiplying the simulated rates with a time weighted efficiency should therefore correct the results for the gadolinium shift. To avoid approximations, the detection efficiency as function of  $n_{Gd}$  has to be obtained from repeating the complete neutron production, propagation, and capture simulation for different  $n_{Gd}$ .

As already mentioned in Sect. 5.4.4, a more sophisticated detector response model may better describe module 51, leading to a more accurate simulation efficiency  $\epsilon_{MT}$  and reduced uncertainties in the model parameter. For the NMM we see no obvious possibility to reduce the parameter uncertainty, as the detector response model seems to agree well with reference measurements.

However, even in the view of the above uncertainties, it should be noted that this work is a significant improvement compared to the often quoted uncertainty of a factor two for Monte Carlo simulations of muon-induced neutron production, see the discussion in Sect. 3.5.4.

To summarize, we could determine accurately the statistical, systematic, and theoretical uncertainties of the simulated quantities. We considered the influence of the flux normalization, the detector response model, and alternative models for the muon spectrum and for the gamma cascade. By defining appropriate ratios between the simulated absolute rates, the relative uncertainties could be reduced by a factor of 1.3, i.e. from 43 % for  $\bar{R}_{n,MC}$  to 32 % for  $\bar{\tilde{R}}_{n,MC}$ . This use of the correlation between the rates will enable a more precise assessment of Geant4 in Sect. 6.1.

### 5.5.5 *Background Estimation*

As discussed in Sect. 4.1.2, ambient neutrons and the radioactive contamination of the liquid scintillator have to be considered as sources of background. Based on the

full geometry implementation<sup>31</sup> (Sect. 5.1), physics list (Sect. 5.2), and the detector response model with the best fitting parameter set (Sect. 5.4), we estimate the background contribution to neutron candidates and neutron cascade candidates for multiple hit and coincident hit signatures. By comparing the expected number of background events to each other, we will show the superiority of the coincident hit signature over the multiple hit signature and thereby justify their use in this work.

To match the multiple hit signature of a candidate for neutron cascades, NMM events require at least one secondary. To match the coincident hit signature, they must be in coincident with a muon telescope event. In both cases the secondary hits are the neutron candidates, see Sect. 4.3 for the definitions. Valid background to NMM events can be produced by ambient neutrons, <sup>214</sup>Bi-decays, and accidental coincidences in the following ways:

Ambient neutrons produce NMM events by nuclear recoils during their thermalization (primary hit) and subsequent capture in the active volume of the NMM (secondary hit) (Sect. 4.2.1).

Uranium contamination of the liquid scintillator can lead to NMM events with at least one secondary via the <sup>214</sup>Bi–<sup>214</sup>Po stage of the uranium decay chain [16, 54, 68]; the  $\beta^-$ -decay of <sup>214</sup>Bi with the endpoint energy of 3.27 MeV can act as primary hit. With the half-life of 164.3  $\mu$ s the <sup>214</sup>Po daughter nucleus undergoes a subsequent  $\alpha$ -decay with  $E_\alpha = 6.61, 6.90$ , or 7.69 MeV, acting as secondary hit.

Both processes can therefore easily create candidates for neutron cascades and neutrons in the multiple hit signature and thus contribute to the background rate  $R_{\text{bg}}$ . However, to match the coincidence signature, also the muon telescope must trigger. Due to the high threshold of muon module 51 of the muon telescope, it is highly unlikely that these background processes can match the coincidence signature and  $R_{\text{bg}} = 0$  is expected.

An additional option is the accidental coincidence between a muon leading to a muon telescope event and an NMM event with at least one hit, caused by an ambient neutron or a decay of <sup>214</sup>Bi. An NMM event with only one hit alone, the primary hit, would not qualify as a neutron cascade candidate, neither via the multiple hit signature nor via the coincident hit signature. It needs the accidental coincidence with a muon telescope event to qualify. The rate  $R_{\text{acc}}$  of these accidental coincidence events is [34]

$$R_{\text{acc}} = 2 \frac{N_{\text{prim}}}{T_{\text{MC}}} R_\mu \tau_{\text{DAQ}} \quad (5.97)$$

where  $R_\mu = 5.788 \text{ d}^{-1}$  is the measured muon rate (Sect. 4.5),  $\tau_{\text{DAQ}} = 59.3 \mu\text{s}$  (Sect. 4.4.4) is the measured DAQ window width, and  $N_{\text{prim}}$  is the number of NMM events with at least the primary hit caused by background sources, deduced from dedicated Geant4 simulations with live-time  $T_{\text{MC}}$ , see Tables 5.13 and 5.14.

---

<sup>31</sup>For the following results the muon veto was simulated in its *closed* configuration, as it is during the physics run of EDELWEISS. Auxiliary simulations on a smaller statistics show that the event rate due to ambient neutrons is reduced to  $R_{\text{open}}/R_{\text{close}} = 68\%$  in the *open* veto configuration. In this configuration the EDELWEISS polyethylene shield is placed above the neutron counter and shields it against ambient neutrons from the ceiling.

In the following, we will discuss these simulations and then derive the related rates  $R_{\text{acc}}$  and  $R_{\text{bg}}$ . To estimate  $R_{\text{bg}}$  and  $N_{\text{prim}}$  due to ambient neutrons, we start tracking neutrons in the concrete wall of the implemented LSM geometry, as suggested by V. A. Kudryavtsev [41]. Neutrons from the rock were neglected as they are mostly absorbed by the concrete [41]. The decay of uranium and thorium together with the spontaneous fission of  $^{238}\text{U}$  are considered as neutron sources, with a specific activity  $A_{\text{U}}$ ,  $A_{\text{Th}}$  per volume  $V$  of

$$\frac{dA_{\text{U}}}{dV} = 1.009 \times 10^{-7} \text{ cm}^{-3} \text{ s}^{-1} \quad (5.98)$$

$$\frac{dA_{\text{Th}}}{dV} = 1.331 \times 10^{-8} \text{ cm}^{-3} \text{ s}^{-1}. \quad (5.99)$$

The activities and the energy spectrum of the resulting neutrons are derived from simulations with the SOURCES4A [67] package and were provided by V. A. Kudryavtsev [41, 43, 63]. For each source,  $N_{\text{n,amb}}$  neutrons were started isotropically and uncorrelated in the concrete volume ( $V = 3.37968 \times 10^8 \text{ cm}^3$ ) via the *General Particle Source* (GPS) interface of Geant4 with energies sampled from the provided energy spectra and normalized to their activity. Our subsequent simulation considers therefore contributions of multiple neutrons per event from the spontaneous fission of  $^{238}\text{U}$ , but treats the emitted neutrons as uncorrelated. For both cases, neutrons from uranium and thorium decays, the highest neutron energy considered is 10 MeV.

Similar to the definition of the muon fluence in Sect. 5.3.3, the fluence was again defined relative to the surface of the liquid scintillator, projected towards the direction of the incident neutron (Eq. 5.27a), and the live-time was normalized relative to the source activities Eqs. 5.98 and 5.99:

$$T_{\text{MC},x} = \frac{N_{\text{n,amb}}}{\frac{dA_x}{dV} V} \quad x = \text{U, Th} \quad (5.100)$$

This results in a total incident flux of

$$\dot{\Phi}_{\text{amb,n}} = 3.4492(72) \text{ cm}^{-2} \text{ s}^{-1} \quad (5.101)$$

ambient neutrons coming to the liquid scintillator of the NMM. The statical uncertainty was calculated similarly to Eq. 5.27b.

Table 5.12 lists the partial fluxes for each source and for the six surfaces of the NMM's active volume. The reduced flux through the bottom side and the east side of the liquid scintillator, compared to the top and west side, is expected: the bottom of the liquid scintillator is shielded by the lead target and the east by the polyethylene shield of EDELWEISS.

The total flux (Eq. 5.101) is in agreement with the  $2.0 \times 10^{-6}$  to  $6.2 \times 10^{-6} \text{ cm}^{-2} \text{ s}^{-1}$  measured by S. Rozov et al. [59] throughout the LSM, but it is higher than the  $2.0(2) \times 10^{-6} \text{ cm}^{-2} \text{ s}^{-1}$  [59] measured at the position of the neutron counter

**Table 5.12** Fluxes  $\dot{\Phi}_n$  of ambient neutrons, entering through the surfaces of the liquid scintillator in the NMM, classified for uranium and thorium decays

Source	$\dot{\Phi}_n (10^{-6} \text{ cm}^{-2} \text{ s}^{-1})$						
	Top	Bottom	North	South	East	West	All
Th	0.1227(10)	0.0730(6)	0.0091(9)	0.0090(6)	0.0548(10)	0.1465(13)	0.415(2)
U	0.902(3)	0.5249(19)	0.064(2)	0.0621(19)	0.395(3)	1.086(5)	3.034(7)
Sum	1.024(3)	0.598(2)	0.073(2)	0.071(2)	0.450(3)	1.233(5)	3.449(7)

Uncertainties are statistical only

prior to its installation (see also Sect. 4.1.2). An explanation may be the different local geometries, since S. Rozov et al. made the measurements before the neutron counter was installed, and its iron and lead parts could alter the local neutron field by absorption, production, and reflection. Therefore, the simulation of the incident neutron flux is suitable for the estimation of the expected ambient background. It supports also [49], which attests Geant4 good capabilities for low energy ( $\lesssim 5 \text{ MeV}$ ) neutron transport.

The second background source, the radioactive contamination of the liquid scintillator was modelled by randomly placing  $N_{\text{BiPo}}$  nuclei of  $^{214}\text{Bi}$  at rest in the scintillator volume and simulating the subsequent decay. We assumed that the uranium decay chain is in secular equilibrium, and that the activity of  $^{214}\text{Bi}$ -decays equals the uranium decay. As typical value for the uranium contamination we used the upper limit measured by the Borexino collaboration for pseudocumene [1, type ‘purchase grade’] as activity  $A_{214\text{Bi}}$  per mass  $m$ :

$$\frac{dA_{214\text{Bi}}}{dm} = 10^{-4} \text{ Bq kg}^{-1}, \quad (5.102)$$

For  $V = 1 \text{ m}^3$  of liquid scintillator with a density of  $0.88 \text{ g cm}^{-3}$  (Sect. 4.2.1) the simulation has a live-time of:

$$T_{\text{MC, BiPo}} = \frac{N_{\text{BiPo}}}{\frac{dA_{214\text{Bi}}}{dm} V \rho} \quad (5.103)$$

Tables 5.13 and 5.14 summarize our studies on ambient neutron background due to U, Th decays in the walls of LSM and on contamination of the liquid scintillator with  $^{214}\text{Bi}$ . Table 5.13 gives an overview of the amount of simulated Geant4 events used for the background investigation, the equivalent live-times, the amounts of NMM events with at least the primary hit, and NMM events that qualify as neutron cascade candidate according to the multiple hit signature and according to the coincident hit signature.

Based on these events, Table 5.14 lists the obtained background rate of NMM events for multiple hit signature, coincident hit signature, and accidental coincidences with incident muons.

For the experimental live-time of 964.5 days (Table 4.2), 666 events from all three background sources are expected to match the multiple hit signature.

**Table 5.13** Characteristics of used data sets: total number  $N_0$  of simulated Geant4 events, activity  $A$  of particular source, live-time  $T_{\text{MC}}$ , number of NMM events with at least a primary hit  $N_{\text{prim}}$ , number of neutron cascade candidates according to multiple hit ( $N_{\text{multiple}}$ ) and coincident hit signature ( $N_{\text{coinc}}$ )

Type	$N_0$	$A$ (Bq)	$T_{\text{MC}}$ (d)	$N_{\text{prim}}$	$N_{\text{multiple}}$	$N_{\text{coinc}}$
Th	132,532,378	4.4984	341.000(30)	51,439	50	0
U	931,149,240	34.1010	316.038(10)	348,182	172	0
$^{214}\text{Bi}$	8,400,000	0.088	1104.80(38)	1,233,036	0	0

For details see text

**Table 5.14** Rates of NMM events  $R_{\text{bg}}$  caused by ambient neutrons and  $^{214}\text{Bi}$ -decays for different signatures, and rate of random coincidences  $R_{\text{acc}}$

Source	$R_{\text{bg}}$	$R_{\text{acc}}$	
		Multiple hit signature ( $10^{-1} \text{ d}^{-1}$ )	Coincident hit signature ( $10^{-3} \text{ d}^{-1}$ )
Th	1.466(207)	$0.0^{+3.8}_{-0.0}$	1.20(2)
U	5.442(415)	$0.0^{+4.1}_{-0.0}$	8.75(16)
$^{214}\text{Bi}$	$0.000^{+0.012}_{-0.000}$	$0.0^{+1.2}_{-0.0}$	8.86(16)
Sum	6.908(464)	$0.0^{+9.1}_{-0.0}$	18.81(23)

For the sum, the errors are quadratically added, except the upper limits for the coincident hit signature which are linearly added. For details see text

Contrary, no NMM event that would match the coincident hit signature was found for the detector threshold implemented in the detector response model. Therefore, we give an upper limit at 68 % CL according to G. J. Feldman and R. D. Cousins [23], equivalent to a combined background of at most 8.8 events within the experimental live-time.

In case of accidental coincidences, the rate of a single coincidence is given, i.e. one muon in coincidence with one ambient neutron or one  $^{214}\text{Bi}$  decay. Combined, this results in 0.02 events for the experimental live-time. It is also an upper limit for the cases of  $n$ -folded coincidences between one muon and several ambient neutrons or  $^{214}\text{Bi}$  decays.

Comparing the combined background from ambient neutrons and liquid scintillator contamination, for both real and accidental coincidences, to the simulated signal rates for muon-induced neutron cascade candidates ( $0.1549 \text{ d}^{-1}$ , Eq. 5.64), the coincident signature provides a very clear signal with a lower limit on the signal-to-noise ratio of  $S/N = 17$ .

Contrary, the multiple hit signature has not such a good discriminative power, since the integral background rate is of the same order as the signal rate. An improvement is expected for higher multiplicities: as the physics of ambient neutrons and  $^{214}\text{Bi}$  decay produces only one secondary hit, background for NMM events with higher multiplicity would be the accidental coincidences only. Assuming the same order of magnitude as for the accidental coincidences with muons ( $1.88 \times 10^{-5} \text{ d}^{-1}$ , Table 5.14), this value would be below the expected signal rates even at higher multiplicities, as lowest rate evaluated in Table 6.1 is  $4 \times 10^{-4} \text{ d}^{-1}$  for  $M_{\text{n,can}} = 14$ .

In summary, the coincident signature provides a clear signal ( $S/N = 17$ ) for candidates of muon-induced neutrons. The good agreement between the simulated ambient neutron flux and literature values underlines the reliability of the simulations. In comparison with the multiple hit signature, this justifies the usage of the coincident hit signature to determine the rate of  $\mu$ -induced neutrons in this work.

### 5.5.6 Prospect to Deduce Neutron Multiplicity and Energy Spectra

The measured multiplicity (Fig. 4.20) and energy spectra (Fig. 4.19) of neutron *candidates* are convolved with the detector response. In this section, we study the prospect of future work to deconvolve the measurement and the detector response to deduce further properties of the muon-induced neutrons.

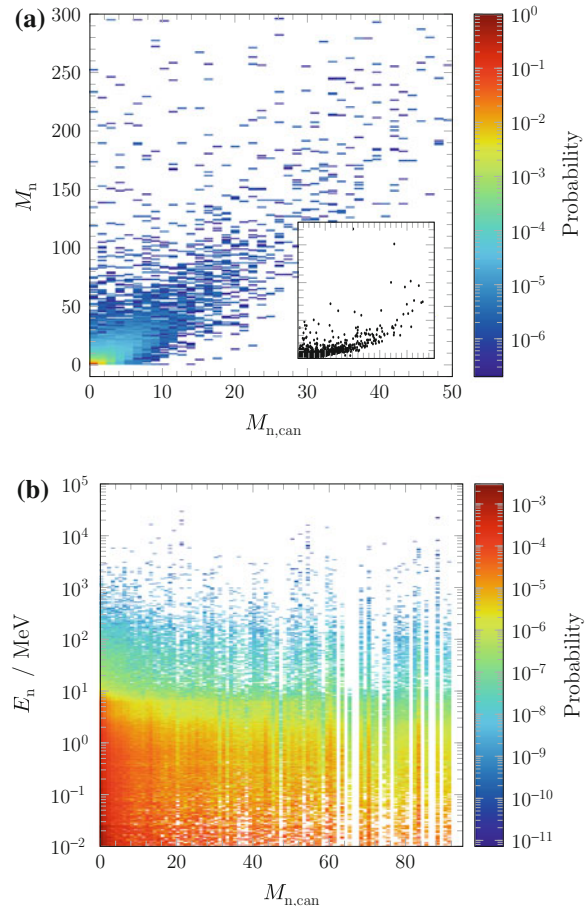
The measured multiplicity spectrum is in general not identical to the neutron multiplicity spectrum, and the differential detection efficiency is non-trivial due to the non-ideal geometry and reactions like  $^{12}\text{C}(n, x n)$ ,  $x > 1$  in the liquid scintillator of the NMM, see Sect. 4.1.3. However, the detailed simulations of the detector response in Sect. 5.4 results in Fig. 5.36a, showing the correlation between the effective neutron multiplicity  $M_n$  and the multiplicity of the detected neutron candidates  $M_{n,\text{can}}$ , see Sect. 5.5.3 for their definition. The strong relation makes an attempt promising to unfold the measured neutron multiplicity spectrum, Fig. 6.3a. However, as a first step the influence of the systematic uncertainties on the correlation has to be studied.

The task to reconstruct the neutron energy spectrum from the detected multiplicity of the neutron candidates is motivated by the following idea: High energy neutrons are likely to produce showers of secondary neutrons. Therefore the multiplicity of detected neutron candidates should be related to the energy spectrum of emitted neutrons. Indeed, as Fig. 5.36b shows, there is a relation between neutron energies and detected neutron candidates.<sup>32</sup> However, the correlation is weak: it seems that most of the neutron candidates are caused by neutrons with energies below 10 MeV, probably evaporated neutrons. Only the lowest multiplicities are weakly affected by more energetic neutrons. This may be explained as follows: high energetic neutrons pass through the NMM without capture. If the primary neutron transfers enough energy to the secondary ones, also these neutrons may be above the threshold for successful thermalization and capture. Albeit these not-thermalized, high energetic neutrons are suspected to produce proton recoils, and hence secondary hits in the NMM, most of them may be removed by the 1  $\mu\text{s}$  cut introduced to remove PMT afterpulses, see Sect. 4.3. For example a neutron with a kinetic energy of 100 MeV will pass through the detector within  $\approx 20$  ns.

---

<sup>32</sup>One may wonder, why there are gaps at high multiplicities, e.g. at  $M_{\text{can}} = 66, 67$ , albeit the statistic seems high enough within a given high multiplicity bin to span several decades in probability, e.g. for  $M_{\text{can}} = 80$ . This may be explained as follows: Albeit there are few events with a high multiplicity of neutron *candidates*, these events can still contain up to several hundred *neutrons*, cf. Fig. 5.36a.

**Fig. 5.36** Simulated correlation between neutron properties when they leave the lead target and the multiplicity  $M_{n,\text{can}}$  of detected neutron candidates (maximum 91) per Geant4 event: **a** probability as function of  $M_{n,\text{can}}$  and the effective neutron multiplicity  $M_n$  (maximum at 3594). The inset shows the whole  $M_{n,\text{can}} - M_n$ -plane up to  $100 \times 3600$  as scatter plot. **b** Probability as function of  $M_{n,\text{can}}$  and the neutron energy  $E_n$ . Both plots contain  $N = 662,122$  Geant4 events in all eight data sets, see Table 5.5, normalized to the live-time



One may speculate to remove the cut and to reject the afterpulses by other techniques, e.g. pulse shape analysis as the pulse traces of each NMM hit is recorded, but up to now this was not used. Albeit the quality of pulse shape analysis deteriorates with increasing detector volume, it is possible in large volume detectors as demonstrated in [6] and it is possible for the used scintillator BC-525 [7]. Templates for proton recoils could be constructed from the primary NMM hit of AmBe monitor data by removing the hits from gamma rays. Pure templates of hits caused by gamma rays could be obtained by the second NMM hit caused via  $\text{Gd}(\text{n}, \gamma)$  during the AmBe monitoring measurements.

Therefore, it should be quite possible to unfold the recorded multiplicity spectrum of neutron candidates to obtain the neutron multiplicity spectrum. Contrary, a reconstruction of the neutron energy spectrum is uncertain and if possible only with a considerable modified re-analysis of the measured data.

## References

1. Alimonti G et al (1998) A large-scale low-background liquid scintillation detector: the counting test facility at Gran Sasso. *Nucl Instrum Methods Phys Res Sect A* 406(3):411–426. doi:[10.1016/S0168-9002\(98\)00018-7](https://doi.org/10.1016/S0168-9002(98)00018-7)
2. Annis M, Wilkins HC, Miller JD (1954) Nuclear interaction of fast  $\mu$  mesons. *Phys Rev* (2nd Ser) 94(4):1038–1045. doi:[10.1103/PhysRev.94.1038](https://doi.org/10.1103/PhysRev.94.1038)
3. Araújo H et al (2005) Muon-induced neutron production and detection with GEANT4 and FLUKA. *Nucl Instrum Methods Phys Res Sect A* 545(1–2):398–411. doi:[10.1016/j.nima.2005.02.004](https://doi.org/10.1016/j.nima.2005.02.004). arXiv:[hep-ex/0411026](https://arxiv.org/abs/hep-ex/0411026)
4. Araújo H et al (2008) Measurements of neutrons produced by high-energy muons at the Boulby Underground Laboratory. *Astropart Phys* 29(6):471–481. doi:[10.1016/j.astropartphys.2008.05.004](https://doi.org/10.1016/j.astropartphys.2008.05.004)
5. Arnold R et al (2005) Technical design and performance of the NEMO 3 detector. *Nucl Instrum Methods Phys Res Sect A* 536(1–2):79–122. doi:[10.1016/j.nima.2004.07.194](https://doi.org/10.1016/j.nima.2004.07.194)
6. Back H et al (2008) Pulse-shape discrimination with the counting test facility. *Nucl Instrum Methods Phys Res Sect A* 584(1):98–113. doi:[10.1016/j.nima.2007.09.036](https://doi.org/10.1016/j.nima.2007.09.036)
7. Banerjee K et al (2007) Characteristics of Gd-loaded liquid scintillators BC521 and BC525. *Nucl Instrum Methods Phys Res Sect A* 580(3):1383–1389. doi:[10.1016/j.nima.2007.06.019](https://doi.org/10.1016/j.nima.2007.06.019)
8. Barlow R (2003) Asymmetric errors. In: Lyons L, Mount R, Reitmeyer R (eds) *Proceedings of the conference on statistical problems in particle physics, astrophysics and cosmology (PHYSTAT2003)*, Stanford, 8–11 Sept 2003. Stanford Linear Accelerator Center, Menlo Park, pp 250–255. <https://www.slac.stanford.edu/econfl/C030908/papers/WE02.pdf> SLAC-R-703
9. Barlow R (2003) Asymmetric systematic errors. arXiv:[physics/0306138](https://arxiv.org/abs/physics/0306138) [hepex]
10. Beckerts KH, Wirtz K (1964) *Neutron physics*. Springer, Berlin
11. Bellini G et al [Borexino Collaboration] (2013) Cosmogenic backgrounds in Borexino at 3800 m water-equivalent depth. *J Cosmol Astropart Phys* 2013(08):049. doi:[10.1088/1475-7516/2013/08/049](https://doi.org/10.1088/1475-7516/2013/08/049). arXiv:[1304.7381](https://arxiv.org/abs/1304.7381) [physics.insdet]
12. Bergamasco L (1970) Experimental results on the pion and neutron production by muons at 60 and 110 m w.e. *Nuovo Cim B* 66(1):120–128. doi:[10.1007/BF02710194](https://doi.org/10.1007/BF02710194)
13. Bergamasco L, Costa S, Picchi P (1973) Experimental results on neutron production by muons at 4300 m w.e. *Nuovo Cim A* 13:403–412. doi:[10.1007/BF02827344](https://doi.org/10.1007/BF02827344)
14. Berger C et al [Fréjus Collaboration] (1989) Experimental study of muon bundles observed in the Fréjus detector. *Phys Rev D* 40(7):2163–2171. doi:[10.1103/PhysRevD.40.2163](https://doi.org/10.1103/PhysRevD.40.2163)
15. Birks JB (1964) *The theory and practice of scintillation counting*. International series of monographs on electronics and instrumentation, vol 27. Pergamon Press, Oxford
16. Browne E (2003) Nuclear data sheets for  $A = 210$ . *Nucl Data Sheets* 99(3):649–752. doi:[10.1006/ndsh.2003.0011](https://doi.org/10.1006/ndsh.2003.0011)
17. Chauvie S (2004) Geant4 low energy electromagnetic physics. In: Seibert JA et al (ed) *IEEE, nuclear science symposium and medical imaging conference. Including the symposium on nuclear power system, 14th room temperature semiconductor X-and gamma-ray detectors workshop and special focus workshops*, Roma, Italy, 16–22 Oct 2004. *IEEE nuclear science symposium conference record*, vol 3. IEEE Computer Society Press, Los Alamitos, pp 1881–1885. doi:[10.1109/NSSMIC.2004.1462612](https://doi.org/10.1109/NSSMIC.2004.1462612)
18. Chazal V et al (1998) Neutron background measurements in the underground laboratory of Modane. *Astropart Phys* 9(2):163–172. doi:[10.1016/S0927-6505\(98\)00012-7](https://doi.org/10.1016/S0927-6505(98)00012-7)
19. Cowan G (1998) *Statistical data analysis*. Clarendon Press, Oxford
20. Crouch MF, Sard RD (1952) The distribution of multiplicities of neutrons produced by cosmic-ray  $\mu$ -mesons captured in lead. *Phys Rev* (2nd Ser) 85(1):120–129. doi:[10.1103/PhysRev.85.120](https://doi.org/10.1103/PhysRev.85.120)
21. Devroye L (1986) *Non-uniform random variate generation*. Springer, Berlin
22. Engineering ToolBox: Beech. <http://www.engineeringtoolbox.com>. Accessed 24 Dec 2012. The Engineering ToolBox homepage > Material Properties > Wood Densities

23. Feldman GJ, Cousins RD (1998) Unified approach to the classical statistical analysis of small signals. *Phys Rev D* 57(7):3873–3889. doi:[10.1103/PhysRevD.57.3873](https://doi.org/10.1103/PhysRevD.57.3873)
24. Gaisser TK (1991) Cosmic rays and particle physics. 1. publ., repr. ed. Cambridge University Press, Cambridge
25. Garny S et al (2009) GEANT4 transport calculations for neutrons and photons below 15 MeV. *IEEE Trans Nucl Sci* 56(4):2392–2396. doi:[10.1109/TNS.2009.2023904](https://doi.org/10.1109/TNS.2009.2023904)
26. Geant4 Collaboration (2009) Geant4 user's guide for application developers. Version: geant4 9.3. <http://geant4.web.cern.ch/geant4/UserDocumentation/UsersGuides/ForApplicationDeveloper/BackupVersions/V9.3/fo/BookForAppliDev.pdf>
27. Geant4 Collaboration (2009) Physics reference manual. Version: geant4 9.3. <http://geant4.web.cern.ch/geant4/UserDocumentation/UsersGuides/PhysicsReferenceManual/BackupVersions/V9.3/fo/PhysicsReferenceManual.pdf>
28. Geant4 homepage: Processes. [http://geant4.web.cern.ch/geant4/support/proc\\_mod\\_catalog/processes/](http://geant4.web.cern.ch/geant4/support/proc_mod_catalog/processes/). Accessed 12 May 2012. Geant4 homepage > User Support > Process/model catalog > Processes
29. Gorshkov GV, Zyabkin VA (1968) Production of neutrons in Pb, Cd, Fe, and Al under the influence of cosmic-ray muons at a depth of 150 m water equivalent (trans: Adashko JG). *Sov J Nucl Phys* 7(4):470–474. Ori. pub. as *Yad Fiz* 7:770–777 [in Russian]
30. Gorshkov GV, Zyabkin VA (1970) Neutron production in Pb at a depth of 150 m w.e. under the influence of cosmic-radiation mesons traveling at large zenith angles (trans: Adashko JG). *Sov J Nucl Phys* 12(2):187–190. Orig. pub. as *Yad Fiz* 12:340–346 [in Russian]
31. Gorshkov GV, Zyabkin VA, Yakovlev RM (1973) Production of neutrons in Pb, Cd, Fe, and Al by high energy muons (trans: Adashko JG). *Sov J Nucl Phys* 18(1):57–61. Org. pub. as *Yad Fiz* 18:109–117 [in Russian]
32. Gorshkov GV, Zyabkin VA, Yakovlev RM (1971) Production of neutrons in Pb, Cd, Fe, and Al and fission of Pb nuclei by cosmic rays in the depth range 0–1000 m water equiv (trans: Robinson CS). *Sov J Nucl Phys* 13(4):450–452. Orig. pub. as *Yad Fiz* 13:791–796 [in Russian]
33. Groshev L et al (1968) Compendium of thermal-neutron-capture  $\gamma$ -ray measurements part II  $Z = 47$  to  $Z = 67$  (Ag to Ho). *Nucl Data Sheets Sect A* 5(1–2):1–242. doi:[10.1016/S0550-306X\(68\)80008-4](https://doi.org/10.1016/S0550-306X(68)80008-4). As cited in Ref. [65]
34. Grupen C, Shwartz BA (2008) Particle detectors, 2nd edn. Cambridge monographs on particle physics, nuclear physics, and cosmology, vol 26. Cambridge University Press, Cambridge
35. Heinrich J, Lyons L (2007) Systematic errors. *Annu Rev Nucl Part Sci* 57(1):145–169. doi:[10.1146/annurev.nucl.57.090506.123052](https://doi.org/10.1146/annurev.nucl.57.090506.123052)
36. Horn OM (2007) Simulations of the muon-induced neutron background of the EDELWEISS-II experiment for Dark Matter search. Scientific report FZKA 7391 (Forschungszentrum Karlsruhe. <http://bibliothek.fzk.de/zb/berichte/FZKA7391.pdf>) PhD dissertation, Universität Karlsruhe (TH). <http://digibib.ubka.uni-karlsruhe.de/volltexte/1000007402>
37. Horton-Smith G (2006) Additional gadolinium support for GLG4sim. <http://neutrino.phys.ksu.edu/GLG4sim/Gd.html>. Accessed 23 Jan 2013
38. International Commission on Radiation Units and Measurements (2011) Fundamental quantities and units for ionizing radiation (revised) (In: ICRU Report 85, special issue). *J ICRU* 11(1). doi:[10.1093/jicru/ndr012](https://doi.org/10.1093/jicru/ndr012)
39. Jahnke U et al (2003) A combination of two  $4\pi$  detectors for neutrons and charged particles: part I. The Berlin neutron ball—a neutron multiplicity meter and a reaction detector. *Nucl Instrum Methods Phys Res Sect A* 508(3):295–314. doi:[10.1016/S0168-9002\(03\)01652-8](https://doi.org/10.1016/S0168-9002(03)01652-8)
40. Koi T (2006) Thermal neutron scattering from nuclei within chemically bound atoms in Geant4. Presented at the IEEE 2006 nuclear science symposium and medical imaging conference, San Diego, CA, US, 29 Oct–1 Nov 2006. <http://geant4hadronics.wikispaces.com/file/view/Thermal+neutron+scattering+from+nuclei+within+chemically+bound.pdf>
41. Kudryavtsev VA (2010) Background of neutrons from  $(\alpha, n)$  reactions. E-mail message to author, 9–10 June 2010
42. Kudryavtsev VA Composition of steel used for EDELWEISS-II support structure. Made available via internal SVN server of the EDELWEISS collaboration

43. Kudryavtsev VA (2013) Definition of neutron yield and reference for the energy distribution of neutrons from  $(\alpha, n)$  reactions. E-mail message to author, 24 June 2013
44. Kudryavtsev V, Pandola L, Tomasello V (2008) Neutron- and muon-induced background in underground physics experiments. *Eur Phys J A* 36(2):171–180. doi:[10.1140/epja/i2007-10539-6](https://doi.org/10.1140/epja/i2007-10539-6)
45. Kudryavtsev V (2009) Muon simulation codes MUSIC and MUSUN for underground physics. *Comput Phys Commun* 180(3):339–346. doi:[10.1016/j.cpc.2008.10.013](https://doi.org/10.1016/j.cpc.2008.10.013)
46. Kudryavtsev VA Simulation of muons at LSM. Internal note for the EDELWEISS collaboration
47. Laible F (2012) Untersuchung der Langzeitstabilität eines Flüssigszintillators im Untergrundlabor von Modane (in German). Bachelor's thesis, Karlsruher Institut für Technologie (KIT)
48. Landau LD (1944) On the energy loss of fast particles by ionization In: Ter Haar D (ed) (1965) Collected papers of L. D. Landau. Pergamon Press, Oxford. Chap. 56. Orig. pub. as: *Zh Eksp Teor Fiz* 8:201 [in Russian]
49. Lemrani R et al (2003) Low energy neutron propagation in MCNPX and GEANT4. *Nucl Instrum Methods Phys Res Sect A* 560(2):454–459. doi:[10.1016/j.nima.2005.12.238](https://doi.org/10.1016/j.nima.2005.12.238). arXiv:[hep-ex/0601030](https://arxiv.org/abs/hep-ex/0601030)
50. Levin A, Moisan C (1996) A more physical approach to model the surface treatment of scintillation counters and its implementation into DETECT. In: Guerra AD (ed) IEEE, nuclear science symposium and medical imaging conference, Anaheim, CA, USA, 2–9 Nov 1996. IEEE nuclear science symposium conference record, vol 2. IEEE Computer Society Press, Los Alamitos, pp 702–706. doi:[10.1109/NSSMIC.1996.591410](https://doi.org/10.1109/NSSMIC.1996.591410)
51. Lindote A et al (2009) Simulation of neutrons produced by high-energy muons underground. *Astropart Phys* 31:366–375. doi:[10.1016/j.astropartphys.2009.03.008](https://doi.org/10.1016/j.astropartphys.2009.03.008). arXiv:[0810.1682](https://arxiv.org/abs/0810.1682) [hep-ex]
52. Motta D, Schönert S (2005) Optical properties of bialkali photocathodes. *Nucl Instrum Methods Phys Res Sect A* 539(1–2):217–235. doi:[10.1016/j.nima.2004.10.009](https://doi.org/10.1016/j.nima.2004.10.009)
53. Motta D, Zbiri K [On behalf of the Double Chooz Collaboration] (2005) Simulations for Double Chooz. Presented at the MANDsim workshop, Manhattan, KS, US, 14–15 June 2005. [http://neutrino.phys.ksu.edu/MAND-sim/MAND-sim%20talks/DoubleChooz\\_motta.pdf](http://neutrino.phys.ksu.edu/MAND-sim/MAND-sim%20talks/DoubleChooz_motta.pdf)
54. National Nuclear Data Center. NuDat: Search and plot nuclear structure and decay data interactively. <http://www.nndc.bnl.gov/nudat2>
55. Persiani R (2011) Measurement of the muon-induced neutron flux at LNGS with the LVD experiment. PhD dissertation, Università di Bologna. [http://www.bo.infn.it/lvd/pubdocs/phdThesis\\_PersianiRino.pdf](http://www.bo.infn.it/lvd/pubdocs/phdThesis_PersianiRino.pdf)
56. Reichhart L et al (2013) Measurement and simulation of the muon-induced neutron yield in lead. *Astropart Phys* 47:67–76. doi:[10.1016/j.astropartphys.2013.06.002](https://doi.org/10.1016/j.astropartphys.2013.06.002). arXiv:[1302.4275](https://arxiv.org/abs/1302.4275) [physics.ins-det]
57. Rhode W (1993) Study of ultra high energy muons with the Fréjus detector. PhD dissertation, Bergische Universität Gesamthochschule Wuppertal. <http://hdl.handle.net/10068/260384> WUB-DIS 93-11
58. Roithner Lasertechnik. RLT420-3-30-Violet LED Lamp. Roithner Lasertechnik, Vienna
59. Rozov S et al (2010) Monitoring of the thermal neutron flux in the LSM underground laboratory. arXiv:[1001.4383v1](https://arxiv.org/abs/1001.4383v1) [astro-ph.IM]
60. Saint-Gobain Crystals (2005) BC400, BC-404, BC-408, BC-412, BC-416-premium plastic scintillators. Saint-Gobain Crystals, Nemours
61. Saint-Gobain Crystals (2005) BC-525 Gd loaded mineral oil based liquid scintillator. Saint-Gobain Crystals, Nemours
62. Schmidt B et al [EDELWEISS collaboration] (2013) Muon-induced background in the EDELWEISS dark matter search. *Astropart Phys* 44:28–39. doi:[10.1016/j.astropartphys.2013.01.014](https://doi.org/10.1016/j.astropartphys.2013.01.014). arXiv:[1302.7112](https://arxiv.org/abs/1302.7112) [astro-ph.CO]
63. Tomasello V, Kudryavtsev V, Robinson M (2008) Calculation of neutron background for underground ground experiments. *Nucl Instrum Methods Phys Res Sect A* 595(2):431–438. doi:[10.1016/j.nima.2008.07.071](https://doi.org/10.1016/j.nima.2008.07.071)

64. Tretyak V (2010) Semi-empirical calculation of quenching factors for ions in scintillators. *Astropart Phys* 33(1):40–53. doi:[10.1016/j.astropartphys.2009.11.002](https://doi.org/10.1016/j.astropartphys.2009.11.002)
65. Trzciński A et al (1999) A monte-carlo code for neutron efficiency calculations for large volume Gd-loaded liquid scintillation detectors. *J Neutron Res* 8(2):85–117. doi:[10.1080/10238169908200048](https://doi.org/10.1080/10238169908200048)
66. Wei Y (1993) Untersuchung der neutrinoinduzierten Myonen im Fréjus-Untergrunddetektor (in German). PhD dissertation, Bergische Universität Gesamthochschule Wuppertal. WUB-DIS 93-8
67. Wilson WB et al (1999) SOURCES 4A: A code for calculating  $(\alpha, n)$ , spontaneous fission, and delayed neutron sources and spectra. Technical report LA-13639-MS. Los Alamos National Laboratory. <https://www.fas.org/sgp/othergov/doe/laml/docs1/00460139.pdf>
68. Wu S-C (2009) Nuclear data sheets for  $A = 214$ . *Nucl Data Sheets* 110(3):681–748. doi:[10.1016/j.nds.2009.02.002](https://doi.org/10.1016/j.nds.2009.02.002)
69. Yeh M, Garnov A, Hahn R (2007) Gadolinium-loaded liquid scintillator for high precision measurements of antineutrino oscillations and the mixing angle,  $\theta_{13}$ . *Nucl Instrum Methods Phys Res Sect A* 578(1):329–339. doi:[10.1016/j.nima.2007.03.029](https://doi.org/10.1016/j.nima.2007.03.029)
70. Zbiri K (2011) GdHPCapture. E-mail message to author, 24 March 2011
71. Zbiri K (2010) Remark on the studies of the muon-induced neutron background in the liquid scintillator detectors. *Nucl Instrum Methods Phys Res Sect A* 615(2):220–222. doi:[10.1016/j.nima.2010.01.035](https://doi.org/10.1016/j.nima.2010.01.035)

# Chapter 6

## Assessment of Geant4 to Simulate the Neutron Yield in Lead at LSM

As discussed in Chap. 2, muon-induced neutrons are an important background for experiments like EDELWEISS which can only be estimated by MC simulations. Two pieces of information are critical for the understanding of this background: The actual neutron yield at the experimental site and the confirmation of the reliability of the used MC program, here Geant4.

We will discuss both aspects for the muon-induced neutron production at the LSM, the site of the EDELWEISS experiment, by comparing the results of the dedicated neutron counter experiment (Chap. 4) with the predictions of detailed MC simulations (Chap. 5) in two stages. First, the capability of Geant4 to simulate correctly the detector response to muon-induced neutrons, and hence the neutron production itself, is discussed in Sect. 6.1. Second, the actual neutron yield at the LSM is calculated, and a comparison with existing measurements at other underground sites is discussed in Sect. 6.2.

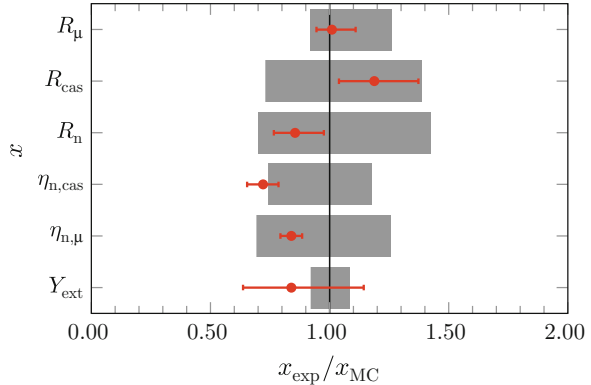
### 6.1 MC Prediction of Muon-Induced Neutron Candidates

To assess Geant4's reliability to simulate the detector response to muon-induced neutrons, we discuss the agreement between measurement (see Sect. 4.5.2) and simulation (Sect. 5.5.3) of neutron candidates, neutron cascade candidates, and muon candidates. Section 6.1.1 contains the discussion of the obtained counting rates, and Sect. 6.1.2 the differential rate spectrum of the neutron candidates. Excluded from the assessment is the neutron yield  $Y_{\text{ext}}$  and the implications for Geant4, which will be discussed in detail in Sect. 6.2.

#### 6.1.1 Counting Rate

In this section we discuss the agreement between the measured and simulated count rates of neutron candidates  $R_n$ , neutron cascade candidates  $R_{\text{cas}}$ , and muon candidates

**Fig. 6.1** Measured quantities (red points) relative to the Geant4 predictions (black line). Shown are the total uncertainties, i.e. the linear sum of statistical and systematic uncertainties for the measurement (red error bars), and for the simulation the linear sum of statistical, systematic, and theoretical uncertainties (gray boxes)



$R_\mu$  and the ratios  $\eta_{n,\text{cas}}$ ,  $\eta_{n,\mu}$ , i.e. in total five quantities. Here, we state the linearly combined uncertainties; the classification in statistical, systematic, and theoretical uncertainties are given in Sect. 5.5.3.

Figure 6.1 compares the measured quantities with the prediction from the Geant4 simulation, normalized to the central value of the simulation. As shown, there is a good agreement between the measurement and simulation for all quantities, taking into account the linearly combined uncertainties of the measurement (red error bars) and simulation (gray error bar), but the assessment is limited by the precision of the simulation. In detail, the assessment for the five quantities is as follows:

The central value of the *absolute* rate of neutron candidates  $R_n$  differs between simulation ( $(3.8^{+1.6}_{-1.1}) \times 10^{-1} \text{ d}^{-1}$ , Eq. 5.65) and experiment ( $(3.2^{+0.5}_{-0.3}) \times 10^{-1} \text{ d}^{-1}$ , Eq. 4.35) by

$$\frac{R_{n,\text{MC}} - R_{n,\text{exp}}}{R_{n,\text{exp}}} = +17\% \quad (6.1)$$

with respect to the measurement. The experimental precision is 16 % and the simulation has a precision of 43 %. The latter is dominated by systematic effects of the detector response model like the shift in the gadolinium content of the NMM or uncertainties in the time normalization, see Table 5.10 for details. Conversely, the experimental precision is limited by the statistics, see Sect. 4.5.2. However, the precision of the simulation is rather low. As discussed in Sect. 5.5.4, an improved detector response model of the muon telescope and by including the gadolinium shift in the detector response model of the NMM may improve the precision of the simulation by  $\approx 20\%$ .

A more precise comparison between simulation and measurement is possible via the ratio  $\eta_{n,\mu}$  (Eq. 4.31), i.e. the neutron candidate rate normalized to the muon rate. The relative uncertainty of the simulated value ( $(6.6^{+1.7}_{-2.0}) \times 10^{-2}$ , Eq. 5.67) is 31 %, being smaller than for  $R_n$ , because systematic uncertainties in the muon telescope model and in the muon flux normalization are cancelled. The precision of

the measurement ( $(5.5^{+0.3}_{-0.5}) \times 10^{-2}$ , Eq. 4.39) increased only slightly, being 9 %. The ratio of detected neutrons to muons  $\eta_{n,\mu}$  (Eq. 4.31) differed by

$$\frac{\eta_{n,\mu,MC} - \eta_{n,\mu,exp}}{\eta_{n,\mu,exp}} = +18\%. \quad (6.2)$$

between simulation and measurement. The agreement between simulation and measurement is better than the  $-21\%$  obtained in [14]<sup>1</sup> for the ZEPLIN-III experiment.

At first sight, the rate of neutron cascade candidates  $R_{cas}$  behaves similar to  $R_n$ : with respect to the measurement ( $(1.8^{+0.3}_{-0.2}) \times 10^{-1} d^{-1}$ , Eq. 4.36), the central value of the simulation ( $(1.5^{+0.6}_{-0.4}) \times 10^{-1} d^{-1}$ , Eq. 5.64) deviates by

$$\frac{R_{cas,MC} - R_{cas,exp}}{R_{cas,exp}} = -16\%. \quad (6.3)$$

Again, the assessment is limited by the precision of the simulation of 39 % compared to 13 % for the measurement. Nevertheless, the simulation *under-produces* the cascade candidates, contrary to the *overproduction* of neutron candidates.

This contrary behaviour is also clearly indicated by the  $\eta_{n,cas}$  ratio (Eq. 4.31), i.e. the neutron candidate rates normalized to the rate of neutron cascade candidates. The simulated value ( $2.4^{+0.4}_{-0.6}$ , Eq. 5.66) is bigger than the measured value ( $1.75^{+0.2}_{-0.17}$ , Eq. 4.38) by

$$\frac{\eta_{n,cas,MC} - \eta_{n,cas,exp}}{\eta_{n,cas,exp}} = +39\%. \quad (6.4)$$

The consequences of these findings will be discussed in more detail in Sect. 6.2.3.

The rate of simulated muon candidates  $R_\mu$  ( $(5.7^{+1.5}_{-0.5}) d^{-1}$ , Eq. 5.63) differs only by

$$\frac{R_{\mu,MC} - R_{\mu,exp}}{R_{\mu,exp}} = -1.1\% \quad (6.5)$$

from the measured value ( $(5.79^{+0.6}_{-0.08}) d^{-1}$ , Eq. 4.37). Despite this small deviation, the precision of the simulation is, at 26 %, again low: The great uncertainty represents the conservative approach describing the correctness of the detector response model of the muon telescope, see the discussion in Sect. 5.4.4.

We also note the good agreement between the simulated average energy of the muon candidates ( $267^{+8}_{-11}$  GeV, Eq. 5.74) and the average muon energy measured by the Fréjus experiment (255.0 (45) GeV, [15]).

In conclusion, Geant4 is able to accurately predict the experimentally obtained count rates of candidates for muon-induced neutrons and muon-induced neutron cascades in end-to-end simulations. As Fig. 6.1 shows, all the deviations are well

<sup>1</sup>Reichhart et al. state a measured ‘muon-induced neutron detection rate’ of 0.346 compared to a simulated value of 0.275 [14].

within 30 % relative to the simulation. This is a clear improvement to the often cited ‘factor 2’ deviation [1, 11]. An even further increase in precision of the MC predictions may be achieved with an improved model of the detector response.

### 6.1.2 Differential Counting Spectra

We will further investigate the agreement between measurement and simulation of muon induced neutron candidates. For that purpose we will study the rate spectra with respect to energy deposit in the liquid scintillator  $E_{\text{dep}}$ , time difference between a muon candidate and any neutron candidate  $\Delta t$ , and multiplicity  $M_{n,\text{can}}$ . All spectra show *absolute* rates, i.e. the simulation is *not* scaled to the measurement.

To compare with the experimental results shown in Sect. 4.5, the simulated energy spectra are given as the sum of the signals from the opposite PMTG<sub>1</sub><sup>N</sup> and PMTG<sub>5</sub><sup>N</sup> in ADC units, see Fig. 4.6 for the position of these PMTs.

Figure 6.2a shows the energy spectrum of the muon-induced neutron candidates and Fig. 6.2b shows the spectrum of the accompanied muon candidates. The time

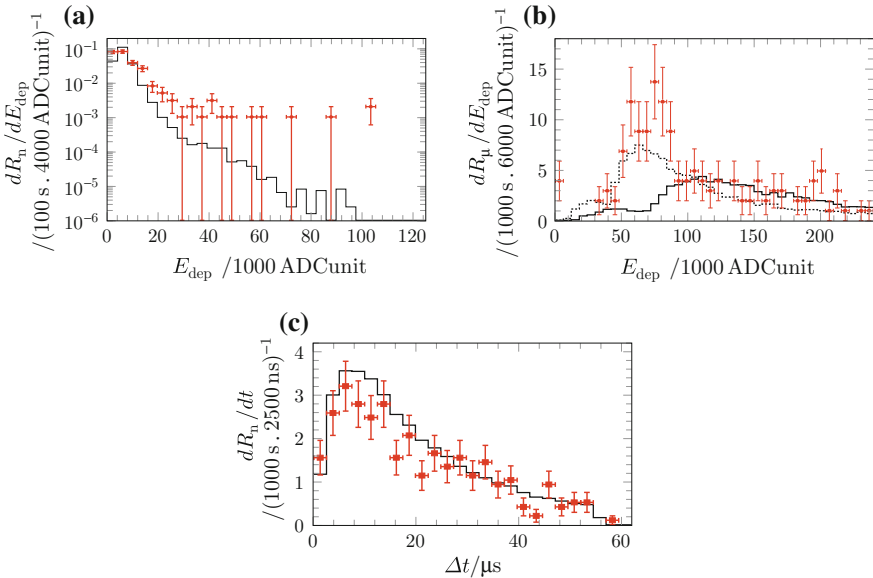


**Fig. 6.2** Measured (data points) and simulated (histogram) differential rate spectra in the case of detected candidates for muon-induced neutrons: **a** shows the energy spectrum for the neutron candidates and **b** for the corresponding muon candidates without additional scaling (solid histogram,  $\langle E_{\text{dep}} \rangle = 1.786(9) \times 10^5 \text{ ADCunit}$ ) and with energy scaling (dashed histogram,  $\langle E_{\text{dep}} \rangle = 1.026(5) \times 10^5 \text{ ADCunit}$ ). Both spectra are recorded by PMTG<sub>1</sub><sup>N</sup> + PMTG<sub>5</sub><sup>N</sup>. The time difference  $\Delta t$  between the muon candidate and any following neutron candidates are shown in **c**. For details see text

differences between the neutron candidates and the corresponding muon candidate is shown in Fig. 6.2c. In all three cases the MC prediction is based on the standard configuration, i.e. best fitting parameter of the detector response model and the standard parameter for the muon generator as listed in Tables 5.2 and 5.7. Therefore, it does not contain systematic uncertainties.

The spectrum of the energy deposits caused by the neutron candidates in Fig. 6.2a deviates between simulation and measurement. The experimental distribution is wider than the simulated one and features a high energy tail.<sup>2</sup> The measured count rate of high energy events exceeds the simulation. However, the measured events occur in the same energy range as predicted by Geant4. Also tentative studies [12] seem to confirm that the measured tail contains physical events and no artefacts, e.g. caused by PMT saturation after a passing muon. The correlation of these excess events with muon candidates and their high energy most likely exclude decays of radio-isotopes as sources. A possible source may be highly energetic muon-induced particles, e.g. neutrons. The plausibility of this source is further discussed in Sect. 6.2.3. However, future work has to show whether the measured high energy events are a significant excess or if they are in agreement with the systematic uncertainties of the simulation.

At first sight, no agreement is achieved for the shape of the muon energy spectrum Fig. 6.2b (solid histogram). However, this may be explained by an imperfection in the method used to calibrate the detector response model. The prompt signal of the through-going muon ( $E_{\text{vis}} \approx E_{\text{dep}} \approx 100 \text{ MeV}$ ) was measured with the NMM, which was calibrated by an AmBe reference source. The maximal visible energy of this source is  $E_{\text{vis}} \approx 10 \text{ MeV}$ , see Fig. 5.17. Therefore, the absolute energy scale between calibration data and physics data differs by a factor 10. This, together with non-linearities in the detector response, such as the saturation effect discussed in Sect. 4.2.5, may motivate a different effective energy scale to match simulated and measured energy deposits for muons. Indeed, scaling the simulated data by a factor 0.574 to match the measured mean energy improves the agreement (Fig. 6.2b, dashed histogram). Tentative investigations indicate that the remaining deviation may be within the systematic uncertainty of the detector response model.

The deviation of the energy spectra between measurement and simulation raises the question whether the detector response model is accurate enough and if it may affect the determination of the neutron yield (Sect. 6.2). The calculation of the neutron yield depends, via the neutron detection efficiency, on the correct simulation of neutron transport and detection. However, the agreement between measured and simulated counting rates in Sect. 6.1.1 disproves a possible influence of the deviating energy spectra on the neutron transport and detection. The reliability of the detector response model in terms of neutron detection is also strengthened by the agreement between simulation and measurement in the timing (Fig. 6.2c) and multiplicity spectra (Fig. 6.3).

---

<sup>2</sup>The tail is on the higher energy side of the Gd ( $n, \gamma$ )-peak in Fig. 6.2a, with the highest neutron binding energy  $S_n = 8.5 \text{ MeV}$  for  $^{155}\text{Gd}$ . Therefore, the tail contains events with  $E_{\text{dep}} >> 8.5 \text{ MeV}$ .

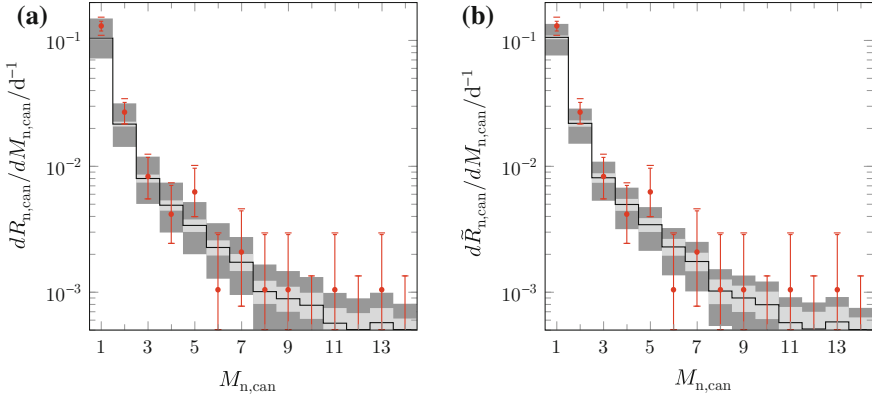


**Fig. 6.3** Comparison between measured (red points) and simulated (black histogram) multiplicity spectrum  $dR_{n,\text{can}}/dM_{n,\text{can}}$ : **a** For unscaled rate  $R_{n,\text{can}}$  and **b** for rate scaled to the measured muon candidate rate  $\tilde{R}_{n,\text{can}}$  as function of the multiplicity  $M_{n,\text{can}}$ . The *small red error bars* and the *light gray band* indicate the statistical uncertainty at 68 % CL. The *dark gray band* indicates the combined uncertainty of the simulation, i.e. statistical, systematic, and theoretical uncertainty. The *large red error bars* indicate the combined uncertainty of the measurement, i.e. statistical and systematic uncertainty. For details see text

The time spectrum in Fig. 6.2c shows good agreement within the uncertainties. The overall offset, which is especially clear in the moderation phase at  $\Delta t < 8 \mu\text{s}$ , indicates the general overproduction of neutron candidates in the simulation, see Fig. 6.1.

The absolute differential rate of neutron candidates as a function of the multiplicity of the neutron cascade candidates is calculated in a similar manner to the neutron candidate rate in Sect. 5.5.3. For each simulated data set *i*c, see Sect. 5.3.2, the muon induced neutron candidates with a given multiplicity are counted and normalized to the live-time, see Table 6.1 for the individual amounts. In accordance with Sect. 5.5.3, the multiplicity  $M_{n,\text{can}}$  is defined as the number of neutron candidates per neutron cascade candidate. The multiplicity spectrum (Fig. 6.3a) results from the sum over all data sets. It is *not* the multiplicity spectrum of emitted neutrons in lead, but contains also neutrons from other sources, see Fig. 5.28 for the general source distribution. The possibility to obtain the multiplicity spectrum of neutrons emitted from lead is discussed in Sect. 5.5.6.

Whereas Fig. 6.2 shows only the statistical uncertainties of the MC data, the multiplicity spectrum in Fig. 6.3 also shows the systematic uncertainty. We assumed that the relative systematic uncertainty on the differential neutron candidate rate is the same as in the neutron candidate rates, i.e.  $^{+39.23}_{-27.15}\%$  (Table 5.10).

We find good agreement between simulation and measurement over the whole measured multiplicity range. At low multiplicities the assessment is limited by the systematic uncertainties of the simulation, at higher multiplicities it is limited by the statistics of the measurement.

**Table 6.1** Number of candidates for muon-induced neutrons  $N_{n,\text{can,MC}}$  in the simulated data sets  $i$  and resulting rate  $R_{n,\text{can,MC}}$ 

$M_{n,\text{can}}$	$N_{n,\text{can,MC}}$	$c = +$				$c = -$				$R_{n,\text{can,meas}} (\text{d}^{-1})$
		$i = 1$	$i = 2$	$i = 3$	$i = 4$	$i = 1$	$i = 2$	$i = 3$	$i = 4$	
1	753	1321	3466	1746	431	1358	3226	1498	(1.049 $^{+0.022}_{-0.022}$ stat $^{+0.411}_{-0.285}$ sys $^{+0.020}_{-0.020}$ theo) $\times 10^{-1}$	
2	41	267	761	561	7	230	670	455	(2.16 $^{+0.10}_{-0.10}$ stat $^{+0.85}_{-0.59}$ sys $^{+0.05}_{-0.05}$ theo) $\times 10^{-2}$	
3	5	94	288	227	3	80	241	207	(7.98 $^{+0.59}_{-0.59}$ stat $^{+3.13}_{-2.17}$ sys $^{+0.21}_{-0.21}$ theo) $\times 10^{-3}$	
4	4	43	146	149	3	52	176	124	(4.88 $^{+0.46}_{-0.46}$ stat $^{+1.92}_{-1.33}$ sys $^{+0.13}_{-0.13}$ theo) $\times 10^{-3}$	
5	2	33	124	91	1	38	103	84	(3.38 $^{+0.39}_{-0.38}$ stat $^{+1.32}_{-0.92}$ sys $^{+0.09}_{-0.09}$ theo) $\times 10^{-3}$	
6	0	29	88	61	0	17	67	62	(2.25 $^{+0.32}_{-0.31}$ stat $^{+0.88}_{-0.61}$ sys $^{+0.06}_{-0.06}$ theo) $\times 10^{-3}$	
7	0	13	60	58	0	9	67	45	(1.72 $^{+0.28}_{-0.25}$ stat $^{+0.67}_{-0.47}$ sys $^{+0.05}_{-0.05}$ theo) $\times 10^{-3}$	
8	0	11	42	38	0	7	28	30	(1.00 $^{+0.22}_{-0.20}$ stat $^{+0.39}_{-0.27}$ sys $^{+0.03}_{-0.03}$ theo) $\times 10^{-3}$	
9	0	7	34	24	0	9	28	22	(8.80 $^{+2.13}_{-1.87}$ stat $^{+3.45}_{-2.39}$ sys $^{+0.25}_{-0.25}$ theo) $\times 10^{-4}$	
10	0	10	28	23	0	4	29	12	(7.79 $^{+2.01}_{-1.72}$ stat $^{+3.06}_{-2.12}$ sys $^{+0.21}_{-0.21}$ theo) $\times 10^{-4}$	
11	0	3	26	12	0	6	15	19	(5.61 $^{+1.80}_{-1.45}$ stat $^{+2.20}_{-1.52}$ sys $^{+0.17}_{-0.17}$ theo) $\times 10^{-4}$	
12	0	3	20	16	0	4	18	8	(4.99 $^{+1.78}_{-1.34}$ stat $^{+1.96}_{-1.35}$ sys $^{+0.14}_{-0.14}$ theo) $\times 10^{-4}$	
13	0	2	21	14	0	4	23	14	(5.68 $^{+1.73}_{-1.40}$ stat $^{+2.23}_{-1.54}$ sys $^{+0.18}_{-0.18}$ theo) $\times 10^{-4}$	
14	0	1	18	9	0	2	19	12	(4.49 $^{+1.62}_{-1.16}$ stat $^{+1.76}_{-1.22}$ sys $^{+0.15}_{-0.15}$ theo) $\times 10^{-4}$	

The statistical uncertainty indicates 68% CL. For details see text

The systematic uncertainty of the simulation is reduced by normalization to the simulated muon candidate rate and scaling to the measured muon candidate rate, as discussed in Sect. 5.5.4. The simulation is still in agreement with the measurement, as shown in the relative multiplicity spectrum in Fig. 6.3b. However, we note that the deviation of the central values may indicate an underproduction of low-multiplicity events in the simulation.

In conclusion, the simulation agrees well with the measurement in terms of absolute multiplicity and timing distribution of the neutron candidates. On the other hand, the agreement between the simulated and measured energy spectra is not as good. The measured neutron candidates feature a high energy tail that is not predicted by the simulation. A possible explanation will be discussed in Sect. 6.2.3. In the case of the muon candidates, the deviation may be explained by experimental saturation effects, which were not implemented in the detector response model.

## 6.2 Cosmic Induced Neutron Production Yield at LSM

Based on the measured rates of neutron candidates  $R_n$  and muon candidates  $R_\mu$  (see Sect. 4.5.2) and the simulated neutron detection efficiency  $\bar{\epsilon}_n$  and muon track lengths  $\langle X \rangle$  in the detector target (Sect. 5.5.3), the cosmic induced neutron production yield at the LSM is calculated in Sect. 6.2.1. Subsequently, in Sect. 6.2.2 we discuss its agreement with existing measurements. Deviation from the Geant4 simulations are interpreted in terms of the implemented neutron shower model in Sect. 6.2.3. Finally, the neutron production at shower equilibrium is estimated in Sect. 6.2.4 from scaling of the measured neutron yield in a thin target with a factor derived from MC.

### 6.2.1 Calculation of the Neutron Yield

Based on Eq. 3.64a, the neutron yield is calculated from the number of detected neutron candidates per detected muon candidate  $\eta_{n,\mu}$ , corrected by the neutron detection efficiency  $\bar{\epsilon}_n$  and normalized to the mean target thickness along the muon track  $\langle X \rangle$ . In the context of the discussion in Sect. 5.5.2, we call this quantity the *external neutron yield*, as it includes the self-absorption by the target itself and the muon-induced shower in the target is not necessarily in equilibrium. It is the basis for the calculation of the *equilibrium neutron yield* in Sect. 6.2.4, which is corrected for self-absorption.

During its 964.5 live-time days, the neutron counter measured  $N_{n,\text{exp}} = 313$  neutron candidates in coincidence with  $N_{\mu,\text{exp}} = 5583$  muon candidates, see Table 4.2. This results in a ratio of  $\eta_{n,\mu} = (5.5^{+0.3}_{-0.5}) \times 10^{-2}$  (Eq. 4.39, linearly combined uncertainty).

MC simulations based on Geant4 9.2p01 establish a detection efficiency for neutrons produced in lead of  $\bar{\epsilon}_n = 15^{+3}_{-4} \%$  (Eq. 5.77, linearly combined uncertainty), thus making it possible to calculate the number of neutrons from the number of neutron candidates. The definition of the efficiency consider the actual detection, the

transport from neutron source to the active volume of the neutron counter, and the fraction of neutrons from the lead target to all neutrons produced in the surrounding of the detector, see Sect. 5.5.3.

The average energy of the detected muons depends on the muon telescope detection threshold, and this is also true for the average target thickness along the track of detected muons. The simulation takes this into account via a detector response model of the muon telescope, and gives a result of  $\langle E_\mu \rangle = 267^{+8}_{-11}$  GeV (Eq. 5.74, linearly combined uncertainty) and  $\langle X \rangle = 135.2(3)$  g cm<sup>-2</sup> (Eq. 5.75b, linearly combined uncertainty).

Therefore, the external neutron yield from Eq. 3.64a at the LSM is:

$$Y_{\text{ext,exp}} = (2.708 \pm 0.158_{-0.489}^{\text{stat} +0.812^{\text{sys}}} \pm 0.011^{\text{theo}}) \times 10^{-3} \text{cm}^2 \text{g}^{-1} \quad (6.6)$$

The angled brackets indicate that the yield is measured for the LSM spectrum of muons.

The calculation of the uncertainties closely follows the methods established in Sect. 5.5.4. The uncertainties due to limited statistics in simulation and experiment are based on straight-forward error propagation, assuming uncorrelated uncertainties. Systematic uncertainties are calculated via the shift method, and these are caused by possible background in the experimental data and uncertainties in the MC detector response model used for the estimation of the detection efficiency. Also, the theoretical uncertainty is introduced via the MC simulation. It states the difference between three different configurations of the MC model with respect to the average over them. These configurations are the standard configuration, an alternative parametrization of the incoming muon flux, and an alternative model for the gamma cascade caused by the neutron capture on gadolinium; see Sect. 5.5.4 for details.

The individual contributions to the uncertainty are listed in Table 6.2. It shows that the uncertainty of the external neutron yield, linearly combined to at most 36 %, is dominated by the uncertainty of the neutron detection efficiency. As discussed in Sect. 5.5.4, this uncertainty itself is dominated by a 10 % uncertainty due to the precipitation of the gadolinium out of the liquid scintillator in the active volume of the detector (see Sect. 4.4.2). If the simulation could include this well-monitored change in future work, as outlined in Sect. 5.5.4, the precision of the simulation would be increased. Nevertheless, the detector efficiency is most likely the most sensitive factor for future changes due to updates in Geant4, which will affect the neutron transport and detection. The muon-induced neutrons feature a hard spectrum up to  $\approx 30$  GeV, see Fig. 5.31, which may be affected by future Geant4 updates, as only the neutron transport below  $\lesssim 15$  MeV seems reliably implemented in Geant4 [13].

In conclusion, the measured external neutron yield is calculated as  $(2.7^{+1.0}_{-0.7}) \times 10^{-3} \text{cm}^2 \text{g}^{-1}$  at  $267^{+8}_{-11}$  GeV. Its value depends via the neutron detection efficiency on Geant4 9.2p01 simulations, which may change due to future Geant4 updates.

**Table 6.2** Statistical, systematic, and theoretical uncertainties for the experimental external neutron yield  $\langle Y_{\text{ext,exp}} \rangle$  relative to its average value

$\delta Y_{\text{ext,exp}} (\%)$	
Statistical uncertainty	$\pm 5.84$
Systematic uncertainties	
$\eta_{n,\mu,\text{exp}} - \delta$	-2.83
$\bar{\epsilon}_n \pm \delta$	<b>-15.07</b> <b>+29.79</b>
$\langle X \rangle \pm \delta$	-0.17 +0.21
Sum	+30.00 -18.08
Theoretical uncertainties	
Standard configuration	+0.41
APS	-0.22
GCM	-0.19
Sum	$\pm 0.41$
Sum	+36.25 -24.33

The alternative muon parameter set is denoted as APS and the alternative gamma cascade model as GCM. Statistically significant deviation are printed bold. For details see text

### 6.2.2 Neutron Yield in Comparison with Existing Measurements

As discussed in Sect. 5.5.2, the external neutron yield is experimentally accessible, but it depends on the target geometry. Therefore, in order to compare our results with existing results from other works, one has to select compatible experiments. In particular, a large difference in target thickness can affect the external neutron yield, since the thickness affects the development of the muon-induced shower inside the target. As reported in Sect. 3.5.1, most of the existing experiments [4–10] used targets with 10 to 35 cm thickness, similar to the 10 cm thick target of the neutron counter. Hereafter, this selection is called *thin target data*. Hence, these results should be compatible with the results of this work, Eq. 6.6, with respect to the development of the muon-induced cascade. Note that ZEPLIN-II and ZEPLIN-III [2, 14] state an equilibrium neutron yield not compatible with Eq. 6.6, as will be discussed in Sect. 6.2.4.

Figure 6.4 shows in analogy to Fig. 3.6a the thin target data (black) together with the result of this work (red). Based on the fit of  $Y(\langle E_\mu \rangle)$  (Eqs. 3.66 and 3.71a) to the thin target data (solid black line), a neutron yield of  $5(4) \times 10^{-3} \text{ cm}^2 \text{ g}^{-1}$  (Eq. 3.74) was estimated for the LSM. Considering the great uncertainty of the thin target data,

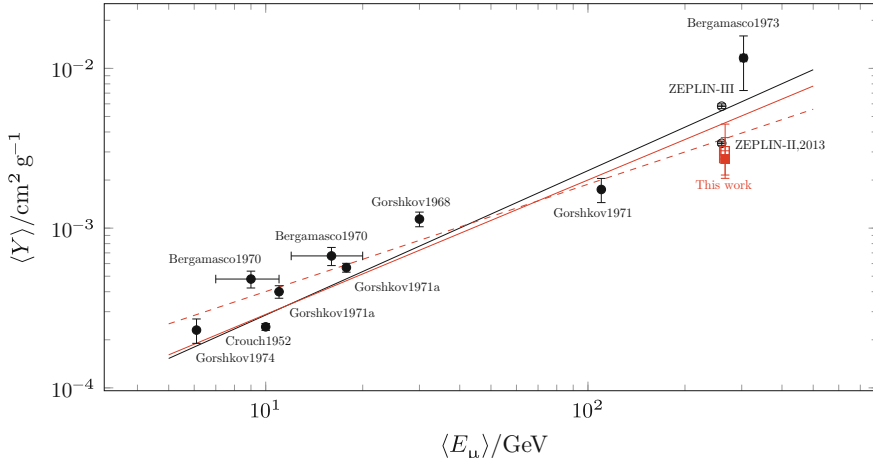


**Fig. 6.4** Average external neutron yield  $\langle Y_{\text{ext}} \rangle$  (filled symbol) as function of the average muon energy  $\langle E_\mu \rangle$  for the thin target data [4–10] (black circles) and for the results of this work (red square). The lines indicate fits of  $Y(\langle E_\mu \rangle) = c_1 \langle E_\mu \rangle^\alpha$  (Eq. 3.66) to different subsets: The black solid line is a fit to all previously mentioned thin target data, the red solid line corresponds to the fit of thin target data including the results of this work, and the dashed red line includes again this work, but excludes Crouch1952 [6]. Also shown is the equilibrium neutron yield  $\langle Y_{\text{equi}} \rangle$  (open symbols) as obtained in this work and for ZEPLIN-II, ZEPLIN-III [14], which is not included in any fit. For details see text

they are in agreement with the results of this work  $(2.7^{+1.0}_{-0.7}) \times 10^{-3} \text{cm}^2 \text{g}^{-1}$  (Eq. 6.6). To specify the agreement between data and fit, the RMS of the residuals between data and fit is used, as discussed in Sect. 3.5.4.

At first sight, the deviation between fit and this work is 106 %, even worse than the 46 % of Bergamasco1973 [5], which was previously the highest deviation.

Including the results of this work in the fit returns (Fig. 6.4, solid red line)

$$c_1 = 4.2(15) \times 10^{-5} \text{cm}^2 \text{g}^{-1} \quad (6.7a)$$

$$\alpha = 0.84(13) \quad (6.7b)$$

and decreases the deviation between this work and the fit to 69 %. However, it is still the greatest deviation, the deviation for Bergamasco1973 [5] changes to 56 %. The overall agreement between data and fit, again expressed as the RMS of the residuals, is 38 %.

A possible explanation is given by the great statistical influence of Crouch1952 [6] on the overall data set: As already discussed in Sect. 3.5.4, this low  $Y$ -value with very small uncertainties drives the fit to high values for the index  $\alpha$ . Generally, one would expect the same index as for the neutron yield in liquid scintillator ( $\alpha = 0.69(3)$ , Eq. 3.68b), as it should be independent on the target, see the discussion in Sect. 3.5.4.

Excluding Crouch1952 [6] changes the fit to (Fig. 6.4, dashed red line)

$$c_1 = 8.5(22) \times 10^{-5} \text{cm}^2 \text{g}^{-1} \quad (6.8a)$$

$$\alpha = 0.67(9), \quad (6.8b)$$

resulting in an excellent agreement of the index  $\alpha$  between neutron production in lead and liquid scintillator. The agreement between fit and the set of experimental data is 30 %, the maximum deviation is 66 % for Bergamasco1973 [5], whereas the deviation of this work is reduced to 35 %. In comparison, exclusion of both Crouch1952 [6] and this work results in  $\alpha = 0.70(10)$  (Eq. 3.72b), hence this work increases slightly the precision, but otherwise does not influence much the result of the fit.

In summary, this work is in agreement with the thin data sets [4–10]. The previously noted tension between Crouch1952 [6] and [4–9] is more pronounced. Exclusion of Crouch1952 [6] decreases the deviation of this work with the fit on the data from 56 to 35 %. Additionally, an improved agreement between the indices  $\alpha$  for lead and liquid scintillator can be achieved.

### 6.2.3 Neutron Yield in Comparison with Geant4 Simulations

Based on the measured neutron yield and neutron candidate rates, we discuss possible effects on the neutron modelling in Geant4. Albeit the simulation reproduce the measured values within the uncertainties, the deviation of the central values may be interpreted in a consistent way. Also, possible changes due to newer Geant4 versions will be discussed.

Compared to the measurement ( $(2.7^{+1.0}_{-0.7}) \times 10^{-3} \text{cm}^2 \text{g}^{-1}$ , Eq. 6.6), the predicted external neutron yield by Geant4 9.2p01 ( $(3.2^{+0.3}_{-0.4}) \times 10^{-3} \text{cm}^2 \text{g}^{-1}$ , Eq. 5.73b) is bigger by a factor of

$$Y_{\text{ext,MC}} / Y_{\text{ext,exp}} = 1.18 \pm 0.07^{\text{stat}} {}^{+0.37^{\text{sys}}}_{-0.31} \pm 0.03^{\text{theo}}, \quad (6.9)$$

see also Fig. 6.1.

This is reflected by the pure neutron candidate to muon candidate ratio, i.e.  $\eta_{n,\mu} = (6.56^{+1.70}_{-1.96}) \times 10^{-2}$  (Eq. 5.67) predicted by Geant4 9.2p01 compared to a measured value of  $(5.5^{+0.33}_{-0.49}) \times 10^{-2}$  (Eq. 4.39). With a value of  $2.43^{+0.43}_{-0.59}$  (Eq. 5.66), the neutron content per neutron cascade candidate  $\eta_{n,\text{cas}}$  is also larger in Geant4 9.2p01 than in the measurement with  $1.75^{+0.20}_{-0.16}$  (Eq. 4.38).

The overproduction of neutrons per neutron cascade is *not* accompanied by an overproduction of neutron cascades per muon. On the contrary, the ratio  $\eta_{n,\mu} / \eta_{n,\text{can}}$  indicates less cascades in Geant4 than in measurement: respectively  $(2.7^{+0.6}_{-0.7}) \times 10^{-2}$  and  $(3.2^{+0.2}_{-0.4}) \times 10^{-2}$ .

Therefore, Geant4 9.2p01 may produce more high multiplicity cascades than measured. This is in agreement with the indication of Fig. 6.3, which shows an underproduction of neutrons in Geant4 at multiplicities  $\leq 2$ . If the experimental excess of high energy neutron candidates, see Sect. 6.1.2, is confirmed and established as significant in future work, one may speculate about the relation to the deficit of simulated low multiplicity events. By simulating more neutrons per cascade, the initial energy may be distributed over more secondary neutrons, leading to fewer high energy neutron candidates with small multiplicity.

The indication of an underproduction at low multiplicities also seems stable for more recent Geant4 versions. Hints for this are reported in [14] for Geant4 9.5p01 and a lead target, and in [3] for Geant4 9.6p01 and a hydrocarbon target. Conversely, the general neutron production is changed, as in [14] an underproduction for Geant4 9.5p01 by  $-21\%$  with respect to the measurement is reported.<sup>3</sup>

In conclusion, the measured neutron yield is remarkably well reproduced by simulations performed with Geant4 9.2p01. However, the slight deviations of the central values may indicate a general neutron overproduction per muon due to increased neutron content per neutron cascade, leading to a deficit of low multiplicity events.

#### 6.2.4 Neutron Production at Shower Equilibrium

The result for the external neutron yield (Eq. 6.6) is specific to the target used, and therefore only comparable for similar experiments. To obtain a target independent result, called the equilibrium neutron yield in Sect. 5.5.2, the approach of Eq. 5.55 can be used in two steps. First, the external neutron yield is used to calibrate a MC simulation of the measurement. Second, the calibrated MC is used to simulate the equilibrium neutron yield in an idealized target. This method is used in [14] to obtain the results for the ZEPLIN-II and ZEPLIN-III measurements (hereafter called *ZEPLIN results*) at Boulby, which are of special interest as the average muon energy at Boulby is with 260 GeV [14] similar to the 267 GeV (Eq. 5.74) obtained for LSM. Up to now, the ZEPLIN results are the only experimental results for the equilibrium neutron yield in lead.

We combined the two steps used to obtain the equilibrium neutron yield in a single factor  $Y_{\text{equi,MC}}/Y_{\text{ext,MC}}$  (Eq. 5.60b). Geant4 9.2p01 simulations with  $Y_{\text{equi,MC}}/Y_{\text{ext,MC}} = 1.122(15)$  (Eq. 5.60b) predict that for LSM the external neutron yield is nearly identical to the equilibrium neutron yield. As the study in Sect. 5.5.2 shows, the increased neutron production in equilibrium is roughly completely cancelled by the environmental factor. In the idealized simulations, used to determine the equilibrium neutron yield, the enhanced neutron production, probably caused by the muon shower, is missing.

---

<sup>3</sup>Reichhart et al. state a measured ‘muon-induced neutron detection rate’ of 0.346 compared to a simulated value of 0.275 [14].

Although the factorization in Eq. 5.60b was useful to discuss the physical contributions in Sect. 5.52, a more convenient factorization in terms of error calculation is

$$Y_{\text{equi}} = Y_{\text{equi,MC}} \frac{\eta_{n\mu, \text{exp}}}{\eta_{n\mu, \text{MC}}} \quad (6.10)$$

based on Eqs. 3.6a, 4.31, 5.55, 5.73b and 5.76.

Based on the measurements at LSM (Eq. 4.39) and simulations with Geant4 9.2p01 (Eqs. 5.56 and 5.67) we obtain an equilibrium neutron yield of

$$Y_{\text{equi}} = (3.05 \pm 0.18^{\text{stat}} \pm 1.18^{\text{sys}} \pm 0.07^{\text{theo}}) \times 10^{-3} \text{cm}^2 \text{g}^{-1}. \quad (6.11)$$

for a 266.5 GeV  $\mu^-$  beam on the idealized lead target of  $272.2 \times 105.5 \times 282$  cm, i.e.  $3087 \times 1197 \times 3198$  g cm $^{-2}$ .

Again the statistical uncertainty of  $Y_{\text{equi}}$  results from uncorrelated error propagation. The theoretical uncertainty is calculated similarly as in Sect. 6.2.1. The sources for the systematic uncertainties<sup>4</sup> are also the same arising from possible background in the experimental value of  $\eta_{n,\mu,\text{meas}}$  and model dependencies for the simulated values  $\eta_{n,\mu,\text{MC}}$ . The individual contributions are listed in Table 6.3. Obviously, via the additional simulation of  $Y_{\text{equi,MC}}$ , this scaled number is more dependent on Geant4 simulations and the actual Geant4 version than the external neutron yield.

Our value for the equilibrium neutron yield is in agreement with the latest update from ZEPLIN-II ( $3.4(1) \times 10^{-3} \text{cm}^2 \text{g}^{-1}$ , [14]), but smaller than the results from ZEPLIN-III ( $5.8(2) \times 10^{-3} \text{cm}^2 \text{g}^{-1}$ , [14]), see Fig. 6.4. As both ZEPLIN results were measured and simulated for the same underground site, the question arises of how to interpret their differences with each other, and the partial disagreement with our results. Discussion in [14] indicates that in comparison with ZEPLIN-III, the ZEPLIN-II results are more susceptible to inaccuracies in the Geant4 code due to a more complicated detector design. If one would consequently ignore the ZEPLIN-II results, our results would be in disagreement with the ZEPLIN results.

However, there are two possible refutations: First, as ZEPLIN-II and ZEPLIN-III measured at the same site, they should report the same yield. Therefore, the deviation between ZEPLIN-II and ZEPLIN-III may contribute as systematic effect to the uncertainties. Second, the ZEPLIN results are obtained with Geant4 9.5p01 simulations. Therefore, the value of our work may also change with an updated Geant4 version. As discussed in Sect. 5.5.2 via the factorization in Eq. 5.60b, the scaling does not depend on the absolute neutron yield, which increased by a factor of 1.265(6) (Eq. 5.61) relative to Geant4 9.2p01, but it depends more on the neutron contribution from the environment (laboratory hall, rock overburden, detector support structure, etc.). Therefore, a prediction of the changed value is not possible without repeating the detailed simulations in Sect. 5.5.1.

<sup>4</sup>We note that  $Y_{\text{equi,MC}}$  has no associated systematic uncertainties, as it was simulated under ideal conditions, i.e. no poly-energetic muon spectrum and no detector response that could introduce uncertainties.

**Table 6.3** Statistical, systematic, and theoretical uncertainties for the equilibrium neutron yield  $Y_{\text{equi}}$  relative to its average value

$\delta Y_{\text{equi}} (\%)$	
Statistical uncertainty	$\pm 5.90$
Systematic uncertainties	
$\eta_{n,\mu,\text{exp}} - \delta$	-2.85
$\eta_{n,\mu,\text{MC}} \pm \delta$	<b>-18.58</b> <b>+38.75</b>
Sum	+38.75 -21.43
Theoretical uncertainties	
Standard configuration	-0.30
APS	+2.22
GCM	-1.92
Sum	$\pm 2.22$
Sum	+46.86 -29.54

The alternative muon parameter set is denoted as APS and the alternative gamma cascade model as GCM. Statistically significant deviation are printed bold. For details see text

At present and regarding the differences between ZEPLIN-II and ZEPLIN-III, we conclude that our equilibrium neutron yield is not contradicted by the ZEPLIN results. Furthermore, our results may provide additional information to solve the tension between ZEPLIN-II and ZEPLIN-III results.

## References

1. Araújo H et al (2005) Muon-induced neutron production and detection with GEANT4 and FLUKA. *Nucl Instrum Methods Phys Res Sect A* 545(1–2):398–411. doi:[10.1016/j.nima.2005.02.004](https://doi.org/10.1016/j.nima.2005.02.004). arXiv:[hep-ex/0411026](https://arxiv.org/abs/hep-ex/0411026)
2. Araújo H et al (2008) Measurements of neutrons produced by high-energy muons at the Boulby underground laboratory. *Astropart Phys* 29(6):471–481. doi:[10.1016/j.astropartphys.2008.05.004](https://doi.org/10.1016/j.astropartphys.2008.05.004)
3. Bellini G et al [Borexino Collaboration] (2013) Cosmogenic backgrounds in Borexino at 3800 m water-equivalent depth. *J Cosmol Astropart Phys* 2013(08):049. doi:[10.1088/1475-7516/2013/08/049](https://doi.org/10.1088/1475-7516/2013/08/049). arXiv:[1304.7381](https://arxiv.org/abs/1304.7381) (physics.insdet)
4. Bergamasco L (1970) Experimental results on the pion and neutron production by muons at 60 and 110 m w.e. *Nuovo Cim B* 66(1):120–128. doi:[10.1007/BF02710194](https://doi.org/10.1007/BF02710194)
5. Bergamasco L, Costa S, Picchi P (1973) Experimental results on neutron production by muons at 4300 m w.e. *Nuovo Cim A* 13:403–412. doi:[10.1007/BF02827344](https://doi.org/10.1007/BF02827344)
6. Crouch MF, Sard RD (1952) The distribution of multiplicities of neutrons produced by cosmic-ray  $\mu$ -mesons captured in lead. *Phys Rev (2nd Ser)* 85(1):120–129. doi:[10.1103/PhysRev.85.120](https://doi.org/10.1103/PhysRev.85.120)

7. Gorshkov GV, Zyabkin VA (1968) Production of neutrons in Pb, Cd, Fe, and Al under the influence of cosmic-ray muons at a depth of 150 in water equivalent (trans: Adashko JG). Sov J Nucl Phys 7(4):470–474. Orig. pub. as Yad Fiz 7:770–777 [in Russian]
8. Gorshkov GV, Zyabkin VA (1970) Neutron production in Pb at a depth of 150 m w.e. under the influence of cosmic-radiation mesons traveling at large zenith angles (trans: Adashko JG). Sov J Nucl Phys 12(2):187–190. Orig. pub. as Yad Fiz 12:340–346 [in Russian]
9. Gorshkov GV, Zyabkin VA, Yakovlev RM (1973) Production of neutrons in Pb, Cd, Fe, and Al by high energy muons (trans: Adashko JG). Sov J Nucl Phys 18(1):57–61. Orig. pub. as Yad Fiz 18:109–117 [in Russian]
10. Gorshkov GV, Zyabkin VA, Yakovlev RM (1971) Production of neutrons in Pb, Cd, Fe, and Al and fission of Pb nuclei by cosmic rays in the depth range 0–1000 m water equiv (trans: Robinson CS). Sov J Nucl Phys 13(4):450–452. Orig. pub. as Yad Fiz 13:791–796 [in Russian]
11. Horn OM (2007) Simulations of the muon-induced neutron background of the EDELWEISS-II experiment for dark matter search. Scientific report FZKA 7391. Forschungszentrum Karlsruhe. <http://bibliothek.fzk.de/zb/berichte/FZKA7391.pdf>. Orig. pub. as PhD dissertation, Universität Karlsruhe (TH), 2007. <http://digibib.ubka.uni-karlsruhe.de/volltexte/1000007402>
12. Kozlov VY (2012/2013) Analysis of neutron counter data and dead time. E-mail messages to author, 1–9 Oct 2012 and 3 July 2013
13. Lemrani R et al (2006) Low energy neutron propagation in MCNPX and GEANT4. Nucl Instrum Methods Phys Res Sect A 560(2):454–459. doi:[10.1016/j.nima.2005.12.238](https://doi.org/10.1016/j.nima.2005.12.238). arXiv:[hep-ex/0601030](https://arxiv.org/abs/hep-ex/0601030)
14. Reichhart L et al (2013) Measurement and simulation of the muon-induced neutron yield in lead. Astropart Phys 47:67–76. doi:[10.1016/j.astropartphys.2013.06.002](https://doi.org/10.1016/j.astropartphys.2013.06.002). arXiv:[1302.4275](https://arxiv.org/abs/1302.4275) (physics.ins-det)
15. Rhode W (1993) Study of ultra high energy muons with the Fréjus Detector. PhD dissertation, Bergische Universität Gesamthochschule Wuppertal. <http://hdl.handle.net/10068/260384> (WUB-DIS 93-11)

# Chapter 7

## Conclusion and Outlook

Since about 80 years astronomical observations of gravitationally bound systems indicate a disagreement between visible matter and the involved dynamic mass, leading to the *problem of missing mass*. From the beginning, the existence of *dark matter* was proposed as possible explanation of this problem [42]. Albeit the hypothesis of dark matter is supported by various experimental results based on techniques as different as observation of the cosmic microwave background, primordial nucleosynthesis, strong and weak gravitation lensing, it is still challenged by the alternative hypothesis of modified gravitational theories, see Sect. 2.1.1. To further strengthen the dark matter paradigm, the discovery of a particle constituent is necessary. A possible candidate for such a constituent is the *WIMP*, which may be the lightest supersymmetric particle, i.e. a neutralino  $\chi$  in the minimal supersymmetric standard model, see Sect. 2.1.2.

Therefore, since roughly 30 years [20, 23] various efforts are undertaken to identify the constituent of the galactic dark matter by searching for its interaction with earth based targets. According to the minimal supersymmetric standard model, the most likely interaction would be elastic scattering of a WIMP off a target nuclei. This work was performed within the EDELWEISS collaboration which searches for the WIMP-induced nuclear recoils in cryogenic germanium crystals at the LSM. Combining the results from EDELWEISS-II [10] with the results from the CDMS II (Ge) experiment [4], both collaborations found no evidence for dark matter and could set the world leading upper limit on the scalar interaction of galactic WIMPs with germanium targets. The combined limit is with  $\sigma_{\chi,N}^{\text{SI}} < 3.3 \times 10^{-8} \text{ pb}$  at 90 % CL minimal at  $m_\chi c^2 = 90 \text{ GeV}$  [5]. It is third only to the results of the XENON100 experiment  $\sigma_{\chi,N}^{\text{SI}} < 2.0 \times 10^{-9} \text{ pb}$  at  $m_\chi c^2 = 55 \text{ GeV}$  [7] and LUX experiment  $\sigma_{\chi,N}^{\text{SI}} < 7.6 \times 10^{-10} \text{ pb}$  at  $m_\chi c^2 = 33 \text{ GeV}$  [7], which used liquid xenon as target. These exclusions are in tension with observed signal excesses over the known background in the experiments CDMS II (Si) [3], CoGeNT [1, 2], and CRESST [6] and the modulation observed with DAMA [13, 18, 19], see Figs. 2.10 and 2.11.

This tension motivated further searches with increased sensitivity and well understood background. To improve the sensitivity of EDELWEISS in its third stage (EDELWEISS-III) up to  $\sigma_{\chi, \text{N}}^{\text{SI}} < 2 \times 10^{-9} \text{ pb}$  within 12,000 kg.d exposure [12], an increase of the target mass and a reduction of the background is necessary. Whereas the background of  $\alpha$ -,  $\beta$ -, and  $\gamma$ -particles caused electron recoils, which can be suppressed by the dual readout of ionisation and heat signals of the EDELWEISS detectors, neutron-induced nuclear recoils are an indiscriminate background as they are barely distinguishably from WIMP induced nuclear recoils. Therefore, the incoming neutron flux above the detection threshold has to be reduced by various techniques depending on its origin. Ambient neutrons from uranium/thorium decay or  $(\alpha, n)$ -reactions are moderated below the detection threshold with passive shields made of polyethylene. Muon-induced neutrons originating in the experimental set-up, mostly in the lead shield, are suppressed by tagging the parent muon with a muon-veto system based on plastic scintillators [38]. This still leaves the possibility of neutrons with kinetic energies up to several GeV which are created by muons outside the muon veto. These muons can not be tagged, but the neutrons can penetrate the polyethylene shield without sufficient moderation. Whereas for EDELWEISS-II the muon-induced neutrons were only a minor source of background, this is not the case for EDELWEISS-III: Albeit the rate of background from unrejected muon-induced neutron is expected to be reduced due to an improved duty cycle of the muon veto, the background of ambient neutrons is more efficiently reduced by improved radiopurity and an additional polyethylene shield. Consequently, muon-induced neutrons will contribute, with at maximum 0.6 evts in 3000 kg.d, to the neutron background as much as ambient neutrons [11, 38], see Sect. 2.3.3 for details.

The increased relative contribution of muon-induced neutrons to the background of the direct dark matter search EDELWEISS highlights the importance of a reliable understanding of this kind of background source. Albeit EDELWEISS is able to measure the rate of muon-induced neutrons caused by tagged muons in situ, the rate is low<sup>1</sup> due to the rare process and the shielding of 4800 mwe against muons at LSM. Whereas this is an advantage in context of background reduction for the dark matter search, it limits the data set to study muon-induced neutron production in its own. Hence, one has to rely on Monte Carlo (MC) simulations. This is especially true for the fraction of muon-induced background which originate from outside the muon-veto.

However, modelling of muon-induced neutron production is not straight forward. As several, energy and target dependent production processes for muon-induced neutrons exist, the simulation depends on a correctly implemented local muon flux, geometry and libraries to describe the physical processes.

To obtain the local muon spectrum, the atmospheric muon flux has to be transformed to the local muon flux by considering the site specific energy loss and the local geometry, see Sects. 3.1–3.3. The local geometry of the experimental site has to be implemented in a detailed way, as the various materials can act as production

---

<sup>1</sup>Within 1504 kg.d exposure, a rate of muon-induced nuclear recoils, as expected from muon-induced neutrons, of 0.035evts kg.d<sup>1</sup> is stated in [11], equivalent to 53 events.

target for muon-induced neutrons. In particular, heavy materials like lead or neutron absorbers like the hydrogen rich plastic parts are of special interest. Within this geometry the simulation has to consider production processes ranging from low energy  $\mu^-$ -capture to high energy muon spallation. It also has to take into account the contribution from hadronic and electromagnetic showers that can be started in the rock overburden of the underground site, see Sect. 3.4. This complex situation is reflected by the great variance (76 %) of the simulated neutron production due to the chosen process models and its implementation on the neutron production, see Table 3.4.

Albeit the muon-induced neutron yield was measured in lead, a straightforward MC reproduction of these experimental results is difficult for three reasons (Sect. 3.5): for a muon energy of several hundred GeV (the average energy at the LSM is 255.0 GeV [37]) only sparse data exist. This is especially true for heavy materials like iron or lead which have a high neutron yield and which are therefore interesting for background estimations. Furthermore the few data [9, 16, 25, 36] are not in mutual agreement. Finally, for some older results like [16, 25], the published documentation of the experimental set-up is not as detailed as it would be needed for a reliable comparison with MC simulations. The importance of a detailed documentation is increased by the possible contamination of the results with muon-induced neutrons created outside of the targets, i.e. in the detector support structure and the walls of the underground site. Combining the uncertainty of the exact experimental set-up and the above mentioned uncertainty in the implemented physics model, the deviation between simulation and measurement is often given by a factor two or more, e.g. [8, 9, 28, 29, 32–34].

This lack of reliable data about the neutron production yield in lead and the debatable accuracy of the MC simulations motivated this work and its four main objectives: first, collect a sufficient data set of muon-induced neutrons at the LSM under well documented conditions. Second, simulate the neutron production at LSM in detail with Geant4 by considering the actual experimental set-up and the local environment. Third, make an assessment of Geant4’s accuracy by comparing the simulation with the previous measurement as reference. Finally, quantify the muon-induced neutron production yield at LSM.

For the measurement of muon-induced neutrons, we contributed to the design and installation of a dedicated neutron detector and the related DAQ electronics at LSM [30]. The neutron detector consisted of two sub-detectors: A neutron multiplicity meter (NMM), which is based on 10001 liquid scintillator loaded with 0.2 % w/w gadolinium (BC-525) and equipped with a lead target, in coincidence with a muon telescope consisting of two detector modules, see Sect. 4.2 for details. After thermalization, the produced neutrons are detected via the delayed scintillation signal caused by the  $Gd(n, \gamma)$  reaction and the subsequent absorption of the gammas. An offline search identified candidates for muon-induced neutrons based on a coincidence between a tagged muon and an event in the NMM with at least two signals: the first signal belongs to the muon, any secondary signal is a candidate for muon-induced neutrons (Sect. 4.3). Test measurements with an AmBe source showed clear evidence for captured neutrons (Fig. 4.18), proving the suitability of

the NMM for neutron detection. Similar, the energy spectrum of the tagged events in the muon telescope shows clearly the typical Landau-distribution which is expected for throughgoing muons (Fig. 4.19).

As detailed information about the experimental set-up are important for the simulation of this measurement, also the long term stability of the detector was monitored during the data taking from 2009 to 2012. A well-known problem of gadolinium loaded liquid scintillator is their chemical instability, leading to a deterioration of their transparency and precipitation of the solved gadolinium. Therefore, continuous monitor measurements with an AmBe source and an LED-based light pulser were performed. Based on Geant4 simulations, we could relate the experimental time distribution of the neutron capture process with the gadolinium content of the scintillator, see Fig. 4.14. Consequently, we determined a decrease of the gadolinium content from the nominal value of 0.2 % w/w at the begin of the measurement to 0.14 % w/w (Eq. 4.22) at the end. We also contributed to the development and installation of the LED-based light pulser to monitor the scintillator transparency (Sect. 4.4.3). In combination with Geant4 simulations of the light propagation in the NMM, the light pulser allowed the deduction of the attenuation length of the liquid scintillator. The observed deterioration of the attenuation length, dropping from 11.4 to 4.9 m, see also Fig. 4.16, is in agreement with literature values published for a scintillator which is chemically similar to the used BC-525. The lower value is still above the minimal attenuation length guaranteed by the manufacture (table A.5). During the run of the NMM, the deterioration was compensated by the PMT gain via increased high tension. As a result of the good performance of the LED-pulser, also newer modules of the EDELWEISS muon veto are equipped with LED-pulser modules to monitor the optical stability of the plastic scintillator.

In a long term measurement campaign from April 2009 to October 2012, the detector could accumulate a live-time of 964.5 d under controlled conditions. During this live-time, a sample of 5583 tagged muons in coincidence with 313 candidates for muon-induced neutrons within 181 neutron cascades were measured, see Table 4.2. Considering the shielding of 4800 mwe against muons at LSM and the rare occurrence of muon-induced neutron production, the data set can be considered as high statistic. It is about six times higher than the set of muon-induced neutrons identified via the EDELWEISS bolometer and muon-veto: within 1504 kg.d exposure, 53 muon-induced nuclear recoils, as expected from muon-induced neutrons, were identified in germanium bolometers [38]. Due to the used signature in coincidence with tagged muons, the data set collected within this work has a low background contribution from ambient neutrons and possible uranium contamination of the liquid scintillator (Table 5.14). Based on Geant4 simulations, we can state a signal-to-noise ration of 17, see Sect. 5.5.5 for details.

With the measured high statistics sample for muon-induced neutron candidates as reference, the reliability of Geant4 to simulate muon-induced neutron production was assessed. As the neutron production depends on the muon energy and on the available targets in the detector and in its surrounding, detailed three dimensional models of the muon flux at the LSM and of the detector geometry within the LSM cavern were implemented. However, to compare the simulated neutron production with the

measured neutron candidates, also a detector response model had to be included in the simulation. Consequently, we developed an end-to-end Geant4 simulation of muon-induced neutron production and detection: It models the muon propagation through the rock and concrete walls of LSM, the shower development, the neutron production and propagation in a detailed three dimensional copy of the detector in the LSM, the neutron detection, and the detector response including the event building in a consistent way.

The implemented geometry spans several levels of accuracy: starting with a newly developed model of the neutron counter based on technical drawings, over the existing, detailed model of the near-by EDELWEISS set-up [29], an approximate model of the more distant NEMO3 experiment, to the LSM cavern, see Figs. 5.1 and 5.2. We added the simplified model of the NEMO3 experiment, which was installed in LSM for most of the run-time of the neutron detector, as its massive iron parts and neutron shields affect the local neutron field.

Within the Geant4 geometry, the three-dimensional muon flux was propagated through at least 5 m of rock which allows the muon-induced showers to reach equilibrium. Consequently, the simulation tracks all electromagnetic and hadronic shower products and includes their influence on the detector. The simulated muon flux was generated with an improved version of a muon generator [29], taken into account the three-dimensional topography of the rock overburden [40] and the measured energy loss of muons in LSM rock [37], see as well Sect. 5.3. In total, we simulated about  $5.5 \times 10^7$  muons ( $\mu^+/\mu^- \approx 1.37$ ) ranging in energy from 2 GeV to 20 TeV, representing at least 99.997 % of the local muon flux at the LSM (Table 5.5). With this configuration, we could perfectly reproduce the angular flux spectra measured by the Fréjus collaboration with high statistics [17, 40], see Fig. 5.6. Also the average kinetic muon energy of  $267_{-11}^{+8}$  GeV is in agreement with 255.0(45) GeV measured by the Fréjus collaboration [37]. The agreement, in both angular distribution and average energy, highlights the reliability of the muon generator. This was also confirmed by an independent test against data obtained from the EDELWEISS muon veto [38].

The simulated muon flux over the four decades in energy enables the simulation of neutron production processes from low energies, like  $\mu^-$ -capture, to high energies, like muon spallation. To implement this processes we take the physics list defined in [29], which aimed for a high precision modelling of muon-induced neutron production, and updated it to Geant4 9.2p01, the latest version used within this work. We extended the physics list by optical light propagation, radioactive decay, and a dedicated high precision model for neutron capture on gadolinium provided by the Double Chooz collaboration [35, 41] to model the detector response (Sect. 5.2).

We considered the detector response of the muon telescope and the NMM with a calibrated model on an event-by-event base (Sect. 5.4). As we identified candidates for muon-induced neutrons mainly on their multiplicity within an event, not only the energy response had to be considered but also the clustering of single signals within the event and ADC windows. To fix the free parameters, the model was fitted to AmBe calibration measurements via a five dimensional log likelihood fit (Sect. 5.4.4). For the energy scale, the detector response model reconstructs the ADC values which

are directly equivalent to the experimental values. Therefore, we found it most suitable to express the results of our simulation in ADC units instead of expressing the experimental results in eV, as this respects the detachment of simulation and measurement.

The model considered the influence of the PMT gain and resolution, and the DAQ trigger threshold for the muon telescope and the NMM. In case of the NMM, also the light propagation and the ionisation quenching [21] is taken into account. The model of the light propagation is based on a three-dimensional propagation of the scintillation light through the actual, optical active volume of the NMM and its absorption on the photocathodes of the PMTs. The model treats the attenuation length of the liquid scintillator as a free parameter, which was determined via calibration measurement with AmBe. As already mentioned, the light propagation model was also used to monitor the transparency of the scintillator.

The ionisation quenching depends on the quenching factor  $kB$  as free parameter, determined via the AmBe calibration to  $kB = 0.016(4) \text{ g MeV}^{-1} \text{ cm}^{-2}$ . As far as we know, this is the first measurement of  $kB$  for BC-525. The value is well in the range expected from chemically similar scintillators,  $0.0094\text{--}0.035 \text{ g MeV}^{-1} \text{ cm}^{-2}$  [39], which further supports our trust in the detector response model.

Applying best fitting values for all the above mentioned parameters, the simulation agrees well with the AmBe calibration measurements, expressed by the ratio of simulated to measured event rates. For the muon telescope this is 0.88 (Eq. 5.54) and for the NMM it is 0.95 (Eq. 5.52b). These deviations between the simulation and the calibration measurement are taken into account as systematic uncertainties.

By convoluting the muon flux, the neutron production processes, and the detector response, we simulated a data set of candidates for muon-induced neutrons, identified by the same signature as used in the experiment (Sect. 5.5).

Throughout the implemented geometry, around  $1.1 \times 10^7$  neutrons are produced by the  $5.5 \times 10^7$  simulated muons. Out of this, roughly  $1.3 \times 10^5$  neutrons terminate in the liquid scintillator of the neutron detector, see Fig. 5.26. Albeit over 95.5 % of these neutrons are produced within a distance of 1.19 m around the neutron counter, see Fig. 5.27, a detailed implemented geometry is still necessary. Only 78.2 % of the  $1.3 \times 10^5$  neutrons are produced in the lead target, see Fig. 5.28 for a detailed list of the production volumes. Therefore, a simplified simulation with only the lead target would underestimate the detected neutron rate by 21.8 %.

However, the simulated rate of muon-induced neutrons is not directly comparable to the measured rate of *candidates* for muon-induced neutrons, as the latter may be affected by pile-ups or contamination of other secondary particles of the muon shower, e.g. gammas from bremsstrahlung. To consider these effects, we applied the detector response model to the *full* simulation of muon-induced interactions, not only to the subset of muon-induced neutrons. Consequently the *simulated* rate of neutron candidates can be compared to the *measured* rate of neutron candidates.

This direct comparison between simulation and measurement allowed us to assess the capability of Geant4 9.2p01 to model the detector response for muon-induced neutrons. In this assessment we considered three types of uncertainties: statistical uncertainties due to limited statistics of the data sets, systematic uncertainties mostly

due to uncertainties in the parameters for the detector response model, and theoretical uncertainties mostly due to the chosen model for the incident muon flux, see Tables 5.10 and 5.11 for details.

Within the uncertainties, we find good agreement between simulation and measurement. Therefore, we state the accuracy of Geant4 to simulate muon-induced neutron events by the deviation between the central values. This deviation of the *absolute* integral rate of neutron candidates  $R_n$  differs between simulation  $(3.8_{-1.1}^{+1.6}) \times 10^{-1} \text{d}^{-1}$  (Eq. 5.65) and experiment  $(3.2_{-0.3}^{+0.5}) \times 10^{-1} \text{d}^{-1}$  (Eq. 4.35) by (Eq. 6.1)

$$\frac{R_{n,MC} - R_{n,exp}}{R_{n,exp}} = +17\%$$

with respect to the measurement. The experimental precision is 16 % and the simulation has a precision of 43 %. The latter is dominated by systematic effects of the detector response model like the shift in the gadolinium content of the NMM or uncertainties in the time normalization, see the discussion in Sect. 5.5.4 for details. Conversely, the experimental precision is limited by the statistics, see Sect. 4.5.2. The agreement between simulation and measurement is clearly better than the often cited factor two, see Fig. 6.1, and also better than the 76 % expected from Table 3.4. For the rate of detected neutrons per muon, our simulation has a deviation of 18 % from the measurement (Eq. 6.2), which is in absolute terms less than the recently obtained -21 % for ZEPLIN-III and Geant4 9.5p01 [36].

Whereas the simulation *over-produces* neutron candidates, it *under-produces* the rate of cascade candidates  $R_{cas}$ , but again agrees within the uncertainties. With respect to the measurement  $(1.8_{-0.2}^{+0.3}) \times 10^{-1} \text{d}^{-1}$  (Eq. 4.36), the central value of the simulation  $(1.5_{-0.4}^{+0.6}) \times 10^{-1} \text{d}^{-1}$  (Eq. 5.64) is smaller by (Eq. 6.3)

$$\frac{R_{cas,MC} - R_{cas,exp}}{R_{cas,exp}} = -16\%.$$

Again, the assessment is limited by the precision of the simulation of 39 % compared to 13 % for the measurement. This under-production considering the central values is reflected by the multiplicity spectrum. The event topology is indicated by the *absolute* rate of neutron candidates as function of the neutron candidate multiplicity per neutron cascade. Also in this case an agreement between simulation and measurement within the uncertainties is found, as shown in Fig. 6.3. In literature, often only a *relative* agreement was achieved, e.g. [36].

Also the energy spectrum of the neutron candidates (Fig. 6.2a) shows an interesting feature: at energies  $\gtrsim 50 \text{ MeV}$  it shows a clear experimental excess over the simulation, possibly due to an underproduction of energetic muon-induced neutrons in Geant4. However, in this work the systematic uncertainties were only considered for the integral rates and the multiplicity spectrum, not for the energy spectrum of the neutron candidates. Therefore, it is the task of future works to evaluate the statistical significance of this excess.

Although the measured rate of muon-induced neutrons can be reproduced by simulation within the uncertainties, we argue that the deviation of the central values may be explained in a consistent way, see Sect. 6.2.3. The over-production of neutrons in parallel with the under-production of neutron cascades may lead to a higher average neutron multiplicity in the simulation and to the deficit at low multiplicity cascades. Albeit we found an agreement of the simulated and measured multiplicity spectra within the uncertainty (Fig. 6.3), the central values show a deviation at low multiplicities. As consequence of the higher average neutron multiplicity, the available energy per cascade is distributed over more neutrons, leading to less high energy neutrons in Geant4 compared to the measurement. The indication of an underproduction at low multiplicities also seems stable for more recent Geant4 versions. Hints to this are reported in [36] for Geant4 9.5p01 and lead as a target, and in [14] for Geant4 9.6p01 and a hydrocarbon target. Conversely, the general neutron production is changed, as in [36] an underproduction for Geant4 9.5p01 by  $-21\%$  with respect to the measurement is reported.

Albeit the direct comparison between the end-to-end simulation of muon-induced neutron production and detection and the dedicated measurement at the LSM makes the assessment of Geant4 possible, it is still specific to the used detector. A more detector-independent quantity to specify the muon-induced neutron production at the LSM is the *neutron yield* (Eq. 3.64a), i.e. the ratio of neutron candidates to muons corrected by the neutron detection efficiency and by the average target thickness along the muon tracks.

From the full Geant4 simulation we deduced the detection efficiency and target thickness. The detection efficiency for muon-induced neutrons from the lead target, i.e. the ratio between simulated neutrons emitted from the lead target to simulated number of neutron candidates in the neutron counter, is  $\bar{\epsilon}_n = 15^{+3}_{-4}\%$  (Eq. 5.77). This efficiency reflects also the contribution of neutrons that may be produced elsewhere, but scatter inside the lead target. For the triggered muons, the simulation returns an average column density of the lead target of  $\langle \bar{X} \rangle = 135.2(3) \text{ g cm}^{-2}$  (Eq. 5.75b). Based on these quantities from the simulation together with the measured numbers of muon and neutron candidates, we deduced a neutron yield (Eq. 6.6) of

$$\langle Y \rangle = (2.7^{+1.0}_{-0.7}) \times 10^{-3} \text{ cm}^2 \text{ g}^{-1}$$

for  $\langle \bar{E}_\mu \rangle = 267^{+8}_{-11} \text{ GeV}$  (Eq. 5.74). As the used target is *thin*, the muon-induced shower inside the target can not reach equilibrium, therefore the neutron yield is still detector-specific as it depends on the target thickness. However, it can be compared to similar thin targets [15, 16, 22, 24–27]. Albeit [22] seems to be a valid measurement, we note that it introduces a strong tension in the data set, see the discussion in Sects. 3.5.4 and 6.2.2. Depending whether we include [22] in the data set or not, the relative residual between our measurement and a fit  $Y = c_1(E_\mu)^\alpha$  (Eq. 3.66) to the data set vary between 69 and 35 %.

To reduce the dependency of the neutron yield on the target thickness, one can define the *equilibrium* neutron yield by scaling the measured neutron yield for a thin target to the neutron yield for a target thick enough to reach equilibrium, usually placed in vacuum [9, 31, 33, 36]. We note, that this method increases the dependence on the used MC package in exchange to a decreased detector dependence. So far, only the ZEPLIN collaboration [36] has published values for the equilibrium neutron yield in lead, but their values are of special interest for this work: they were obtained with the experiments ZEPLIN-II and ZEPLIN-III at the Boulby underground facility which has an average muon energy of 260 GeV [36], similar to the 267 GeV (Eq. 5.74) we obtained for LSM. Therefore, one would expect similar neutron yields at Boulby and LSM.

With Geant4 9.2p01, we scaled our measured neutron yield to the neutron yield in a  $3198 \text{ g cm}^{-2}$  thick lead target placed in vacuum, a thickness comparable to [36]. For this configuration, we find an equilibrium neutron yield (Eq. 6.11) of

$$Y_{\text{equi}} = (3.1_{-0.9}^{+1.4}) \times 10^{-3} \text{ cm}^2 \text{ g}^{-1}.$$

Within the uncertainties, this value is in agreement with the results of the earlier ZEPLIN-II experiment ( $Y_{\text{equi}} = 3.4(1) \times 10^{-3} \text{ cm}^2 \text{ g}^{-1}$ , [36]), but not with the results of ZEPLIN-III ( $Y_{\text{equi}} = 5.8(2) \times 10^{-3} \text{ cm}^2 \text{ g}^{-1}$ , [36]). However, as both ZEPLIN-II and ZEPLIN-III measured at the same site, they should report the same yield. Therefore, the deviation between the ZEPLIN-II and ZEPLIN-III can be considered as a kind of systematic uncertainty for their measurement in addition to the stated uncertainty. Hence, we conclude that our equilibrium neutron yield is not contradicted by the ZEPLIN results. Furthermore, our results may provide additional information to solve the tension between the ZEPLIN-II and ZEPLIN-III results.

Because of the increased column density ( $3198 \text{ g cm}^{-2}$ ), one expects a higher equilibrium neutron yield compared to the one in the thin target of  $135.2(3) \text{ g cm}^{-2}$ . However, the equilibrium neutron yield is only  $1.122(15)$  (Eq. 5.60b) times the size of the thin target. We found that the expected increase of the neutron yield due to the increased thickness is nearly completely cancelled by changing the LSM environment with the vacuum surrounding. As we already corrected for the influence of incident neutrons on the target via the neutron detection efficiency, this strong contribution of the environment on the neutron yield may be associated with a boosted neutron production inside the lead target by the muon shower which is present in full geometry, but missing in a vacuum as surrounding. Therefore, *cosmic-induced neutrons* may be a better description instead of *muon-induced neutrons*, as the latter focus only on the primary muon whereas the simulation highlights also the importance of the secondary shower products. See the discussion in Sect. 5.5.2 for more details.

In summary, within this work we contributed to the design and installation of a dedicated neutron counter at the LMS to collect a reference data set of candidates for muon-induced neutron. We developed and calibrated an end-to-end simulation in Geant4 9.2p01 of the muon-induced neutron production and detection. By comparing the simulation to the measurement, we can state an agreement within uncertainties

in integral rate and in event topology. The central values of the neutron candidate rate differs by 15 %. Finally, for the first time we quantified a neutron yield in lead at LSM of  $\langle Y \rangle = (2.708^{+0.98}_{-0.10}) \times 10^{-3} \text{ cm}^2 \text{ g}^{-1}$  for  $\langle E_\mu \rangle = 267^{+8}_{-11} \text{ GeV}$ , scaled to an equilibrium neutron yield of  $Y_{\text{equi}} = (3.1^{+1.4}_{-0.9}) \times 10^{-3} \text{ cm}^2 \text{ g}^{-1}$ .

These results show that Geant4 is a reliable tool to simulate muon-induced neutron production and detection, if the experimental geometry and detector response are implemented properly and in full detail. Therefore, Geant4 can be used for future investigations of muon-induced neutrons to model background for direct dark matter searches like EDELWEISS or the future EURECA experiment.

EDELWEISS, as well as EURECA if it will be built at LSM, may further benefit from this work, as the measured muon-induced neutrons may serve as reference data also for future simulations. As the detailed implementation of the detector geometry and response is available to the EDELWEISS collaboration via an SVN repository, it should be possible to validate the muon-induced neutron production also in more recent Geant4 versions against the measured data set of muon-induced neutron candidates, maybe even on a regular base. In Appendix A.3.3 we find no predictable complication for a possible migration of our simulation code to more recent Geant4 versions. Even if the compatibility of our implementation to the most recent Geant4 version breaks at some point in the future, the detailed description of the detector geometry, materials, and DAQ parameters in this work should make a migration or even re-implementation possible. We regard this as an advantage compared to the limited documentation of especially the older experiments reported in literature.

Besides this direct use as test benchmark, this work may inspire also further investigations of the muon-induced neutron production at LSM: a more precise neutron yield for lead, deduction of neutron yields for further materials, the de-convolution of the multiplicity and energy spectra for muon-induced neutrons.

It should be possible to increase the precision by reducing the systematic uncertainties of the simulation and the measurements. For the latter, the systematic uncertainty is determined by the dead time estimation. This estimated uncertainty could be replaced by a correction of the live-time by the exact dead time. Similar for the simulation, the estimated uncertainty due to the gadolinium precipitation could be replaced by an efficiency correction for the gadolinium decrease over time, based on the AmBe monitor measurements. A further reduction of the systematic uncertainty of the simulation may be possible by an improved detector response model for the muon telescope, see the discussion in Sect. 5.5.4.

Similar to the measurement of the neutron yield in lead, it should be possible to determine the neutron yield in iron by adopting a detection efficiency for neutrons from the iron support structure of the neutron counter. The deduction for the neutron yield in liquid scintillator would be more complicated, as target and detector are identical in this case.

As discussed in Sect. 5.5.6, also an deconvolution of measured multiplicity and energy spectra of the *neutron candidates* seems possible to obtain further information of the *neutron* production.

This work demonstrates, that Geant4 can reliably model the production and detection of muon-induced neutrons once all relevant production processes and a detailed description of the detector response and geometry are implemented in the model. Thus, one of the most prominent background sources for Dark Matter search can be accurately modelled and eventually suppressed.

## References

1. Aalseth CE et al [CoGeNT Collaboration] (2011) Results from a search for light-mass dark matter with a *p*-type point contact germanium detector. *Phys Rev Lett* 106(13):131301. doi:[10.1103/PhysRevLett.106.131301](https://doi.org/10.1103/PhysRevLett.106.131301). arXiv:[1002.4703](https://arxiv.org/abs/1002.4703) [astro-ph]
2. Aalseth CE et al [CoGeNT Collaboration] (2011) Search for an annual modulation in a *p*-type point contact germanium dark matter detector. *Phys Rev Lett* 107(14):141301. doi:[10.1103/PhysRevLett.107.141301](https://doi.org/10.1103/PhysRevLett.107.141301). arXiv:[1106.0650](https://arxiv.org/abs/1106.0650) [astro-ph.CO]
3. Agnese R et al [CDMS Collaboration] (2013) Dark matter search results using the silicon detectors of CDMS II. arXiv:[1304.4279](https://arxiv.org/abs/1304.4279) [hep-ex]
4. Ahmed Z et al [CDMS II Collaboration] (2010) Dark matter search results from the CDMS II experiment. *Science* 327(5973):1619–1621. doi:[10.1126/science.1186112](https://doi.org/10.1126/science.1186112)
5. Ahmed Z et al [CDMS and EDELWEISS collaborations] (2011) Combined limits on WIMPs from the CDMS and EDELWEISS experiments. *Phys Rev D* 84(1):011102. doi:[10.1103/PhysRevD.84.011102](https://doi.org/10.1103/PhysRevD.84.011102). arXiv:[1105.3377](https://arxiv.org/abs/1105.3377) [astro-ph.CO]
6. Angloher G et al (2012) Results from 730 kg days of the CRESST-II dark matter search. *Eur Phys J C* 72:1971. doi:[10.1140/epjc/s10052-012-1971-8](https://doi.org/10.1140/epjc/s10052-012-1971-8). arXiv:[1109.0702](https://arxiv.org/abs/1109.0702)
7. Aprile E et al [XENON100 Collaboration] (2012) Dark matter results from 225 live days of XENON100 data. *Phys Rev Lett* 109(18):181301. doi:[10.1103/PhysRevLett.109.181301](https://doi.org/10.1103/PhysRevLett.109.181301). arXiv:[1207.5988](https://arxiv.org/abs/1207.5988) [astro-ph.CO]
8. Araújo H et al (2005) Muon-induced neutron production and detection with GEANT4 and FLUKA. *Nucl Instrum Methods Phys Res Sect A* 545(1–2):398–411. doi:[10.1016/j.nima.2005.02.004](https://doi.org/10.1016/j.nima.2005.02.004). arXiv:[hep-ex/0411026](https://arxiv.org/abs/hep-ex/0411026)
9. Araújo H et al (2008) Measurements of neutrons produced by high-energy muons at the Boulby Underground Laboratory. *Astropart Phys* 29(6):471–481. doi:[10.1016/j.astropartphys.2008.05.004](https://doi.org/10.1016/j.astropartphys.2008.05.004)
10. Armengaud E et al [EDELWEISS Collaboration] (2011) Final results of the EDELWEISS-II WIMP search using a 4-kg array of cryogenic germanium detectors with interleaved electrodes. *Phys Lett B* 702(5):329–335. doi:[10.1016/j.physletb.2011.07.034](https://doi.org/10.1016/j.physletb.2011.07.034). arXiv:[1103.4070](https://arxiv.org/abs/1103.4070) [astro-ph.CO]
11. Armengaud E et al [EDELWEISS Collaboration] (2013) Background studies for the EDELWEISS dark matter experiment. *Astropart Phys* 47:1–9. doi:[10.1016/j.astropartphys.2013.05.004](https://doi.org/10.1016/j.astropartphys.2013.05.004). arXiv:[1305.3628](https://arxiv.org/abs/1305.3628) [physics.ins-det]
12. Arnaud Q [For the EDELWEISS collaboration] (2014) The EDELWEISS Experiment Status. In: Augé E, Dumarchez J, Trần Thanh Vân J (eds) *Proceedings of the 49th RENCONTRES DE MORIOND. Cosmology*, (La Thuile, Aosta Valley, Italy, Mar. 22–29, 2014), pp 175–178 ARISF. [http://moriond.in2p3.fr/Proceedings/2014/Moriond\\_Cosmo\\_2014.pdf](http://moriond.in2p3.fr/Proceedings/2014/Moriond_Cosmo_2014.pdf)
13. Belli P et al (2011) Observations of annual modulation in direct detection of relic particles and light neutralinos. *Phys Rev D* 84(5):055014. doi:[10.1103/PhysRevD.84.055014](https://doi.org/10.1103/PhysRevD.84.055014). arXiv:[1106.4667](https://arxiv.org/abs/1106.4667) [hep-ph]
14. Bellini G et al [Borexino Collaboration] (2013) Cosmogenic Backgrounds in Borexino at 3800 m water-equivalent depth. *J Cosmol Astropart Phys* 2013(08):049. doi:[10.1088/1475-7516/2013/08/049](https://doi.org/10.1088/1475-7516/2013/08/049). arXiv:[1304.7381](https://arxiv.org/abs/1304.7381) [physics.ins-det]

15. Bergamasco L (1970) Experimental results on the pion and neutron production by muons at 60 and 110 m w.e. *Nuovo Cim B* 66(1):120–128. doi:[10.1007/BF02710194](https://doi.org/10.1007/BF02710194)
16. Bergamasco L, Costa S, Picchi P (1973) Experimental results on neutron production by muons at 4300 m w.e. *Nuovo Cim A* 13:403–412. doi:[10.1007/BF02827344](https://doi.org/10.1007/BF02827344)
17. Berger C et al [Fréjus Collaboration] (1989) Experimental study of muon bundles observed in the Fréjus detector. *Phys Rev D* 40(7):2163–2171. doi:[10.1103/PhysRevD.40.2163](https://doi.org/10.1103/PhysRevD.40.2163)
18. Bernabei R et al (2008) First results from DAMA/LIBRA and the combined results with DAMA/NaI. *Eur Phys J C* 56(3):333–355. doi:[10.1140/epjc/s10052-008-0662-y](https://doi.org/10.1140/epjc/s10052-008-0662-y)
19. Bernabei R et al (2010) New results from DAMA/LIBRA. *Eur Phys J C* 67(1–2):39–49. doi:[10.1140/epjc/s10052-010-1303-9](https://doi.org/10.1140/epjc/s10052-010-1303-9)
20. Bertone G (ed) (2010) Particle dark matter: observations, models and searches. Cambridge University Press, Cambridge
21. Birks JB (1964) The theory and practice of scintillation counting. International series of monographs on electronics and instrumentation 27. Pergamon Press, New York
22. Crouch MF, Sard RD (1952) The distribution of multiplicities of neutrons produced by cosmic-ray  $\mu$ -mesons captured in lead. *Phys Rev 2nd ser* 85(1):120–129. doi:[10.1103/PhysRev.85.120](https://doi.org/10.1103/PhysRev.85.120)
23. Gaitskell RJ (2004) Direct detection of dark matter. *Annu Rev Nucl Part Sci* 54(1):315–359. doi:[10.1146/annurev.nucl.54.070103.181244](https://doi.org/10.1146/annurev.nucl.54.070103.181244)
24. Gorshkov GV, Zyabkin VA (1968) Production of neutrons in Pb, Cd, Fe, and Al under the influence of cosmic-ray muons at a depth of 150 m water equivalent (trans: Adashko JG). *Sov J Nucl Phys* 7(4):470–474. Orig. pub. as *Yad Fiz* 7:770–777 (1968) [in Russian]
25. Gorshkov GV, Zyabkin VA (1971) Neutron production in Pb at a depth of 150 m w.e. under the influence of cosmic-radiation mesons traveling at large zenith angles. (trans: Adashko JG). *Sov J Nucl Phys* 12(2):187–190. Orig. pub. as *Yad Fiz* 12:340–346 (1970) [in Russian]
26. Gorshkov GV, Zyabkin VA, Yakovlev RM (1974) Production of neutrons in Pb, Cd, Fe, and Al by high energy muons (trans: Adashko JG). *Sov. J. Nucl. Phys* 18(1):57–61. Orig. pub. as *Yad Fiz* 18:109–117 (1973) [in Russian]
27. Gorshkov GV, Zyabkin VA, Yakovlev RM (1971) Production of neutrons in Pb, Cd, Fe, and Al and fission of Pb nuclei by cosmic rays in the depth range 0–1000 m water equiv (trans: Robinson CS) *Sov J Nucl Phys* 13(4):450–452. Orig. pub. as *Yad Fiz* 13:791–796 (1971) [in Russian]
28. Hemmings-Yeomans R, Akerib D (2007) A neutron multiplicity meter for deep underground muon-induced high-energy neutron measurements. *Nucl Instrum Methods Phys Res Sect A* 574(1):89–97. doi:[10.1016/j.nima.2007.01.137](https://doi.org/10.1016/j.nima.2007.01.137)
29. Horn OM (2007) Simulations of the muon-induced neutron background of the EDELWEISS-II experiment for Dark Matter search. Scientific report FZKA 7391. Forschungszentrum Karlsruhe. <http://bibliothek.fzk.de/zb/berichte/FZKA7391.pdf>. Orig. pub. as PhD Dissertation, Universität Karlsruhe (TH). <http://digibib.ubka.uni-karlsruhe.de/volltexte/1000007402>
30. Kozlov VY [For the EDELWEISS Collaboration] (2008) Studies of the muon-induced neutron background in LSM: detector concept and status of the installation. In Identification of dark matter 2008, proceedings of science IDM2008 (Stockholm, Sweden, Aug. 18–22, 2008). Trieste: SISSA, p 86. arXiv:[0902.4858v1](https://arxiv.org/abs/0902.4858v1) [astro-ph.IM]
31. Kudryavtsev VA (2013) Definition of neutron yield and reference for the energy distribution of neutrons from  $(\alpha, n)$  reactions. 2013. E-mail message to author, June 24, 2013
32. Kudryavtsev V, Pandola L, Tomasello V (2008) Neutron-and muon-induced background in underground physics experiments. *Eur Phys J A* 36(2):171–180. doi:[10.1140/epja/i2007-10539-6](https://doi.org/10.1140/epja/i2007-10539-6)
33. Lindote A et al (2009) Simulation of neutrons produced by high-energy muons underground. *Astropart Phys* 31:366–375. doi:[10.1016/j.astropartphys.2009.03.008](https://doi.org/10.1016/j.astropartphys.2009.03.008). arXiv:[0810.1682](https://arxiv.org/abs/0810.1682) [hep-ex]
34. Mal'gin A, Ryazhskaya O (2008) Neutrons from muons underground. *Phys At Nucl* 71(10):1769–1781. doi:[10.1134/S1063778808100116](https://doi.org/10.1134/S1063778808100116)
35. Motta D, Zbiri K [On behalf of the Double Chooz Collaboration] (2005) Simulations for Double Chooz. Presented at the MANDsim Workshop, Manhattan, KS, US, 14–15 June 2005. [http://neutrino.phys.ksu.edu/MAND-sim/MANDsim%20talks/DoubleChooz\\_motta.pdf](http://neutrino.phys.ksu.edu/MAND-sim/MANDsim%20talks/DoubleChooz_motta.pdf)

36. Reichhart L et al (2013) Measurement and simulation of the muon-induced neutron yield in lead. *Astropart Phys* 47:67–76. doi:[10.1016/j.astropartphys.2013.06.002](https://doi.org/10.1016/j.astropartphys.2013.06.002). arXiv:[1302.4275](https://arxiv.org/abs/1302.4275) [physics.ins-det]
37. Rhode W (1993) Study of Ultra High Energy Muons with the Fréjus Detector. PhD Dissertation, Bergische Universität Gesamthochschule Wuppertal. <http://hdl.handle.net/10068/260384>. WUB-DIS 93-11
38. Schmidt B et al [EDELWEISS collaboration] (2013) Muon-induced background in the EDELWEISS dark matter search. *Astropart Phys* 44:28–39. doi:[10.1016/j.astropartphys.2013.01.014](https://doi.org/10.1016/j.astropartphys.2013.01.014). arXiv:[1302.7112](https://arxiv.org/abs/1302.7112) [astro-ph.CO]
39. Tretyak V (2010) Semi-empirical calculation of quenching factors for ions in scintillators. *Astropart Phys* 33(1):40–53. doi:[10.1016/j.astropartphys.2009.11.002](https://doi.org/10.1016/j.astropartphys.2009.11.002)
40. Wei Y (1993) Untersuchung der neutrinoinduzierten Myonen im Fréjus-Untergrunddetektor' [in German]. PhD Dissertation, Bergische Universität Gesamthochschule Wuppertal, WUB-DIS 93-8
41. Zbiri K (2011) GdHPCapture. E-mail message to author, March 24, 2011
42. Zwicky F (1933) Die Rotverschiebung von extragalaktischen Nebeln [in German]. *Helv Phys Acta* 6(2):110–127. doi:[10.5169/seals-110267](https://doi.org/10.5169/seals-110267)

# Appendix

## A.1 The Cosmological Framework

The expansion of the Universe since the big bang followed the field equation of Einstein's general relativity. Under the assumption that the Universe is homogeneous and isotropic at large scales, a particle propagating in such a Universe on a trajectory is given by the *Robertson-Walker* metric [57]:

$$d\tau^2 = dt^2 - a(t)^2 \left[ \frac{dr^2}{1 - kr^2} + r^2 (d\theta^2 + \sin^2 \theta d\phi^2) \right]. \quad (\text{A.1})$$

Here,  $\tau$  is the proper time of the particle and  $t, r, \theta, \phi$  are comoving coordinates. The *curvature parameter*  $k = -1, 1, 0$  indicates a universe with negatively curved, positively curved, or flat geometry, respectively.

The *scaling parameter*  $a(t)$  describes the expansion of the Universe and is determined by the *Friedmann* equations [57]:

$$\left( \frac{\dot{a}}{a} \right)^2 + \frac{k}{a^2} = \frac{8\pi G\rho}{3} \quad (\text{A.2})$$

$$\frac{-2\ddot{a}}{a} - \left( \frac{\dot{a}}{a} \right)^2 + \frac{k}{a^2} = 8\pi Gp, \quad (\text{A.3})$$

with Newton's gravitational constant  $G$ . The matter content of the universe is characterized by its pressure  $p$  and energy density  $\rho$ .

Under the assumption that the Universe consists only of non-relativistic matter, relativistic radiation, and vacuum energy, the first Friedmann Eq. (A.2) can be expressed by [57]:

$$\left(\frac{\dot{a}}{a}\right)^2 = H_0^2 \left( \Omega_m \hat{a}^{-3} + \Omega_r \hat{a}^{-4} + \Omega_\Lambda + (1 - \Omega_T) \right), \quad \hat{a} = a/a_0 \quad (\text{A.4})$$

$$\text{with } H_0 = \left. \frac{\dot{a}}{a} \right|_{t_0}, \quad (\text{A.5})$$

where  $a_0 = a(t_0)$  is the scaling parameter at the present epoch  $t_0$  and  $H_0$  the present Hubble's constant. The  $\Omega$ 's [57]

$$\Omega_i = \frac{\rho_i(a_0)}{\rho_c}. \quad (\text{A.6})$$

are the contributions of non-relativistic matter ( $\Omega_m$ ), relativistic matter or radiation ( $\Omega_r$ ), and vacuum energy ( $\Omega_\Lambda$ ) to the total energy density of the universe  $\Omega_T = \rho/\rho_c$ ,  $\Omega_T = \sum_i \Omega_i$ , normalized to the *critical density* [57]:

$$\rho_c = \frac{3H_0^2}{8\pi G}. \quad (\text{A.7})$$

Observations of the cosmic microwave background by the PLANCK observatory [2] are in agreement with a flat universe  $\Omega_T = 1$  and lead to the following energy budget of the Universe:

$$\Omega_\Lambda = 0.683 \quad (\text{A.8a})$$

$$\Omega_m = 0.313 \quad (\text{A.8b})$$

$$\Omega_{\text{cdm}} = 0.263 \quad (\text{A.8c})$$

$$\Omega_b = 0.0486 \quad (\text{A.8d})$$

$$\Omega_v < 0.0156. \quad (\text{A.8e})$$

As motivated in Sect. 2.1.2, the difference between  $\Omega_m$  and  $\Omega_b$  is expressed by the density of *cold dark matter*  $\Omega_{\text{cdm}} = \Omega_m - \Omega_b$ . Similarly, the difference  $\Omega_T - \Omega_m \approx \Omega_\Lambda$  together with SN1a measurements [50] indicates a non-vanishing vacuum energy as *dark energy*.

Therefore the present Universe is dominated by cold dark matter and dark energy ( $\Lambda$ ). Consequently, the cosmological standard model is named the  $\Lambda$ CDM universe.

## A.2 Gaisser Parametrization of Sea Level Muon Flux

Within the framework of deep underground experiments (e.g. [4, 38, 55]), often an approximative solution to Eq. 3.7a, the *Gaisser parametrization* [23], is used as starting point to calculate the remaining muon flux underground.

The 14 approximations given in literature [23, 42] are:

**Approximation 1** The net flux of incoming cosmic rays is described by a power law with energy independent spectral index gamma [42, p. 195].

**Approximation 2** As the energy regime is above the nuclear binding energy of  $\approx 5$  MeV, the nucleons are considered as free (superposition principle) [23, pp. 29f.], [20, p.473] and only the net nucleon flux is considered [24, p. 269]

$$I_N(E) \approx 1.8 \times 10^4 (E/1 \text{ GeV})^{-(\gamma+1)} \frac{\text{nucleons}}{\text{m}^2 \text{ s sr GeV}} \quad (\text{A.9})$$

**Approximation 3** The cross section for interactions between the incident cosmic ray particle and the nuclei in the atmosphere can be reduced to nucleon–nucleon cross section via the multiple scattering theory of Glauber and the wounded nucleon picture [23, pp. 54, 204]

**Approximation 4** The atmosphere is isothermal

$$X_v = X_0 e^{-h/h_0} \quad (\text{A.10})$$

with the scale height  $h_0$  and the atmospheric depth at ground  $X_0$  [23, p. 34].

**Approximation 5** The earth curvature is neglected. From Fig. 3.1 follows the relation between altitude  $h$  and track length  $l$

$$h = R \sqrt{1 + \left( \frac{l \sin \theta^*}{R} \right)^2} + l \cos \theta^* - R \quad (\text{A.11})$$

$$\approx l \cos \theta + \frac{l^2}{2R} \sin^2 \theta \quad (\text{A.12})$$

For a flat Earth  $\theta \leq 60^\circ$  it is further approximate as [23, p. 34]:

$$h \approx l \cos \theta^*. \quad (\text{A.13})$$

**Approximation 6** called approximation A according to [23, pp. 30–31], [42, p. 197]:

1. Ignoring the energy dependence of the interaction cross section and therefore of the interaction length:  $\lambda_i = \text{const.}$
2. The cross section obeys the Feynman scaling:

$$F_{ij}(E_i, E_j) = F_{ij}(x_L) \quad (\text{A.14})$$

$$x_L = E_i/E_j \quad (\text{A.15})$$

with the Feynman scale  $x_L$  [21]. In reality the cross section rises slowly with energy, e.g. the rise of the cross section for inelastic proton-proton scattering is about 25 % between 1 GeV and 1 TeV [23, pp. 31, 53]

**Approximation 7** *The flux factorizes as  $N_i(E_i, X) = g(E_i) \cdot h(X)$  [23, p. 30], [42, p. 197].*

**Approximation 8** *Neglecting nucleon production by mesons  $\pi^\pm$  and  $K \rightarrow n, p$  [23, p. 31], [42, p. 200].*

**Approximation 9** *Neglecting the coupling  $K \rightarrow \pi$ , because the kaon flux is only one tenth of the pion flux [42, p. 200] [23, p. 33].*

**Approximation 10** *Neglecting nucleon–antinucleon reactions [23, p. 33].*

**Approximation 11** *Ignore mesons with heavier flavour content, e.g. charmed D and  $\Lambda_c$ . As they decay nearly immediately after production, their contribution to the muon flux is called prompt muons [17]. Their decay becomes finally suppressed at  $10^8$  GeV and they start to interact. Due to their immediate decay the prompt muon flux is isotropic [23, pp. 40, 83] and can be described by the ratio of prompt muons to pions  $R_c < 2 \times 10^{-3}$  [3, p. 4].*

**Approximation 12** *Treat the pions and kaons as relativistic [23, p. 69].*

**Approximation 13** *Ignore the energy loss of muons along their trajectories in the atmosphere of roughly 2 GeV [24, p. 270].*

**Approximation 14** *Treat muons as stable, they have a decay length of 15 km at 2.4 GeV [24, p. 270].*

Under the Approximation 6 the source term Eq. 3.7b simplifies to [42, p. 197]:

$$S_{ij} = E^{-(\gamma+1)} \frac{N_i(X)}{\lambda_{\text{int},j}} Z_{ij} \quad (\text{A.16})$$

Here the  $Z_{ij}$  are the spectral weighted moments of the inclusive cross sections [23, p. 31], [22, 25]:

$$Z_{ij} = \int_0^1 x_L^{\gamma+1} F_{i,j}(x_L) dx_L \quad (\text{A.17})$$

that determined the uncorrelated fluxes of particles, values are given in [42, p. 210]. For  $\gamma = 1$  the  $Z_{ij}$  describe the averaged energy transferred to particle  $j$  [23, p. 31], [1, pp. 347f.].

By assuming an isothermal atmosphere (Eq. A.10) and ignoring the earth curvature (Eq. A.13), therefore only valid for  $\theta \leq 60^\circ$ , the decay length (Eq. 3.6) approximates to [23, p. 35]:

$$\lambda_{\text{dec},i}(E_i, X) = \frac{X \cos \theta^*}{h_0} \frac{E_i}{m_i c^2} c \tau_i \quad (\text{A.18})$$

$$= \rho(X) \frac{E_i \cos \theta}{\epsilon_i} \quad (\text{A.19})$$

With the critical energy for pions (kaons) of  $\epsilon_\pi = 115 \text{ GeV}$  ( $\epsilon_K = 850 \text{ GeV}$ ) [24]. Particles with  $E \gg \epsilon$  have longer decay lengths than the interaction length and will interact rather than decay.

A correction for these approximations is possible by replacing the zenith angle  $\theta$  by an adapted angle  $\theta^*$  [69]. By including all corrections due to the atmosphere density model and the track geometry within  $\theta^*$ , the validity of relation Eq. A.18 and the value of  $\epsilon$  are maintained. The correction is most precisely done by numerical calculation of the air density profile along the particle trajectory, see [3, 12].

At larger values,  $\theta^*$  can be interpreted as the zenith angle at the production vertex [3] and can be calculated as [55]:

$$\theta^* = \arcsin \left( \frac{R}{R + H} \sin \theta \right) \quad (\text{A.20})$$

where  $H$  is approximating the production height of the muons in the atmosphere. Depending on the zenith angle the production height rises from 17 km at  $\theta = 0^\circ$  to 32 km at  $\theta = 90^\circ$ , but has little influence on the correction for  $\cos \theta \leq 0.3$  [3, p.3]. Several values for  $H$  are used in the literature: [55, pp. 18, 20] use the mean interaction height for protons (as protons are the main constituents of the primary cosmic rays) of 18.6 km, [3] use 17 km, [39, p. 4] use 32 km, [12, p. 2] use 19.28 km, and [42, p. 204] use 30 km. For the last value a precision of 5% is reported with respect to more elaborated calculations [42, p. 204].

By neglecting the coupling of mesons to nucleons (Approximation 8) and using Eq. A.9 as boundary condition at  $X = 0$ , the net nucleon flux can be written as [23, p. 31]:

$$\dot{\phi}_N(E_N, X) = \dot{\phi}_{N,0} e^{-X/\Lambda_N} E^{-(\gamma+1)} \quad (\text{A.21})$$

i.e. the shape of nucleon flux follows the power law of the primary particle [33], [23, p. 31] that is attenuated in  $X$  with a attenuation length  $\Lambda_N$ :

$$\frac{1}{\Lambda_i} = \frac{1}{\lambda_i} (1 - Z_{ii}) \quad (\text{A.22})$$

Separate fluxes for n and p instead of a net flux Eq. A.21 are given in [42, p. 200].

By neglecting kaon production from pions (Approximation 9) the meson fluxes ( $\dot{\phi}_M$ ,  $M = K, \pi$ ) decouple. By the additional Approximations 6 and 10 the meson fluxes are obtained by inserting Eq. A.21 in the source term of Eq. 3.7a [23, p. 33], [42, p. 200]:

$$\frac{d\dot{\phi}_M(E_M, X)}{dX} = - \left( \frac{1}{\Lambda_M} + \frac{\epsilon_M}{E_M X \cos \theta} \right) \dot{\phi}_M + \frac{Z_{N,M}}{\lambda_N} \dot{\phi}_N(E_M, X) \quad (\text{A.23})$$

with the solution

$$\dot{\phi}_M(E_M, X) = \frac{Z_{N,M}}{\lambda_N} \dot{\phi}_N(E_M, X) \int_0^X \left( \frac{X'}{X} \right)^{\epsilon_M/E \cos \theta} \exp \left( \frac{X'}{\Lambda_M} - \frac{X'}{\Lambda_N} \right) dX' \quad (\text{A.24})$$

A solution taking into account the regeneration and mixing of the kaons ( $K^+$ ,  $K^-$ , and  $K^L$ ) and the coupling  $\pi \rightarrow K$  is given by [42, p. 199].

As any heavy mesons are ignored (Approximation 11), only pions and kaons contribute to the muon flux [23, p. 40]

$$\pi^\pm \rightarrow \mu^\pm + \nu_\mu (\bar{\nu}_\mu) \quad (B_{\pi\mu} \approx 100\%) \quad (\text{A.25})$$

$$K^\pm \rightarrow \mu^\pm + \nu_\mu (\bar{\nu}_\mu) \quad (B_{K\mu} \approx 63.5\%), \quad (\text{A.26})$$

where the  $B_{ij}$  are the branching ratios for the decay channel  $i \rightarrow j$ . The energy scale of the parent mesons is transferred to the energy scale of the muons via  $dn_{ij}/dE_i$  and is for unpolarized and relativistic mesons (Approximation 12) [23, pp. 41, 69]:

$$\frac{dn_{ij}(E_i, E_j)}{dE_i} = B_{ij} \frac{1}{1 - m_i^2/m_j^2} \frac{1}{m_j}, \quad (\text{A.27})$$

where  $m_i, m_j$  are the masses of the parent and daughter particles, respectively.

By neglecting the muon energy loss (Approximation 13) the flux is described by [23, pp. 39, 69]:

$$\dot{\phi}_\mu(E_\mu) = \int_0^{X_0} \sum_j \int_{E_{\min}}^{E_{\max}} \frac{dn_{\mu j}(E_\mu, E')}{dE_\mu} \frac{1}{\Lambda_j} \dot{\phi}_j(E', X) dE' dX. \quad (\text{A.28})$$

The sum goes over all fluxes of the parent particles  $j$  within  $[E_{\min}, E_{\max}]$  that give rise to muons with  $E_\mu$ , weighted by their attenuation length  $\Lambda_j$ . Inserting  $N_\pi$  and  $N_K$  (Eq. A.24), and  $dn_{\mu\pi}/dE_\mu$  and  $dn_{\mu K}/dE_\mu$  (Eq. A.27) in Eq. A.28 results in the cascade equation of the muon flux at sea level. For an equation consider the continuous energy loss, see [42, p. 205] and references there in.

An approximate solution is given by the well known *Gaisser parametrization*:

$$\frac{d\dot{\phi}_{\mu,0}}{dE_{\mu,0} d\Omega_0} = \frac{0.14}{\text{cm}^2 \text{s sr GeV}} \left( \frac{E_{\mu,0}}{\text{GeV}} \right)^{-2.7} \left( \frac{1}{1 + \frac{1.1E_{\mu,0} \cos \theta_0}{115\text{GeV}}} + \frac{0.054}{1 + \frac{1.1E_{\mu,0} \cos \theta_0}{850\text{GeV}}} \right) \quad (\text{A.29})$$

$$\approx AE^{-\gamma_\mu} \quad (\text{A.30})$$

The energy dependence follows the power law of the primary particle. The depth dependence of the attenuation lengths  $\lambda_{\text{dec},\pi}, \lambda_{\text{dec},K}$  is expressed via Eq. A.18, leading to the two cosine terms. For  $E_\mu \ll \epsilon_K, E_\mu \ll \epsilon_\pi$  the slope of the muon spectrum is the same as the slope of the primary spectrum:  $\gamma_\mu \rightarrow \gamma$ . For  $E_\mu \gg \epsilon_{K,\pi}$  the

muon spectrum become steeper:  $\gamma_\mu \rightarrow \gamma + 1$ . For the comparison of experimental results obtained under different zenith angles, the vertical muon flux is corrected by the cosine dependence [9]:

$$\dot{\Phi}_0 = \dot{\Phi} \cos \theta \quad (\text{A.31})$$

As the muon flux is based on the assumption of negligible earth curvature (Eq. A.18) and stable muons (Approximation 14), it is only valid for  $\theta \leq 60^\circ$  [23] and  $E_{\mu,0} > 100 \text{ GeV} / \cos \theta$ , respectively. Within this energy range the distance between muon production vertex and sea level under a zenith angle  $\theta$  is shorter than the decay length. The Gaisser parametrization can be corrected for the used approximations:

- The earth curvature and different atmosphere density profiles are considered by the  $\theta^*$  correction (see page 341).
- The contribution of prompt muons can be considered by adding the ratio of prompt muons to pions  $R_c$  [3, p. 4].
- The muon decay can be taken into account by weighting the differential flux with the survival probability:

$$P(E_\mu) = \exp \left( -l \cdot \frac{m_\mu c^2}{E_\mu \tau_\mu c} \right), \quad (\text{A.32})$$

cf. [63, p. 1014] and Eq. 3.6. The muon track length  $l$  can be obtained from simulations of air showers, e.g. [12, p. 4].

- The muon energy  $E_\mu$  can be corrected by the muon energy loss (see Eq. 3.11a) along the muon propagation from production to ground [55, p. 21], [63, p. 1014].

As the muons reaching LSM have a minimal energy at sea level in the order of TeV, the Gaisser parametrization with the  $\theta^*$  correction is sufficient until energies in the EeV range, where the spectral index changes (Eq. 3.3), and the prompt muon contribution becomes significant (Approximation 11).

## A.3 Used Software: Geant4 and Auxiliary Programs

### A.3.1 Overview of the Used Software

For the MC simulations within this work (see Chap. 5) the programme package *Geant4* [5, 6] was used because it covers the full range between muon interaction at a TeV energy scale over high precision thermal neutron interaction to optical processes. A short introduction to Geant4 related terms is given in Appendix A.3.2.

Within this work two event generators were used: For the generation of muons the one described in Sect. 5.3.1, and for the simulation of the response of the neutron

detector and for the simulation of its background the *General Particle Source* (GPS, `G4GeneralParticleSource`) was used in Sect. 5.5.5.

The physical processes were based in most cases on models and cross sections delivered with the used Geant4 version and described in detail in Sect. 5.2. The only exception is the class `GdNeutronHPCapture` [47, 75] developed by the CHOOZ collaboration. It describes the deexcitation of the gadolinium nucleus after neutron capture with higher precision than the default Geant4 model and is discussed in more detail in Sect. 5.4.1.

For data storage and analysis the *ROOT* package was used: For each event the produced muon and neutron tracks and generated hits within the sensitive volumes were stored in a user designed ROOT event class and written to file. Albeit these are quite extended amounts of data, they are nevertheless strongly reduced in comparison to the full amount of data generated during an event. Afterwards these skimmed data were the input for the ROOT based offline event building and analysis through the algorithm described in Sect. 5.4.3. This splitting in a Geant4 governed part of data generation and a ROOT governed part of event building and data analysis was a main advantage during the detector calibration Sect. 5.4.4: The detector response only affects the event building and not the data generation. To fit the parameter of the detector response model to the calibration data, only the event building had to be executed several times with different parameter values and not the data generation in the entire Geant4 simulation. This saved CPU-time.

The parameters of the simulation (energy range of the primary particle, verbosity of stored information, enabling of visualisation, etc.) were set via macro files using user defined commands, i.e. it was running in batch mode. Several instances (*jobs*) of the simulation programme were running in parallel on the TESLA computer cluster of the Institute of Nuclear Physics (IKP) at KIT. The TESLA cluster is managed by a *SUN Grid engine* and consists of up to 738 nodes, most of them are part of an Intel XEON E5649 hexa-core CPU.

To ensure unique random numbers over the several jobs, the `TRandom3(0)` random number generator from the ROOT package was used [60, pp. 20, 176, 234]. Based on a *Universally Unique Identifier*, ‘the seed is guaranteed to be unique in space and time’ [59]. Spot tests of the run jobs found only unique seeds. The actual seeds for the random number generator were stored as part of the data for each event. It was therefore possible to re-run certain events in order to visualize them, or to study them in more details.

It turned out that the job-level parallelism used for this work was sufficient for events with low energetic primary particles, as they produce small amounts of secondary particles so that the CPU-time per event is small. In contrast, events with a large amount of secondaries, like events with high energetic primary particles, need more time per event. Therefore the parallelization of the simulation of secondaries within one track as proposed in [15, 16] may be a useful improvement for future work.

The simulation and the ROOT based programs were compiled and run under Ubuntu with the kernel, GNU Compiler Collection, and CLHEP versions stated in Table A.1. The implemented detector geometry was visualized with *DAWN* and the

**Table A.1** Used software for this work

Program	Version	Source
Geant4	9.2.p01	<a href="http://geant4.cern.ch/">http://geant4.cern.ch/</a>
PhotonEvaporation	2.0	
RadioactiveDecay	3.2	
G4EMLOW	6.2	
G4NDL	3.13	
G4ABLA	3.0	
RealSurface	1.0	
GdHPNeutrons	1.0.0	[47, 75]
CLHEP	2.0.4.5	<a href="http://proj-clhep.web.cern.ch">http://proj-clhep.web.cern.ch</a>
DAWN	3.90b	<a href="http://geant4.kek.jp/~tanaka/DAWN/About_DAQN.html">http://geant4.kek.jp/~tanaka/DAWN/About_DAQN.html</a>
HepRAPP	3.15.0	<a href="https://www.slac.stanford.edu/~perl/heprep/">https://www.slac.stanford.edu/~perl/heprep/</a>
ROOT	5.32	<a href="http://root.cern.ch/">http://root.cern.ch/</a>
Ubuntu	10.04 LTS	<a href="http://www.ubuntu.com/">http://www.ubuntu.com/</a>
Kernel	2.6.32-47	
GNU compiler collection <sup>a</sup>	4.4.3	
Wolfram MATHEMATICA	8	<a href="http://www.wolfram.com/mathematica/">http://www.wolfram.com/mathematica/</a>
GetData GRAPH	2.25	<a href="http://getdata-graph-digitizer.com/">http://getdata-graph-digitizer.com/</a>
DIGITIZER		

<sup>a</sup>With enabled C++11 support via `-std=c++0x` option during compilation

particle tracks within this geometry with *HepRAPP*. For the analytical calculation in Sect. 5.3.1 the computer algebra system *Wolfram MATHEMATICA* under Windows XP was used. Some reference values from literature, like [30] in Fig. 5.12c, were digitized with *GetData GRAPH DIGITIZER*.

### A.3.2 Structure of a Geant4 Application

Geant4 implements the physical interaction (or physical *processes*) of particles within a given detector volume of specific shape (*geometry*) and material in an object oriented way as classes, see [5, 6]. A fixed set of physical processes, geometries and material compositions defines a *run*. Within a run an *event* is the sum of all interactions subsequently caused by the *primary particle*. The initial parameters of this primary particle have to be specified by the user either directly event-by-event or by a dedicated algorithm called an *event generator*, e.g. the *general particle source* (GPS, `G4GeneralParticleSource` [26]) was used in this work for the start of optical photons, neutrons from AmBe, and  $^{214}\text{Bi}$  nuclei, see Sects. 5.4.2, 5.4.4 and 5.5.5 respectively.

The trajectory (or *track*) of each particle through the geometry is approximated by discrete segments (*steps*). For each step the interactions with the material are calculated according to the implemented physical processes, including continuous energy loss along the track and discrete energy loss via decay or production of secondary particles. The lost energy is then deposited in the surrounding material, or carried away by the secondary particles and finally deposited elsewhere. For each physical process that is applicable to the particle, the corresponding interaction length in the current material is calculated. The step length is then the minimum among all those interaction lengths and the distance to the volume boundary. To prevent infrared divergences the user has to specify a *range cut*: In case the step length is shorter than the range cut, the track is killed and the remaining energy of the particle is deposited. The volumes are hierarchically ordered according to a mother-daughter relation. At the top of the hierarchy is the *world volume*, the centre of this volume defines also the point of origin of the global coordinate system.

If an energy deposit happens within a volume the user has declared *sensitive* a *hit* is generated. It is up to the user to define what information about the particle, its track or step is stored within a hit. The current event is terminated when each particle has decayed or left the simulated geometry, and a new event is started with new primary particles.

Geant4 by itself provides only a framework, the user has to implement the detector geometry, the list of physical processes (*physics list*), and the primary particle generation. In this work *Geant4 simulation* or *simulation* refers to the Geant4 framework plus the user's implementations.

### A.3.3 Relevant Revision History of Geant4

The models and cross sections used in Geant4 affect significantly the results of muon and neutron production, and transport simulations (see Sect. 3.6). To estimate the possible effects of different Geant4 releases on the results of this work, this section list the changes in the muon and hadronic/neutron physic between consecutive Geant4 releases, and afterwards assets the changes. It is based on the release notes from the Geant4 homepage.<sup>1</sup> It starts with version 9.0 (first version after 8.4p01 used in [34]), over version 9.2p01 (used in this work) to version 9.5 (the current stable release). The list skips pure technical improvements (code reorganizing, removing of compiler warnings, etc.), and new high performance, but simplified models (e.g. G4NeutronRadCapture, conserves four-momentum in neutron capture, but produce only one photon.).

It is clear that without dedicated benchmark simulations no quantitative evaluation is possible. This is especially true for the several more technical fixes (e.g. the

---

<sup>1</sup>[http://geant4.web.cern.ch/geant4/support/source\\_archive.shtml](http://geant4.web.cern.ch/geant4/support/source_archive.shtml): Home > User Support > Archive.

‘Re-Parameterized Gheisha-style’ model introduced in version 9.1), which may have a significant influence only in specific user cases.

The three most significant qualitative changes for muon-induced neutron production between version 8.2p01 (used in [34]) and version 9.2p01 (used in this work) are in our opinion: The bugfix in the angular distribution of nucleons with the LEP model (version 9.0). Second, the change in the muon bremsstrahlung process (version 9.1), keeping in mind that muon-induced bremsstrahlung shower contribute to neutron production. The third change is in the pre-compound model (versions 9.1 and 9.2), leading to an increase of neutron production in lead and changes of the shape of the low energetic neutron spectrum.

By migrating the simulation based on this work to version 9.5p01 we expect changes in the low and high energy regime: A better description of the low energetic neutron behaviour (neutron transport, deexcitation, and fragmentation of atoms excited by neutrons), important for the simulation of the detector response to neutrons and low energetic neutron production. For muon-induced neutron reactions the changes in version 9.5 in the handling of muon nuclear reactions are relevant.

From a technical point of view the changes in the low energy packages and in the muon multiple scattering (both in version 9.3) have to be considered if the simulation described in this work should be migrated to newer versions of Geant4. Considering the various fixes and improvements applied to all models used in this simulation and the extension of the data bases, a migration to the newest Geant4 version would be the most practical solution.

## Version 9.0

- Elastic cross section for low energy neutrons upgraded and tuned in CHIPS model, add high energy, heavy nuclei nA correction.
- New module for Livermore LLNL neutron-induced and spontaneous fission model is now available.
- Bug fixes in LEP models remove an un-physical peak at 180 degrees and reduce the number of very low energy nucleons produced. The net effect is to shift the angular distributions forward by about 5–10° and increase the mean secondary kinetic energy by roughly 20–30 MeV. Effects of this size occur at incident particle energies of 2–10 GeV. At higher energies the effect is small. Benchmark tests show little change in shower shape.

**Version 9.0p01** No fix seems relevant.

**Version 9.0p02** Contains fix affecting CHIPS.

## Version 9.1

- Contains cross sections for four additional isotopes in neutron HP.
- Bug fixes and completed implementation of theory in G4PreCompoundModel and G4Evaporation have produced a 10–15 % increase in neutron flux for 2.5 GeV/c protons incident on Pb.

- Bug fix in quasi-elastic, which may influence the shower shape, it should be now a bit shorter and wider when using QGSC/QGSP physics lists.
- G4MuBremsstrahlungModel: Improved simulation of the high-energy gamma tail for muon Bremsstrahlung (rare process, important for background simulation—NA49).
- G4MuMultipleScattering, G4MuMscModel: new classes for simulation of multiple scattering for muons (beta-version).
- First version of a ‘Re-Parameterized Gheisha-style’ model. This version is essentially a re-factored copy of the low energy parameterized model which also contains several bug fixes and physics improvements.
- New developments in pre-equilibrium stage to reflect the literature and units expected for the exciton model: introducing a  $R_j$  factor into the probability calculation; correcting the units for the Pauli Blocking Factor

**Version 9.1p01** Contains fix affecting photonuclear/electronuclear cross sections and CHIPS.

**Version 9.1p02** Contains fix affecting CHIPS, muon capture, and neutron HP cross sections.

**Version 9.1p03** Contains fix affecting pre-compound model.

## Version 9.2

- New data for neutron cross sections, G4NDL.3.13: Added isotopes, and correct wrong entries in some inelastic and capture data
- Several fixes in neutron HP, improved energy and angular distributions for both scattered neutron and recoil targets, fixed missing inelastic gamma-ray lines, fixed too many secondaries production in nd reactions.
- New multiple-scattering model G4WentzelVIModel used in new muon physics processes.
- Missing pieces of theory were added and several code fixes were made to G4PreCompoundModel and related classe, resulting in more realistic neutron spectra at low energies.

**Version 9.2p01** Contains fix affecting pre-compound model.

**Version 9.2p02** Contains fix affecting neutron HP and parton string.

## Version 9.2p03

**Version 9.2p04** Contains fix affecting CHIPS.

## Version 9.3

- All Low Energy Electromagnetic Physics process classes have been entirely redesigned. No significant changes on the physics outcomes are expected due to the new software design of process and model classes, or from these new implementations of data loading and interpolation methods.
- It is recommended to replace the G4MultipleScattering physics process with G4MuMultipleScattering for muons, using G4UrbanMscModel90 by default
- Improvements in the deexcitation code (G4CompetitiveFission, G4FermiBreakup, etc.) produce better agreement with IAEA benchmark data below 200 MeV.
- Fixes in G4MuIonisation.
- More precise simulation near cross section threshold in G4AnnihiToMuPair.
- The validity of the pion-nuclear cross sections in G4PiNuclearCrossSections, and the nucleon-nuclear cross sections in G4NeutronInelasticCrossSections and G4ProtonInelasticCrossSections has been extended to 100 TeV, by assuming a constant cross section at very high energies.
- The CHIPS model has been extended with hadronic interactions covering all energies for all hadronic particles; in addition hadron- and lepton-nuclear reactions are extended to high energies ( $\sim$ TeV). CHIPS ion-ion elastic scattering model is also now available. Added eight new cross section classes and bug fixes in pA cross sections. Tuning of the G4QCollision for better description of the pA interactions ( $E < 290$  MeV).
- Changes to G4BinaryCascade to protects against energy non-conservation.

**Version 9.3p01** Contains fix affecting CHIPS.

**Version 9.3p02** Contains fix affecting CHIPS, neutron HP, parton string, and muon nuclear interactions.

#### Version 9.4

- New data set G4NDL.3.14.
- G4NEUTRONXS-1.0, new data set for evaluated neutron cross section data on natural composition of elements.
- G4PII-1.2, new data set for shell ionisation cross sections
- Changed default multiple scattering models to G4WentzelVIModel for muons.
- G4MuPairProductionModel: added sampling recoil of a primary particle.
- G4MuIonisation: use G4ICRU73QOModel for mu- for  $E < 0.2$  MeV (G4Bragg-Model in past).
- Fix in G4MuonMinusCaptureAtRest.
- Improved spectra of nuclear gamma deexcitation including Doppler broadening simulation.
- Fermi Break-up Model and GEM evaporation are used by default providing improved production of light fragments in nuclear fragmentation at low energy.
- Fermi breakup was extended to include fragments with  $1 < A < 5$ . Several improvements were made to bring the model closer to the original one of Botvina. Use hybrid of Fermi breakup and GEM models for  $A < 20$ . Several other improvements were made to the evaporation models.

- Several fixes in CHIPS, updated proton elastic and CHIPS parameters, added pion elastic, implemented isotope-wise CHIPS elastic for neutrons.
- Several fixes in neutron HP.
- Several fixes in parton-string, improved low mass string fragmentation.
- Several fixes in pre-compound model.

**Version 9.4p01** Contains fix affecting muon energy loss and CHIPS.

**Version 9.4p02** Contains fix affecting CHIPS and neutron HP.

**Version 9.4p03** Contains fix affecting electronuclear corss sections.

**Version 9.4p04** Contains fix affecting CHIPS.

## Version 9.5

- New data set versions: G4NDL.4.0, G4NEUTRONXS-1.1.
- Binary cascade: The excitation energy used for re-scattering was improved. The large energy non-conservation observed for hydrogen targets was fixed.
- Nuclear deexcitation models have been improved to allow G4PhotoEvaporation to be used for nuclei with  $Z > 100$ . Several improvements were also made to the Fermi-Breakup model to improve behavior for light ( $A < 17$ ) target nuclei.
- A new module which handles quasi-elastic scattering has been created. It is extracted and now separate from the CHIPS code where it originated. It is used by all physics lists.
- New translations of alternative neutrons database (ENDF, JENDL, JEFF, MENDL, CENDL), are being made available.
- Thermal scattering is enabled in the HP neutron models and the appropriate data files have been added to ENDF/B-VII, with the exception of para (ortho) H and D, liquid (solid) methane and benzene.
- Several fixes in neutron HP.
- Improved muon-nuclear reactions are implemented in G4VDMuonNuclearModel. Here, the LEP models that used to handle the meson interactions are replaced by the Bertini Cascade. A new cross section class, G4KokoulinMuonNuclearXS, was developed which splits out the cross section code which was formerly hard-coded into the old muon-nuclear process. Added G4MuonNuclearProcess, meant to replace the old process G4MuNuclearInteraction by separating model and cross section classes.
- New model G4VDMuonNuclearModel to replace old-style G4MuNuclearInteraction and G4ParametrizedHadronicVertex based on GHEISHA. Removed G4MuNucleusProcess and G4MuNucleusInteractionModel classes. These were the old GHEISHA-style models no longer used.
- G4ElectroNuclearCrossSection: corrected numerical instability adding numerical protections in methods computing equivalent photon energy,  $Q^2$ , and virtual factor.
- Binary Cascade: Several fixes, including a fix of a large energy non-conservation for Hydrogen target.

- Several fixes in CHIPS.
- Several fixes in parton-strong model.
- Several fixes in pre-compound model

**Version 9.5p01** Contains fixes affecting muon energy loss, G4WentzeVIModel, CHIPS, and neutron HP.

**Table A.2** Application ranges of the used Geant4 models for inelastic reactions

Process Model	$E_{\min}$ (GeV)	$E_{\max}$ (GeV)
Neutron inelastic scattering		
G4NeutronHPInelastic	0	0.0199
G4PreCompoundModel	0.0195	0.070
G4BinaryCascade	0.065	6.1
LEP	6.0	12.1
QGSP	12	100,000
Proton inelastic scattering		
G4PreCompoundModel	0	0.070
G4BinaryCascade	0.065	6.1
LEP	6.0	12.1
QGSP	12	100,000
Photo-nuclear reaction		
G4GammaNuclearReaction	0	3.5
QGSC	3	100,000
Electron-nuclear reaction		
G4ElectronNuclearReaction	3	10,000
Charged pions ( $\pi^{\pm}$ ) inelastic scattering		
G4CascadeInterface	0	1.5
LEP	1.4	12.1
QGSP	12	100,000
Kaons ( $K^{\pm}, K_{S/L}^0$ ) inelastic scattering		
LEP	0	12.1
QGSP	12	100,000
d, t, and $\alpha$ inelastic scattering		
LEP	0	0.100
G4BinaryLightIonReaction	0.080	40
$^3\text{He}$ and generic ions inelastic scattering		
G4BinaryLightIonReaction	0	30

For cases not listed, the same values as in QGSP\_BIC\_HP version 1.0 are used

## A.4 Geant4 Implementation of the Neutron Counter

### A.4.1 Application Range of Physic Models

Table A.2 list the used application ranges in energy for the models in the physics list of this work, based on [34], see Sects. 3.6 and 5.2. Only models are listed that differ from the implementation in the Geant4 physics list QGSP\_BIC\_HP version 1.0.

LEP denoted GEISHA based, particle specific low energy models, e.g. G4-LENNeutronInelastic, G4LEPionPlusInelastic, G4LEAlphaInelastic. QGSP is a G4TheoFSGenerator, using a G4QGSModel together with a G4PreCompoundModel for the fragmentation of the excited nucleus. QGSC used instead of G4PreCompoundModel a CHIPS model (G4StringChips-ParticleLevelInterface). G4BinaryCascade, G4BinaryLightIonReaction are both binary cascades, whereas G4CascadeInterface implements the Bertini cascade [27]. G4GammaNuclearReaction, G4ElectronNuclearReaction are based on the CHIPS model [28].

### A.4.2 Material Definitions

The simulations in this work relay partial on materials defined by Geant4 (G4\_Ga1-actic, G4\_Ar, G4\_Fe, G4\_Al, G4\_Pb) and partial on dedicated definitions listed in Table A.3. This is especially true for the liquid scintillator and the Fréjus rock (FrejusRock3 [11]), which will be discussed in more details on page 350. If not stated otherwise natural isotope compositions are applied.

#### A.4.2.1 Definition of Liquid Scintillator

The composition of the liquid scintillator (implemented as `liqScintillator`) in the NMM is defined dynamically, based on the user's specification of the gadolinium content. As the elemental abundance and density affect the detection efficiency via the macroscopic neutron capture cross section, the respective values are adjust to the used gadolinium content. The calculation for a given gadolinium fraction is based on the following assumptions: The first assumption is that the components masses  $m_X$  sum up to the total mass  $M = \sum m_X$  of the liquid scintillator. Within this assumption the partial density  $\rho_X$  of a component as function of its abundance  $n_X$  with respect to the scintillator volume  $V$  is defined as

**Table A.3** Composition of the materials implemented in Geant4

Material	Density (g cm <sup>-3</sup> )	Component	Fraction (% w/w)
Air	0.129	N	70
		O	30
BiAlkali	1.3	K <sub>2</sub> CsSb	100
BorosilicateGlass	2.51	O	53.9562
		Si	37.722
		Na	2.8191
		Al	1.1644
		B	0.40064
		K	0.3321
FrejusConcrete2	2.4	O	49.68
		Ca	36.78
		C	7.78
		Si	2.69
		H	1.09
		Mg	0.78
		Fe	0.52
		Al	0.48
		Ti	0.09
		P	0.07
		K	0.02
		Na	0.01
		Mn	0.01
FrejusRock3	2.65	O	49.40
		Ca	30.60
		Si	6.93
		C	5.94
		Al	2.58
		Fe	1.90
		H	1.00
		Mg	0.84
		Na	0.44
		K	0.21
		Ti	0.07
		P	0.06
		Mn	0.03
Lead	11.36	<sup>82</sup> <sub>207.19</sub> Pb	100
LimeGlass	2.53	SiO <sub>2</sub>	72.7
		Na <sub>2</sub> O	14.0
		CaO	9.0

(continued)

**Table A.3** (continued)

Material	Density (g cm <sup>-3</sup> )	Component	Fraction (% w/w)
		MgO	4.0
		Al <sub>2</sub> O <sub>3</sub>	0.15
		K <sub>2</sub> O	0.03
		TiO <sub>2</sub>	0.02
		Fe <sub>2</sub> O <sub>3</sub>	0.1
liqScintillator	$\rho$	Gd	$n_{Gd}$
		C	$n_C$
		H	$n_H$
Paraffin	0.75	C <sub>12</sub> H <sub>26</sub>	100
Plexiglass	1.19	C <sub>5</sub> H <sub>8</sub> O <sub>2</sub>	100
PolyEthylen	0.94	C <sub>86</sub> H <sub>14</sub>	100
Polystyrol	1.050	C <sub>8</sub> H <sub>8</sub>	100
PVT	1.032	C <sub>19</sub> H <sub>21</sub>	100
S235JR	7.85	Fe	97.798
		Mn	1.4
		Cu	0.55
		C	0.17
		P	0.035
		S	0.035
		N	0.012
Steel	7.85	Fe	94.0
		Mn	1.6
		Co	1
		Cr	1
		Ni	1
		Cu	0.6
		Si	0.6
Wood	0.8	C	0.2
		C <sub>6</sub> H <sub>10</sub> O <sub>5</sub>	100

For the definition of  $\rho$ ,  $n_H$ ,  $n_C$ , and  $n_{Gd}$  see text

$$\begin{aligned}
 \rho_X &= \frac{m_X}{V} \\
 &:= \frac{n_X \sum m_X}{V} \\
 &= n_X \frac{M}{V} \\
 &= n_X \rho
 \end{aligned} \tag{A.33}$$

For a scintillator loaded with  $n_{\text{Gd}} = 0.2\% \text{ w/w}$  gadolinium a density of  $\rho = 0.88 \text{ g cm}^{-3}$  is stated in the data sheet (Table A.5), resulting in  $\rho_{\text{Gd}} = 0.0018 \text{ g cm}^{-3}$ .

The second assumption is that the empirical formula of the hydrocarbon of the liquid scintillator ( $\text{C}_{100}\text{H}_{156}$ ) does not change by a changing gadolinium loading, i.e. the relation of the stoichiometric fractions  $x_i$  is constant and the same as the relation of the amounts of substance:

$$\frac{x_{\text{C}}}{x_{\text{H}}} = \frac{100}{156} := \frac{m_{\text{C}}/A_{\text{C}}}{m_{\text{H}}/A_{\text{H}}} \quad (\text{A.34})$$

where  $A_X$  are the averaged atomic weights according to [72].

As a consequence of Eqs. A.33 and A.34 the partial densities of hydrogen and carbon are

$$\rho_{\text{H}} = \frac{x_{\text{H}}A_{\text{H}}}{x_{\text{H}}A_{\text{H}} + x_{\text{C}}A_{\text{C}}} (\rho - \rho_{\text{Gd}}) \quad (\text{A.35})$$

$$\rho_{\text{C}} = \frac{x_{\text{C}}A_{\text{C}}}{x_{\text{H}}A_{\text{H}} + x_{\text{C}}A_{\text{C}}} (\rho - \rho_{\text{Gd}}) \quad (\text{A.36})$$

resulting in  $\rho_{\text{H}} = 0.1017 \text{ g cm}^{-3}$  and  $\rho_{\text{C}} = 0.7765 \text{ g cm}^{-3}$  for  $n_{\text{Gd}} = 0.2\% \text{ w/w}$ . The definition of the partial densities is consistent as they sum up to the total density  $\rho = 0.88 \text{ g cm}^{-3}$ .

With this two assumption the density of the liquid scintillator and the abundances of hydrogen and carbon can be calculated as:

$$\rho = \frac{\rho_{\text{H}} + \rho_{\text{C}}}{1 - n_{\text{Gd}}} \quad (\text{A.37})$$

$$n_{\text{H}} = \frac{\rho_{\text{H}}}{\rho} \quad (\text{A.38})$$

$$n_{\text{C}} = \frac{\rho_{\text{C}}}{\rho} \quad (\text{A.39})$$

#### A.4.2.2 LSM Rock and Concrete Composition

For the Fréjus rock<sup>2</sup> several compositions are given in the literature [11, 34, 39, 41, 44, 55], which can be traced back to the three primary sources [11, 44, 55].

For a better comparability of the different sources Table A.4 list the relative *elemental* abundance by weight  $n_i$ . The relative *material* abundance by weight  $n_j$  used in [11] was converted by:

$$n_i = \sum_j \frac{x_{ji}A_i}{\sum_i x_{ji}A_i} n_j \quad (\text{A.40})$$

<sup>2</sup>Identified as ‘schistes lustrés’ [40] in french, ‘glossy schist’ [41] in english, and ‘Bündener Schiefer’ [55] in german.

**Table A.4** Chemical composition of the Fréjus rock and LSM concrete given in literature, rounded to two decimal places

Reference	$Z^2$ (A)	Z (A)	$\rho$ (g cm $^{-3}$ )	$n_H$ (% w/w)	$n_C$ (% w/w)	$n_O$ (% w/w)	$n_{Na}$ (% w/w)	$n_{Mg}$ (% w/w)
<b>Fréjus rock</b>								
[9]	5.87(2)	0.50	2.73(1)	—	—	—	—	—
[55] <sup>a</sup>	5.04	0.499	2.74	—	11.12	61.94	—	0.74
[11, 41] <sup>b</sup>	6.22 <sup>c</sup>	0.503 <sup>c</sup>	2.65	1.02	6.10	48.61	0.45	0.84
[44]	—	—	—	1.00	6.00	49.00	0.44	0.84
<b>LSM concrete</b>								
[11]	—	—	2.40	1.25	7.46	48.99	0.01	0.78
Reference	$n_{Al}$ (% w/w)	$n_{Si}$ (% w/w)	$n_P$ (% w/w)	$n_S$ (% w/w)	$n_K$ (% w/w)	$n_{Ca}$ (% w/w)	$n_{Ti}$ (% w/w)	$n_{Mn}$ (% w/w)
[9]	—	—	—	—	—	—	—	—
[55]	3.60	10.28	—	0.26	0.65	10.40	—	0.04
[11, 41]	2.65	6.96	0.07	—	0.21	30.59	0.07	0.03
[44]	2.60	7.00	0.06	—	0.31	30.75	0.07	0.03
<b>Fréjus rock</b>								
[9]	—	—	—	—	—	—	—	—
[55]	3.60	10.28	—	0.26	0.65	10.40	—	0.04
[11, 41]	2.65	6.96	0.07	—	0.21	30.59	0.07	0.03
[44]	2.60	7.00	0.06	—	0.31	30.75	0.07	0.03
<b>LSM concrete</b>								
[11]	0.58	2.71	0.07	—	0.02	36.81	0.10	0.01
								0.52

<sup>a</sup>Average composition between LSM and surface, based on 18 measurements, possibility remains of local inequalities [55, p. 58]

<sup>b</sup>Rock composition near LSM

<sup>c</sup>Values according to [39]

Here the index  $j$  goes over the materials (e.g.  $\text{SiO}_2$ ,  $\text{Al}_2\text{O}_3$ ) and the index  $i$  goes over the elements (e.g. Si, Al, O). For the atomic weight  $A_i$  of element  $i$  the mean atomic weight according to [72] is taken and  $x_{ij}$  is the stoichiometric fraction of element  $i$  in material  $j$  (e.g.  $x = 2$  for Al in  $\text{Al}_2\text{O}_3$ ). For [11] only the ‘major elements concentration’ in [11, Table 2] are considered. It is further assumed that the ‘weight loss on ignition’ in [11] was caused by 50 % w/w  $\text{H}_2\text{O}$  and 50 % w/w  $\text{CO}_2$ .

As pointed out by [39] the rock compositions near the LSM [11, 44] are in mutual agreement, whereas they differ from the *average* composition between LSM and the surface given in [55].

For the composition of the concrete used for the walls at LSM only one reference [11] exist, its elemental composition is also listed in Table A.4. For the conversion from material abundance to elemental abundance the same method and assumption as for the rock was used.

#### A.4.3 Optical Properties

In the detector response model, see Sect. 5.4.2, we include reflection and absorption within the active volume of the NMM in the detector response model. The optical interaction are characterized by the *absorption length*  $\alpha^{-1}(\lambda)$  of optical volumes and the complex *refraction index*  $n(\lambda) + i\kappa(\lambda)$  of optical surfaces. Both quantities are functions of the wavelength  $\lambda$ .

First we define some relation, needed to calculate the absorption length  $\alpha^{-1}$  for a given material from the literature. Considering a light beam of intensity  $I_0$  that gets attenuate to an intensity  $I$  after passing a material of thickness  $x$  with refraction index  $n + i\kappa$ . In this case the *absorbance*  $A(\lambda)$  is a function of the wavelength  $\lambda$  and is related to the *transmittance*  $T(\lambda)$  via [18, 66]

$$A(\lambda) = -\log_{10} T(\lambda), \quad (\text{A.41})$$

$$T(\lambda) = \frac{I(\lambda)}{I_0(\lambda)}. \quad (\text{A.42})$$

The transmittance depends via the *Beer-Lambert law* on the thickness  $x$  [18]:

$$I(\lambda) = I_0(\lambda) e^{-\alpha(\lambda) \cdot x}. \quad (\text{A.43})$$

The *absorption coefficient*  $\alpha(\lambda)$  is connected to the imaginary part  $\kappa(\lambda)$  of the refraction index by [18]

$$\alpha(\lambda) = \frac{\kappa(\lambda) \cdot 4\pi}{\lambda}, \quad (\text{A.44})$$

which can be modelled as a damped oscillator with resonance frequency  $\omega_0$  and damping coefficient  $\gamma$  [18]:

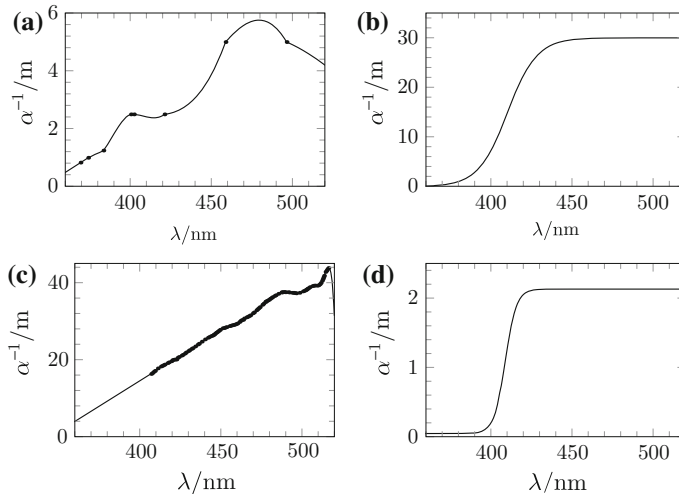


**Fig. A.1** Interpolated absorption length  $\alpha^{-1}$  as function of the wavelength  $\lambda$  for: **a** borosilicate glass [36, p. 14, SchottglassBK7], **b** lime glass [52, Fig. 1.5], **c** paraffin [19, Fig. 5.8, dashed curve], **d** acrylic glass [7, Fig. 5, curve ‘G’]

$$\kappa(\omega) = A \cdot \frac{\gamma\omega}{(\omega_0^2 - \omega^2)^2 + \gamma^2\omega^2}, \quad \omega = \frac{2\pi \cdot c}{\lambda}. \quad (\text{A.45})$$

and a normalisation  $A$ .

In the modelled detector (Sect. 5.4.2), we considered complex refraction spectra for iron [49], aluminium [65], and the bialkali photocathode [46]. For air [13], argon [70], borosilicate glass [36], and acrylic glass [14] only the real part of the refraction spectra is implemented.<sup>3</sup> In case of paraffin [8] and lime glass [51] only the constant refraction index was used. Absorption spectra for borosilicate glass [36], acrylic glass [7], paraffin [19], and lime glass [52] were calculated from the cited sources by using Eqs. A.41 and A.42. We omitted the absorption in the thin ( $< 4$  cm) layers of argon and air as negligible. Figure A.1 shows the resulting absorption spectra.

The absorption length of the liquid scintillator BC-525<sup>4</sup> used in the NMM is not given in the data sheet [62]. However, as we argued in Sect. 4.2.1, we expect that the scintillator presented in [74] is an approximative model of the used BC-525. Figure A.2a shows the absorption spectrum given in [74]. We fit the individual absorption bands in the spectrum with Eq. A.45. Given the approximative character of the spectrum, we used only the spectral shape in the detector response model by normalizing the fit to  $\alpha^{-1}(\lambda = 440 \text{ nm})$ , Fig. A.2b. The absolute scale is a free parameter of the model, see Sect. 5.4.2.

<sup>3</sup>The actual data for air and argon were accessed through the *Refractive Index Database* [53].

<sup>4</sup>BC-525 (Saint-Gobain Crystals).

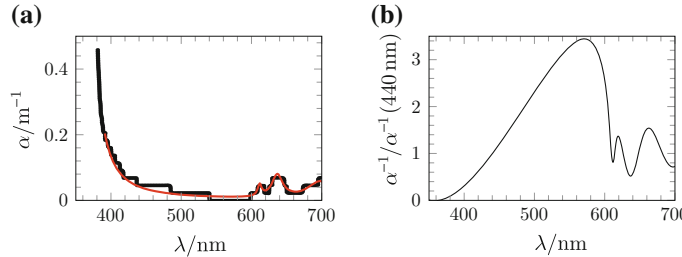


**Fig. A.2** Absorption spectrum of liquid scintillator as function of the wavelength  $\lambda$ : **a** Absorption coefficient  $\alpha(\lambda)$  of gadolinium loaded liquid scintillator [74, Fig. 3, curve ‘0.2 % Gdin20 % PC80 % dodecane’], fitted with (Eq. A.45) (*solid line*). **b** Reciprocal of the fit, i.e. absorption length  $\alpha^{-1}(\lambda)$ , normalized to  $\alpha^{-1}(440\text{ nm})$

## A.5 Technical Properties of the Neutron Counter

### A.5.1 Technical Drawings of the Neutron Counter

The implemented geometry in Sect. 5.1 is based on the technical drawings of the neutron counter. Simplified drawings of the complete neutron counter and of the acrylic glass container in particular are shown in Figs. A.3 and A.4 respectively. Both figures consist of a side view, a top view, and a cut parallel to plane A–A, which is indicated in the side view.

The neutron counter consist in principal of two parts: the muon module 50 of the muon telescope on top of the neutron multiplicity meter (NMM). The innermost part of the NMM is the acrylic glass container, which is shown as part 10 in Figs. A.3, and A.4 shows it in more details. It is divided in three chambers: the two outermost chambers (part 13) contain the 8 inch PMTs (part 6) and 2 inch PMTs (part 7) immersed in paraffin, the innermost chamber is the active volume filled with liquid scintillator (part 14). It is connected to the siphon (part 3), placed in an aluminium safety container (part 4) on top of module 50, to prevent overpressure. The plastic scintillator (part 2) of module 50 is placed on the wooden cover (part 1) of the NMM. The acrylic glass container is placed in aluminium safety container (part 8) on top of the lead target (part 11). The iron support structure consists of 2 cm thick plates with dimension of 740 mm  $\times$  395 mm on the long side (part 9) and 740 mm  $\times$  315 mm on the short side (part 5) of the neutron counter. The bottom plate was 1 cm thick (part 12). Not shown on the drawings are two styrofoam layers: one of 5 mm thickness is placed between the acrylic glass body and the aluminium safety container, the second one of 17.9 mm thickness is placed between the safety container and the lead target.

For the sake of simplicity, some details were omitted, e.g. the dimensions of the drilling and the dimensions of the siphon. The functionality of the neutron counter and its parts are described in Sect. 4.2.

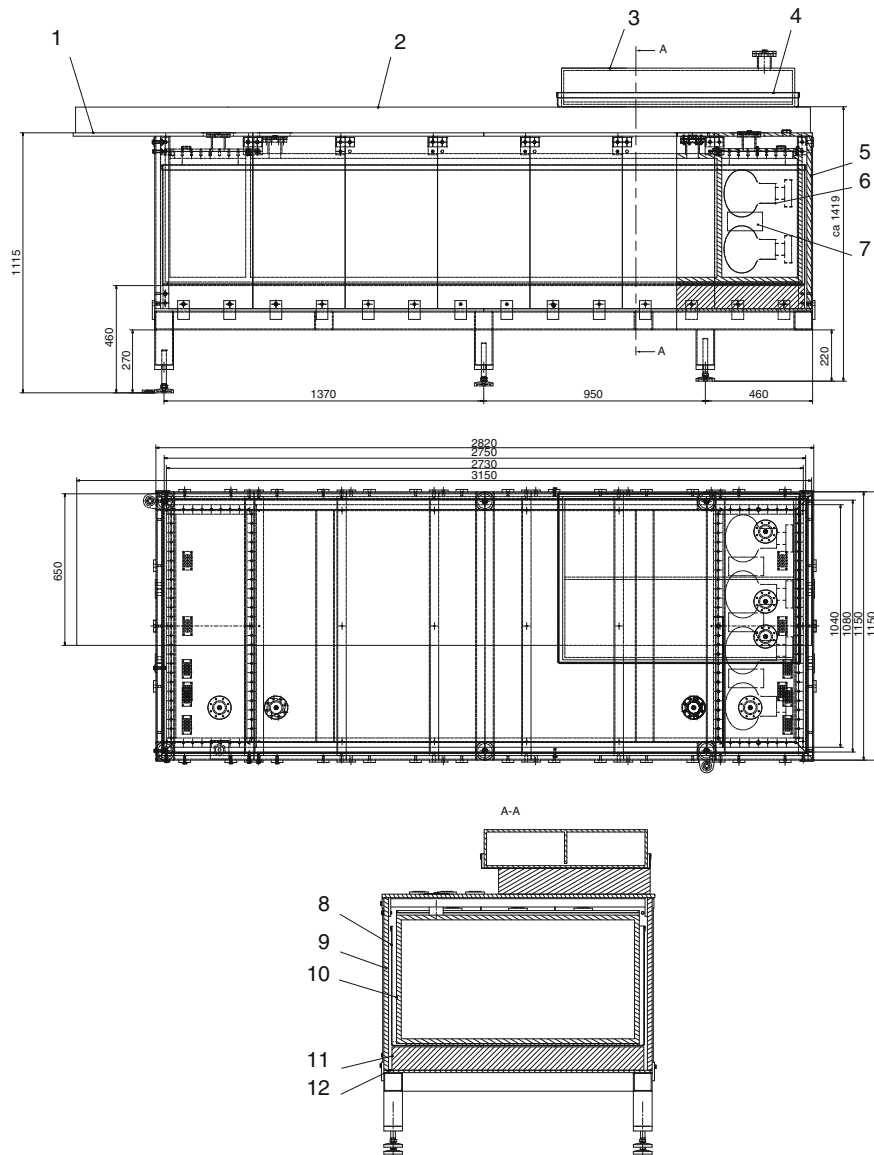


**Fig. A.3** Side view, top view, and cut parallel to plane A–A of the neutron counter, all dimensions are given in millimetre. Figure adapted from the technical drawing. For the description of the numbered parts, see text

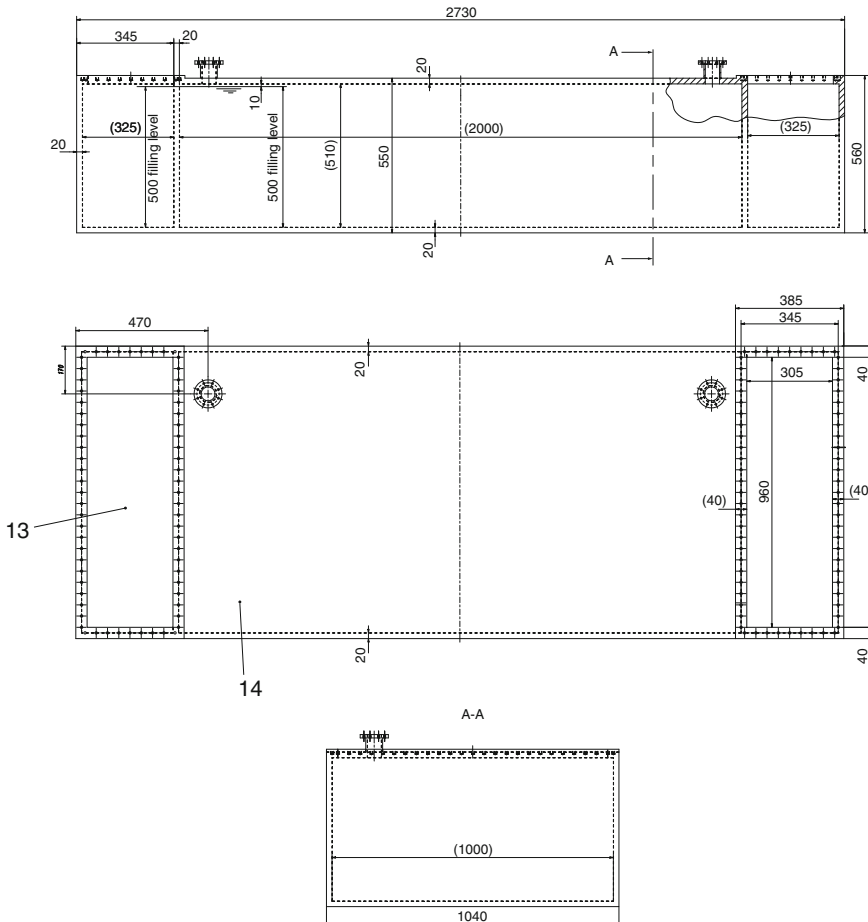


**Fig. A.4** Side view, top view, and cut parallel to plane A–A of the acrylic glass container, all dimensions are given in millimetre. Figure adapted from the technical drawing. For the description of the numbered parts, see text

### A.5.2 Properties of the Used Scintillators

This section list the properties of the used scintillators according to the data sheets. The liquid scintillator BC-525 (Table A.5) was used in the NMM, the plastic scintillator BC-412 (Table A.6) was used in module 50.

**Table A.5** Physical properties of the used scintillator BC-525 according to the manufacturer's data sheet [62]

Property	Value
Scintillation properties	
Light output relative to Anthracene	55 %
Decay time, short component	3.8 ns
Bulk light attenuation	>4.5 m
Wavelength of maximum emission	425 nm
Atomic composition	
Density of hydrogen atoms	$6.00 \times 10^{22} \text{ cm}^{-3}$
Density of carbon atoms	$3.85 \times 10^{22} \text{ cm}^{-3}$
Ration of hydrogen to carbon atoms	1.56
Density of electrons	$29.9 \times 10^{22} \text{ cm}^{-3}$
General technical data	
Gadolinium content	0.2 % w/w
Density	0.88 g cm <sup>-3</sup>
Refractive index	1.49
Flash point	81 °C

Contrary to the stated gadolinium loading of 0.5 % w/w in the data sheet, the used liquid scintillator is loaded with 0.2 % w/w gadolinium

**Table A.6** Selected physical properties of the used scintillator BC-412 according to the manufacturer's data sheet [61]

Property	Value
Scintillation properties	
Light output relative to Anthracene	60 %
Rise time	1.0 ns
Decay time	3.3 ns
Bulk light attenuation	4.0 m
Wavelength of maximum emission	434 nm
Atomic composition	
Density of hydrogen atoms	$5.23 \times 10^{22} \text{ cm}^{-3}$
Density of carbon atoms	$4.74 \times 10^{22} \text{ cm}^{-3}$
Ration of hydrogen to carbon atoms	1.104
Density of electrons	$3.37 \times 10^{22} \text{ cm}^{-3}$
General technical data	
Density	1.032 g cm <sup>-3</sup>
Refractive index	1.58

### A.5.3 Properties of Photomultiplier Tubes

This section describes the details of the used neutron PMTs (PMT<sup>N</sup>): the voltage divider, the gain parameter, an estimation of the single electron response, and a characterization of the after-pulse proneness.

#### A.5.3.1 Voltage divider

The PMT<sup>N</sup> are operated on negative high tension, i.e. the anode is grounded, otherwise a coupling capacitor between anode and subsequent electronic would be necessary causing a decreased time resolution [10, p. 84]. The low-pass R14, C4 prevent noise from the power supply [32, p. 93]. The voltage divider itself is not equally spaced, but has higher voltages near the photocathode (along R1, R2, R3) and the anode (R8, R19, R10–R12) compared to the middle ones (R4–R7) (so called *tampered voltage divider* [32, pp. 90f.]). The higher voltages near the photocathode increase the electric fields in the optical-electronic input system and hence the collection efficiency. The increased electric fields near the anode prevent the build-up of space charges, caused by the high number of secondary electrons on the latter dynode stages, that could disturb the linearity of the PMT response. As the space between the last dynode and the anode is smaller than the inter-dynode space, the voltage between them (R12) can be again smaller as the previous, last inter-dynode voltage (R11), but still create a high electric field strength. The serial decoupling capacitors (C1–C3) increase the linearity of the PMT response by supplying charge, additional to the one delivered by the current through the divider, for pulse formation [32, p. 88]. With a load of  $100\ \Omega$  (R13) a parallel coupled pair of PMTs match the  $50\ \Omega$  input impedance of the data acquisition electronics (see Sect. 4.2.4).

This voltage divider design is similar to the one used in [48]: According to [48, Fig. 4.1.2] it also has a tampered resistive divider, decoupling capacitors, but the low-pass filter is placed at the signal connection instead at the supply connector, because the photocathode is grounded instead of the anode.

#### A.5.3.2 Gain Parametrization

The 16 neutron PMTs with 8 in. diameter (PMT<sup>N</sup>) of the NMM were divided in eight groups and the anode signals of the two PMTs within a given group were added passively, see Sect. 4.2.1. Albeit each individual PMT was connected to a individual high tension line, PMTs with similar gain were selected for a given group. The 2 in. muon PMTs (PMT<sup>M</sup>) of the muon telescope were similar grouped, see Sect. 4.2.2.

To measure the gain parameters  $A$  and  $K$ , the respective PMT was placed in a light tight box where it was illuminated through a diffuser by a pulsed LED<sup>5</sup> at

---

<sup>5</sup>RLT420-3-30 (Roithner Lasertechnik).

**Table A.7** Properties of the neutron PMTs ( $\text{PMT}_{i,j}^N$ ): serial number, the gain parameters  $A$ ,  $K$ , and the gain  $G$  at reference high tension  $-1000$  V is given for the used PMTs

PMT ID	Serial number	$A (10^{-24})$	K	$G (-1000 \text{ V})$
Neutron PMTs—high gain				
1.1	SA1723	0.4	9,0238	471
1.2	SA1593	1	8,9294	614
2.1	SA1680	3	8,7786	650
2.2	SA1709	1	8,9446	682
5.1	SA1718	1	8,7078	133
5.2	SA1653	3	8,8827	133
6.1	SA1652	4	8,8522	144
6.2	SA1800	4	8,9561	295
Neutron PMTs—low gain				
3.1	SA1638	5	8,7670	1000
3.2	SA1626	50	8,4341	1003
4.1	SA1634	4	8,7653	791
4.2	SA1670	1	8,9831	890
7.1	SA1807	1	8,8746	421
7.2	SA1614	1	8,8807	439
8.1	SA1607	1	9,0233	1175
8.2	SA1664	3	8,8854	1359

$\bar{\lambda} = 423$  nm, the same type as used in the light pulser (Sect. 4.2.3). The output light intensity was controlled via the light pulse width and the LED supply voltage. It was held constant whereas the PMT supply voltage  $U$  was varied. The integrate anode response pulse  $Q$  was measured and corrected for the pedestal  $P$ , i.e. the integrate anode response when the PMT is not illuminated. The gain parameters were obtained by fitting the measured  $Q(U)$ -values with [32]

$$Q - P = A \cdot U^K. \quad (\text{A.46})$$

The gain parameters  $A$ ,  $K$  of the  $\text{PMT}^N$  are listed in Table A.7 together with the gain  $G$  at a reference high tension of  $-1000$  V. This reference gain was used to select PMTs with similar gains for the PMT groups. The division in *low gain* and *high gain* PMTs is discussed in Sect. 4.2.1. Table A.8a lists the actual applied high tension, based on the adjustment procedure described in Sect. 4.2.5. As the PMTs used in the modules 50 and 51 of the muon telescope were already tested and characterized for the KARMEN experiment [48], we do not list their parameter, but list only the applied high tension in Table A.8b.

In the tables, the individual  $\text{PMT}_{i,j}^N$  are identified by two indices:  $i = 1, \dots, 8$  identified the PMT group and  $j = 1, 2$  the given PMT within this group. For the muon telescope, both modules 50 and 51 had each two PMT groups, one at the north end of the module (marked with ‘N’ in the table) and one at the south end (‘S’).

**Table A.8** Applied supply voltage of (a) the neutron PMTs and of (b) the muon PMTs

(a)	PMT ID	High tension line		High tension (V)					2011-03-14	2011-06-06	
		<2009-12-22	>2009-12-22	2008-09-24	2008-12-15	2009-06-23	2010-03-13	2010-03-14			
Neutron PMTs—high gain											
	1.1	112	144	-1100	-1212	-1212	-1224	-1224	-1255		
	1.2	113	152	-1100	-1280	-1280	-1293	-1293	-1340		
	2.1	114	145	-1100	-1244	-1201	-1212	-1212	-1205		
	2.2	115	153	-1100	-1142	-1101	-1111	-1111	-1130		
	5.1	116	148	-1100	-1237	-1237	-1249	-1249	-1230		
	5.2	117	156	-1100	-1189	-1189	-1201	-1201	-1220		
	6.1	118	149	-1100	-1337	-1290	-1303	-1303	-1325		
	6.2	119	157	-1100	-1198	-1158	-1167	-1167	-1200		
Neutron PMTs—low gain											
	3.1	120	146	-1100	-1129	-1129	-1140	-1140	-1172		
	3.2	121	154	-1100	-1213	-1213	-1225	-1225	-1280		
	4.1	122	147	-1100	-1163	-1123	-1135	-1135	-1150		
	4.2	123	155	-1100	-1128	-1090	-1101	-1101	-1120		
	7.1	124	150	-1100	-1225	-1225	-1237	-1237	-1250		
	7.2	125	158	-1100	-1218	-1218	-1230	-1227	-1200		
	8.1	126	151	-1100	-1245	-1202	-1212	-1215	-1240		
	8.2	127	159	-1100	-1110	-1072	-1082	-1084	-1105		

(continued)

Table A.8 (continued)

		High tension line			High tension (V)					
		2008-09-24	2008-10-31	2008-12-11	2008-12-15	2009-08-12	2009-12-22	2010-01-14	2010-09-30	2011-02-11
<b>Module 51</b>										
N	38	-1600	-1600	-1600	-1600	-1600	-1650	-1650	-1600	-1700
S	39	-1600	-1600	-1600	-1600	-1598	-1650	-1650	-1598	-1700
<b>Module 50</b>										
N	54	-1450	-1350	-1450	-1400	-1450	-1450	-1510	-1400	-1520
S	55	-1450	-1350	-1450	-1400	-1450	-1450	-1490	-1398	-1500

In case of the neutron PMTs, the allocation of the high tension lines changed on 2009-12-22

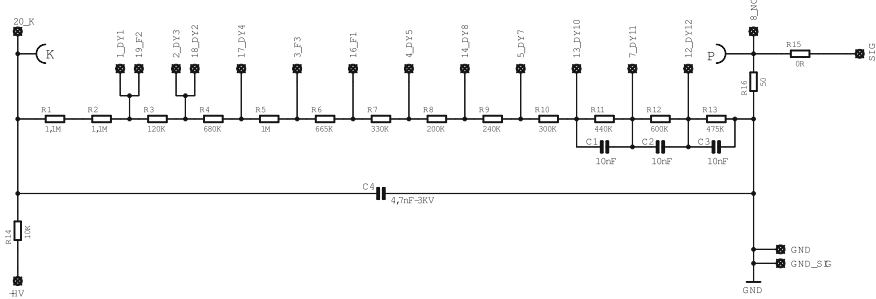


**Fig. A.5** Voltage divider of the  $\text{PMT}^N$ 's. Figure adapted from technical drawing, for details see text

### A.5.3.3 Single Electron Response

The time resolution of a PMT depends on the *single electron response* (SER) and the energy resolution depends on the *single electron spectrum* (SES), i.e. the distribution of the amplitudes of SERs. The SER gives the *transit time difference*  $\bar{t}_{c,a}$  [52, pp. 4–14, 4–17f.], i.e. the time between absorbing a photon on the photocathode and generating an anode pulse and the *response pulse width*  $t_w$  [52, pp. 2–9, 4–11], i.e. the FWHM of the SER. The SES gives the *single electron resolution*  $\nu_{t,ca}$  [52, pp. 2–8, 3–17], i.e. the FWHM of the SES peak. Contrary to the previous reported gain parameters, these parameters were not measured in this work, but generic values were estimated for each type of PMT.

For the muon PMTs ( $\text{PMT}^M$ ),<sup>6</sup> the data sheet [51] list the values of  $\bar{t}_{c,a} \approx 30 \text{ ns}$ ,  $t_w \approx 4 \text{ ns}$ , and  $\nu_{t,ca} = 70 \text{ \%}$ . By eye, the last one seems in agreement with an actual measured SES [54, Fig. 4.4b], unfortunately [54] gives no quantitative values.

For the neutron PMTs ( $\text{PMT}^N$ ),<sup>7</sup> the data sheet [31] gives the following values:  $\bar{t}_{c,a} \approx 55 \text{ ns}$ ,  $t_w \approx 2.4 \text{ ns}$ . However, this values may differ from our case: albeit we used a voltage divider design that was similar to the one used in the data sheet, we used different resistors.

For the same type of PMT and a voltage divider design similar to the one we used (see Fig. A.5), C. Oehler [48] report measurements of SER and SES for different *inter-stage voltages* between cathode and first dynode  $U_{c,d1}$ , and between first dynode and anode  $U_{d1,a}$ . The differences between voltage dividers with the same design but different resistors can be effectively described by the voltages  $U_{c,d1}$ ,  $U_{d1,a}$ . Therefore, we can estimate  $\bar{t}_{c,a}$ ,  $t_w$  for the voltage divider we used from the average supply voltage ( $\approx -1200 \text{ V}$ , Table A.8) and the work of C. Oehler. For the voltage divider shown in Fig. A.5, we obtain with the given average supply voltage the following inter-stage voltages:  $U_{c,d1} \approx -364 \text{ V}$ ,  $U_{d1,a} \approx -835 \text{ V}$ . These voltages lead to a single electron resolution of  $\nu_{t,ca} \lesssim 40 \text{ \%}$ , cf. [48, Fig. 5.7, 5.8], and to a response

<sup>6</sup>Photonis XP2262 (PHOTONIS).

<sup>7</sup>Hamamatsu Photomultiplier Tube R5912 (HAMAMATSU PHOTONICS K.K.).

pulse width of  $t_w \lesssim 1.2$  ns, cf. [48, Figs. 5.11, 5.12]. Therefore, as a conservative upper limit, we used for the *response pulse width*  $t_w$  the value from the data sheet:

$$t_w < 2.4 \text{ ns.} \quad (\text{A.47})$$

It is included in the detector response model of the NMM (see Sect. 5.4.2) to consider the timing resolution of the neutron PMTs. The transit time difference  $\bar{t}_{c,a}$  is not further considered, as its value is dominated by the geometry of the optical-electronic input system [52, p. 4–14], which is the same for each PMT of a given type (PMT<sup>N</sup>, PMT<sup>M</sup>).

#### A.5.3.4 Afterpulse Measurements

The set-up was the same as used in the gain measurement. The PMT was illuminated by a pulsed LED ( $\nu = 497$  Hz) and the anode pulse traces were accumulated on a storage oscilloscope for a time window of  $\tau \ll 1/\nu$ , triggered by the LED controller. Afterwards manually the pulses  $n$  over a threshold  $U_{\text{th}}$  were counted. The resulting fraction

$$F_{\tau, U_{\text{th}}} = \frac{n}{n_0} \quad (\text{A.48})$$

relates them to the total number of light pulses  $n_0 = \tau \nu$ . Results for different supply voltage are listed in Table A.9.

#### A.5.4 Properties of Used DAQ Electronic Modules

This section document the used parts of the DAQ electronics, the mapping of the PMT groups to the ADC and TDC channels, and the measured pedestals of the ADC channels.

**Table A.9** Afterpulse fraction  $F_{\tau, U_{\text{th}}}$  as function PMT high tension  $U$ , threshold  $U_{\text{th}}$ , and time window width  $\tau$

$U$ (V)	$\tau$ ( $\mu\text{s}$ )	$U_{\text{th}}$ (mV)	$F_{\tau, U_{\text{th}}}$
900	1.8	36	$1.8(10) \times 10^{-4}$
900	1.8	236	$0.7(8) \times 10^{-4}$
900	9.5	36	$7.9(12) \times 10^{-4}$
900	9.5	236	$5.1(13) \times 10^{-4}$
1300	1.8	36	$2.8(4) \times 10^{-3}$
1300	1.8	236	$2.19(14) \times 10^{-3}$
1300	9.5	36	$3.6(10) \times 10^{-2}$
1300	9.5	236	$0.9(2) \times 10^{-2}$

**Table A.10** Allocation of the CAMAC crate

Slot	ID	Type	Serial number
1	–	CES LA3310—LogicAnalyzer	29
2	–	CES DSM3320	87
3	–	–	–
4	DISC <sup>M<sub>1</sub></sup>	LeCroy 4413—discriminator	B23663
5	–	–	–
6	DISC <sup>M<sub>2</sub></sup>	LeCroy 4413—discriminator	B23676
7	–	–	–
8	DISC <sup>M<sub>3</sub></sup>	LeCroy 4413—discriminator	B23602
9	–	–	–
10	DISC <sup>M<sub>4</sub></sup>	LeCroy 4413—discriminator	B236282
11	–	–	–
12	DISC <sup>M<sub>5</sub></sup>	LeCroy 4413—discriminator	A48573
13	–	–	–
14	DISC <sup>M<sub>6</sub></sup>	LeCroy 4413—discriminator	B23640
15	–	–	–
16	SCA <sup>M<sub>1</sub></sup>	LeCroy 4434—scaler	????59
17	–	–	–
18	SCA <sup>M<sub>2</sub></sup>	LeCroy 4434—scaler	A80735
19	–	–	–
20	SCA <sup>M<sub>3</sub></sup>	LeCroy 4434—scaler	A80637
21	–	–	–
22	–	In-house made power supply for splitter/delay cards	–
23	–	–	–
24	–	Hytec CCA2 Crate Controller	–
25	–	–	–

#### A.5.4.1 Used Electronic Modules

For documentation, this section list the allocation of the CAMAC crate (Table A.10) and the VME crate (Table A.11). As there is the possibility of unwanted interaction between modules in the same crate all electronic modules are listed regardless if they where used for this work.

Both tables are order by ascending slot number where slot one is located on the left side of the crate. The ID of the module given in the *second column* is introduced in Sect. 4.2.4: Modules of the muon veto are indicated by the superscript M, modules of the NMM are indicated by the superscript N. The *third column* contains the manufacture in short form and the type number of the module. Where possible the serial number of the electronic module is given in *column four*. For the VME

**Table A.11** Allocation of the VME crate

Slot	ID	Type	Serial number	VME base address
1	–	Wiener VME to PCI interface	–	0x120000
2	LED <sup>N</sup>	In-house made LED controller	1	0x584300
3	TDC <sup>M</sup>	CAEN V767—TDC	181	0xee0000
4	LED <sup>M</sup>	In-house made LED controller	2	0x584400
5	LU <sub>1</sub> <sup>M</sup>	CAEN V512—Logic unit	27	0xca0000
6	–	–	–	–
7	LU <sub>2</sub> <sup>M</sup>	CAEN V512—Logic unit	26	0xcb0000
8	–	–	–	–
9	LU <sub>3</sub> <sup>M</sup>	CAEN V512—Logic unit	28	0xca0000
10	–	In-house made veto card	1	0xad0000
11	–	In-house made time module	2	0xedc600
12	ADC <sub>2</sub> <sup>M</sup>	CAEN V792—QDC	314	0xba0000
13	ADC <sub>1</sub> <sup>M</sup>	CAEN V792—QDC	326	0xbb0000
14	ADC <sub>3</sub> <sup>M</sup>	CAEN V792—QDC	339	0xbc0000
15	TDC <sup>N</sup>	LeCroy 1176—TDC	B32674	0xf00000
16	LU <sup>N</sup>	In-house made logic unit	2	0x9b5200
17	DISC <sup>N</sup>	CAEN V895B—Discriminator	227	0xa00000
18	SCA <sup>N</sup>	CAEN V830—Scaler	17	0xaa0000
19	–	CAEN V785NC—ADC	–	0xfe0000
20	ADC <sup>N</sup>	CAEN VX1720 – ADC	105	0xe00000
21	–	CES 8210—CAMAC Branch Driver	–	0x800000

modules also the VME base address is given in *column five*; it is necessary to access the modules via VMEbus.

#### A.5.4.2 Mapping of the PMTs to the DAQ Electronic Modules

Table A.12 list the mapping of the neutron PMT groups  $\text{PMTG}_i^N$  to the input channels of the DAQ electronic modules. Software thresholds were activated on the ADC input channels of the muon telescope ( $\text{ADC}_i^M$ ). For the channels relevant for the muon telescope the values are: 112 ADCunit for  $\text{ADC}_1^M.\text{In}03$  and 144 ADCunit for  $\text{ADC}_1^M.\text{In}11$ ,  $\text{ADC}_1^M.\text{In}23$ , and  $\text{ADC}_1^M.\text{In}31$ .

After passing the discriminator (DISC<sup>N</sup>) and the logical unit (LU<sup>N</sup>), the neutron PMT groups ( $\text{PMTG}_i^N$ ) are mapped to the input channels of the TDC (TDC<sup>N</sup>) in the following ways:

**Table A.12** Mapping of the PMT groups to the input channels of the DAQ electronic modules

PMT group	Discriminator	Scaler	Logic unit	ADC	TDC
PMTG <sub>1</sub> <sup>N</sup>	DISC <sup>N</sup> .In1	SCA <sup>N</sup> .In0	LU <sup>N</sup> .InA1A3	ADC <sup>N</sup> .In0	—
PMTG <sub>2</sub> <sup>N</sup>	DISC <sup>N</sup> .In2	SCA <sup>N</sup> .In1	LU <sup>N</sup> .InA2A4	ADC <sup>N</sup> .In1	—
PMTG <sub>5</sub> <sup>N</sup>	DISC <sup>N</sup> .In3	SCA <sup>N</sup> .In2	LU <sup>N</sup> .InA5A7	ADC <sup>N</sup> .In2	—
PMTG <sub>6</sub> <sup>N</sup>	DISC <sup>N</sup> .In4	SCA <sup>N</sup> .In3	LU <sup>N</sup> .InA6A8	ADC <sup>N</sup> .In3	—
PMTG <sub>3</sub> <sup>N</sup>	DISC <sup>N</sup> .In5	SCA <sup>N</sup> .In4	LU <sup>N</sup> .InB1B3	ADC <sup>N</sup> .In4	—
PMTG <sub>4</sub> <sup>N</sup>	DISC <sup>N</sup> .In6	SCA <sup>N</sup> .In5	LU <sup>N</sup> .InB2B4	ADC <sup>N</sup> .In5	—
PMTG <sub>7</sub> <sup>N</sup>	DISC <sup>N</sup> .In7	SCA <sup>N</sup> .In6	LU <sup>N</sup> .InB5B7	ADC <sup>N</sup> .In6	—
PMTG <sub>8</sub> <sup>N</sup>	DISC <sup>N</sup> .In8	SCA <sup>N</sup> .In7	LU <sup>N</sup> .InB6B8	ADC <sup>N</sup> .In7	—
PMTG <sub>N</sub> <sup>M50</sup>	DISC <sub>1</sub> <sup>M</sup> .In4	SCA <sub>1</sub> <sup>M</sup> .In4	LU <sub>1</sub> <sup>M</sup> .InA3	ADC <sub>1</sub> <sup>M</sup> .In3	TDC <sup>M</sup> .In3
PMTG <sub>S</sub> <sup>M50</sup>	DISC <sub>1</sub> <sup>M</sup> .In12	SCA <sub>1</sub> <sup>M</sup> .In12	LU <sub>1</sub> <sup>M</sup> .InB3	ADC <sub>1</sub> <sup>M</sup> .In11	TDC <sup>M</sup> .In11
PMTG <sub>N</sub> <sup>M51</sup>	DISC <sub>2</sub> <sup>M</sup> .In8	SCA <sub>1</sub> <sup>M</sup> .In24	LU <sub>1</sub> <sup>M</sup> .InC7	ADC <sub>1</sub> <sup>M</sup> .In23	TDC <sup>M</sup> .In23
PMTG <sub>S</sub> <sup>M51</sup>	DISC <sub>2</sub> <sup>M</sup> .In16	SCA <sub>1</sub> <sup>M</sup> .In32	LU <sub>1</sub> <sup>M</sup> .InD7	ADC <sub>1</sub> <sup>M</sup> .In31	TDC <sup>M</sup> .In31

For the mapping of the neutron PMT groups PMTG<sub>i</sub><sup>N</sup> to the TDC, see Eq. A.49

$$TDC^N.In0 = PMTG_1^N \vee PMTG_2^N \quad (A.49a)$$

$$TDC^N.In1 = PMTG_5^N \vee PMTG_6^N \quad (A.49b)$$

$$TDC^N.In2 = PMTG_3^N \vee PMTG_4^N \quad (A.49c)$$

$$TDC^N.In3 = PMTG_7^N \vee PMTG_8^N \quad (A.49d)$$

$$TDC^N.In4 = (PMTG_1^N \vee PMTG_2^N) \wedge (PMTG_5^N \vee PMTG_6^N) \quad (A.49e)$$

$$TDC^N.In5 = (PMTG_3^N \vee PMTG_4^N) \wedge (PMTG_7^N \vee PMTG_8^N) \quad (A.49f)$$

$$TDC^N.In6 = T_M \quad (A.49g)$$

$$TDC^N.In7 = F_{LED} \quad (A.49h)$$

also the flag of the LED pulser  $F_{LED}$  and the trigger signal of the muon veto  $T_M$  are connected, see Sect. 4.2.4.

For the detector response model described in Sect. 5.4, the mapping of PMTs  $i$  to ADC channels  $n$  is encoded by the matrix

$$(M_{in}) = \begin{pmatrix} 0 & 0 & 0 & 0 & 0 & 0 & 0 & 0 \\ 1 & 0 & 0 & 0 & 0 & 0 & 0 & 0 \\ 0 & 1 & 0 & 0 & 0 & 0 & 0 & 0 \\ 0 & 0 & 0 & 0 & 1 & 0 & 0 & 0 \\ 0 & 0 & 0 & 0 & 0 & 1 & 0 & 0 \\ 0 & 0 & 1 & 0 & 0 & 0 & 0 & 0 \\ 0 & 0 & 0 & 1 & 0 & 0 & 0 & 0 \\ 0 & 0 & 0 & 0 & 0 & 0 & 1 & 0 \end{pmatrix}, \quad (A.50)$$

see Sect. 5.4.3.

**Table A.13** Gaussian mean value of the pedestal distribution for the used ADC input channels of the muon telescope

Channel	Date 2009-06-24
3	62.5(0.2)
11	76.7(0.01)
23	49.93(0.01)
31	56.79(0.01)

#### A.5.4.3 Pedestals of the ADC Channels

For the ADCs of the neutron multiplicity meter (NMM) ( $ADC^N$ ) and the muon telescope ( $ADC^M$ ), the pedestal of a given input channel was recorded by providing a trigger signal to the DAQ electronic that was uncorrelated to the signals of the respective detector. For the muon telescope the muon modules of the EDELWEISS muon veto were used as trigger source. For the NMM the internal test pulse generator of the NMM logic unit  $LU^N$  with a frequency of 50 kHz was used. For the NMM, this measurement were repeated during the run of the neutron counter to document possible shifts of the DAQ electronic, see also Sect. 4.4.4. The Tables A.13 and A.14 list the mean value of a Gaussian fitted to the respective data set. For the muon telescope the software thresholds were disable during the pedestal measurements, as otherwise the pedestals would not have been recorded.

In case of the NMM pedestals, the shift of channel  $i$  is specified as the maximal deviation of the pedestal measurements  $P_i$  from the mean pedestal  $\bar{P}_i$  relative to it:

$$\Delta P_i = \max \frac{|P_i - \bar{P}_i|}{\bar{P}_i} \quad (\text{A.51})$$

During the run of the neutron counter, the  $ADC^N$  module LeCroy 1182 was exchanged with CAEN VX1720 on September 9, 2009. The pedestal of the module LeCroy 1182 was measured only one time during the short usage. Therefore, the pedestal shift is only calculated for the longer used CAEN VX1720.

#### A.5.5 Optical and Electrical Parameters of the Light Pulser

The functionality of the LED based light pulser ( $LED^N$ ) is described in Sect. 4.2.3. Here, we list selected properties of the used type of LED<sup>8</sup> in Table A.15 and the supply voltages that were applied during the usage of the light pulser in Table A.16.

The supply voltage for each LED is generated on the LED driver module [37] by two 8 bit digital to analog converter (DAC). The maximal output voltage of DAC1 is 2.5 and 5 V for DAC2. The LED supply voltage is the sum of these two DAC

<sup>8</sup>RLT420-3-30 (Roithner Lasertechnik).

**Table A.14** Gaussian mean value of the pedestal distribution for the used ADC input channels of the NMM

Channel	Date and ADC type				Shift (%)
	2008-11-19	2009-11-15	2010-02-15	2010-06-30	
	LeCroy 1182	CAEN VX1720	CAEN VX1720	CAEN VX1720	
0	368.89(0.04)	240,192(0.14)	243,964(0.13)	243,991(0.10)	1.04
1	324.14(0.03)	242,915(0.14)	246,758(0.08)	246,756(0.09)	1.04
2	310.84(0.04)	241,784(0.16)	245,573(0.15)	245,581(0.16)	1.04
3	335.69(0.04)	240,015(0.14)	243,819(0.13)	243,872(0.15)	1.05
4	306.34(0.07)	241,328(0.15)	245,143(0.13)	245,168(0.16)	1.05
5	378.59(0.05)	242,773(0.10)	246,619(0.14)	246,603(0.15)	1.04
6	349.29(0.08)	242,891(0.16)	246,711(0.15)	246,734(0.18)	1.04
7	328.48(0.05)	240,555(0.14)	244,376(0.09)	244,396(0.15)	1.05

**Table A.15** Selected properties of the used LED at 25 °C according to the data sheet [58]

Property	Typical value	Minimal and maximal values
Electro-optical properties		
Forward voltage	3.3 V	<4.0 V
Reverse current		<10 µA
Radiant flux	3 mW	<6 mW
Viewing angle	30°	–
Peak wavelength	423 nm	420–425 nm
Spectral width	20 nm	–
General technical data		
Power dissipation	120 mW	–
Continuous forward current	30 mA	–
Reverse voltage	5 V	–

**Table A.16** Mapping of LEDs to output channels of the driver module LED<sup>N</sup>, the settings of the DACs, and the resulting supply voltages

Channel	LED ID	DAC1	DAC2	Supply voltage (V)
0	G	0x89	0x99	6.343
1	M	0x99	0x99	6.500
2	H	0x98	0x99	6.490
3	I	0xa7	0x99	6.637
4	C	0x9e	0x99	6.549
5	K	0x94	0x99	6.451
6	D	0x7c	0x99	6.216
7	S	0x38	0xff	7.549

controlled voltages plus an offset of 2 V. The resulting voltage range is 2–9.5 V with a resolution of 10 mV.

Table A.16 contains in the *first column* the ID of the output channel of LED<sup>N</sup>, in the *second column* the alphabetic ID of the LED connected to the output channel, in the *third and fourth columns* the hexadecimal values for DAC1, DAC2 respectively, and in the *fifth column* the resulting supply voltage.

## A.6 AmBe as Reference Neutron Source

In general, an AmBe neutron source consist of a mixture of <sup>241</sup>AmO as  $\alpha$ -emitter and beryllium as target [29]. The primary neutron spectrum is the result of the <sup>9</sup>Be ( $\alpha$ , n) <sup>12</sup>C reaction of the slowed down  $\alpha$ -particles [29, 68].

With a maximal energy of the  $\alpha$ -particle of 5.48 MeV [29], the <sup>12</sup>C is produced either in its ground state, first excited state, or second excited state [29, 68]. Therefore, the primary neutron spectrum consists of three neutron groups from the three levels of <sup>12</sup>C, reaching up to a kinetic neutron energy of around 11 MeV [29, 68].

The first excited state of <sup>12</sup>C decays to the ground state via emission of a  $\gamma$ -ray of 4.438 MeV [43]. This results in a  $\gamma$ -to-n ratio of [43]:

$$B_{\gamma,n} = 0.575(28). \quad (\text{A.52})$$

This primary spectrum is modified most prominently by inelastic scattering on <sup>9</sup>Be, but also by inelastic scattering on <sup>241</sup>Am and <sup>16</sup>O, as well as <sup>9</sup>Be (n,2n) and <sup>241</sup>Am (n, f) reactions [68]. Especially below 1 MeV, the multi-body breakup <sup>9</sup>Be ( $\alpha$ ,  $\alpha$  n) <sup>8</sup>Be add a neutron continuum [68]. As consequence of these secondary processes, the neutron intensity below 2.5 MeV depends on the source size and activity [45, 68].

During the run of the neutron counter we used an uncollimated AmBe source to measure the detector response to neutrons and  $\gamma$ -rays. Usually, the source is used by EDELWEISS for neutron calibration measurements. The AmO and Be powder is enclosed by a cylindrical lead container of 5 mm diameter and 3 cm length, which itself is placed in a 10 cm long metal cylinder [73]. To our knowledge, the neutron activity is

$$A_{\text{AmBe},n} = 20 \text{ Bq}. \quad (\text{A.53})$$

It is in agreement with a slightly higher activity of 21(4) Bq stated in [73]. Within the uncertainty, the measured  $\gamma$ -to-n ratio is  $B_{\gamma,n} = 0.591(27)$  [73] is in agreement with Eq. A.52.

In the Geant4 simulations, see Sects. 4.4.2 and 5.4.4, the AmBe source is modeled as an isotropic point source via the G4GeneralParticleSource interface. To

model the neutron spectrum, we used the energy spectrum provided by Geant4,<sup>9</sup> reaching up to 10 MeV. We take Eq. A.53 as neutron activity and Eq. A.52 as  $\gamma$ -to-n ratio. Within the uncertainties, these values are in agreement with the ones given in [73]. Also the agreement between simulation and measurement in Sect. 5.4.4 shows that these values are suitable.

## A.7 Discussion of the Muon Flux Measured by the Fréjus Experiment

As mentioned in Sect. 5.3.3, the definition of the muon flux used by the Fréjus experiment [9] is not clear, at least within the EDELWEISS collaboration: on one hand the former Fréjus collaboration member and former EDELWEISS collaboration member G. Chardin proposes in private communication to use a horizontal plane as reference surface. This would be equivalent to measure the vertical flux component.<sup>10</sup> On the other hand, EDELWEISS collaboration member V. A. Kudryavtsev propose in private communications and in [39] to use a sphere as reference surface. As the surface of a sphere is always perpendicular to the direction of all incoming muons this is equivalent to the definition proposed of the ICRU [35].

To further complicate the issue their exist a compilation of data sets containing supposed measured raw muon numbers of the Fréjus experiment, circulating via private communication. As all this concerns an over 20 years old measurement, the private statements and memories have to be handled with care.

As this data set will be important for the further discussion we will describe it in more detail. As obtained from V. A. Kudryavtsev, it consists of three plain text files:

`Nb_muons_360x90_Rhode.txt` seems to contain 492,095 supposed muons divided in an array of 360 bins in azimuth and 90 bins in zenith direction. `Acceptance_360x45_Rhode.txt` seems to contain the acceptance area of the Fréjus detector, the file name suggest a listing for 360 x 45 directions in the azimuth–zenith-plane. The file `frejus.dat` seems to contain the rock overburden for  $360 \times 45$  directions in the azimuth–zenith-plane. V.A. Kudryavtsev obtained the files from W. Rhode, who works on the Fréjus data in the 1990s (e.g. [55, 56]) and state a live-time of  $1.03150728 \times 10^8$  s. Hereafter we will refer to this data set as *Rhode-compilation*.

To break the dependence on private communicated data, V. A. Kudryavtsev propose to reverse engineer the reference values from [9], based on the files from the Rhode-compilation. It is therefore important to collect as much additional data as possible, especially to answer the question if the supposed muons contained in the

---

<sup>9</sup>In the used Geant4 version 9.2p01, the binned spectrum is stored under `/geant4/examples/advanced/underground_physics/ambe_spectrum.mac`.

<sup>10</sup>Given a fluence  $\Phi$  of particles from direction  $(\theta, \phi)$ , defined according to [35], the vertical component can be *calculated* as  $\Phi_v = \Phi \cos \theta$ . It can be *measured* by counting the particle from all directions that cross a horizontal plane of  $1 \text{ m}^2$ .

Rhode-compilation are really muons ( $5.31 \text{ m}^{-2} \text{ d}^{-1}$  [9]), or muon-induced events within the Fréjus detector. In the latter case the question is if they are single muon events ( $4.73 \text{ m}^{-2} \text{ d}^{-1}$  [9]), or all events containing also higher multiplicities ( $4.98 \text{ m}^{-2} \text{ d}^{-1}$  [9]). The answer to this question decide which reference value from [9], given above in parenthesis, has to be taken to compare with the result from this reverse engineering.

The importance of the correct chosen reference value from [9] in reverse engineering the flux definition is highlighted in [39]: V.A. Kudryavtsev used the data from the Rhode-compilation to adjust his muon propagator and obtained a simulated flux of  $4.36 \text{ m}^{-2} \text{ d}^{-1}$  [39] for a horizontal plane as reference surface, and  $5.62 \text{ m}^{-2} \text{ d}^{-1}$  [39] for a sphere. Compared to the all muon rate of  $5.31 \text{ m}^{-2} \text{ d}^{-1}$  [9] this results would support a sphere as reference surface, compared to the single event rate of  $4.73 \text{ m}^{-2} \text{ d}^{-1}$  [9] it would support the horizontal plane as reference surface. V.A. Kudryavtsev cite private communication with W. Rhode that the Rhode-compilation based on *all muons*, therefore it seems plausible to compare it to  $5.31 \text{ m}^{-2} \text{ d}^{-1}$  [9]. The conclusion would be a surface of a sphere as reference, in contradiction with the statement of G. Chardin.

But there are two reasons to doubt that the Rhode-compilation is based on all muons: In current private communication W. Rhode state that the data are more probably based on single muon events. Also the live-time associated with the Rhode-compilation is identical to the live-time of single muon events as given in [55].

To pinpoint the origin of the Rhode-compilation the number of muons (492,095) can be compared to the various published data sets: In [9] a total of 420,334 events for zenith angle less than  $60^\circ$  are reported, containing 407,775 single muon events, and 436,679 muons in total for a live-time of  $2.12544 \times 10^9$ s. A different selection in [55] results in 481,817 single muon events in  $1.03151 \times 10^8$ s live-time and 8780 events with higher multiplicity in  $6.64425 \times 10^7$ s live-time, both values after cuts. In [71] a value of 492,083 muons after cut is given for a live-time of  $1.03151 \times 10^8$ s. These is the reference with the smallest deviation to the 492,095 muons in question. As the live-time is the same as the live-time of single muon events in [55], it seems plausible that these are also single muon events.

Stopping the argumentation here and rely on [39], we would conclude that the Rhode-compilation based on single muon events, therefore the results from [39] has to be compared to  $4.73 \text{ m}^{-2} \text{ d}^{-1}$  [9]. As consequence the reference surface is the horizontal plane, in agreement with the statement of G. Chardin. Unfortunately there is a further aspect one has to respect: According to [9] the flux is restricted to muons with a zenith angle less than  $60^\circ$ . This cut is not included in [39], therefore we have to do an additional attempt to reverse engineer the value of  $4.73 \text{ m}^{-2} \text{ d}^{-1}$  [9] from the Rhode-compilation.

This attempt is based on the hypothesis that the flux is obtained by

$$\dot{\phi} = \sum_{\theta \leq 60^\circ} \sum_{\phi} \frac{N_{\theta,\phi}}{T A_{\theta,\phi}} \quad (\text{A.54})$$

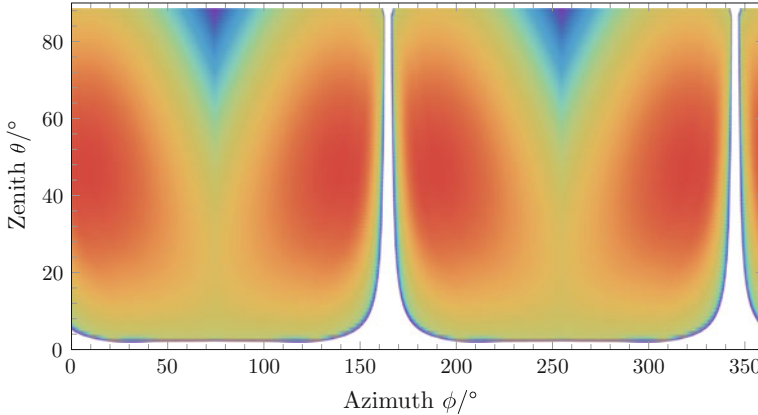


**Fig. A.6** The acceptance area of the Fréjus detector for  $360 \times 90$  directions in the azimuth–zenith-plane according to the Rhode-compilation, see text for details

where  $N_{\theta,\phi}$  are the values from `Nb_muons_360x90_Rhode.txt`, according to the previous argumentation assumed to be single muon events measured by the Fréjus detector, see Fig. 3.3 for illustration. As live-time  $T = 1.03151 \times 10^8$  s is used. The  $A_{\theta,\phi}$  are the acceptance area from `Acceptance_360x45_Rhode.txt`. The acceptance area is also described in [64], but there a division in  $180 \times 90$  directions in the azimuth–zenith-plane and an azimuth symmetry is stated. By handling the values from `Acceptance_360x45_Rhode.txt` in this way the acceptance area shown by Fig. A.6 is obtained, similar to the one shown in [63, Fig. 6.4]. The calculation results in  $4.82 \text{ m}^{-2}\text{d}^{-1}$ , in agreement with  $4.73 \text{ m}^{-2}\text{d}^{-1}$  [9] for single muon events. This reduce the question of the correct definition of the flux used in [9] to the question of the definition of the acceptance area. According to [71] it seems the acceptance area is mainly the geometrical surface of the Fréjus detector projected on direction  $(\theta, \phi)$  corrected by further detection efficiencies. This is in agreement with the flux definition by the ICRU [35] and by V. A. Kudryavtsev.

The results of this reverse engineering forced us to the following conclusion: The flux given in [9] is defined as number of particles crossing a surface perpendicular to the particle direction divided by the area and divided by the live-time. The surface of a given detector has therefore to be projected along the direction of the incident particle in contradiction to the statement by G. Chardin. It is equivalent to the measurement of the flux through a sphere, therefore it is also in contradiction with the values obtained in [39]: It gives  $5.62 \text{ m}^{-2}\text{d}^{-1}$  [39] for a sphere, but has to be most likely compared to the single muon rate of  $4.73 \text{ m}^{-2}\text{d}^{-1}$  [9] as discussed above. The discrepancy between [9] and [39] may be due to the  $60^\circ$  cut. The conclusion is certainly unsatisfied and open to further discussion, but for this work we will adopt it.

## References

1. Adair RK, Kasha H (1977) Cosmic-Ray Muons. In: Hughes VW, Wu CS (eds) Muon physics. Chap 4, Vol 1: Electromagnetic interactions. Academic Press, New York
2. Ade PAR et al [Planck Collaboration] (2013) Planck 2013 results: XVI. Cosmological parameters. *Astron Astrophys* 571:A16. doi:[10.1051/0004-6361/201321591](https://doi.org/10.1051/0004-6361/201321591). arXiv:[1303.5076](https://arxiv.org/abs/1303.5076) [astro-ph.CO]
3. Aglietta M et al [LVD Collaboration] (1999) Upper limit on the prompt muon flux derived from the LVD underground experiment. *Phys Rev D* 60(11):112001. doi:[10.1103/PhysRevD.60.112001](https://doi.org/10.1103/PhysRevD.60.112001). arXiv:[hep-ex/9906021](https://arxiv.org/abs/hep-ex/9906021)
4. Aglietta M et al [LVD Collaboration] (2003) Study of single muons with the Large Volume Detector at the Gran Sasso Laboratory. *Phys At Nucl* 66(1):123–129. doi:[10.1134/1.1540666](https://doi.org/10.1134/1.1540666). arXiv: [hep-ex/0202006v1](https://arxiv.org/abs/hep-ex/0202006v1)
5. Agostinelli S et al [GEANT4 Collaboration] (2003) GEANT4 - a simulation toolkit. *Nucl Instrum Methods Phys Res Sect A* 506(3):250–303. doi:[10.1016/S0168-9002\(03\)01368-8](https://doi.org/10.1016/S0168-9002(03)01368-8)
6. Allison J et al (2006) Geant4 developments and applications. *IEEE Trans Nucl Sci* 53(1):270–278. doi:[10.1109/TNS.2006.869826](https://doi.org/10.1109/TNS.2006.869826)
7. Altuglas International (2000) Plexiglas Acrylic sheet: Optical & transmission characteristics. Philadelphia, PA
8. Aralaguppi MI, Jadar CV, Aminabhavi TM (1999) Density, refractive index, viscosity, and speed of sound in binary mixtures of cyclohexanone with Hexane, Heptane, Octane, Nonane, Decane, Dodecane, and 2,2,4-Trimethylpentane. *J Chem Eng Data* 44(3):435–440. doi:[10.1021/je9802266](https://doi.org/10.1021/je9802266)
9. Berger C et al [Fréjus Collaboration] (1989) Experimental study of muon bundles observed in the Fréjus detector. *Phys Rev D* 40(7):2163–2171. doi:[10.1103/PhysRevD.40.2163](https://doi.org/10.1103/PhysRevD.40.2163)
10. Burle Industries (1989) Photomultiplier Handbook. Lancaster, PA: Burle Industries
11. Chazal V et al (1998) Neutron background measurements in the underground laboratory of Modane. *Astropart Phys* 9(2):163–172. doi:[10.1016/S0927-6505\(98\)00012-7](https://doi.org/10.1016/S0927-6505(98)00012-7)
12. Chirkin D (2007) Fluxes of atmospheric leptons at 600 GeV - 60 TeV. arXiv: [hep-ph/0407078](https://arxiv.org/abs/hep-ph/0407078)
13. Ciddor PE (1996) Refractive index of air: New equations for the visible and near infrared. *Appl Opt* 035(9):1566–1573. doi:[10.1364/AO.35.001566](https://doi.org/10.1364/AO.35.001566) Ref. As cited in [53]
14. Clark LB, Kaplan DG (1987) The measurement of UV/VIS transmission characteristics of intraocular lenses. *Appl Spectrosc* 41(2):334–336. <http://as.osa.org/abstract.cfm?URI=as-41-2-334>
15. Cooperman G, Nguyen VH, Malioutov I (2006) Parallelization of Geant4 using TOP-C and Marshalgen. In: Fifth IEEE international symposium on network computing and applications (NCA'06), Cambridge, MA, US, 24–26 July 2006.

IEEE computer society, technical committee on distributed processing. IEEE Computer Society Press, Los Alamitos (CA), pp 48–55. doi:[10.1109/NCA.2006.45](https://doi.org/10.1109/NCA.2006.45)

16. Cooperman G et al (2002) Using TOP-C and AMPIC to port large parallel applications to the computational grid. In: 2nd IEEE international symposium on cluster computing and the grid (CCGrid 2002), Berlin, Germany, 22–24 May 2002. IEEE computer society. Los Alamitos: IEEE Computer Society Press, p 120. doi:[10.1109/CCGRID.2002.1017119](https://doi.org/10.1109/CCGRID.2002.1017119)
17. Costa C (2001) The prompt lepton cookbook. *Astropart Phys* 16(2):193–204. doi:[10.1016/S0927-6505\(01\)00105-0](https://doi.org/10.1016/S0927-6505(01)00105-0) Ref. As cited in [24]
18. Demtröder W (2009) Experimentalphysik. Vol. 2: Elektrizität und Optik [in German]. 5th ed. Springer, Berlin
19. Eitel K (1991) Untersuchung organischer Flüssigszintillatoren auf spektrale Abschwächung, Lichtausbeute und Pulse Shape-Verhalten [in German]. Master's thesis, Universität Karlsruhe (TH)
20. Engel R, Heck D, Pierog T (2011) Extensive air showers and hadronic interactions at high energy. *Annu Rev Nucl Part Sci* 61(1):467–489. doi:[10.1146/annurev.nucl.012809.104544](https://doi.org/10.1146/annurev.nucl.012809.104544)
21. Feynman RP (1969) Very high-energy collisions of hadrons. *Phys Rev Lett* 23(24):1415–1417. doi:[10.1103/PhysRevLett.23.1415](https://doi.org/10.1103/PhysRevLett.23.1415) Ref. As cited in [1]
22. Frazer WR et al (1972) Limiting fragmentation and the charge ratio of cosmic-ray muons. *Phys Rev D* 5(7):1653–1657. doi:[10.1103/PhysRevD.5.1653](https://doi.org/10.1103/PhysRevD.5.1653) Ref. As cited in [23]
23. Gaisser TK (1991) Cosmic rays and particle physics. 1. Publ., repr. ed. Cambridge University Press, Cambridge
24. Gaisser T, Stanev T (2010) Cosmic rays. In: Nakamura K et al Chap. 24. Review of particle physics particle data group. *J Phys G: Nucl Part Phys* 37(7A):075021. doi:[10.1088/0954-3899/37/7A/075021](https://doi.org/10.1088/0954-3899/37/7A/075021)
25. Garraffo Z, Pignotti A, Zgrablich G (1973) Hadronic scaling and ratios of cosmic-ray components in the atmosphere. *Nucl Phys B* 53(2):419–428. doi:[10.1016/0550-3213\(73\)90454-9](https://doi.org/10.1016/0550-3213(73)90454-9) Ref. As cited in [23]
26. Geant4 Collaboration (2009) Geant4 user's guide for application developers. Version: geant4 9(3). <http://geant4.web.cern.ch/geant4/UserDocumentation/UsersGuides/ForApplicationDeveloper/BackupVersions/V9.3/fo/BookForAppliDev.pdf>
27. Geant4 Collaboration (2009) Physics reference manual. Version: geant4 9(3). <http://geant4.web.cern.ch/geant4/UserDocumentation/UsersGuides/PhysicsReferenceManual/BackupVersions/V9.3/fo/PhysicsReferenceManual.pdf>
28. Geant4 homepage: Processes (2012) Geant4 homepage > User Support > Process/model catalog > Processes. [http://geant4.web.cern.ch/geant4/support/proc\\_mod\\_catalog/processes/](http://geant4.web.cern.ch/geant4/support/proc_mod_catalog/processes/). Accessed 05 Dec 2012
29. Geiger K, Zwan LVD (1975) Radioactive neutron source spectra from  ${}^9\text{Be}(\alpha, n)$  cross section data. *Nucl Instrum Methods* 131(2):315–321. doi:[10.1016/0029-554X\(75\)90336-5](https://doi.org/10.1016/0029-554X(75)90336-5)

30. Groshev L et al (1968) Compendium of thermal-neutron-capture  $\gamma$ -ray measurements part II  $Z = 47$  to  $Z = 67$  (Ag to Ho). Nucl Data Sheets Sect A 5(1–2):1–242. doi:[10.1016/S0550-306X\(68\)80008-4](https://doi.org/10.1016/S0550-306X(68)80008-4). Ref. As cited in [67]
31. Photonics Hamamatsu (1998) Photomultiplier Tube R5912. Hamamatsu Photonics, Hamamatsu
32. Hamamatsu Photonics (2006) In: Hakamata T et al (eds) Photomultiplier tubes: basics and applications, 3rd edn. Hamamatsu Photonics KK Electron Tube Division, Hamamatsu
33. Heitler W, Jánossy L (1949) On the absorption of meson-producing nucleons. Proc Phys Soc London, Sect A 62(6):374–385. doi:[10.1088/0370-1298/62/6/306](https://doi.org/10.1088/0370-1298/62/6/306). Ref. As cited in [23]
34. Horn OM (2007) Simulations of the muon-induced neutron background of the EDELWEISS-II experiment for Dark Matter search. Scientific report FZKA 7391. Forschungszentrum Karlsruhe. [http://bibliothek.fzk.de/zb/berichte/FZK\\_A7391.pdf](http://bibliothek.fzk.de/zb/berichte/FZK_A7391.pdf). Orig pub as PhD diss, Universität Karlsruhe (TH). <http://digbib.ubka.uni-karlsruhe.de/volltexte/1000007402>
35. International Commission On Radiation Units And Measurements (2011) Fundamental quantities and units for ionizing radiation (revised). In ICRU Report 85, special issue. J ICRU 11(1). doi:[10.1093/jicru/ndr012](https://doi.org/10.1093/jicru/ndr012)
36. ISPOptics (2010) ISP optics infrared catalog. ISP Optics, Irvington <http://www.ispoptics.com/CatalogDownload.htm>
37. Jokisch S (2010) Neutrondetector - VME-LED-Module Version 1.0. Internal manual for the EDELWEISS collaboration
38. Kudryavtsev VA, Spooner NJC, McMillan JE (2003) Simulations of muon-induced neutron flux at large depths underground. Nucl Instrum Methods Phys Res, Sect A 505(3):688–698. doi:[10.1016/S0168-9002\(03\)00983-5](https://doi.org/10.1016/S0168-9002(03)00983-5). arXiv: [hep-ex/0303007](https://arxiv.org/abs/hep-ex/0303007)
39. Kudryavtsev VA Simulation of muons at LSM. Internal note for the EDELWEISS collaboration
40. Laboratoire Souterraine de Modane (1991)
41. Lemrani R et al (2006) Low energy neutron propagation in MCNPX and GEANT4. Nucl Instrum Methods Phys Res, Sect A 560(2):454–459. doi:[10.1016/j.nima.2005.12.238](https://doi.org/10.1016/j.nima.2005.12.238). arXiv: [hep-ex/0601030](https://arxiv.org/abs/hep-ex/0601030)
42. Lipari P (1993) Lepton spectra in the earth's atmosphere. Astropart Phys 1(2):195–227. doi:[10.1016/0927-6505\(93\)90022-6](https://doi.org/10.1016/0927-6505(93)90022-6)
43. Liu Z et al (2007) The 4.438 MeV gamma to neutron ratio for the Am-Be neutron source. Appl Radiat Isot 65(12):1318–1321. doi:[10.1016/j.apradiso.2007.04.007](https://doi.org/10.1016/j.apradiso.2007.04.007)
44. Lubashevsky A, E-mail message to Kudryavtsev VA. Ref. as cited in [39]
45. Marsh JW, Thomas DJ, Burke M (1995) High resolution measurements of neutron energy spectra from Am-Be and Am-B neutron sources. Nucl Instrum Methods Phys Res Sect A 366(2–3):340–348. doi:[10.1016/0168-9002\(95\)00613-3](https://doi.org/10.1016/0168-9002(95)00613-3)

46. Motta D, Schönert S (2005) Optical properties of bialkali photocathodes. *Nucl Instrum Methods Phys Res, Sect A* 539(1–2):217–235. doi:[10.1016/j.nima.2004.10.009](https://doi.org/10.1016/j.nima.2004.10.009)
47. Motta D, Zbiri K [On behalf of the Double Chooz Collaboration] (2005) Simulations for double Chooz. Presented at the MANDsim Workshop, Manhattan, KS, US, 14–15 June 2005. [http://neutrino.phys.ksu.edu/MAND-sim/MAND-sim%20talks/DoubleChooz\\_motta.pdf](http://neutrino.phys.ksu.edu/MAND-sim/MAND-sim%20talks/DoubleChooz_motta.pdf)
48. Oehler C (1996) Untersuchung der Eigenschaften hemisphärischer 8-inch Photomultiplier für einen großvolumigen Wasser-Čerenkov-Detektor [in German]. Scientific report FZKA 5695. Forschungszentrum Karlsruhe, 1996. Orig. pub. as master's thesis, Universität Karlsruhe (TH). [in German]
49. Paquin RA (1995) Properties of metals. In: Bass M (ed) Chap 35. *Handbook of optics*. Vol. 2: Devices, measurements, and properties. 2nd ed. McGraw-Hill, New York
50. Perlmutter S et al (1999) Measurements of  $\Omega$  and  $\Lambda$  from 42 high-Redshift supernovae. *Astrophys J* 517(2):565–586. doi:[10.1086/307221](https://doi.org/10.1086/307221)
51. Photonis (1998) Photomultiplier Tubes Xp2262 Product Specification: A standard fast, 12-stage, 51mm (2") tube. Brive: Photonis
52. Photonis (2002) In: Flyckt S-O, Marmonier C (eds) Photomultiplier tubes: principles and application, Rev edition. Photonis, Brive
53. Polyanskiy M, Refractive index database <http://refractiveindex.info>
54. Reichenbacher J (1998) Untersuchung der optischen Eigenschaften grossflächiger Plastiksintillatoren für den KARMEN-Upgrade [in German]. Scientific report FZKA 6202. Forschungszentrum Karlsruhe, 1998. Orig. pub. as master's thesis, Universität Karlsruhe (TH). [in German]
55. Rhode W (1993) Study of Ultra High Energy Muons with the Fréjus Detector. PhD diss., Bergische Universität Gesamthochschule Wuppertal. <http://hdl.handle.net/10068/260384>. WUB-DIS 93-11
56. Rhode W et al [Frejus Collaboration] (1996). Limits on the flux of very high-energetic neutrinos with the Frejus detector. *Astropart Phys* 4:217–225. doi:[10.1016/0927-6505\(95\)00038-0](https://doi.org/10.1016/0927-6505(95)00038-0)
57. Rich J (2010) Fundamentals of cosmology. 2nd ed. Springer, Berlin. doi:[10.1007/978-3-642-02800-7](https://doi.org/10.1007/978-3-642-02800-7)
58. Roithner Lasertechnik. RLT420-3-30 - Violet LED Lamp. Roithner Lasertechnik, Vienna
59. ROOT homepage: TRandom3 (2013) ROOT homepage > Documentation > Reference Guide > Old version 5.32.0 > TRandom3. <http://root.cern.ch/root/html532/TRandom3.html>. Accessed 14 Sep 2013
60. ROOT team (2009) ROOT: An Object-Oriented Data Analysis Framework; Users Guide 5.26. Ed Antcheva I, Couet O. [http://root.cern.ch/download/doc/Users\\_Guide\\_5\\_26.pdf](http://root.cern.ch/download/doc/Users_Guide_5_26.pdf)
61. Crystals Saint-Gobain (2005) BC400, BC-404, BC-408, BC-412, BC-416 - Premium Plastic Scintillators. Saint-Gobain Crystals, Nemours
62. Crystals Saint-Gobain (2005) BC-525 Gd Loaded Mineral Oil Based Liquid Scintillator. Saint-Gobain Crystals, Nemours

63. Schröder F, Rhode W, Meyer H (2001) Muon flux simulation and comparison with Frejus measurements'. In Proceedings of the 27th International Cosmic Ray Conference. (Hamburg, Germany, Aug. 7–15, 2001). Göttingen: Copernicus Gesellschaft, 2001. pp 1013–1016. ADS: 2001ICRC....3.1013S
64. Schröder F (2001) Simulation und beobachtung von Luftschaubern unter großen Zenitwinkeln [in German]. PhD diss., Bergische Universität Gesamthochschule Wuppertal. WUB-DIS 2001–17
65. Smith D Y, Shiles E, Inokuti M (1998) The optical properties of metallic aluminum. In: Palik ED (ed) Handbook of optical constants of solids. Chap. 13. Vol. 1. Elsevier, Amsterdam. <http://www.knovel.com/knovel2/Toc.jsp?BookID=1669>
66. Transmittance (2013) <https://en.wikipedia.org/wiki/Transmittance>. Accessed 11 Nov 2013
67. Trzciński A et al (1999) A monte-carlo code for neutron efficiency calculations for large volume Gd-loaded liquid scintillation detectors. J Neutron Res 8(2):85–117. doi:[10.1080/10238169908200048](https://doi.org/10.1080/10238169908200048)
68. Vijaya A, Kumar A (1973) The neutron spectrum of Am-Be neutron sources. Nucl Instrum Methods 111(3):435–440. doi:[10.1016/0029-554X\(73\)90199-7](https://doi.org/10.1016/0029-554X(73)90199-7)
69. Volkova LV (1969) Scientific report 72. Lebedev Physical Institute. Ref. As cited in [12, 23]
70. Weber MJ (2002) Handbook of optical materials. Laser and Optical Science and Technology Series. CRC Press, Boca Raton. Ref. As cited in [53]
71. Wei Y (1993) Untersuchung der neutrinoinduzierten Myonen im Fréjus-Untergrunddetektor [in German]. PhD diss., Bergische Universität Gesamthochschule Wuppertal. WUB-DIS 93–8
72. Wieser ME (2006) Atomic weights of the elements 2005 (IUPAC Technical Report). Pure Appl Chem 78(11):2051–2066. doi:[10.1351/pac200678112051](https://doi.org/10.1351/pac200678112051)
73. Wunderle A (2011) Modellierung von Neutronensignaturen in Germanium-Bolometern des EDELWEISS Experiments [in German]. Master's thesis, Karlsruher Institut für Technologie (KIT)
74. Yeh M, Garnov A, Hahn R (2007) Gadolinium-loaded liquid scintillator for highprecision measurements of antineutrino oscillations and the mixing angle,  $\theta_{13}$ . Nucl Instrum Methods Phys Res, Sect A 578(1):329–339. doi:[10.1016/j.nima.2007.03.029](https://doi.org/10.1016/j.nima.2007.03.029)
75. Zbiri K (2011) GdHPCapture. E-mail message to author, March 24

# Curriculum Vitae

**Holger Kluck** was born on the 28th of August 1982 in Heidelberg (Germany). He started to study physics at the University of Karlsruhe (Germany) in 2002 where he received a Master of Science degree in physics in 2007. For his master thesis he developed a prototype detector for the investigation of muon-induced neutrons, a prominent kind of background for dark matter searches. During his Ph.D. studies, Holger joined the EDELWEISS and EURECA collaborations and investigated the production of muon-induced neutrons at the Modane underground laboratory. His investigations included a dedicated measurement campaign at the underground laboratory and comparison with Monte Carlo models. He was also responsible for the data acquisition electronics and software of the muon veto system of EDELWEISS. In 2013 he obtained his Ph.D. at the Karlsruher Institut of Technology with a *magna cum laude* grade.



Since 2014, Kluck is a postdoctoral researcher at the Vienna University of Technology and at the Institute of High Energy Physics of the Austrian Academy of Sciences. Searching for dark matter remains the major topic of his research interests, bringing his experience in background investigations into the CRESST experiment. In addition, he is developing electronics and readout concepts for future dark matter searches such as EURECA.

## References

The following list gives an overview of Holger Kluck's publications until the end of 2014.

- Strauss R et al. (2014) Electron/gamma and alpha backgrounds in CRESST-II Phase 2. *J Cosmol Astropart Phys.* arXiv:[1410.4188](https://arxiv.org/abs/1410.4188) [physics.ins-det]
- Strauss R et al (2014) A detector module with highly efficient surface-alpha event rejection operated in CRESST-II Phase 2. *Eur Phys J C.* arXiv:[1410.1753](https://arxiv.org/abs/1410.1753) [physics.ins-det]
- Gütlein A et al (2014) Impact of Coherent Neutrino Nucleus Scattering on Direct Dark Matter Searches based on CaWO4 Crystals. *Astropart Phys.* arXiv:[1408.2357](https://arxiv.org/abs/1408.2357) [hep-ph]
- Angloher G et al (2014) Results on low mass WIMPs using an upgraded CRESST-II detector. *Eur Phys J C* 74(12):3184. doi:[10.1140/epjc/s10052-014-3184-9](https://doi.org/10.1140/epjc/s10052-014-3184-9). arXiv:[1407.3146](https://arxiv.org/abs/1407.3146) [astro-ph.CO]
- Angloher G et al (2014) EURECA Conceptual Design Report. *Phys Dark Universe* 3:41–74. doi:[10.1016/j.dark.2014.03.004](https://doi.org/10.1016/j.dark.2014.03.004)
- Armengaud E et al [EDELWEISS Collaboration] (2013) Axion searches with the EDELWEISS-II experiment. *J Cosmol Astropart Phys* 2013(11):067. doi:[10.1088/1475-7516/2013/11/067](https://doi.org/10.1088/1475-7516/2013/11/067). arXiv:[1307.1488](https://arxiv.org/abs/1307.1488) [astro-ph.CO]
- Armengaud E et al [EDELWEISS Collaboration] (2013) Background studies for the EDELWEISS dark matter experiment. *Astropart Phys* 47:1–9. doi:[10.1016/j.astropartphys.2013.05.004](https://doi.org/10.1016/j.astropartphys.2013.05.004). arXiv:[1305.3628](https://arxiv.org/abs/1305.3628) [physics.ins-det]
- Schmidt B et al [EDELWEISS collaboration] (2013) Muon-induced background in the EDELWEISS dark matter search. *Astropart Phys* 44:28–39. DOI:[10.1016/j.astropartphys.2013.01.014](https://doi.org/10.1016/j.astropartphys.2013.01.014). arXiv:[1302.7112](https://arxiv.org/abs/1302.7112) [astro-ph.CO]
- Armengaud E et al [EDELWEISS Collaboration] (2012) Search for low-mass WIMPs with EDELWEISS-II heat-and-ionization detectors. *Phys Rev D* 86(5):051701(R). doi:[10.1103/PhysRevD.86.051701](https://doi.org/10.1103/PhysRevD.86.051701). arXiv:[1207.1815](https://arxiv.org/abs/1207.1815) [astro-ph.CO]
- Cox G et al (2012) A multi-tiered data structure and process management system based on ROOT and CouchDB. *Nucl Instrum Methods Phys Res, Sect A* 684:63–72. doi:[10.1016/j.nima.2012.04.049](https://doi.org/10.1016/j.nima.2012.04.049)
- Ahmed Z et al [CDMS and EDELWEISS collaborations] (2011) Combined limits on WIMPs from the CDMS and EDELWEISS experiments. *Phys Rev D* 84(1):011102. doi:[10.1103/PhysRevD.84.011102](https://doi.org/10.1103/PhysRevD.84.011102). arXiv:[1105.3377](https://arxiv.org/abs/1105.3377) [astro-ph.CO]
- Armengaud E et al [EDELWEISS Collaboration] (2011) Final results of the EDELWEISS-II WIMP search using a 4-kg array of cryogenic germanium detectors with interleaved electrodes. *Phys Lett B* 702(5):329–335. doi:[10.1016/j.physletb.2011.07.034](https://doi.org/10.1016/j.physletb.2011.07.034). arXiv:[1103.4070](https://arxiv.org/abs/1103.4070) [astro-ph.CO]
- Kozlov VY et al (2010) A detection system to measure muon-induced neutrons for direct dark matter searches. *Astropart Phys* 34(2):97–105. doi:[10.1016/j.astropartphys.2010.06.001](https://doi.org/10.1016/j.astropartphys.2010.06.001). arXiv:[1006.3098](https://arxiv.org/abs/1006.3098) [astro-ph.IM]
- Armengaud E et al [EDELWEISS Collaboration] (2010) First results of the EDELWEISS-II WIMP search using Ge cryogenic detectors with interleaved electrodes. *Phys Lett B* 687(4–5):294–298. doi:[10.1016/j.physletb.2010.03.057](https://doi.org/10.1016/j.physletb.2010.03.057). arXiv:[0912.0805](https://arxiv.org/abs/0912.0805) [astro-ph.CO]
- Broniatowski A et al [EDELWEISS Collaboration] (2009) A new high-background-rejection dark matter Ge cryogenic detector. *Phys Lett B* 681(4):305–309. doi:[10.1016/j.physletb.2009.10.036](https://doi.org/10.1016/j.physletb.2009.10.036). arXiv:[0905.0753](https://arxiv.org/abs/0905.0753) [astro-ph.IM]